Victor Apollonov

High-Conductivity Channels in Space



Springer Series on Atomic, Optical, and Plasma Physics

Volume 103

Editor-in-chief

Gordon W. F. Drake, Department of Physics, University of Windsor, Windsor, ON, Canada

Series editors

James Babb, Harvard-Smithsonian Center for Astrophysics, Cambridge, MA, USA Andre D. Bandrauk, Faculté des Sciences, Université de Sherbrooke, Sherbrooke, QC, Canada

Klaus Bartschat, Department of Physics and Astronomy, Drake University, Des Moines, IA, USA

Philip George Burke, School of Mathematics and Physics, Queen's University, Belfast, UK

Robert N. Compton, Knoxville, TN, USA

Tom Gallagher, University of Virginia, Charlottesville, VA, USA

Charles J. Joachain, Faculty of Science, Université Libre Bruxelles, Bruxelles, Belgium

Michael Keidar, School of Engineering and Applied Science, George Washington University, Washington, DC, USA

Peter Lambropoulos, FORTH, IESL, University of Crete, Iraklion, Crete, Greece Gerd Leuchs, Institut für Theoretische Physik I, Universität Erlangen-Nürnberg, Erlangen, Germany

Pierre Meystre, Optical Sciences Center, University of Arizona, Tucson, AZ, USA

The Springer Series on Atomic, Optical, and Plasma Physics covers in a comprehensive manner theory and experiment in the entire field of atoms and molecules and their interaction with electromagnetic radiation. Books in the series provide a rich source of new ideas and techniques with wide applications in fields such as chemistry, materials science, astrophysics, surface science, plasma technology, advanced optics, aeronomy, and engineering. Laser physics is a particular connecting theme that has provided much of the continuing impetus for new developments in the field, such as quantum computation and Bose-Einstein condensation. The purpose of the series is to cover the gap between standard undergraduate textbooks and the research literature with emphasis on the fundamental ideas, methods, techniques, and results in the field.

More information about this series at http://www.springer.com/series/411

Victor Apollonov

High-Conductivity Channels in Space



Victor Apollonov Prokhorov General Physics Institute Moscow, Russia

ISSN 1615-5653 ISSN 2197-6791 (electronic) Springer Series on Atomic, Optical, and Plasma Physics ISBN 978-3-030-02951-7 ISBN 978-3-030-02952-4 (eBook) https://doi.org/10.1007/978-3-030-02952-4

Library of Congress Control Number: 2018958957

© Springer Nature Switzerland AG 2018

This work is subject to copyright. All rights are reserved by the Publisher, whether the whole or part of the material is concerned, specifically the rights of translation, reprinting, reuse of illustrations, recitation, broadcasting, reproduction on microfilms or in any other physical way, and transmission or information storage and retrieval, electronic adaptation, computer software, or by similar or dissimilar methodology now known or hereafter developed.

The use of general descriptive names, registered names, trademarks, service marks, etc. in this publication does not imply, even in the absence of a specific statement, that such names are exempt from the relevant protective laws and regulations and therefore free for general use.

The publisher, the authors and the editors are safe to assume that the advice and information in this book are believed to be true and accurate at the date of publication. Neither the publisher nor the authors or the editors give a warranty, express or implied, with respect to the material contained herein or for any errors or omissions that may have been made. The publisher remains neutral with regard to jurisdictional claims in published maps and institutional affiliations.

This Springer imprint is published by the registered company Springer Nature Switzerland AG The registered company address is: Gewerbestrasse 11, 6330 Cham, Switzerland

Preface

For many years, attempts to create super-long conductive channels were made to study the upper atmosphere and to settle special tasks, related to energy transmission. Consequently, the program to develop "Impulsar" attracted great interest, since this program combining high-voltage, high-repetition-rate electrical source can be useful to solve the above-mentioned problems. This could be considered a "renaissance of Nikola Tesla ideas" for the days of high-power lasers. The principle behind the production of super-long conductive channels can be concisely described as follows. "Impulsar"-LJE vehicle-propulsion takes place under the influence of powerful high repetition rates of pulse-periodic laser radiation. In the experiments, CO₂-laser and solid-state Nd YAG laser systems have been used. Active impulse appears, thanks to air breakdown (<30 km) or to the breakdown of ablated material onboard (>30 km), placed in the vicinity of the focusing mirror-acceptor of the breakdown waves. With each pulse of powerful laser, the device rises up, leaving a bright and dense trace of products with a high degree of ionization and metallization by conductive nanoparticles due to the ablation process. The investigation of conductive dust-plasma properties in our experiments has been produced on the basis of two very effective approaches: high-power laser-controlled ablation of various materials and by the electrical explosion of wire. In this work, experimental and theoretical results of conductive-canal modeling will be presented. The estimations show that, based on already experimentally demonstrated figures of specific thrust impulse, the lower layers of the ionosphere can be reached in several hundred seconds and that is enough to keep the high level of channel conductivity and stability with the help of a high-repetition-rate high-voltage generator. At present, many laboratories continue the search for an efficient laser-based lightning-protection system and to produce a controlled high-conductivity channel in the atmosphere that is capable of conducting a short-circuit current in a natural or artificial electrical circuit. A 1.5-fold increase in the length of the discharge gap broken under laser irradiation has been demonstrated when switching is extended (~1 m) by high-voltage (up to 390 kV) electric discharges with 100-ns UV pulses of a KrF laser. Laser-based lightning-protection systems, as they are known, rely on the so-called long laser spark, which provides the conditions for vi Preface

connecting a thunderstorm cloud with a grounded metal rod, i.e., a classical lightning rod. Maximum lengths (~ 16 m) of the laser-spark-controlled electric discharge at a voltage of 3000 kV were obtained in Russia and Japan using a 0.5 kJ short-pulse CO_2 laser with spherical optics. Such control conductivity channels can be used in energy transmission, overvoltage protection systems, transport of charged-particle beams, plasma antennas, and so on.

productive theoretical and experimental investigation high-repetition-rate P-P mode of operation for high-power lasers (COIL, HF/DF) has also now been achieved. The experimental realization of the P-P regime has been demonstrated for 100 KW GDL and LD-pumped SSL. A greater than two orders of magnitude ratio of peak to average power with minimal energy loss has been obtained. Both the high efficiency and excellent beam quality of disk lasers mean that they can be widely used in modern science and industry for a very large range of applications, including the treatment of the surface of dielectric materials in microelectronics, cutting, drilling, welding, polishing and cleaning of the surface, and other technological operations with solid and composite materials. Disk lasers can be used effectively for other important challenges faced by science and technological advances in the future. Today, we can say that the creation of a megawatt-class mono-module P-P disk lasers with large cross sections of the active medium opens up great prospects for their use to solve the set of problems: small satellites launching by lasers, formation of super-long conductive channels in space and the atmosphere, cleaning space debris from of near-Earth space, and so on.

In the first part of High-Conductivity Channels in Space, scientific problems involving electric discharge guided by a continuous laser-induced spark are considered. The purpose of this chapter is to estimate the CO₂-laser energy required for producing CLS in a practical lightning-protection system. Taking into account the estimates of the plasma-channel length required to initiate a lightning discharge and a linear-energy input of 200 J m⁻¹ required for the CLS production, which was experimentally obtained in this work, the output laser energy should be not less than few kJ. At present, there already exist many CO₂ lasers with an output energy of 5–10 kJ for laser-based technology development, and further improvement of their output characteristics is under intense attention. It is important to note that we provide an understated estimate that does not take into account the increase in the transverse dimension of the laser-induced spark with the increasing cone angle that was reported in this chapter.

Lightning strikes on industrial objects like petrochemical complexes, nuclear power plants, ultrahigh-voltage transmission lines and substations, and rocket-launching devices may turn out to be extremely hazardous. The electromagnetic pulse from a close-range strike of lightning can also result in a breakdown of telecommunication equipment and its operation, computer networks, and control systems. Consequently, stringent requirements are imposed at present for lightning-protection measures. The traditional lightning-protection systems used currently are not always in a position to ensure the desired level of efficiency. This stimulates the quest for new approaches to solve this problem. This is the subject matter of the second chapter of our book. Laser protection against lightning is one

Preface vii

of the most prospective trends being developed actively at present. While using this approach, it is assumed that the lightning-discharge channel being developed is guided toward the conventional rod of the metal lightning rod along the plasma channel formed as a result of the laser-induced breakdown of the atmosphere.

Our experimental studies have shown that, in spite of its discontinuous structure, a LLS created in the vicinity of an earthed electrode may capture the channel of leader discharge that develops in the gap between the electrode and a CAC. The capture takes place for an electric field of a quite high strengths at the electrode, its value being close to that of the field required for the emergence of an ascending positive leader in the absence of a laser spark in the gap.

The creation of a LLS near the tip of an earthed electrode enables a considerable decrease in the time of formation of a stable leader that starts propagating toward the cloud and captures a part of the LLS. As a result, its velocity increases compared to the case when the discharge develops in the absence of a laser spark in the gap. This circumstance is of fundamental importance for laser systems for lightning protection. Indeed, owing to its interaction with the laser spark, the leader discharge developing from the tip of the lightning rod may well precede the ascending discharges from the object being protected during its advance toward an approaching descending leader, capturing the latter and thus protecting the object.

Lightning and the ecology of the atmosphere is the topic under consideration in Chap. 3. Taking into account recent experimental data and based on them, theoretical estimations have created a new description of OES as an open dissipation system, supported in the state of dynamic equilibrium by the entering it energy flow, in the first turn of radiant energy of the sun. It has been established that electrical energy is generated predominantly in the regions of reduced atmospheric pressure and in the zones of cold fronts and comprises in average 5×10^{13} George. which is two orders of magnitude higher than the energy concentrated in the orbital spherical capacitor the Earth-ionosphere. The average speed of the dissipation of electrical energy, namely 4×10^{11} W, exceeds the speed of the dissipation of energy in the tectonic and magmatic processes and is characterized by an OES as a completely dynamic system with a very short time of the renovation of electrical energy. The process of the transformation of energy in the atmosphere is accompanied by the generation of dissipative structures of various scales and in the details of convective systems and aero-electrical structures, which clearly are possible to visualize in the form of the global processes of the accumulation of electrical energy and its dissipation in the atmosphere. In the near future, and on the basis of higher than aforesaid, the study of power engineering of the atmosphere and the structure and dynamics OES will remain a vital problem of atmospheric electricity.

It is necessary to say a few words about the interrelationship of atmospheric electricity and the formation of the composition of the atmosphere and climate of our planet. Over many years, attempts have been made to the create conducting channels of adequate length for the study of the upper atmosphere and the solution of special problems. In this connection, great interest has been focused on the "Impulsar" program that combines high-power/energy lasers and the high-voltage

viii Preface

high-frequency Tesla's source which can be useful in the solution of the cited problems.

Part II of High-Conductivity Channels in Space is devoted to the problems of the interaction of optical pulsating discharges with gas. The reason for that consideration is to analyze a new set of physical effects produced by laser light in the atmosphere. The transformation of high-repetition-rate pulse-periodic laser radiation into a low-frequency OSW in an OPD has been studied for the first time. Unlike a continuous optical discharge, no physical constraints are imposed on the velocity of OPD propagation in a gas. In contrast to a single laser spark, the SWs generated by an OPD merge to form a QSW propagating in a preferred direction in the surrounding gas. About 25% of the laser power is transformed into SW in an OPD, which may exert a considerable influence on the surrounding medium. An OPD can be stationary or move at a high velocity in a gas. Stable SW generation occurs only for certain relationships between the radiation intensity, laser-pulse repetition rate, their filling factor, and the OPD velocity. The OPD generates a QSW in the surrounding space if it is stationary or moves at a subsonic velocity and its parameters satisfy the above conditions. The mechanism of SW merging operates in various media over a wide range of pulsation energies. The results of preliminary investigations show that the efficiency of the laser radiation can be increased substantially when a QSW is used for producing thrust in a laser jet engine and eventually for producing a long conductive channel.

The ensuing chapter has the goal to investigate the mechanism of SW merging in a LJE that was proposed for use in projects involving the launching of light SC into orbit and later for the production of a super-long conductive channel. With the help of a focusing reflector, repetitively pulsed radiation produces laser sparks that, in turn, should generate SW. A part of the momentum of the latter is imparted to the SC. In Part II, we propose a new approach to develop an efficient LJE, which is based on the merging of SW generated by an OPD at short radiation pulses with a high-pulse repetition rate. In this case, the OPD energy is transformed most efficiently in an LJE into a constant force accelerating the motion of an SC. High-power GDL, which may generate pulses with time duration $t_r = 150$ –250 ns and a pulse repetition rate of up to 100 kHz under a continuous pumping of the active medium, offers great promise for use in the LJE consists of an RA. The model presented in the book is based on the estimates and numerical simulation in the two-dimensional axisymmetric approximation for thrust pulses generated by the OPD.

It is very important that the LJE is considerably more economical than traditional engines operating on chemical fuel. At the initial stage of the flight, the atmospheric air is used as the working substance and—beyond the atmosphere—as a small space-borne store of a gas or easily sublimated substance. In this case, the specific cost of freight launching into outer space can be reduced to 200–500 USD kg⁻¹, i.e., approximately by two orders of magnitude compared to the current cost. The possibility of maintaining the parameters of the orbit at a specified level with the help of the laser system used for launching is also highly estimated.

Preface

At present, the possibility of building an LJE is being investigated in the developed countries all over the world. For example, at present, such systems are being developed in the USA within the framework of the "Lightcraft" project. Thus, the Lightcraft Technologies Company has successfully tested a rocket model, which rose to 70 m for 12.7 s under the action of a jet produced by high-power laser radiation. A 10 kW low-repetition-rate pulse-periodic CO₂ laser was used in the experiments. The reactive momentum was produced by carrying out a special polymer material from a concave surface located in the lower part of the rocket irradiated by the laser beam.

As early as 1973, the possibility of building a LJE has been investigated by our team under the supervision of Acad. A. M. Prokhorov at the Lebedev Physics Institute, Academy of Science of the USSR. The engine unit operated by irradiating a reflector located at its rear part by a laser beam. The reflector concentrated laser radiation in the air, which resulted in a microexplosion and produced the reactive thrust. The tests of reflectors of various types, which served simultaneously as receivers of the incident shock wave providing the thrust, were successful.

A LJE uses repetitively pulsed-laser radiation and the atmospheric air as a working substance. A reflector to focus the radiation is located in the tail of the SC. The propulsion is produced by the action of the periodic shock waves produced by laser sparks on the reflector. The laser air-jet engine is attractive due to its simplicity and high efficiency. It was pointed out in many papers that the LJE can find applications for launching SC if $\sim 100~\rm kJ$ repetitively pulsed lasers with hundred-hertz pulse repetition rates are developed, and the damage of the optical reflector under the action of shock waves and laser plasma is eliminated. These problems can be solved by using high-pulse repletion rates ($f \sim 100~\rm kHz$), an optical pulsed discharge, and the merging of shock waves. The efficiency of the use of laser radiation in the case of short pulses at high-pulse repetition rates is considerably higher. It is shown in this book that factors damaging the reflector and a triggered device cannot be eliminated at low-pulse repetition rates and are of the resonance type.

Many laboratories of the world still continue the search for an efficient laser-based lightning-protection system and for producing controlled high-conductivity channels in space that are capable of conducting a short-circuit current in a natural or artificial electrical circuit. Laser-based lightning-protection systems, as they are known, rely on the LLS, which provides the conditions for connecting a thunder-storm cloud with a grounded metal rod, i.e., a classical lightning rod. Maximum lengths (~16 m) of the laser-spark-controlled electric discharge at a voltage of 3 mV were achieved in Russia and Japan using a 0.5 kJ pulsed CO₂ laser with spherical optics. Such control conductivity channels can be used in energy transmission, overvoltage protection systems, transport of charged-particle beams, plasma antennas, etc. It is shown in our book that a laser spark produced using conical optics demonstrates much better characteristics from the point of view of the formation of conductivity channels in the atmosphere. Currently, among the huge variety of lasers, only two types are being actively studied for use in the formation of laser-spark-controlled high-conductivity channels in the atmosphere:

x Preface

sub-microsecond pulsed gas and chemical lasers (CO₂, DF) and femtosecond solid-state lasers.

The main advantage of femtosecond lasers is their ability to produce super-long ionized channels (so-called filaments) with a characteristic diameter of about 100 μm in the atmosphere along the laser-beam propagation direction. With an estimated electron density of 10^{16} cm⁻³ in these filaments and laser wavelengths in the range of 0.5-1.0 um, the plasma hardly absorbs the laser light. In this case, the length of the track consisting of many filaments is determined by the laser intensity and can reach many miles at a femtosecond pulse energy of ~ 100 mJ. However, these lasers could not be used to form long high-conductivity channels in atmosphere. The ohmic resistance of the thus formed conducting channels turns out to be very high, and the gas in the channels cannot be strongly heated. We determined the range of sizes of copper and copper oxide particles (from 50 nm to 300 µm) and their minimum volume density ($\sim 0.1 \text{ kg/m}^3$) that are necessary to provide an electric breakdown in order to form a plasma channel according to the "Impulsar" program. The results of the model experiments showed that nanoparticles in the plasma channel can merge into larger aggregates during LRE operation. The experiments on electric breakdown showed also that a high-conductivity channel with a diameter of ~ 8 mm and a minimum specific resistance of ~ 5 Ω/m is implemented at the maximum introduced specific energy: ~ 200 J/m. At a larger channel diameter, the specific energy is proportional to the squared ratio of diameters, and the minimum average electric-field strength in the channel decreased to the level of ~ 50 V/cm.

When using the controlled electrical breakdown in a plasma channel that is produced by an exploding wire and is capable of passing a current in the short-circuit mode, one should know the temperature and radius of the channel. The notion of the radius of the channel refers to its part through which a main fraction of the current passes at the main stage of the discharge. Quantities such as the expansion rate of the channel and its maximal diameter, which is observed in a high-conductivity high-temperature area, are of importance for describing the specific energy deposition and pressure at the front of a cylindrical shock wave that propagates in the atmosphere. A spark-discharge channel in the atmosphere usually can be studied by using Tepler's shadow method combined with a rotating mirror method. In Chap. 9, we use a simple technique that does not require optical-detection methods to see how the expansion rate of the conductivity channel produced by the explosion of a thin copper wire depends on time for a maximal possible specific energy. A new experimental technique for determining the high-conductivity channels' expansion rate as a function of the propagation time has been suggested and is described in this chapter. This technique was applied in experiments on the controlled breakdown and extended up to 1.9-m gaps produced by an exploding wire for a maximal specific energy deposited into a channel of about 1 kJ/m. With this technique, the main parameters of the breakdown, namely the specific energy deposited into the discharge channel and the variation in the resistivity of the discharge gap, were measured as accurate up to 5%. In terms of the equilibrium plasma model, these data allow us to find the maximal temperature in Preface xi

the discharge channel and thereby more accurately determine the breakdown voltage and specific energy deposition in considering controlled breakdowns over great lengths.

Since the 1970s, the possibility of using LJE to launch light satellites into orbit has attracted the attention of researchers. The solution of related problems is still of current interest. Specifically, this relates to an increase in the efficiency—the coupling coefficient J_r of using laser radiation (the ratio of the propulsion to the radiation power)—by several times and the prevention of the shock damage of the apparatus, which appears when high-power repetitively pulsed-laser radiation with low repetition rates f is used.

To solve these problems, it was proposed to use repetitively pulsed radiation with $f \sim 100$ kHz, the OPD, and the effect of merging shock waves produced by the OPD. The merging criteria were confirmed in experiments. The OPD is laser sparks in the focus of repetitively pulsed radiation, which can be at rest or can move at high velocities. The high-frequency repetitively pulsed regime is optimal for continuously pumped Q-switched high-power lasers. In this case, the pulse energy is comparatively small and the stationary propulsion is possible.

Part III, Lasers and Laser Components for High-Conductivity-Channel Implementation, is devoted to various aspects of laser-power sources and unique laser components for wireless power transmission in space development. As was shown also in Part I, to form a high-conductivity channels in the atmosphere that could commute an artificial or natural discharge (lightning), the gas must be heated to a temperature from 6000 to 8000 K, when thermal ionization begins. This condition is crucial because the high initial electron density in the atmosphere is a necessary but not sufficient condition for realizing high conductivity in a long atmospheric channel. It is important not only to produce but also to maintain the electron density in an atmospheric channel that is sufficient for the breakdown. During gas heating, thermal ionization becomes the main mechanism of electron "production" in the channel. Specifically, this is the main reason why the streamer mechanism cannot lead directly to an electric breakdown in the presence of high electron density (filaments) in a cold channel. In the case of sub-microsecond CO₂ or DF lasers with a high energy per pulse (several hundreds of joules), long conducting laser-plasma channels can be formed with conical optics. In contrast to spherical optics, one can use methods of dynamic correction of lenses to increase aberrations and elongate the focal segment by passing to a conical phase front.

A completely different approach to the formation of a conducting channel can be realized using high-repetition-rate P-P lasers. The motion of a light-driven engine under irradiation by a high-frequency P-P laser with a pulse energy sufficient to produce a breakdown in the focus of the optical system of a LJE gives rise to a continuous conducting channel in air as a result of the formation of a mixture of aerosol with atmospheric air and its subsequent ionization. In this case, according to the calculations, the aforementioned range of laser-pulse repetition rates provides continuity of the conducting channel at optimal velocities of the focusing system. Indeed, each laser pulse focused by the optical system forms some extended plasma region with a high conductivity, which occupies a relatively small segment of the

xii Preface

focusing-system trajectory. If the laser pulses have a low repetition rate, these regions will form somewhat like a dashed line at some velocities of the focusing system. If the pulse repetition rate exceeds 10 kHz and the motion velocities are optimal for solving the problem stated, these high-conductivity regions will have no discontinuities, and a continuous conducting channel will be formed. However, when the moving optical system enters rarefied atmospheric layers, a problem of medium deficits arises. To solve it, the displaced optical system must have an efficient source of an appropriate medium (a material containing microscopic metal particles, which can easily be sublimated under laser irradiation) in the vicinity of the focus.

Currently, in technological processes with high-average power (over 1-kW) lasers, advantage is taken only of sources operating in two regimes—continuous and P-P with a repetition rate from a few to hundreds of Hz at pulse durations within tens to thousands of microseconds and even milliseconds. In this case, the discussed processes usually rely on purely thermal mechanism because use is made of the possibility of a laser source to deliver a sufficient amount of energy to a small area of the surface of the material being processed. High-repetition-rate P-P laser systems with a high average power, which provide the required pulse train durations from a few to hundreds of nanoseconds, enable implementation of a fundamentally different mechanism of interaction of radiation with matter-sublimation (ablation), ensuring a local energy release not only in space but also in time. This results in an explosive local evaporation of a substance without an intermediate liquid phase. This mechanism can significantly extend the range of technological applications of laser sources. However, it has found no real use in practice because of the great complexity of its implementation in the case of the mean powers required in a significant number of technologies. In general, such mean-power lasers are used in microsurface treatment, product marking, scribing, term cleavage, microdrilling, and laser-induced chemical etching.

However, a more differentiated and balanced assessment of the many innovations in the field of laser shows that there is no such thing as a perfect design—or an ideal laser. There is always room for improvement and further development. It is possible that, in the near future, a laser with the disk geometry of the active medium will become the dominant technology. However, despite this, a number of existing laser technologies (with some exceptions, of course) will continue to improve for quite a long time. Based on these considerations, we must continue to develop most types of lasers, each time clearly specifying their undeniable technological niche and knowing well their advantages and disadvantages.

The high efficiency and excellent beam quality of disk lasers mean that they can be widely used in modern science and industry for a very wide range of applications, including the treatment of the surface of dielectric materials in microelectronics, cutting, drilling, welding, polishing and cleaning of the surface, and other technological operations with superhard and fragile metals and composite materials. P-P Q-switched disk lasers and high-average-power, mode-locked laser systems ensure optimal conditions for ablation (sublimation) of a material. A number of advantages of high-repetition-rate P-P lasers emitting short pulses, as applied to a

Preface xiii

wide range of industrial technologies, are the basis of many modern concepts of disk lasers. High-intensity light with an insignificant thermal lens effect in the central high-loaded zone of the active medium has led to the lifting of restrictions on the brightness of the pump diode.

The question arises as to how the average power of a few megawatts can be achieved on the basis of solid-state lasers. And it is this power that is needed to address many problems associated with the removal of debris from near-Earth space, with launching of missiles with the help of lasers, with the creation of long-range conducting channels, and others. Fiber lasers are not applicable for these purposes because of the smallness of the area of the exit pupil of the fibers and hence the impossibility of operation of such lasers in the high-frequency P-P regime with high peak power at an average power of a few megawatts. The laser system based on "slabs" also seems difficult to implement as adjustment of the system and its maintenance in a safe operation mode are comparable to the complexity of working with a multi-element system for the solution to the problem of controlled thermonuclear fusion. Proceeding from these considerations, the answer is quite clear: Such a laser can and should be based on the mono-module disk laser geometry!

Consider the most important aspects of the problem of static POE fabrication—the most important component of high-power/energy laser system. The task of this part of our book is to investigate the conditions needed to achieve high optical-damage thresholds for a mirror surface. We obtained and describe here the expressions for the limiting intensities, leading to the optical destruction of POE, and the stability parameters of optical surfaces based on them. This set of theoretical and experimental works in the field of high-power/energy optics led to one very important point: Effective development of any of the areas of modem cutting-edge technologies, as a rule, yields results not only in the related fields of technological applications, but also in completely different branches of science and technology. Thus, the appearance of one- and two-dimensional cooled high-power laser diode arrays, large astronomical cooled POE based on silicon carbide and complex composite materials is largely a consequence of the success of power optics—a recognized effective donor for many areas of science and advanced technology of the twenty-first century.

It is important to very clearly conclude here that the very near future will reveal the details of a physical–technical solution regarding the best laser that will be used effectively for the many important challenges and technological advances faced by science. However, today we can say that the creation of a class of high-power/energy, high-frequency P-P lasers with large cross sections of the active medium and high compactness and low weight will open up great prospects for their use in solving the problems of launching small satellites by lasers, the formation of super-long conductive channels in space (vacuum and atmosphere), the clearing space debris from the near-Earth space, and other special tasks of our time.

Acknowledgements

The author of the book expresses his gratitude to N. Akhunov, G.G. Baitsur, V.I. Borodin, S.A. Chetkin, S.I. Derzhavin, K.N. Firsov, Goncharov, V.V.K.Kh. Kazakov, I.G. Kononov, V.V. Kuzminov, V.Yu. Khomich. V.N. Motorin, V.V. Ostanin, S.A. Savranskii, A.G. Safronov, S.K. Semenov, Yu.A. Shakir, V.A. Shmakov, A.N. Shults, S.F. Sholev, V.A. Shurygin, A.A. Sirotkin, V.R. Sorochenko, V.N. Tishchenko, G.V. Vdovin, Yu.P. Voinov, V.A. Yamshchikov, and S.I. Zienko. While working in the field of high-power/energy lasers and on important new applications, the author of this book was the scientific supervisor of and advisor to separate studies that were conducted in conjunction with the above researchers.

The author also believes it important to note fruitful cooperation with A.J. Alcock, A.A. Aliev, A.I. Artemyev, V.A. Alekseev, V.N. Antsiferov, G.I. Babayants, Yu. A. Broval'skii, F.V. Bunkin, S.V. Bilibin, P.I. Bystrov, O.D. Baklanov, H.A. Baldis, A.I. Barchukov, A.A. Belevtsev, R.E. Beverly III, V.D. Borman, G.V. Bush, Yu. I. Bychkov, M.V. Gartman, Yu.V. Danchenko, P.B. Corkum, A.V. Ermachenko, M.V. Fedorov, B.A. Frolov, A.E. Hill, D.S. Joins, Yu.L. Kalachev, N.V. Karlov, S.Yu. Kazantsev, V.S. Khmelev, V.I. Konov, I.N. Konovalov, O.B. Kovalchuk, V.V. Kralin, A.A. Kuchinsky, B.B. Kudabaev, N.V. Kudrov, G.P. Kuzmin, N.V. Karlov, V.V. Kiyko, V.I. Kislov, B.Sh. Kishmakhov, V.K. Konyukhov, A.P. Kunevich, V.N. Lugovoi, V.N. Lukanin, E.A. Narusbek, V.F. Losev, G.A. Mesyats, V.R. Minenkov, J-C. De Miscault, P.I. Nikitin, B.I. Nikolaev, V.F. Oreshkin, L.M. Ostrovskaya, N.N. Polyashev, S.S. Pel'tsman, N.V. Pletnyev, D.A. Polukhin, A.M. Prokhorov, N.A. Raspopov, R.E. Rovinskii, V.E. Rogalin, V.N. Rodin, E.V. Khristyan, M.I. Tsypin, A.V. Shirkov, A.A. Shubin, A.V. Saifulin, A.A. Sazykin, B.V. Semkin, B.G. Shubin, V.M. Sobolev, E.A. Sviridenkov, A.G. Suzdaltsev, V.F. Tarasenko, R.S. Taylor, V.I. Troyan, I.S. Tsenina, V.P. Tomashevich, E.E. Trefilov, N.D. Ustinov, D.M. Velimamedov, Yu.M. Vas'kovskii, R. Walter, A. Watanabe, A.V. Yushin, N.S. Zakharov and M.I. Zhavoronkov, L.N. Zakhar'ev who made significant contributions to the development of high-power/energy lasers and realization of new applications.

Contents

Part 1		ligh Conductivity Channels for a Laser Lightning-Protection ystem		
1]	Electric-Discharge Guiding by a Continuous Laser-Induced			
	Spar	k		
	1.1	Introduction		
	1.2	Experimental Setup		
	1.3	Experimental Results and Discussion		
	1.4	Conclusions		
References				
.]	Experimental Simulation of a Laser Lightning-Protection			
	Syste	em		
2	2.1	Introduction		
	2.2	Experimental Setup		
2	2.3	Experimental Results and Analysis		
	2.4	Conclusions		
]	Refe	rences		
]	Ligh	tning and Ecology of Atmosphere		
(3.1	Introduction		
(3.2	Power of Lightning		
	3.3	Lightning in the Natural Capacitor "Earth-Cloud"		
	3.4	Lightning in the Natural Capacitor "Cloud-Ionosphere"		
2	3.5	Orbital Electrical Socket		
2	3.6	Conclusions		
1	Refe	rence		

xviii Contents

Part		«Impulsar» as a Background for High Conductivity Channels Realization
4	4.1 4.2 4.3 4.4 4.5	raction of an OPD with a Gas Introduction
5	Mec 5.1 5.2 5.3	hanism of SW Merging in a LJE 5 Introduction 5 Efficient Laser Jet Engine 5 Conclusions 6 rences 6
6	6.1 6.2 6.3 6.4 6.5 6.6 6.7	Based on the Resonance Merging of SW Introduction 66 Parameters of a Spark in the LJE. 66 Mechanism of the Resonance Merging of SW in a LJE 77 Spherical OPD 77 LJE Parameters in the Monoreflector Scheme 77 Array Reflector 77 LJE Based on the Resonance Merging of SW 88 6.7.1 Mechanism and Scheme of Acceleration 88 6.7.2 Advantages of the Method 88 6.7.3 The LJE Parameters (Initial Data) 88 Conclusions 88 rences 88
7	7.1 7.2 7.3	: The Action of SW at Low Laser Pulse Repetition Rates Introduction 8 LJE Parameters 8 Conclusions 9 rences 9
8	8.1 8.2 8.3 8.4 8.5	Introduction
	8.6	Formation of Electrical Discharges in a Plasma Channel Produced by a Solid-State Laser

Contents xix

	8.7	Experimental Results	112			
	8.8	Conclusions	113			
	Refer	rences	114			
9	High	Conductivity Channel Expansion Data Massurements	117			
9	nigi i 9.1	Conductivity Channel Expansion Rate Measurements Introduction	117			
	9.1	Formation of Controlled Electrical Discharges in a Channel	11/			
	7.2	Produced by the Explosion of a Wire	120			
	9.3	Conclusions	126			
		rences	126			
10		oulsar»: New Application for High Power/Energy High				
10	Repetition Rate Pulse-Periodic Lasers					
	10.1	Introduction	129 129			
	10.2	Experimental Setup	130			
	10.3	Results of Measurements	133			
		10.3.1 Control Measurements	133			
		10.3.2 Stationary Regime	134			
		10.3.3 Pulsed Regime	136			
	10.4	The Impact of Thermal Action	138			
	10.5	The Dynamic Resonance Loads	141			
	10.6	Matrix of Reflectors	142			
	10.7	Super Long Conductive Channel for Energy Transfer	143			
	10.8	Conclusions	145			
	Refer	rences	145			
Par	t III	Lasers and Laser Components for High Conductivity				
		Channels Implementation				
11	Lase	r Power Source for Wireless Power Transmission				
	in Sp	pace	149			
	11.1	Introduction	149			
	11.2	High Conductivity Channel Formation	152			
	11.3	High-Frequency Pulse-Periodic Solid-State and Gas-Dynamic				
		Lasers	153			
	11.4	Pulse-Periodic HF/DF and COIL Lasers	157			
	11.5	Bright Future—High Power/Energy Mono-Module				
		Disk Laser	158			
	11.6	Conclusions	161			
	Refer	rences	161			
12	High Power/Energy High Repetition Rate Lasers					
	12.1	Introduction	163			
	12.2	Comparison of CW and P-P Regimes of Operation	163			
	12.3	Solid-State Lasers	165			
	12.4	High-Frequency Intra-Cavity Loss Modulation	166			

xx Contents

	12.5	Carbon Dioxide Lasers	166		
	12.6	High-Frequency P-P Regime	167		
	12.7	Conclusions	169		
	Refer	rences	169		
13	High Power/Energy Lasers and New Applications				
	13.1	Introduction	171		
	13.2	Lasers for Laser Jet Engine Development	171		
	13.3	Long Conducting Channel and New Set of Applications	174		
	13.4	Lightning Control	178		
	13.5	Manifestation of Atmospheric Electricity Existence	180		
	13.6	Sprites and Jets Investigation	184		
	13.7	Conclusions	186		
	Refer	rences	186		
14	High Power/Energy Disk Lasers				
	14.1	Introduction	189		
	14.2	Disk and Fiber Lasers	190		
	14.3	Design and Physical Foundations of Disk Laser Operation	191		
	14.4	Laws of Scaling of Disk Lasers	192		
	14.5	Regenerative Amplification of Pulses	195		
	14.6	Prospects for Scaling the Power/Energy of Disk Lasers	196		
	14.7	Conclusions	198		
	Refer	ences	198		
15	High Power/Energy Molecular Lasers				
	15.1	Introduction	201 201		
	15.2	Physical Model of SSVD Formation	202		
	15.3	Experiments	206		
	15.4	High Power/Energy HF (DF) Lasers	214		
	15.5	Discussion	226		
	15.6	Conclusions	232		
	Refer	ences	234		
16	High	Power/Energy HF (DF) Lasers	237		
	16.1	Introduction	237		
	16.2	A New Form of SSVD	238		
	16.3	Non-chain HF (DF) Lasers Pumped by SIVD	249		
	16.4	Wide Aperture Non-chain HF (DF) Lasers	253		
	16.5	Conclusions	253		
	Refer	rences	255		
17	High Power/Energy Optics				
	17.1	Introduction	257257		
	17.2	Static POEs Based on Monolithic Materials	258		
	- · ·-	17.2.1 Thermal Stress State of a Solid Body Exposed to	_20		
		Laser Radiation	259		

Contents xxi

		17.2.2	Continuous-Wave Irradiation	262
		17.2.3	Pulsed Irradiation	267
		17.2.4	Repetitively Pulsed Irradiation	269
		17.2.5	Criteria for the Optical Surface Stability	271
		17.2.6	Irreversible Changes in the Optical Surface	274
	17.3	Static O	PEs Based on Materials with a Porous Structure	275
		17.3.1	Temperature Field in Porous Structures Under	
			Convective Cooling	275
		17.3.2	Convective Heat Transfer in a Porous Structure	277
		17.3.3	Hydrodynamics of a Single-Phase Flow in a Porous	
			Structure	277
		17.3.4	Effect of the Coolant Inlet and Outlet Conditions on	
			the Hydraulic Characteristics of the POE	279
		17.3.5	Thermal Conductivity of Porous Structures in POEs	280
		17.3.6	Thermal Deformation of the Optical Surface	280
		17.3.7	Liquid-Metal Coolants in POEs Based on Porous	
			Structures	282
	17.4	Adaptiv	e POEs and Optical Systems Based on Them	286
	17.5		OEs Based on Multilayer Honeycomb Structures	288
	17.6		OEs Based on Composite Materials	290
	17.7		ower/Energy Optics and Its New Applications	293
		_	Cooling of Laser Diode Assemblies	293
			New Generation of High Power/Energy Optics Based	
			on Silicon Carbide	294
	17.8	Conclus	ions	295
	Refer			295
40				
18			ogies for High Power/Energy Lasers Based	•
			res, New Technologies and Materials	299
	18.1		ction	299
	18.2		opproaches for High Power/Energy	
			Development	302
	18.3		ystems of Propellant Ignition	303
	18.4		C-Mirror Manufacturing Technology Capabilities	310
	18.5		ions	315
	Refer	ences		315
Cor	ıclusio	ns		317
Ind	ex			319

About the Author

Victor Apollonov is the leading specialist in the area of basic principles of creation and development of high-power/energy laser systems and high-power/energy laser radiation interaction with matter. He has made an outstanding input into creation and development of new branches of science—physical and technical fundamentals of high-power/energy laser optics and adaptive optics, investigation of physical processes in a large-scale self-controlled volume discharges, creation of highpower/energy continuous wave, pulsed and high-repetition-rate pulse-periodic laser systems, high-intensity laser radiation interaction with matter, high-power/energy laser application for an effective protection of valuable objects and water surface cleaning from oil films, medical applications for UV lasers. Recent results of his investigations related to the laser diode arrays phase-locking, mechanisms of shock waves merging for a rocket launch by high-repetition-rate pulse-periodic laser light, super-long conductive channel based on the electrical breakdown in a dust plasma produced by mechanism of ablation, high-repetition-rate optical pulsating discharge applications, space debris elimination by laser, scalable mono-module disk laser, and high-power/energy laser applications in the Arctic are under very intensive implementation in our country and abroad. He is the author of 1923 publications (19 books, 92 chapters, 710 presentations and 148 patents, 954 articles, inf. from Research Gate). He is a high-profile scientist and well known around all over the world, and for more than 49 years of his international scientific activity, he has participated and organized more than 60 international conferences, symposiums, and workshops, and prepared 32 candidates and doctors of physics and mathematics. For the last 5 years, his scientific department "High-power lasers" has fulfilled more than 65 R&D contracts with customers from Japan, UK, Germany, France, China, Korea, Singapore, and USA. He is the General Director of "Energomashtechnika" Ltd. He is the member of European and American Physical Society, SPIE, AIAA, American Society for QE and the member of specialized scientific council of Russia. He is a full member of Russian Academy of Natural xxiv About the Author

Science and Academy of Engineering Sciences, member of the Presidium RANS. He is the laureate of State Prize of USSR (1982) and of Russia (2001). In 2017, he has got the "EcoWorld-2017" international prize.

Research Interests

High-power/energy laser systems, high-power/energy static and adaptive optics, lasers for ecology, new applications for high-power/energy lasers (energy transfer, satellite launching, space debris cleaning, etc.)



Prof. Victor Apollonov, Gagarin's center, September 2008

Acronyms

ASE Amplified spontaneous emission

CAC Charged aerosol cloud

CLS Continuous laser-induced spark

CO₂ Carbon dioxide

COIL Chemical laser based on oxygen and iodine

CTF Controlled thermonuclear fusion

CW Continuous wave
EB Electric breakdown
EFW Exploding fine wire
GDL Gas dynamic laser

HF/DF Chemical laser based on hydrogen and fluorine

IR Infrared
KJ Kilo joule
LD Laser diode
LJE Laser jet engine
LLS Long laser spark

MMDL Mono-module disk laser
OES Orbital electrical socket
OPD Optical pulsating discharge
POE Power optical element

OF Ouartz fiber

QSW Quasi-stationary wave

RA Reflector array

SBC Spectral beam combining

SC Spacecraft
SiC Silicon carbide

SIVD Self-initiated volume discharge

SSL Solid-state laser

xxvi Acronyms

SSVD Self-sustained volume discharge

SW Shock waves UV Ultraviolet

YFL Ytterbium fiber laser

Part I High Conductivity Channels for a Laser Lightning-Protection System

Chapter 1 Electric-Discharge Guiding by a Continuous Laser-Induced Spark



1.1 Introduction

The solution of some scientific and applied problems requires the production of long plasma channels in the atmospheric air with controllable location and shape. Such channels can find application for energy transfer [1–3], the transportation of charged particle beams [4, 5], the production of plasma antennas [6], and for lightning protection [7–10]. In the investigation of these problems, considerable attention was given to the control of the trajectory of an electric discharge or, in other words, to the production of guided electric discharges [1–3, 11, 12].

One of the most promising methods for producing a plasma channel or controlling the trajectory of an electric discharge is the exposure of gas to laser radiation. Of all kinds of laser action, an optical breakdown leads to the longest and most intense gas perturbation. The length of optical breakdown channel, called a long laser spark (LLS), under real atmospheric conditions can amount to tens of metres and over [13, 14], which makes it possible to produce guided electric discharges several metres long [1, 8].

In [9], the length of a guided discharge was equal to 16 m for a 3-MV voltage across the discharge gap and a 460-J output energy of a pulsed CO₂ laser used to obtain the LLS. However, an LLS produced by spherical optics consists of separate breakdown nuclei located at random in the caustic of the focusing element, i.e., it is immanently discontinuous. For this reason it has not been possible to attain good reproducibility in attempts to control the trajectory of very long discharges with the use of an LLS. This is also evidenced by the results of the tests of a laser lightning-protection system under real thunderous conditions in Japan, which failed because two events of time coincidence of a thunderbolt to the lightning rod with the triggering of a laser were observed, but the trajectories of the lightning channel and the LLS did not coincide [10].

A continuous optical breakdown channel devoid of gaps, or a continuous laser-induced spark (CLS), can be obtained by focusing laser radiation with a conic

lens (an axicon) [15]. A \sim 1-m long CLS was experimentally obtained [16] by focusing Nd-laser radiation ($\lambda=1.06\,\mu m$) with an axicon. The electrical characteristics of a 9–12 cm long CLS produced by a Nd laser emitting 40-ns pulses were investigated in [3]. For an output laser energy of 100 J, the resistance of the spark under investigation was $0.5-1\,\Omega$. On applying a voltage of 1–25 V across the spark, the electric current reportedly started flowing immediately after the optical breakdown. The results of [3] demonstrate that the efficient control of the trajectory of electric discharges is possible using CLSs produced by focusing laser radiation with conic optics. However, considerably longer CLSs may be needed for practical applications. For instance, estimates made in [17] show that the plasma channel length in real lightning protection systems should be equal to \sim 20 m.

Increasing the wavelength of laser radiation results in a lowering of the optical breakdown threshold, which should permit increasing the CLS length—a parameter critical for practical applications [18]. In this paper, we investigate the feasibility of producing a CLS with the use of a CO_2 laser ($\lambda=10.6\,\mu m)$, and also the feasibility of its application for guiding electric discharges and transferring the electric potential.

1.2 Experimental Setup

The schematic diagram of the setup for studying CLSs is shown in Fig. 1.1. The radiation of an electric-discharge TS-300 CO₂ laser [19] with a maximum output energy of 300 J and the radiation divergence at half-maximum of $\sim 3.5 \times 10^{-4}$ rad was focused with conic aluminium mirrors (1) with a cone angle $\gamma = 177.8$ or 179.16°. The angle of incidence of the laser beam (2) on the focusing mirror did not exceed 5°. The radiation of a laser spark in the visible range was recorded with a fast photodiode (3) and was also photographed with an Olympus C-3030 digital camera (4).

The laser beam with a cross section in the form of a frame with external and internal dimensions of 10×10 cm and 3.3×3.3 cm, respectively, was formed by

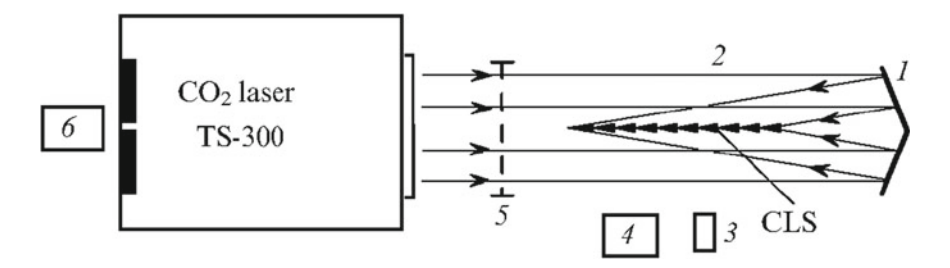


Fig. 1.1 Schematic of the setup for CLS production: (1) conic mirror; (2) laser beam; (3) photodiode; (4) digital photographic camera; (5) transmission bolometer; (6) photodetector

an unstable telescopic resonator with a magnification M=3. The output laser energy was recorded with a transmission bolometer (5) in every shot; the shot-to-shot energy spread was within 5%. The output laser energy was varied during experiments by varying the pressure of the working laser medium and the voltage of the pump source, because introducing plastic film or metal mesh filters into the laser beam resulted in beam wafefront distortions and deterioration of CLS quality.

The shape of output laser pulses was monitored with an FP-3 photon drag detector (6) through the alignment opening in the rear resonator mirror. Typical oscilloscope traces of an output laser pulse are given in Fig. 1.2. One can see from Fig. 1.2a that the shape of the output pulse is typical for electric-discharge CO_2 lasers—a short (\sim 40 ns) primary peak and a long (\sim 3 µs) tail. Due to spontaneous modelocking, the pulse was modulated with short (\sim 3 ns) peaks spaced at \sim 10-ns intervals (see Fig. 1.2b).

The electrical CLS characteristics were investigated employing the circuit shown in Fig. 1.3a. The ends of two metal rods 2 mm in diameter were introduced into the CLS plasma. The rods were connected to oppositely (relative to the common ground) charged capacitors C with capacitances of 0.25 μ F each and were variously spaced in different experiments. The highest capacitor charging voltage was 50 kV, so that the potential difference across the rods could be as high as 100 kV. When studying the electric breakdown of the air between the metal rod and the CLS plasma column, one or both rods were shifted perpendicular to the CLS axis through a distance required in the experiment. The polarity of the rod moved aside could be altered.

The circuit for studying the electric field distortion and potential transfer with the aid of an LLS is shown in Fig. 1.3b. In these experiments, one of the rods dipped into the plasma was connected to a resistive voltage divider $(R_1 = 5 \text{ k}\Omega, R_2 = 60 \Omega)$. The other rod remained connected to the capacitor, whose charging voltage did not exceed 600 V, allowing us to avoid the development of ionisation in the electric field.

The electric field perturbation and the potential transfer during the production of a CLS were also investigated employing a capacitive voltage divider. The high-voltage arm of the divider was the capacitance between the CLS plasma channel, or the electric-discharge channel, and the metal plate mounted on the divider. This capacitance could be varied by varying the plate area and the distance between the plate and the plasma channel. A ceramic capacitor, whose second plate was connected to the grounded body of the divider, served as the low-voltage arm.

The voltage dividers were calibrated directly at the measurement site by applying voltage drops of different amplitude across them from a capacitor C (see Fig. 1.3b). When calibrating the capacitive divider, the CLS was simulated by metal rods of different diameters. As in the setup of Fig. 1.1, the instants of spark initiation and the electric-discharge development in it during the study of electrical CLS characteristics were recorded with a fast photodiode. The signals from the photodetectors and voltage dividers were recorded employing a Tektronix TDS 220 oscilloscope with a pass band of 100 MHz.

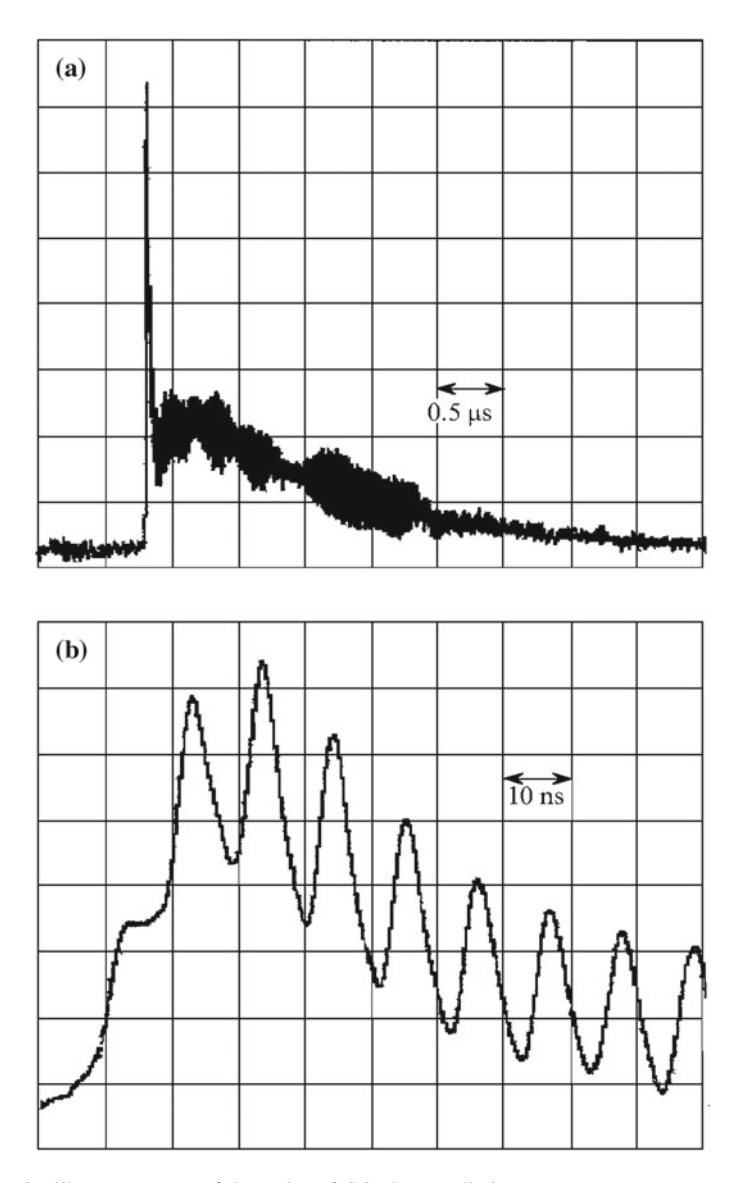


Fig. 1.2 Oscilloscope traces of the pulse of CO₂-laser radiation

1.3 Experimental Results and Discussion

The photograph of a CLS produced by focusing the CO_2 -laser radiation with a conic mirror with a cone angle $\gamma = 177.8^{\circ}$ is shown in Fig. 1.4a. One can see that the laser spark looks like a continuous column consisting of bright cone-shaped elements. The breaks characteristic of the sparks produced by beam focusing with

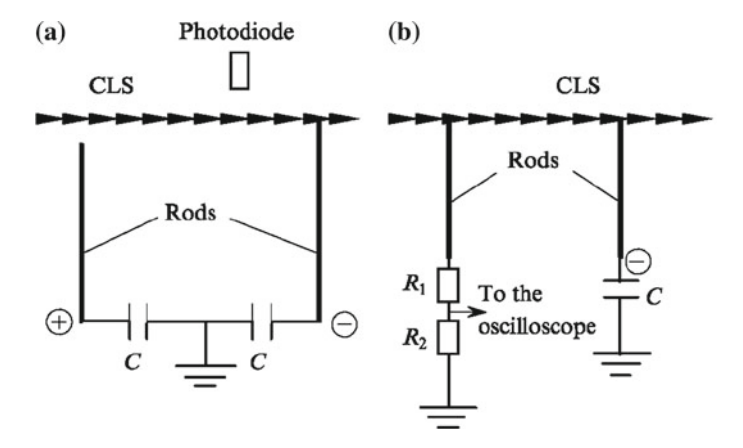


Fig. 1.3 Circuits for studying the electrical characteristics of a CLS

spherical optics are absent in this case. This pattern is observed for an output laser energy of $180{\text -}300$ J. The CLS length, determined by the cone angle and the beam dimensions in the cross section of the cone, was equal to ~ 90 cm. The CLS onset is displaced from the mirror surface because the radiation is absent in the beam centre. When the output laser energy was less than 150 J, at the ends of the spark, where the input of laser energy is lower than in the central region, visible breaks appeared in accordance with the energy distribution over the beam section.

The photograph of a CLS fragment is shown in Fig. 1.4b, in which the longitudinal spark structure in the form of bright cone-shaped elements is clearly visible. The same structure was observed when the CLS was produced by Nd-laser radiation [3, 16], but the structure period and the transverse dimension of the CLS were significantly smaller than in the case under study due to the different emission wavelengths of Nd and CO₂ lasers.

For comparison, Fig. 1.4c shows the photograph of an LLS obtained by using the mirror with a cone angle $\gamma=179.16^\circ$ for an output CO₂-laser energy of 300 J. One can see that the increase in cone angle, as expected, led to the increase in the spark length up to ~ 3 m. However, the spark was no longer continuous, because the laser energy inputted per unit length of the spark was not high enough. The transverse dimension of the plasma nuclei in the spark also increased appreciably (by a factor of ~ 1.5). However, even for an output laser energy insufficiently high to produce a continuous channel, the radiation focusing with a conic mirror makes it possible to attain a higher density of plasma nuclei per unit length of the spark compared to that obtained by focusing with spherical optics (the spark lengths being equal) because of the more uniform distribution of laser radiation energy over the spark length.

Estimates made on the basis of photographs show that to produce an almost continuous spark structure by focusing the CO_2 -laser beam with a conic mirror, a linear laser energy input of $\sim 200 \text{ J m}^{-1}$ is required. Note that these estimates are

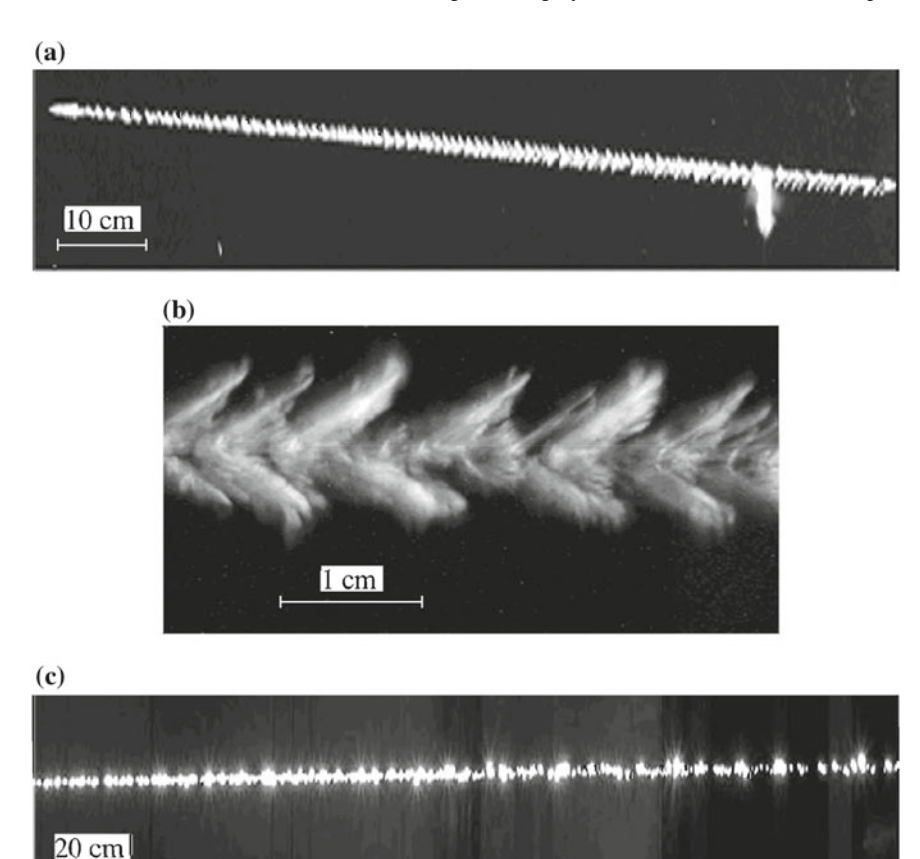


Fig. 1.4 Photographs of an LLS produced by CO_2 -laser radiation focusing with a conic mirror with a cone angle $\gamma = 177.8$ (a, b) and 179.16° (c)

valid only for the shape of output laser pulses shown in Fig. 1.2. The use of techniques for raising the peak output power, for instance, by injecting a nanosecond pulse into the resonator [20], will reduce the output laser energy required for the CLS production.

The electrical properties of the laser spark were investigated by focusing radiation with a mirror with a cone angle $\gamma=177.8^\circ$ (the total spark length was ~90 cm). These studies confirmed that these sparks can be efficiently applied for electric-discharge guidance. Even for an output laser energy of 140 J, when noticeable discontinuities were observed at the spark ends and the length of the continuous part did not exceed 50 cm, an electric breakdown was observed in the spark between the rods immersed into the spark plasma and spaced at d=80 cm for a minimal average electric intensity $E_{\rm min}\approx 77$ V cm⁻¹.

Figure 1.5 shows the average propagation velocity $V_{\rm ch}$ of the conducting channel of laser-guided discharge along the spark as a function of the average electric intensity in the gap E for d=80 cm and an output laser energy of 140 J. The velocity $V_{\rm ch}$ was estimated from the time interval between the signals from the photodiode corresponding to the instants of laser spark initiation and the appearance of the guided discharge. One can see from Fig. 1.5 that for $E=385~{\rm V~cm}^{-1}$, the channel velocity $V_{\rm ch}=4\times10^7~{\rm cm~s}^{-1}$.

The experiments on the electric breakdown of the air gaps between the CLS column and the metal rod were performed using the circuit shown in Fig. 1.3a for a 100-kV voltage across the rods, an output laser energy of 270 J, and a horizontal rod separation d=45 cm. For a positive polarity of the rod displaced relative to the CLS, the longest vertical distance H between the rod upper end and the CLS plasma column at which the electric breakdown occurred amounted to 13 cm. The photograph of a laser-guided discharge in this case is shown in Fig. 1.6.

Figure 1.7 shows the oscilloscope trace of signals from the photodiode recorded under the same conditions. The first peak in the oscilloscope trace reflects the CLS production, while the other, with a ~ 100 -µs delay, corresponds to the current of the guided discharge. Under the same experimental conditions and a negative

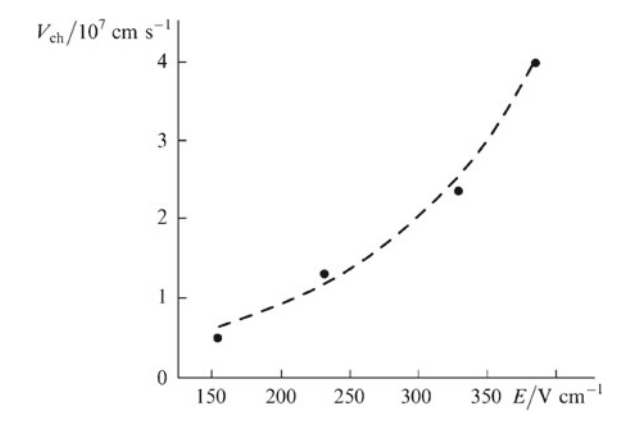


Fig. 1.5 Velocity of propagation of the conducting channel $V_{\rm ch}$ as a function of the electric field intensity E



Fig. 1.6 Photograph of a CLS-guided electric discharge

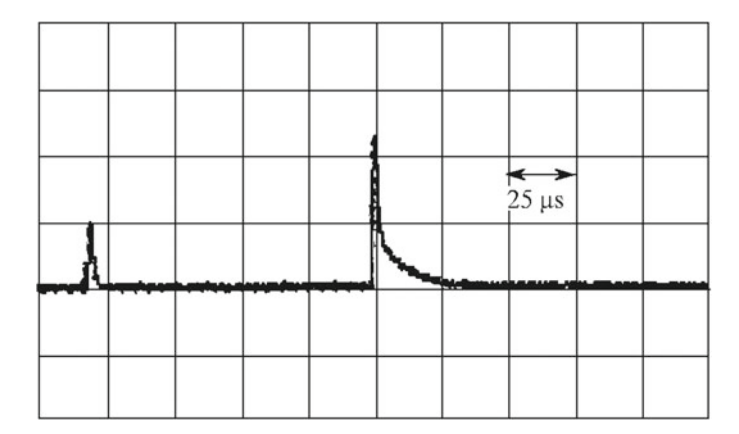


Fig. 1.7 Oscilloscope trace of the signal from the photodiode: the CLS radiation (the first peak) and the radiation of CLS-guided electric discharge (the second peak)

polarity of the rod, the longest distance H at which the electric breakdown of the air gap occurred was only 6 cm. Therefore, upon the breakdown of the air gap between the CLS plasma column and the rod, we observed a distinct polarity effect indicating that the real transverse dimension of the CLS is significantly larger than that demonstrated by the photographs (~ 1 cm). Indeed, when the CLS was replaced by metal rods of different diameters, the polarity effect in the air gap breakdown comparable to the polarity effect observed in the CLS-guided discharge experiment manifested itself only for a rod diameter of over 4 cm.

Therefore, our experiments showed that the CLS produced by focusing the CO₂-laser radiation with a conic mirror behaves similarly to a conducting rod, its conductivity, as follows from the oscilloscope trace in Fig. 1.7, persisting for a rather long period of time.

The CLS conductivity and the feasibility of transferring the electric potential via the CLS were investigated using the circuit shown in Fig. 1.3b for an output CO₂laser energy of 150 J. Under these conditions, only the central \sim 65-cm long part of the spark was continuous. The distance d between the rods immersed into the CLS plasma was varied between 10 and 60 cm. The position of the rod under potential remained invariable in the experiment, and only the rod connected to the resistive voltage divider was moved. The polarity of the rod under potential was negative. Figure 1.8 shows the oscilloscope traces of the signals from the voltage divider and the photodiode (recording the CLS plasma emission) obtained for d = 10 cm. One can see that these signals commence simultaneously, i.e., the CLS is conducting since the instant of its initiation. The leading edge of the voltage pulse at the divider has a characteristic step shape, the regions of rapid voltage build-up being replaced with the regions of slow voltage growth. The voltage rise time τ_f and, accordingly, the CLS plasma conductivity rise time are independent of the rod separation d and are equal to $\sim 28 \,\mu s$. The large duration τ_f points to an important role of gas dynamic processes in the production of CLS conductivity.

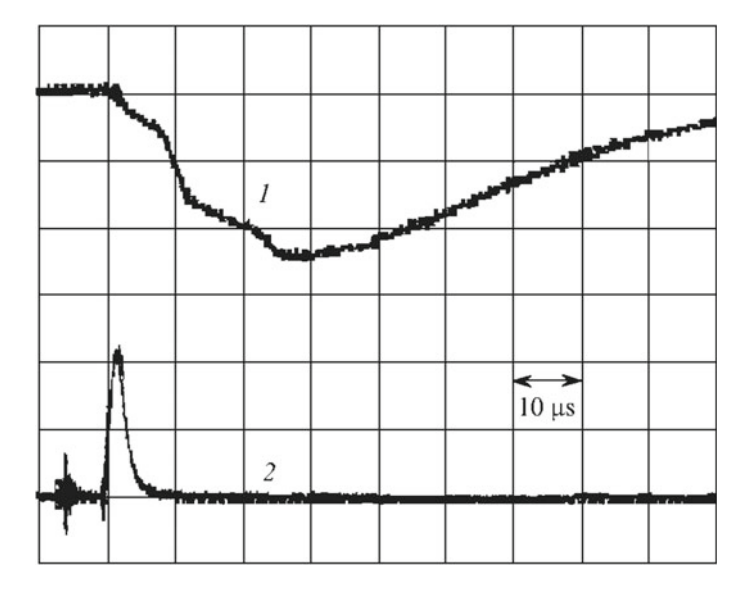


Fig. 1.8 Oscilloscope traces of the signals from the voltage divider at the spark axis (1) and from the photodiode (2)

Fig. 1.9 Dependence of U/U_0 on the distance d between the rods dipped into the CLS plasma

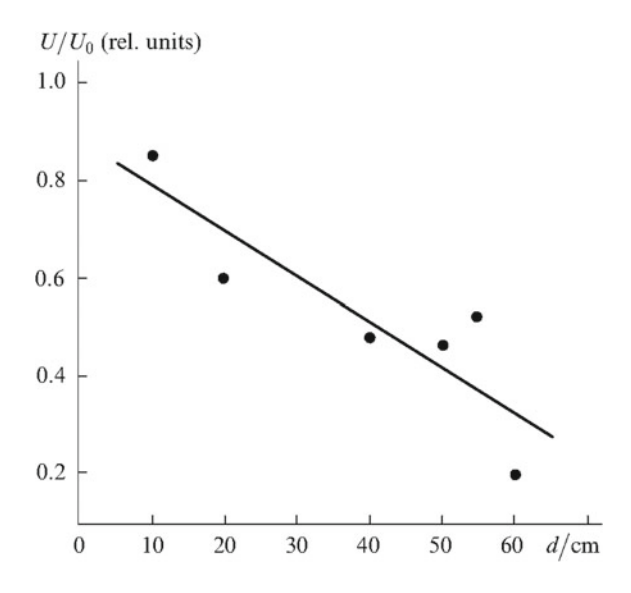


Figure 1.9 shows the ratio U/U_0 (where U is the voltage amplitude recorded by the resistive divider and U_0 is the charging voltage of the rod under potential) as a function of the distance d between the metal rods immersed into the CLS plasma. This dependence reflects the CLS-assisted potential transfer. The scatter of points may be due to an inaccurate mounting of the movable rod in the plasma channel.

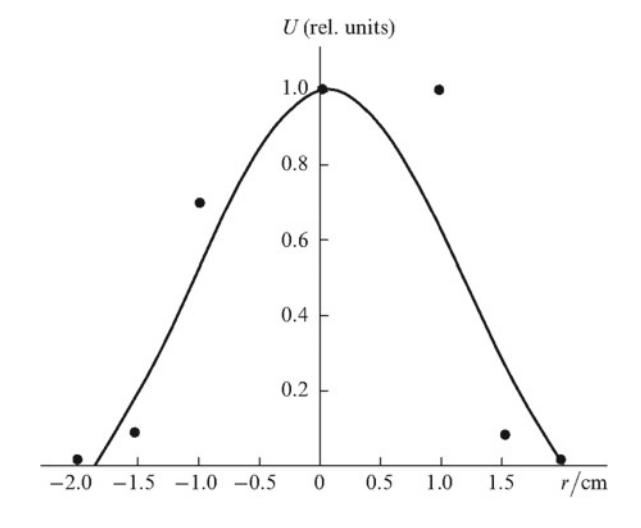
This dependence allows us to estimate, taking into account that the resistance of the resistive divider is $R_{\rm d}=5.06~{\rm k}\Omega$, the resistance $R_{\rm s}$ of the CLS produced with a conic mirror: $R_{\rm s}=988~\Omega$ for $d=10~{\rm cm}$ and $R_{\rm s}=23.9~{\rm k}\Omega$ for $d=60~{\rm cm}$ (the resistance per unit length is $100-400~\Omega~{\rm cm}^{-1}$). This result confirms that the CLS conductivity is high. Note that a CLS produced by focusing a laser beam with a spherical mirror is not conducting at all due to the immanent structural discontinuities between the plasma nuclei.

In the experiment being outlined, for d > 70 cm no signal from the resistive divider was detected as well. This indicates that the spark is nonconducting due to the appearance of breaks in its structure (recall that the experiment was performed for an output laser energy of 150 J). However, the capacitive divider produced signals as d was increased up to 90 cm, which confirms the existance of significant electric-field distortions in the gap induced by the spark under study, despite the discontinuities in the spark structure. This is consistent with the results of measurements of the breakdown fields along the spark considered above.

Of immediate interest was the investigation of electrical conduction of the CLS in its cross section in connection with the discovery of polarity effect in the electric breakdown of CLS-rod air gaps. For this purpose, the rod connected to the resistive voltage divider was displaced perpendicular to the CLS axis. This experiment was conducted for a separation d = 10 cm and an output CO₂-laser energy of 270 J.

Figure 1.10 shows the voltage amplitude U recorded by the voltage divider as a function of the distance r between the upper end of the measuring rod and the CLS axis. One can see that the maximum distance r at which the signal from the divider is still recorded is equal to ~ 2 cm. This is consistent with the results of the experiment on the modelling of polarity effect when the CLS was simulated by metal rods of different diameters. Figure 1.11 shows the oscilloscope traces of the signals from the resistive divider and the photodiode recorded for r=1.5 cm. Note that the voltage rise time $\tau_f \approx 3$ μ s in Fig. 1.11 is substantially (about an order

Fig. 1.10 Voltage U across the divider as a function of the distance r between the CLS axis and the tip of the rod



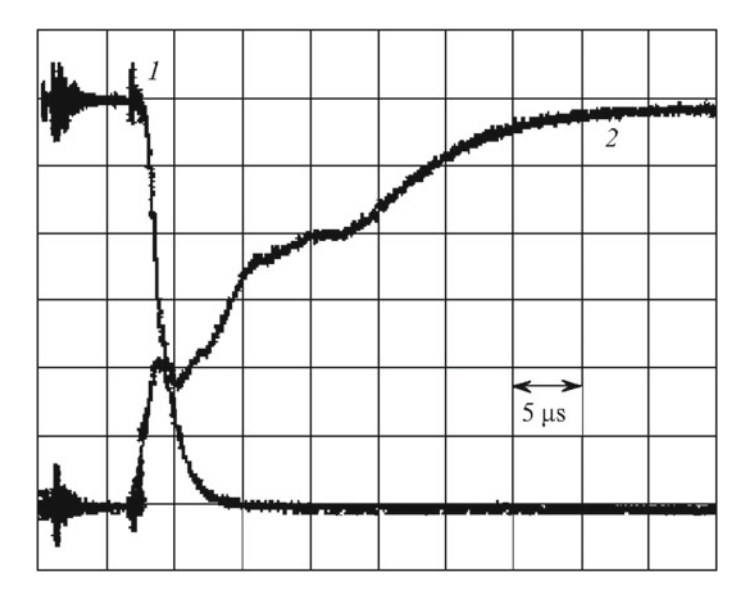


Fig. 1.11 Oscilloscope traces of the signals from the voltage divider (I) and the photodiode (2) for r = 1.5 cm

of magnitude) shorter than the corresponding time in the oscilloscope trace of the voltage signal shown in Fig. 1.8 and the voltage drop from the peak value in Fig. 1.11 occurs considerably faster than in Fig. 1.8.

Note that the duration τ_f in Fig. 1.11 is approximately equal to the duration of the initial period of rapid voltage build-up in Fig. 1.8. Therefore, we can assume that the initial CLS conductivity, both on the axis and in the peripheral regions of the CLS (in the cross section), is due to the photoionisation of air by the radiation of initial nuclei of optical breakdown. The ionisation corona around a spark produced by focusing a laser beam with a short-focus lens was earlier observed in [21]. However, we believe that this interesting effect invites further investigation.

1.4 Conclusions

In conclusion, we estimate the CO_2 -laser energy required for producing CLSs in a real lightning protection system. Taking into account the estimates [17] of the plasma-channel length required to initiate a lightning and a linear energy input of 200 J m⁻¹ required for the CLS production, which was experimentally obtained in our work, the output laser energy should be ~ 4 kJ. At present there already exist CO_2 lasers with an output energy of 5 kJ, and further improvement of their output characteristics is also possible [22]. Note, however, that we give here an understated

estimate that does not take into account the increase in the transverse dimension of the laser-induced spark with increasing cone angle, which was observed in our work.

References

- 1. V.V. Apollonov, S.M. Silnov, High Power P-P Lasers, NOVA (2014)
- 2. V.V. Apollonov, High Power Lasers in Our Life, NOVA (2015)
- 3. M.Yu. Marin, V.I. Pil'skii, L.Ya. Polonskii et al., Zh. Tekh. Fiz. 57, 1507 (1987)
- 4. J.N. Olsen, R.J. Leaper, J. Appl. Phys. 53, 3397 (1982)
- 5. T. Ozaki, S. Miyamoto, K. Imasaki, S. Nakai, C. Yamanaka, J. Appl. Phys. 58, 2145 (1985)
- 6. Dwyer T.J., Greig J.R., Murphy D.R, et al. IEEE Trans. Antennas Propag. AP-32, 141 (1984)
- 7. G.N. Aleksandrov, V.L. Ivanov, G.D. Kadzov, et al. Elektrichestvo (2), 47 (1980)
- 8. T. Yamanaka, S. Uchida, Y. Shimada et al., Proc. SPIE Int. Soc. Opt. Eng. 281, 3343 (1998)
- 9. F. Kinoshita, Y. Morooka, M. Uchiumi, et al. *Proceedings of XII International Conference on Gas Discharge and their Applications* (Greifswald, Germany, 1997), p. 475
- 10. S. Uchida, E. Shimura, H. Yasuda et al., Opt. Zh. 66(3), 36 (1999)
- 11. G.N. Aleksandrov, G.D. Kadzov, V.Yu. Petrun'kin, et al. Zh. Tekh. Fiz. 47, 2122 (1977)
- 12. O.B. Danilov, S.A. Tul'skii Zh. Tekh. Fiz., 48, 2040 (1978)
- 13. L.M. Vasilyak, S.P. Vetchinin, I.O. Kovalev, G.P. Kuz'min, D.N. Polyakov, A.M. Prokhorov, Pis'ra Zh. Tekh. Fiz. **16**(1), 1 (1990)
- 14. V.N. Parfenov, L.M. Pakhomov et al., Pis'ma Zh. Tekh. Fiz. 2, 731 (1976)
- 15. F.V. Bunkin, V.V. Korobkin et al., Kvantovaya Elektron. 10, 443 (1983)
- 16. S.S. Bychkov, MYu. Marin, L.N. Pyatnitskii, Trudy IOFAN 50, 166 (1995)
- E.M. Bazelyan, Yu.P. Raizer, The Physics of Lightning and Lightning Protection (Fizmatlit, Moscow 2001)
- 18. Apollonov V.V. et al., in 25th International Conference on Phenomena in Ionized Gases (Nagoya, Japan, Vol. l, p. 259. (2001)
- 19. V.V. Apollonov et al., J. Opt. Soc. Am. B 8, 220 (1991)
- 20. V.V. Appollonov, A.M. Prokhorov et al., Kvantovaya Elektron. 15, 1766 (1988)
- 21. G.A. Askar'yan, M.S. Rabinovich et al., Pisam Zh. Teor. Eksp. Fiz. 1(6), 18 (1965)
- Apollonov V.V., Prokhorov A.M. et al., Proceedings of International Forum on Advanced High Power Lasers and Application (Osaka, Japan, 1999), p. 63

Chapter 2 Experimental Simulation of a Laser Lightning-Protection System



2.1 Introduction

The problem of protection of terrestrial objects against lightning has not been solved satisfactorily so far. Lightning strikes on industrial objects like petrochemical complexes, nuclear power plants, ultrahigh voltage transmission lines and substations, rocket-launching devices, etc., may turn out to be extremely hazardous. The electromagnetic pulse from a close-range strike of lightning also results in a breakdown of telecommunication equipment and its operation, computer networks, and control systems. Consequently, stringent requirements are imposed at present on lightning protection measures [1, 2]. The traditional lightning protection systems being used currently are not always in a position to ensure the desired level of efficiency. This stimulates the quest for new approaches to solve this problem.

Laser protection against lightning is one of the most prospective trends that are being developed actively at present [3, 4]. While using this approach, it is assumed that the lightning discharge channel being developed is guided towards the conventional rod of the metal lightning rod along the plasma channel formed as a result of the laser-induced breakdown of the atmosphere. This method is based on the concept of an 'active' lightning rod, when a laser beam can be used for 'triggering' and guiding a positive ascending leader from the tip of a lightning rod to a negatively charged thunderstorm cloud. It is expected that in contrast to the traditional approach, the use of laser spark will make it possible to control efficiently the very process of protection from lightning, ensure the selectivity of lightning capture, and provide safety of tall objects and large areas.

In most experimental works, the effect of the laser spark length on the process of discharge development was studied only in the gaps between electrodes [5, 6], and an attempt at striking a lightning in the field tests with the help of a long laser spark was made only in [3, 7]. Two cases of simultaneous occurrence of a strike on the lightning rod and triggering of a laser were registered in [7], but the lightning channel did not coincide with the optical breakdown channel. On the other hand,

it is known from the experiments on initiation of discharge in the gap between electrodes that a long laser spark completely determines the development of the leader channel and its position in space [5]. However, the conditions under which a long laser spark can initiate an ascending leader or trap a lightning strike are not clear, and the field tests of laser protection against lightning carried out in [3, 7] could not provide an answer to these questions.

Since field experiments are quite complex and expensive, it seems expedient to continue laboratory-scale studies of lightning protection systems. However, such studies must be carried out under conditions of the most appropriate simulation of the actual thunderstorm situation.

In this work, we investigate experimentally the interaction of a laser spark with discharges induced by an artificial cloud of charged aqueous aerosol. The results presented in this chapter were published partly in [8].

2.2 Experimental Setup

Figure 2.1 shows the experimental setup consisting of two main parts; a charged aerosol generator [9] and a 50-J pulsed CO_2 laser [10].

The charged aerosol cloud (CAC) is produced by the condensation-type charged aqueous aerosol generator (1) in which a subsonic convergent nozzle with a diameter 6 mm of the outlet aperture is used. For a working pressure of 3–8 atm in the vapour generator, the velocity of outflow of the turbulent vapour jet into the

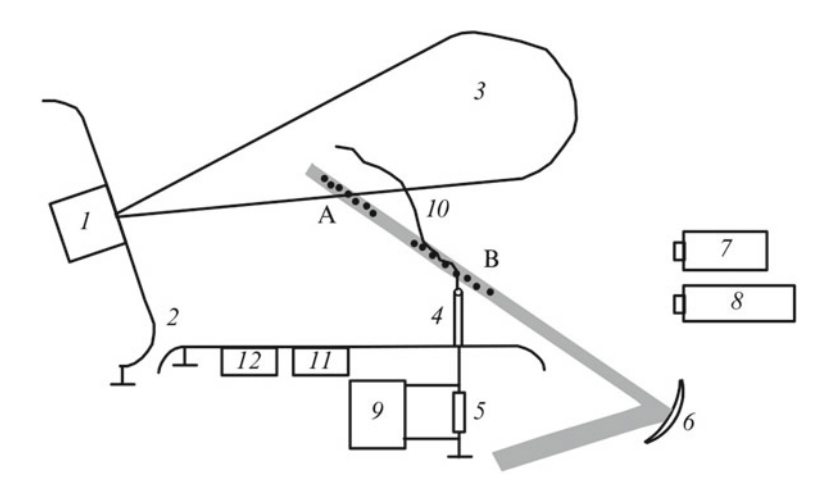


Fig. 2.1 Schematic of the experimental setup: (1) charged aqueous aerosol generator; (2) earthed surface; (3) charged aerosol cloud; (4) electrode rod; (5) current shunt; (6) spherical mirror; (7) digital camera; (8) video camera; (9) current measuring instrument; (10) channel discharge; (11) string sensor for electric field strength; (12) dynamic aerial; (A and B) two positions of a laser spark

atmosphere is 400–430 m s⁻¹. The results of measurement of the outflow velocity in various cross sections of a charged turbulent flow are given in [9].

The charging unit of the charged aerosol generator ensures a loss current in the range $80\text{--}150~\mu\text{A}$. The positively or negatively charged aerosol cloud (3) having a volume of several cubic meters is formed at a height of 1--3 m above an earthed metal surface (2). The CAC voltage may be as high as 1.5~MV. An electric field of strength up to $12~\text{kV}~\text{cm}^{-1}$ at the earthed surface and up to $22~\text{kV}~\text{cm}^{-1}$ near the CAC boundaries is produced in the gap between CAC and the earthed surface [11, 12].

When the experiments were carried out, an electrode rod (4) with a spherical or conical tip was placed on the earthed surface under the CAC. The height of the electrode could be varied from 10 to 58 cm, and the radius of curvature of its tip varied from 2 to 20 mm. The $\rm CO_2$ laser beam was directed in such a way that a long laser spark was formed in the gap between the CAC and the rod after reflection at the concave mirror (6) with radius of curvature 3.6 m. The spark was formed in the CAC near its boundaries (version A) or near the tip of the rod (version B). The laser spark had a length up to 50 cm. The angle between the direction of propagation of the spark and the horizontal surface could be varied from 40 to 70°. The laser spark had a discontinuous structure (up to 15 globular plasma formations along the laser beam), which is characteristic of long sparks obtained by focusing laser radiation with the help of spherical optics.

The measuring part of the experimental complex included low-inductance current shunts (5) (10 and 4 Ω) for measuring the discharge current in the gap between the CAC and the electrode rod. The signal from the shunts was supplied to the oscillograph (9) (Tektronix TDS 220). A digital camera (7) and a video camera (5) recorded the optical pattern of a long laser spark and channel discharges (10) in this gap. The electric field produced by CAC was monitored by a string-type sensor (11) mounted on the earthed surface (2). A dynamic aerial (12) whose signal was fed to a storage oscilloscope C8-17 tracked the variation of charge in the cloud due to discharge phenomena.

2.3 Experimental Results and Analysis

In this work, we present the experimental results obtained for a negatively charged aerosol cloud, since this situation is the closest to real thunderstorm patterns in our climatic conditions.

The experiment was carried out as follows. The charge of the CAC was increased to a value for which the electric field formed by it in the gap between the CAC and the rod was sufficient for creating ascending discharges from the tip of the rod. The laser was triggered manually, and a long laser spark was produced in the gap at arbitrary instants relative to the discharge processes occurring between the cloud and the rod on the surface.

Series of experiments were carried out for two positions of the laser spark in the discharge gap (A and B, see Fig. 2.1.) and for two heights of the rod above the

surface (58 and 29 cm). The pressure, temperature and relative humidity of the air were 740 mm Hg, 18 °C and 70% respectively.

During the spark formation at the tip of the electrode rod (version B, height of the rod 58 cm, electric field strength of CAC 12–16 kV cm $^{-1}$ near the tip of the rod), a strong correlation was revealed between the emergence of the laser spark and the development of the main discharge between the cloud and the rod at the surface. In this case, a part of the leader channel of the main discharge in the vicinity of the tip of the rod developed along a segment of the laser spark (Fig. 2.2). It is significant that the leader discharge is guided not along the entire spark, but only along a part of the spark, which is not characterised by the highest density of plasma formations per unit length. The spark segment in the vicinity of the CAC boundaries does not participate in this process. Figure 2.3 shows a typical oscillogram of the discharge current passing through the rod in the case of 'capture' of its channel by a laser spark. The oscillogram shows all the stages of the discharge evolution, including the streamer corona burst about 2 μ s after the optical breakdown (which is transformed into a leader within about 2–4 μ s), and the main discharge stage of duration ~ 1 μ s following the leader after 1–3 μ s.

If the height of the rod is reduced to 29 cm (the spark is also formed in the region B, the electric field strength near the tip of the rod is 10–14 kV cm⁻¹), only solitary acts of capture of the discharge channel by the laser spark are recorded. In this case, the duration of all discharge stages was much longer than on the oscillogram screen even in the case of capture.



Fig. 2.2 Photograph of a discharge with a laser spark in the gap

Fig. 2.3 Oscillograms of the discharge current I in the presence of a laser spark (upper beam) and the shape of the laser pulse W (lower beam)

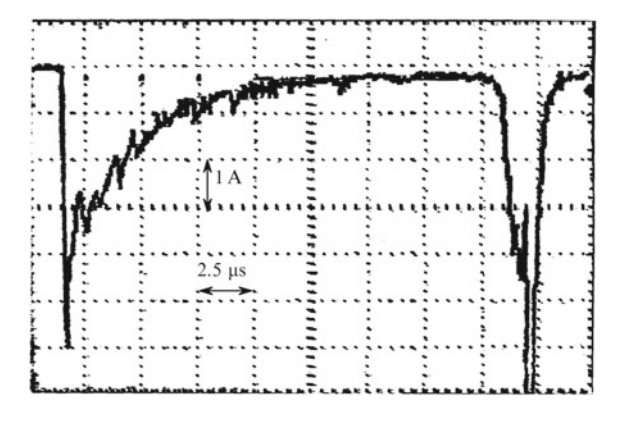


If the laser spark was in the region A, no connection between its emergence and the formation and evolution of the discharge was observed for all the heights of the electrode rod in spite of a high electric field strength (10–16 kV cm⁻¹) in this region (a total of 20 laser shots was carried out for this purpose).

To determine the role of the laser spark in the evolution of the discharge, we carried out a series of experiments for studying the discharges in the gap between the CAC and the rod without the laser spark. Figure 2.4 shows a typical oscillogram of the discharge current passing through the rod in this case. The oscillogram clearly shows all the stages of the discharge evolution, including the corona burst, leader stage and the main stage. However, the duration of these stages is much longer than in the case when a laser spark is present in the gap (Fig. 2.3).

A comparison of the discharge characteristics in the gap between the CAC and the rod, obtained with/without a laser spark in the gap, and an analysis of the conditions of their evolution show that the laser spark formed at the tip of an earthed electrode does not facilitate the emergence of ascending leader discharges if the electric field

Fig. 2.4 Oscillogram of the discharge current *I* in the absence of a laser spark



of the cloud is weaker than that required for the development of a discharge in the absence of a spark. A fairly high probability of discharge channel capture by a laser spark is observed only for large values of the cloud charge, when the electric field of the CAC is in a position to initiate an ascending leader even in the absence of a spark. Consequently, the emergence of a leader with or without a laser spark occurs for close values of the external electric field produced by CAC. However, a long laser spark formed in the vicinity of an earthed electrode may accelerate the process of formation of a stable leader and its propagation towards the CAC.

Table 2.1 contains the results of processing of the current oscillograms for discharges 'captured' by the laser spark, as well as the discharges observed without a laser spark. It can be seen that the formation of a laser spark near the tip of the electrode rod leads to a manifold decrease in the duration $T_{\rm cor}$ of the streamer corona burst before its transformation into a leader discharge, while the maximum current $I_{\rm cor}$ of the streamer corona and the charge $Q_{\rm cor}$ transferred by it decrease by just about 30%. On the whole, similar relations hold between the duration of the streamer corona burst and the transferred charge for discharges with and without a laser spark. It can be assumed that the presence of a laser spark near the tip of the

Table 2.1 Leader discharge parameters with and without a laser spark in the gap

Measured parameters	Mean values of measured parameters and their spread	
	Duration $T_{\rm cor}$ of the streamer corona burst before the emergence of the leader/ μs	2.37
1.22-5.88		4.2-11.2
Maximum streamer corona current I _{cor} /A	3.37	3.95
	1.88-5.0	2.46-5.0
Charge $Q_{\rm cor}$ of the corona burst/ μC	5.0	6.7
	2.07-15.8	2.8-14.8
Mean leader current $I_{\rm lead}/A$	1.52	0.11
	0.93-3.07	0.08-0.15
Duration T_{lead} of the leader current stage/ μ s	1.25	13.0
	0.68-2.07	5.6-22.9
Leader charge $T_{\rm lead}/\mu C$	1.8	1.68
	0.84-3.68	0.4–2.6
Amplitude $I_{\rm m}$ of the main discharge current/A	5.0	4.9
	4.4–5.4	4.2-5.3
Duration $T_{\rm m}$ of the main discharge stage/ μ s	1.05	3.4
	0.75-1.61	2.23-6.25
Charge $Q_{\rm n}$ of the aerosol cloud neutralized at the main discharge stage/ μ C	3.64	5.76
	2.38-6.05	2.49-8.21
$Q_{ m IV}\!/Q_{ m lead}$	2.28	6.7
	0.98-3.79	1.1-22.6

rod in the streamer corona region accelerates the process of its transformation into the first leader segment.

The velocity of propagation of the leader increases by almost an order of magnitude under the influence of a laser spark, thus decreasing the duration $T_{\rm lead}$ of the leader stage of discharge from 13 to 1.25 μs . In turn, the average leader current in the presence of a laser spark is an order of magnitude higher than without the spark (more than 1.5 A on the average as against 0.11 A). As a result, the total charge of the leader is found to be almost identical in both cases.

Thus, a laser spark accelerates the propagation of a leader discharge if it traps the emerging leader. The laser spark may increase the average velocity of the leader manifold. This is in accord with the results obtained in [5, 6] according to which the presence of a long laser spark in the discharge gap increases the velocity of propagation of the leader by more than an order of magnitude in comparison with its velocity in the unperturbed gap. It is significant that the gap is covered the more rapidly, the larger the segment of the laser spark coinciding with the leader channel.

This effect is manifested clearly in our experiments also upon an increase in the length of the discharge gap between the CAC and the rod due to a decrease in the height of the rod (from 58 to 29 cm) on the earthed surface. In spite of the development of the ascending leader over the laser spark region, this led to an increase in the average time T_{lead} of its propagation from 1.25 to 5.7 μ s, since the total length of the gap increases and the part covered by the laser spark decreases.

The parameters of the main discharge also differ significantly in the presence of a spark in the gap and without it. Although the current amplitudes of the main discharge in both cases are 4–5 A (Table 2.1), the duration $T_{\rm m}$ of the main discharge stage and the charge $Q_{\rm n}$ neutralised in this time decrease to less than half as a result of 'capture' of the discharge. In both cases, a nearly identical growth of the main stage duration $T_{\rm m}$ is observed upon an increase in the time $T_{\rm lead}$ of propagation of the leader (Fig. 2.5).

In spite of the similarity in the increase in $T_{\rm m}$ and the increase in $T_{\rm lead}$, the dependences of the charge $Q_{\rm n}$ neutralised at the main discharge stage on the leader charge $Q_{\rm lead}$ are of different types for charges with a spark and without it. In the absence of a spark, a tendency towards a decrease in the value of $Q_{\rm n}$ upon an increase in the leader charge $Q_{\rm lead}$ is manifested clearly. On the contrary, a weak increase in the value of $Q_{\rm n}$ upon an increase in the leader charge $Q_{\rm lead}$ is observed in the presence of a spark. It must be noted that the fraction of the charge left by the leader in the total charge neutralised at the main discharge stage ($Q_{\rm n}/Q_{\rm lead}$) is much smaller for discharges without a laser spark in the gap than in the presence of the spark (on the average, $Q_{\rm n}/Q_{\rm lead} \approx 6.7$ in the presence of the spark and 2.28 without it), especially for small values of the leader charge. For higher leader charges, only the charge left by the preceding leader is virtually neutralised under all conditions at the main discharge stage; i.e., $Q_{\rm n}/Q_{\rm lead} \rightarrow 1$.

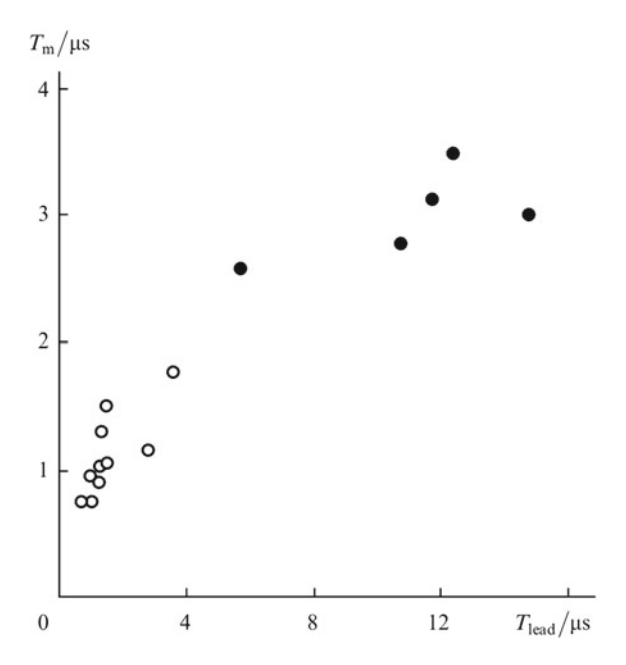


Fig. 2.5 Duration $T_{\rm m}$ of the main discharge stage as a function of the duration $T_{\rm lead}$ of the leader current in the presence (open circle) and absence (filled circle) of a laser spark

2.4 Conclusions

Our experimental studies have shown that, in spite of its discontinuous structure, a long laser spark created in the vicinity of an earthed electrode may capture the channel of leader discharge developing in the gap between the electrode and a CAC. The capture takes place for a quite high electric field strength at the electrode, its value being close to that of the field required for the emergence of an ascending positive leader in the absence of a laser spark in the gap.

The creation of a laser spark near the tip of an earthed electrode allows a considerable decrease in the time of formation of a stable leader which starts propagating towards the cloud and captures a part of the laser spark. As a result, its velocity increases compared to the case when the discharge develops in the absence of a laser spark in the gap. This circumstance is of fundamental importance for laser systems of lightning protection. Indeed, owing to its interaction with the laser spark, the leader discharge developing from the tip of the lightning rod may well precede the ascending discharges from the object being protected during its advance towards an approaching descending leader, capture the latter and thus protect the object.

References 23

References

 International Electrotechnical Commission Standard: IEC 1024-1, Protection of Structures Against Lightning. Part 1: General Principals (1990)

- 2. International Electrotechnical Commission Standard: IEC 1312-1, Protection Against Lightning Electromagnetic Impulse (LEMP). Part 1: General Principals (1994)
- 3. T. Yamanaka, S. Uchida, Y. Shimada et al., in *Proceedings of SPIE—The International Society for Optical Engineering*, vol 3343 (1998), p. 281
- 4. E.M. Bazelyan, YuP Raizer, Usp. Fiz. Nauk 170, 753 (2000)
- L.M. Vasilyak, Materialy konferentsii po fizike nizkotemperaturnoi plazmy FNTP-98, in Proceedings of the Conference on Low-Temperature Plasma Physics, Part 2, Petrozavodsk (1998) p. 135
- 6. L.M. Vasilyak, S.P. Vetchinin, D.N. Polyakov, Elektrichestvo 1, 59 (1991)
- 7. S. Uchida, E. Shimura, H. Yasuda et al., Opt. Zh. **66**(3), 36 (1999)
- 8. V.V. Apollonov et al, in *Proceeding 25th International Conference on Phenomena in Ionized Gases*, vol. 4, Nagoya, Japan (2001), p. 65
- 9. I.P. Vereschagin, K.V. Antsupov, V.V. Bazutkin, A.A. Beloglovsky, L.M. Makalsky, O.A. Nikitin, V.S. Sysoev, A.G. Temnikov, in *Proceeding. 21st International Conference on Lightning Protection*, Berlin, Germany (1992), p. 25
- 10. V.V. Apollonov et al., J. Opt. Soc. Am. B 8(2), 220 (1991)
- 11. A.G. Temnikov, A.V. Orlov, Elektrichestvo 8, 18 (1996)
- 12. I.P. Vereschagin, A.G. Temnikov, M.A. Koshelev, L.M. Makalsky. in *Proceeding 9th international symposium on high voltage engineering*, Graz, Austria (1995), p. 2165

Chapter 3 Lightning and Ecology of Atmosphere



3.1 Introduction

Lightning is an electrical spark discharge that usually manifests as a bright flash of light and is accompanied by thunder. The electrical nature of lightning was first studied by the American physicist B. Franklin, who carried out experiments that attempted to extract electricity from thunderstorms. Similarly, the famous Russian scientists M. Lomonosov and G. Rikhman also investigated the nature of electricity. In addition to Earth, lightning occurs on the surface of other planets, including Venus, Jupiter, Saturn and Uranus.

3.2 Power of Lightning

Let us pause and take a moment to discuss the processes behind the appearance of lightning. Most frequently lightning appears in rain clouds known as thunderstorms. Additionally, lightning can be formed in layered rain clouds, in the ash plumes of volcanic eruptions, in tornados, and in dust storms. Usually linear lightning is observed, which is related to so-called electrode-less discharges, since they begin and end in accumulations of charged particles. Until recently, their properties were not clearly explained, although they were clearly distinguished from discharges between electrodes.

Although the average length of lightning is 2–5 km, some discharges stretch in the atmosphere up to the distance to 150 km. Meanwhile, lightning shorter than several hundred meters does not occur. Lightning appears in electric fields of considerably weaker strength than inter-electrode discharges. The collection of the charges transferred by lightning occurs for thousandthds of a second between huge numbers of small particles that are well isolated from each other. These particles are typically located within in a volume of several km³.

There are two main types of lighting: intra-cloud lightning which passes between clouds and ground-based lightning that strikes the earth. Perhaps the most well studied process is how lightning develops inside clouds. For lightning to appear, a relatively small and critical volume of cloud must form an electric field with a sufficient tension for electrical discharge, which is approximately 1 MV/m. Meanwhile, the rest of the cloud must have a field with an average tension of approximately 0.1-0.2 MV/m that is sufficient for maintaining discharge. As lightning discharges, the electrical energy of the cloud is converted into heat and light. The processes governing ground-based lightning consist of several stages. In the first stage, once the electric field reaches a critical value it propels free electrons in the air towards the earth at significant speeds. These electrons collide with air molecules, thereby ionizing them. As a result, electron avalanches appear, through which passes a stream of electrical discharges that are known as streamers. These are highly conductive channels, which, after merging, create bright thermo-ionized channels with high conductivity, observed as the stepped leader of a lightning strike. The motion of leader to the earth's surface occurs by steps of several tens of meters with a speed of approximately 50 million meters per second, after which its motion stops by tens of microseconds and the glow drastically weakens. In the subsequent stage, the leader moves again by tens of meters. Steps where the leader is moving are accompanied by a bright glow, during the intermittent stops the glow weakens. These processes are repeated during the motion of leader to the earth's surface with an average speed of 200 km per second.

The field strength at the leader is strengthened in proportion to its speed towards the earth and by the action of any reciprocal streamers that are ejected from objects protruding from the earth's surface. These reciprocal streamers are connected to the leader and allow the use of lightning rods. In the final stage, the reverse discharge of lightning follows the channel ionized by the leader from the ground upwards. This massive discharge has currents ranging from tens of amperes to hundreds of thousands of amperes and is characterized by its bright flash, which noticeably exceeds the brightness of leader, and by its high speed of advance, which is initially about 100 million meters per second, decreasing to about 10 million meters per second at the end of the discharge. The channel of the main discharge can have temperatures exceeding 25 thousand degrees Celsius. The length of the channel of lightning can be from one to ten kilometers with a diameter of several centimeters.

Afterwards, both the strength of the ionization current along the channel and its glow weaken. In the final stage, the current of lightning can last the hundredth and even tenths of seconds and reaches hundred and thousands of amperes. These protracted lightning discharges frequently cause fires. However, most discharges occur within the cloud. Discharges at high altitudes can create an arrow-shaped leader that moves continuously at thousands of kilometers per second. The brightness of its glow is close to the brightness of a stepped leader. When arrow-shaped leaders reach the earth's surface, a second strike follows that is similar to the first. Usually lightning includes several repeated discharges and can be as many as several tens of discharges. The duration of repeated lightning can exceed one second. Strip lightning is created when wind displaces the channel of

repeated lighting strikes. When lightning enters directly into soil it can sinter quartz sand and minerals to form unique fulgurites. Intra-cloud lightning usually only includes the leader stages and their length varies from 1 to 150 km. The portion of intra-cloud lightning grows in proportion to displacement to the equator, changing from 0.5 in the temperate latitudes to 0.9 in the equatorial strip. The passage of lightning is accompanied by changes in electrical and magnetic field power, radio emission, and so-called atmospheric disturbances. The probability that lightning can kill a ground-based object grows in proportion to its height and with the electrical conductivity of soil on the surface or at a certain depth. The action of lightning conduction is based on these factors. If there is an electric field in the cloud that is sufficient for maintaining the discharge but insufficient for its appearance, then lightning can still be "provoked" using long wire cables and products of aircraft or rocket engine combustion as initiators. This method can be used to cause lightning in the layered rain and cumulus congestus clouds.

To illustrate the enormous power of lightning and the significant frequency of their occurence around the world, let us examine an article from the British press about "Marakaibo's lighthouse" (Venezuela). Every day around the world, there are more than three million discharges of lightning (i.e. more than a thousand every second). The greatest frequency of discharges occurs in the tropical and subtropical zones of the terrestrial globe. Some of these record places include the following: Ale hook in Columbia (270 days in the year with the lightning); Tororo in Uganda (274 days); Bogor in Java in Indonesia (283 days). A completely extraordinary light storm occurs in Venezuela in the mouth of Katatumbo river that leads into Marakaibo Lake. This spectacle can be seen one hundred eighty days of the year at night for more than ten hours at a time. These light shows are completely silent because their intercloud discharges occur at altitudes up to 10 km. Meanwhile, the sky is illuminated by bright flashes approximately 300 times an hour, which comprises more than one million electrical discharges per year with current strengths from 100 to 400 thousand amperes each. These discharges are visible from the ocean for many tens of kilometers and for many centuries were used by seafarers as a natural lighthouse known as "The Lighthouse of Marakaibo". This unique phenomenon is created by the mixture of wind from the Andes with the hot and humid air rising from the earth's swampy surface in the environment of Marakaibo. Air rising from the surface of swamps consists of methane, which is created from rotting plants. The power of each flash of lightning could illuminate all of the lamps of South America. If only this enormous energy could somehow be harnessed by humanity for domestic purposes.

3.3 Lightning in the Natural Capacitor "Earth-Cloud"

Why does lighting and sparkle? Electric charges are accumulated in clouds, leading to the breakdown of air, which is accompanied by a flash of light and by the formation of a acoustic shock wave. In other words, thunder and lightning are the

manifestation of the existence of atmospheric electricity. Over the last two and one-half of centuries, the fundamental connection between thunderstorm phenomena and electricity was reliably confirmed by numerous studies of geophysicists, meteorologists, specialists on lightning protection. However, in the last two decades, a qualitative jump in the improvement of the methods of observations has led to many unexpected discoveries in the study of thunderstorm clouds, lightning, and the orbital scale of the atmospheric electrical chain. The renewed interest in the problems of atmospheric electricity has made it possible to look differently at the mechanisms of shaping of electric field and its role in the dynamics of the atmosphere and ionosphere of the Earth.

The heart of atmospheric electrical machine is actually the contribution of thousands of thunderstorms within the troposphere that are simultaneously working together. Thunderstorm clouds do not last for long and only exist for several hours. However, the occurence of a few thunderstorms will draw others which form nearby in the lower atmosphere. Contemporary satellite measurements and ground-based systems of the registration of lightning give researchers sufficiently reliable maps of the allocation of frequencies of lightning flashes over the Earth's surface. The average flash rate above the surface of ocean is lower than that above the continents in the tropics. The reason for this asymmetry is the intense convection in the continental regions, where the land is effectively heated by solar radiation. The quick ascent of thoroughly heated air that is saturated by moisture contributes to the formation of powerful convective clouds that develop vertically, the upper part of which has temperatures lower than 40 °C. As a result, particles of ice are formed known as soft hail or hail, whose interaction against the background of rapidly ascending air current leads to the separation of charges. Cloud heights over large bodies of water are typically lower than those above the continents and the processes of electrization are less effective above the ocean. Recently, the differences in the concentrations of the aerosols found above the ocean and above the continents have been discussed. Since aerosols serve as the condensation nuclei necessary for forming particles in supercooled air, their abundance above land increases the probability of electrization of clouds. However, quantitative analysis of this factor requires more detailed experiments.

Approximately 78% of all lightning is recorded between 30°S. and 30°N. In Africa (Rwanda), the maximum value of the average density of the number of flashes per unit of the earth's surface exceeds 80 km⁻². The Kongo river has a flowing area of 3 million km² and it regularly demonstrates the greatest lightning activity on the planet, although other equatorial centers abound with thunderstorms. It appears that a significant contribution to the global thunderstorm activity is provided by the centers of thunderstorms in the subtropics and middle latitudes. Some of them, for example in northern Argentina and Paraguay, lead in the annual rate of lightning flashes. The study of the statistical features of specific regions requires further improvement of satellite and ground based of mapping thunderstorms. These studies are conducted with the consideration that lightning activity is extremely sensitive to the climate of the planet, reacting to changes in the temperature, humidity, radiation conditions, and the composition of the atmosphere.

Progress in the studies of atmospheric electricity is foremost connected with the mechanisms of the generation and dissipation of electrical energy in the atmosphere. The main concept here is the so-called electrical dynamo, or the generation of a quasi-stationary electric field and a space charge in a flowing weakly-conductive medium. In the simplest formulation of a dynamo, very wide intervals of time-spatial scales are manifested. This means that an electric field would arise on the scale of several kilometers with a strength of about 30 kV/cm, allowing for the breakdown of dry air under standard conditions and the random traffic of charges due to the collisions of cloud solid or liquid particles. This leads to the addition of micro-currents into the macroscopic current with a relatively high value (several amperes) that is required for the rapid (tens of seconds) process of the separation of charges. It is evident from casual observation that within ripe thunderstorm cells, lightning discharges occur regularly every 15–20 s. In essence, the mechanism of charging acting in the cloud is very effective although the average electric charge density rarely exceeds several nCl/m³.

As showed by measurements of the electric field on the earth's surface and also inside the cloud medium (on balloons, aircraft, and rockets), the average "main" negative charge of a typical thunderstorm cloud is several tens of coulombs and occupies altitudes corresponding to air temperatures of -10 to -25 °C. The "basic" positive charge is also several tens of coulombs and it is located above basic negative charge. Therefore, a large part of cloud-earth lightning discharges return to the earth as a negative charge. The lower part of the cloud frequently reveals small positive charges of approximately 10 Cl. To explain the 3-layer structure of the field and charge in thunderstorm clouds, one must examine the mechanisms of the separation of charges. These mechanisms depend on factors such as temperature, phase composition of medium, and the spectrum of the sizes of cloud particles. The value of the charge that is transferred from the electric field for one collision is very important. From this parameter, all mechanisms can be subdivided into inductive and non-inductive classes. For the inductive class of mechanisms, the charge q depends on the value and direction of an external electric field and is connected with the polarization of the interacting particles. Meanwhile, non-inductive charge exchanges between particles in an explicit form that does not depend on the field strength. In spite of the abundance of different microphysical mechanisms of electrization, many authors now consider non-inductive charge exchanges to be the main form. These exchanges involve collisions between small crystals of ice with sizes up to tens of micrometers and particles of soft hail with dimensions on the order of several millimeters.

Experiments have established the presence of a characteristic temperature at which the sign of charge q reverses, which typically lies between -15 and -20 °C. This feature has gained popularity because the typical temperature profile in the cloud can be used to explain the 3-layer distribution of charge density. Recent experiments have shown, however, that many thunderstorm clouds possess an even more complex structure of space charge. It is especially interesting to note that mesoscale convective systems (having horizontal scales from ten to hundreds of kilometers) serve as an important source of thunderstorm activity. Their

characteristic feature is the presence of a united electrical structure, which includes the region of intensive convection and is sometimes extended several hundred kilometers beyond the stratified region. In the region of stratification the ascending currents are relatively weak but the electric field has a steady multilayer structure. Near the zero isotherm, a narrow layer of space charge is formed with a thickness of several hundred meters and a critical charge for the high lightning activity of mesoscale convective systems. However, the mechanisms and laws governing the formation of the layer of positive charge near the zero isotherm remains the subject of debate.

Other examples of the work of electrical dynamos include the electrization and discharge phenomena within dust and snow storms, within volcanic eruptions, in nuclear explosions in the atmosphere, and in technological processes that involve the mixture of aerosol flows, for example in the flour-grinding and cement industries. The presence of powerful convective and turbulent flows in thunderstorm clouds and the aforementioned cases of electrization suggest that the interaction of large charged particles with the sizes of 0.1–10 mm with the particles of micrometer size in the moving conducting gas medium plays an important role for electrical dynamos. The poly-phase and multi-flow nature of the medium leads to the effective transformation of mechanical energy into electrical energy.

The problem of the initiation of lightning discharge remains unanswered and involves many complex questions. Let us pause briefly to examine two of them. First, as measurements on balloons, rockets, and aircraft have shown, the maximum tension of electric field in the thunderstorm clouds does not usually exceed 2 kV/cm, which is substantially lower than the threshold of the breakdown of dry air at the heights in question, which is on the order of 10 kV/cm. In the thunderstorm cloud, however, the discharge is developed in humid air, which contains particles of different size. It is natural to assume that the threshold of the field is reached in a compact spatial domain on the scale of less than 10 m or more generally on the microscale because of field strengthening on the particles. Furthermore, it happens in a sufficiently short period, so that common sensors of field do not have that required spatial or time resolution for proper measurement. The development of avalanches of fast "run-away" electrons with energies on the order of 1 meV can serve as the alternative explanation to initiation of spark in the sufficiently weak field. Such electrons can be accelerated in the field of cloud because of a drop in braking power occurs with an increase in the energy of particle. The threshold for the development of an avalanche is almost an order of magnitude lower than the usual threshold for the breakdown of dry air. Therefore, when seeding particles that are highly energized by cosmic rays are present, the development of avalanches in the cloud can give birth to localized regions of high conductivity that are capable of initiating a spark.

The second question arises because the classical theory of gas discharge cannot explain the cloud medium's rapid passage into the conducting state during the preliminary stage of lightning. Recently, a new scenario of this stage had been proposed and investigated that is connected with the cloud reaching a regime of self-organized criticality. In this model, electrical cells with significant dimensions

of 1–30 m randomly grow in space and time. Small-scale breakdowns between pairs of cells can cause "chain reaction" of intra-cloud micro-discharges, or the development of the stochastic process "of the metallization" of intra-cloud medium. This model describes the experimentally observed features of the preliminary stage of the lightning discharge through the dynamics of micro-discharges and characteristics of its radio emission.

The study of thunderstorm phenomena includes experiments on the artificial initiation of lightning, or triggered lightning. In order to create a discharge in the atmosphere under the thunderstorm cloud, a rocket is used which leaves behind a significant trail of soot in the spent oxidizer that is capable of conducting electricity. Initiation occurs with the sufficiently high tension of field on the earth's surface under the cloud, not less than 5-10 kV/m. The first classical diagram of the initiation of discharges was realized with a rocket pulling a wire from onboard of research vessel in 1960. Since then, thousands of successful experiments have been carried out studying the physics of the ascending and arrow-shaped leaders, the return shock, and the mechanism of the sudden strengthening of the luminosity of lightning channel because of the sharp current amplification have all been investigated in great detail. Today, new possibilities of controlling lightning discharges have been opened with the aid of lasers. Powerful lasers are capable of organizing extensive plasma cylinders in air which can initiate and direct the lightning discharges similar to the conducting channels used to trigger lightning from metallic wires or from the products of the combustion of special geodetic rockets.

In 1925, Ch. Wilson indicated the possibility of accelerating electrons to relativistic energies in the field of a thunderstorm cloud. This hypothesis was confirmed recently through a series of experiments showing the generation of relativistic particles and quanta of high-frequency emission in the atmosphere that correlate with thunderstorm activity. Measurements on balloons revealed an anomalous increase in the intensity of X-ray and gamma-radiation more than two or three orders of magnitude over the course of approximately one minute with a maximum of the spectrum in the region 50-60 keV. Ground observations also revealed intense flashes of X-radiation with energy of quanta of several hundred keV, whose appearance coincided with the creation of the lightning leader's flash and with the arrow-shaped leader of trigger lightning. Finally, publications in the last several years have shown results from satellite observations of the splashes of gamma-quanta MeV-foot level, X-ray, and ultraviolet radiation of atmospheric origin. To explain these phenomena, a number of works investigate the atmospheric electrodynamics, or more precisely, the generation of the run-away electrons and their breakdown. Energetic quanta can arise from the bremsstrahlung of the fast electrons which interacts with air molecules. Models describe different situations, including the development of avalanches of fast electrons when the extensive air is showered by cosmic rays and the breakdown of run-away electrons in the strong field of the stepped leader of lightning. One should note that an increase in the number of fast electrons in the field of a thunderstorm cloud in the presence of extensive air showers is accompanied by the generation of a large quantity of secondary particles, leading to the generation of current pulses and radio emission. If the energy of the primary particles are sufficiently great $(10^{17}-10^{19} \text{ eV})$, the short (several microseconds) pulses of radio emission can have enormous energy (up to 1 meV), which explains the appearance of the so-called narrow bipolar pulses that are sometimes observed during ground-based and satellite measurements and correlate with thunderstorm activity. The formation of such intensive current pulses is of interest both for understanding of the mechanism of the generation of lightning and for studying cosmic rays with extremely high energies. It is interesting that in thunderstorm clouds where the cellular structures of the electric field have amplitudes exceeding the threshold "of running away" proves to be essential for the process of accelerating electrons to relativistic energies. The randomly oriented electrical cells together with this acceleration greatly increase the time of life of relativistic electrons in the cloud because of the diffusive nature of their trajectories. This makes it possible to explain the significant duration of the splashes of X-ray and gamma-radiation and the nature of their interrelation with the lightning flashes. The role of cosmic rays for atmospheric electricity must be further clarified experimentally to study their correlation with thunderstorm phenomena.

3.4 Lightning in the Natural Capacitor "Cloud-Ionosphere"

The surge in interest of atmospheric electricity in the last century has led to observations of various discharge phenomena. The first of which are known as sprites, which occur in the middle atmosphere and correlate with daily thunderstorm activity where the glowing region stretches up to 85–90 km above the earth and whose flash durations last from ones to tens of milliseconds. Similarly, elves are observed stretching to heights of 70–90 km with durations less than 100 s. Finally, jet discharges have been observed starting from the upper part of clouds and extend sometimes to mesospheric heights with a speed of about 100 km/s. Measurement of high-altitude discharges and diagnostics of their characteristics are complicated by their short time of life and the sporadic nature of lightning discharges. Therefore, until now the physical models of sprites, elves, and jets remain the subject of intense discussions. Presently, sprites are perhaps the best understood of the three phenomena. Jets and their physical examination is the most interesting subject of future works.

The optical flash of sprites in the mesosphere appears several milliseconds after discharge from the cloud to the earth, sometimes across distances of tens of kilometers horizontally from the channel of lightning. Discharge ignites above a critical altitude, since the threshold of the breakdown of air falls exponentially with its height. Conversely, the amplitude of the disturbances of the electric field, which

appear when powerful lightning flashes in the cloud-earth capacitor, decreases relatively slowly with altitude following a power law and at heights extending approximately 75 km into the atmosphere that exceed the threshold of breakdown. In the last decade, the study of high-altitude discharges in the atmosphere became the subject of extensive investigations and greatly developed the direction of geophysical electrodynamics. Although the accumulation of data characterizing the morphology of these phenomena is by no means completed, it is already possible to switch over to a study of more specific features of the structure and dynamics of high-altitude discharges and their role in the orbital electrical chain and the balance of low components of the atmosphere. Experiments and theoretical calculations show that these discharges must be considered as a part of the dynamic process which includes the formation of the structure of the field, the charge in the cloud, and lightning discharges to the earth.

Different approaches to simulations are widely discussed, including the attraction mechanism of the run-away electrons. Models of the generation of electric field in the middle atmosphere have been generated in great detail that consider the special features of the charge distribution and its dynamics in convective systems at orbital scales which serve as the basic source of positive discharges to the earth. Accordingly, a physical model has been developed that describes the fine structure and dynamics of sprites. Sprites are represented as the network of micro-discharges —streamers—and as a self-sustaining process in an external field. Together with the metallizing process of thunderstorm clouds that was already mentioned, yet another example of self-organizing behavior is found when the dynamics of high-altitude discharge is caused by reaching the threshold of the so-called directed flow along the branched conducting channels which overlap the entire length of a sprite. The immediate prospects for studying high-altitude discharges in the atmosphere involve conducting coordinated ground-based and space experiments and also with the development of new methods of measurement of the parameters of high-altitude discharges through the use of radio-wave and laser diagnostics.

The electrical field of the atmosphere is extremely variable. The tension of the vertical component of the field sags due to ground-winds and thunderstorm cloudiness that can reach several kV/m horizontally.

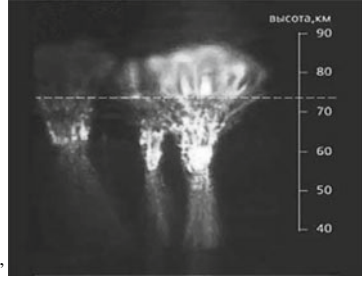


Photo of "Sprite"



Photo of "Jet"

Therefore, the growth of clear weather corresponds to conditions where wind speeds do not exceed 6 m/s and in the absence of any sediments, hoarfrost, fog, or lower cloudiness. But even under these conditions near the earth's surface there is an electric field with a tension of approximately 150 V/m, along which the weakly conducting air flows with electric current having a density of several pa/m². This field changes in time and space and these fluctuations range up to tens of percent relative to the average value. The measurements of electric field, current, and conductivity under the conditions of clear weather serve as powerful means of studying the electrical state of the atmosphere. However, this information is only useful when divided between planetary and orbital scales, from the order of the height of neutral atmosphere at 100 km to the local disturbances of the electrical parameters. The latter, in turn, are directly connected with both the changes in the ionic-aerosol composition and with the dynamics of the conducting medium. Various studies have established that the boundary layer of the atmosphere is characterized by the presence of aeroelectrical structures which are manifested by pulsations of an electric field with a power-law spectrum with short-term periods from ones to several hundred seconds.

The electrodynamics of fog is of special interest. Full-scale observations show that under the conditions of fog in the frequency band 10^{-2} –1 Hz, power-law spectra of the pulsations of field also occur, but the intensity of these pulsations increases more an order of magnitude compared to the conditions for clear weather. This is explained by the diffusion of charged drops in the lowest layer of the atmosphere. The result of structural-temporal analysis made it possible to isolate two forms of the electrical state of fog, the first of which is characterized by the formation of intensive aeroelectrical structures and the second by chaotic variations in the field and current.

3.5 Orbital Electrical Socket

Electricity growth during clear weather is inseparably connected with the thunderstorm electricity, as it composes a part of the distributed current outline or the orbital electrical socket (OES) of the atmosphere. A sharp increase in the conductivity of air with the height causes the formation of the OES in the atmosphere. Near the earth's surface, the conductivity of air is very small and comprises $(2-3) \times 10^{-14}$ S/m, which corresponds to the concentration of light ions of approximately 10^3 cm⁻³. At increasingly high altitudes above 40 km, because of an increase in the ionization level by galactic cosmic rays as well as by ultraviolet and X-radiation from the sun, conductivity grows almost exponentially with a characteristic scale of 6 km. At the height of the lower boundary of the ionosphere (about 80 km) it increases to more than 10 orders of magnitude in comparison with the troposphere. The conductivity of the earth in the surface layer and all of the water in the ocean also exceeds the conductivity of the boundary layer of the atmosphere by 10-12 orders of magnitude. Thus, the constantly functioning thunderstorm generators prove to be concentrated in the narrow weakly conducting layer between the earth's surface and the ionosphere.

Frequently a simplified description of the OES extends from the earth's surface to the lower boundary of the ionosphere (70-80 km.) and is considered as one gigantic spherical capacitor at an orbital scale which is discharged in the regions of clear weather and charged in the regions of thunderstorm activity. In this case, the quasi-stationary currents of charging are not locked completely to the earth near the thunderstorm clouds, but are instead partially involved in the superincumbent region of high conductivity and spread on the ionosphere. The precisely quasi-stationary currents are considered to bear responsibility for the maintenance of a potential difference of 350 kV between the ionosphere and Earth. Since the upper part of the majority of thunderstorm clouds is positively charged, the potential of the ionosphere also proves to be positive, and in the regions of clear weather the electric field is directed downwards, thereby causing conduction currents which close the OES. If the action of these generators ceased, a potential difference between the earth's surface and the ionosphere would disappear in less than 10 min. The orbital electric generator, caused by the nonmonolithic nature of the rotation of the plasma sheath of planet, can serve together with thunderstorm generators as a potentially important source of atmospheric electricity. In order to understand the mechanisms of how OES works and its role in the system of solar to terrestrial connections, their spatial and temporal dynamics must be studied through high-precision measurements of their electric field and current on orbital scales and through measurements of the integral activity of thunderstorm generators. Likewise, it is necessary to create adequate models of thunderstorm generators that give the possibility to calculate quasi-stationary and pulsed currents, and also show how the generators contribute to the complete power engineering of the OES. The results of calculations show that the contribution of mesoscale convective systems in OES can substantially exceed the contribution of single thunderstorms. In spite of the significant disturbance of electric potential in the region of convection, which reaches hundreds of megavolts, the basic contribution to the complete vertical current and structure of currents within mesoscale convective systems are determined by region stratifications. Taking into account recent experimental data and based on theoretical estimations, a new description of OES shows them as an open dissipation system that is supported in a state of dynamic equilibrium by the energy

flowing into it, principally from the radiant energy of the sun. It has been established that electrical energy is generated predominantly in regions of reduced atmospheric pressure and in cold fronts, comprising on average 5×10^{13} George, which is two orders of magnitude higher than the energy concentrated in the orbital spherical capacitor between the earth and ionosphere. The average speed of the dissipation of electrical energy is 4×10^{11} W, exceeding the speed of the dissipation of energy in tectonic and magnatic processes and characterizes the OES as a completely dynamic system with a very short time of renewal of electrical energy. The process of the transformation of energy in the atmosphere is accompanied by the generation of the dissipative structures of different scales, in particular convective systems and aeroelectrical structures, that clearly it is possible to visualize them in the form of global processes of the accumulation of electrical energy and its dissipation in the atmosphere. On the basis of this information, in the near future the study of power engineering of the atmosphere and the structure and dynamics of OES will remain one of the vital problems of atmospheric electricity [1].

3.6 Conclusions

In conclusion of Part I (Chaps. 1–3), it is necessary to include a few words about the interrelation of atmospheric electricity with the formation of the composition of atmosphere and climate of planet. Many years were undertaken attempting to create conducting channels long enough to study the upper atmosphere. Accordingly, the program "Impulsar" is of great interest. This program combines high power/energy lasers with a high-voltage high-frequency Tesla's source which can be useful to solve the aforementioned problems.

Reference

1. V.V. Apollonov, High Power/Energy Lasers in Our Life (Nova, New York, 2015)

Part II «Impulsar» as a Background for High Conductivity Channels Realization

Chapter 4 Interaction of an OPD with a Gas



4.1 Introduction

The transformation of high repetition rate pulse-periodic laser radiation into a low-frequency quasi-stationary wave (QSW) in an optical pulsed discharge (OPD), which was studied for the first time in [1], is considered in [2]. Unlike a continuous optical discharge, no physical constraints are imposed on the velocity of OPD propagation in a gas. In contrast to a single laser spark, the shock waves (SW) generated by an OPD are merged to form a QSW propagating in a preferred direction in the surrounding gas. About 25% of the laser power is transformed into SW in an OPD, which may exert a considerable influence on the surrounding medium.

The mechanism of wave merging can be described as follows. Periodic perturbations (e.g., SW) with an initial velocity exceeding the sound speed C_0 are successively generated in a continuous medium. The velocity V_0 of propagation of the pulsation region is lower than C_0 . The SW combine to the form a QSW if the parameters of the pulsations and the medium satisfy the criteria formulated in this study. Depending on the space-time structure of the pulsations, the mechanism manifests itself in the form of effects characterised by a long elevated-pressure region.

This mechanism does not impose any constraints on the type of the medium and the source of pulsations, and its energy (which is important for producing long waves). The QSW can move from the source, which has a point size in a preferred direction. The SW can also combine during supersonic propagation of an OPD [3], but the length of the combined SW in a direction perpendicular to its front is small. The initial stage of QSW was observed in water upon successive detonation of two charges [4]. In the studies devoted to thermooptical generation of sound in a liquid [5, 6], the SW spectrum could be rearranged by varying the laser pulse repetition rate f^0 , or by modulating the high-frequency component by a low-frequency signal of frequency F^0 . It was found that the fraction of power at the frequency F^0 is small

and proportional to the ratio F^0/f^0 . The mechanism of SW formation considered in this work is free from such a constraint; on the contrary, its efficiency increases for large values of f^0 at which waves are merged. For example, it was shown experimentally [7] that the fraction of power at a frequency ~ 36 Hz can be increased several times by increasing f^0 from 100 to ~ 250 kHz.

Like [2, 7, 8], the present chapter is aimed at studying the interaction between an OPD and a gas medium under the conditions when the wave merging mechanism is manifested. Earlier, we considered the situations when the OPD is stationary or moves along the laser beam axis at a constant relative velocity $M_0 = V_0/C_0 < 1$. The criteria for merging SW into QSW in air were determined in [2].

Here, we determine the conditions under which an OPD stably generates periodic SW, and study the behaviour of QSW in various media in a wide energy range of laser sparks. The applicability of QSW in a laser engine is also substantiated.

Let us briefly discuss the importance of the problems being studied here. It is found experimentally that an OPD exists at any gas velocity $V_0 = 0-400 \text{ m s}^{-1}$ if the radiation power exceeds a certain threshold value. However, the transformation of laser radiation into intense interacting SW is possible only for a certain ratio of the parameters of the OPD and the medium. Hence, it is important to find the conditions for the formation of OSW in various gases and to determine whether any constraints are imposed on the spark energy. Apart from the acoustics, OPD and QSW are also of interest for solving aerospace problems. For example, it was found experimentally [3] that the aerody-namic drag decreases approximately to half its value if an OPD is initiated in front of a body in an incoming supersonic flow. The creation of high-power OPD sustained by laser or microwave radiation was considered in [9]. Increasing the coupling factor J characterising the efficiency of laser radiation application for speeding up an aircraft is one of the main problems in the development of a laser engine [10, 11]. We believe that the value of J can be increased substantially by using QSW and high power/energy pulses of duration $\sim 0.1-1$ µs with a high pulse repetition rate (tens of kHz). Great progress in the development of such lasers was achieved in [12] where an average power $\sim 10 \text{ kW}$ of periodic pulses was attained and the possibility of its further increase was demonstrated.

4.2 Conditions of Stable SW Generation

An OPD can propagate in a moving gas with an unchanged focal length, or in a stationary gas with a moving focus of the laser beam. For a low pulse repetition rate f^0 , the periodic laser pulses successively produce a chain of isolated sparks on the axis along which the focus moves. As the value of f^0 increases, the sparks form a channel with a high temperature and a low density of decaying laser plasma in the gas [13–15]. Calculations show that the pressure in the sparks levels out under thermal expansion with the surrounding gas pressure over a time $t_c = 0.38 \ t_d$ (t_d is the

dynamic time, see below). Under the conditions of our experiment, $t_c \sim 15$ –20 µs. By this time, the gas concentration in a spark decreases to ~ 2 –5% of the unperturbed gas concentration N_0 . The gas concentration is restored to the level N_0 due to turbulent heat and mass transfer with a characteristic time of ~ 1 –2 ms [14, 15]. It can be assumed that the necessary condition for obtaining a stable OPD and efficient generation of SWs is that the focus of radiation must leave the low-gas-density region over the time $1/f^0$ between two laser pulses. This corresponds to the following relation between OPD parameters: $f^0 < V_0/L_s$ if the spark length L_s is much larger than the spark radius r_0 [13]. For a spherical spark, the minimum distance between the centres of the sparks is determined by the relation [2]:

$$f = t_{\rm d} f^0 < f_{\rm b} = 2.5 M_0. \tag{4.1}$$

The time and distance are normalised to the dynamic time $t_{\rm d}=R_{\rm d}/C_0$ and the dynamic radius $R_{\rm d}=(q/p_0)^{1/3}$ (in metres) respectively, where q is the spark energy (in joules) and p_0 is the unperturbed gas pressure (in pascals). A single spark can be treated as an explosion [16]; for this reason, the quantities $t_{\rm d}$ and $R_{\rm d}$ used in the theory of a point explosion can also be applied for describing OPDs. Straight line (1) in Fig. 4.1 shows the dependence of the threshold frequency on M_0 ; above this line, the focus cannot leave the low-pressure region.

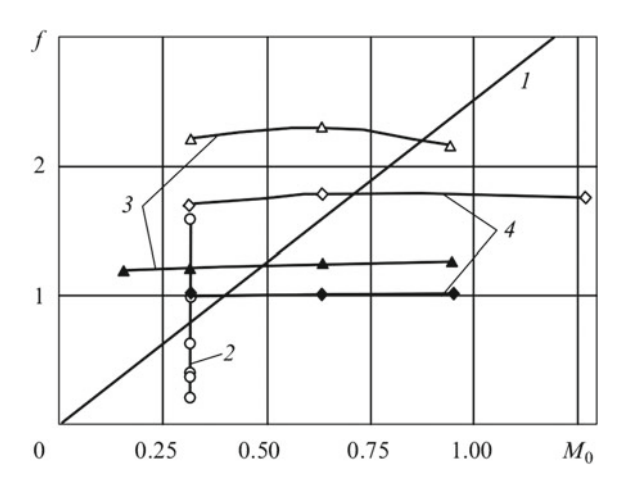


Fig. 4.1 Theoretical dependence (1) of the maximum laser pulse repetition rate f on the velocity M_0 of OPD motion [the OPD stably generates SWs in the region below line (1)] and experimental values of f and M_0 (symbols for which the SW pressure was measured for the averaged power W = 1.3 kW of the absorbed laser radiation, average SW power $W_a = 140$ W, $f^0 = 51$ kHz, $q \approx 25$ mJ (♦); W = 1.3 kW, $W_a = 50$ –76 W, $f^0 = 116$ kHz, $q \approx 11$ mJ (♦); W = 0.764 kW, $W_a = 58$ –179 W, $f^0 = 53.8$ kHz, $q \approx 40$ mJ (♠); W = 0.35 kW, $W_a = 26$ –31 W, $f^0 = 104$ kHz, $q \approx 33$ mJ (♠). The experimental points (circles) correspond to variation of f^0 for $V_0 = \text{const.}$ The symbols on lines (2) and (4) correspond to an OPD generating repetitively pulsed SWs, while symbols on line (3) correspond to an OPD generating SW trains with a repetition rate $F^0 = 1.2$ kHz

4.3 Experimental Setup

Expression (4.1) was verified in the following experiment. An OPD in stationary argon (in a chamber) or in an argon jet effusing into the atmosphere was produced by 1- μ s pulses from $a \sim 1.5$ -kW CO₂ laser. The jet and the radiation propagated in the same direction along the common axis. In this case, the OPD as an SW source is stationary relative to air. The jet was narrow (diameter 3 or 6 mm) and had little effect on SW passed into air.

The pressure in the SW was measured with a piezo-electric transducer located at a distance of 5 cm from the OPD on a fine passing through the OPD at an angle of 90° to the jet axis. Such a position of the transducer was chosen taking the weakened effect of the background into account. At small distances from the OPD, the background intensity is much lower than the intensity of SWs generated by the OPD. The intensity of laser radiation incident on an OPD and transmitted through it was measured.

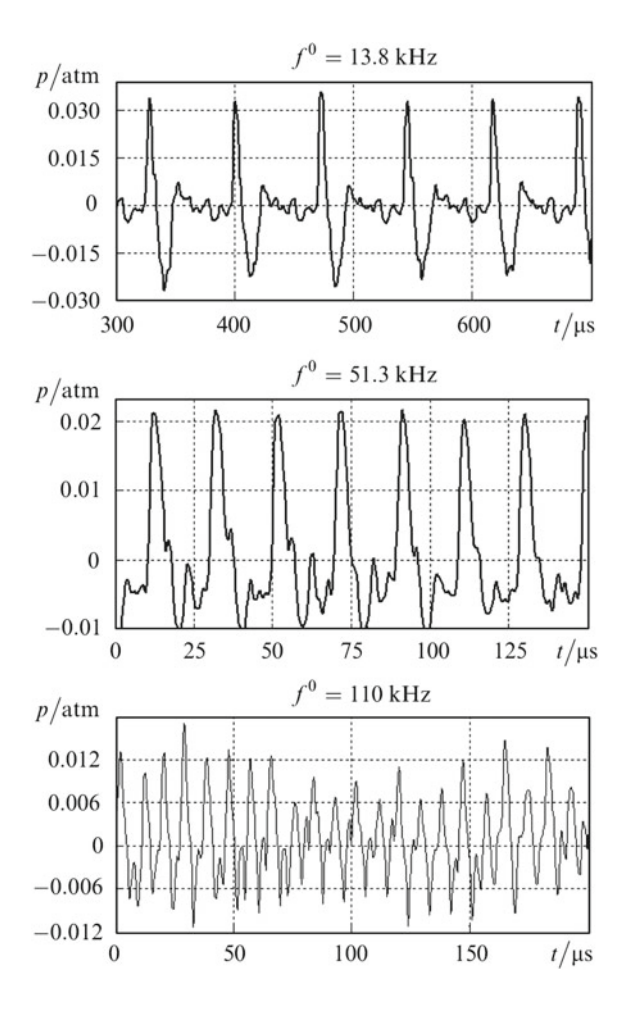
We studied the regimes of periodic laser pulses or periodic trains of laser pulses with a repetition rate $f^0 \approx 20-120$ kHz. The repetition rate of pulse trains was $F^0 = 1.2$ kHz. Accordingly, the OPD produced periodic SWs or SW trains. The effect of the jet velocity $M_0 = V_0/C_0$ and frequency $f = f^0t_{\rm d}$ on the SW generation stability and the efficiency of transformation of laser radiation into SW were studied.

Figure 4.1 shows some values of M_0 and f at which the SW pressure was measured. The jet velocity V_0 was varied at a fixed pulse repetition rate f^0 , or vice versa. The SW generation efficiency can be estimated from the shape of signals from the piezoelectric transducer (Figs. 4.2 and 4.3) and the mean SW power (Fig. 4.4). One can see from the time dependence of pressure that each laser pulse produces SW in the entire range of parameters being studied. However, SW are unstable for $f > f_b$; their average power and the efficiency η of transformation of laser radiation into SW decrease. The SW instability is a consequence of the fact that weaker pressure jumps and, hence, weaker SW, are produced in a hot gas.

We found in experiments that OPD burns and efficiently absorbs radiation $(\eta \sim 70\%)$ in the entire velocity range under study (up to 400 m s⁻¹), including the case of a stationary gas. The value of η differs from 100% because the breakdown developed over a time of \sim 200 ns and the leading edge of the pulse was partly absorbed. The value of η can be as high as \sim 90–95% if the pulse has a steep front and its intensity is much higher than the breakdown threshold of the gas. We also considered the limiting case, when periodic laser pulses with a repetition rate $f^0=1$ or 30 kHz produced an OPD in stationary argon (under a pressure $p_0=1$ atm). Measurements of parameters of incident and transmitted laser radiation show that each laser pulse was absorbed in the OPD.

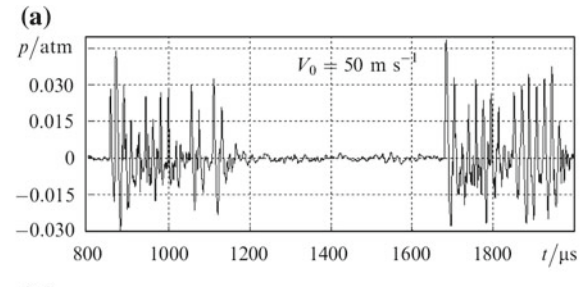
To confirm this result, we measured emission of the OPD spark plasma using a streak camera. The time sweep was carried out along the spark axis coinciding with the radiation beam and jet axis. Figure 4.5 shows the streak camera traces obtained for the case when the OPD was produced by periodic laser pulses with a repetition

Fig. 4.2 Pressure oscillograms for repetitively pulsed SWs in the case of an OPD burning in a jet $(V_0 = 100 \text{ m s}^{-1})$ for various frequencies f^0



rate $f^0 = 100$ kHz and burned in the jet moving at a low velocity $V_0 = 100$ m s⁻¹. The point with coordinates f = 2.2 and $M_0 = 0.316$ in Fig. 4.1, which lies in the unstable SW generation region, corresponds to these parameters. The following conclusions can be drawn from an analysis of this and other pictures. Each laser pulse produces a spark. The velocity of propagation of the plasma front towards the beam is close to the velocity of light-detonation mode. The position of the focus on the axis is repeated regularly from pulse to pulse. During the pause $\sim 1/f^0 = 10$ µs between the pulses, the gas in the jet moves over a distance $\sim V_0/f^0 = 0.1$ cm, which is much smaller than the spark length $L_{\rm s} \sim 0.5$ cm. Consequently, sparks are produced in the channel formed by the previous sparks. One can see from Fig. 4.5 that for z > 0 (z is the coordinate along the axis of the radiation beam and the jet), the slope of the luminescence region corresponds to a velocity of the order of 0.5–1 km s⁻¹. This is a manifestation of the effect of plasma acceleration due to its

Fig. 4.3 Pressure oscillograms for SW trains for various values of V_0 , W = 610 W, $W_a = 58$ W, $\eta = 9.5\%$ (a) and W = 764 W, $W_a = 179$ W, $\eta = 23.4\%$ (b). The repetition rate of the trains $F^0 = 1.2$ kHz, the SW repetition rate in trains $f^0 = 179$ W 53.4 kHz, the jet diameter is 3 mm



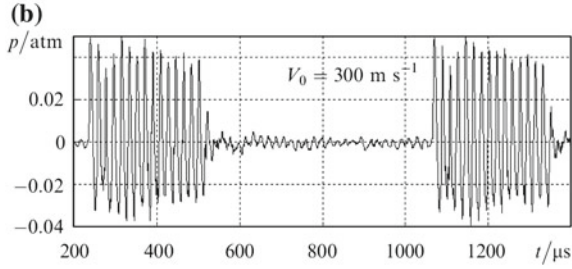
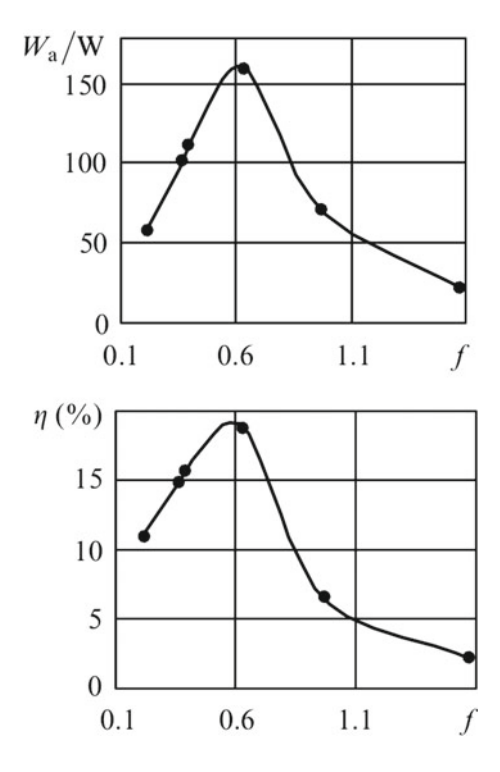


Fig. 4.4 Dependence of the average SW power and the efficiency of transformation of laser radiation absorbed in an OPD into SWs on the dimensionless frequency f. The OPD is produced by periodic laser pulses in a jet propagating at a velocity $V_0 = 100 \text{ m s}^{-1}$



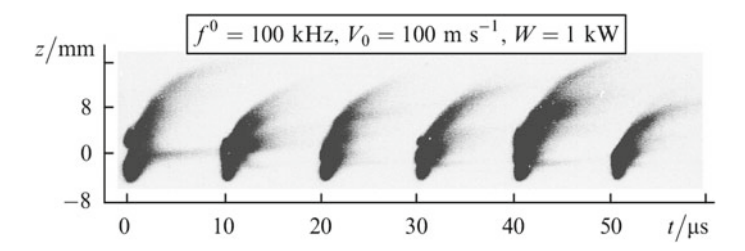


Fig. 4.5 Streak camera traces of the OPD spark plasma emission. The sweep is carried out along the z axis coinciding with the direction of propagation of laser radiation and the jet. The focus is situated at the point z=0

outflow from the high-pressure region to the 'vacuum' channel formed by the moving OPD [17].

Detailed investigations of an OPD burning at low values of V_0 and at $V_0 = 0$ are beyond the scope of this study. We can provide only a qualitative explanation of this process. The necessary condition for the burning of a OPD is that the gas concentration in the focal region should be restored during the pause $1/f^0$ between laser pulses to such a level for which not only the optical breakdown can occur at the focus, but also the conditions are created for the observed light-detonation mode (streak camera traces) of the motion of the plasma front towards the beam. This is a must for efficient absorption of laser radiation. The characteristic time t_1 of turbulent thermal conductivity responsible for the restoration of concentration is of the order of 1 ms [14] (for a single spark). Since $t_1 \ll 1/f^0$, this is not the main mechanism. The most probable reason behind maintaining a fixed gas density and the conditions for OPD burning is the combined action of the convective thermal flow and strong pulsations of the gas concentration in the vicinity of the focal region. We can estimate the gas velocity in the focal region required for replacement of the gas as $\sim 0.5 d_c f^0 \sim 30 \text{ m s}^{-1}$, where $d_c \sim 0.2 - 0.3 \text{ cm}$ is the spark cavity diameter.

4.4 Combination of OPD-Generated SW

According to the above hypothesis, the wave combination mechanism operates in various media for all energies and all types of pulsation sources. The following questions are considered in the present study: can we introduce a universal criterion of wave combination for different gases? Does the mechanism hold for an arbitrary pulsation energy? Which constraints on the parameters of the pulsation source (OPD) are imposed due to the requirement of nonlinearity of interaction of the source with the medium? The wave combination mechanism allows us to analyse the results obtained in [2, 7, 8] from a unified point of view.

Certain constraints were employed in the course of our investigations. We considered a stationary OPD or one propagating in a gas at a constant velocity

lower than C_0 . Equations of gas dynamics in the two-dimensional axisymmetric approximation were solved. For a better generalisation of the results, the spark shape was simulated by a sphere, the velocity (V_0) of the OPD was varied as well as the spark repetition rate and the spark energy $(q = 10^{-3} - 10^3 \text{ J})$. Calculations were made for air and inert gases xenon, argon and helium, in which the sound speeds are substantially different $(C_0 = 340, 169, 316 \text{ and } 965 \text{ m s}^{-1} \text{ respectively})$. A detailed description of some properties of a QSW in air and the derivation of the criterion for its existence are given in [2].

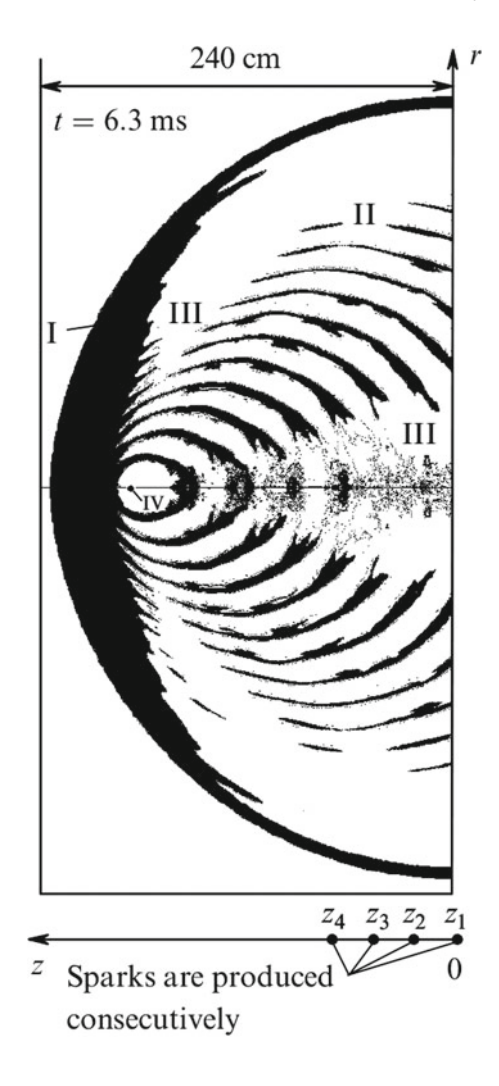
OSW formation by a moving OPD. Figure 4.6 shows a QSW and a part of the field of SW produced by an OPD. On the whole, the perturbation field has the shape of a sphere expanding with the sound speed C_0 . Periodic laser pulses of short duration ($\sim 0.5-1 \mu s$) successively produce laser sparks at the beam focus. The focus moves in the gas and a train of sparks is formed, each spark producing a SW. At subsonic OPD velocities ($M_0 \approx 0.6 - 0.9$), the SWs catch up with one another and produce a region of elevated pressure (QSW) in front of the OPD, which pulsates only at the trailing edge of the QSW in the vicinity of the OPD. Figure 4.7 shows the pressure distribution in the QSW on the OPD axis. The time and distance along the z axis are normalised to t_d and R_d , respectively. The wave whose length L at the asymptote (more than ~ 100 sparks) is equal to $\sim (10-30)R_{\rm d}$ (i.e., much larger than the compression phase length for a SW from a single spark) is regarded as a low-frequency QSW. For the sake of better visualisation, Figs. 4.6 and 4.7a show only the initial stage of QSW formation corresponding to n = 11 sparks. Figure 4.7b shows the QSW pressure corresponding to a later instant of time and n = 280. The QSW propagates in the same direction as OPD. SW form a directional field pattern in the opposite direction due to interaction with the plasma trace and the low-pressure phase of the QSW. If the QSW formation conditions are not satisfied, the SW field resembles that produced by a moving acoustic source (Doppler effect).

SW merging conditions. The SW produced by a moving OPD combine to form a QSW if any two of the three dimensionless parameters $(M_0 = V_0/C_0, z_s = z_{\rm sp}/R_{\rm d}, f = f^0t_{\rm d})$ satisfy certain requirements $(z_{\rm sp})$ is the separation between the centres of sparks) [2]. The parameters M_0 and z_s are convenient for the case of detonation, while the pair M_0 and f is suitable for an OPD. The parameter M_0 is of special importance since a QSW is formed only for $M_0 < 1$. The conditions for merging of SWs and formation of a QSW can be formulated in terms of M_0 and f:

$$2.5M_0 > f > 5.88(1 - M_0)^{1.5}. (4.2)$$

This relation can be used to determine the velocity range $0.6 < M_0 < 1$ in which an OPD produces SW that form a QSW (Fig. 4.8). The left-hand side of formula (4.2) corresponds to line (1). Below this line, the OPD generates SWs stably. The right-hand side defines the range of parameters M_0 and f [above curve (2)] in which the SWs combine to form a QSW. Consequently, a QSW is formed in the region between the curves (1) and (2), to the right of the point of their intersection.

Fig. 4.6 Pressure field in SW produced by a moving OPD and the diagram of QSW formation. Dark shade corresponds to $p > p_0$, and the light shade to $p \le p_0$ [I—QSW, II—SW, III—shadow region $(p \sim p_0)$, IV—last spark]. The OPD moves from right to left at a velocity $V_0 = 300 \text{ m s}^{-1}$ in air; $p_0 = 1 \text{ atm}$, $q = 10^3 \text{ J}$, $f^0 = 2.5 \text{ kHz}$, $R_d = 21.5 \text{ cm}$, $t_d = 632.4 \text{ µs}$, f = 1.58, $M_0 = 0.882$



Expression (4.2) was derived for the air. Because the SW compression phase length (in dimensionless form) depends weakly on the type of the gas, it could be expected that condition (4.2) is also applicable for other gases. In order to verify this, we carried out a number of calculations whose dimensionless parameters are presented in Fig. 4.8. The practical significance of inequality (2) is that it makes it possible to determine the OPD parameters required for producing a QSW. Note also that the computation of a single version (~ 100 sparks) may require several hundred hours of machine time on a modern PC.

If the SW parameters are stable, each point on the M_0 , f plane in Fig. 4.8 corresponds to a large number of combinations of independent dimensional quantities V_0 , f^0 , q, p_0 , ρ_0 , and γ_0 , where ρ_0 , and γ_0 are the gas density and adiabatic exponent. For example, the point + in Fig. 4.8 corresponds to calculations

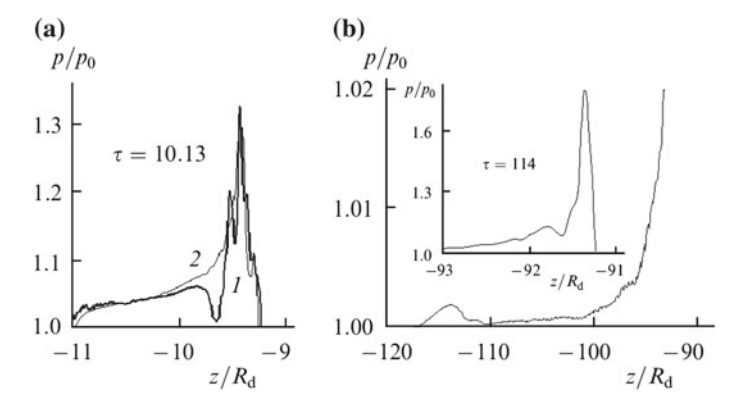


Fig. 4.7 Gas pressure distribution in a QSW on the z axis at various instants $\tau = t/t_{\rm d}$ in the case of SW generated **a** in air for $p_0 = 1$ atm, $M_0 = 0.882$, $V_0 = 300$ m s⁻¹, f = 1.58, $q = 10^3$ J (1) and 10^{-3} J (2), and **b** in helium for $p_0 = 1$ atm, $M_0 = 0.8$, $V_0 = 772$ m s⁻¹, f = 2.46, $f^0 = 400$ kHz, q = 0.021 J. The OPD propagates from right to left

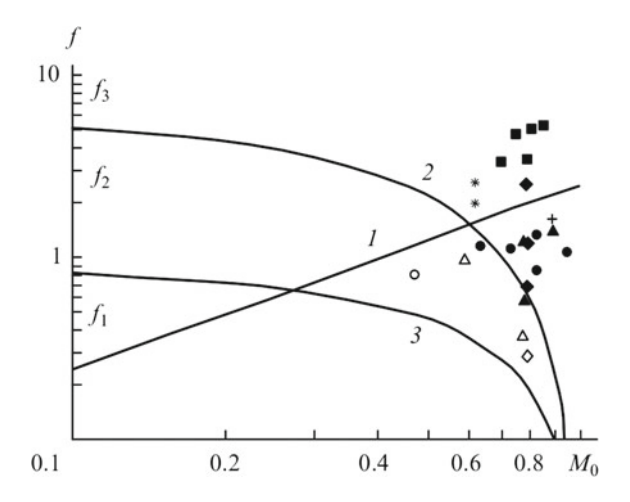


Fig. 4.8 Theoretical dependences of the repetition rate f on the velocity M_0 of OPD motion; the OPD stably generates SW in the region below line (1); SW produce a QSW above curve (2); SWs do not interact with one another below curve (3). The OPD produces a QSW on the right of the point of intersection of curves (1) and (2). The symbol + corresponds to an OPD in air for $q = 10^{-3}$ and 10^3 J (see Figs. 4.6 and 4.7). Symbol * corresponds to an OPD in air for an unstable energy absorption; ♦, ♦—He, Δ , ▲—xenon, o, ●—argon, and ■—water (explosion from two charges) [4]. Dark symbols correspond to the case when SW produce a QSW, while light symbols correspond to the case when no QSW are produced. The computational parameters are close to the experimental ones when the average power $W \sim 1.5$ kW, and the spark energy q = 0.015–0.1 J

performed in air for spark energies $q = 10^{-3}$ and 10^3 J. Figure 4.7a shows the pressure distribution in a QSW. The criteria of QSW formation are satisfied in the entire energy range $q = 10^{-3}$ to 10^3 J investigated by us.

Between curves (2) and (3), the SW interaction decreases as we move away from curve (2) and approach curve (3). In this case, the pressure pulsations increase over the entire length of the QSW. SW do not interact with one another below curve (3). Curve (3) corresponds to the dependence $f(M_0) = (1 - M_0)(t_d/t_s) \sim 0.81(1 - M_0)$. This expression was obtained from the condition $V_0/f^0 = C_0(1/f^0 - t_s)$, where t_s is the time measured from the beginning of a laser pulse to the instant when an SW is detached completely from the cavity.

For $f > 2.5M_0$ [the region above line (1)], the beam focus does not manage to leave the cavity formed by the preceding spark. Here the OPD generates SW intermittently, which may affect the structure of the QSW even if the wave merging condition is satisfied. Points * in Fig. 4.8 corresponds to the computations carried out for such a case. Their height is equal to the spread of frequencies f created by the instability of the absorbed energy $\sim 0.015-0.034$ J. The dependence of q on gas concentration was taken into consideration during computations. The problem of QSW formation criteria under conditions of instability of OPD parameters has not been studied extensively. However, it is obvious that the spread of dimensional parameters of OPD will correspond to a certain region in Fig. 4.8, and SW will form a QSW if this region is situated above curve (2). For example, we carried out computations in which the parameters were changed in such a way that the trajectories on the plane of Fig. 4.8 correspond to a smooth transition from the region above curve (2) to the lower part of the plane, and vice versa. In this case, the QSW was found to disintegrate into isolated fragments.

Merging of SW generated by a stationary OPD. An OPD can produce SW in a stationary gas also if the constraint imposed by formula (4.1) on the stability of SW formation is removed. In our experiments and in [7, 8], an OPD burning in a narrow argon jet generated SW and was stationary relative to the air in which the SWs propagated. In this case, two different values of M_0 should be used. The gas velocity in the jet must satisfy condition (4.1) for stable generation of SW by an OPD, which gives

$$M_{01} > 0.4f$$
.

The OPD is stationary relative to the air in which the interaction of SW takes place, hence $M_0 = 0$ on the right-hand side of formula (4.2). Three frequency regions can be singled out in this case (see Fig. 4.8):

- (1) the region $f_1 < 0.8$, in which SW do not interact with one another;
- (2) the region $0.8 < f_2 < 5.88$, corresponding to the transient region in which SWs combine partially;
- (3) the region $f_3 > 5.88$, in which SWs combine.

Figure 4.2 corresponds to the region of frequencies f_1 (13.8 kHz), while Figs. 4.2 and 4.3 correspond to the region of frequencies f_2 (51.3 and 53.4 kHz respectively).

Repetitively pulsed SW regime. An OPD is produced by periodic laser pulses. The shape of an SW and its power spectrum are determined by the frequency f [7].

In the f_1 and f_2 frequency regions, the fundamental harmonic of the spectrum corresponds to the pulse repetition rate f. In the f_1 region, the SW power is mainly contained in higher harmonics. This is due to the fact that the duration of an SW is much shorter than $1/f_1$. In the f_2 region, most of the SW power is concentrated in the first harmonic. Investigations were not made for the f_3 region.

Periodic SW train regime. An OPD is produced by periodic trains of laser radiation with a low repetition rate $F \ll f$. The trains are filled with pulses having a high repetition rate f corresponding to the frequency range f_2 or f_3 . The OPD generates SW trains with the same frequencies F and f (Fig. 4.3).

In the f_2 region, SWs interact only partly since the SW compression phases do not combine. At frequency $f\approx 2$ ($f^0\approx 120\,\mathrm{kHz}$), the spectrum of SW trains contains a high- intensity component at a train repetition rate $F\ll f$ [7]. However, the main part of power in the SW spectrum was at a frequency $\sim f$.

According to calculations made in [8], SW com-pression phases in the train combine in the f_3 region. A unified wave (an analogue of a QSW) is produced. If the train duration is much longer than 1/f the QSW length is also much larger than the length of the SWs from which it was formed. In this case, the power of periodic trains is mainly concentrated at frequency F. This distinguishes our method from the traditional methods based on low-fre-quency modulation of a high-frequency acoustic signal, in which the power ratio is very small and proportional to F^0/f^0 . We could not generate a QSW in the f_3 region in our experiments since this requires a high-power laser with a pulse repetition rate $\sim 250 \text{ kHz}$.

Restrictions on the gas pressure, energy, and spark radius. No restrictions are imposed in expression (4.2) on the spark energy and other OPD parameters. The restrictions on the most important parameters of the problem can be deter-mined from the condition under which the following mechanism operates: sparks (or another source) should produce SW. We do not consider here the restrictions associated with the generation of pulsations.

The maximum admissible pulse duration $t_{\rm max}$ can be determined from the condition that the gas remains stationary during the time of energy supply to the gas. In this case, the pressure is maximal. According to the results of our calculations and measurements made in [14, 15], the time $t_{\rm c}$ corresponding to the fast stage of laser spark propagation is equal to $\sim 0.14t_{\rm d}$. Consequently, $t_{\rm max}=0.1$ $t_{\rm c}=0.014t_{\rm d}$. For q=1–5 J, we obtain $t_{\rm c}\approx 9$ –15 μs and $t_{\rm max}=0.9$ –1.5 μs . Let us determine the relation between energy q, spark radius r_0 , and unperturbed gas pressure p_0 , for which

$$p/p_0 > b_1 \gg 1, (4.3)$$

and the mean free path l of particles in the gas is much smaller than the value of $r_*/l = r_* N_0 \sigma > b_2 \sim 100$ (σ is the scattering cross section). It follows from the results of calculations that the value of b_1 must not be smaller than ~ 10 ; otherwise, the fraction of energy carried away by SWs decreases. Upon thermal expansion of a spark, the gas concentration in it decreases in proportion to $\sim (r_0/R_c)^3$, while the value of l increases. Hence, we should take the cavity radius R_c instead of r_0 for r_*

at the final stage of the adiabatic expansion of the spark. In this case, $l \approx (a/p_0)$ $(R_c/r_0)^3$, where the parameter $a \approx a_1(T_0/273 \text{ K})$ takes into account the type of the gas $(a_1 = 0.006 \text{ for air})$ and the temperature dependence of the initial concentration [18]. Using formula (4.3) and the condition $R_c/l > b_2$, we obtain

$$r_{01} < \frac{q^{1/3}}{p_0^{1/3}} \left[\frac{3(\gamma - 1)}{4\pi b_1} \right]^{1/3} \approx 0.17 \frac{q^{1/3}}{p_0^{1/3}},$$
 (4.4)

$$r_{02} > \frac{(ab_2)^{\gamma/(\gamma+1)}q^{1/[3(\gamma+1)]}}{p_0^{(3\gamma+1)/[3(\gamma+1)]}} \left[\frac{3(\gamma-1)}{4\pi} \right]^{1/[3(\gamma+1)]} \approx 0.5 \frac{q^{0.152}}{p_0^{0.7}}, \tag{4.5}$$

where γ is the adiabatic exponent. The following simplification was made while deriving formula (4.5): $(r_0/R_c)^3 \ll 1$, which is admissible for $b_1 \sim 10$ or more.

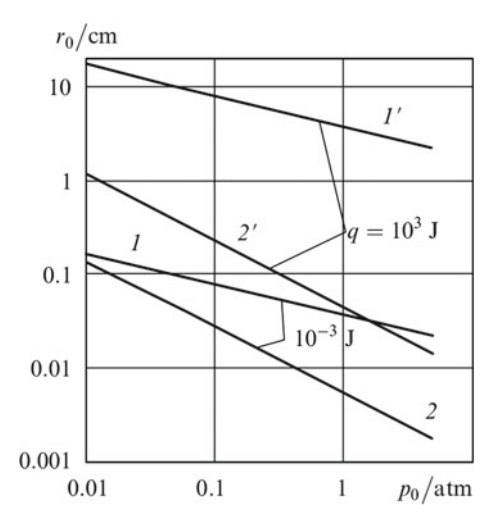
Equating relations (4.4) and (4.5), we find the point of their intersection on the r_0 , p_0 plane:

$$p_{0} = \frac{(ab_{2})^{3/2}b_{1}^{(\gamma+1)/(2\gamma)}}{\sqrt{q}[3(\gamma-1)/(4\pi)]^{1/2}} \approx \frac{20}{\sqrt{q}},$$

$$r_{0} = \left[\frac{3(\gamma-1)}{4\pi ab_{2}}\right]^{1/2} \frac{\sqrt{q}}{b_{1}^{(3\gamma+1)/(6\gamma)}} \approx 0.063\sqrt{q}.$$
(4.6)

The parameters in expressions (4.4)–(4.6) were taken for air at $T_0 = 300$ K and $\gamma = 1.2$. Formulas (4.4)–(4.6) define the region on the r_0 , p_0 plane in which a source produces SW. Of the three quantities q, r_0 , p_0 only one is independent. The admissible values for the remaining two quantities are obtained with the help of formulas (4.4)–(4.6). Figure 4.9 shows the dependences (4.4) and (4.5) for

Fig. 4.9 Limiting values of the spark radius r_0 and air pressure p_0 for spark energies $q = 10^{-3}$ and 10^3 J. Curves (1), (1') and (2), (2') correspond respectively to maximum and minimum values of r_0 . The operational range of the wave combination mechanism is bounded by curves (1) and (2) for a given value of q



 $q = 10^{-3}$ and 10^3 J respectively. The requirement of the formation of an SW upon energy absorption is met in the region between curves (4.1) and (4.2) to the right of the point of their intersection with coordinates r_0 , p_0 .

QSW in a laser engine. One of the methods for producing thrust in a laser engine can be described as follows. Periodic laser pulses are incident on a focusing reflector producing periodically repeated laser sparks at the focus. The sparks generate SW producing an alternating force at the reflector (compression and low-pressure phases in SW). The coup-ling factor J characterizing the efficiency of employment of laser radiation is equal to $\sim 100-500 \text{ N MW}^{-1}$ (see, for example, [11, 19]).

Here, we suggest that a plane QSW be used for a substantial increase in the value of J. The QSW produces a high constant pressure on a large area of the reflector. A simplified scheme permitting calculations in the 2D axisymmetric approximation can be described as follows. The OPD has the shape of a disc whose plane is perpendicular to the reflector axis and whose radius r_0 is much larger than its length L and smaller than the distance (~ 20 –50 cm) between the OPD and the reflector.

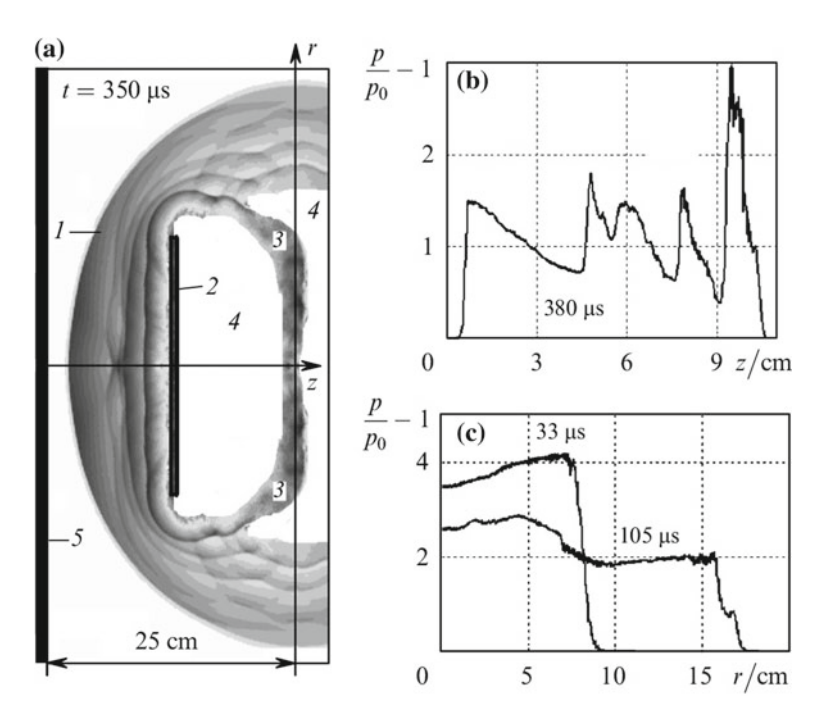


Fig. 4.10 Pressure distribution **a** over radius r in a plane QSW interacting with the wall 350 ps after the initiation of an OPD [(1)—QSW; (2)—OPD; (3)—SWs from the previous pulse; (4)—plasma region; (5)—wall], **b** over the z axis (z is measured from the wall; the last spark is located at a point z = 12.8 cm) and **c** over the wall (time t is measured from the instant of collision of the QSW with the wall at t = 380 µs). The OPD propagates in air ($p_0 = 0.1$ atm) from right to left at a velocity ~ 370 ms⁻¹; $r_0 = 12$ cm, L = 0.5 cm, $q \approx 100$ J, and $f^0 = 20$ kHz

The SW generated in the direction of the reflector merge to form a QSW in the region between the OPD and the reflector. Such an idealisation might correspond to a 2D OPD matrix produced synchronously by many beams. Details of the formation of a plane QSW and its model will be presented elsewhere.

We carried out computer simulation to estimate the coupling factor J in the case when a plane QSW is used in a laser engine. The OPD parameters were as follows: L = 0.5 cm, $r_0 = 10-15$ cm, and $q \sim 100$ J. The repetition rate f^0 was chosen from the conditions of formation of a plane QSW, which differ from conditions (4.2). The simulation technique consisted in the following. At the initial stage, the OPD burns in a free gaseous space. After the passage of several hundred microseconds, a QSW is formed in front of the OPD, in which the gas flows at a velocity $\sim 300 \text{ m s}^{-1}$ in the same direction as the OPD. After this, a wall with which the wave interacts appears on the path of the QSW. Figure 4.10 shows the results of computations in air for p_0 = 0.1 atm. The range of the high-pressure region increases with time due to the curvature of the leading front of the OSW. After a certain interval of time, an excess pressure $\Delta p = p/p_0 - 1$ is established at the wall, its characteristic value being ~ 2 for a range $R_a \approx (1.5 - 2)r_0$. For the computation conditions used by us, the coupling factor $J \approx 10\pi R_a 2\Delta p p_0/(q f^0) \approx$ 1000 и 1000 N MW⁻¹ (where q is in kJ, f^0 is in kHz, and p_0 is in atm). It follows from our computations that $J \approx 2000 \text{ N MW}^{-1}$ for $p_0 = 1$ atm.

4.5 Conclusions

Thus, an OPD can be stationary or move at a high velocity in a gas. However, stable SW generation occurs only for a certain relation between the radiation intensity, laser pulse repetition rate, their filling factor, and the OPD velocity. The OPD generates a QSW in the surrounding space if it is stationary or moves at a subsonic velocity and its parameters satisfy the above conditions. The mechanism of SW merging operates in various media in a wide range of pulsation energies. The results of preliminary investigations show that the efficiency of the laser radiation can be increased substantially when a QSW is used for producing of thrust in a laser jet engine and finally for producing of a long conductive channel [20, 21].

References

- P.K. Tret'yakov, G.N. Grachev, A.I. Ivanchenko, V.L. Krainev, A.G. Ponomarenko, V.N. Tishchenko, Dokl. Akad. Nauk SSSR 336, 466 (1994)
- V.V. Apollonov, V.I. Kislov, V.N. Tischenko, in Proceedings GCL—High Power Laser Conference (SPIE, Prague, 2004)
- P.K. Tret'yakov, G.N. Grachev, V.L. Krainev, A.G. Ponomarenko, V.N. Tishchenko, Dokl. Akad. Nauk SSSR, 351, 339 (1996)
- 4. S.V. Stebnovskii, Prikl. Mat. Teor. Fiz. (4), 87 (1978)

- A.I. Bozhkov, F.V. Bunkin, A1.A. Kolomenskii, A.I. Malyarovskii, V.G. Mikhalevich, Trudy FI AN, 156, 123 (1984)
- 6. L.M. Lyamshev, Usp. Fiz. Nauk 151, 479 (1987)
- 7. V.N. Tishchenko, G.N. Grachev, V.I. Zapryagaev, A.V. Smirnov, A.V. Sobolev, Kvantovaya Elektron. 32, 329 (2002) [Quantum Electron. 32, 329 (2002)]
- 8. V.N. Tishchenko, G.N. Grachev, A.I. Gulidov, V.I. Zapryagaev, V.G. Posukh, Kvantovaya Elektron. 31, 283 (2001) [Quantum Electron. 31, 283 (2001)]
- 9. A.G. Ponomarenko, V.N. Tischenko, G.N. Grachev, V.M. Antonov, A.I. Gulidov, A.V. Melekhov, S.A. Nikitin, V.G. Posukh, I.F. Shaikhislamov, in *Perspectives of MHD and Plazma Technologies in Aerospace Application* (Moscow, IVTAN, 1999), pp. 82–92
- V.P. Ageev, A.I. Barchukov, F.V. Bunkin, V.I. Kononov, A.M. Prokhorov, A.S. Silenok, N.I. Chapliev, Kvantovaya Elek-tron. 4, 2501 (1977) [5ov. J. Quantum Electron. 7, 1430 (1977)]
- 11. C.R. Phipps, Proc. SPIE Int. Soc. Opt. Eng. 4065, 502 (2000)
- 12. V.V. Apollonov, V.I. Kislov, A.G. Suzdal'tsev, A.B. Egorov, Kvantovaya Elektron. 33, 753 (2003) [Quantum Electron. 33, 753 (2003)]
- 13. G.N. Grachev, A.G. Ponomarenko, A.L. Smirnov et al., Laser Phys. 6(2), 376 (1996)
- V.N. Tischenko, V.M. Antonov, A.V. Melekhov et al., J. Phys. D Appl. Phys. 31, 1998 (1998)
- 15. V.N. Tishchenko, Opt. Atmos. Okean. 11, 228 (1998)
- 16. F.V. Bunkin, V.M. Komissarov, Akust. Zh. 19, 306 (1973)
- 17. V.N. Tishchenko, A.I. Gulidov, Pis'ma. Zh. Tekh. Fiz. 26, 77 (2000)
- 18. Yu.P. Raizer, Gas Discharge Physics (Springer, Berlin 1997); (Nauka, Moscow, 1987)
- 19. M.V. Powers, C. Zaretzky, L.N. Myrabo AIAA Paper, (86–1761) (1986)
- 20. V.V. Apollonov, Wallace J. Laser Focus World, August, 17 (2004)
- 21. V.V. Apollonov, S.M. Silnov, High Power P-P Lasers (NOVA, 2014)

Chapter 5 Mechanism of SW Merging in a LJE



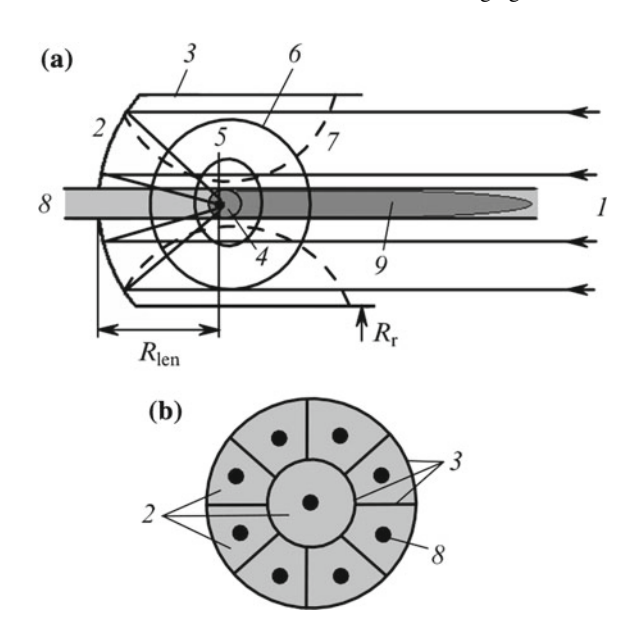
5.1 Introduction

A laser jet engine (LJE) is proposed for use in projects involving the launching of light spaceships into orbit [1, 2] and later for a super long conductive channel production [3]. With the help of a focusing reflector, repetitively pulsed radiation produces laser sparks (Fig. 5.1) which, in turn, should generate shock waves (SW). A part of the momentum of the latter is imparted to the spacecraft (SC). The radiation parameters proposed for realising an LJE are average power 1–3 MW, pulse repetition rate $f \approx 100-300$ Hz, energy $q \approx 10$ kJ, pulse duration $t_{\rm r} = 15-30$ µs. These parameters of an LJE are far from optimal. A specific pulse is maximal if a spark is produced in the vicinity of the reflector, but then thermal destruction of its surface and shielding of the emerging radiation by the laser plasma become inevitable. Apart from this, the reflector of the SC is subjected to strong shock loads.

5.2 Efficient Laser Jet Engine

In the chapter we propose a new approach to develop an efficient LJE, which is based on the merging of SWs generated by an optical pulsating discharge (OPD) at short radiation pulses with a high pulse repetition rate [3, 4]. In this case, the OPD energy is transformed most efficiently in an LJE into a constant force accelerating the motion of an SS. High-power gas-dynamic lasers, which may generate pulses with $t_{\rm r} = 150$ –250 ns and a pulse repetition rate of up to 100 kHz under a continuous pumping of the active medium, offer great promise for the use in the LJE technology [5, 6]. The use of repetitively pulsed lasers is especially efficient if the LJE consists of a reflector array (RA). The model presented below is based on the estimates and numerical simulation in the two-dimensional axisymmetric approximation for thrust pulses generated by the OPD.

Fig. 5.1 Scheme of the reflector (a) and possible structure of the reflector array (b) in a laser jet engine:
(1) repetitively pulsed laser radiation; (2) end face of the reflector: the collector of radiation and mechanical momentum; (3) reflector side wall; (4) cavity; (5) OPD; (6) SW; (7) reflected SW; (8) gas jet; (9) plasma jet



Our approach is illustrated in Fig. 5.1 and can be formulated as follows. Repetitively pulsed laser radiation with a pulse energy $Q \approx 200 \text{ J}$, f = 100 kHz and an average power $W_a \approx 20$ MW [3, 5] is supplied at the input of an RA consisting of N = 9 reflectors. Each laser pulse is divided into N parts so that $q \sim Q/N$, $W_{\rm p} = W_{\rm a}/N$. It is also possible to use the RA in the form of a ring having a circular central reflector with cylindrical walls, and the remaining eight reflectors constituting the outer part of the ring. All the reflectors have side walls and a spherical end face which receives the mechanical momentum and focuses the laser radiation. An OPD burns in each reflector in a gas jet injected through a nozzle at the centre of the reflector. The jet carries the plasma away from the OPD region, which is necessary for the efficient generation of subsequent SW. The gas jet velocity exceeds 1 km s⁻¹. Rapidly propagating SW generated by the OPD merge to form a quasistationary wave (QSW) which fills the entire volume of the cylinder. The surface of the reflector is subjected to a force $F_a \sim \pi R_r^2 \delta P$ [R_r is the radius of the reflector, $\delta P = (P - P_0) > 0$ is the excess pressure, P_0 being the atmospheric air pressure]. The force F_a is constant (time-independent) if the gas flow is created in the reflector in the same direction as the gas jet, but has a subsonic velocity $\sim 300 \text{ m s}^{-1}$. In the opposite case, it becomes necessary to use laser pulse trains with a frequency F, the pulse repetition rate in the trains being $f \gg F$. The duration τ_t of the trains is limited by the time in which the density of air decreases in the reflector. The gas is replaced during the pause $\tau_p \sim a_p R_{\rm len}/C_0$ between the pulse trains (R_{len} is the length of the cylindrical part of the reflector, C_0 is the velocity of light in air, and the coefficient $a_p \approx 1 - 2$).

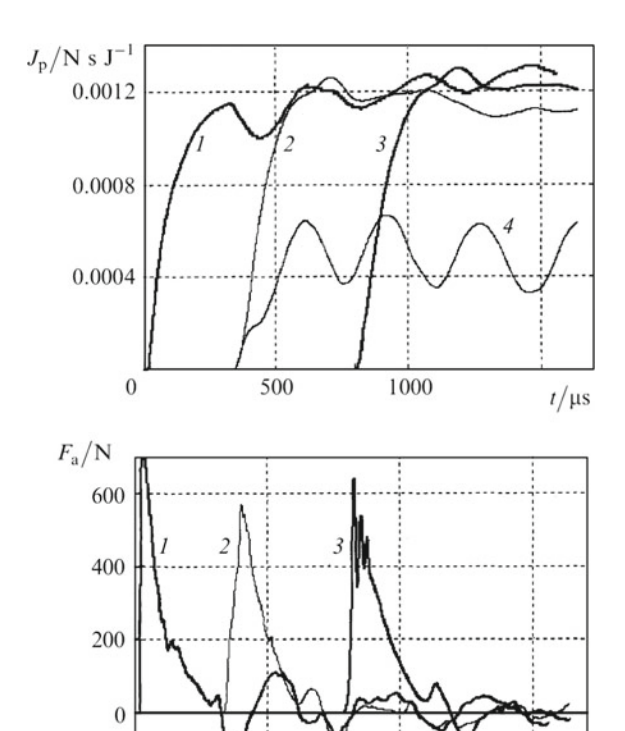
Reflection at the side walls makes it possible to gather $\sim 1/2$ of the total momentum of the OSW or a solitary SW at the surface of the reflector. The

formulation of the problem thus becomes close to the one in the model of a plane explosion in which the specific momentum $J_{\rm p}$ is maximal. Figure 5.2 shows the force $F_{\rm a}$ and the specific momentum $J_{\rm p}$ calculated for various relations between $R_{\rm len}$ and $R_{\rm r}$. Here, in contrast to the conventional schemes, the dependence of $J_{\rm p}$ on the separation between the OPD and the reflector or on the form of the reflector is not critical. Hence, we can neglect the thermal and impact action of laser plasma on the reflector.

The laser pulse duration t_r is chosen taking into account the following conditions. The fraction of the energy carried away by an SW is maximal if the entire pulse energy is absorbed in the spark during a time shorter than the time $t_e \approx (q/P_0)^{1/3}$ of broadening of the laser spark, where q is the pulse energy in joules and t_e is measured in microseconds. The beam diameter at the reflector is $d_b \approx F_f$ (F_f is the focal length of the reflector and d_b is measured in cm). Hence, the mechanism of optical breakdown (light detonation wave or infrasonic radiation wave) operates over a short distance from the focus (equal to the spark length Z_p) and for a short duration t_r . Beyond this, the radiation may be absorbed in the disintegrating plasma for a certain time t_e . For a constant power W over the pulse duration, the spark

-200

Fig. 5.2 Time dependence of the force F_a and momentum $J_{\rm p}$ produced by a laser spark with energy q = 54.8 Jlocated on the cylinder axis at a distance $\Pi_{1 \text{ and } 1} = 3$ (curve 1), 16 (curve 2), and 32 cm (curve 3), acting on the side wall of the cylinder. Curve (4) was obtained for Π_{1e} = 16 cm for the reflector diameter 5 cm. The pulsation of $J_{\rm f}$ is the result of reflection of SWs at the side walls and their motion over the reflector surface



500

1000

 $t/\mu s$

length Z_p , the energy q absorbed over it, and the instant t_r of time of decay of the light detonation wave [3] are defined as follows:

$$\begin{split} Z_{\rm p} \frac{d_{\rm b}}{F_{\rm f}} &= 0.013 \left(\frac{W}{P_0}\right)^{1/2} \left\{ 1.93 + \ln P_0 + \ln \left[\left(\frac{W}{P_0}\right)^{1/2} (6.3 + \ln P_0)^{3/4} \right] \right\}^{3/4}, \\ \frac{q}{P_0} \frac{d_{\rm b}}{F_{\rm f}} &= 0.0014 \left(\frac{W}{P_0}\right)^{3/2} \left\{ 1.93 + \ln P_0 + \ln \left[\left(\frac{W}{P_0}\right)^{1/2} (6.3 + \ln P_0)^{3/4} \right] \right\}^{5/4}, \\ t_{\rm r} \frac{d_{\rm b}}{F_{\rm f}} &= 0.0014 \left(\frac{W}{P_0}\right)^{1/2} \left\{ 1.93 + \ln P_0 + \ln \left[\left(\frac{W}{P_0}\right)^{1/2} (6.3 + \ln P_0)^{3/4} \right] \right\}^{5/4}, \end{split}$$

where *W* is measured in megawatts. If the value of *q* is given, *W*, $t_{\rm r}$ and $Z_{\rm p}$ have the following values: $W=21.7(qd_{\rm f}/E_{\rm f})^{0.617}$, $t_{\rm r}=0.0455(qF_{\rm f}/d_{\rm f})^{0.381}$, and $Z_{\rm p}=0.194q^{0.352}(F_{\rm f}/d_{\rm f})^{0.648}$ at $P_{01}=1$ atm; $W=15(qd_{\rm f}/F_{\rm f})^{0.588}$, $t_{\rm r}=0.665q^{0.411}$ ($F_{\rm f}/d_{\rm f})^{0.588}$, and $Z_{\rm p}=0.357q^{0.365}(F_{\rm f}/d_{\rm f})^{0.635}$ at $P_{02}=0.1$ atm. Putting q=100 J and $P_{0}=1$ atm, we obtain $t_{\rm r}=0.263$ µs, W=372 MW and $Z_{\rm p}=1$ cm. Thus the optimal pulse duration for the LJE is 0.2–0.3 µs.

The mechanism of the merging of SW in an LJE is operative under the following conditions. SW leave the jet and merge to form a QSW if $f \geq 5.88C_0/R_d$, which is always observed in the present formulation. The OPD glowing in the gas jet transforms laser radiation into SWs if $V_{\rm g} \geq 86f^{2/3}(W_{\rm n}/P_{\rm g})^{1/3}$ (i.e., if $V_{\rm g} > 1.2 \times 10^5$ cm s⁻¹), where $V_{\rm g}$ is the velocity of the gas jet, $P_{\rm g}$ is the static gas pressure in the jet in atmospheres, f is measured in hertz, and $W_{\rm n}$ is the average laser radiation power in megawatts. The conditions of departure of an SW from the jet and demolition of the OPD plasma are met for a jet radius (in cm) $R_{\rm g} = 0.11(q/P_{\rm g})^{1/3} \approx 0.11q^{1/3}$.

The reflector array must meet the following requirements. Its transverse diameter (~ 1 m) is determined by the conditions of radiation transportation in atmosphere and the prevention of breakdown at the surface of the reflector. The reflector radius is $R_{\rm r}\approx 0.43\delta^{1/2}(q/P_{\rm g2})^{1/3}$ and the length of the sidewalls is $L_{\rm r}\sim 2R_1\approx 2a_{\rm r}R_{\rm r}$ ($a_{\rm r}=0.5-1$). Here, $\delta\approx 0.03$ is the acceptable fraction of radiation losses at the OPD plasma, and $F_{\rm g2}=0.1$ atm is the gas pressure in the jet. Note that $R_{\rm r}/R_{\rm d}\approx 1$ atm. The force $F_{\rm a}$ acting on the reflector surface and the specific force J are defined respectively as follows:

$$F_{\rm a} \approx \frac{81.4q^{0.67}P_0^{0.45}}{a_{\rm r}^{1.64}P_{\rm g2}^{0.12}\delta^{0.18}}, \quad J \equiv \frac{F_{\rm a}}{W_{\rm n}} \approx \frac{81.4 \times 10^6 P_0^{0.45}}{a^{1.64}fq^{1/3}P_{\rm g2}^{0.12}\delta^{0.18}},$$

where F_a is measured in newtons and J in N MW⁻¹. The RA is subjected to a force $F_{MR} = NF_a$.

Table 5.1 The parameters of a reflector array and monoreflector in an LJE

				•									
LJE type	×	f (kHz)	q (J)	$R_{ m r}$	R _{len}	$F_{ m al}$	F_{a2}	J_1	J_2	V_{gl}	$V_{ m g2}$	$R_{\rm g1}$	Rg2
			(cm)	(cm)	(cm)	(kN)	(kN)	$(N MW^{-1})$	$(N MW^{-1})$	(km s^{-1})	(km s^{-1})	(cm)	(cm)
Mono-reflector	1	20	1000	50	25	64	23	2600	930	1.73	3.72	1	2.4
	1	100	200	31	15	21.8	7.73	906	317	5.05	10.88	0.64	1.4
	1	100	200	31	9.5	50.1	17.78	2084	729	5.05	10.88	0.64	1.4
RA	1	100	25	15.5	5	12.5	4.45	4168	1458	2.52	5.44	0.32	0.7
	8	100	200	06	5	100^{a}	35.6^{a}	4168	1458	2.52	5.44	0.32	0.7
												l	

The duration $\tau_{\rm t}$ of the pulse trains can be estimated as the time in which the first SW in a train covers the distance from OPD to the reflector surface and back (lower estimate): $\tau_{\rm t}=4.6\times 10^{-4}q^{1/3}$. Here and below, $\delta=0.03$, $P_{\rm g2}=0.1$, $a_{\rm p}=1$. The ratio of the times $\tau_{\rm p}/\tau_{\rm t}=0.5a_{\rm p}\times L_{\rm p}/R_{\rm len}$ and their minimum value is equal to $0.5a_{\rm p}$. The pulse train frequency for one reflector is $F=2090/q^{1/3}$, their energy is $q_{\rm t}=4.63\times 10^{-4}W_{\rm n}q^{1/3}$, the average radiation power in the train is $W_{\rm m}=2W_{\rm n}/3$, and the average force in the train is $F_{\rm am}\approx 2F_{\rm a}/3$. By optimising the reflector, it is possible to increase $\tau_{\rm t}$ and the energy transformation efficiency of the laser generating the trains.

The parameters of a reflector array and monoreflector in an LJE are compared in Table 5.1. The average power supplied to the reflector array and to the monoreflector is equal to 20 MW. We did not consider the problems of optimisation of the number *N* of reflectors or the RA geometry. The RA structure should be chosen by taking into account its use for controlling the flight trajectory and

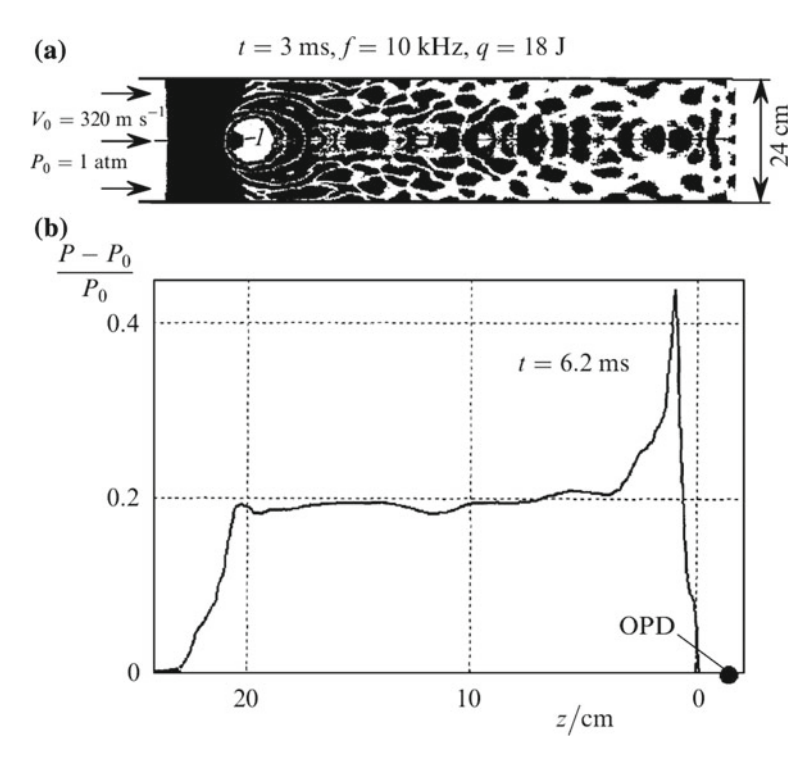
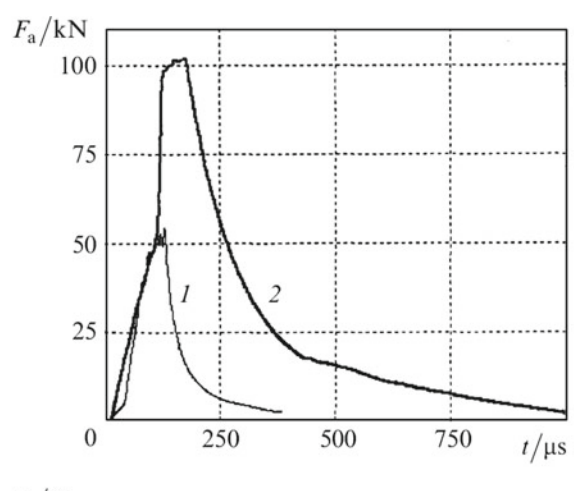


Fig. 5.3 a Air pressure field generated during an OPD burning in (1) an infinite cylinder of diameter 24 cm for an incident air flow velocity $V_0 = 320 \text{ m s}^{-1}$ and $P_0 = 1 \text{ atm}$, for a two-dimensional axially symmetric distribution of pressure at the instant t = 3 ms after the ignition of the OPD (in the dark regions $P > P_0$); and **b** distribution of excess air pressure in a QSW along the cylinder axis at t = 6.2 ms (before ignition of the next spark); the distance along the z axis is measured from the trailing edge of the QSW in the vicinity of the OPD; a plane QSW in which the pressure is independent of the distance from the cylinder axis is formed in front of the OPD

producing the required jet energy and the force of traction of the engine. The array whose data are presented in Table 5.1 contains eight spherical reflectors with cylindrical walls, and the radiation losses associated with nonoptimal 'packing' are not taken into account. Indices '1' and '2' in the notation correspond to the initial $(P_0 = 1 \text{ atm})$ and final $(P_0 = 0.1 \text{ atm})$ LJE modes. Parameters in the first two rows are calculated at various frequencies f for $a_r = R_{\rm len}/R_r = 0.5$. By reducing a_r to extremely low values (~ 0.3), high values of F_a can be attained for f = 100 kHz (3rd row in Table 5.1.). The use of radiation with a frequency f > 50 kHz is hampered in a multireflector LJE-the jet has to move at a very high velocity $(V_g \approx 5-10 \text{ km s}^{-1})$. The last two rows show the parameters for an individual reflector as well as an RA as a whole for f = 100 kHz ($a_r = 0.3$). In this case, the specific force J is much stronger while the jet velocity is lower. The values of V_g correspond to an SC velocity range during its acceleration, which facilitates the jet formation. A significant advantage of the RA is the possibility of controlling the

Fig. 5.4 Time dependences of the force F_a and mechanical momentum J_{3} produced upon collisions of a plane OSW with the end face of the cylinder 350 us after the ignition of the OPD (curve 1) and after 1950 µs when the wall is at a distance of 100 cm from the point of start of the OPD (curve 2) (the time is measured from the instant of collision). The parameters of the two-dimensional OPD are as follows: radius $R_0 = 10$ cm, layer thickness L = 1 cm, pulse energy q = 330 J, frequency f = 50 kHz, velocity of motion along the cylinder axis $V_0 = 480 \text{ m s}^{-1}$, cylinder radius $R_r = 26$ cm



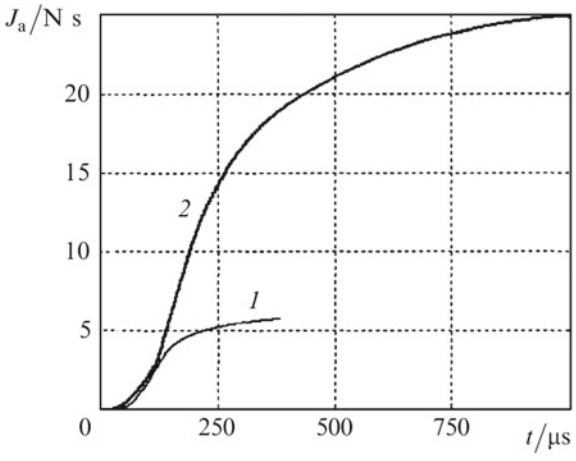
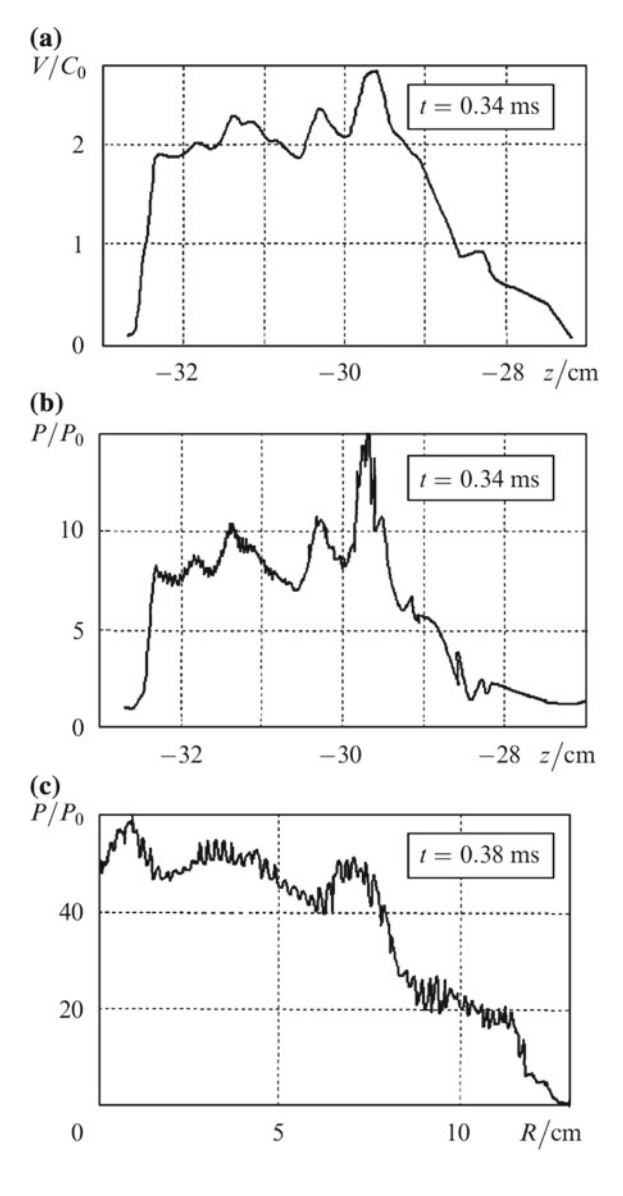


Fig. 5.5 Distribution of the gas velocity and pressure in a plane QSW along the z axis (a, b) and along the radius (c) for the instant of time before (a, b) and during collision (c) of a OSW with the end face of the cylinder. The QSW is produced by a plane OPD moving to the left with a velocity $V_0 = 830 \text{ m s}^{-1} \text{ under the}$ following conditions: $P_0 = 0.1$ atm, radius $R_0 = 8$ cm, layer thickness L = 0.5 cm, f = 50 kHz, q = 140 J. Measurements along the z axis are made from the point of start of the OPD, and R is measured from the axis



flight trajectory with the help of an LJE. For example, the variation of jet parameters in an appropriate reflector can lead to a variation of the traction force in it, thus producing a rotational moment on the RA.

The results of model calculations presented below show that the use of a plane QSW can increase the traction force J considerably and make it possible to impart energy to the supersonic gas flow. Such a wave can be formed under conditions of a point OPD in the presence of side walls and for a subsonic velocity of the OPD moving relative to the gas. Figure 5.3 shows the gas-dynamic perturbations

produced when a OPD burns in a cylinder ($R_r \approx 2R_d$). One can see that a plane QSW, in which the pressure is constant along the radius and along the direction of motion of the OPD, is formed in front of the point OPD. The specific force corresponding to an excess pressure $\delta P = 0.2$ atm is $J = F_a/W_n = 900/0.18 = 5000 \text{ N MW}^{-1}$. If a point OPD glows in a supersonic flow, the SW are carried away by the flow [7] and cannot be used for accelerating the SS.

Constraints on the gas velocity are removed under the conditions of a 'plane' OPD which is an array of synchronously pulsating point OPDs. Since there are no sidewalls between OPD, the SW generated by the OPD array merge to form a plane QSW. Calculations show that the pressure in it varies weakly over distances comparable with the characteristic size of the OPD array. Hence, such a wave can create a continuously operating traction force. Figure 5.4 shows the force F_a and the mechanical momentum J_a produced by a plane SW upon interaction with the wall. Here the plane OPD moves in a cylinder. Momentum is accumulated in the direction of propagation of the OPD as a result of interaction with the sidewalls. The specific force calculated at half-height $F_a/2$ is J = 2900 N MW⁻¹. Figure 5.5 shows the distributions of pressure and gas velocity in a plane QSW formed during the motion of a plane OPD in infinite space (along the radius) with a supersonic velocity $V_0 = 830$ m s⁻¹. The mass velocity of the gas is approximately equal to V_0 , the total pressure P is ~ 6 atm, and the specific traction force is ~ 1300 N MW⁻¹.

5.3 Conclusions

Thus, the mechanism of the merging of SW transforms laser radiation into a plane QSW which produces a steady thrust in the spacecraft. Together with an RA and a gas jet, the QSW makes it possible to increase the specific force of traction to a record-high level exceeding 2500 N MW⁻¹, prevent thermal and impact action on the reflector and shielding of the radiation by laser plasma, as well as to use high-power pulse-periodic gas-dynamic lasers generating radiation with a pulse repetition rate up to 100 kHz for LJE operation.

References

- 1. A. Kantrowitz, Astronaut. Aeronaut. **10**(5), 74 (1972)
- 2. V.V. Apollonov, High Power Lasers in Our Life (NOVA, New York, 2015)
- V.V. Apollonov, V.N. Tischenko, Proceedigs of GCL-High Power Laser Conference (Prague, SPIE, 2004)
- 4. V.N. Tishchenko, V.V. Apollonov et al., Kvantovaya Elektron. 34, 941 (2004)
- V.V. Apollonov, 3rd International Symposium on Beamed Energy Propulsion (Troy, New York, 2004)
- 6. V.V. Apollonov, V.I. Kislov, A.G. Suzdal'tsev, Kvantovaya Elektron 33, 753 (2004)
- 7. P.K. Tretyakov et al., Dokl. Ros. Akad. Nauk **351**, 339 (1996)

Chapter 6 LJE Based on the Resonance Merging of SW



6.1 Introduction

According to expert estimates, the market for commercial satellite launches for various purposes increased by 50% in 2007 compared to 2005. Taking this factor into account, investigations are being performed in developed countries on the development of new rocket engines that will provide an alternative to modern engines that operate on chemical fuel, which is often far from being ecologically faultless.

A laser jet engine (LJE) is one of the most promising new classes of rocket engines. During the initial part of its trajectory, this spacecraft engine provides thrust under the action of a long train of laser pulses directed from the Earth.

It is very important to note that the LJE is considerably more economical than traditional engines that operate on chemical fuel. At the initial stage of flight, the atmospheric air is used as the working substance. Beyond the atmosphere, the working substance is a small space-borne store of gas or easily sublimated substance. In this case, the specific cost of launching freight to outer space can be reduced down to 200–500 USD kg⁻¹, i.e., approximately by two orders of magnitude compared to the cost at present. Additionally, the possibility of maintaining orbit at a specified level with the help of the laser system used for launching is estimated to be exceptional.

At present, the possibility of building LJE is being investigated in developed countries all over the world. For example, currently such systems are being developed in the USA within the framework of the Lightcraft project. The Lightcraft Technologies Company has successfully tested a rocket model which rose to 70 m in 12.7 s under the action of a jet produced by high-powered laser radiation. A 10-kW low repetition rate pulse-periodic CO₂ laser was used in the experiments. The reactive momentum was produced by irradiating a special polymer material with the laser beam. This material was carried in a concave surface located in the lower part of the rocket.

As early as 1973, the possibility of building a LJE has been investigated by our team under the supervision of Acad. A.M. Prokhorov at the Lebedev Physics Institute, Academy of Science of the USSR. The engine unit operated by irradiating a reflector located at its rear by a laser beam. The reflector concentrated laser radiation in air, which resulted in a microexplosion that produced the reactive thrust. The tests successfully used reflectors of various types, which simultaneously served as receivers of the incident shock wave providing the thrust.

Note that all of these experiments were performed using low-power ($10~\rm kW$) electric-discharge $\rm CO_2$ lasers, whereas in order to place various high-tech equipment (e.g. for communication, Internet, photomonitoring) in orbit, a considerably higher radiation power is required. For example, to put a satellite weighing $1000~\rm kg$ in orbit, a laser with the output power of no less than $10~\rm MW$ is required. Presently, such a laser can only be gas-dynamic, because in this case the principles of laser and rocket technologies are extremely similar. In addition, to avoid the screening of laser radiation by the plasma produced during engine operation and to increase the laser operation efficiency, the laser should emit short enough pulses with a high repetition rate.

In the opinion of experts (classical rocket designers), LJE can be used in low-cost single-stage rockets for the orbital injection of nano- and microsatellites of mass 10–100 kg, on which basis commercial launches will be performed in the near future. During the first stage of flight of such an apparatus at heights up to 30–50 km, the atmospheric air can be used as the working substance and then, before orbital injection, the space-borne store of fuel in amounts not exceeding 15–20% of the satellite weight can be employed.

The experience in the development of high power/energy lasers has been accumulated at A.M. Prokhorov General Physics Institute RAS and at Energomash Research and Production Association. The repetitively pulsed regime in high power/energy and well-developed cw lasers has been successfully studied in recent years at Eneromashtekhnika Joint-Stock Company in collaboration with the General Physics Institute RAS, both of whom have made contributions to the development of the mechanism of efficient utilisation of laser energy in LJE. This allows these institutions to begin the cooperative experimental development of a superpower repetitively pulsed gas-dynamic laser, an LJE as a part of a light SiC carrier with a control system and a ground launching system with the aim of building a global super-broadband, super-high-speed laser communication space Internet network. This complex of works should become an important step preceding the future launches of superlight satellites to a low circumterrestrial orbit and even the launches of piloted spacecraft. The realisation of this project will make it possible to build economical reusable LJEs for launching civil and military payloads to outer space.

The main advantage of a new approach is that the source of motion energy and the payload are uncoupled in space, and the starting weight of a rocket can be considerably reduced, from 705 tons (Proton rocket) down to a few tons of only a payload. As early as the beginning of the 20th century, great K.E. Tsiolkovsky

6.1 Introduction 67

predicted that future rockets will be launched with the help of electromagnetic waves directed from an external energy source (lasers did not exist at that time).

Three recent symposia devoted to this problem have shown that high-powered lasers emitting 100–150-ns pulses at a pulse repetition rate of 50–100 kHz developed in our country attract great interest of foreign researchers. Such operation regimes were attained for a high-power gas-dynamic CO₂ laser and it can also be used in other high-power lasers (HF/DF lasers, diode-pumped Nd:YAG lasers, and chemical oxygen-iodine lasers). At present, a 10–20-MW gas-dynamic laser with a variable temporal structure of radiation is being developed in our country. The efficiency of using laser energy in a new lasing regime was considerably increased, which made it possible to change the estimates of payload weight from a few tens to hundreds and thousands of kilograms. Note also that the outlook for various applications have stimulated investigations in this field in Germany, Japan, England, France, China, Brazil and other countries. It is assumed by almost all researchers involved in these studies that a gas-dynamic laser is the most promising system from the point of view of its scaling based on rocket technology up to the level of a few tens of megawatts and with respect to other important parameters.

By now there exist two directions in the study of the possibility of using laser radiation in aerospace problems: the orbital injection of light spacecraft [1–9] and the reduction of aerodynamic resistance acting on bodies moving at high velocities in the atmosphere [10, 11]. To obtain jet propulsion, repetitively pulsed radiation from a laser is focused on a reflector near the rear end of a rocket to produce periodic laser sparks. The sparks generate shock waves, which transfer a part of their momentum to the reflector [1]. The spark repetition rate f is usually limited by the time of the gas change in the reflector and is about 100-300 Hz. To achieve the high average radiation power $\overline{W} \sim 20$ MW, it is necessary to use laser pulses of energy $q = \overline{W}/f \sim 200 - 70$ kJ. At low air pressures (at heights above 15 km), a long-lived plasma sphere produced by one pulse occupies almost the entire volume of the reflector (see below), resulting in the screening of subsequent pulses for approximately ~ 10 ms. The technical difficulty of this method is caused by strong shock loads and mechanical resonances appearing in the rocket structure at high pulse energies q (200 kJ) (approximately 50 g in the trotyl equivalent). In the case of short pulses ($t_r \sim 100-200$ ns) in a LJE, $\sim 95\%$ of laser pulse energy is absorbed and $\sim 30\%$ of the energy is transformed to shock waves. However, the use of high-energy beams with low repetition rates and, hence, with a very high peak power is limited by the optical breakdown in the beam path and on the reflector surface.

We proposed a method to overcome these difficulties, which is based on the use of short laser pulses with a high repetition rate [9, 12] and the resonance merging of shock waves generated by an optical pulsed discharge (OPD) [1–4]. In addition, we showed that the specific thrust can be increased by several times by transforming the radial component of the shock wave to the longitudinal component.

6.2 Parameters of a Spark in the LJE

Laser radiation was focused with a reflector, which can have the form of a hemisphere or paraboloid. Figure 5.1a (Chap. 5) presents the typical dimensions of the reflector, focusing region, one spark, and a cavern produced by the spark. The distance $F_{\rm f}$ between the focal point and reflector should be small ($F_{\rm f}/R_{\rm d} < 0.2$), which follows from the conditions to achieve a high value of recoil momentum $J(R_{\rm d})$ is the dynamic radius). To avoid the optical breakdown on the reflector and according to the radiation transport conditions, the beam diameter $d_{\rm b}$ on the reflector should be large. If the radiation intensity exceeds the optical breakdown threshold, a plasma front propagates towards the laser beam and the air is heated and ionised due to the absorption of laser radiation. Because the radiation intensity in a sharply focused beam rapidly decreases (geometrical factor), the detonation regime of the plasma front propagation is disrupted a small distance from the focus. Then, radiation is absorbed in the decaying plasma for some time. The limiting length $Z_{\rm p}$ of a laser spark in the photodetonation regime is

$$Z_{\rm p} \frac{d_{\rm b}}{F_{\rm f}} = 0.013 \left(\frac{W}{P_0}\right)^{1/2} \left\{ 1.93 + \ln P_0 + \ln \left[\left(\frac{W}{P_0}\right)^{1/2} (6.3 + \ln P_0)^{3/4} \right] \right\}^{3/4}. \tag{6.1}$$

Here, d_b [cm] is the beam diameter on the lens, F_f [cm] is the focal distance, W [MW] is the laser pulse power, and P_0 [atm] is the air pressure. If radiation is switched off at the instant t_r before the quenching of the photodetonation regime, the spark length for a given power is

$$Z_{\rm p} = 0.67 \left(\frac{F_{\rm f}}{d_{\rm b}}\right)^{2/5} \left(\frac{W}{P_0}\right)^{1/5} t_{\rm r}^{3/5}.$$
 (6.2)

By equating expressions (6.1) and (6.2), we find the instant of time at which the photodetonation regime decays:

$$t_{\rm r} \frac{d_{\rm b}}{F_{\rm f}} = 0.014 \left(\frac{W}{P_0}\right)^{1/2} \left\{ 1.93 + \ln P_0 + \ln \left[\left(\frac{W}{P_0}\right)^{1/2} (6.3 + \ln P_0)^{3/4} \right] \right\}^{5/4}$$
 (6.3)

where t_r is measured in microseconds. The specific laser radiation energy absorbed for the time t_r is

$$\frac{q}{P_0} \frac{d_b}{F_f} = 0.014 \left(\frac{W}{P_0}\right)^{3/2} \left\{ 1.93 + \ln P_0 + \ln \left[\left(\frac{W}{P_0}\right)^{1/2} (6.3 + \ln P_0)^{3/4} \right] \right\}^{5/4}.$$
(6.4)

These dependences can be approximated in the following convenient to use form:

For
$$P_0 = 1$$
 atm For $P_0 = 0.1$ atm $Z_p = 0.0336W^{0.57}F_f/d_f$, $Z_p = 0.0667W^{0.62}F_f/d_f$, (6.5)

$$t_{\rm p} = 0.0068W^{0.618}F_{\rm f}/d_{\rm f}, \quad t_{\rm p} = 0.01W^{0.7}F_{\rm f}/d_{\rm f},$$
 (6.6)

$$q = 0.0068W^{1.62}F_{\rm f}/d_{\rm f}, \quad q = 0.01W^{1.7}F_{\rm f}/d_{\rm f}.$$
 (6.7)

Here, t_p is the action time of the photodetonation regime and d_f is the threshold diameter of the absorption region at which the photodetonation regime is quenched.

By using these expressions, we estimated the parameters of a laser spark experimententally [7], where for the pulse energy q=280 J and $t_{\rm r}\sim30$ ms, we have $\overline{W}\sim10$ MW. By substituting this value into (6.5)–(6.7), we obtain for $P_0=0.1$ atm that $Z_{\rm p}=0.28$ cm, $t_{\rm r}=0.05$ μ s, and q=0.5 J and for $P_0=1$ atm that $Z_{\rm p}=0.12$ cm, $t_{\rm r}=0.028$ μ s, and q=0.238 J. It follows from this data that for $\overline{W}\sim10$ MW the photodetonation regime cannot provide efficient absorption of laser pulses. At low intensities, the regime of a subsonic radiation wave also does not exist. In this case, the mechanism of a slow combustion wave, whose propagation velocity is too small (a few tens of metres per second), also probably does not act. It is possible that radiation was absorbed due to the successive action of optical breakdown in the focus, a photodetonation wave, a subsonic radiation wave, and bremsstrahlung absorption in the expanding plasma for ~15 μ s.

Let us find the optimal values of W and t_r for the absorbed energy q. The corresponding expressions are obtained from (6.5)–(6.7):

For
$$P_0 = 1$$
 atm For $P_0 = 0.1$ atm $W = 21.7(qd_f/F_f)^{0.617}$, $W = 15(qd_f/F_f)^{0.588}$, (6.8)

$$t_{\rm r} = 0.0455 (qF_{\rm f}/d_{\rm f})^{0.381}, \quad t_{\rm r} = 0.0665 q^{0.411} (F_{\rm f}/d_{\rm f})^{0.588},$$
 (6.9)

$$Z_{\rm p} = 0.194 q^{0.352} (F_{\rm f}/d_{\rm f})^{0.648}, \quad Z_{\rm p} = 0.357 q^{0.365} (F_{\rm f}/d_{\rm f})^{0.635}.$$
 (6.10)

The numerical values of these parameters for $d_{\rm f}/F_{\rm f}=1$ and different values of P_0 and q are presented in Table 6.1.

Table 6.1 The	e numerical valu	ies of basic par	ameters for $d_{\rm f}$	$/F_{\rm f}=1$ and di	fferent values	of P_0 and q
q/J	$P_0 = 0.1 \text{ atm}$			$P_0 = 1$ atm		
	137/1/1/37	7 lom	t luc	147/N/ISX7	7 lom	t luc

q/J	$P_0 = 0.1 \text{ a}$	tm		$P_0 = 1$ atm	$P_0 = 1$ atm		
	W/MW	$Z_{\rm p}$ /cm	t _r /μs	W/MW	$Z_{\rm p}$ /cm	$t_{\rm r}/\mu{ m s}$	
10	58.1	0.83	0.17	90	0.44	0.11	
100	225	1.97	0.439	372	0.98	0.263	
1000	873	4.52	1.13	1540	2.21	0.63	
280 [7]	411	2.86	0.665	702	1.41	0.39	

Thus, of principal interest for LJE are pulses of duration $\sim 0.2~\mu s$. The laser pulse energy is limited by the condition of radiation transport without losses: $q=\pi D_{\rm r}^2 q_{\rm b}/4\approx 15-40~{\rm kJ}$. It is assumed here, based on the condition of a weak divergence of radiation at long paths from a radiation source to a reflector, that the beam diameter is $D_{\rm r}=100~{\rm cm}$ [1] and $q_{\rm b}\approx 2-5~{\rm J}$ cm⁻² is the threshold energy density (the laser wavelength is $10.6~\mu m$) above which emission is observed in the atmosphere and acoustic effects appear, which are caused by the heating of aerosols [14]. The optical breakdown threshold in a gas on aerosols is $10-50~{\rm J}~{\rm cm}^{-2}$ depending on their concentration and size (in wide-aperture beams). Therefore, the conditions of energy transport and absorption in sparks allow the use of repetitively pulsed laser radiation with the average power of $\overline{W}\approx 20~{\rm MW}$, or more specifically, short laser pulses with a high pulse repetition rate.

The maximum laser pulse energy is limited by the condition of obtaining a high efficiency use of laser radiation for producing thrust. The momentum carried by a shock wave in a free gas is nonzero only at small distances from the explosion centre [14]. The specific momentum for a parabolic reflector is maximal $(J_1 \sim 550 \text{ N s J}^{-1})$ at the distance R_1 , for which $R_1/R_d \sim 0.1$, where $R_d = 2.15(q/P_0)^{1/3}$ is the dynamic radius (the dimensional units cm, J, and atm are used). As the ratio R_1/R_d increases from ~ 0.1 to 0.33, the value of J_1 decreases from ~ 550 down to 200 N s J^{-1} .

The possibility of using small values of R_1/R_d in LJEs is limited by the formation of long-lived plasma with the characteristic radius comparable to the reflector size. At the late stages of the thermal expansion of a spark, a cavern is formed with a low density ($\rho \ll \rho_0$) and a high temperature (~ 8000 K) of the ionised gas. The movement of the contact boundary of a hot region ceases when pressure in the cavern and surrounding gas are equalised. In the spherical spark approximation, the cavern radius $R_{\rm cav}$ during the equalisation of pressures can be obtained from the expressions

$$\frac{R_{\text{cav}}}{R_{\text{d}}} = \frac{0.49r_0^{0.29}}{(q/P_0)^{0.097}},\tag{6.11}$$

$$\frac{t_{\text{cav}}}{t_d} \approx 0.374. \tag{6.12}$$

Here, r_0 [cm] is the initial radius of the spark, $t_d = R_d/C_0$ is the dynamic time, and C_0 is the speed of sound. By setting $r_0 \approx Z_p/2$, from (6.11) we obtain the estimate for the cavern radius for the entire pressure range $P_0 = 0.1-1$ atm:

$$R_{\rm cav}/R_{\rm d} \approx 0.25(F_{\rm f}/d_{\rm f})^{0.19} \approx 0.15 - 0.25.$$
 (6.13)

One can see from (6.13) that the ratio $R_{\text{cav}}/R_{\text{d}}$ is independent of the gas energy and pressure; its value being in the range of values of R_1/R_{d} where the maximum specific recoil momentum produced by the shock wave is achieved. For a

hemispherical reflector, the maximum of the specific momentum J_1 is achieved for $R_1/R_{\rm d}\approx 1$, its value is, however, small ($J_1<250~{\rm N~s~J^{-1}}$). In this case, the plasma size is smaller than the reflector size.

Let us examine the cavern radius and its formation time for the laser energy $q = 10^5$ J and pressures $P_0 = 1$ and 0.05 atm. The average power of the laser is $\overline{W} = 2 \times 10^7$ W and the pulse repetition rate is f = 100 Hz. We consider the start stage of a spacecraft and the end of its acceleration stage in the LJE regime (for higher parameters of the laser, the ablation regime begins). For $P_0 = 1$ atm, we have $R_{\text{cav}} = 15-25$ cm and $t_{\text{cav}} = 1.1$ ms, and for $P_0 = 0.1$ atm $-R_{\text{cav}} = 32-54$ cm and $t_{\text{cav}} = 2.36$ ms. If $t > t_{\text{cav}}$, the laser plasma is cooled due to its turbulent mixing with a cold surrounding gas. The characteristic time of this process is more than an order of magnitude exceeds t_{cav} from [15–17].

We considered here a spherical spark. However, real sparks in LJEs have a conical shape with a large cone angle, which makes the situation even worse. Under certain conditions at the late stage of spark expansion, a cumulative jet can be formed [18, 19] in which a gas moves to the cone base (in our case, to the reflector). The plasma shape is no longer simply connected and resembles a torus. Thus, in the case of the maximum radiation pulse, the plasma contacts the reflector surface, which can result in damage of the reflecting layer. To reduce the gas-replacement time in the reflector, we proposed the use of an air jet. However, this does not solve the problem of the negative action of a large plasma sphere on the environment.

6.3 Mechanism of the Resonance Merging of SW in a LJE

The resonant merging of individual shock waves into a low-frequency quasi-stationary wave occurs generally as follows. Shock waves with an initial velocity greater than the speed of sound C_0 are produced successively in a continuous medium. The propagation velocity V_0 of the pulsation region is lower than C_0 . Shock waves merge to produce a quasi-stationary wave if the parameters of pulsation and the medium satisfy certain criteria. Depending on the spatiotemporal structure of pulsations, this merging is characterised by a number of properties, principal of which is a long length of the high-pressure region. The wave-merging mechanism imposes no restrictions on the type of a medium, pulsation source, and its energy. Depending on the structure of pulsations, the quasi-stationary wave may have different shapes.

We will show that the merging of the waves into a quasi-stationary wave solves the above-considered problems of radiation screening and thermal action of the laser plasma in a LJE. In addition, the quasi-stationary wave allows one to considerably increase the efficiency of using laser radiation due to an increase in the specific thrust (per unit power). Let us estimate the laser pulse energy and pulse repetition rate required for solving this problem. We will consider two methods based on the use of a spherical and 'planar' OPD. In both cases, a plane

quasi-stationary wave is formed by using both the OPD and reflector geometry and also by a proper coupling of the laser radiation energy.

Thus, the merging of shock waves into a quasi-stationary wave provides the reduction of the laser pulse energy, thereby solving the problem of a large size $R_{\rm cav}$ of the plasma, because for the pulse energy $\sim 1000~{\rm J}$ and a high pulse repetition rate, the transverse dimensions of plasma (caverns) of the OPD are small compared to the reflector diameter; the plasma itself is drawn out from the reflector by a jet injected to the central part of the reflector. In addition, the quasi-stationary wave and the engine geometry used allow the introduction of the laser radiation energy into a gas away from the reflector surface, which removes the problem of screening and thermal action; also, the specific thrust (recalculated to the average radiation power unit) increases.

6.4 Spherical OPD

In the general case a reflector has the shape a cylinder of length $L_{\rm r}$, whose end is a receiver of repetitively pulsed laser radiation focused on the cylinder axis. The radiation intensity in the focus exceeds the optical breakdown threshold $q_{\rm b}$ in the atmospheric air. The value of $q_{\rm b}$ depends on the size and concentration of aerosol particles in the atmosphere and is 20–50 J cm⁻² [13] for 1-µs pulses. A gas jet injected through the reflector end has a high velocity and is used for discharging the OPD plasma (the radius of caverns does not exceed the jet radius) and providing the efficient conversion of laser radiation to shock waves. The jet can be formed with the help of an air collector. The cylinder walls transform the spherical shock waves' radial component of momentum into the longitudinal direction.

On the reflector, the input trains of laser pulses producing an OPD are incident. The train repetition rate F depends on the gas-replacement time in the reflector. The pulses in a train have a high (tens of kilohertz) repetition rate at which individual shock waves merge to produce an extended region of elevated pressure—a quasi-stationary wave. Such a wave in a free gas would have a spherical shape and pressure in it would rapidly decrease as its leading edge moves away from the OPD. In the limited space and for a certain relation between the reflector size and the OPD power, constant pressure appears to act for a time that is no shorter than the laser pulse train duration. The negative excess pressure on the receiving reflector and the force produced by it, which decelerates a spacecraft, can appear only after switching off radiation during the replacement of the heated gas by the atmospheric air. Unlike the case of a spherical or cylindrical explosion, the negative momentum of the unloading phase of a plane shock wave is small [14].

Let us estimate the parameters of a LJE of the required power for the acceleration scheme of a spacecraft described above. We assume that the pulse energy q is given. It is necessary to determine the optimal parameters of the reflector, jet, the pulse repetition rate in trains, and the train repetition rate. We assume that the

73

average laser radiation power required for placing light spacecrafts in orbit is $\overline{W} \approx 10 - 20$ MW.

We will also take into account that, to avoid a decrease in the average power of a gas-dynamic laser, laser radiation should be modulated at a frequency of no less than 20 kHz. This imposes the restriction $q < 10^3$ J on the laser pulse energy. To avoid optical breakdowns in the path and on the reflector, the characteristic radius R_r of the reflector should be 30–50 cm.

Earlier [1–3], we found the conditions under which a pulsed source of shock waves (for example, an OPD) produces the extended region of elevated pressure—a quasi-stationary wave. The length of this wave considerably exceeds the length of the compression phases of shock waves from which it is formed. The source of waves can be immobile or can move at a subsonic speed. The OPD in a LJE is immobile and burns in the focus of laser radiation. In the absence of walls, such a discharge can produce a spherically symmetric quasi-stationary wave. Due to reflection of the latter from the walls, the radial component of its momentum is partially transformed to the longitudinal component. An excess pressure is established over the entire volume of the cylinder. The geometry of the problem then becomes approximately the case of a one-dimensional plane explosion at which the recoil momentum is maximal. The reflecting part of the reflector, which also serves as a receiver of the recoil momentum, is subjected to a force which weakly changes during the action of the laser pulse train.

The OPD produces a quasi-stationary wave when the conditions of stable generation of shock waves and the merging of their train are fulfilled. In the general case these conditions are

$$2.5M_0 > f^0 > 5.88(1 - M_0)^{1.5}, (6.14)$$

where $M_0 = V_0/C_0$ is the dimensionless velocity of the OPD propagation in a free gas along some line and $f^0 = ft_d$ is the dimensionless pulse repetition rate. The left-hand side of (6.14), which restricts the region of stable generation of shock waves, can be written in the form

$$f_{\rm p} = \frac{V_{\rm J}}{2R_{\rm cav}} = \frac{2.5V_{\rm J}}{R_{\rm d}} \left(\frac{P_{\rm J}}{P_0}\right)^{1/3}.$$
 (6.15)

Here, P_0 is the air pressure in the reflector at the beginning of the action of the laser pulse train and $P_{\rm J}$ and $V_{\rm J}$ are the static pressure and velocity of a gas in the jet where the OPD is burning. If the laser pulse repetition rate is equal to the limiting frequency $f_{\rm p}$ of generation of shock waves or lower, the laser plasma is carried out from the focal region during the period between pulses. Each spark is produced in a fresh gas, and the OPD transforms $\sim 30\%$ of the laser radiation energy to periodic shock waves.

The OPD burns in the jet, and the shock waves generated by the OPD merge into a quasi-stationary wave in the surrounding air, which can be considered immobile

with respect to the OPD. Therefore, $M_0 = 0$ in the right-hand side of (6.14), and the condition of shock-wave merging can be written in the form

$$f_{\rm q} = 5.88C_0/R_{\rm d},\tag{6.16}$$

where f_q is the OPD frequency at which the quasi-stationary wave is established. Thus, the conditions for the efficient conversion of laser radiation to shock waves and their merging to quasi-stationary waves can be written in the form

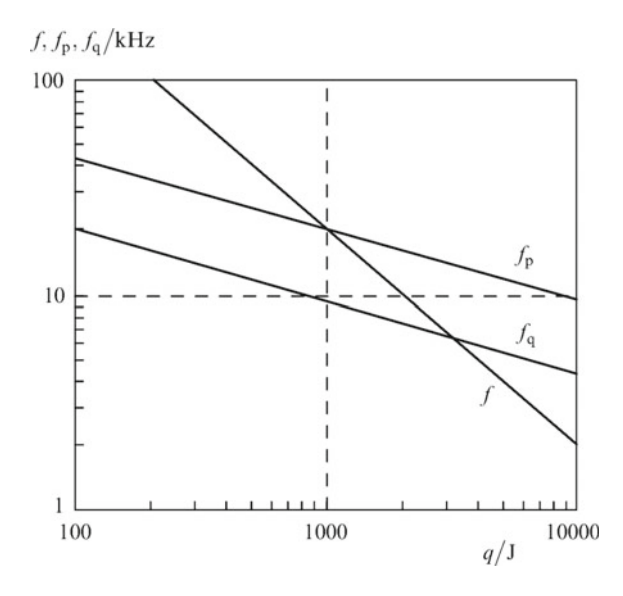
$$f_{q} < f < f_{p}.$$
 (6.17)

Here, the laser pulse repetition rate is

$$f = \overline{W}/q. \tag{6.18}$$

Figure 6.1 shows the dependences (6.15), (6.16), and (6.18) for $\overline{W}=20$ MW. According to (6.17), the working range of the q and f values is limited by a part in curve (6.18) between the intersection points with curves f_p and f_q . The values of f_p and f_q depend on the laser pulse energy, gas pressure in the reflector and jet, and the jet velocity V_J ; note that the gas pressure and jet velocity can change during the acceleration of a spacecraft. This ambiguity in the choice of radiation parameters can be eliminated in the following way. Let us assume that the air pressure at the start of the spacecraft is $P_0 = P_{01}$. As the height and velocity of the flight increase, the values of P_0 and P_J decrease and $P_0 = P_{02}$ at the end of the LJE action. We assume for the convenience of precision that $P_0 = 1$ atm and $P_{02} = 0.1$ atm. Because $f_p \sim P_J$ and $f_q \sim P_0$, curves f_p and f_q in Fig. 6.1 are displaced downwards

Fig. 6.1 Conditions of the merging of shock waves into a quasi- stationary wave for the average OPD power $\overline{W}=20$ MW, laser pulse repetition rate $f=\overline{W}/q=20$ kHz and gas pressure $P_0=0.1$ atm



with increasing height. We will consider the part of the curve f between its intersection points with the curve f_q for $P_{01} = 1$ atm and curve f_p for $P_{02} = 0.1$ atm as the working range of q and f. In this case, the boundary values of q and f are

$$q_{\text{max}} = \frac{2.2 \times 10^8}{P_{01}^{1/2}} \left(\frac{\overline{W}}{C_0}\right)^{3/2} = 35\overline{W}^{3/2},$$

$$f_{\text{min}} = 4.52 \times 10^{-3} C_0^{3/2} \left(\frac{P_{01}}{\overline{W}}\right)^{1/2} = \frac{28.3 \times 10^3}{\overline{W}^{1/2}},$$
(6.19)

$$q_{\min} = \frac{8 \times 10^8}{P_{\text{J}2}^{1/2}} \left(\frac{\overline{W}}{V_{\text{J}2}}\right)^{3/2},$$

$$f_{\max} = 1.25 \times 10^{-3} V_{\text{J}2}^{3/2} \left(\frac{P_{\text{J}2}}{\overline{W}}\right)^{1/2}.$$
(6.20)

The average power \overline{W} in (6.19) and (6.20) is expressed in megawatts. Let us take into account the restriction $f \approx 20$ kHz imposed on the minimal pulse repetition rate in a gas-dynamic laser. By replacing $f_{\rm max}$ by f we find the gas jet velocity at the final acceleration stage of the spacecraft to be:

$$V_{\rm J2} = 86f^{2/3} \left(\frac{\overline{W}}{P_{\rm J2}}\right)^{1/3};\tag{6.21}$$

the corresponding limiting frequency is

$$f_{\rm p} = 100 f^{2/3} \left(\frac{\overline{W}}{q}\right)^{1/3}.$$
 (6.22)

The pulse repetition rate and energy can have arbitrary values between their minimum and maximum values. The jet velocity $V_{\rm J}$ can always be selected so that the OPD plasma will be carried out from the focal region during the period between pulses. However, as q increases, the diameter of the gas jet and plasma trace also increases, resulting in the screening of radiation on the path to the reflector, making it necessary for an unacceptably large diameter of the reflector. The velocity $V_{\rm J}$ can be found from (6.21) by replacing $P_{\rm J2}$ by $P_{\rm J}$, which depends on the current value of $P_{\rm 0}$. By assuming that $\overline{W}=20$ MW and $f=2\times 10^4$ Hz, we obtain $V_{\rm J}=1.73\times 10^5$ and 3.7×10^5 cm s⁻¹ for $P_{\rm J}=1$ and 0.1 atm, respectively. Here, $V_{\rm J}$ is the jet velocity in the combustion zone of the OPD located at a distance $R_{\rm I}\sim (1-2)R_{\rm d}$ from the nozzle that the jet is issued from. Therefore, the total pressure in the jet should considerably exceed the pressure in the reflector. The velocity $V_{\rm J}$ is related to the quasi-stationary pressure $P_{\rm br}$ upon deceleration of the gas flow by the expression

$$V_{\rm J} = \frac{2C_{\rm J}}{\gamma - 1} \left[\left(\frac{P_{\rm br}}{P_{\rm J}} \right)^{(\gamma - 1)/\gamma} - 1 \right]^{1/2}.$$
 (6.23)

By assuming that $P_{\rm br} \sim 2P_{\rm r} \sim 4P_0$, $P_{\rm J} = P_0$, the speed of the jet is $C_{\rm J} \approx 3.4 \times 10^4~{\rm cm s^{-1}}$, and the adiabatic parameter is $\gamma = 1.4$, we obtain $V_J = 1.19 \times 10^5~{\rm cm~s^{-1}}$ ($P_{\rm r}$ is the gas pressure after the OPD is switched on). This value is lower than that required for maintaining a stable generation of shock waves.

The jet radius should satisfy two opposing requirements: on the one hand, it should be sufficiently large compared to $R_{\rm cav}$ to provide the removal of the OPD plasma from the reflector, and on the other, the condition $R_{\rm J} \ll R_{\rm cav}$ should be fulfilled, because otherwise a great part of the energy of shock waves will be removed by the supersonic jet and will not enter the surrounding gas. The latter follows both from the geometric factor and the condition that the shock wave should have an intensity allowing for its propagation through the jet-immobile gas interface without losses. These conditions can be satisfied simultaneously when the cavern and jet radii are related by the expression

$$R_{\rm J} = 0.3R_{\rm cav} = 0.05R_{\rm dJ} = 0.11(q/P_{\rm J})1/3 \,[{\rm cm}],$$
 (6.24)

where $R_{\rm dJ}$ is the dynamic radius of the jet.

In this case, optical breakdowns occur in the jet and the plasma being formed expands outside of the jet. In the case of a high longitudinal component of the velocity, the plasma located outside the region of radius $R_{\rm J}$ also will be carried away from the reflector. Upon acceleration of the spacecraft, pressures $P_{\rm 0}$ and $P_{\rm J}$ decrease. In the pressure range $P_{\rm J}=1-0.1$ atm for a fixed value of $q_{\rm J}$ the value of $R_{\rm J}$ should increase approximately twofold. Otherwise the high-velocity jet will remove not only the OPD plasma but also the shock waves generated by it. To avoid this, either the parameters of the jet and radiation should be changed according to (6.24) or all of the parameters should be fixed by maintaining $P_{\rm J}$ at the level of 1 atm (by using an appropriate air collector).

In experiments [11, 20], the OPD burned in a jet flowing out into immobile air. The radii of caverns and the plasma jet were ~ 2 mm, while the gas jet radius was varied from 1.5 to 3 mm. In these experiments, which were performed at velocities $V_{\rm J} < 500~{\rm m~s}^{-1}$, no effect of $R_{\rm J}$ on the generation of shock waves was observed. Note, however, that sparks had the shape of a cone with the length exceeding the diameter of its base by approximately a factor of five.

The jet structure strongly changes under the action of the OPD. Two limiting cases can be considered. If $f \ll f_{\rm p}$, traces consist of the isolated regions of the decaying laser plasma. For $f \approx f_{\rm p}$, the OPD forms a continuous plasma jet with the limiting velocity (with respect to the reflector) $V_{\rm p} \approx V_{\rm J} + C_{\rm p}$ [21–23]. For a high energy density absorbed in a spark, the sound speed in the plasma is $C_{\rm p} \approx (2-3) \times 10^5$ cm s⁻¹. Also note that away from the OPD (at a distance of ~ 2 m), the jet radius can increase up to $\sim 2R_{\rm cav}$. This is caused by its slowing down and turbulent cooling after the end of adiabatic expansion (for $t > t_{\rm q}$). At this stage, the

4 Spherical OPD 77

gas temperature decreases from $\sim 8000~\mathrm{K}$ to ambient temperatures and the density is restored.

Based on the transverse size of the jet, radiation power losses in the laser plasma can be determined:

$$\delta \overline{W} = \frac{R_{\text{cav}}^2}{R_{\text{r}}^2} = \frac{0.04R_{\text{dJ}}^2}{R_{\text{r}}^2} = \frac{0.185(q/P_{\text{J}})^{2/3}}{R_{\text{r}}^2}.$$
 (6.25)

Let us find the reflector radius, by assuming that some level of losses, for example, δW is the limiting admissible level:

$$R_{\rm r} = \frac{0.2R_{\rm dJ}}{\delta W^{1/2}} = \frac{0.43(q/P_{\rm J2})^{1/3}}{\delta W^{1/2}}.$$
 (6.26)

For $\delta W \approx 0.03$, $P_{\rm J} = 0.1$ atm, and q = 1000 J, the reflector radius is $R_{\rm r} = 53$ cm. It is obvious that for $P_{\rm J} \sim 1$ atm, $R_{\rm r}$ will be approximately half this value; however, its value should be the same as at the end of the acceleration stage of the spacecraft. Note that the value $R_{\rm r} \sim 50$ cm also satisfies the conditions of radiation transport.

Let us determine the accelerating force produced by the OPD on the reflector shown in Fig. 6.1. The principal difference of our approach from other known LJE schemes with low optical breakdown repetition rates is that the OPD produces a quasi-stationary wave occupying the entire volume of a cylinder. Thus, we are dealing with a planar geometry of the problem in which the specific recoil momentum is maximal, whereas the negative excess pressure is minimal. The excess pressure $\delta P = P - P_0$ on the cylinder end, the force F_a acting on the end, and the specific thrust F_a/\overline{W} are

$$\delta P = P_0 (R_{\rm d}/R_{\rm sp})^{1.64} [atm],$$
 (6.27)

$$F_{\rm a} = \pi R_{\rm r}^2 \delta P,\tag{6.28}$$

$$F_{\rm a}/\overline{W} = \pi R_{\rm r}^2 \delta P/(q\overline{W}),\tag{6.29}$$

where $R_{\rm sp}$ is the distance between the OPD and cylinder walls, which is approximately equal to the focal distance of the reflector. Let us assume that $R_{\rm sp} = a_{\rm r}R_{\rm r}$, where $a_{\rm r} = 0.5-1$. Note that the ratio of the reflector radius to the dynamic radius for $P_0 = P_{01} = 1$ atm is close to unity:

$$\frac{R_1}{R_{\rm d1}} = \frac{0.2}{\delta W^{1/2}} \left(\frac{P_{01}}{P_{\rm J2}}\right)^{1/3}.$$
 (6.30)

For $P_0 = P_{01} = 1$ atm, we obtain the ratios $R_r/R_{d1} = 1.15$ and 2.47 for two different pressures of the jet $P_{J2} = 1$ and 0.1 atm. This means that if $R_1 \approx R_r$, the pressure on the reflector end can be considered uniformly distributed and described by expression (6.27). This is all the more true because a shock weave reflected from

the cylinder side will act on the periphery of the reflector. The excess pressure is constant or grows during the pulse train:

$$\delta P = 14 P_0^{0.45} P_{J2}^{0.55} \frac{(\delta W)^{0.82}}{a^{1.64}} \text{ [atm]}.$$
 (6.31)

The force acting on the reflector is

$$F_{\rm a}[{\rm N}] = 10\pi R_{\rm r}^2 P_0 \left(\frac{R_{\rm d}}{aR_{\rm r}}\right)^{1.64} = 10\pi R_{\rm r}^{0.36} P_0 \left(\frac{R_{\rm d}}{a}\right)^{1.64}.$$
 (6.32)

The specific force (per 1 MW of the average power) is

$$J[\text{NMW}^{-1}] = \frac{F_a}{\overline{W}} = \frac{192 \times 10^6 P_0^{0.45}}{a^{1.64} f q^{1/3}}.$$
 (6.33)

In the simplest LJE scheme, a spacecraft is accelerated under the action of laser pulse trains following with the repetition rate F. The repetition rate of laser pulses in trains is $f \gg F$. Each laser pulse train produces the OPD, which in turn generates a train of shock waves merging into a quasi-stationary wave. The air in the reflector heats up considerably within a time τ_t and its density decreases. As a result, further input of laser radiation can be inefficient. After switching off radiation, the gas in the reflector is replaced by cold atmospheric air. The duration of this process is $\tau_p \sim a_p L_r/C_0$. Here, $a_p \approx 1-2$ is a coefficient depending on the geometry of the reflector and spacecraft and the velocity of the latter. The minimal duration τ_t , of the train is equal to the time for a shock wave produced by the first spark of the train to propagate along the distance from the OPD to the reflector and back:

$$\tau_{\rm t} = \frac{2R_{\rm 1}}{C_0} = \frac{2R_{\rm r}}{C_0} = \frac{0.86}{C_0 \delta^{1/2}} \left(\frac{q}{P_{12}}\right)^{1/3} = 4.63 \times 10^{-4} q^{1/3}. \tag{6.34}$$

Hereafter, it is assumed in final expressions that the admissible screening level of radiation is $\delta=0.03$, the pressure in the jet at the end of the shock-wave amplification regime is $P_{\rm J2}=0.1$ atm, and $a_{\rm p}=1$. The ratio of characteristic times $\tau_{\rm p}/\tau_{\rm t}=0.5a_{\rm p}L_{\rm p}/R_1$ achieves the minimal value $0.5a_{\rm p}$ when the OPD burns on the open end of the cylinder. The average value of the accelerating force is

$$\overline{F}_{a} = F_{a} \frac{1}{1 + \tau_{p} / \tau_{t}} = \frac{2}{3} F_{a}.$$
 (6.35)

The train repetition rate F, their energy $q_{\rm t}$, and average power \overline{W} are

$$F = \frac{3.95 \times 10^4 \delta^{1/2}}{1 + 0.5 a_{\rm p}} \left(\frac{P_{\rm J2}}{q}\right)^{1/3} \approx \frac{2090}{q^{1/3}},\tag{6.36}$$

6.4 Spherical OPD 79

$$q_{\rm t} = \overline{W}\tau_{\rm t} = \frac{0.86\overline{W}}{C_0\delta^{1/2}} \left(\frac{q}{P_{\rm J2}}\right)^{1/3} = 4.63 \times 10^{-4}\overline{W}q^{1/3},\tag{6.37}$$

$$\overline{W} = q_{t}F = \frac{\overline{W}}{1 + \tau_{p}/\tau_{t}} = \frac{\overline{W}}{1 + 0.5a_{p}} = \frac{2}{3}\overline{W}.$$
(6.38)

Note that these relations were obtained for the lower bound of the minimal duration of the train. The results of preliminary calculations show this value can be increased by several times due to the properties of the quasi-stationary wave and geometry of the reflector–receiver of the recoil momentum.

6.5 LJE Parameters in the Monoreflector Scheme

Let us determine the LJE parameters by using the model considered above. We assume that the average power of laser pulse trains is 20 MW, the air pressure at the start of a spacecraft is $P_0 = P_{01} = 1$ atm, and $P_0 = P_{02} = 1$ atm at the end of the LJE operation. In addition, we assume that the static pressure in the jet is equal to the surrounding air pressure ($P_J = P_0$).

The obvious advantages of the scheme considered above compared to traditional methods are a higher efficiency of utilising laser radiation and the absence of laser-plasma contact with the optical surface of the reflector and the absence of laser radiation screening. In addition, this scheme is technologically simple. For $\overline{W}\approx 20$ MW, the following laser parameters are optimal: the pulse energy q=1 kJ, the pulse repetition rate f=20 kHz, the duration of laser pulse trains $\tau_t=5$ ms, and the train repetition rate F=200 Hz. However, gas-dynamic lasers can efficiently generate pulses with a pulse repetition rate of f>50 kHz [9]. In this case, the velocity of a gas jet injected to the reflector proves to be too high for technical realisation in model experiments on a test stand.

6.6 Array Reflector

An array reflector is shown schematically in Fig. lb. All parameters (with the subscript m) in the expressions presented below refer to one reflector of the array; then, the number N of elements is summed $[R_{\rm cav}/R_{\rm d}\approx 0.25(F_{\rm f}/d_{\rm f})^{0.19}\approx (0.15-0.25)R_{\rm cav}{}_m=R_{\rm cav}/N^{1/3}]$:

$$f_{pm} = \frac{V_{Jm}}{2R_{cav\,m}} = \frac{2.5V_{Jm}}{R_{dm}} \left(\frac{P_{Jm}}{P_0}\right)^{1/3} = f_p N^{1/3},$$
 (6.39)

$$f_{qm} = 5.88C_0/R_{dm} = f_q N^{1/3},$$
 (6.40)

$$f_{q} < f < f_{p}$$
. (6.41)

Here, the laser pulse repetition rate is

$$f_m = \overline{W}_m / q_m = f, \tag{6.42}$$

$$q_{\max m} = \frac{2.2 \times 10^8}{P_{01}^{1/2}} \left(\frac{\overline{W}_m}{C_0}\right)^{3/2} = \frac{q_{\max}}{N^{3/2}},$$

$$q_{\min m} = \frac{8 \times 10^8}{P_{12m}^{1/2}} \left(\frac{\overline{W}_m}{V_{12m}}\right)^{3/2} = \frac{q_{\min}}{N^{3/2}},$$
(6.43)

$$f_{w \max m} = 1.25 \times 10^{-3} V_{\text{J}2m}^{3/2} \left(\frac{P_{\text{J}2m}}{\overline{W}_m} \right)^{1/2} = N^{1/2} f_{w \max}.$$
 (6.44)

In these expressions and below, the average power is given in megawatts. Let us take into account the restriction $f \approx 20$ kHz on the minimal pulse repetition rate in a gas-dynamic laser. By equating this value of f to $f_{w \text{ max}}$, we find the velocity of the gas jet at the final acceleration stage of the spacecraft:

$$V_{J2m} = 85f^{2/3} \left(\frac{\overline{W}_m}{P_{12m}}\right)^{1/3} = \frac{V_{J2}}{N^{1/3}}.$$
 (6.45)

By substituting $V_{\rm J2}$ into (6.39), we obtain

$$f_{\rm pm} = 100 f^{2/3} \left(\frac{\overline{W}_m}{q_m}\right)^{1/3} = f_{\rm p}.$$
 (6.46)

Here, f is the fixed value of the laser pulse repetition rate and q is the argument of the function $f_{\rm D}$ shown in Fig. 6.1. The jet velocity is

$$V_{\rm J} = \frac{2C_{\rm J}}{\gamma - 1} \left[\left(\frac{P_{\rm brm}}{P_{\rm Jm}} \right)^{(\gamma - 1)/\gamma} - 1 \right]^{1/2}, \tag{6.47}$$

$$R_{\text{J}m} = 0.3 R_{\text{cav}\,m} = 0.05 R_{\text{dJ}m} = 0.11 (q_m/P_{\text{J}m})^{1/3} [\text{cm}] = R_{\text{J}}/N^{1/3}.$$
 (6.48)

The losses of the average radiation power in the laser plasma in the mth element of the reflector are

6.6 Array Reflector 81

$$\overline{\delta}_m = \frac{R_{\text{cav}\,m}^2}{R_{rm}^2} = \frac{0.04R_{\text{dJ}m}^2}{R_{rm}^2} = \frac{0.185(q_m/P_{\text{J}m})^{2/3}}{R_{rm}^2}.$$
(6.49)

Let us determine the reflector radius assuming that the level of losses $\delta W = 0.03$ is the limiting admissible level:

$$R_{\rm rm} = \frac{0.2R_{\rm dJm}}{\delta_{m}^{1/2}} = \frac{0.43(q_m/P_{\rm J2m})^{1/3}}{\delta_{m}^{1/2}} = \frac{R_{\rm r}}{N^{1/3}},\tag{6.50}$$

where δ_m are radiation losses in the laser plasma per element of the array reflector. For a square array reflector, half of the square side is

$$R_M = R_{\rm rm} N^{1/2} = R_{\rm r} N^{1/6}$$
.

The excess pressure producing the accelerating thrust is

$$\delta P = P_0 (R_d/R_1)^{1.64} [atm],$$
 (6.51)

$$F_{a} = \pi R_{r}^{2} \delta P,$$

$$\frac{F_{a}}{\overline{W}} = \frac{\pi R_{r}^{2} \delta P}{W},$$
(6.52)

$$\frac{R_{\rm rm}}{R_{\rm d1m}} = \frac{0.2}{\delta^{1/2}} \left(\frac{P_{01m}}{P_{\rm J2m}}\right)^{1/3} = \frac{R_{\rm r}}{R_{\rm d1}},\tag{6.53}$$

$$\delta P_m = 14 P_{0m}^{0.45} P_{\text{J2}m}^{0.55} \frac{\delta^{0.82}}{a^{1.64}} \text{ [atm]}, \tag{6.54}$$

where $a = (R_d/R_{d1})^{1.64}$.

Let us determine the average values of parameters for periodic laser pulse trains (with the subscript *t*). The train duration is

$$\tau_{tm} = \frac{2R_{1m}}{C_0} = \frac{2R_{rm}}{C_0} = \frac{0.86}{C_0 \delta_m^{1/2}} \left(\frac{q_m}{P_{J2m}}\right)^{1/3} = 4.63 \times 10^{-4} q_m^{1/3} = \frac{\tau_t}{N^{1/3}}.$$
 (6.55)

The average force acting on an element of the array reflector in periodic trains is

$$\overline{F}_{am} = F_{am} \frac{1}{1 + \tau_{pm}/\tau_{tm}} = \frac{2}{3} F_{am} = \frac{2}{3} \frac{F_a}{N^{2/3}}.$$
 (6.56)

The force acting on the entire array reflector is

$$\overline{F}_{aM} = N\overline{F}_{am} = \frac{2}{3}F_aN^{1/3} = \overline{F}_aN^{1/3}.$$

The train repetition rate is

$$F_m = F_M = \frac{3.95 \times 10^4 \delta_m^{1/2}}{1 + 0.5 a_{\text{pm}}} \left(\frac{P_{\text{J2}m}}{q_m}\right)^{1/3} \approx \frac{2090}{q_m^{1/3}} = N^{1/3} F.$$
 (6.57)

The pulse train energy per element of the array reflector is

$$Q_{tm} = \overline{W}_m \tau_{tm} = \frac{0.86 \overline{W}_m}{C_0 \delta_m^{1/2}} \left(\frac{q_m}{P_{12m}}\right)^{1/3} = 4.63 \times 10^{-4} \overline{W}_m q_m^{1/3} = \frac{Q}{N^{4/3}}, \quad (6.58)$$

where Q is the train energy for a monoreflector.

The train energy in the array reflector consisting of N elements is

$$Q_{\mathrm{t}M} = N \overline{W}_m au_{\mathrm{t}m} = rac{Q}{N^{1/3}}$$
 .

The average radiation power of periodic trains for the array reflector is

$$\overline{W}_{tM} = Q_{tM} F_M = \overline{W}_t = \frac{2}{3} \overline{W}. \tag{6.59}$$

The specific force acting on the array reflector is

$$J_M [N MW^{-1}] \equiv \frac{F_{aM}}{\overline{W}_{cM}} = JN^{1/3}.$$
 (6.60)

6.7 LJE Based on the Resonance Merging of SW

6.7.1 Mechanism and Scheme of Acceleration

Laser pulses with a high repetition rate produce an OPD. Shock waves generated by the OPD merge to produce a high-pressure region, a quasi-stationary wave, thereby creating a permanent accelerating force. An air jet injected to the reflector provides the stable generation of shock waves and removal of the laser plasma from the reflector. An array reflector allows one to use high-powered laser pulses with a high repetition rate. Short 100–200-ns laser pulses are efficiently absorbed when radiation is sharply focused upon the reflector. The cylindrical walls of a receiver of a mechanical momentum convert a part of the radial component of the

quasi-stationary wave's momentum to the longitudinal component acting on the reflector. This makes it possible to considerably increase pressure and, therefore, the efficiency of utilising laser radiation.

6.7.2 Advantages of the Method

- (i) The specific thrust is $J = 1000-2500 \text{ N MW}^{-1}$, which is several times higher than the level achieved earlier (200–500 N MW⁻¹).
- (ii) The method eliminates the problems inherent in traditional methods (see Sect. 6.3) such as radiation screening by the laser plasma (in the case of low-energy laser pulses, the transverse size of the laser plasma is small), thermal action of the laser plasma on the reflector (the OPD is removed from the reflector surface), and shock loads (a constantly acting force is produced).

6.7.3 The LJE Parameters (Initial Data)

- (i) The average power of repetitively pulsed laser radiation is $\overline{W} = 20$ MW and the radius of the radiation receiver (reflector) is $R_r \sim 50$ cm.
- (ii) Radiation receivers consist of N = 1-10 elements, each of them containing a reflector (served also as receiver of the mechanical momentum) and having cylindrical walls.
- (iii) A gas-dynamic CO₂ laser emitting 10.6-μm pulses at a pulse repetition rate of 50–100 kHz is used. The lasing efficiency decreases at lower pulse repetition rates.
- (iv) The air pressure at the start of the spacecraft is $P_0 = 1$ atm and at the end of the LJE operation—0.1 atm (at height ~ 30 km).

6.7.3.1 Monoreflector

The reflector radius is selected for conditions of low radiation losses in the laser plasma ($\delta = 0.03$). The excess pressure is

$$\delta P = 14P_0^{0.45}P_{12}^{0.55} \frac{\delta^{0.82}}{a_{\perp}^{1.64}} = 0.68P_0^{0.45} \text{ [atm]}, \tag{6.61}$$

where $P_{J2} = 0.1$ atm is a pressure in the jet at the end of the LJE regime; $a_r = R_1/R_r = 0.5$; and R_1 is the distance from the OPD to the reflector. The force acting on the reflector is

$$F_{\rm a} [{\rm N}] = 10\pi R_{\rm r}^2 \delta P = \frac{201q^{0.67}P_0^{0.45}}{a_{\rm r}^{1.64}} = 62q^{0.67}P_0^{0.45}.$$
 (6.62)

The rate and radius of the gas jet are

$$V_{\rm J} \ [{\rm ms}^{-1}] = 0.86 f^{2/3} \left(\frac{\overline{W} \ [{\rm MW}]}{P_{\rm J}}\right)^{1/3},$$
 (6.63)

$$R_{\rm J} = 0.11 (q/P_{\rm J})^{1/3} \,[{\rm cm}].$$
 (6.64)

We determine from (6.61)—(6.64) the LJE parameters for the pulse repetition rates $f = 2 \times 10^4$ and 10^5 Hz. Parameters at the start of the spacecraft ($P_0 = 1$ atm) are denoted by the subscript 1 and by 2 at the end of the LJE operation ($P_0 = 0.1$ atm).

Laser pulse repetition rate is $f = 2 \times 10^4$ Hz.

The pulse energy is q = 1000 J, the reflector radius is $R_r = 50$ cm, and the distance from the OPD to the reflector is $R_1 = 25$ cm.

The forces acting on the reflector are $F_{a1} = 64 \times 10^3$ N and $F_{a2} = 23 \times 10^3$ N. The specific forces (per 1 MW of average power) are $J_1 = 2600$ N MW⁻¹ and $J_2 = 930$ N MW⁻¹.

The gas jet velocities are $V_{\rm J1} = 1725 \text{ m s}^{-1}$ and $F_{\rm J2} = 3716 \text{ m s}^{-1}$.

The jet radii are $R_{J1} = 1$ cm and $R_{J2} = 2.4$ cm.

Laser pulse repetition rate is $f = 10^5$ Hz.

The pulse energy is q = 200 J, the reflector radius is $R_r = 31$ cm, and the distance from the OPD to the reflector is $R_1 = 15$ cm.

The forces acting on the reflector are ($F_a=21.8P_0^{0.45}$ [N]) $P_{al}=21.8\times10^3$ N and $P_{a2}=7.73\times10^3$ N.

The specific forces (per 1 MW of average power) are $(J = 906P_0^{0.45})$ $J_1 = 906 \text{ N MW}^{-1}$ and $J_2 = 317 \text{ N MW}^{-1}$.

By decreasing the distance R_1 down to 9.5 cm ($a_r = 0.3$), we can increase the force and the specific force. In this case, the parameters F_a and J increase by a factor of 2.3: $F_{a1} = 50.1 \times 10^3$ N, $F_{a2} = 17.78 \times 10^3$ N, $J_1 = 2084$ N MW⁻¹ and $J_2 = 729$ N MW⁻¹.

The gas jet velocities are $V_{\rm J1} = 5048~{\rm m~s}^{-1}$ and $V_{\rm J2} = 10{,}880~{\rm m~s}^{-1}$.

The jet radii are $R_{11} = 0.64$ cm and $R_{12} = 1.4$ cm.

The production of such a jet in the LJE is complicated by the fact that even for the pulse repetition rate f = 50 kHz, the jet velocity is too high: $V_{J1} = 3175$ ms⁻¹ and $V_{J2} = 6840$ ms⁻¹.

Thus, an LJE with a monoreflector has good parameters and can be realised using a laser pulse repetition rate of $\sim\!20$ kHz. At higher pulse repetition rates, the LJE stabilisation is complicated by the necessity of using high-velocity ($\sim\!5$ km s⁻¹) gas jets. Another disadvantage of the monoreflector is that controlling flight with the laser engine is complicated.

6.7.3.2 Array Reflector

The problems of the development of the LJE based on the merging of shock waves generated by laser pulses with a high ($\sim 100 \text{ kHz}$) repetition rate and of the control of the flight trajectory with the help of the LJE can be solved by using an array reflector consisting of N monoreflectors. The array is irradiated by laser pulses with the energy q and average power \overline{W} . We assume that the radii R_{rm} of the elements of the array reflector are the same and the elements are irradiated by laser pulses with the same parameters $q_m = q/N$ and $W_m = \overline{W}/N$ $W_m = W/N$. The array reflector produces an array of OPDs, which are stabilised by a jet with the velocity V_{Jm} and do not interact with each other.

The parameters with subscripts m and M in the expressions presented below correspond to the element and array, respectively; if these subscripts are absent, the notation refers to the monoreflector for the energy q and average power \overline{W} . The number of elements should provide the solution of the problem of a high-velocity jet. We assume that N=8 (there is no point in using a greater value of N). The numerical values presented after expressions (6.65)–(6.70) were obtained for $\overline{W}=20$ MW ($W_m=2.5$ MW), $f=10^5$ Hz, q=200 J ($q_m=40$ J), and $a_{rm}=0.3$. As before, parameters at the start of the spacecraft ($P_0=1$ atm) are denoted by the subscript 1 and by the subscript 2 at the end of the LJE operation ($P_0=0.1$ atm).

The radius of the cylinder of an elementary reflector is

$$R_{rm} = \frac{0.2R_{dJm}}{\delta_m^{1/2}} = \frac{0.43(q_m/P_{J2m})^{1/3}}{\delta_m^{1/2}} = \frac{R_r}{N^{1/3}} = 15.5 \text{ cm},$$
(6.65)

and the distance from the reflector to focus is ~ 5 cm.

The characteristic size of the array reflector is ~ 90 cm. The excess pressure is

$$\delta P_m = 14 P_{0m}^{0.45} P_{J2m}^{0.55} \frac{\delta^{0.82}}{a_m^{1.64}} = 1.56 P_0^{0.45} \text{ [atm]},$$
 (6.66)

therefore, $\delta P_{m1} = 1.56$ atm and $\delta P_{m2} = 0.55$ atm.

An element of the array reflector is subjected to the average force

$$F_{am} [N] = \frac{81.4q_m^{0.67}P_{0m}^{0.45}}{a_m^{1.64}P_{Dm}^{0.12}\delta_m^{0.18}} = \frac{F_a}{N^{0.67}} = \frac{F_a}{4},$$
(6.67)

which gives $F_{am1} = 12.5 \times 10^3$ N and $F_{am2} = 4.45 \times 10^3$ N.

The array reflector is subjected to the average force

$$F_{aM} = NF_{am} = N^{1/3}F_a, (6.68)$$

therefore, $F_{aM1} = 100 \times 10^3 \text{ N}$ and $F_{aM2} = 35.6 \times 10^3 \text{ N}$.

An element of the array reflector is subjected to the specific force (per 1 MW of average power)

$$J_m[\text{N MW}^{-1}] = \frac{F_{am}}{\overline{W}_m}; \quad \frac{81.4 \times 10^6 P_{0m}^{0.45}}{a_m^{1.64} f q_m^{1/3} P_{D_{c}}^{0.12} \delta_m^{0.18}} = \frac{170 \times 10^6 P_{0m}^{0.45}}{a^{1.64} f q_m^{1/3}} = N^{1/3} J, \quad (6.69)$$

which gives $J_{m1} = 4170 \text{ N MW}^{-1}$ and $J_{m2} = 1460 \text{ N MW}^{-1}$.

The specific force for the array reflector is the same as for one element:

$$J_M = F_{aM}/\overline{W} = N^{1/3}J.$$

The jet velocities in the reflectors are

$$V_{J2m} = 86f^{2/3} \left(\frac{\overline{W}_m}{P_{I2m}}\right)^{1/3} = \frac{V_{J2}}{N^{1/3}},\tag{6.70}$$

and $V_{J1} = 2520 \text{ m s}^{-1} \text{ and } V_{J2} = 5440 \text{ m s}^{-1}$.

Note in the conclusion of this section that

- (i) the flight can be controlled by varying the thrust of a laser engine in the corresponding elements of the array reflector; and
- (ii) the increase in the number of reflector elements is accompanied by the increase in the aerodynamic resistance in air collectors.

6.8 Conclusions

In this chapter, we called attention to a 'renaissance' in the field of laser jet propulsion supported in many countries. We confirmed that Russia still occupies a leading place in the development of laser systems and control of the laser radiation parameters, as well as in the investigation of new mechanisms of the LJE propulsion. The high efficiency of gas-dynamic lasers with a variable temporal structure of radiation for launching various nano- and microsatellites into space and maintaining them in orbit is discussed.

Taking into account the advances of Russia in the development of high-power gas-dynamic lasers as the main element of the efficient LJE for launching small satellites, we proposed the "Impulsar" project, which is the logical continuation and development of pioneering papers of Prokhorov and Bunkin [24], for realisation in our country and development of international collaboration in space with the aim to create the next generation of communication systems, long range wireless energy transfer lines, and so on.

References 87

References

 V.V. Apollonov, V.N. Tishchenko, Kvantovaya Elektron. 34, 1143 (2004); V.V. Apollonov, V.N. Tishchenko, Proc. SPIE GCL/HPL, Vol. 5777, Prague, (2004)

- 2. V.N. Tishchenko, V.V. Apollonov et al., Kvantovaya Elektron. 34, 941 (2004)
- 3. V.V. Apollonov, in Proceedings SPIE ISBEP-3, vol. 5779 (Troy, NY, USA, 2004), p. 205
- V.P. Ageev, A.I. Barchukov, F.V. Bunkin, A.M. Prokhorov Kvantovaya Elektron. 4, 2501 (1977)
- V. Apollonov, Yu. Baturin, A. Bashilov, B. Katorgin, P. Mizin, A. Shurov, in *Proceedings SPIE ISBEP-4*, vol. 5779, (Nara, Japan, 2005), p. 22
- 6. V. Apollonov, in Proceedings SPIE ISBEP-4, vol. 5779, (Nara, Japan, 2005), p. 33
- W.O. Schall, W.L. Bohn, H.-A. Eckel, W. Mayerhofer, W. Riede, E. Zeyfang, Proc. SPIE Int. Soc. Opt. Eng. 4065, 472 (2000)
- 8. V. Apollonov, V. Tishchenko, G. Grachev, in *Proceedings SPIE ISBEP-4*, Vol. 5779 (Nara, Japan, 2005), p. 73
- 9. V.V. Apollonov, V.I. Kislov, A.G. Suzdal'tsev, Kvantovaya Elektron. 33, 753 (2003)
- 10. V.Yu. Borzov, V.M. Mikhailov, I.V. Rybka, A.S. Yur'ev et al., Inzh.-Fiz. Zh 66, 515 (1994)
- P.K. Tret'yakov, A.F. Garanin, G.N. Grachev, V.L. Krainev, A.G. Ponomarenko, V.N. Tishchenko, Dokl. Ross. Akad. Nauk. 351, 339 (1996)
- 12. Wallace J. Laser Focus World, August, 17 (2004)
- 13. V.N. Tishchenko, Kvantovaya Elektron. 33, 823 (2003)
- G.N. Grachev, A.G. Ponomarenko, A.L. Smirnov, V.N. Tischenko, P.K. Tret'jacov Laser Phys. 6(2), 376 (1996)
- 15. A.A. Zemlyanov (ed.) Vozdeistvie lazernogo i VCh izluchenii na vozdushnuyu sredu, (Effect of Laser and Microwave Radiations on Air) (Nauka, Novosibirsk, 1992)
- 16. S.R. Korbeinikov Teoriya tochechnogo vzryva, (Theory of a Point Explosion) (Nauka, 1971)
- 17. S.N. Kabanov, L.I. Maslova et al., Zh. Tekh. Fiz. 60, 37 (1990)
- 18. V.N. Tischenko, V.M. Antonov et al., J. Phys. D: Appl. Phys. 31, 1998 (1998)
- 19. V.N. Tishchenko, Opt. Atmos. Okean. 11, 228 (1998)
- 20. I.A. Bufetov, A.M. Prokhorov, V.B. Fedorov et al. Dokl. Akad. Nauk SSSR, 261, 586 (1981)
- 21. V.N. Kondrashev, N.B. Rodionov, S.F. Sitnikov, et al. Zh. Tekh. Fiz. 56, 89 (1986)
- 22. V.N. Tishchenko, G.N. Grachev et al., Kvantovaya Elektron. 32, 329 (2002)
- 23. V.N. Tishchenko, A.I. Gulidov Pis'ma Zh. Tekh. Fiz. 26, 77 (2000)
- 24. F.V. Bunkin, A.M. Prokhorov Usp. Fiz. Nauk, 119, 425 (1976)

Chapter 7

LJE: The Action of SW at Low Laser Pulse Repetition Rates



7.1 Introduction

A laser jet engine (LJE) uses repetitively pulsed laser radiation and the atmospheric air as a working substance [1–4]. In the tail part of a rocket a reflector focusing radiation is located. The propulsion is produced due to the action of the periodic shock waves produced by laser sparks on the reflector. The laser air-jet engine is attractive due to its simplicity and high efficiency. It was pointed out in papers [3, 4] that the LJE can find applications for launching space crafts if ~ 100 -kJ repetitively pulsed lasers with pulse repetition rates of hundreds hertz are developed and the damage of the optical reflector under the action of shock waves and laser plasma is eliminated. These problems can be solved by using high pulse repletion rates ($f \sim 100$ kHz), an optical pulsed discharge, and the merging of shock waves [5, 6]. The efficiency of the use of laser radiation in the case of short pulses at high pulse repetition rates is considerably higher. It is shown in this paper that factors damaging the reflector and a triggered device cannot be eliminated at low pulse repetition rates and are of the resonance type.

7.2 LJE Parameters

Let us estimate the basic LJE parameters: the forces acting on a rocket in the cases of pulsed and stationary acceleration, the wavelength of compression waves excited, in the rocket body by shock waves, the radius R_k of the plasma region (cavern) formed upon the expansion of a laser spark. We use the expressions for shock-wave parameters obtained by us. A laser spark was treated as a spherical region of radius r_0 in which the absorption of energy for the time $\sim 1~\mu s$ is accompanied by a pressure jump of the order of tens and hundreds of atmospheres. This is valid for the LJE in which the focal distance and diameter of a beam on the reflector are

comparable and the spark length is small. The reflector is a hemisphere of radius R_r . The frequency f is determined by the necessity of replacing hot air in the reflector by atmospheric air.

Let us estimate the excess of the peak value $F_{\rm m}$ of the repetitively pulsed propulsion over the stationary force $F_{\rm s}$ upon accelerating a rocket of mass M. It is obvious that $F_{\rm s}=Ma$, where the acceleration $a=(10-20)g_0\approx 100-200~{\rm m~s}^{-2}$. The peak value of the repetitively pulsed propulsion is achieved when the shock-wave front arrives on the reflector. The excess pressure in the shock wave (with respect to the atmospheric pressure P_0) produces the propulsion $F_i(t)$ and acceleration a of a rocket of mass M. The momentum increment produced by the shock wave is

$$\delta p_{\rm i} = \int_{0}^{1/f} F_{\rm i}(t) \cong F_{\rm a} t_{\rm a} \quad ({\rm N s}), \tag{7.1}$$

Here, F_a is the average value of the propulsion for the time t_a of the action of the compression phase of the shock wave on the reflector, and $F_m \approx 2F_a$. By equating δp_i to the momentum increment $\delta p_s = F_s/f = aM/f$ over the period under the action of the stationary propulsion F_s , we find

$$\Delta = F_{\rm m}/F_{\rm s} = 2/(ft_{\rm a}).$$

The value of Δ , as shown below, depends on many parameters. The momentum increment per period can be expressed in terms of the coupling coefficient J as $\delta p_i = JQ$, where Q [J] is the laser radiation energy absorbed in a spark. The condition $\delta p_i = \delta p_s$ gives the relation

$$W = aM/J (7.2)$$

between the basic parameters of the problem (W = Qf is the absorbed average power of repetitively pulsed radiation, and $J \approx 0.0001 - 0.0012$ N s J⁻¹ [3, 4, 6].

The action time of the compression phase on the reflector is $t_a \sim R_c/V$, where $V \approx k_1 C_0$ is the shock-wave velocity in front of the wall ($k_1 \sim 1.2$) and $C_0 \approx 3.4 \times 10^4$ cm s⁻¹ is the sound speed in air. The length R_c of the shock-wave compression phase can be found from the relation

$$\frac{R_{\rm c}}{R_{\rm d}} = 0.26 \left(\frac{h}{R_{\rm d}}\right)^{0.32}.\tag{7.3}$$

Here, h is the distance from the spark centre to the reflector surface and $R_d \approx 2.15(Q/P_0)^{1/3}$ is the dynamic radius of the spark (distance at which the

7.2 LJE Parameters 91

pressure in the shock wave becomes close to the air pressure P_0). In this expression, R_d is measured in cm and P_0 in atm. The cavern radius can be found from the relation

$$\frac{R_{\rm k}}{R_{\rm d}} = 0.6 \left(\frac{r_0}{R_{\rm d}}\right)^{0.29} = 0.22 - 0.3 \approx 0.25.$$
 (7.4)

Final expression (7.4) corresponds to the inequality $r_0/R_d < 0.03 - 0.1$, which is typical for laser sparks (r_0 is their initial radius). Let us find the range of P_0 where the two conditions are fulfilled simultaneously: the plasma is not in contact with the reflector surface and the coupling coefficient J is close to its maximum [3, 4, 7]. This corresponds to the inequality $R_k < h < R_d$. By dividing both parts of this inequality by R_d , we obtain $R_k/R_d < h/R_d < 1$, or $0.25 < h/R_d < 1$. As the rocket gains height, the air pressure and, hence, h/R_d decrease. If we assume that at the start ($P_0 = 1$ atm) the ratio $h/R_d = 1$, where h and R_d are chosen according to (7.2), then the inequality $0.25 < h/R_d < 1$ is fulfilled for $P_0 = 1 - 0.015$ atm, which restricts the flight altitude of the rocket by the value 30–40 km (h = const.).

The optimal distance h satisfies the relation $h/R_d \approx 0.25b_i$, where $b_i \approx 4-5$. By substituting h/R_d into (7.3), we find the length of the shock-wave compression phase and the time of its action on the reflector:

$$\frac{R_{\rm c}}{R_{\rm d}} \approx 0.17 b_{\rm i}^{0.32},$$
 (7.5)

$$t_{\rm a} = \frac{0.17b_{\rm i}^{0.32}R_{\rm d}}{k_{\rm l}C_0} = \frac{s_{\rm l}Q^{1/3}}{P_0^{1/3}} = \frac{s_{\rm l}}{P_0^{1/3}} \left(\frac{aM}{Jf}\right)^{1/3},\tag{7.6}$$

where $s_1 = 0.37 b_i^{0.32}/(k_1 C_0) \approx 9 \cdot 10^{-6} b_i^{0.32}$. From this, by using the relation $\Delta = F_m/F_a = 2/(ft_a)$ we find

$$\Delta = \frac{2P_0^{1/3}}{s_1 f^{2/3} W^{1/3}} = \frac{2P_0^{1/3} Q^{2/3} J}{s_1 a M} = \frac{2}{s_1 f^{2/3}} \left(\frac{P_0 J}{a M}\right)^{1/3}.$$
 (7.7)

Of the three parameters Q, W, and f, two parameters are independent. The third parameter can be determined from expression (7.2). The conditions $l/f \sim t_a$ and $\Delta \approx 1-2$ correspond to the merging of shock waves [5].

The important parameters are the ratio of t_a to the propagation time $t_z = L/C_m$ of sound over the entire rocket length L (C_m is the sound speed in a metal) and the ratio of t_z to 1/f. For steel and aluminum, $C_m = 5.1$ and 5.2 km s⁻¹, respectively. By using (7.6), we obtain

$$U = \frac{t_{\rm a}C_{\rm m}}{L} = \frac{s_{\rm 1}C_{\rm m}}{LP_{\rm o}^{1/3}}Q^{1/3}.$$
 (7.8)

Here, L is measured in cm and $C_{\rm m}$ in cm s⁻¹. Expression (7.8) gives the energy

$$Q = \frac{35.4P_0}{b_i^{0.96}} \left(U \frac{C_0}{C_{\rm m}} \right)^3 L^3. \tag{7.9}$$

From the practical point of view, of the most interest is the case $U\gg 1$, when the uniform load is produced over the entire length L. If $U\ll 1$, the acceleration is not stationary and the wavelength of the wave excited in the rocket body is much smaller than L. If also $C_{\rm m}/f\ll L$, then many compression waves fit the length L. The case $U\approx 1$ corresponds to the resonance excitation of the waves. Obviously, the case $U\leq 1$ is unacceptable from the point of view of the rocket strength.

By using the expressions obtained above, we estimate Δ , U, and $R_{\rm k}$ for laboratory experiments and a small-mass rocket. We assume that $b_{\rm i}=4$, $J=5\times 10^{-4}$ N s J⁻¹, and $s_{\rm i}=1.4\times 10^{-5}$. For the laboratory conditions, $M\approx 0.1$ kg, $R_{\rm r}\approx 5$ cm, L=10 cm, and a=100 m s⁻². The average value of the repetitively pulsed propulsion $F_{\rm IP}$ is equal to the stationary propulsion, $F_{\rm IP}=F_{\rm s}=10$ N; the average power of repetitively pulsed radiation is $W=F_{\rm IP}/J=20$ kW, and the pulse energy is $Q_{\rm p}=W/f$. We estimate the frequency f and, hence, $Q_{\rm p}\approx Q$ for the two limiting cases.

At the start, $P_0 \approx 1$ atm and the cavern radius R_k is considerably smaller than R_r . Here, as in the unbounded space, the laser plasma is cooled due to turbulent thermal mass transfer. For $Q_p < 20$ J, the characteristic time of this process is 2–5 ms [8, 9], which, corresponds to f = 500–200 Hz. If $R_k \sim R_r$ ($P_0 < 0.1$ atm), the hot gas at temperature of a few thousands of degrees occupies the greater part of the reflector volume. The frequency f is determined by the necessity of replacing gas over the entire volume and is $\sim 0.5 C_0/R_r \sim 850$ Hz [3, 4]. Let us assume for further estimates that f = 200 Hz, which gives $Q_p = 100$ J. We find from (7.7) and (7.8) that $\Delta = 74$ and U = 3.5. This means that the maximum dynamic propulsion exceeds by many times the propulsion corresponding to the stationary acceleration. The action time of the shock wave is longer by a factor of 3.5 than the propagation time of the shock wave over the model length. For $P_0 = 1$ and 0.01 atm, the cavern radius is $R_k = 2.5$ and 11.6 cm, respectively.

Let us make the estimate for a rocket by assuming that $M \approx 20$ kg, $R_r \approx 20$ cm, L = 200 cm, and a = 100 m s⁻². The average repetitively pulsed propulsion is $F_{\rm IP} = F_{\rm s} = 2000$ N, the average radiation power is W = 4 MW, for f = 200 Hz the pulse energy is $Q_{\rm p} = 20$ kJ, $\Delta = 12.6$, U = 1, $R_{\rm k} = 14.7$ and 68 cm ($P_0 = 1$ and 0.01 atm), and $F_{\rm m} = 25.6$ kN = 2560 kg. One can see that the repetitively pulsed acceleration regime produces the dynamic loads on the rocket body which are an order of magnitude greater than $F_{\rm s}$. They have the resonance nature because the condition $U \sim 1$ means that the compression wavelengths are comparable with the rocket length. In addition, as the rocket length is increased up to 4 m and the pulse repetition rate is increased up to 1 kHz, the oscillation eigenfrequency $C_{\rm m}/L$ of the rocket body is close to/(resonance).

7.3 Conclusions 93

7.3 Conclusions

Thus, our estimates have shown that at a low pulse repetition rate the thermal contact of the plasma with the reflector and strong dynamic loads are inevitable. The situation is aggravated by the excitation of resonance oscillations in the rocket body. These difficulties can be eliminated by using the method based on the merging of shock waves [4, 5]. Calculations and experiments [10] have confirmed the possibility of producing the stationary propulsion by using laser radiation with high pulse repetition rates. The method of scaling the output radiation power is presented in [11].

References

- 1. A.R. Kantrowitz, Astronaut. Aeronaut. **10**(5), 74 (1972)
- 2. A.N. Pirry, M. Monsler, R. Nebolsain, Raket. Tekh. Kosmonavt. 12, 112 (1974)
- V.P. Ageev, A.I. Barchukov, F.V. Bunkin, V.I. Konov, A.M. Prokhorov, A.S. Silenok, N.I. Chapliev, Kvantovaya Elektron. 4, 2501 (1977); Sov. J. Quantum Electron. 7, 1430 (1977)
- 4. F.V. Bunkin, A.M. Prokhorov, Usp. Fiz. Nauk 119, 425 (1976)
- 5. V.N. Tishchenko, V.V. Apollonov et al., Kvantovaya Elektron. 34, 941 (2004)
- 6. V.V. Apollonov, V.N. Tishchenko, Kvantovaya Elektron. 34, 1143 (2004)
- 7. V.P. Korobeinikov, *Zadachi teorii tochechnogo vzryva* (Problems of the theory of point explosions) (Nauka, Moscow, 1985)
- 8. S.N. Kabanov, L.I. Maslova et al., Zh. Tekh. Fiz. 60, 37 (1990)
- 9. V.N. Tishchenko, V.M. Antonov, A.V. Melekhov, S.A. Nikitin, V.G. Posukh, P.K. Tret'yakov, I.F. Shaikhislamov, Pis'ma. Zh. Eksp. Teor. Fiz. 22, 30 (1996)
- G.N. Grachev, V.N. Tishchenko, V.V. Apollonov, A.I. Gulidov, A.L. Smirnov, A.V. Sobolev, M.I. Zimin, Kvantovaya Elektron. 37, 669 (2007)
- 11. V.V. Apollonov, V.I. Kislov, A.G. Suzdal'tsev, Kvantovaya Elektron. 33, 753 (2003)

Chapter 8 Simulation of High Conductivity Channels in Space



8.1 Introduction

At present, many laboratories still continue the search for an efficient laser-based lightning protection system [1–3] and for producing a controlled high conductivity channels in space [4–8], capable of conducting a short-circuit current [9] in a natural or artificial electrical circuit. Authors of [7] demonstrated a 1.5-fold increase in the length of the discharge gap broken under laser irradiation when switching extended (~ 1 m) high-voltage (up to 390 kV) electric discharges by 100-ns UV pulses of a KrF laser. Laser-based lightning protection systems, as is known, rely on the so-called long laser spark, which provides the conditions for connecting a thunderstorm cloud with a grounded metal rod, i.e., a classical lightning rod. Maximum lengths (~ 16 m) of the laser-spark-controlled electric discharge at a voltage of 3 mV were obtained in Russia and Japan [3] using a 0.5-kJ pulsed CO₂ laser with spherical optics. Such control conductivity channels can be used in energy transmission, overvoltage protection systems, transport of charged particle beams, plasma antennas, etc. [8].

8.2 Lasers for Producing Sparks in the Atmosphere

It was shown in [10, 11] that a laser spark produced using conical optics demonstrates much better characteristics from the point of view of formation of conductivity channels in the atmosphere. Currently, among the huge variety of different lasers, only two types are being actively studied to be used in the formation of laser-spark-controlled high conductivity channels in the atmosphere: submicrosecond pulsed gas and chemical lasers (CO₂, DF) and femtosecond solid-state lasers [4, 6, 12].

The main advantage of femtosecond lasers is the ability of producing superlong ionized channels (so-called filaments) with a characteristic diameter of about 100 μ m in atmosphere along the laser beam propagation direction. With an estimated electron density of 10^{16} cm⁻³ in these filaments and the laser wavelength in the range of 0.5–1.0 μ m, the plasma hardly absorbs the laser light. In this case, the length of the track consisting of many filaments is determined by the laser intensity and can reach many miles at a femtosecond pulse energy of ~ 100 mJ. However, these lasers could not be used to form long high-conductivity channels in atmosphere. The ohmic resistance of the thus formed conducting channels turned out to be very high, and the gas in the channels could not be strongly heated (the femtosecond laser energy is less than 1 J). In particular, an electric breakdown (EB) controlled by radiation of a femtosecond solid-state laser was implemented in [5, 6] only at a length of 3 m (with a voltage of 2 mV across the discharge gap).

As was shown in [13, 14], to form a high-conductivity channel in the atmosphere, which could commute an artificial or natural discharge (lightning), the gas must be heated to a temperature from 6000 to 8000 K, when thermal ionization begins. This condition is crucial, because the high initial electron density in the atmosphere is a necessary but not sufficient condition for realizing high conductivity in a long atmospheric channel. As was mentioned in [13], it is important not only to produce but also to maintain the electron density in an atmospheric channel that is sufficient for the breakdown. During gas heating thermal ionization becomes the main mechanism of electron 'production' in the channel. Specifically this is the main reason why the streamer mechanism cannot lead directly to an electric breakdown in the presence of high electron density (filaments) in a cold channel [13].

In the case of submicrosecond CO₂ or DF lasers with a high energy per pulse (several hundreds of joules), long conducting laser-plasma channels can be formed with conical optics. In contrast to spherical optics, one can use methods of lens dynamic correction to increase aberrations and elongate the focal segment by passing to a conical phase front [11]. For example, an axicon transforms the phase front of a plane wave so that it becomes conical rather than spherical and converges to the z axis at an angle γ . For small angles ($\gamma \ll 1^{\circ}$), it is simply expressed in terms of the angle γ at the axicon base and the refractive index N of the axicon material: $\gamma = (N-1)\alpha$. Each ring element of a conical wave front with a radius R and width δR is focused into an axial element of length $\delta z = \delta R/\gamma$ and the entire focal segment has the length $L = R/\text{tg } \gamma = R/\gamma$ [11]. This length can be made significant. For example, at R = 10 cm and $\gamma = 0.5^{\circ}$, it amounts to $L \sim 11$ m. The cylindrical symmetry of focusing suggests that the type of transverse intensity distribution is independent of the coordinate z, a situation corresponding to a 'diffractionless' wave beam. In reality, such beams also undergo diffraction; however, the diffraction energy loss from the central part of the beam is compensated for by the distributed lateral supply of radiation. Note that the theoretical length of the focal segment formed by the axicon is independent of the laser beam energy and power and is determined by only the beam diameter. At R = 100 cm and $\gamma = 0.5^{\circ}$, it amounts to $L \sim 110$ m. According to our estimates, when using CO₂ lasers with an energy of ~ 5 kJ per pulse, the length of these channels for wide laser beams and conical optics can be fairly large (much more than 100 m).

When laser radiation is focused by an axicon in a real experiment, the longitudinal intensity distribution I(z) along the focal length L depends on z, since the transverse intensity distribution I(R) of the input beam is transformed by the axicon into the longitudinal distribution I(z) of the Bessel beam. When the radiation intensity in the beam reaches the threshold, there occurs a breakdown in the medium and an extended plasma channel is formed along the focal length of the axicon [11]. Initially, the channel has a diameter of 20–100 μ m and a length that is on order of the focal length L of the axicon. If the breakdown is stable, the plasma channel, in contrast to the case of spherical optics, becomes continuous for few nanoseconds. The density of the plasma, depending on the parameters of the medium, the wavelength λ , and other experimental conditions, varies from 10^{17} to 3 cm⁻³, the temperature reaches 30–40 eV, and specific conductivity is $10 (\Omega \text{ m})^{-1}$. A few microseconds later the channel expands to 10 mm. Accordingly, the temperature drops to 1 eV and retains at this level for about 100μ s, followed by a relaxation of the plasma [11].

Figure 8.1a shows a scheme of focusing laser radiation by a conical lens and a photograph of a plasma channel in scattered heating radiation with a wavelength $\lambda = 1.06 \ \mu m$ at the breakdown onset ($\tau_u \approx 50 \ \text{ns}$, exposure time 5 ns, delay time $t_{\rm d}$ = 0 ns) [11]. The channel structure is affected by the combination of such parameters as the pulse width and the angle γ . For example, for a long pulse, laser-supported detonation may arise at inhomogeneities of the channel structure [15], as a result of which the structure becomes herringbone [11]. The photograph of a continuous lasers spark (CLS) in Fig. 8.1b was obtained by focusing CO₂-laser radiation in the atmosphere by a conical mirror with an opening angle $\gamma = 177.8^{\circ}$ [8]. One can see that a laser spark looks like a continuous cord, composed of bright tapered elements. There are no discontinuities that are characteristic of sparks produced by focusing radiation by spherical optics. A similar pattern was observed at laser energies below 300 J [8]. In the photograph of a CLS fragment in Fig. 8.1c the longitudinal structure of the spark looks like a set of bright tapered elements, which are in contact and equally spaced. Figure 8.1d shows a photograph of the electric breakdown in the atmosphere for a channel formed by a CLS. When studying the spark between two rods immersed in its plasma and spaced by d = 80 cm [8], an electric breakdown occurred at a laser energy of 140 J and minimum average electric field strength $E_{\min} \approx 77$ V/cm.

The up-to-date experiments aimed at implementing laser-spark-guided electric discharges shows another fundamental difference in the case of femtosecond solid-state and long-wavelength lasers. In the presence of a laser-plasma channel composed of filaments, the breakdown voltage decreased by 30% [5]. The use of CO_2 and DF lasers made it possible to reduce it by a factor of more than 10.

As was pointed out in [16], the guiding properties of CLS (with a high voltage delayed by $T = 10-20 \mu s$) are similar to the action of a chain of metal balls. After an optimal time of $\sim 10-20 \mu s$, the expansion of individual breakdown 'zones' leads

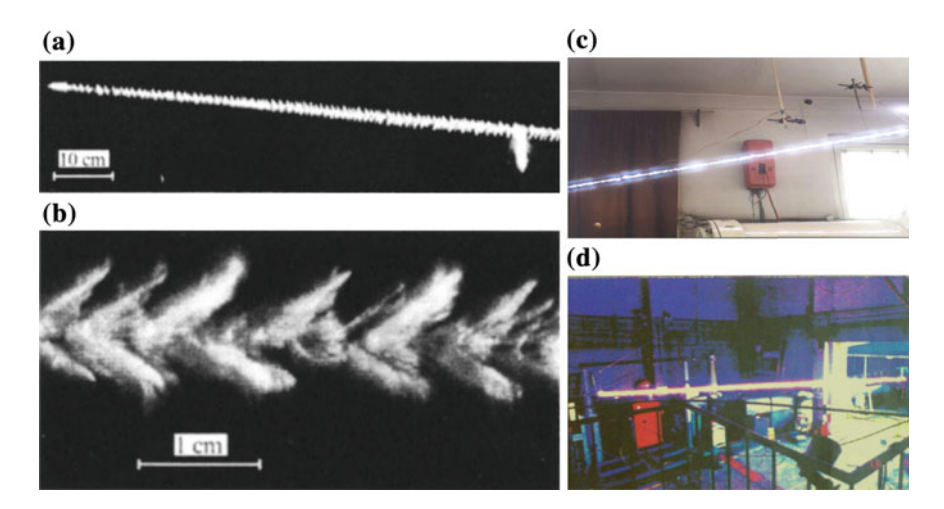


Fig. 8.1 a Schematics of focusing laser radiation by a conical lens (CL) and a photograph of the channel in scattered heating laser radiation (LR) with a wavelength 1.06 μ m at the breakdown onset (50 ns, exposure time 5 ns, delay time = 0) [11]; **b**, **c** photographs of a continuous laser spark for CO₂-laser radiation focused by a conical mirror with an opening angle = 177.8°; and **d** a photograph of electric breakdown in atmosphere in a CLS-induced channel

to the formation of a continuous quasi-cylindrical conducting channel with a low gas density (~ 0.1 of the normal density), high equilibrium temperature (2700–2900 K), and electron density in the range from 10^7 to 10^8 cm⁻³.

8.3 Use of a Pulse-Periodic Laser

Another approach to the formation of a conducting channel relies on the application of a pulse-periodic laser. It was shown in [17] that electric-discharge and gas-dynamic lasers with a high peak power can operate in a high-frequency pulse-periodic regime. This lasing regime allows one to produce a long conducting channel in the atmosphere, which exists for a long time. To this end, it is necessary to align a laser beam with an inverted Cassegrain telescope system, which consists of two spherical mirrors. The first (main) mirror of large diameter is immobile, while the second mirror can move according to a certain law. When moving the second mirror, the common real focus of the system changes its position in time from infinity to some minimum value, which is determined by the optical scheme of the telescope. Calculations show that, at a certain repetition frequency of laser pulses and a certain motion law for the second mirror, continuous extended plasma channels can be formed. However, practical implementation of this scheme with a 'running' focus meets a number of fundamental difficulties. The light distribution in the focal plane, yielded by a well correlated lens, is in essence due to the Fraunhofer

diffraction. The specific features of the out-of-focus 3D monochromatic images of a point source, obtained with a round hole, were considered for the first time by Lommel. Along the optical z axis, the length of the focal segment that determines the longitudinal size of the energy-accumulation region depends quadratically on the focal length of the system. The transverse size of this region is proportional to the focal length and the angular divergence of laser radiation; therefore, the volume within which energy is concentrated is proportional to the focal length in the fourth power. For this reason, to form a homogeneous plasma channel several kilometres long, one must use a pulse-periodic laser with a shaped pulse energy and the second telescope mirror moving according to a complex program. A practical implementation of this method with a pulse-periodic CO_2 laser with an average power of 1 kW yielded a continuous plasma channel ~ 1 m long [18].

8.4 Formation of a Current-Conducting Channel According to the "Impulsar" Program

A completely different approach to the formation of a current-conducting channel can be realized using laser firing according to the Impulsar program [19]. According to "Impulsar" program the motion of the vehikle under irradiation by a high-frequency pulse-periodic laser with a pulse energy sufficient for producing a breakdown in the focus of the optical system of a laser reactive engine (LRE) gives rise to a continuous conducting channel in air as a result of the formation of a mixture of aerosol [20] with atmospheric air and its subsequent ionization [19]. In this case, according to the calculations, the aforementioned range of laser pulse repetition rates provides continuity of the conducting channel at optimal velocities of the focusing system. Indeed, each laser pulse focused by the optical system forms some extended plasma region with a high conductivity, which occupies a relatively small segment of the focusing system trajectory. If the laser pulses have a low repetition rate [21], these regions will form somewhat like a dashed line at some velocities of the focusing system. If the pulse repetition rate exceeds 10 kHz and the motion velocities are optimal for solving the problem stated, these high-conductivity regions will have no discontinuities, and a continuous conducting channel will be formed. However, when the moving optical system enters rarefied atmospheric layers, a problem of medium deficit arises. To solve it, the displaced optical system must have an efficient source of an appropriate medium (a material containing microscopic metal particles, which can easily be sublimated under laser irradiation) in the vicinity of the focus. In particular, one can use copper oxide (CuO) nanopowder [22], which provides synthesis of conducting aerosol copper particles upon laser heating. The presence of aerosol particles of heavy metals in the sublimated material makes it possible to increase the specific impulse of the LRE thrust, simultaneously with increasing the channel conductivity.

To implement a long conducting channel, one must solve several problems:

- (i) development of a high-frequency pulse-periodic CO_2 laser with an average power $P \sim 100-150$ kW and a peak power sufficient for initiating a breakdown in the focus of the LRE optical system;
- (ii) development of a system of dynamic correction for the wave front of a wide-aperture laser beam with a diameter $D \sim 10$ cm in the presence of small-scale turbulence in atmosphere;
- (iii) consideration of the laser radiation absorption and scattering by aerosol particles in the LRE exhaust;
- (iv) alignment of the starting position of LRE with the laser and the pulsed high-voltage (up to several MV) source;
- (v) obtainment of maximally possible specific impulse of the LRE thrust to reduce the time of aerosol channel formation:
- (vi) choice of the material of aerosol heavy-metal particles and their dispersion composition that could provide high channel conductivity upon heating to the sublimation temperature in the LRE;
- (vii) determination of the lower limit for the size of dispersion aerosol particles to ignite electric breakdown of a channel capable of transmitting a current, corresponding to a short-circuit current in natural or artificial electric circuits at a minimally possible average strength of electric field.

To address the latter two problems, we conducted a series of experiments. The results obtained are reported below. We consider urgent the problems of determining the dynamics of change in the channel conductivity at long delay times and its maintenance at the optimal level by introducing additional high-frequency generators into a chain; they will be analyzed in the next stage of the Impulsar program.

8.5 Formation of an Electrical Breakdown in the Channel Formed by an Exploding Thin Wire

The formation of a conducting channel based on the "Impulsar" technology was simulated using the results of the laboratory experiments on a controlled electric breakdown in an atmospheric channel containing aerosols [22, 23] of hot copper and copper oxide (CuO, Cu₂O) particles, formed as a result of wire explosion. Note that the proposed method for generating particles of variable size with a necessary concentration appears to be fairly efficient in terms of the price—quality criterion when one must carry out many experiments aimed at modeling the optimal conditions for high conductivity. There are a number of factors facilitating the electric breakdown (including the streamer stage) of long gaps in an atmospheric channel formed as a result of wire explosion at average external electric fields.

As was noted in [14], the main problem in the analysis of the formation of a spark channel in a discharge gap in atmosphere using a field of arbitrary

configuration is to determine the mechanism of gas heating, which provides thermal ionization of the gas in the spark channel. The heating in the discharge channel was generally believed to be caused by the increase in the concentration of the charged particles supplied by shock gas ionization. However, the concentration of charged particles in the range of 10^{11} to 10^{13} cm $^{-3}$ is limiting for shock ionization. The development rate of thermal processes in a gas is limited by the velocity of the electrons that transform the electric field energy to the thermal energy of gas molecules. The thermal inertia of the gas excludes the possibility of step changes in its temperature and therefore, its conductivity, both during heating and cooling the channel.

It was noted in [13] that ionization in a highly ionized plasma differs significantly from the similar process in a weakly ionized plasma, where molecules are ionized by the electrons gaining energy directly from the electric field. A field in a highly ionized plasma supplies energy to all gas electrons. The latter are thermalized as a result of collisions and obey Maxwell's distribution. The gas is ionized by the electrons that acquire sufficient energy during the energy exchange with other particles rather than directly from the field. It is much easier to maintain a highly ionized equilibrium plasma than a weakly ionized nonequilibrium plasma, because the former situation requires a much weaker field. For example [13], in an equilibrium plasma column of nitrogen arc at atmospheric pressure, which burns in a cooled tube of radius r = 1.5 cm at a current i = 10 A, the field supporting the arc column has a strength $E=10 \text{ V cm}^{-1}$. Under these conditions, T=8000 K, the gas density $N_{\rm a}=10^{18} \text{ cm}^{-3}$, $n_{\rm e}=2\times10^{15} \text{ cm}^{-3}$, the degree of ionization $x_1=n_{\rm e}/N=2\times10^{-3}$, and $E/N_{\rm a}=10^{-17} \text{ V cm}^2$. In a nonequilibrium glow discharge column in nitrogen, the strength of the discharge-supporting field is larger by an order of magnitude: $E = 200 \text{ V cm}^{-1}$. Such a sharp difference is caused by the difference in the nature of ionization processes. In the case of weakly ionized plasma, the field must be sufficiently strong to accelerate electrons to an energy of 13-15 eV (ionization threshold). At the same time, for highly ionized equilibrium plasma, the field can be much weaker, because in this case it is sufficient to accelerate electrons to only $k_{\rm T} \sim 1$ eV. As was indicated in [13], electrons supply atoms with energy, and, during the energy exchange, all particles jointly concentrate energy in separate electrons, which serve as ionization sources.

Our experiments on the formation of a high-conductivity channel in atmosphere was performed with a PEV-2 copper wire in an enamel shell; the wire was 90–155 cm long and had a diameter of 90 mm. Figure 8.2a shows a schematic of the experimental setup; the arrangement of the sensors for measuring current by a Rogowski loop and voltage on the capacitor battery using a voltage divider; and the position of the end face of polished quartz fiber, which transfers radiation from the discharge channel to a high-speed pin-photodiode. The end face of the polished quartz fiber was located at a distance of 2–10 cm from the wire axis near the discharge cathode or anode. The shape of the current pulse was measured using a differential screened Rogowski loop with a time resolution of \sim 30 ns [24].

The shape of the voltage pulse across the discharge gap was determined with the aid of a screened voltage divider of mixed type (connected to the capacitor battery

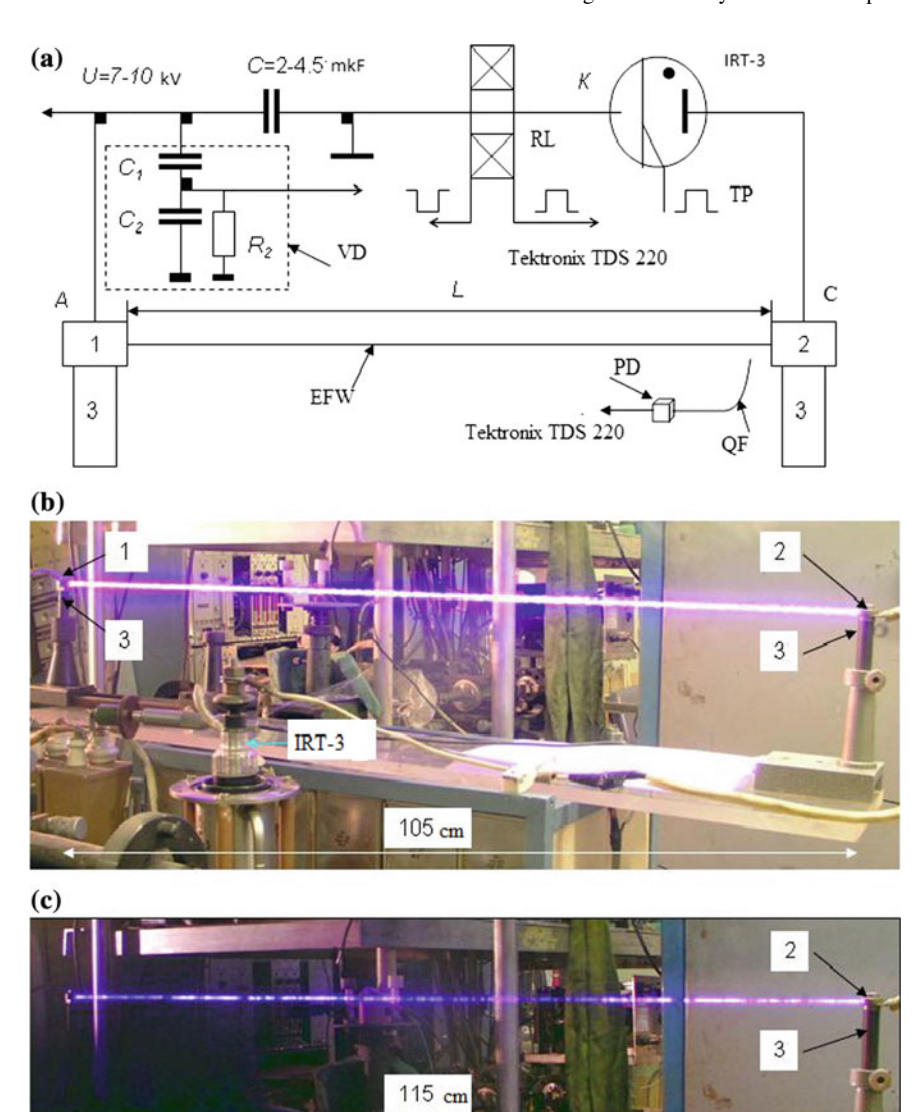


Fig. 8.2 a Schematics of the experiment on igniting an electric breakdown in a wire-explosion channel for a horizontally oriented wire: (1, 2) brass electrodes, (3) ebonite insulators, (IRT-3) ignitron switcher, (RL) Rogowski loop, (VD) voltage divider, (TP) triggering pulse, (EFW) exploding fine wire, (PD) photodiode, (QF) silica fiber, (A) anode, and (C) cathode; **b** a photograph of controlled electric breakdown; and **c** a photograph of wire explosion in the absence of breakdown)

anode), which yields a measurement error of $\sim 1\%$ at a width of the current-pulse leading edge >1 µs [25]. Recording was performed using a Tektronix TDS 220 digital oscilloscope. The capacitor with a capacitance C=2 µF was charged from a voltage source to $U_0=7$ –10 kV. When switched on by an external triggering pulse from a controlled discharger (IRT-3 ignitron), the capacitor was discharged through a copper wire 90 µm in diameter (with allowance for the enamel shell, the wire diameter was ~ 110 µm). As the experiments showed, the presence of an enamel shell facilitates the formation of a thin straight-line electric breakdown channel with a conducting region 4–8 mm in diameter in atmosphere and promotes a unique mechanism of aerosol formation in the form of balls 330–20 µm in diameter with a black surface (oxidized during wire explosion). Large pieces of the enamel shell (up to 10 cm long) remain integer, with burn-through areas on the surface. During the wire explosion and electric breakdown, the enamel shell stabilizes the spatial arrangement of the balls in the channel, which are centers of ionization plasma formations.

Figure 8.2b shows a photograph of electric breakdown in a channel formed during explosion of a horizontally oriented wire (D90 µm, length 105 cm). This photograph was recorded through an FS-1 blue filter and a neutral NS-9 filter by an OLYMPUS C-5050 ZOOM digital camera. At an exposure of 1.6 s the photographs have an integral character; i.e., the exposure during photographing the discharge was determined by the discharge duration. The digital camera matrix operated with a maximum resolution. When taking pictures of the entire discharge channel, the distance l from the wire centre to the digital camera objective was ~2 m. To reveal the electric breakdown details: sizes of individual hot particles formed during the wire explosion and the diameter of the channel and the inhomogeneities in the structure of channel luminescence, we took pictures in the macroscopic regime, in which the digital camera objective was located rather close (at 25–50 cm) to the wire. When taking pictures of the wire explosion products, l was chosen to be 3 cm (supermacroscopic regime). The digital camera was used in the ZOOM regime. The spherical shape of the wire explosion products (D330-20 μm) is primarily explained by the effect of surface tension forces on the molten copper drops during their formation. The large spread of particle diameters is explained by the fragmentation and aggregation of metal drops during wire explosion [26]. The black color of the particles is due to the formation of copper oxide on their surface as a result of the interaction of copper drops with air oxygen. The oxidation is reversible; i.e., upon heating to ~ 1200 K, copper oxide is reduced to copper [22]. During the wire explosion, the oxygen concentration in the channel formed should sharply decrease as a result of the oxidation. It was shown in this experiment that, by the instant of electric breakdown, the voltage across the discharge gap $U_a = 7 \text{ kV}$ provides the electric field strength in the channel $E_c = U_a/$ $d \gg 67 \text{ V cm}^{-1}$.

At the storage capacitance $C = 2 \mu F$, depending on the charging voltage and wire length, wire explosion may occur without electric breakdown. Figure 8.2c shows a photograph of a channel ($D90 \mu m$, length 115 cm) formed as a result of explosion in the absence of electric breakdown. It can be seen that the channel

structure is intermittent: it consists of individual isolated plasma zones of superheated drops of wire material [27–29]. At a charging voltage $U_0=10~\rm kV$ and storage capacitance $C=2~\mu F$, the voltage across the capacitor battery decreases to 7.6 kV by the end of the wire explosion. At a constant charging voltage U_0 , the maximum pulse current during wire explosion is mainly determined by the initial wire resistance R_0 and amounts to 1.25 kA. When changing the length of 90- μ m copper wire within 90–155 cm, the measured resistance ranged from 2.7 to 4.2 W. At $U_0=10~\rm kV$ and $C=2-4~\mu F$, the maximum amplitude of the pulse current was in the range of 1–1.4 kA. After the wire explosion, a current $i=10~\rm A$ flows for some time through the hot channel and then decays to zero. As a result, the residual voltage across the capacitor battery decreases to 7 kV. Despite the presence of residual current after the wire explosion, which heats additionally the channel, the electric breakdown does not occur at these parameters of the discharge circuit. The amount of energy W spent on wire explosion, calculated from the current and voltage characteristics, was found to be $\sim 35~\rm J$.

In the series of experiments performed on a horizontally oriented wire, the capacitance of the capacitor battery was taken to be constant: $C=2~\mu F$; the only variable parameters were the wire length (90–155 cm) and charging voltage (7–10 kV). It was found experimentally that, at a wire length of 100 cm, the minimum charging voltage at which there is no electric breakdown in the gap does not exceed 7 kV; a value corresponding to the minimum accumulated energy: $W_0=49~\rm J$.

In the next series of experiments on the electric breakdown in a channel, we considered a vertically oriented wire. This version is preferred, because it takes into account the possible influence of the vertical component of electric field at the Earth's surface on the electric breakdown in the channel formed by wire explosion.

Figure 8.3a shows a photograph of electric breakdown in a channel formed by a vertically oriented wire ($D90~\mu m$, length 143 cm) at the initial stored energy $W_0 = 190~J$, which corresponds to the charging voltage $U_0 = 10~kV$ and the storage capacitance $C = 3.8~\mu F$. The electric breakdown can be seen in the oscillograms of discharge channel current, voltage, and luminescence, which were recorded by a high-speed pin-photodiode with a time resolution of = 1 ns. The light arrived at the photosensitive area of pin photodiode through a silica fiber $\sim 2~m$ long, whose polished receiving end face was located near the discharge anode at a distance of 1.5–4 cm from the discharge channel. The radiation pulse width at half maximum was $\sim 30~\mu s$ and hardly differed from the corresponding current pulse width during electric breakdown (the light-pulse oscillogram in Fig. 8.3e shows only the arc phase of the breakdown). The oscillogram of the discharge current (Fig. 8.3b, d) indicates that it is close to zero during the current pause [30, 31], whose duration is $DT = 140~\mu s$. The results of our studies showed that the current during the pause amounted to 10–50 A (depending on the discharge-circuit parameters).

There are many theories explaining this phenomenon; they will be considered elsewhere. As was shown in [31], the electric breakdown delay for a copper wire depends on the average electric field strength $E_{\rm c}$ in the channel at the instant when the arc phase of the breakdown begins. The voltage oscillogram demonstrates that the breakdown occurred at a voltage of ~ 8.4 kV. Using the current and voltage

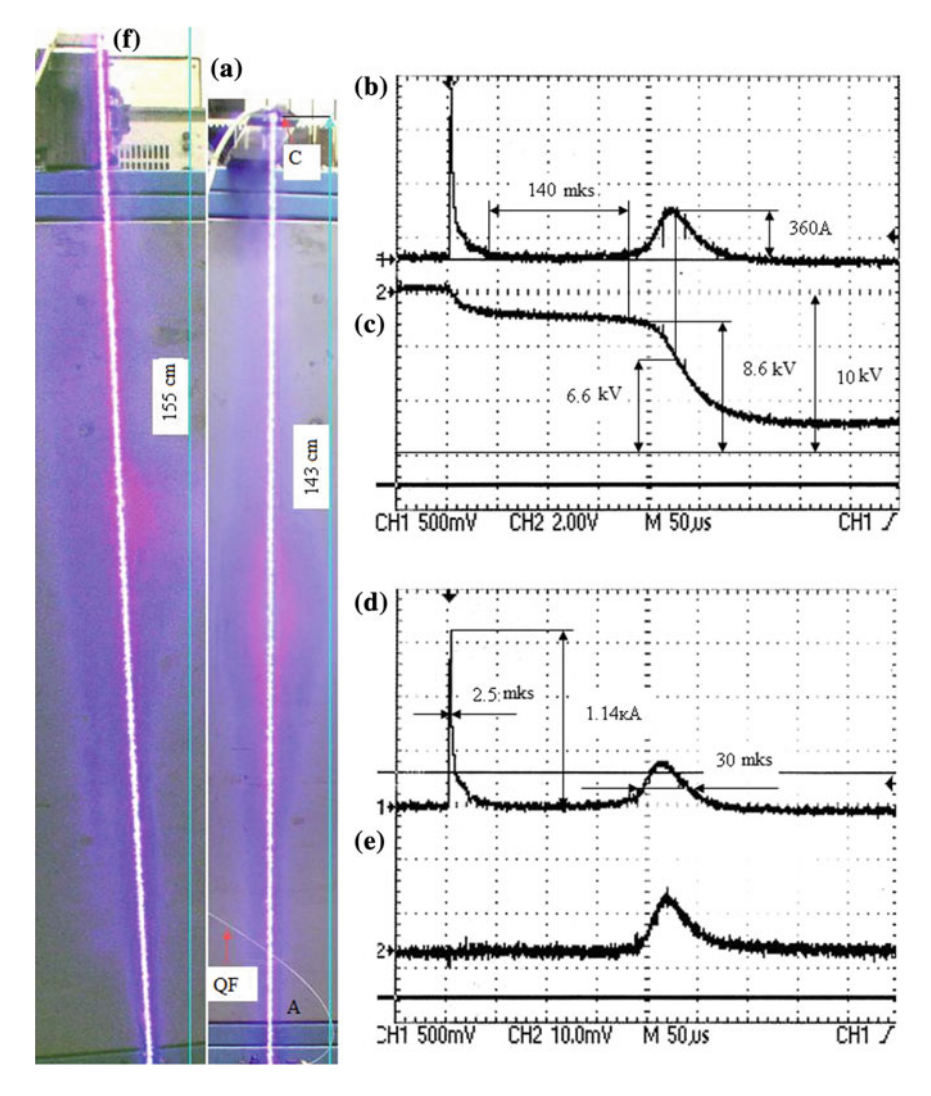


Fig. 8.3 a Photograph of controlled electric breakdown for explosion of a vertically oriented wire (the interelectrode length is 143 cm); **b–e** oscillograms of the discharge channel (**b**, **d**) current, (**c**) voltage, and (**e**) luminescence at a capacitance $C = 3.8 \mu F$ and charging voltage $U_0 = 10 \text{ kV}$; and **f** a photograph of controlled electric breakdown at $C = 4.5 \mu F$, charging voltage $U_0 = 10 \text{ kV}$, and an interelectrode distance of 155 cm

oscillograms, one can also determine the channel resistance during the electric breakdown at the instant corresponding to $I_{\rm max}=360$ A. In this case, $R_{\rm min}=17$ W. Here, in contrast to the data of [32, 33], the discharge-channel diameter is of little importance, because the discharge is slow, and the inductive component can be neglected when estimating the voltage drop across the discharge channel. In Fig. 8.3b, which illustrates the case of the electric breakdown in a channel formed

by wire explosion at $C=3.8~\mu\text{F}$ and inductance $L=2~\mu\text{H}$, the wave resistance $\rho=(L/C)^{0.5}=0.7~\Omega$. Judging by the volt–ampere characteristics of the discharge gap, $L\approx 143~\text{cm}$ in the case of the electric breakdown at $R_{\rm p}\approx 18~\Omega$, $R_{\rm p}>2\rho$ and $R_{\rm p}>1.4~\Omega$, which corresponds to the aperiodic shape of the discharge.

It was noted in [9] that the channel resistance is affected by the amount of energy released in the channel rather than the current through the latter. At a wire length of 143–152 cm and the maximum capacitance $C_{\rm max}=4.5~\mu \rm F$, a breakdown in a channel formed by wire explosion occurred with a probability close to 100%. Figure 8.3f shows a photograph of a controlled electric breakdown at $C=4.5~\mu \rm F$, $U_0=10~\rm kV$, and an interelectrode distance of 155 cm. In this experiment, an electric breakdown was ignited at a voltage of \sim 8.3 kV. The duration of the current pause was $\Delta T \approx 200~\mu \rm s$. At a wire length of 152–159 cm, an electric breakdown occurred with a probability of \sim 30%. For wires longer than 159 cm the breakdown probability (at the same parameters of the scheme) was close to zero. Thus, the average minimum electric field strength in the channel formed by wire explosion, at which breakdown can occur, is $E_{\rm min} \approx 52~\rm V/cm$. The suggestion about the possibility of long-term support of current breakdown with an amount of accumulated energy increased by an order of magnitude and the same charging voltage was partially confirmed. This problem will be considered in detail elsewhere.

The channel for recording radiation in the visible wavelength range has a low sensitivity, because it detects only the radiation entering the angular aperture of the polished receiving end face of the quartz fiber. If the distance between the end face and the discharge channel is reduced to minimum (~ 1.5 cm), one can detect the following phases in the oscillogram of a visible-light pulse. During the first 16 μ s after the wire explosion, the visible light intensity is low (the wire explosion gives rise to radiation with wavelengths in the range of $\lambda \approx 2.5$ –0.5 μ m) [29]. Then the oscillogram of visible light pulse exhibits the radiation corresponding to the streamer (weak), leader (weak), and arc phases of the breakdown.

An analysis of many photographs indicates that the electric breakdown trajectory (broken line, circle, etc.), which is set by spanned copper wire, is highly controllable and contains no branchings. The experiments revealed that the vertical orientation of exploded wire is indeed preferred in the case of streamer breakdown of maximally long gaps ($L_{\rm max} = 159$ cm) at $U_0 = 10$ kV and $C_{\rm max} = 4.5$ μF .

Let us analyze the requirements to an ionized formation that can initiate electric breakdown. The minimal conditions that are necessary for initiating a streamer were reported in [13]. We will consider a uniform conducting sphere with a radius R_s , placed in a uniform field of strength E_0 . To form a self-propagating plasma channel, the external field must be displaced from the plasma formation and amplified beyond it. To displace the external field from the entire volume of the sphere, charges must be nonuniformly distributed over the surface, and there must be no less than $N = 3\varepsilon_0\pi R^2 E_0/e$ electrons in the field. Taking into account that the radius of this formation should be no less than a-1 (a is the effective ionization coefficient), we can estimate the lower limit of the number of electrons at which a streamer may arise [13] as follows: $N_{\min} \approx 3\varepsilon_0\pi E_0/e\alpha^2$. As an example, we will consider air at atmospheric pressure. At the breakdown field strength $E_0 = 31.4 \text{ kV/cm}$ and effective ionization

coefficient $\alpha=12.4~{\rm cm}^{-1}$, we have $N_{\rm min}=2\times10^9$. The smaller the plasma formation radius, the more severe the limitation on the plasma density is. At the minimally allowable value $R\sim\alpha^{-1}$ the electron concentration in air at atmospheric pressure should be $N_{\rm min}\sim4\times10^{11}~{\rm cm}^{-3}$. The plasma formation size R also must be no smaller than the ionization length α^{-1} , in a field with a strength equal to the external field strength or even somewhat higher. In air at atmospheric pressure the ionization length is $\alpha^{-1}\sim0.8~{\rm mm}$. If the initial size of plasma formation in a homogeneous field satisfies the aforementioned requirements, this formation should generate ionization waves to both sides along the field, thus forming a plasma channel. The plasma channel development is accompanied by amplification of the field at both leader heads [13].

Our experiments showed that all above requirements to an ionized formation [13], which must be fulfilled to ignite an electric breakdown, are implemented in the channel of the discharge gap formed by wire explosion with the aforementioned parameters. The characteristics of separate plasma formations ($R_{\rm s} \sim 0.5$ –4 mm, average distances $l \sim 3-5$ mm, and temperature $T \sim 3000-5000$ °C) with clusters of superheated drops and their aggregates at the centre, as well as low oxygen content in the wire-explosion channel, reduce significantly the average field strength that is necessary for electric breakdown. Note that the size of individual plasma formations exceeds that of superheated drops of wire material by one to two orders of magnitude. The average density of the wire-explosion products in the channel is $\rho \sim 0.1 \text{ kg/m}^3$. The electric field in separate spherical plasma fractions can be amplified by a factor of no more than 3. Further studies should reveal new factors leading to electric breakdown in the channel produced by wire explosion at $E_c = 52$ V/cm. We should note the original work by Komel'kov [34], who analyzed the leader-discharge channel. We showed that the specific resistance per unit length in the channel of leader positive retarded discharge is 11.8 W/cm, while the longitudinal gradient along the channel in the end of the leader phase is 55.5 V/cm. The main parameters of the leader channel turned out to be the same as in the case of arc discharge. The result obtained in [34] was interpreted in [13] as not quite correct because of incorrect analysis of the discharge-gap voltage oscillograms. Our results disprove the conclusion of [13].

To check the influence of the size of individual plasma formations in the channel on the mechanism of electric breakdown, we performed experiments with explosion of a copper wire $L \sim 30\text{--}36$ cm long and Ø 90 μ m in diameter at U_0 = 10 kV and C_{max} = 4.5 μ F, i.e., at a much higher specific energy contribution. The channel formed by wire explosion with these parameters contains a fairly large number of wire-material nanoparticles [22], whereas large particles (individual plasma formations) are completely absent. In this case, the second requirement to the development of streamer mechanism of breakdown in the channel is violated. As a consequence, a fivefold decrease in the gap length did not lead to breakdown at the corresponding parameters of the discharge circuit. It occurred only for wires not shorter than $L \geq 60$ cm, a minimum value at which the size of plasma formations in the wire explosion channel became sufficiently large to implement a streamer breakdown.

8.6 Formation of Electrical Discharges in a Plasma Channel Produced by a Solid-State Laser

We also investigated the regime of electric breakdown in a plasma channel containing evaporated aerosol particles of metals and their compounds, which is formed by focusing radiation of a solid-state laser, operating in the modified spike regime, onto targets made of different materials [35, 36]. To form a plasma plume on a target, we used a phosphate glass laser with a wavelength $\lambda = 1.054~\mu m$, operating in a modified lasing regime with a peak power of 100-500~kW.

Photographs of lasers operating in this regime are shown in Fig. 8.4a, b. Solid-state lasers of this type are unique. Actually, they are laser hyperboloids (concerning the way of extracting radiation from a totally reflecting flat cavity through a round hole of large diameter, which can be seen in the upper photograph). Lasers of this type can produce large plasma plumes in both pulsed and pulse-periodic regimes. A laser pulse with a width up to 700 us consisted of many (approximately 150) high-contrast pulses 150-300 ns wide with an average repetition rate of 200 kHz (Fig. 8.4c). The radiation divergence at the laser output $\alpha \sim 4 \times 10^{-4}$ rad, was close to the diffraction one. The total energy per laser burst reached ~ 30 J (see the laser in Fig. 8.4a). Graphite, vinyl plastic, textolite, ferrite, Permalloy, and carbonyl core were used as targets. Their exposure to focused laser radiation led to the formation of a cloud of rapidly expanding plasma, which contained aerosol particles of evaporated target material $\sim 50-1000$ nm in size. No large particles were found in the plasma cloud. Note that a copper target cannot be used to form an electric breakdown in this plume, because evaporated large copper drops have velocities of several hundred meters per second and cannot form a quasi-stationary channel for electric breakdown.

The conductivity of this plasma has been studied little, while the dynamics of changes in its properties is of great interest to search for the ways of forming (according to the Impulsar program) superlong high conductivity channels in order to transfer energy at large distances. The experiments were performed with a system of electrodes, between which an electric discharge was ignited (Fig. 8.5). An anode in the form of a copper cylinder was connected to the high-voltage output of the capacitor battery with a capacitance $C = 2 \mu F$, which was charged to a voltage of $U_0 = 10 \text{ kV}$. A duraluminum cathode(K) had a hole Ø 6 mm in diameter, through which laser radiation was guided to the target using a lens with a focal length of F = 300 mm. The distance between the electrodes was $L \sim 80 \text{ mm}$. The photo of the plasma plume on the target made of graphite is shown in panel (b). The results of image processing on the PC with the use of the HSB color model are presented in panel (c).

At a laser pulse energy below 30 J the gap was switched using the plasma formed on the target. Typical photographs of the electric breakdown in atmosphere on a graphite target (at a laser burst energy of 12 J) for a gap ~ 70 mm wide, obtained using an FS-1 filter, a neutral NS-9 filter, and an OLYMPUS C-5050 ZOOM digital camera, are shown in Fig. 8.6. In highly inhomogeneous fields,

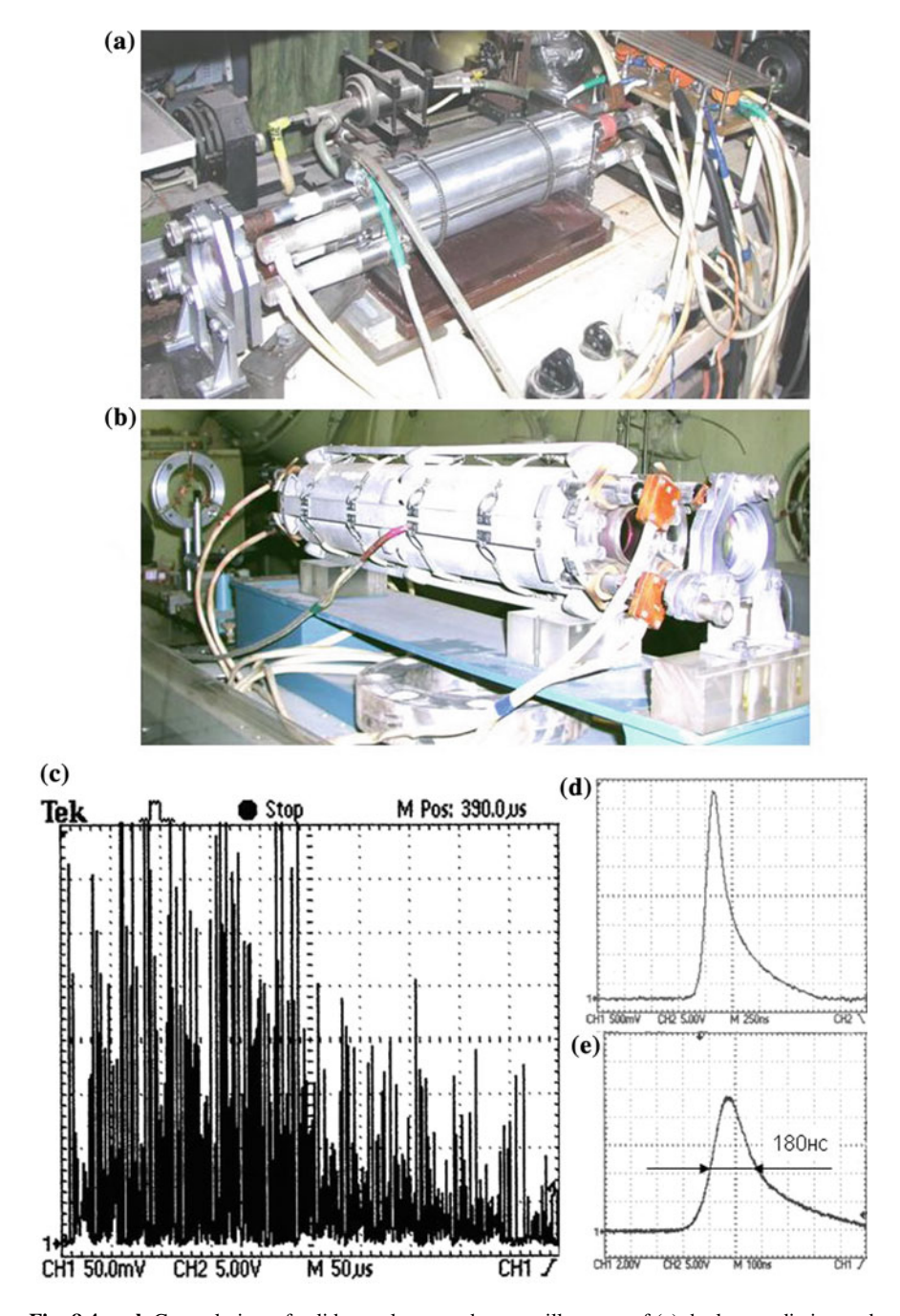


Fig. 8.4 $\,$ a, b General view of solid-state lasers and c-e oscillograms of (c) the laser radiation and $(d,\,e)$ separate laser pulses

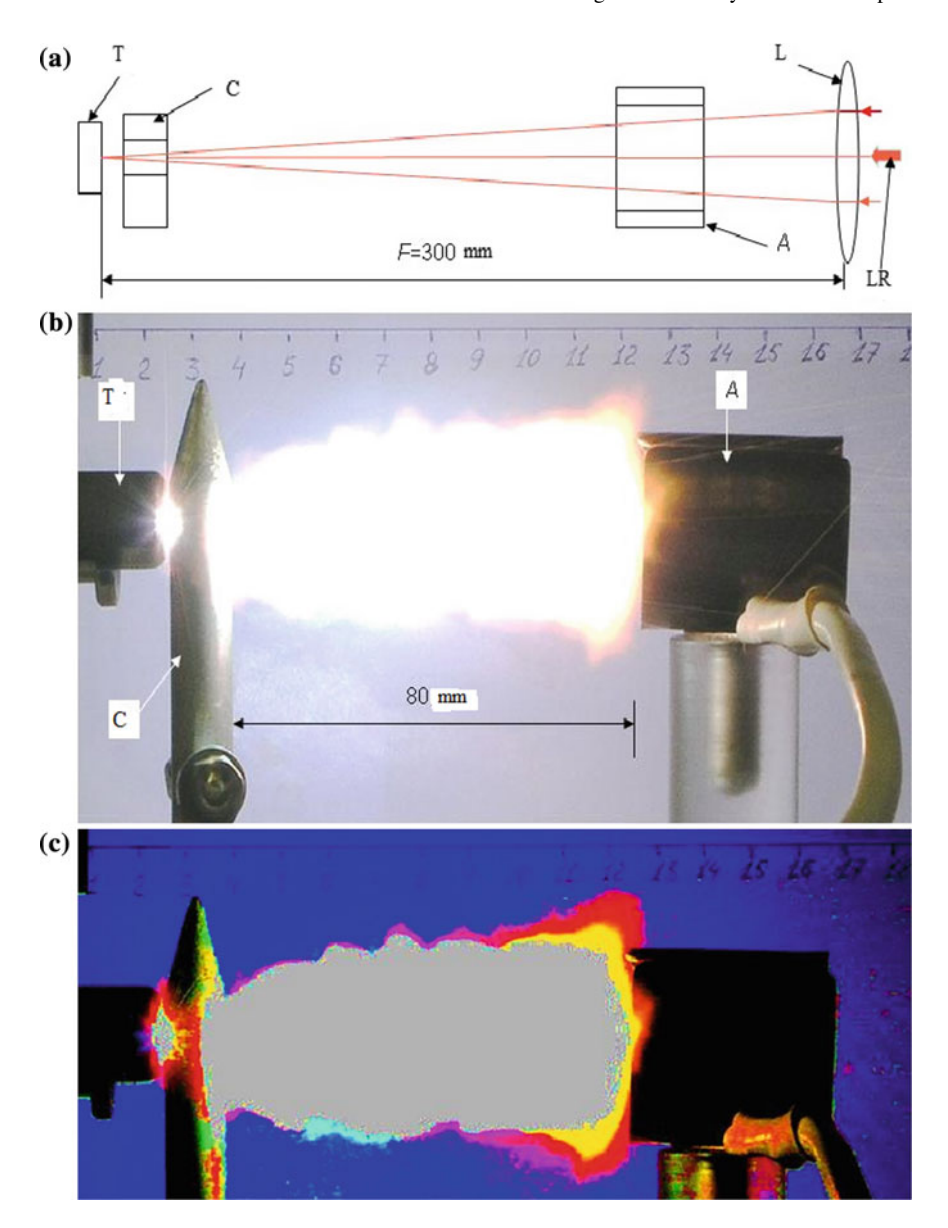


Fig. 8.5 a Schematics of the system for studying the conductivity of plasma plume products (T indicates a target), \mathbf{b} a photograph of a plasma plume on a graphite target, and \mathbf{c} the results of image processing in the system of HSB color coordinates

streamers are formed primarily in the regions of maximum field strength near the electrodes and, depending on the voltage polarity, are directed either to the anode or to the cathode [13]. In the photographs in Fig. 8.6 the streamer directed to the anode

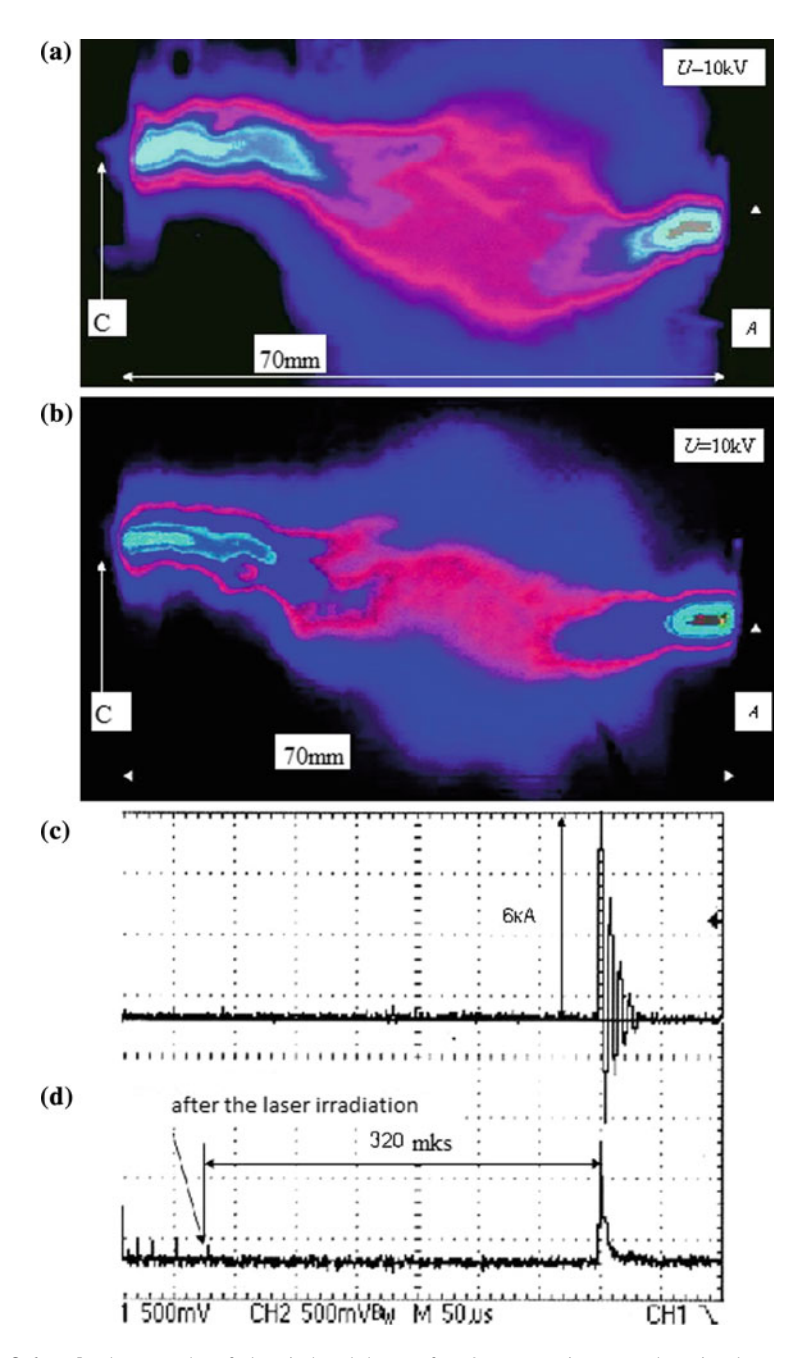


Fig. 8.6 a, b Photographs of electric breakdown of a 70-mm gap in atmosphere in plasma-plume products (photographing through an FS-1 filter and a neutral NS-9 light filter) and the results of image processing in the system of HSB color coordinates, $\bf c$ a current oscillogram at electric breakdown of the gap (voltage $U_0=10$ kV, storage capacitance C=2 μF) in plasma plume, and $\bf d$ a luminescence oscillogram for the discharge channel in aerosol plasma

develops more rapidly than that directed to the cathode. Streamers overlap at a distance of ~ 25 mm from the anode, and an electric breakdown of the gap occurs.

An analysis of this process shows that the breakdown has a random trajectory, as well as a natural lightning. In addition, the results of experiments with different targets show that electric breakdown occurs at a minimum average electric field strength of ~ 300 V/cm. The experiments revealed also that the electric breakdown delay (which is shown in the oscillograms of discharge-circuit current and luminescence) for the graphite target, could exceed 300 μs after the laser irradiation. In Fig. 8.6c, the capacitance C=2 μF . The current oscillogram indicates that the damping oscillation period T=8 μs ; therefore, the discharge inductance is 0.8 μH . The contour wave resistance $\rho\approx 0.6$ Ω . According to the current—voltage characteristics of the $L\approx 70$ mm discharge gap for the graphite target, the discharge gap resistance is $R_{\rm p}\approx 0.5$ Ω , a value corresponding to an oscillatory discharge with a high damping decrement. The long breakdown delay with respect to the laser irradiation onset is apparently caused by the closing of the discharge gap by the expanding vapor of the target material and discharge-gap preionization by UV radiation of the plasma plume.

The targets made of other materials were characterized by a shorter possible delay. Changing the delay for the voltage pulse applied to the capacitor, one can measure the plasma characteristics at different instants and thus estimate the conductivity of the channel at different stages of its cooling and expansion. In our opinion, the strong electric field in these experiments is due to the absence of large particles in the erosion-plasma cloud. To carry out successfully the Impulsar program, we believe it necessary to study the dynamics of plasma conductivity and the residual aerosol products after cooling the plasma.

8.7 Experimental Results

Below we report the estimated values of the channel conductivity, which were obtained both in our previous experiments on the breakdown of atmospheric air using long- and short-wavelength radiation and the experiments with aerosol plasma.

- (i) For the plasma channels obtained on graphite, ferrite, Permalloy, and carbonyl core targets using a phosphate glass laser, the gap specific resistance was 10 Ω /m and the specific breakdown voltage was \sim 300 V/cm.
- (ii) For the plasma containing a set of dispersion and condensation aerosols, which was obtained by wire explosion, the gap specific resistance was $\sim 5~\Omega/m$ and the specific breakdown voltage was $\sim 50~V/cm$.
- (iii) For the plasma channel formed by a pulsed CO_2 laser with a conical focusing optics, the gap specific resistance was 100–400 Ω /cm and the specific breakdown voltage was ~ 80 V/cm.

(iv) For the plasma channel obtained with the aid of a femtosecond pulsed laser, the gap specific resistance was ~ 0.1 MW/m and the specific breakdown voltage was ~ 7.5 kV/cm [4].

These estimates, based on the results of the electric-breakdown experiments, show that a voltage of 7 MB, at a total introduced energy of ~ 300 kJ, is sufficient to form a plasma channel ~ 1 km long and 8 mm in diameter. Note that the minimum specific resistance of the channel depends strongly on the specific introduced energy; the transverse size of plasma formations; the concentration and size of aerosol particles; the repetition rate of laser pulses and their energy; and the humidity, temperature, and many other parameters of the medium where a conducting channel is formed. The results of the studies show that the discharge plasma has a high conductivity and can efficiently be used to form a high conductivity channel in order to transfer energy over long distances.

8.8 Conclusions

We determined the range of sizes of copper and copper oxide particles (from 50 nm to 300 $\mu m)$ and their minimum volume density ($\sim\!0.1~kg/m^3$) that are necessary to provide an electric breakdown in order to form a plasma channel according to the "Impulsar" program. The results of the model experiments showed that nanoparticles in the plasma channel can merge into larger aggregates during the LRE operation. The experiments on electric breakdown showed also that a high conductivity channel with a diameter of $\sim\!8$ mm and a minimum specific resistance of $\sim\!5~\Omega/m$ is implemented at the maximum introduced specific energy: $\sim\!200~J/m$. At a larger channel diameter, the specific energy is proportional to the squared ratio of diameters. The minimum average electric field strength ($\sim\!52~V/cm$) in the channel, at which a streamer-leader electric breakdown of the discharge gap begins, is due to the following factors:

- (i) the presence of dispersion and condensation aerosols of hot particles of copper oxide (CuO, Cu₂O) and copper with oxidized surface (smaller than 300 μ m in diameter) in the channel for a long time (1–10 μ s) due to their low mobility;
- (ii) the presence of superheated metal drops at the centre of plasma formations, which are in the metastable (unstable) state at temperatures $T \sim 3000-5000$ °C and play a role of hot dots [31] during thermionic emission;
- (iii) formation of large linear aggregates of aerosol particles [20], which are formed during wire explosion;
- (iv) low oxygen content in the channel as a result of fast oxidation of aerosol particles formed during wire explosion.

References

- 1. V.V. Apollonov et al., J. Opt. Soc. Am. B 8, 220 (1991)
- 2. G.N. Alexandrov et al., Elektrichestvo 12, 47 (1980)
- 3. F. Kinoshita, Y. Morooka, M. Uchiumi et al., in *Proceedings of XII International Symposium on Gas Discharge and their Applications* (Greifswald, Germany, 1997) p. 475
- 4. J.-C. Diels, W. Rudolph, *Ultrashort Laser Pulse Phenomena: Fundamentals, Techniques, and Applications on Femtosecond Time Scale* (Acad. Press, Burlington, 2006)
- 5. J. Kasparian, M. Rodriquez, G. M'ejean et al., Science 301, 61 (2003)
- 6. L. Berge, S. Skupin, R. Nuter, J.-P. Wolf, Rep. Prog. Phys. 70, 1633 (2007)
- V.D. Zvorykin, A.O. Levchenko, N.N. Ustinovskii, Kvantovaya Elektron. 41, 227 (2011)
 Quantum Electron. 41, 227 (2011)
- 8. V.V. Apollonov, L.M. Vasilyak, S.Yu. Kazantsev et al., Kvantovaya Elektron. **32**, 115 (2002) [Quantum Electron. **32**, 115 (2002)]
- 9. E.M. Bazelyan, YuP Raizer, Fizika molnii i molniezashchita (Physics of Lightning and Lightning Protection) (Fizmatlit, Moscow, 2001)
- 10. V.V. Apollonov, Opt. Eng. 44, 1 (2005)
- 11. L.N. Pyatnitskii, V.V. Korobkin, Trudy IOFAN 57, 59 (2000)
- 12. http://www.teramobile.org/publis.html
- E.M. Bazelyan, YuP Raizer, Iskrovyi razryad (Spark Discharge) (Izd-vo μFTI, Moscow, 1997)
- 14. G.N. Aleksandrov, Zh. Tekh. Fiz. 37, 288 (1967)
- 15. Yu.P. Raizer, Lazernaya iskra i rasprostranenie razryadov (Laser Spark and Propagation of Discharges) (Nauka, Moscow, 1974)
- E.I. Asinovskii, Vasilyak L.M. Entsiklopediya nizkotemperaturnoi plazmy. Vvodnyi tom. Kniga II (Encyclopedia of Low-temperature Plasma: Introduction. Book II) (Nauka, Moscow, 2000), p. 234
- P.K. Tret'yakov, G.N. Grachev, A.I. Ivanchenko, V.L. Krainev, A.G. Ponomarenko, V.N. Tishchenko, Dokl. Akad. Nauk. 336, 466 (1994); V.V. Apollonov, V.I. Kislov, A.G. Suzdal'tsev, Kvantovaya Elektron. 33, 753 (2003)
- 18. Grachev G.N., Ponomarenko A.G., Smirnov A.L., Statsenko P.A., Tishchenko V. N., et al. Kvantovaya Elektron. **35**, 973 (2005); V.V. Apollonov, in *Proceedings of X International Conference on Photonics and Optoelectronics* (Wuhan, China, 2009), p. 13
- V.V. Apollonov et al., Sposob sozdaniya tokoprovodyashchikh kanalov v neprovodyashchei srede (Method for the Formation of Conducting Channels in a Nonconducting Medium), RF Patent No. 2400005 May 20, (2009)
- 20. N.A. Fuks, Mekhanika aerozolei (Mechanics of Aerosols) (Izd-vo AN SSSR, Moscow, 1955)
- V.P. Ageev, A.I. Barchukov, F.V. Bunkin et al., Kvantovaya Elektron. 4, 2501 (1977) [Sov. J. Quantum Electron. 7, 1430 (1977)]
- 22. http://www.nanosized-powders.com
- 23. Rukhadze A.A., Shpigel' N.S. *Elektricheskii vzryv provodnikov (Electric Explosion of Conductors)* (Mir, Moscow, 1965), p. 341
- N.I. Gerasimenko, N.A. Grashina, A.G. Medvedkov, A.B. Meshcheryakov, N.V. Pletnev, Prib. Tekh. Eksp. 1, 212 (1988)
- 25. G.M. Goncharenko, in *Trudy MEI. Vyp. 45. Elektroenergetika* (Proceedings of MEI. Issue. 45: Electric Power Engineering) (Izd-vo MEI, Moscow, 1963), p. 146
- 26. V.N. Gavrilov, E.A. Litvinov, Zh. Prikl. Mekh. Teor. Fiz. 34, 28 (1993)
- I.F. Kvartskhava, A.A. Plyutto, A.A. Chernov, V.V. Bondarenko, Zh. Eksp. Teor. Fiz. 30, 42 (1956)
- 28. M.M. Martynyuk, Zh. Tekh. Fiz. 44, 1262 (1974)
- B.P. Peregud, K.B. Abramova, Dokl. Akad. Nauk SSSR, 157, 837 (1964); K.B. Abramova,
 V.P. Valitskii, Yu.V. Vandakurov, N.A. Zlatin, B.P. Peregud, Dokl. Akad. Nauk SSSR, 167,
 778 (1966)

References 115

- 30. N.A. Protopopov, vm Kul'gavchuk, Zh. Tekh. Fiz. **31**, 557 (1961)
- 31. A.E. Vlasto's J. Appl. Phys., 38, 4993 (1967); A.E. Vlasto's J. Appl. Phys. 39, 3081 (1968)
- 32. A.F. Aleksandrov, V.V. Zosimov, S.P. Kurdyumov, Yu.P. Popov, A.A. Rukhadze, I.B. Timofeev, Zh. Eksp. Teor. Fiz. 61, 1841 (1971)
- 33. A.F. Aleksandrov, A.A. Rukhadze, Fizika sil'notochnykh elektrorazryadnykh istochnikov sveta (Physics of High-Current Electric-Discharge Light Sources) (Atomizdat, Moscow, 1976)
- 34. V.S. Komel'kov, Dokl. Akad. Nauk SSSR 58, 57 (1947)
- 35. V.V. Apollonov, N.V. Pletnev, *Sposob neodnorodnogo vyvoda energii svobodnoi generatsii vysshikh poperechnykh tipov kolebanii iz lazera i lazer* (Method for the Inhomogeneous Extraction of the Energy of Free Higher Transverse Lasing Modes from a Laser and a Laser), RF Patent No. 2239921 (November 10, 2004)
- 36. R. Sinton, R. van Herel, W. Enright, P. Bodger, J. Appl. Phys. 110, 093303 (2011)

Chapter 9 High Conductivity Channel Expansion Rate Measurements



9.1 Introduction

When using a controlled electrical breakdown [1, 2] in a plasma channel that is produced by an exploding wire [3–8] and is capable of passing a current in the short-circuit mode, on should know the temperature and radius of the channel [9]. The notion of the radius of the channel refers to its part through which a main fraction of the current passes at the main stage of the discharge [9]. Quantities such as the expansion rate of the channel and its maximal diameter, which is observed in a high-conductivity high-temperature area, are of importance for describing the specific energy deposition and pressure at the front of a cylindrical shock wave that propagates in the atmosphere. In [10, 11], a spark discharge channel in the atmosphere was studied using the Tepler's shadow method combined with mirror scanning (rotating mirror method). For the spark channel, we took a highly (almost completely) ionized conducting area. The radial expansion of this area may be associated with the following processes:

- (i) heat transfer, which leads to the expansion of the high-temperature (hence, highly ionized) area;
- (ii) diffusion of electrons and ions in the radial field of the spark;
- (iii) photoionization.

A shock wave that propagates with a velocity of about 1 km/s results from a pressure step of several tens of atmospheres [10]. This step cannot be attributed to photoionization even within a heavily confined region, since photoionization cannot raise the pressure by several tens of times [11]. Consequently, a process that causes a sharp pressure step (explosive process) is expected to occur at the initial stage of the discharge [10, 11]. For a spark discharge, an energy of 0.1–1.0 J per one centimeter of the channel length is released within 5×10^{-7} s after breakdown. This energy is comparable to that being released after the detonation of explosives. Thus, the expansion of the channel is actually initiated by an explosive process. In a

thin channel produced by breakdown, the temperature, and hence, pressure of the gas rise. This generates a cylindrical shock wave that propagates with a velocity much higher than sound velocity a_0 ($a_0 = 340$ m/s in the undisturbed atmosphere at room temperature). Calculations show that, at the shock wave front and immediately behind it, the temperature is about 10,000 K; this high temperature provides the intense ionization of the channel [10]. As the shock wave propagates, the temperature at its front declines and, as follows from data of optical investigations by the Tepler's method and similar methods, the SW front moves away from the channel. The further expansion of the channel is due to the motion of the gas as a whole and the continuous release of the current energy in the channel. The expansion rate of the channel [10, 11] depends on the energy E(t) released in the channel by time instant t and on gas parameters, namely, the density of the gas and ratio γ of its specific heats in calculating γ . The ionization and dissociation processes must be taken into consideration.

In [12], optical phenomena related to the expansion of the spark discharge channel were studied. For a specific energy deposition of about 3 J/cm, the boundaries of blue-violet (4700-3700 Å) and IR (7000-10,000 A) radiations propagate at the same velocity, only within 0.4-0.5 µs after the beginning of the discharge until the diameter of the channel becomes equal to 2.5 mm. The time instant of the velocity of the short-wave radiation boundaries changes and sharply coincides with the first maximum of the current in the discharge circuit. Comparing the sweeps of the shock wave and IR radiation [12], one can see that the IR radiation boundary coincides with the trailing edge of the shock wave. It follows from the sweep pictures that the leading edge of IR radiation becomes sharp when it is limited by the gas thickening in the shock wave. The shock wave has a steep front; an area of roughly uniform density; and a smooth trailing edge, which is sometimes called the sheath of the channel. It has been shown [12] that the formation of the channel and its structure can be conceived as follows. For the time of the current rise in the first quarter of the oscillation cycle, the energy release in the spark continuously grows. The discharge plasma expands explosively with a supersonic velocity. When the current reaches a maximum the energy deposition into the channel drops. As a result, the plasma expansion slows down and an SW is detached from the channel front. Between the plasma at the center of the discharge, which emits cw radiation, and the SW, a layer of a hot neutral gas arises, which emits IR radiation in the form of arcs.

In [13], reasons for the experimentally observed spark channel expansion are considered. According to [14], the conductivity a of air plasma rises sharply with temperature in the temperature range $T = (0.4-1.2) \times 10^4$ K and achieves saturation at ionization temperature $T_i > 1.5 \times 10^4$ K [15]. Irrespective of the mechanism responsible for primarily heating air to temperature Ti, its further heating is due to the Joule energy of the discharge current, since the efficiency of the heating mechanism sharply drops. The expansion rate of the channel is calculated based on the mechanism of primarily heating the gas to temperature T_i , and the amount of the Joule heat in the channel may influence the rate of this process. As stated in [13], shock loading of the gas at maximal velocities of the shock front (bow wave),

9.1 Introduction 119

D = 2-5 km/s, is provided by low temperatures at the front: $T = (2-7) \times 10^{-5}$ 10^3 K < T_i . Therefore, the boundary of the spark channel, which moves with the above velocity, cannot be a shock front. In the model suggested in [13], the energy spectral density of radiation reaches a maximum in the wavelength interval $\lambda_{\rm m} =$ 62-50 nm for spark channel temperature T = 4-5 eV. Most of this radiation is absorbed by cold air layers at the boundary of the channel. Intense light absorption serves as a main mechanism of air heating in the subsequent development of the spark, when the shock front is detached from the boundary of the channel. In this case, the channel is at the shock wave tail, the gas density in it is small, and the radiation becomes optically thin. In both cases, the width of the radiatively heated area can be estimated from coefficient $\chi_v \setminus 1/l_v$ of large quantum absorption. Energy hv of large quanta equals ionization energy J of air molecules [16]. For $T = 1.2 \times 10^4$ K and $N_0 = 5 \times 10^{18}$ cm⁻³ in the channel, the spectral mean free path of heating quanta equals $l_v = 1/\chi_v = 0.59 \times 10^{-2}$ cm [13]. This value of l_v is roughly two orders of magnitude greater than the spark channel radius. This allows us to consider the channel boundary as a thin layer of light absorption and gas ionization. Calculations show [13] that the electron heat conductivity may play a considerable role in an area of high temperature gradients near the boundary. The electron heat flux is absorbed at the boundary in a layer Δr ; $l_v \approx 0.6 \times 10^{-2}$ cm thick; that is, a thin layer at the boundary of the channel is jointly heated by radiation and heat conduction. In the cases considered above, the hot zone shifts toward new portions of the cold gas, which may be considered as the wave motion of some thin heating and ionization front or as the motion of an ionization wave. In [13], the rates of the ionization wave front at the early and advanced stages of spark channel expansion were estimated from the energy balance at the front. At the early stage, the expansion rate of the spark channel was found to be $D_{\Sigma,e} = 1.14 - 2.77$ km/s, while the contribution of electron heat conduction is negligibly small under the given conditions. At later instants of time, e.g., at $t = 5 \mu s$, the propagation rate of the ionization wave was $D_{\rm v.e} = 420$ m/s. Now, electron heat conductivity plays a significant role and makes a major contribution to the propagation Rte of the ionization wave front.

In [17], experimental data in favor of the Lim theory were reported. The data were obtained in terms of a model of an intense cylindrical shock wave. A 30-mm-high cylindrical pentaerythritol tetranitrate (PETN) charge with outer and inner radii of 30 and 4 mm, respectively, was exploded, and the SW velocity as a function of the propagation time or the distance from the surface of the charge was determined using an ionization probe and an oscilloscope. The reciprocal shock wave velocity U^{-1} versus time $t^{1/2}$ dependence for Mach numbers in the interval 7–14 was linear in agreement with Lin's calculations. The deviation from linearity for Mach numbers less than three, which was predicted by Lin, may be associated with a finite size of the explosive charge. Similar experimental data that support the Lin theory were also obtained by Bennett [18, 19], who applied the same model. As an SW source, Bennett used the explosion of a 2-cm-long thin wire with a diameter of 90–160 μ m and a stored energy of 118 J.

In this chapter, we use a simple technique that does not require optical detection methods [10–12] to see how the expansion rate of the conductivity channel produced by the explosion of a thin copper wire depends on time for a maximal possible specific energy (about 1 kJ/m). Unlike the result obtained in [17], the $U^{-1}(t^{1/2})$, the dependence obtained in this work for a thin (90 μ m in diameter) exploding wire and Mach numbers less than three is linear.

9.2 Formation of Controlled Electrical Discharges in a Channel Produced by the Explosion of a Wire

Here, as well as in experiments [1, 2] on the formation of a controlled highconductivity channels in atmosphere, we used a vertically placed enamel-coated conductor made of PEV02 copper. Its length L, diameter, and capacitance C were L = 133 cm, 90 µm, and C = 90 µF, respectively. Voltage U_0 applied to the conductor was equal to 8.6 kV. Figure 9.1 show the schematic of the experimental setup; sensors used to measure the current with a Rogowski loop (RL) and the voltage across the capacitor bank using a voltage divider (VD); and the end face of a polished quartz fiber (QF), which transmits a radiation from the discharge channel to a fast pin photodiode (PD) with a time resolution of about 1 ns. In contrast to the setup described in [1, 2], our setup has a grounded ring electrode (RE), which is placed symmetrically with respect to the exploding fine wire (EFW) near the anode (15 cm distant from it). In a controlled breakdown initiated in the atmospheric channel that is produced by the exploding wire (EW), the discharge current partly closes on the ring electrode. Knowing that the inner diameter of the ring and time interval Δt between the onset of breakdown and the instant the plasma channel is completely closed (as judged from the current waveform), one can find the mean expansion rate for a given radius of the ring. The photos of capturing rings made of copper and duralumin with inner diameters of 19.0–36.5 mm are presented in Fig. 9.1b. The shape of the current pulse was determined using a screened differential Rogowski loop with a time resolution of about 30 ns and constant of integration $\theta = L_{\Sigma}/2R \approx 380 \,\mu s$ [20]. The shape of the voltage across the discharge gap was determined using a screened voltage divider of a mixed type [21], which was connected to the anode of the capacitor bank. This voltage divider gives a measuring error of 1% for the width of the current pulse leading edge $\tau_{\phi} \ge 1 \,\mu s$ [21] (for details of the voltage divider functioning, see [2, 21]). The advantage of this voltage divider is that it does not shunt a low-current source of discharge voltages. As a detector, a Tektronix TDS 220 digital oscilloscope was applied. A capacitor with capacitance $C = 74.8 \, \mu\text{F}$ was charged from a discharge voltage source to $U_0 = 8.6 \text{ kV}.$

The general operating principles of the charging voltage source upgraded by us are described in [22]. The output voltage of the source can be gradually controlled in the interval 2–12 kV. The maximal charging current is 5 mA. Unlike the voltage

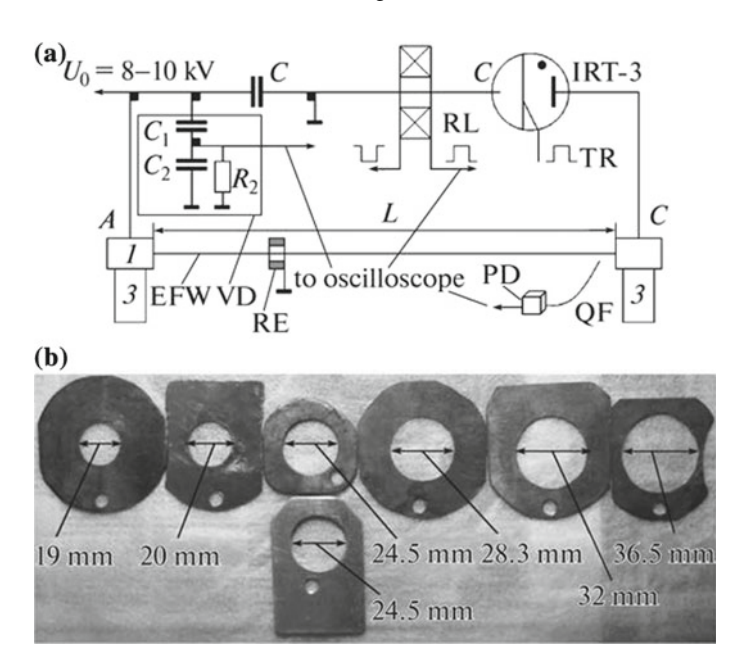


Fig. 9.1 a Electrical circuit to initiate breakdown in a channel produced by an exploding vertical copper wire: (1, 2) brass electrodes; and (3) ebonite insulators. IRT-3, ignitron (switch); RL, Rogowski loop; VD, voltage divider; TR, trigger; EFW, exploding fine wire; PD, photodiode; QF, quartz fiber; A, anode; C, cathode; and RE capturing ring. **b** Photos of several capturing copper rings with diameters from 19.0 to 36.5 mm and one duralumin ring 24.5 mm in diameter

source circuit suggested in [22], our voltage source uses a K140UD8-chip-based comparator, which is simple to tune and does not require add-on components. This voltage source offers the following advantages;

- (i) small weight and sizes in combination with a relatively high power,
- (ii) automatic system for charging the capacitor bank to a desired voltage and its maintenance accurate to 0.5%,
- (iii) high efficiency and reliability,
- (iv) capability of withstanding shorts at the output.

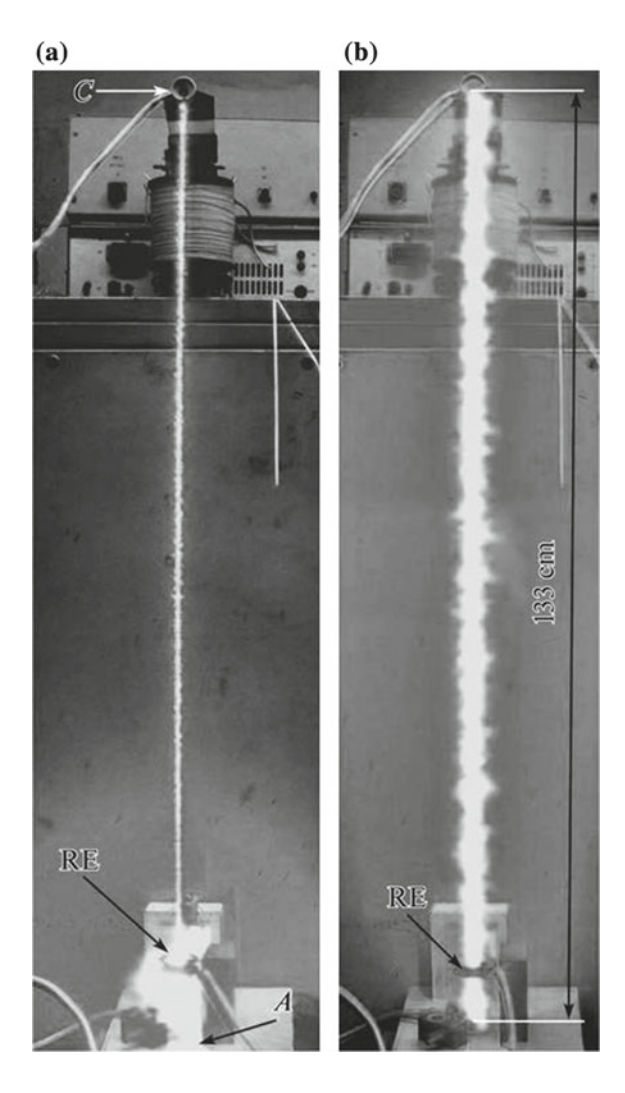
The charging voltage was measured using a C53 electrostatic voltmeter a high-ohmic voltage divider accurate to 0.5%.

When an external triggering pulse is applied to a controlled discharger (IRT-3 ignitron), the capacitor is discharged through the copper exploding 90 μ m, in diameter. In this work, we studied electrical breakdown in an atmospheric channel produced by the explosion of the 133-cm-long wire 90 μ m in diameter. The initial stored energy was about 2.8 kJ, and the specific electric field strength in the channel was $E \approx 59$ V/cm. It was shown [6] that if breakdown is associated with the explosion of a long wire, the discharge channel expands monotonically. Therefore, it seems more appropriate to consider the mean expansion rate of the channel, rather

than the value of its radius at a given instant of time, in order to estimate the discharge geometry. The expansion rate depends on specific energy W (energy per unit discharge length) linearly [6]. In this work, this energy is determined with the help of the grounded capturing ring electrode with an inner diameter of 19–40 mm.

The photos of the breakdown in the channel in the presence and absence of a capturing ring 20 mm in diameter are shown in Fig. 9.2a, b, respectively. Photographing was carried out manually using an OLYMPUS C-5050ZOOM digital camera through an FS-1 blue filter combined with an NS-9 neutral filter. Photographing conditions are described in [1, 2]. In Fig. 9.2a it is shown that in the presence of the capturing ring with an inner diameter of 20 mm, the Joule energy of the discharge current heats the channel only until the channel touches the grounded

Fig. 9.2 Photos of an electrical breakdown for vertical position of 133-cm-long exploding wire in a presence and b absence of the capturing ring 20 mm in diameter. A is anode; C is cathode



ring. Then, the current totally flows to ground, bypassing the discharge (ignitron). The corresponding time interval Δt was recorded on the current oscillogram by the Rogowski loop, which measures the current passing in the circuit through the discharger. Knowing the radius of the channel and time interval Δt , one can find the mean rate of the conductivity channel expansion for a given capturing ring. With a large set of rings with different diameters at hand, one can derive (with a certain accuracy) the time dependence of the channel instantaneous expansion. In our experiment, we used seven rings with inner diameters from 19 to 40 mm.

The photographs presented in Fig. 9.3 show the breakdown of the channel in the presence of rings (a) 24.5 and (b) 28.3 mm in diameter. The maximal (finite) size of

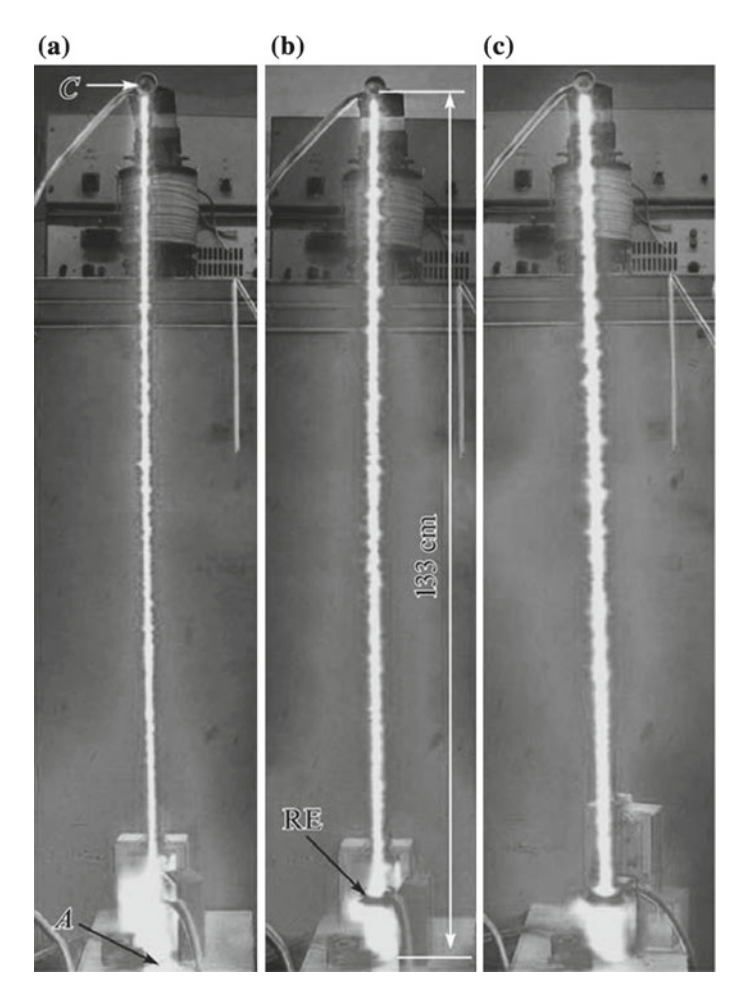


Fig. 9.3 Photos of electrical breakdown for the vertical position of the 133-cm-long exploding wire in the presence of the capturing ring **a** 24.5, **b** 28.3, and **c** 32 mm in diameter. A is anode; C is cathode

the conductive channel grows with the ring diameter. This indicates that, after the expanding channel touches the grounded ring, the energy no longer enters the channel.

Figure 9.4a shows the (1) current and (2) voltage waveforms in the case of a breakdown in the channel produced by a 133-cm-long exploding wire with a diameter of 90 μ m in the presence of a grounded ring with a diameter of 20 mm. The (1) current and (2) voltage waveforms in the case of a breakdown in the channel in the presence of grounded rings with diameters of 24.5 and 28.3 mm are shown in Fig. 9.4b, c, respectively. Finally, Fig. 9.4d shows the (7) current and (2) voltage waveforms for breakdown in the channel in the absence of the capturing ring. When the diameter of the ring grows, so does time Δt it takes for the conducting channel to touch the grounded ring. This is distinctly seen in the current waveforms, in which the current sharply drops at the instant of contact. Knowing time interval Δt and the diameter of the ring, one can find the mean rate of channel expansion over time interval Δt .

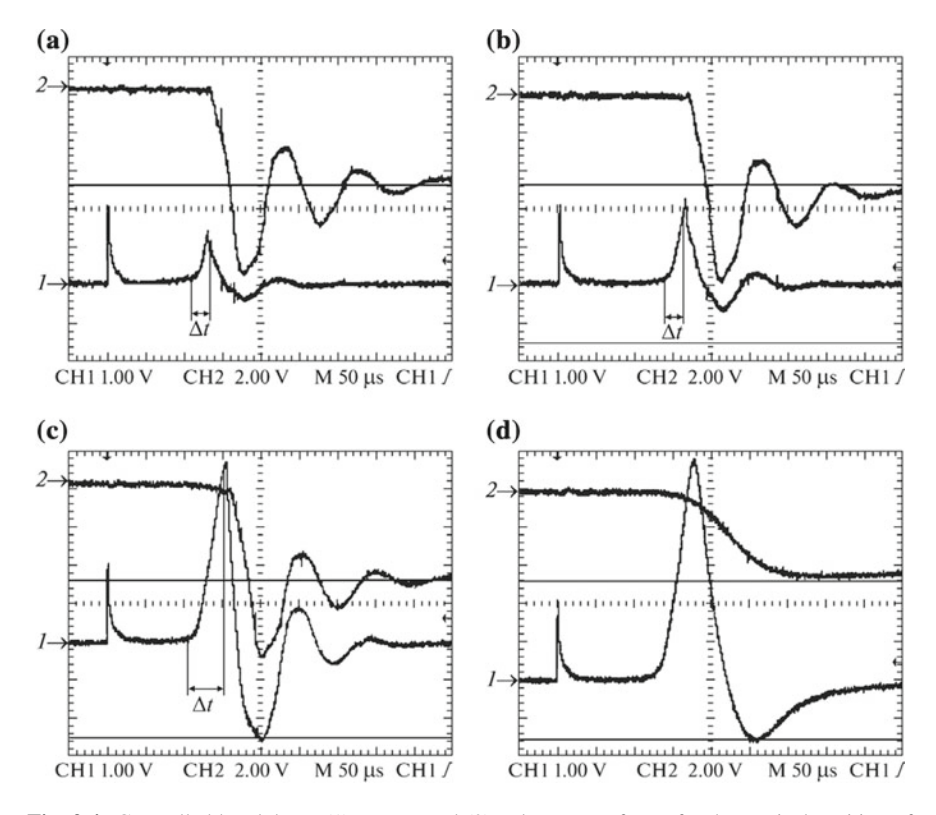


Fig. 9.4 Controlled breakdown (1) current and (2) voltage waveforms for the vertical position of the 133-cm-long exploding wire in the presence of the capturing ring **a** 20, **b** 24.5, **c** 28.3, and **d** without the capturing ring. A is anode; C is cathode

For example, in the experiment the data of which are depicted in Fig. 9.3c (the specific energy deposition is 800 J/m), the means expansion rate of the channel is roughly equal to 400 m/s. The diameter of the ring's conducting area was 32 mm.

It has been found [6] that, in the case of extended (about 100 cm long) discharges, there is a time interval within the first quasi-cycle of the discharge channel over which the discharge radiates as an absolutely black body and a major energy contribution to the discharge is made. Over this time interval, 64% of the energy stored in the capacitor bank is deposited into the discharge. For specific breakdown field strength $E_c = 59$ V/cm, a maximal breakdown channel diameter, and an energy stored in the capacitor bank of 2.8 kJ, we estimated the maximal specific energy deposition into the channel during breakdown. It was found to be about 1 kJ/m.

Figures 9.5a, b plot the experimental dependences of current expansion reciprocal rate U^{-1} on (a) $t^{1/2}$ and (b) channel radius R, and Fig. 9.5c plots channel radius #R versus $t^{1/2}$. Unlike the results obtained in [17] for Mach numbers less than three, this dependence is linear. This agrees with results following from the model of an intense cylindrical shock wave [23] for a small transverse size of a shock wave source (in our case, the exploding wire 90 μ m in diameter). The linear extrapolation of the experimental curves (dashed line in Fig. 9.5) toward higher expansion rates ends in the origin. This means that the explosion of a fine wire simulates the

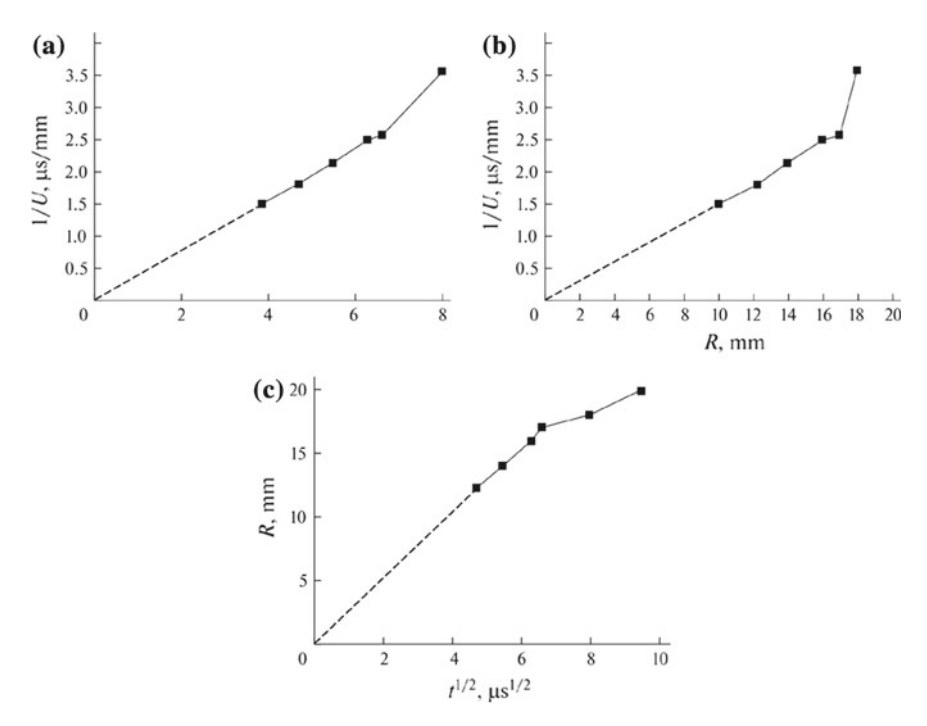


Fig. 9.5 Experimental dependences of the reciprocal channel expansion rate (U^{-1}) on **a** $t^{1/2}$ and **b** channel radius R and **c** dependence of channel radius R on $t^{1/2}$

initiation of an ideal cylindrical shock wave, which is impossible when a 30-mm-high cylindrical PETN charge with inner and outer radii of 4 and 15 mm is exploded [17]. Thus, it can be concluded that the expansion rate of a conductivity channel produced by an exploding wire coincides with the propagation velocity of a cylindrical shock wave in the channel.

9.3 Conclusions

We suggested a new experimental technique for determining the high conductivity channels expansion rate as a function of the propagation time. This technique was applied in experiments on the controlled breakdown of extended (0.6–1.9 m long) gaps produced by an exploding wire for a maximal specific energy deposited into the channel of about 1 kJ/m. With this technique, the main parameters of the breakdown, namely, the specific energy deposited into the discharge channel and the variation in the resistivity of the discharge gap, were measured accurate to 5%. In terms of the equilibrium plasma model, these data allow us to find the maximal temperature in the discharge channel and thereby more accurately determine the breakdown voltage and specific energy deposition in considering controlled breakdown over large lengths. It follows from the experimental dependences of channel expansion rate U and channel radius R on propagation time that, with an accuracy of up to 20%, these parameters coincide with the velocity and radius of an intense cylindrical shock wave generated by an exploding wire for a maximal specific energy deposition into the channel exceeding 1 kJ/m. It should be noted that, in the experiment, we managed to initiate an ideal cylindrical shock wave, the theory of which was developed in [23].

References

- 1. V.V. Apollonov, N.V. Pletnev, Kvantovaya Elektron. 42(2), 130 (2012)
- 2. V.V. Apollonov, N.V. Pletnev, Tech. Phys. 58, 1770 (2013)
- 3. R. Sinton, R. van Herel, W. Enrigh, P. Bodger, J. Appl. Phys. 108, 053304.1 (2010)
- 4. R. Sinton, R. van Herel, W. Enrigh, P. Bodger, J. Appl. Phys. 110, 093303.1 (2011)
- A.F. Aleksandrov, V.V. Zosimov, S.P. Kurdyumov, YuP Popov, A.A. Rukhadze, I.B. Timofeev, Sov. Phys. JETP 34, 979 (1971)
- A.F. Aleksandrov, A.A. Rukhadze, *Physics of High-Current Electric-Discharge Light Sources*, 2nd edn. (Atomizdat, Moscow, 1976; LIBROKOM, Moscow, 2012)
- 7. Exploding Wires, vol. 1 (Plenum, New York, 1959)
- 8. Exploding Wires, vol. 2 (Plenum, New York, 1962)
- 9. E.M. Bazelyan, YuP Raizer, *Physics of Lightning and Lightning Protection* (Fizmatlit, Moscow, 2001)
- I.S. Abramson, N.M. Gegechkori, S.I. Drabkina, S.L. Mandel'shtam, Zh. Eksp. Teor. Fiz. 17, 862 (1947)
- 11. N.M. Gegechkori, Zh Eksp, Teor. Fiz. 21, 493 (1951)

References 127

- 12. M.P. Vanyukov, V.I. Isaenko, L.D. Khazov, Zh. Tekh. Fiz. 25, 1248 (1955)
- 13. YuK Bobrov, Zh. Tekh. Fiz. 44, 2340 (1974)
- 14. Notes on Physics and Chemistry of Low-Temperature Plasma, ed. by L. S. Polak (Nauka, Moscow, 1971)
- 15. YuP Raizer, Usp. Fiz. Nauk 108, 429 (1972)
- 16. YaB Zel'dovich, YuP Raizer, *Physics of Shock Waves and High-Temperature Hydrodynamic Phenomena* (Nauka, Moscow, 1966)
- 17. M. Birk, Y. Manheimer, G. Nahmani, J. Appl. Phys. 25, 1208 (1954)
- 18. F.D. Bennett, Phys. Fluids 1, 347 (1958)
- 19. F.D. Bennett, Phys. Fluids 1, 515 (1958)
- N.I. Gerasimenko, N.A. Grashina, A.G. Medvedkov, A.B. Meshcheryakov, N.V. Pletnev, Prib. Tekh. Eksp. (1), 212 (1988)
- 21. G.M. Goncharenko, Tr. Mosk. Energ. Inst., vol. 45: Elektroenergetics (MEI, Moscow, 1963)
- 22. A.G. Nasonov, L.S. Lantsman, Prib. Tekh. Eksp. (2), 134 (1984)
- 23. S.C. Lin, J. Appl. 25, 54 (1954)

Chapter 10 «Impulsar»: New Application for High Power/Energy High Repetition Rate Pulse-Periodic Lasers



10.1 Introduction

Since the 1970s, the possibility of using a laser jet engine to launch light satellites into orbit has been attracting the attention of researchers [1–9]. The solutions to the problems considered in [3] is still of current interest. This includes an increase in the efficiency of using laser radiation, the coupling coefficient J_r (the ratio of the propulsion to the radiation power), by several times and the prevention of the shock damage to the apparatus, which appears when high-powered repetitively pulsed laser radiation with low repetition rates f is used. For example, for $J_r \sim 0.3$ kN MW⁻¹ (a typical value for the laser jet engine of the 1970s), a mass of 200 kg, and an acceleration of 10 g, the required laser power should be ~ 60 MW (the energy $Q \sim 100$ g in the TNT equivalent, $f \sim 100$ Hz) and the power of the power supply should be 0.5-1 GW. However, it seems unlikely that such a laser will be created in the near future. In our experiments, $J_{\rm r} \sim 1~{\rm kN~MW^{-1}}$ (obtained experimentally) and 3-5 kN MW⁻¹ (estimated under special conditions), which allows us to reduce the laser power by a factor of 7–10. A power of 10–15 MW can already be obtained with the help of gas-dynamic lasers and HF/DF lasers by using the properties of repetitively pulsed lasing with high repetition rates and methods for the power scaling of lasing [10, 11], which have already been tested for CO₂, HF and Nd YAG.

To solve these problems, the use of repetitively pulsed radiation with $f \sim 100$ kHz, optical pulsating discharge (OPD), and the effect of merging of shock waves produced by the OPD [12–14] was proposed. The merging criteria were confirmed experimentally [15]. The OPD is when laser sparks in the focus of repetitively pulsed radiation, which can be at rest or can move at high velocities [16–20]. The high-frequency repetitively pulsed regime is optimal for continuously-pumped Q-switched high-powered lasers. In this case, the pulse energy is comparatively small and stationary propulsion is possible.

The aim of our work is to experimentally verify the possibility of using pulse-periodic laser radiation with a high repetition rate to produce effective stationary propulsion in a laser jet engine and to demonstrate the advantages of this technology for the production of super long conductive canals for energy delivery from space.

10.2 Experimental Setup

In the model considered in [12–14], pulsed and stationary regimes are possible. Figure 10.1 explains the specific features of these regimes. An OPD is produced at the focus of a lens on the axis of a gas jet flowing from a high-pressure chamber or an air intake to a cylindrical reflector. The shock waves generated by the OPD merge to form a quasi-stationary wave, the high-pressure region between the OPD and reflector.

As a result, the propulsion $F_{\rm r}$ appears. In a cylindrical reflector, the coupling coefficient is maximal, $J_{\rm r}=1.1~{\rm N~kW}^{-1}$ [13], acting as a planar explosion [21]. In the pulsed regime, the OPD is produced by trains of laser pulses. A narrow jet of diameter $D_{\rm j}\sim0.3~R_{\rm d}$ [13], which is smaller than the reflector diameter $D_{\rm r}$, carries a plasma out from the OPD region and is necessary for the efficient formation of shock waves. Here, $R_{\rm d}=2A5(q/P_0)^{1/3}$ is the dynamic radius of a spark, q (in J) is

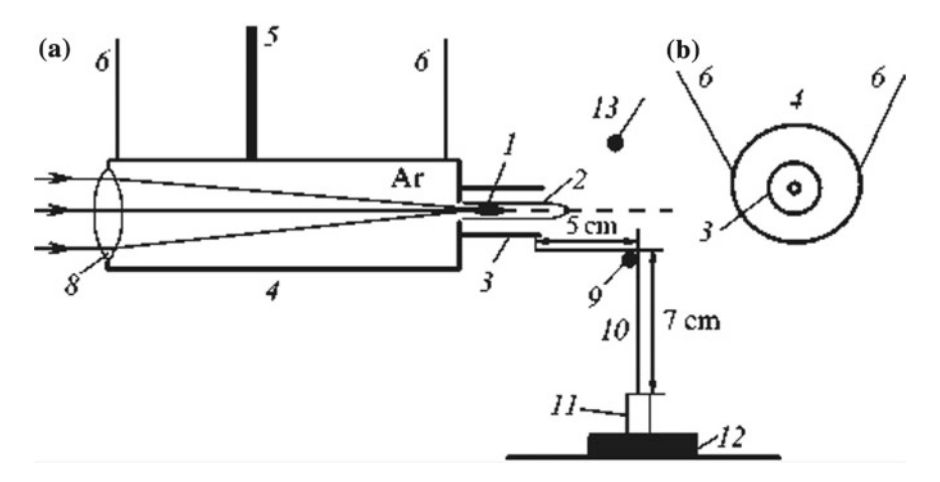


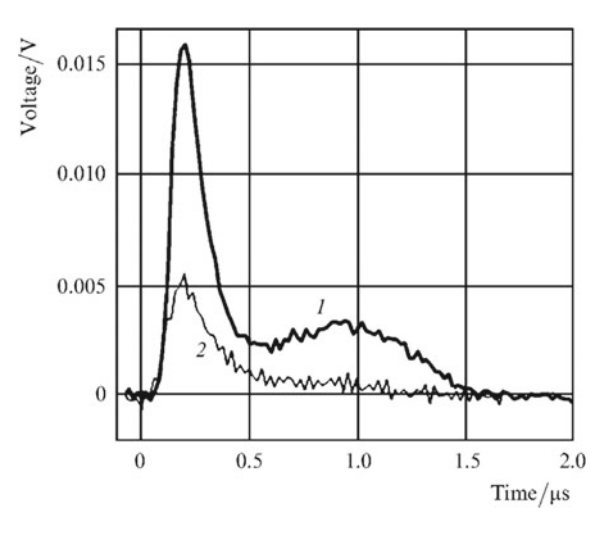
Fig. 10.1 Schematic illustration of the experiment, side (a) and front (b) view: (1) OPD; (2) argon jet; (3) replaceable cylindrical attachment (reflector); (4) high-pressure chamber (rocket model); (5) elastic hose for argon supply; (6) model suspension wires; (7) laser radiation; (8) focusing lens; (9) block; (10) wire connecting cylinder (3) with weight (11); (12) balance; (23) shock-wave pressure gauge

the laser pulse energy absorbed in a spark, and P_0 (in atm) is the gas pressure. Propulsion acts during a pulse train, whose duration is limited by the air heating time. Hot atmospheric air is replaced by cold air during the interval between pulses. In the stationary regime, gas continuously arrives to the reflector from the bottom by forming a jet over the entire section. In experiments in this regime, we have found $D_{\rm j} \sim 2R_{\rm d} \sim 3$ mm, which is comparable with the reflector diameter $D_{\rm r} \sim 5$ mm.

The experiment is shown schematically in Fig. 10.1. The OPD was produced by radiation from a pulsed CO₂ laser. The pulse duration was $\sim 1~\mu s$, the duration of the front peak was 0.2 μs . The pulse repetition rate was varied from 7 to 100 kHz, the pulse energy was 0.1–0.025 J. The peak power was 300–100 kW, the average power of repetitively pulsed radiation was W = 600-1700~V, and the absorbed power was $W_a = \eta W~(\eta \approx 0.7)$. Figure 10.2 shows the shapes of the incident pulse and the pulse transmitted through the OPD region. Note that for a short pulse duration and high power, $\eta \sim 0.95$. Because the radiation intensity at the focus is lower than the optical breakdown threshold in air, the argon jet was used. The length l of sparks along the flow was $\sim 0.5~cm$.

The model of a rocket with a laser jet engine was made from a duralumin cylinder of diameter ~ 8 cm, length ~ 26 cm, and weight of 1.1 kg, which was suspended on four thin wires of length 1.1 m and capable of moving only in the axial direction. A reflector (replaceable cylindrical attachment) was mounted on the chamber end. Laser radiation was directed to the chamber through a lens with a focal distance of 17 cm. The argon jet was formed by flow from a high-pressure chamber through a hole of diameter $\sim 3-4$ mm. The jet velocity V was controlled by the pressure of argon, which was delivered to the chamber through a flexible

Fig. 10.2 Oscillograms of the laser pulse (1) and radiation pulse transmitted through the OPD (2) for f = 50 kHz



hose. The force produced by the jet and shock waves was recorded with the help of a thin (of diameter ~ 0.2 mm) molybdenum wire connected to a weight that stood on a strain-gauge balance (accurate to 0.1 g). The wire length was 12 cm and the block diameter was 1 cm.

The sequence of operations in each experiment was as follows. A weight fixed on a wire was placed on a balance. The model was slightly deviated from the equilibrium position (in the block direction) in order to provide the necessary initial tension of the wire (~ 1 g). The reading $F_{\rm m}$ of the balance was fixed, the jet was switched on, and then the reading of the balance decreased to F_1 . This is done because the rapid jet produces a reduced pressure (ejection effect) in the reflector. After the OPD is switched on, the balance reads the value F_2 . The propulsion $F_{\rm r}$ produced by the OPD is equal to $F_1 - F_2$. The pressure of shock waves was measured with a pressure gauge whose output signal was stored in a PC with a step of ~ 1 µs. The linearity band of the pressure gauge was ~ 100 kHz. The gauge was located at a distance of ~ 5 cm from the jet axis (see Fig. 10.1) and was switched on after the OPD ignition (t = 0). The pressure was detected for 100 ms.

Let us estimate the possibility of shock-waves merging in the experiment and the expected values of F_r and J_r . The merging efficiency depends on the parameters $\omega = fR_{\rm d}/C_0$ and $M_0 = V/C_0$ ($M_0 < 1$), where C_0 is the speed of sound in gas. If the distance from the OPD region to the walls is much larger than $R_{\rm d}$ and the sparks are spherical or their length l is smaller than $R_{\rm d}$, then the frequencies characterizing the interaction of the OPD with gas are:

$$\omega_0 \approx 2.5 M_0,\tag{10.1}$$

$$\omega_1 \approx 0.8(1 - M_0),\tag{10.2}$$

$$\omega_2 \approx 5.9(1 - M_0)^{1.5}. (10.3)$$

For $\omega < \omega_1$, the shock waves do not interact with each other. In the range $\omega < \omega_1 < \omega_2$, the compression phases of the adjacent waves begin to merge and this effect is enhanced as the value of ω approaches ω_2 . In the region $\omega < \omega_2$, the shock waves form a quasi-stationary wave with the length greatly exceeding the length of the compression phase of the shock waves. For $\omega < \omega_0$, the OPD efficiently (up to $\sim 30\%$) transforms the repetitively pulsed radiation to shock waves.

In the pulsed regime the value of M_0 in (10.1) corresponds to the jet velocity. Because shock waves merge in an immobile gas, $M_0 \approx 0$ in (10.2) and (10.3). The frequencies f = 7-100 kHz correspond to $R_{\rm d} = 0.88$ -0.55 cm and $\omega = 0.2$ -1.7. Therefore, shock waves do not merge in this case. In trains where the energy of the first pulse is greater by a factor of 1.5-2 than those of the subsequent pulse ($\omega \approx 2$), then the first shock waves can merge. The propulsion produced by pulse trains is $F_{\rm r} = J_{\rm r} \eta W = 0.3$ N (~ 30 g), where $J_{\rm r} = 1.1$ N kW⁻¹, $\eta = 0.6$, and $W \sim 0.5$ kW. In the stationary regime for $M_0 \sim 0.7$, the shock wave merge because $\omega > \omega_2$ ($\omega = 1.8$, $\omega_2 \approx 1.3$). A quasi-stationary wave is formed between the OPD and the

cylinder bottom. The excess pressure on the bottom is $\delta P = P - P_0 = 0.54 P_0 (R_{\rm d}/r)^{1.64} \approx 0.25 - 0.5$ atm and the propulsion force is $F_{\rm r} \approx \pi (D_{\rm r}^2 - D_{\rm j}^2) \delta P/4 = 0.03 - 0.06$ kg.

10.3 Results of Measurements

10.3.1 Control Measurements

The jet propulsions $F_{\rm j}$ and $F_{\rm r}$ and the excess pulsation pressure $\delta P=P-P_0$ were measured for the model without the reflector. We considered the cases of the jet without and with the OPD. The jet velocity V and radiation parameters were varied. For V=50,100, and 300 m s⁻¹, the propulsion produced by the jet was $F_{\rm j}=6,28$, and 200 g, respectively, and the amplitude of pulsations was $\delta P=5\times 10^{-6},~2\times 10^{-5}$ and 3×10^{-4} atm. The OPD burning in the jet did not change the reading of the balance. This is explained by the fact that the OPD is located at a distance of r from the bottom of a high-pressure chamber, which satisfies the inequality

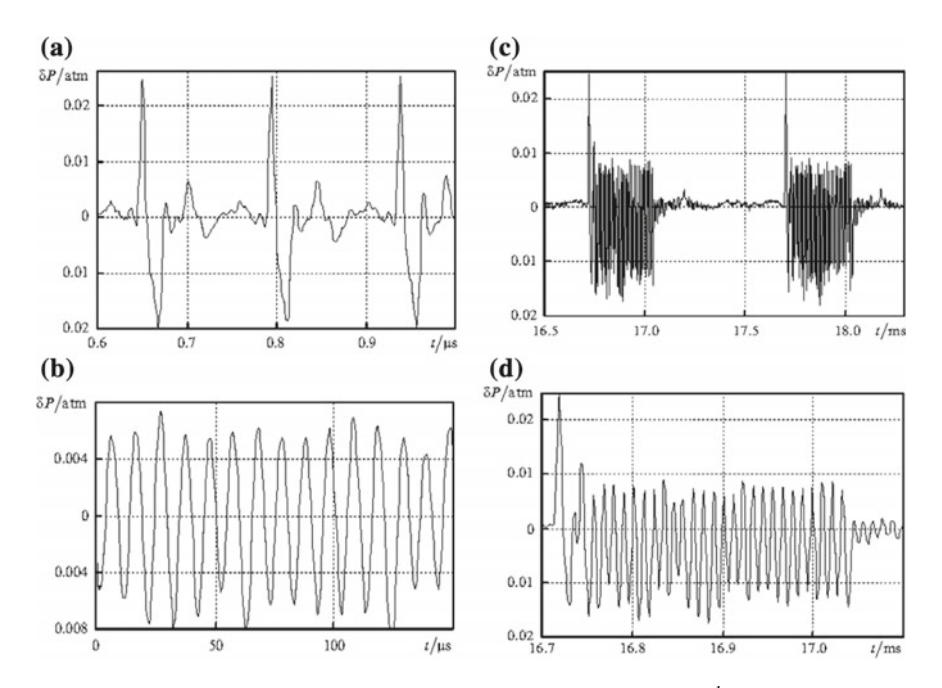


Fig. 10.3 Pressure pulsations produced by the OPD for $V = 300 \text{ ms}^{-1}$ (without reflector), f = 7 kHz, W = 690 W (a); f = 100 kHz, W = 1700 W (b); and f = 100 kHz, the train repetition rate $\phi = 1 \text{ kHz}$, W = 1000 W, the number of pulses in the train N = 30 (c); for a train of shock waves at large scales, parameters are as shown in (c) (d)

 $r/R_{\rm d} > 2$, when the momentum produced by shock waves is small [3, 22]. As follows from Fig. 10.3, pulsations $\delta P(t)$ produced by the OPD greatly exceed pressure fluctuations in the jet.

10.3.2 Stationary Regime

The OPD burned in the flow formed during gas outflow from the chamber through a hole ($D_{\rm j}=0.3$ cm) to the reflector ($D_{\rm r}=0.5$ cm) (Fig. 10.4). In order to avoid the jet from closing, the pressure used in the chamber was set equal to ~ 2 atm because the excess pressure on the reflector bottom was ~ 0.5 atm (see above). The jet velocity without the ODP was V=300 and $400~{\rm ms}^{-1}$, $F_{\rm j}=80$ and $140~{\rm g}$. The OPD was produced by repetitively pulsed radiation with f=50 and $100~{\rm kHz}$ and an average power of $W\approx 1200~{\rm W}$ (the absorbed power was $W_{\rm a}\approx 650~{\rm W}$). Within several seconds after the OPD switched on, the reflector was heated up to a temperature of more than $100~{\rm ^{\circ}C}$.

Figure 10.5 illustrates the time window for the visual recognition of shock waves with the Schlieren system in the presence of plasma. Before 7 μs , the plasma was too bright relative to the LED source and all information of the shock wave was lost. At 7 μs , the shock wave image could be discerned under very close examination. By 10 μs , the shock wave was clearly visible in the image; however, by this time the shock wave had nearly left the field of view. Therefore, a specialized technique was needed to resolve the shock waves at short timescales, when plasma was present.

For f = 50 kHz and $V = 300 \text{ m s}^{-1}$ the propulsion is $F_r = 40 \text{ g}$ and for $V = 400 \text{ m s}^{-1}$ the propulsion is 69 g. The coupling coefficient is $J_r \approx 1.06 \text{ N kW}^{-1}$. The propulsion F_r is stationary because the criteria for the merging of shock-waves in front of the OPD region are fulfilled. Downstream, the shock waves do not merge. One can see this from Fig. 10.5, which shows pressure pulsations

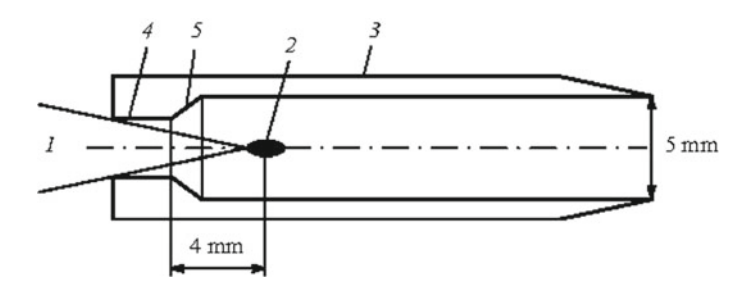


Fig. 10.4 Reflector of a stationary laser engine: (1) repetitively pulsed laser radiation with f = 50 and 100 kHz, W = 1200 W; (2) OPD; (3) reflector; (4) hole of diameter ~ 3 mm through which argon outflows from a high-pressure chamber (~ 2 atm) to the reflector; (5) reflector bottom, the angle of inclination to the axis is $\sim 30^{\circ}$

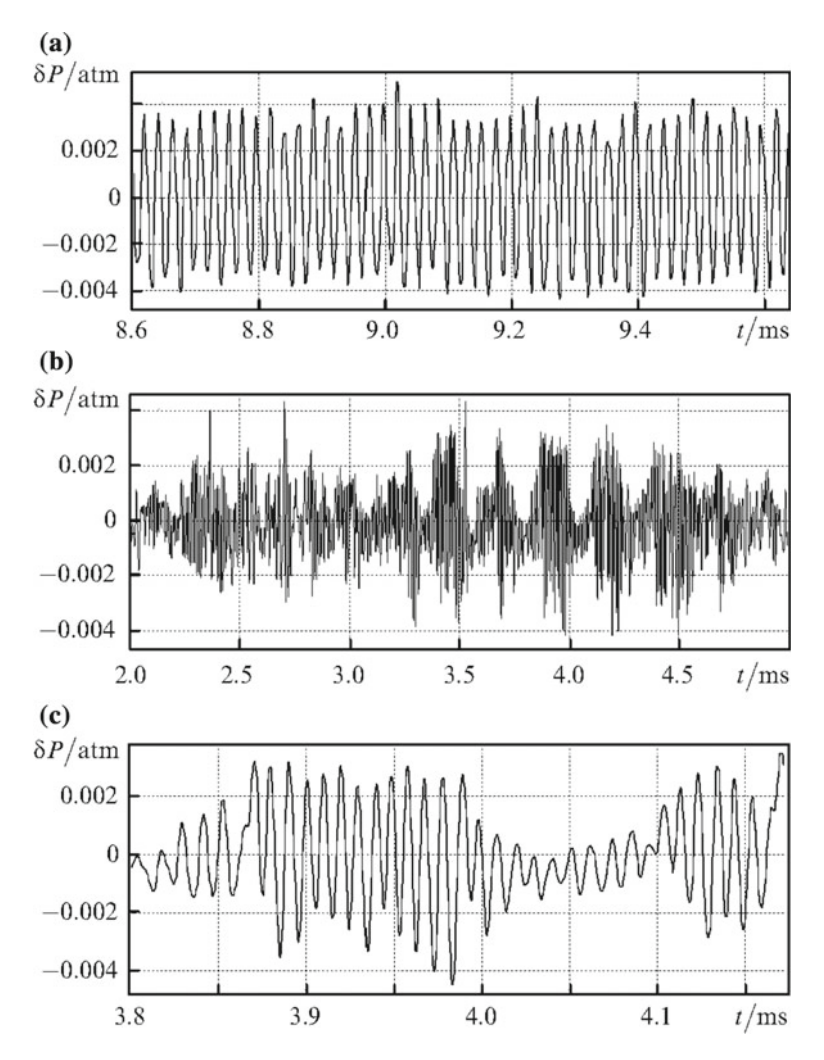


Fig. 10.5 Pressure pulsations δP produced upon OPD burning in the reflector with $D_{\rm r}=0.5$ cm, H=4.6 cm, V=400 m s⁻¹, $D_{\rm j}=0.3$ cm for f=50 kHz, W=1300 W (a) and f=100 kHz, W=1200 W (b, c)

 $\delta P(t)$ measured outside the reflector. They characterize the absorption of repetitively pulsed radiation in the OPD and, therefore, the propulsion. For $f=50~\rm kHz$ the instability is weak $(\pm 5\%)$ and for $f=100~\rm kHz$ the modulation $\delta P(t)$ is close to 100%. The characteristic frequency of the amplitude modulation $f_a\approx 4~\rm kHz$ is close to $C_0/(2H)$, where H is the reflector length. One possible explanation is that at such high frequencies the plasma has no time to be removed from the OPD burning region, which reduces the efficiency of the generation of shock waves. The closure of the jet can also lead to the same result if the pressure in the quasi-stationary wave

is comparable with that in the chamber. Thus, repetitively pulsed radiation can be used to produce stationary propulsion in a laser engine.

10.3.3 Pulsed Regime

To find the optimal parameters of the laser engine, we performed approximately 100 OPD starts. Some of the resulting data is presented in Table 10.1. We varied the diameter and length of the reflector, radiation parameters, and the jet velocity (from 50 to 300 m s⁻¹). For V = 50 m s⁻¹ the ejection effect is small, for $V = 300 \text{ ms}^{-1} \approx C_0$ this effect is strong, and for $V \approx 100 \text{ ms}^{-1}$ the transition regime occurs. In some cases, the cylinder was perforated along its circumference to reduce ejection. The OPD was either produced by radiation pulse trains or in some cases by repetitively pulsed radiation. The structure and repetition rate of pulse trains was selected to replace the heated OPD gas by atmospheric air. The train duration was $\sim 1/3$ of its period and the number of pulses was N = 15 or 30, depending on the frequency f. The heating mechanism was the action of the thermal radiation of a plasma [23], the turbulent thermal diffusivity with the characteristic time $\sim 300 \text{ }\mu\text{s}$ [24], and shock waves.

Table 10.1 Experimental conditions and results of the coupling coefficient J_r measurements

	-						-	_	
f/ kHz	φ/ kHz	D _r /mm, [H/mm]	N	V/ m s ⁻¹	W/ W	F _j /g	F _r /	J _r / N kW ⁻¹	Reflector material
45	RP	5, [46]		300	1300	80	40	0.61	Duralumin
	1		-						
45	RP	5, [46]	-	400	1300	141	69	1.06	Duralumin
100	RP	5, [46]	-	400	1200	155	54	1.08	Duralumin
100	1	15, [50]	30	300	720	49	4	0.085	Duralumin
45	1	15, [50]	15	50	720	0.9	2.1	0.042	Duralumin
45	1	15, [50]	15	300	720	49.1	4.5	0.09	Duralumin
45	1	15, [50]	15	50	720	1.2	1.4	0.028	Duralumin ^a
45	1	15, [50]	15	100	720	6.3	5.6	0.11	Duralumin ^a
45	1	15, [50]	15	300	720	62.7	4	0.08	Duralumin ^a
45	1	15, [50]	5	170	500	17.7	3.5	0.1	Duralumin ^a
45	2	15, [50]	5	100	600	6.3	4.8	0.11	Duralumin ^a
45	2	15, [50]	5	164	600	18.5	7.5	0.18	Duralumin ^a
45	2	15, [50]	5	300	600	70	-4	0.095	Duralumin ^a
12.5	RP	25, [35]	_	60	430	2.4	4	0.13	Quartz
12.5	RP	25, [35]	_	100	430	5	7	0.23	Quartz
12.5	RP	25, [35]	_	150	430	11	11	0.37	Quartz
12.5	RP	25, [35]	_	300	430	51	16	0.53	Quartz
12.5	RP	25, [35]	-	50	430	6	1	0.033	Duralumin ^b
12.5	RP	25, [35]	_	100	430	12	7	0.23	Duralumin ^b
12.5	RP	25, [35]	-	300	430	195	-97	-3.2	Duralumin ^b

Note Laser radiation was focused at a distance of 1 cm from the reflector bottom

^aSix holes of diameter 5 mm over the reflector perimeter at a distance of 7 mm from its exhaust ^bSix holes of diameter 5 mm over the reflector perimeter at a distance of 15 mm from its exhaust

The propulsion $F_{\rm r}$ was monitored while decreasing the reflector diameter and increasing its length. The OPD burned at a distance of ~ 1 cm from the reflector bottom. One can see from Fig. 10.6 that the shock waves produced by the first high-power pulses in trains merge. For f=100 kHz, the pulse energy is low, which manifests in the instability of pressure pulsations in trains. As the pulse energy was approximately doubled at the frequency f=50 kHz, pulsations $\delta P(t)$ were stabilized. An OPD burning in the reflector of a large diameter $(D_{\rm r}/R_{\rm d}\approx 4)$ and at a distance from its bottom satisfying the relation $r/R_{\rm d}\approx 3$ did not produce any propulsion.

Table 10.1 presents some results of the measurements. One can see that the coupling coefficient Jr strongly depends on many parameters, achieving 1 N kW^{-1} in the stationary regime and 0.53 N kW^{-1} in the pulsed regime.

At present, the methods of scaling the power of laser systems and laser engines, which are also used in laboratories, are being extensively developed [10, 25]. Let us demonstrate their application with a few examples. We observed the effect when the OPD produced 'negative' propulsion $F_{\rm t}=-97~{\rm g}$ (see Table 10.1), which corresponds to a deceleration of the rocket. The value of $J_{\rm r}$ can be increased by approximately a factor of 1.5 by increasing the pulse energy and decreasing their duration down to $\sim 0.2~{\rm \mu s}$. An important factor characterizing the operation of a laser engine at high-altitude flight is the efficiency $I_{\rm m}$ of the working gas. The value $I_{\rm m}=0.005~{\rm kg~N^{-1}~s^{-1}}$ can be reduced considerably in experiments by using higher powered/energy radiation. The power of repetitively pulsed radiation should be no less than 10 kW. In this case, $F_{\rm r}$ will exceed all the other forces considerably. For the gas-dynamic effects that influence the value of $F_{\rm r}$, for example, the lowest resistance at the flight velocity $\sim 1~{\rm km~s^{-1}}$ should be taken into account.

Thus, our experiments have confirmed that repetitively pulsed laser radiation produces stationary propulsion with a high coupling coefficient. The development

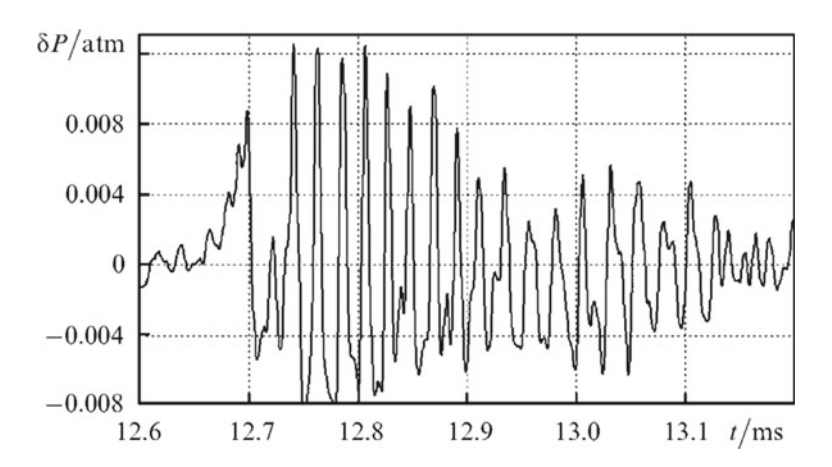


Fig. 10.6 Pressure pulsations δP in the OPD produced by pulse trains with $\phi = 1.1$ kHz, f = 50 kHz, W = 720 W, N = 15, V = 300 m s⁻¹, $D_{\rm r} = 1.5$ cm, H = 5 cm, $D_{\rm j} = 4$ mm, and F = 4.5 g

of the scaling methods for laser systems, the increase in output radiation power, and the optimization of the interaction of shock waves will result in a considerable increase in laser-engine efficiency.

10.4 The Impact of Thermal Action

A laser jet engine (LJE) uses repetitively pulsed laser radiation and the atmospheric air as a working substance [1–3]. A reflector that focuses radiation is located in the tail part of a rocket. The propulsion is produced by the action of periodic shock waves that are produced by laser sparks on the reflector. The laser air-jet engine is attractive due to its simplicity and high efficiency. According to published arguments [26, 27], LAJE can find applications for launching spacecraft if $\sim 100\text{-kJ}$ repetitively pulsed lasers with pulse repetition rates of hundreds hertz are developed and if the damage of the optical reflector under the action of shock waves and laser plasma is eliminated. These problems can be solved by using high pulse repetition rates ($f \sim 100 \text{ kHz}$), optical pulsed discharge, and the merging of shock waves [12, 13]. The efficiency of the use of laser radiation in the case of short pulses at high pulse repetition rates is considerably higher. It is shown in this paper that factors damaging the reflector and a triggered device cannot be eliminated at low pulse repetition rates and are resonant.

Let us estimate the basic LJE parameters, which include the forces acting on a rocket in the cases of pulsed and stationary acceleration, the wavelength of compression waves excited in the rocket body by shock waves, and the radius $R_{\rm k}$ of the plasma region (cavern) formed upon the expansion of a laser spark. We use expressions for shock-wave parameters that were obtained empirically. A laser spark was treated as a spherical region of radius r_0 in which the absorption of energy for the time $\sim 1~\mu s$ is accompanied by a pressure jump on the order of tens and hundreds of atmospheres. This is valid for the LJE in which the focal distance and diameter of a beam on the reflector are comparable and the spark length is small. The reflector is a hemisphere of radius $R_{\rm r}$. The frequency f is determined by the necessity of replacing hot air in the reflector by atmospheric air.

Let us estimate the excess peak value $F_{\rm m}$ of the repetitively pulsed propulsion beyond the stationary force $F_{\rm s}$ upon accelerating a rocket of mass M. It is obvious that $F_{\rm s}=Ma$, where the acceleration $a=(10-20)g_0\approx 100-200~{\rm m~s}^{-2}$. The peak value of repetitively pulsed propulsion is achieved when the shock wave front arrives on the reflector. The excess pressure in the shock wave (with respect to the atmospheric pressure P_0) produces the propulsion $F_j(t)$ and acceleration a of a rocket of mass M. The momentum increment produced by the shock wave is:

$$\delta p_{i} = \int_{0}^{1/f} F_{i}(t) dt \cong F_{a} t_{a} [N \cdot s].$$
 (10.4)

Here, F_a is the average value of propulsion for the time t_a of the action of the compression phase of the shock wave on the reflector and $F_m \approx 2F_a$. By equating δP_i to the momentum increment $\delta p_s = F/f = aM/f$ over the period under the action of the stationary propulsion F_s , we find:

$$\Delta = F_{\rm m}/F_{\rm s} = 2/(ft_{\rm a}). \tag{10.5}$$

The value of Δ , as shown below, depends on many parameters. The momentum increment per period can be expressed in terms of the coupling coefficient J as $\delta Pi = JQ$, where Q [J] is the laser radiation energy absorbed in a spark. The condition $\delta Pi = \delta p_s$ gives the relation:

$$W = aM/J (10.6)$$

which yields the basic parameters of the problem, the absorbed average power of repetitively pulsed radiation W = Qf and $J \approx 0.0001 - 0.0012 \,\mathrm{N\,s\,J^{-1}}$ [3, 13, 26].

The action time of the compression phase on the reflector is $t_a \sim R \mathcal{N}$, where $V \approx k_1 C_0$ is the shock-wave velocity in front of the wall $(k_1 \sim 1.2)$ and $C_0 \approx 3.4 \times 10^4$ cm s⁻¹ is the speed of sound in air. The length R_c of the shock wave compression phase can be found from the relation:

$$\frac{R_{\rm c}}{R_{\rm d}} = 0.26 \left(\frac{h}{R_{\rm d}}\right)^{0.32}.$$
 (10.7)

Here, h is the distance from the spark center to the reflector surface and $R_{\rm d}\approx 2.15(Q/P_0)^{1/3}$ is the dynamic radius of the spark (distance at which the pressure in the shock wave becomes close to the air pressure P_0). In this expression, $R_{\rm d}$ is measured in cm and P_0 in atm. The cavern radius can be found from the relation:

$$\frac{R_{\rm k}}{R_{\rm d}} = 0.6 \left(\frac{r_0}{R_{\rm d}}\right)^{0.29} = 0.22 - 0.3 \approx 0.25.$$
 (10.8)

The final expression (10.8) corresponds to the inequality $r_0/R_d < 0.03 - 0.1$ typical for laser sparks (r_0 is their initial radius). Let us find the range of P_0 where the following two conditions are fulfilled simultaneously: the plasma is not in contact with the reflector surface and the coupling coefficient J is close to its maximum [3, 22, 26]. This corresponds to the inequality $R_k < h < R_d$. By dividing both parts of this inequality by R_d , we obtain $R_k/R_d < h/R_d < 1$, or $0.25 < h/R_d < 1$. As the rocket gains height, the air pressure and, hence, h/R_d decreases. If we assume that at the start ($P_0 = 1$ atm) the ratio $h/R_d = 1$, where h and R_d are chosen according to (10.2), then the inequality $0.25 < h/R_d < 1$ is fulfilled for $P_0 = 1$ –0.015 atm, which restricts the flying altitude of the rocket to values between 30 and 40 km (h = const).

The optimal distance h satisfies the relation $h/R_d \approx 0.25b_i$ where $b_i \approx 4-5$. By substituting h/R_d into (10.7), we find the length of the shock-wave compression phase and the time of its action on the reflector:

$$\frac{R_{\rm c}}{R_{\rm d}} \approx 0.17b_{\rm i}^{0.32},$$
 (10.9)

$$t_{\rm a} = \frac{0.17b_{\rm i}^{0.32}R_{\rm d}}{k_{\rm l}C_0} = \frac{s_{\rm l}Q^{1/3}}{P_0^{1/3}} = \frac{s_{\rm l}}{P_0^{1/3}} \left(\frac{aM}{Jf}\right)^{1/3},\tag{10.10}$$

where $s_1 = 0.37 b_{\rm i}^{0.32}/(k_1 C_0) \approx 9 \times 10^{-6} b_{\rm i}^{0.32}$. From this, by using the relation $\Delta = F_{\rm m}/F_{\rm a} = 2/(Ft_{\rm a})$ we find:

$$\Delta = \frac{2P_0^{1/3}}{s_1 f^{2/3} W^{1/3}} = \frac{2P_0^{1/3} Q^{2/3} J}{s_1 a M} = \frac{2}{s_1 f^{2/3}} \left(\frac{P_0 J}{a M}\right)^{1/3}.$$
 (10.11)

Two of the three parameters Q, W, and f, are independent. The third parameter can be determined from expression (10.6). The conditions $1/f \sim t_a$ and $\Delta \approx 1-2$ correspond to the merging of shock waves [12].

The important parameters are the ratio of t_a to the propagation time $t_z = L/C_m$ of sound over the entire rocket length L (C_m is the speed of sound in a metal) and the ratio of t_z to 1/f. For steel and aluminum, $C_m = 5.1$ and 5.2 km s⁻¹, respectively. By using (10), we obtain:

$$U = \frac{t_{\rm a}C_{\rm m}}{L} = \frac{s_{\rm 1}C_{\rm m}}{LP_0^{1/3}}Q^{1/3}.$$
 (10.12)

Here, L is measured in cm and $C_{\rm m}$ in cm s⁻¹. Expression (10.12) gives the energy:

$$Q = \frac{35.4P_0}{b_i^{0.96}} \left(U \frac{C_0}{C_{\rm m}} \right)^3 L^3.$$
 (10.13)

From a practical point of view, the most interesting case is U > 1, when the uniform load is produced over the entire length L. If U < 1, the acceleration is not stationary and the wavelength of the wave excited in the rocket body is much smaller than L. Also, if $C_m/f < L$, then many compression waves can fit within the length L. The case $U \approx 1$ corresponds to the resonance excitation of the waves. Obviously, the case $U \leq 1$ is unacceptable from the point of view of the rocket's strength.

By using the expressions obtained above, we estimate Δ , U, and R_k for laboratory experiments and a small-mass rocket. We assume that $b_i = 4$, $J = 5 \times 10^4$

N s J⁻¹, and $s_1 = 1.4 \times 10^{-5}$. For laboratory conditions, $M \approx 0.1$ kg, $R_r \approx 5$ cm, L = 10 cm, and a = 100 ms⁻². The average value of the repetitively pulsed propulsion $F_{\rm IP}$ is equal to the stationary propulsion, $F_{\rm IP} = F_{\rm s} = 10$ N, the average power of repetitively pulsed radiation is $W = F_{\rm IP}/J = 20$ kW, and the pulse energy is $Q_{\rm p} = W/f$. We estimate the frequency f and, hence, $Q_{\rm p} \approx Q$ for the two limiting cases.

At the start, $P_0 \approx 1$ atm and the cavern radius R_k is considerably smaller than R_r . Here, as in the unbounded space, the laser plasma is cooled due to turbulent thermal mass transfer. For $Q_p < 20$ J, the characteristic time of this process is 2–5 ms [8, 9], which corresponds to f = 500–200 Hz. If $R_k \sim R_r$ ($P_0 < 0.1$ atm), hot gas at a temperature of a few thousands of degrees occupies the greater part of the reflector volume. The frequency f is determined by the necessity of replacing gas over the entire volume and is $\sim 0.5 \ C_0/R_r \sim 850$ Hz. Let us assume for further estimates that f = 200 Hz, which gives $Q_p = 100$ J. We find from (10.7) and (10.8) that $\Delta = 74$ and U = 3.5. This means that the maximum dynamic propulsion greatly exceeds the propulsion corresponding to the stationary acceleration. The action time of the shock wave is longer than the propagation time of the shock wave over the model length by a factor of 3.5. For $P_0 = 1$ and 0.01 atm, the cavern radius is $R_k = 2.5$ and 11.6 cm, respectively.

10.5 The Dynamic Resonance Loads

Let us estimate the loads for a rocket by assuming that $M \approx 20$ kg, $R_{\rm r} \sim 20$ cm, L = 200 cm, and a = 100 m s⁻². The average repetitively pulsed propulsion is $F_{\rm IP} = F_{\rm s} = 2000$ N, the average radiation power is W = 4 MW, for f = 200 Hz the pulse energy is $Q_{\rm p} = 20$ kJ, $\Delta = 12.6$, U = 1, $R_{\rm k} = 14.7$ and 68 cm ($P_0 = 1$ and 0.01 atm), and $F_{\rm m} = 25.6$ kN = 2560 kg. One can see that the repetitively pulsed acceleration regime produces dynamic loads on the rocket body which are an order of magnitude greater than $F_{\rm s}$. They have a resonant nature because the condition $U \sim 1$ means that the compression wavelengths are comparable with the rocket length. In addition, as the rocket length is increased up to 4 m and the pulse repetition rate is increased up to 1 kHz, the oscillation eigenfrequency $C_{\rm m}/L$ of the rocket body is close to f (resonance).

Thus, our estimates have shown that at a low pulse repetition rate the thermal contact of the plasma with the reflector and strong dynamic loads are inevitable. The situation is aggravated by the excitation of resonance oscillations in the rocket body. These difficulties can be eliminated by using the method based on the merging of shock waves. Calculations and experiments [28] have confirmed the possibility of producing the stationary propulsion by using laser radiation with high laser pulse repetition rates. The method of scaling the output radiation power is presented in [10].

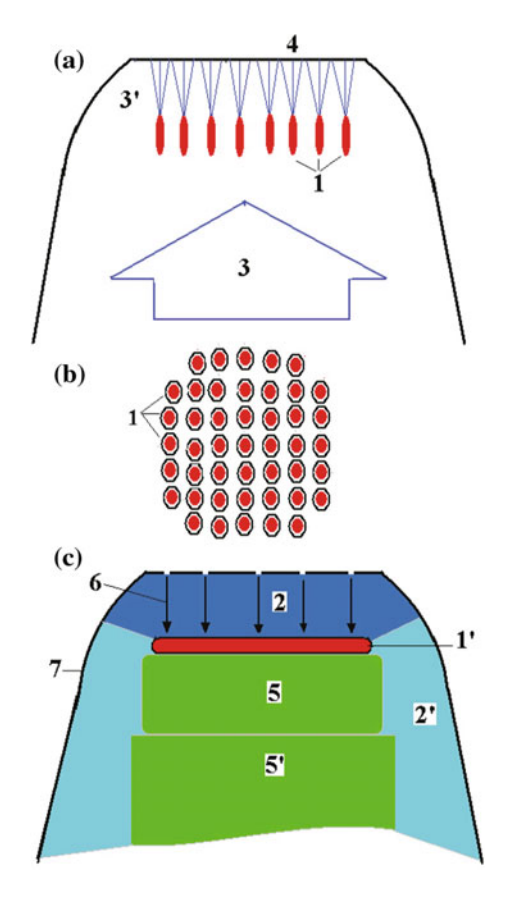
10.6 Matrix of Reflectors

This matrix consists of N-element single reflectors, pulse-periodic radiation with a repetition rate of 100 kHz, pulse energy q, and average power WC. All elements of the matrix are very similar (Fig. 10.7) and radiation comes with the same parameters: qm = q/N, $W_{\rm m} = W_{\rm C}/N$. The matrix of reflectors creates a matrix of OPD, each one stabilized by gas flux with velocity— $V_{\rm jm}$. OPD's do not interact with each other. The structure of the elements of the matrix of reflectors could help find better conditions of gas flux penetration. In our case the number of reflectors was N = 8. Larger values of N are not reasonable.

The following estimations are valid for the boundary conditions: $W_{\rm C}=20$ MW ($W_{\rm m}=2.5$ MW), f=105 Hz, q=200 J ($q_{\rm m}=25$ J), $a_{\rm rm}=0.3$. The index 1 is for — $P_0=1$ atm. (Start of "Impulsar") and index 2 is for $P_0=0.1$ atm. (end of the regime).

The radius of the cylinder for each reflector is:

Fig. 10.7 "Impulsar" engine scheme based on OSW. (a) Focusing system, (b)—OPD matrix, creating flat QSW; (c) plasma created inhomogeneities; (1) OPD elements; (1') Model of OPD (Distance from 1' to 4: less 10 cm); (2) Flat QSW, $(P-P_0)/P_0 \approx 0.5 - 3$; (2') Radial QSW, $(P-P_0)/P_0 < 0.1$; (3) Main beam, $q \sim 100 \text{ J}; 3'$ focused beams $q \sim 3-5$ J, creating OSW matrix; (4) Matrix of focusing elements and air injecting system; (5) OPD matrix of plasma decay; (5') OPD plasma turbulence; (6) Gas flow; (7) Nozzle



10.6 Matrix of Reflectors 143

$$R_{\rm rm} = \frac{0.2 R_{\rm dJm}}{\delta_{\rm m}^{1/2}} = \frac{0.43 (q_{\rm m}/P_{\rm J2m})^{1/3}}{\delta_{\rm m}^{1/2}} = \frac{R_{\rm r}}{N^{1/3}} = 15.5 \, \text{cm}$$

The focus of reflector is ~ 5 cm. The size of matrix is ~ 90 cm. Additional pressure is:

$$\delta P_{\rm m1} = 1.56$$
 atm. and $\delta P_{\rm m2} = 0.55$ atm

The force acting on the matrix is:

$$F_{\text{am1}} = 100 \cdot 103 \,\text{N}, \quad F_{\text{am2}} = 35.6 \cdot 103 \,\text{N}$$

The specific force for each element of the matrix (for MW of average power) is:

$$J_{\text{m1}} \approx 4000 \,\text{N/MW}, \quad J_{\text{m2}} \approx 1500 \,\text{N/MW}$$

The velocities of gas flux in the reflectors of matrix are:

$$V_{\rm J1} = 2520$$
 m/s, $V_{\rm J2} = 5440$ m/s.

Flight control in this case can be accomplished by thrust change for the different elements of the matrix of reflectors. At the same time, such a configuration could be very helpful in the realization of efficient gas exchange in the area of breakdown behind of the reflectors (Fig. 10.7).

Thus, an OPD can be stationary or move at a high velocity in a gaseous medium. However, stable SW generation occurs only for a certain relation between the radiation intensity, laser pulse repetition rate, their filling factor, and the OPD velocity. The OPD generates a QSW in the surrounding space if it is stationary or moves at a subsonic velocity and if its parameters satisfy the aforementioned conditions. The mechanism of SW merging operates in various media in a wide range of laser pulse energies. The results of investigations show that the efficiency of the high repetition rate pulse-periodic laser radiation can be increased substantially when a QSW is used for producing thrust in a laser engine [13, 14].

10.7 Super Long Conductive Channel for Energy Transfer

Powerful lasers are capable of creating the spending channels of large lengths which are located at any distance from a radiator. At relatively small energies of single impulses, the channels are approximately hundreds of meters long. Since 1970, successful attempts of their usage were undertaken to solve the problems of the interception of lightning and to block overload waves on electrical lines. The traditional lightning protection systems being used currently are not always in a position to ensure the desired level of efficiency. This stimulates the quest for new

approaches to solve this problem. Laser protection against lightning is one of the most prospective trends that are being developed actively at the present [29, 30].

While using this approach, it is assumed that the lightning discharge channel being developed is guided towards a conventional metal lightning rod along which the plasma channel forms as a result of the laser induced breakdown of the atmosphere. This method is based on the concept of an active lightning rod, whereby a laser beam can be used to "trigger" and guide a positive ascending leader from the tip of a lightning rod to a negatively charged thunderstorm cloud. It is expected that in contrast to the traditional approach, the use of a laser spark will make it possible to efficiently control the process of protection from lightning, to ensure the selectivity of lightning capture, and to provide safety for tall objects and large areas. The conductive canal in this case is about 10–15 m long and the main advantage of this approach is the immediate appearance of laser produced lightning rods. But the maximum length of the breakdown in the air produced by a laser was registered at a level of 100 m and limited by the optical method of laser energy delivery into the focal point. How is it possible to create a much longer conductive canal?

The ongoing French-German program "Teramobiie" has goal of producing long conductive canals and is based on femto-second multi-photon laser technology. But the goal is to create a very long canal with a very low level of electrical resistivity in comparison with canals produced by infrared laser radiation breakdown. The ionisation of air, produced by ultra-intense and ultra-short pulses can used to channel bolts of lightning. As a "Teramobiie" burst propagates, it creates a sort of straight filament of ionised air which conducts electricity. If the laser were directed toward a dark and threatening thunderhead, it would trigger a lightning bolt that could be safely directed away from doing harm. This capacity has already been demonstrated over a distance of a few meters only using lightning within a laboratory and tests on natural scales are limited by the very high resistivity of the filaments. So what do we do with a mobile terawatt laser, if it is not good enough for lightning control? It can be used very effectively to study the propagation of intense laser light in the atmosphere, detect pollution, and to control the parameters of fast objects in space. Ultra-high intensity lasers have their own special qualities. First, they significantly modify the index of refraction while focusing the light beam along its path, the effect of the latter is the production of a self—guiding laser burst which can travel hundreds of meters. The second effect is that the luminous spectrum widens to yield a white laser whose light is composed of a wide range of wavelengths, which is important for a wide range of applications.

Consequently, the well known "Impulsar" program is of great interest, because this program uses a combination of high-voltage and high-frequency sources that may solve the aforementioned problems. The principle of "Impulsar" operation can be shortly described as follows [31].

Jet propulsion of the device is made with powerful high frequency pulsed-periodic laser radiation. In the experiments the CO₂ laser and solid—state Nd YAG laser systems were used. Active impulses appear thanks to the breakdown of air (<30 km) or to the breakdown of vapour from low-ionizable materials

saturated by nano-particles (dust plasma) which are placed in the vicinity of the focusing mirror, or the acceptor of breakdown waves. With each pulse of the powerful laser, the device rises up, leaving a bright and dense trace of products with high degree of ionization and metallization of nano-particles after ablation. The theoretical estimations and experimental tests show that with the experimentally demonstrated figures of specific thrust, the lower layers of the Ionosphere can be reached in several tens of seconds. These tests also show that a high level of channel conductivity is created with the help of high frequency high voltage generator.

The space around globe represents a series of megavolt class condensers created by Earth's surface, cloudy cover, various layers of ionosphere, and radiating belts. With the help of the high-voltage source of trajectory, the trail of "Impulsar" creates a conductive channel of required length and direction. In process of lifting the vehicle and its trailing conductive channel, the breakdown characteristics of the channel decrease by 5 orders of magnitude (90 km) and density is considerably reduced. Consequently, the process must be prolonged by expanding the sum of micro-discharges and their development as self-supported processes within the external field of all of the studied intervals. It is important to note that presence of such an orbital scale channel also allows us to perform a number of important experiments from the Earth's surface as well as from space. Ball and bead lightning investigation is the most interesting application for the long conductive canal technology based on "Impulsar" due to the intriguing possibility for investigators to set up a stationary laboratory with variable boundary conditions for effective tests. Most likely, their nature is varied. It would appear that natural ball lightning may not be one phenomenon but rather many, each with similar appearances but with different mechanisms of origin, stability criteria, and different properties dependent upon the atmosphere and the environment present at the time of the event.

10.8 Conclusions

Consideration of a large set of available applications of high-powered high-repetition rate pulse-periodic lasers give us strong confidence to explore new horizons of instrumental space science and a wide spectrum of innovative and important applications.

References

- 1. A.R. Kantrowitz, Astronaut. Aeronaut. **10**(5), 74 (1972)
- 2. A. Pirry, M. Monsler, R. Nebolsine, Raket. Tekh. Kosmonavt. 12(9), 112 (1974)
- 3. V.P. Ageev, A.I. Barchukov, F.V. Bunkin, V.I. Konov, A.M. Prokhorov, A.S. Silenok, N.I. Chapliev, Kvantovaya Elektron. 4, 2501, (Sov. J. Quantum Electron. 7, 1430) (1977)

- 4. W. Schall, Proc. SPIE Int. Soc. Opt. Eng. 4065, 472 (2000)
- L.N. Myrabo, Yu. P. Raizer, in 2nd International Symposium on Beamed Energy Propulsion (Japan, 2003), p. 534
- V.E. Sherstobitov, N.A. Kalitieevskiy, V.I. Kuprenyuk, A. Yu. Rodionov, N.A. Romanov, V. E. Semenov, L.N. Soms, N.V. Vysotina, in 2nd *International Symposium on Beamed Energy Propulsion* (Japan, 2003), p. 296
- 7. V. Hasson, F. Mead, C. Larson, in *III International Symposium on Beamed Energy Propulsion*, New York, p. 3
- 8. K. Mori, L. Myrabo, in *III International Symposium on Beamed Energy Propulsion* (Troy, New York, 2004) p. 155
- 9. C.S. Hartley, T.W. Partwood, M.V. Filippelli, L.N. Myrabo, H.T. Nagamatsu, M.N. Shneider, Yu.P. Raizer, in *III International Symposium on Beamed Energy Propulsion* (Troy, New York, 2004), p. 499
- 10. V.V. Apollonov, A.G. Kislov A.G. Suzdal'tsev, Kvantovaya Elektron. 33, 753, (Quantum Electron. 33, 753) (2003)
- G.N. Grachev, A.G. Ponomarenko, A.L. Smirnov, V.B. Shulyat'ev, Proc. SPIE Int. Soc. Opt. Eng. 4165, 185 (2000)
- V.N. Tishchenko, V.V. Apollonov, G.N. Grachev, A.I. Gulidov, V.I. Zapryagaev, Yu.G. Men'shikov, A.L. Smirnov, A.V. Sobolev Kvantovaya Elektron. 34, 941, (Quantum Electron. 34, 941) (2004)
- V.V. Apollonov, V.N. Tishchenko, Kvantovaya Elekton. 34, 1143, (Quantum Electron. 34, 1143) (2004)
- V.V. Apollonov, V.N. Tishchenko, Kvantovaya Elekton. 36, 763, (Quantum Electron. 36, 763) (2006)
- G.N. Grachev, A.G. Ponomarenko, V.N. Tishchenko, A.L. Smirnov, S.I. Trashkeev, P.A. Statsenko, M.I. Zimin, A.A. Myakushina, V.I. Zapryagaev, A.I. Gulidov, V.M. Boiko, A.A. Pavlov, A.V. Sobolev, Kvantovaya Elektron. 36, 470, (Quantum Electron. 36, 470) (2006)
- U. Bielesch, M. Budde, B. Freisinger, F. Ruders, J. Schafer, J. Uhlenbusch, in Proceedings ICPIG XXI (Arbeitsgemeinschaft, Plasmaphysik APP-RUB, p. 253 (1993)
- 17. P.K. Tret'yakov, G.N. Grachev, A.I. Ivanchenko, V.I. Krainev, A.G. Ponomarenko, V.N. Tishchenko, Dokl. Akad. Nauk. **336**(4), 466 (1994)
- 18. N. Myrabo, Yu.P. Raizer, AIAA Paper, No. 94–2451 (1994)
- V. Yu.Borzov, V.M. Mikhailov, I.V. Rybka, N.P. Savishchenko, A.S. Yur'ev, Inzh.-Fiz. Zh. 66(5), 515 (1994)
- G.N. Grachev, A.G. Ponomarenko, A.L. Smirnov, P.A. Statsenko, V.N. Tishchenko, S.I. Trashkeev, Kvantovaya Elektron. 35, 973, (Quantum Electron. 35, 973) (2005)
- 21. A.M. Prokhorov, V.I. Konov, I. Ursu, I.N. Mikheilesku, *Vzaimodeistvie lazemogo izlucheniya s metallami (Interaction of Laser Radiation with Metals)* (Nauka, Moscow, 1988)
- 22. V.P. Korobeinikov Zadachi teorii tochechnogo vzryva (Problems of the Theory of Point Explosion) (Nauka, Moscow, 1985)
- 23. Yu.P. Raizer, Gas Discharge Physics (Springer, Berlin, 1991; Nauka, Moscow, 1987)
- V.N. Tishchenko, V.M. Antonov, A.V. Melekhov, S.A. Nikitin, V.G. Posukh, P.K. Tret'yakov, I.F. Shaikhislamov, Pis'ma Zh. Tekh. Fiz. 22, 30 (1996)
- V.V. Apollonov, V.N. Tishchenko, Kvantovaya Elektron. 37(8), 798, (Quantum Electron. 37 (8), 798) (2007)
- 26. F.V. Bunkin, A.M. Prokhorov, Lisp. Fiz. Nauk. **119**, 425 (1976)
- 27. S.N. Kabanov, L.I. Maslova et al., Zh. Tekh. Fiz. 60, 37 (1990)
- G.N. Grachev, V.N. Tishchenko, V.V. Apollonov, A.I. Gulidov, A.L. Smirnov, A.V. Sobolev, M.I. Zimin, Kvantovaya Elektron. 37, 669, (Quantum Electron. 37, 669) (2007)
- 29. V.V. Apollonov, Opt. Eng. 44(1) (2005)
- 30. G.N., Aleksandrov, V.L. Ivanov, G.D. Kadzov et al., Elektrichestvo (12), 47 (1980)
- 31. Apollonov, V.V. in *Proceedings of High Power Laser Ablation Conference, Santa Fe, USA*, 2010

Part III Lasers and Laser Components for High Conductivity Channels Implementation

Chapter 11 Laser Power Source for Wireless Power Transmission in Space



11.1 Introduction

Currently, many laboratories around the world are continuing the search for an efficient laser-based lightning protection system [1–3] and for producing controllable high conductivity channels in the atmosphere [4–8] that are capable of conducting short-circuit current [9] in natural or artificial electrical circuits. Laser-based lightning protection systems are known to rely on so-called long laser sparks, which provide the conditions for connecting a thunderstorm cloud with a grounded metal rod, i.e., a classical lightning rod. Our team in Russia and Japan obtained maximum lengths (~ 16 m) of the laser-spark-controlled electric discharge at a voltage of 3000 kV using a 0.5-kJ pulsed CO₂ laser with spherical optics [3]. Such controlled conductivity channels can be used for energy transmission, overvoltage protection systems, transport of charged particle beams, plasma antennas, and so forth [8].

It was shown in Part I of this book [10, 11] that a laser spark produced using conical optics demonstrates much better characteristics for the formation of conductivity channels in the atmosphere. Currently, among the huge variety of different lasers, only two types are being actively studied for use in the formation of laser-spark-controlled high conductivity channels in the atmosphere: submicrosecond pulsed gas and chemical lasers (CO2, DF) and femtosecond solid-state lasers [4, 6, 12]. The main advantage of such lasers is the ability of producing ionized channels (filaments) with characteristic diameters of about 100 um in the atmosphere along the direction of laser beam propagation. With an estimated electron density of 10^{16} cm⁻³ in these filaments and the laser wavelength in the range of 0.5-1.0 µm, the plasma poorly absorbs the laser light. In this case, the length of the path consisting of many filaments is determined by the laser intensity and can reach many miles at a femtosecond pulse energy of ~ 100 mJ. However, these lasers could not be used to form long high conductivity channels in the atmosphere. The ohmic resistance of conducting channels formed in such a way turned out to be very high and the gas in the channels could not be strongly heated (the femtosecond laser energy is less than ≤ 1 J). In particular, an electric breakdown (EB) controlled by radiation of a femtosecond solid-state laser was implemented [5, 6] only at a length of 3 m (with a voltage of 2MV across the discharge gap).

As was also shown in Part I [13–15], in order to form high-conductivity channels in the atmosphere which could accommodate an artificial or natural discharge (lightning), the gas must be heated to a temperature from 6000 to 8000 K, when thermal ionization begins. This condition is crucial, because the high initial electron density in the atmosphere is a necessary but insufficient condition for realizing high conductivity in a long atmospheric channel. As was mentioned in [13], it is important to not only produce but also to maintain the electron density in an atmospheric channel that is sufficient for electric breakdown. During gas heating, thermal ionization becomes the main mechanism of electron 'production' in the channel. Specifically, this is the main reason why the streamer mechanism cannot lead directly to an electric breakdown in the presence of high electron density (filaments) in a cold channel [13].

In the case of submicrosecond CO₂ or DF lasers with a high energy per pulse (several hundreds of joules), long conducting laser-plasma channels can be formed with conical optics. In contrast to spherical optics, one can use methods of dynamic lens correction to increase aberrations and to elongate the focal segment by conversion to a conical phase front [11]. For example, an axicon transforms the phase front of a plane wave so that it becomes conical rather than spherical and converges to the z axis at an angle γ . For small angles ($\gamma \ll 1^{\circ}$), it is simply expressed in terms of the angle γ at the base of the axicon and the refractive index N of the axicon material: $\gamma = (N-1)\alpha$. Each ring element of a conical wave front with a radius R and width δR is focused into an axial element of length $\delta z = \delta R/\gamma$ and the entire focal segment has the length $L = R/tg\gamma = R/\gamma$ [11]. This length can be significant. For example, at R = 10 cm and $\gamma = 0.5^{\circ}$, it amounts to $L \sim 11$ m. The cylindrical symmetry of focusing suggests that the type of transverse intensity distribution is independent of the coordinate z, a situation corresponding to a 'diffractionless' wave beam. In reality, such beams also undergo diffraction; however, the diffraction energy loss from the central part of the beam is compensated for by the distributed lateral supply of radiation. Note that the theoretical length of the focal segment formed by the axicon is independent of the laser beam energy and power and is instead determined by only the beam diameter. At R = 100 cm and $\gamma = 0.5^{\circ}$, it amounts to $L \sim 110$ m. According to our estimates, when using CO₂ lasers with an energy of ~ 5 kJ per pulse, the length of these channels for wide laser beams and conical optics can be fairly large (much more than 100 m).

When laser radiation is focused by an axicon in a real experiment, the longitudinal intensity distribution I(z) along the focal length L depends on z, since the transverse intensity distribution I(R) of the input beam is transformed by the axicon into the longitudinal distribution I(z) of the Bessel beam. When the radiation intensity in the beam reaches the threshold, a breakdown in the medium occurs and an extended plasma channel is formed along the focal length of the axicon [11]. Initially, the channel has a diameter of 20–100 μ m and a length that is on order of

11.1 Introduction 151

the focal length L of the axicon. If the breakdown is stable, the plasma channel, in contrast to the case of spherical optics, becomes continuous for a few nanoseconds. The density of the plasma, depending on the parameters of the medium, the wavelength λ , and other experimental conditions, varies from 10^{17} to 3 cm⁻³, the temperature reaches 30–40 eV, and the specific conductivity is 10 $(\Omega \text{ m})^{-1}$. A few microseconds later the channel expands to 10 mm. Accordingly, the temperature drops to 1 eV and retains at this level for about 100 us, followed by a relaxation of the plasma [11]. In contrast to sparks produced by focusing radiation with spherical optics, there are no discontinuities in the case of axicon based sparks. A similar pattern was observed at laser energies below 300 J [8]. In the photograph of a CLS fragment in Part I, the longitudinal structure of the spark looks like a set of bright tapered elements that are in contact and equally spaced. Figures in Part I show a photograph of the electric breakdown in the atmosphere for a channel formed by a CLS. When studying the spark between two rods immersed in plasma and spaced by d = 80 cm [8], an electric breakdown occurred at a laser energy of 140 J and a minimum average electric field strength $E_{\rm min} \approx 77$ V/cm.

The state of the art experiments aimed at implementing laser-spark-guided electric discharges show another fundamental difference in the case of femtosecond solid-state and long-wavelength lasers. In the presence of a laser-plasma channel composed of filaments, the breakdown voltage decreased by 30% [5]. The use of CO_2 and DF lasers made it possible to reduce it by a factor of more than 10.

As was pointed out in [16], the guiding properties of CLS (with a high voltage delayed by 10– $20~\mu s$) are similar to the action of a chain of metal balls. After an optimal time of ~ 10 – $20~\mu s$, the expansion of individual breakdown 'zones' leads to the formation of a continuous quasi-cylindrical conducting channel with a low gas density (~ 0.1 of the normal density), high equilibrium temperature (2700–2900°K), and electron density in the range from 10^7 to $10^8~cm^{-3}$.

Another approach to the formation of a conducting channel relies on the application of a P-P laser. It was shown in [17] that electric-discharge and gas-dynamic lasers with a high peak power can operate in a high-frequency P-P regime. This lasing regime allows one to produce a long conducting channel in the atmosphere that exists for a long time. To this end, it is necessary to align a laser beam with an inverted Cassegrain telescope system, which consists of two spherical mirrors. The first (main) mirror has a large diameter and is immobile, while the second mirror can move within certain constraints. When moving the second mirror, the common real focus of the system changes its position in time from infinity to some minimum value, which is determined by the optical layout of the telescope. Calculations show that, at a certain repetition frequency of laser pulses and a certain motion of the second mirror, continuous extended plasma channels can be formed. However, the practical implementation of this scheme with a 'running' focus meets a number of fundamental difficulties. The light distribution in the focal plane, yielded by a well correlated lens, is in essence due to Fraunhofer diffraction. The specific features of the out-of-focus 3D monochromatic images of a point source, obtained with a round hole, were considered for the first time by Lommel. Along the optical z axis, the length of the focal segment that determines the longitudinal size of the energy-accumulation region depends quadratically on the focal length of the system. The transverse size of this region is proportional to the focal length and the angular divergence of laser radiation. Therefore, the volume within which energy is concentrated is proportional to the focal length to the fourth power. For this reason, to form a homogeneous plasma channel several kilometers long, one should use a P-P laser with accurately shaped pulsed energy and with the small telescope mirror moving according to a complex program. A practical implementation of this method with a P-P $\rm CO_2$ laser with an average power of 1 kW yielded a continuous plasma channel ~ 1 m long [18].

11.2 High Conductivity Channel Formation

A completely different approach to the formation of a conducting channel can be realized using high repetition rate pulse-periodic (P-P) lasers [19]. While under irradiation by a high-frequency P-P laser with a pulse energy sufficient for producing breakdown in the focus of the optical system of a laser reactive engine (LRE), the motion of the lightly driven engine gives rise to a continuous conducting channel in air as a result of the formation of a mixture of aerosol [20] with atmospheric air and its subsequent ionization [19]. In this case, according to the calculations, the aforementioned range of laser pulse repetition rates provides continuity of the conducting channel at optimal velocities of the focusing system. Indeed, each laser pulse focused by the optical system forms some extended plasma region with a high conductivity that occupies a relatively small segment of the focusing system trajectory. If the laser pulses have a low repetition rate [21], these regions will take a form somewhat like a dashed line at certain velocities of the focusing system. If the pulse repetition rate exceeds 10 kHz and the motion velocities are optimal for solving the problem stated, these high-conductivity regions will have no discontinuities, and a continuous conducting channel will be formed. However, when the moving optical system enters rarefied atmospheric layers, a problem of a deficit of the conducting medium arises. To solve it, the displaced optical system must have an efficient source of an appropriate medium (a material containing microscopic metal particles, which can easily be sublimated under laser irradiation) in the vicinity of the focus. In particular, one can use copper oxide (CuO) nanopowder [22], which provides synthesis of conducting aerosol copper particles upon laser heating. The presence of aerosol particles of heavy metals in the sublimated material makes it possible to increase the specific impulse of the LRE thrust, simultaneously increasing the channel conductivity.

To implement a long conducting channel, one must solve several problems:

1. The development of a high-frequency P-P laser with an average power $P \sim 100$ kW and a peak power sufficient for initiating a breakdown in the focus of the LRE optical system.

- 2. The development of a system of dynamic correction for the wave front of a wide-aperture laser beam with a diameter D#10 cm in the presence of small-scale turbulence in atmosphere.
- 3. Consideration of the laser radiation absorption and scattering by aerosol particles in the LRE exhaust.
- 4. Alignment of the starting position of LRE with the laser and the pulsed high-voltage (up to several MV) source.
- 5. Obtainment of maximally possible specific impulse of the LRE thrust to reduce the time of aerosol channel formation.
- 6. Choice of the material of aerosol heavy-metal particles and their dispersion composition that could provide high channel conductivity upon heating to the sublimation temperature in the LRE.
- 7. Determination of the lower limit for the size of dispersion aerosol particles to ignite electric breakdown of a channel capable of transmitting a current, corresponding to a short-circuit current in natural or artificial electric circuits at a minimally possible average strength of electric field.

To address the latter two problems, we conducted a series of experiments. The results obtained are reported below. We consider the urgent problems of determining the dynamics of change in the channel conductivity at long delay times and its maintenance at the optimal level by introducing additional high-frequency generators into a chain.

11.3 High-Frequency Pulse-Periodic Solid-State and Gas-Dynamic Lasers

Currently, technological processes and physical experiments with high average power lasers (over 1 kW) are only advantageous when operating in two regimes: CW and P-P with repetition rates up to hundreds of Hz and at pulse durations within tens to thousands of microseconds or even milliseconds. High-frequency P-P laser systems with a high average power that provides the required pulse train durations from a few to hundreds of nanoseconds allows the implementation of a fundamentally different mechanism of interaction of radiation with matter–sublimation (ablation), thereby ensuring a local energy release not only in space but also in time [23, 24]. This results in an explosive local evaporation of a substance without an intermediate liquid phase. This mechanism can significantly extend the range of physical and technological applications of laser sources.

High-frequency intra-cavity loss modulation is the most effective method of high repetition rate P-P lasers. These were realized in flash lamp-pumped solid-state lasers with an average output power up to 1 kW. Such lasers can be fabricated using existing experience in the field of the calculation and design of laser resonators, thereby allowing their operation at the stability boundary with simultaneous optical decoupling of intra-cavity elements. In industrial applications, stability can be

reached with the help of an active rear mirror, which provides stabilization of the fundamental mode in the cavity. The facility relies on a standard lamp-pumped Nd: YAG laser, which has two 6.3×130 mm active elements. The active elements are mounted in the cavity. In the standard configuration, the laser provides an output power of 500 W with a radiation beam quality of $M^2 = 40$. The experimental setup uses an active cavity, which includes two active mirrors: a rear mirror with a variable radius of curvature and an output mirror with variable reflectivity varying along the radial coordinate. Using the system of active mirrors has made it possible to significantly improve laser radiation quality. The parameter $M^2 = 15$ was obtained with decreasing power down to 350 W. Therefore, the increase in the power density in the focal plane of the lens exceeded one order of magnitude. Additionally, improving the divergence of the output radiation creates the prerequisites for the normal operation of standard acousto-optic modulators used in single-mode lasers. Thus, the O-switched regime can be realized in the frequency range from 10 to 30 kHz at an output power of 250 W. When using a similar approach, the P-P regime has been implemented (Fig. 11.1) at an output power up to 1 kW with a slight deterioration in quality of the output radiation. It is very important to emphasize that very little energy is lost during the transformation process of the CW into the P-P regime.

In principle, if a low-average-power high repetition rate P-P solid-state laser exists, then high-frequency P-P CO₂ lasers with an output power suitable for many purposes are absent. However, the use of high-frequency P-P CO₂ lasers will fundamentally expand the scope of their applications. The possibility of the high-frequency P-P operation of lasers of virtually any power has been demonstrated both theoretically and experimentally. Experimental testing under laboratory conditions suggests the possibility of transferring the available technology to industry. The basic requirement for industrial lasers is their high reliability and

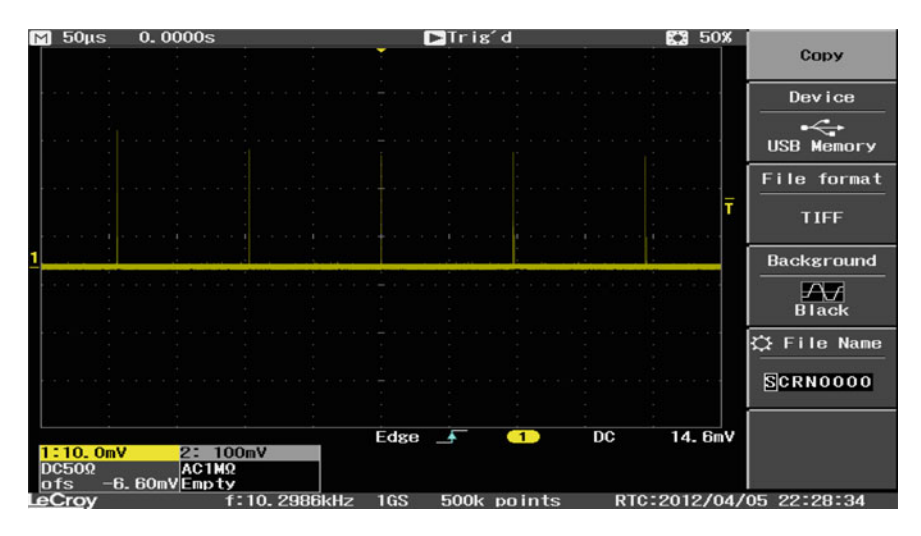


Fig. 11.1 Continuous train of pulses for Nd:YAG laser, P = 1 kW

long-term trouble-free operation. Consequently, it is desirable to ensure the low service requirements of the equipment. In this regard, the development of industrial laser sources requires additional research to obtain maximum stability of the output characteristics, reliability, and service life of the laser. The main direction of the research should be comprised of the optimization of optical schemes of laser resonators operating in the high-frequency P-P regime and the search for solutions that provide a high radiation resistance of the optical elements of lasers [25].

The high-frequency P-P regime fundamentally differs from CW and low-frequency operation modes by the mechanisms of interaction of laser radiation with matter. Experiments show that in the case of high-frequency P-P laser sources, it is necessary to significantly increase the range of many interaction parameters.

These objectives can be achieved through the physical foundations that have been established by our team since 1993 [26]. The emphasis of which involves two main approaches to implement the high-frequency P-P regime in high power/energy lasers. In lasers with a high average output power (GDL, HF/DF, COIL, Mono-module disk laser (MMDL)), unstable resonator configurations are commonly used, owing to the large cross section of the active medium. In resonators of this type, externally injected low-power beams may exert a significant effect on the characteristics of output radiation. One way to realize the control regime is the self-injection of radiation extraction from the resonator and the return of a part of radiation after changing its spatial-temporal characteristics. The transition to the transient lasing mode is effected through the modulation of the self-injecting beam. Earlier, laser versions with radiation self-injection into the paraxial resonator region were studied. However, analysis showed that the power of the beam injected into the paraxial beam region should be comparable to the output laser power in order to efficiently control the resonator of a continuously pumped laser, unlike pulsed systems with regenerative amplification.

The self-injection of a part of the output radiation through the resonator periphery is more efficient; on return to the paraxial resonator region, the injection power significantly rises due to the large number of passages playing a dominant part in the formation of output radiation. In the case of a traditional resonator, the role of waves converging on the resonator axis was found to be insignificant, because their source is a narrow region with a small relative area along the edge of the output mirror. Accordingly, the power of the control wave injected into the resonator is low. This wave has a large divergence and only a small part of which (of the order of 1/Nf, where $Nf \gg 1$ is the Fresnel number) participates in lasing.

The effect of injection waves on the resonator characteristics can be enhanced by matching the beam phase with the resonator configuration and by increasing the radiation power that is returned. In this case, the propagation direction and the wave front curvature of the injection beam should be matched with the resonator configuration such that the injection beam concentrates, after a relatively large number of passages through the resonator, near the optical resonator axis and transforms to a divergent wave that forms the output radiation. The injection beam energy should be high enough to exceed, after its arrival to the resonator axis, the saturation energy of the active medium.

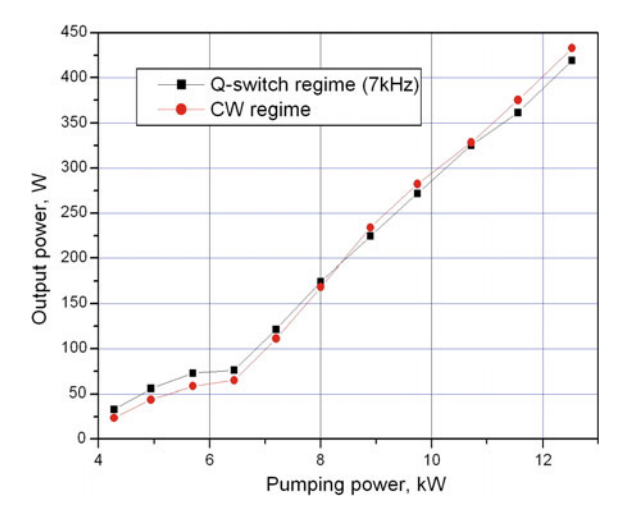
The experimental configuration was realized in a gas-dynamic CO_2 P=100 kW laser with the following parameters: the length of the active medium $L_a=1.2$ m, the unsaturated gain coefficient $g_0=0.6$ m⁻¹, the time it takes the active medium to transit the resonator $\tau=0.92\times 10^{-4}$ s, the relaxation time $\tau_p=2.76\times 10^{-4}$ s, the total go-round resonator time $\tau_f=4.2\times 10^{-9}$ s, the luminescence lifetime $\tau_1=5$ s, the resonator magnification factor M=1.45, and the diameter of output laser aperture a=0.08 m.

The laser resonator is made up of two spherical mirrors with rectangular apertures, which provide a geometrical amplification factor of 1.45. The active medium travels across the optical resonator axis. In the following, all theoretical and experimental data are given for a laser with the aforementioned parameters.

A part of the output laser radiation was diverted by a metallic mirror that is inclined with respect to the injection beam formation system that consists of two spherical mirrors with conjugate focal planes. In the vicinity of the focal plane, the waist of the branched part of the laser beam is formed and a modulator was placed near the waist. The modulator location selected so that the laser beam completely filled the aperture of the modulator. The maximal modulation frequency in our experiments was equal to 33 kHz.

The duration of an individual pulse was about 100–150 ns. We emphasize that the recorded pulse duration was limited by the measuring path bandwidth equal to 50 MHz, as noted above. The amplitudes of individual pulses exceeded the average value of output power by factor –100. The average output power was measured with a calorimeter cooled by running water. It is noteworthy that the average output power in the P-P mode was equal to the output power in the CW laser-operating mode (Fig. 11.2). Good agreement between the experimental and theoretical data for frequencies ranging up to 30 kHz testifies to the adequacy of the proposed model and the possibility of employing this method at higher frequencies in order to convert a CW laser radiation to the P-P operating mode [27].

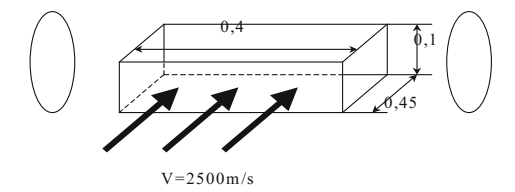
Fig. 11.2 Output power for CW and P-P modes of operation



11.4 Pulse-Periodic HF/DF and COIL Lasers

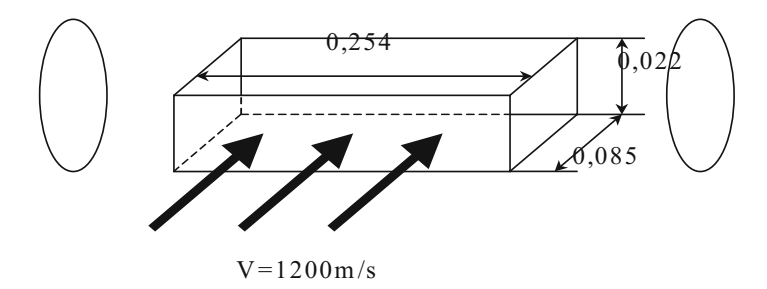
We have performed calculations for two of the most powerful existing lasers in order to determine the temporal structure of radiation and the peak power of pulses after transformation of the CW mode into the P-P mode. The basic parameters for these calculations are presented in the Table 11.1 for HF/DF laser and Table 11.2 for COIL.

(a) HF/DF laser



For this experimental configuration one can draw the following conclusions. First, the P-P mode is valid for the modulation frequency 60–600 kHz. Second, the depth of modulation will be chaotic and structured as bundles of pulses for the frequency gap between 100 and 300 kHz. Third, the duration of bundles will be controlled by a filling factor. For frequencies more than 300 kHz, the depth of modulation will reach 100% (rough pulse structures are very similar to the structure of biting transverse modes). For frequencies more than 450 kHz, one reaches the classical regime of a regularly pulsed train. The duration of pulses should be in the gap of 100–150 ns. The ratio *P* peak/*P* average is within 100–1000.

(b) COIL



All parameters of the system have the same definitions as shown in the table above and from this data one can conclude that the starting modulation frequency of the P-P mode should be higher than 20 kHz. The depth of modulation will be chaotic and structured as bundles of pulses. The duration of bundles will be controlled by a filling factor. For frequencies more than 100 kHz the depth of

Parameter	Value	Parameter	Value
L_a	0.4 m	τ	$0.18 \times 10^{-4} \text{ s}$
L_r	1.0 m	$\tau_{ m p}$	$(2-3) \times 10^{-5} \text{ s}$
<i>g</i> ₀	5–10 m ⁻¹	M	1.4
\overline{C}	3×10^8 m/s	$ au_{ m f}$	3.3×10^{-9} s
A	0.08 m	τ_1	20/330 s

Table 11.1 Parameters of HF/DF laser

where: L_a —active media length; g_0 —unsaturated gain coefficient; g—saturated gain coefficient; C—light velocity; τ —time of active media travel across of the resonator; τ_p —relaxation time; τ_r —round trip time; τ_r —luminescence time; M— magnification of resonator; a—diameter of aperture

Table 11.2 Parameters of COIL

Parameter	Value	Parameter	Value
$L_{\rm a}$	0.254 m	τ	$0.71 \times 10^{-4} \text{ s}$
$L_{\rm r}$	1.5 m	τ_{p}	$(10-12) \times 10^{-5} \text{ s}$
80	56.9 m ⁻¹	M	1.2
С	3×10^8 m/s	$ au_{ m f}$	$5 \times 10^{-9} \text{ s}$
a	0.04 m	$\tau_{ m l}$	2 s

modulation will reach 100%. For frequencies more then 150 kHz, the classical regime of regularly pulsed trains occurs. The duration of pulses should be less than 150 ns. The ratio of $P \operatorname{peak}/P$ average is within 100–1000.

11.5 Bright Future—High Power/Energy Mono-Module Disk Laser

The scaling laws for the MMDL design show that the power limit for CW operation is far beyond 100 kW for a single disk and that the pulsed energy limit is higher than 100 J from one disk in pulsed operation [27]. By cooling the surface of the disk, optical distortion of the laser beam is low and therefore operation of a thin disk laser is possible in its fundamental mode at extremely high output power. The disk laser concept is a laser design for diode-pumped solid-state lasers, which allows the realization of lasers with high output power, very good efficiency, and excellent beam quality. Since the first mention of the principle in 1962 and its demonstration in 1964 by acad. Basov et al. [28], the output power of disk lasers has been increased to 4 kW in CW-operation. Disk lasers (chain of disks) with up to 30 kW are now commercially available for materials processing [29, 30]. The beam quality of commercially available disk lasers is always better than that for rod lasers of similar power levels and laser powers up to 100 W are available with the

fundamental mode ($M^2 < 1.2$). Additionally, the electrical efficiency is higher than all other commercially available solid-state lasers with similar power levels. The disk laser design also allows highly efficient pulsed operation as a high repetition rate P-P laser or as a laser amplifier. In particular, the generation and amplification of ultra-short pulses is possible with a very high average power and a high efficiency. These properties of disk lasers will open the way to a completely new class of pulsed laser systems for materials processing. With all of their outstanding features, disk lasers will not only replace classical laser systems in many applications but will also create new markets for laser technology.

One of the outstanding features of a disk laser is its excellent beam quality, which results from the surface cooling of the laser disk. The laser crystal is disk shaped with a diameter of several mm, depending on the output power and energy and has a thickness of up to 500 µm, depending on the laser active material, the doping concentration, and the pump design. The back side of the disk is coated with material that is highly reflective for both the laser and the pump wavelengths and the front side is anti-reflectively coated for both wavelengths. This disk is mounted with its back side facing a water-cooled heat sink. Due to this mounting and cooling technique, the temperature gradients inside the laser crystal are mainly coaxial to the disk axis and the laser beam axis. The temperature in the radial direction is nearly uniform within the homogeneously pumped central area of the disk. Therefore, these temperature gradients only slightly influence the laser beam propagation through the disk. All of the thermal lens effects and the aspherical parts of the profile of the index of refraction are reduced by more than one order of magnitude compared with rod laser systems. The stress-induced birefringence is even further reduced and can be neglected for real laser systems. Additionally, due to the large surface-to-volume ratio, the heat dissipation from the disk into the heat sink is very efficient, thereby allowing operation at extremely high volume power densities in the disk. Using multiple pumped beams passing through the disk results in a thinner disk and/or a lower doping concentration, thus reducing the thermal effects such as thermal lensing and stress in the disk.

Another advantage is that the effective pump power density is increased so that on the one hand, the demands to the power density of the pump diodes are reduced and on the other hand, quasi-three-level laser materials can also be used with this design. Although quasi-three-level materials offer the possibility of building lasers of the highest efficiency, they are difficult to operate because they show a relatively high absorption of the laser-wavelength. This difficulty is due to the fact that the lower laser level is so close to the ground state that a considerable number of the laser-ions are in the lower laser level when the laser is operated at room temperature. Therefore, it is necessary to pump the material with a high pump power density in order to reach the threshold without increasing the temperature of the crystal too much. Using multiple pumped beam passes through the crystal is therefore the key to achieving a low threshold and a high efficiency, because this helps to simultaneously reduce the thickness of the crystal as well as the doping concentration. This decoupling of laser and pump beam absorption is essential for the operation of quasi-three-level systems. The limit for the possible number of

pump beam passes through the disk is given by the beam quality of the laser diodes, which determines the beam diameter on the parabolic mirror and therefore the number of positions on the mirror that can be used. The better the beam quality of the pump laser diodes, the higher the number of pump beam passes that are possible and the higher the total efficiency of the disk laser will be. When operating the disk, it is easy to scale the output power or energy by simply increasing the pump spot diameter while keeping the pump power density constant. Also, there is no need to increase the brightness of the pump laser diodes. Besides quasi-three-level systems like Ytterbium and Thulium doped materials, nearly all classical laser materials can be operated using a disk design, especially if the absorption of the pump radiation is quite high. This has been demonstrated by using Nd in YAG and other hosts.

Besides the outstanding properties of disk laser designs for CW-operation, they are also well suited for P-P laser systems, especially if a high average output power is required. Until now, high average powered P-P disk laser systems have been developed and demonstrated for the ns-pulse duration regime. These systems show an excellent beam quality and high efficiency. P-P operation could be achieved by inserting an AOM inside the laser resonator. With 140 W pump power, 18 mJ output energy per pulse has been demonstrated at 1 kHz repetition rate and 6 mJ at 10 kHz repetition rate. Using the concept of a master oscillator, the use of a regenerative amplifier allows for pulse amplification of ns-, ps- and fs pulses. The oscillator generates pulses with the desired properties (pulse duration, wavelength and repetition rate) which are amplified to the desired energy in the disk amplifier. The disk amplifier in this scheme is operating independently of the seed laser and is able to amplify any incoming pulse with the right wavelength and a pulse duration which is shorter than the round-trip time of the amplifier resonator. Simulations show that scaling of the output power of one single disk is only limited by amplified spontaneous emission (ASE) if the pump spot diameter becomes increasingly large. Fortunately, the gain of low doped Yb:YAG is rather small so that ASE will occur only at very high pump power levels. For a 9 at.% doped disk with a thickness of 200 µm the power limit occurs at a pumping power beyond 50 kW. Therefore, much more than 20 kW laser power can be extracted in CW-operation from one disk. This power level (20 kW) can be considerably increased further by increasing the pump spot diameter. The limitation set by ASE can then be overcome by using a disk with an undoped cap on top of the original disk, thus reducing the mean radial gain by the square of the ratio between the undoped and the doped material. Simulations also show that the laser power level for operation in the fundamental mode can be increased to nearly the same power level as for multi-mode operation. The reason for this behaviour is that the aspherical part of the residual thermal lens of the disk inside a top-hat pump profile is extremely low and independent of the pump spot diameter itself. The additional phase step at the edge of the pump profile is low and also nearly independent of the pump spot diameter. This phase step can be compensated for by using simple adaptive optics. Scaling the pulse energy of single disk is more strongly limited by ASE than the power under CW operation since the gain under low repetition rate P-P conditions is much higher compared with the CW operation of a disk. Nevertheless, using an undoped cap on top of the disk and some other construction features (proprietary "know-how" which is not presented here) will result in achievable energy levels far beyond 100 J from a single disk geometry.

The concept of TRUPF is very much similar to the CO2 laser which was developed in the 1970s by GPI RAS [30]. That approach was very effective in understanding the many features of high powered lasers development (high power optics, adaptive optics, CW plasma ball in air for new applications and so on). But the corresponding "Zig-Zag" approach for high power laser development is not effective and is gone forever. The only way for multi-MW scale laser development is a MMDL with $D \gg 1$ cm. The MMDL is an innovative laser concept that allows one to build diode pumped solid state lasers with the highest average output powers, the highest efficiency, and the best beam quality, simultaneously. Nearly all operational modes of solid state lasers such as CW, P-P operation can be built using our new design and having better properties than previous designs. Laser output average power of much more than existing level is possible due to our innovative efforts. The scaling laws for disk laser design according to our approach show that the average power limit is far beyond 1 MW for a MMDL. Variation of the radiation temporal structure will help to overcome the following problems:

- preventing an effective energy deposition into a target;
- large losses of energy during propagation in air due to absorption saturation effect for high peak power of pulses;
- much higher extraction of energy from a big volume of a laser active media.

11.6 Conclusions

The physical and technical details have yet to be revealed for a laser that can solve the many important challenges faced by science and technological advances in the future. However, the creation of high power/energy class of high frequency P-P lasers with a large cross section of the active medium, high compactness, and low weight will greatly help solve the current problems of launching of small satellites by lasers, formation of super-long conducting channels in space (vacuum and atmosphere), cleaning of the near-Earth space from space debris, and other special tasks [31, 32].

References

- 1. V.V. Apollonov et al., J. Opt. Soc. Am. B 8, 220 (1991)
- 2. G.N. Alexandrov et al., Elektrichestvo 12, 47 (1980)
- 3. F. Kinoshita, Y. Morooka, M. Uchiumi et al., *Proceedings of the XII International Conference on Gas Discharge and Their Applications* (Greifswald, Germany, 1997)

- 4. J.-C. Diels, W. Rudolph, *Ultrashort Laser Pulse Phenomena: Fundamentals, Techniques, and Applications on Femtosecond Time Scale* (Academic Press, Burlington, 2006)
- 5. J. Kasparian, M. Rodriquez, G. M'ejean et al., Science 301, 61 (2003)
- 6. L. Berge, S. Skupin, R. Nuter, J.-P. Wolf, Rep. Prog. Phys. 70, 1633 (2007)
- 7. V.D. Zvorykin, A.O. Levchenko, N.N. Ustinovskii, Quantum Electron. 41, 227 (2011)
- 8. V.V. Apollonov, L.M. Vasilyak, S.Y. Kazantsev et al., Quantum Electron. 32, 115 (2002)
- E.M. Bazelyan, Y.P. Raizer, Physics of Lightning and Lightning Protection (Fizmatlit, Moscow, 2001)
- 10. V.V. Apollonov, Opt. Eng. 44, 1 (2005)
- 11. L.N. Pyatnitskii, V.V. Korobkin, Trudy IOFAN 57, 59 (2000)
- 12. http://www.teramobile.org/publis.html
- 13. E.M. Bazelyan, Y.P. Raizer, Spark Discharge (Izd-vo MFTI, Moscow, 1997)
- 14. G.N. Aleksandrov, Zh. Tekh. Fiz. 37, 288 (1967)
- 15. Y.P. Raizer, Laser Spark and Propagation of Discharges (Nauka, 1974)
- E.I. Asinovskii, L.M. Vasilyak, Encyclopedia of Low-Temperature Plasma (Nauka, Moscow, 2000)
- 17. V.V. Apollonov, V.I. Kislov, A.G. Suzdal'tsev, Quantum Electron. 33, 753 (2003)
- 18. V.V. Apollonov, High Power P-P Lasers (NOVA, 2014)
- 19. V.V. Apollonov, *Proceedings of the X International Conference on Photonics and Optoelectronics* (Wuhan, China, 2009)
- 20. V.V. Apollonov et al., RF Patent No. 2400005, 20 May 2009
- 21. N.A. Fuks, Mekhanika aerozolei, Mechanics of Aerosols (Izd-vo AN SSSR, Moscow, 1955)
- V.P. Ageev, A.I. Barchukov, F.V. Bunkin et al., Kvantovaya Elektron. 4, 2501 (1977) [Sov. J. Quantum Electron, 7, 1430 (1977)]
- 23. V.V. Apollonov, P.B. Corkum, R.S. Teylor, Appl. Phys. Lett. 35, 147 (1979)
- 24. V.V. Apollonov, V.I. Kislov, A.G. Suzdal'tsev QE 33(9) (2003)
- 25. V.V. Apollonov, A.M. Prokhorov, A.H. Guenther, Laser Phys. 11(8) (2001)
- 26. V.V. Apollonov, Symposium HPLS@A-2012. Istanbul, 10 Sept 2012
- 27. V.V. Apollonov, Nat. Sci. 4, 713 (2012)
- 28. N.G. Basov, O.V. Bogdankevich, A.Z. Grasiuk. IEEE J. QE 2(9) (1966)
- 29. SPIE Events Europe, TRUMPF's R@D (2012)
- A. Giesen, H. Hugel, A. Voss, K. Wittig, U. Brauch, H. Opower, Appl. Phys. B 58, 365 (1994)
- V.V., Apollonov, A.I., Barchukov, A.M. Prokhorov, IEEE J. QE 6, 10 (1974). Report of FIAN (1971)
- 32. V.V. Apollonov, Nat. Sci. 4, 719 (2012)

Chapter 12 High Power/Energy High Repetition Rate Lasers



12.1 Introduction

Currently, in technological processes with high average power (over 1 kW) lasers, advantage is taken only of sources operating in two regimes-continuous and pulse-periodic (P-P) with a repetition rate from a few to hundreds of Hz at pulse durations within tens to thousands of microseconds and even milliseconds. In this case, the discussed processes usually rely on purely thermal mechanism, because use is made of the possibility of a laser source to deliver a sufficient amount of energy to a small area of the surface of a material being processed. High repetition rate P-P laser systems with a high average power, which provide the required pulse train durations from a few to hundreds of nanoseconds, allows implementation of a fundamentally different mechanism of interaction of radiation with matter-sublimation (ablation) ensuring a local energy release not only in space but also in time [1, 2]. This results in an explosive local evaporation of a substance without an intermediate liquid phase. This mechanism can significantly extend the range of technological applications of laser sources. However, it has found no real use in practice because of the great complexity of its implementation in the case of the mean powers required in a significant number of technologies. In general, such mean-power lasers are used in micro surface treatment, product marking, scribing, term cleavage, micro drilling, and laser-induced chemical etching.

12.2 Comparison of CW and P-P Regimes of Operation

It is known that for CW radiation, the threshold power density of evaporation is defined as:

$$q_{\text{cav}} = \frac{kT_{\text{vap}}}{Ar_0},\tag{12.1}$$

where A is the absorption coefficient (A = 1 - R), κ is the thermal conductivity, $T_{\rm vap}$ is the evaporation temperature, and r_0 is the radius of the beam cross section in the focal plane. At $T_{\rm vap} = 3000$ K, A = 0.5 ($\lambda = 1.06$ µm), k = 0.32 W/cm \times K, and $r_0 = 10$ µm, we obtain for steel $q_{\rm cav} = 1.9 \times 10^6$ W/cm². The corresponding laser power is:

$$P_{P-P} = qS, (12.2)$$

where S is the area of the laser spot, and thus $P_{P-P} \approx 6.0 \text{ W}$.

For a P-P laser source with the same parameters and the corresponding thermal regime, the threshold power density can be expressed as:

$$q_{\rm p} = \frac{kT_{\rm vap}}{2A} \sqrt{\frac{\pi}{a\tau}} \tag{12.3}$$

(a is the thermal conductivity 3.45×10^{-2} cm²/s for steel), which gives the value of $q_{\rm p} \approx 0.9 \times 10^6$ W/cm².

In addition, we can calculate the pulse power, $P_{\rm p}$, and the average power $P_{\rm P-P}$: (f is the pulse repetition rate), $P_{\rm P-P}\approx 2.8~{\rm W}$ and $t=10^{-4}~{\rm s}$, $f=50~{\rm Hz}$.

Thus, on the basis of the above-said, we can conclude, in general, the following:

$$\frac{\bar{P}_{\text{P-P}}}{P_{\text{cw}}} = f\tau \frac{r_0}{\sqrt{a\tau}},\tag{12.4}$$

at above stated parameters $\frac{r_0}{\sqrt{a\tau}} \approx 1$ and $\frac{\bar{P}_{p-p}}{P_{cw}} \sim f\tau$. Then for f = 250 Hz and $t = 10^{-4}$ s $\frac{\bar{P}_{p-p}}{P_{cw}} = 10^{-2}$ for f = 1 kHz and nanosecond pulses we have $\frac{\bar{P}_{p-p}}{P_{cw}} = 10^{-6}$.

Thus, for a repetition rate of 30 kHz and pulse duration of 100 ns, i.e., the regime characteristic for the solution to most engineering problems, the ratio is 10^{-3} . Note that the physical processes in the case of P-P cutting are very similar to those of drilling, as the cut is a set of individual holes. Based on the above-said, we can conclude that the P-P regime of laser operation is more advantageous for most processing operation than the CW regime.

Then, let us answer the question: what regime of laser operation, continuous or pulse-periodic, is preferable in terms of quality of materials processing?

For high-quality processing of materials it is necessary to ensure the following conditions:

- (i) The minimum amount of the liquid phase formed during drilling or cutting. The amount of the liquid phase is proportional to $\sqrt{a\tau}$.
- (ii) The maximum amount of liquid phase removed from the drilling or cutting region by vapor pressure. The recoil vapor pressure is proportional to.

Both of these factors indicate that the pulse duration for the P-P regime should be as short as possible based on the mean power requirements. Now we perform the same comparison in terms of requirements on the accuracy of scanning systems used for materials processing. It is evident that for processing conditions (stable product quality) to be stable, it is needed to ensure constant power flux density q. The required q for scanning systems is equal to:

$$q = \frac{hV_{\rm sk}}{d^0} L_{\rm p} \tag{12.5}$$

or with respect to the laser power P this condition is expressed as:

$$\frac{P}{V_{\rm sk}} = hd_0L_{\rm p} = {\rm const} = B. \tag{12.6}$$

On this basis, we can once again confirm our earlier conclusion: from the energy point of view, the P-P regime of laser operation is more preferable for laser cutting or drilling than the CW regime. This means that the stable conditions imply the constant laser power P and beam scanning speed $V_{\rm sk}$. This is especially important for high-speed processing of materials of complex shape. In this case, it is impossible to maintain the same speed on straight lines and sharp turns. If $V_{\rm sk}$ is not a constant and varies according to some law $V_{\rm sk}(t)$, the condition $P = BV_{\rm sk}(t)$ cannot be met fin the case of the CW laser power.

Nowadays, laser technologies are widely used in the manufacture of products made of carbon steel and non-metal materials, such as composites, plastics, glass, rocks, wood, etc. Among the variety of different lasers, solid-state lasers and gas laser systems based on the $\rm CO_2$ molecule have found the most frequent use in industrial applications.

12.3 Solid-State Lasers

Solid-state lasers are most widely used in processing of the materials made of carbon steel and non-metal materials. The use of solid-state lasers for machining nonferrous metals and their alloys is less common. This is mainly due to significant reflectivity of nonferrous metals, which reduces the laser radiation-to-heat conversion efficiency and performance, thereby making the materials processing impossible. It is known that for nonferrous metals and alloys to be processed, more appropriate are high-peak-power Q-switched lasers ensuring ablative material removal mechanism. Experiments on cutting of nonferrous metals in the high-frequency P-P regime show their high efficiency and much higher quality of machining. However, the power of the available solid state lasers operating in this regime is low—typical values of the output power are no more than 1 kW. Low average power does not provide acceptable performance. Increasing average power will open the way for industrial application of these lasers. Comparisons performed for the same average power showed that the speed of cutting of nonferrous metals in

the high-frequency P-P regime exceeds the speed of cutting in the CW regime by more than an order of magnitude in some cases.

The absence of melting of the material ensures the quality of the edges comparable with the quality of mechanical machining without a cold-worked layer, thereby making additional processing unnecessary. Fabrication of industrial solid-state lasers operating in the high-frequency P-P regime with an average output power—1 kW and higher will significantly expand the scope of application of these lasers.

12.4 High-Frequency Intra-Cavity Loss Modulation

This approach is realized in flash lamp-pumped solid-state lasers with an average output power up to 1 kW. Such lasers can be fabricated by using the existing experience in the field of calculation and design of laser resonators, which provide their operation at the stability boundary with simultaneous optical decoupling of intra-cavity elements. In industrial applications, stability can be reached with the help of an active rear mirror, which provides stabilization of the fundamental mode in the cavity. The facility relies on a standard lamp-pumped Nd:YAG laser, which has two $6.3 \times 130 \,\mathrm{mm}$ active elements. The active elements are mounted in the cavity. In standard configuration, the laser provides an output power of 500 W with radiation beam quality $M^2 = 40$. The experimental setup uses the active cavity, which includes two active mirrors—a rear mirror with a variable radius of curvature and an output mirror—with variable reflectivity varying along the radial coordinate. Using the system of active mirrors has made it possible to significantly improve laser radiation quality. The parameter $M^2 = 15$ was obtained with decreasing power down to 350 W. Therefore, the increase in the power density in the focal plane of the lens exceeded one order of magnitude. Besides, improving the divergence of the output radiation creates prerequisites for the normal operation of standard acousto-optic modulators used in single-mode lasers. Thus, the Q-switched regime can be realized in the frequency range from 10 to 30 kHz at an output power of 250 W. When using a similar approach, the O-switched regime at an output power up to 1 kW, with a slight deterioration in quality of the output radiation, has been implemented (see Fig. 11.1.).

12.5 Carbon Dioxide Lasers

If low-average-power Q-switched solid-state lasers exist in principle, high-frequency P-P CO₂ lasers with an output power that is suitable for technological purposes are absent. However, the use of high-frequency P-P CO₂ lasers will fundamentally expand the scope of their applications. One of the most promising applications is the use of CO₂ lasers for glass cutting. Continuous-wave CO₂ lasers

provide high-quality and high-speed cutting of flat glass of virtually any thickness (the method of splitting non-metallic materials was proposed and patented. In recent years, the technique of laser splitting of different materials is increasingly used in mass production. However, this method ensures only a straight cut and is completely unsuitable for complex laminated glass. High-frequency P-P devices emitting pulses of short duration deliver a cut along an arbitrary trajectory, without softening a material. The possibility of high-frequency P-P operation of lasers of virtually any power has been demonstrated both theoretically and experimentally. Experimental testing under laboratory conditions suggests the principle possibility of transferring the available technology to industry. The basic requirement for industrial lasers is the high reliability and long-term trouble-free operation. In this connection, it is desirable to ensure the low serviceability of equipment. In this regard, the development of industrial laser sources requires additional applied research to obtain maximum stability of the output characteristics, reliability and service life of the laser. The main direction of the research should comprise optimization of optical schemes of laser resonators operating in the high-frequency P-P regime and search for solutions that provide high radiation resistance of optical elements of lasers [3, 4].

In addition, it is also advisable to conduct additional research aimed at the commercial development of constructive and technological implementation of the technique of phase-locking of individual lasers (in order to increase the output power without deteriorating the spatial and temporal characteristics of the laser output) in metal and glass processing. The high-frequency P-P regime fundamentally differs from CW and low-frequency operation modes by the mechanisms of interaction of laser radiation with matter. In the future this will require applied research aimed at the refinement of the technologies of cutting, scribing, marking, laser-induced chemical etching, attainment of high-power secondary radiation from plasma, etc. for different boundary conditions of interaction with a wide range of materials. Experiments show that in the case of high-frequency P-P laser sources, it is needed to significantly increase the ranges of variation of many interaction parameters.

12.6 High-Frequency P-P Regime

The above objectives can be achieved through physical foundations, elaborated by our team in this area since 1993 [2]. The emphasis is on the two main approaches to implementation of the high-frequency P-P regime. In lasers with a high average output power (GDL, HF/DF, COIL, Mono-module disk laser (MMDL)) [4–9] use is commonly made of unstable resonator configurations owing to the large cross section of the active medium. In resonators of this type, externally injected low-power beams may exert a significant effect on the characteristics of output radiation.

One way to realize the control regime is the self-injection of radiation extraction from the resonator and return of a part of radiation after changing its spatial-temporal characteristics. The transition to the transient lasing mode is effected through the modulation of the self-injecting beam. Earlier, a study was made of laser versions with radiation self-injection into the paraxial resonator region. However, analysis showed that the power of the beam injected into the paraxial beam region should be comparable with the output laser power to efficiently control the resonator of a continuously pumped laser, unlike pulsed systems with regenerative amplification.

The self-injection of a part of output radiation through the resonator periphery is more efficient: on return to the paraxial resonator region, the injection power significantly rises due to the large number of passages to play the dominant part in the formation of output radiation. In the case of a traditional resonator, the role of waves converging to the resonator axis was found to be insignificant, because their source is a narrow region with a small relative area at edge of the output mirror; accordingly, the power of the control wave injected into the resonator is low. This wave has a large divergence, and only its small part (of the order of 1/Nf, where $Nf \gg 1$ is the Fresnel number) participates in lasing.

The effect of injection wave on the resonator characteristics can be enhanced by matching the beam phase with the resonator configuration and increasing the radiation power returned. In this case, the propagation direction and the wave front curvature of the injection beam should be so matched with the resonator configuration that the injection beam concentrates, after a relatively large number of passages through the resonator, near the optical resonator axis and transforms to a divergent wave that forms the output radiation. The injection beam energy should be high enough to exceed, after its arrival to the resonator axis, the saturation energy of the active medium.

The experimental configuration was realized in a gas-dynamic CO_2 laser with the following parameters: the length of the active medium $L_a=1.2$ m, the unsaturated gain coefficient $g_0=0.6$ m⁻¹, the time it takes the active medium to transit the resonator $\tau=0.92\times 10^{-4}$ s, the relaxation time $\tau_p=2.76\times 10^{-4}$ s, the total goround resonator time $\tau_f=4.2\times 10^{-9}$ s, the luminescence lifetime $\tau_1=5$ s, the resonator magnification factor M=1.45, the diameter of output laser aperture a=0.08 m.

The laser resonator is made up of two spherical mirrors with rectangular apertures, which provided a geometrical amplification factor of 1.45. The active medium travels across the optical resonator axis. In what follows all theoretical and experimental data are given for a laser with the above parameters.

A part of the output laser radiation was diverted by an inclined metallic mirror to the injection beam formation system consisting of two spherical mirrors with conjugate focal planes. In the vicinity of the focal plane there formed the waist of the branched part of the laser beam, and a modulator was placed near the waist. The modulator location was so selected that the laser beam completely filled the aperture of the modulator. The maximal modulation frequency in our experiments was equal to 33 kHz.

The duration of an individual pulse was about 100–150 ns. We emphasize that the recorded pulse duration was limited by the measuring path bandwidth equal, as noted above, to 50 MHz. The amplitudes of individual pulses exceeded the average value of output power by factor—100. The average output power was measured with a calorimeter cooled by running water. It is note worthy that the average output power in the P-P mode was equal to the output power in the CW laser-operating mode. Good agreement between the experimental and theoretical data for frequencies ranging up to 30 kHz testifies to the adequacy of the proposed model and the possibility of employing this method at higher frequencies to convert a CW laser radiation to the P-P operating mode [2, 4, 5].

12.7 Conclusions

Today the only we can say to conclude this chapter is the following. The creation of high power/energy class high repetition rate P-P lasers with a large cross section of the active medium will open up a great prospects for their use in solving the problems of launching of small satellites by lasers, formation of super long high conductivity channels in space (vacuum) and in atmosphere, cleaning of the near-Earth space from space debris and special tasks of our days [10].

References

- 1. V.V. Apollonov, P.B. Corkum, R.S. Teylor, Appl. Phys. Lett. 35, 147 (1979)
- 2. V.V. Apollonov, V.I. Kislov, V.V. Kijko, A.G. Suzdal'tsev, Quantum Electron. 33, 9 (2003)
- 3. V.V. Apollonov, A.M. Prokhorov, A.H. Guenther, Laser Phys. 11, 8 (2001)
- 4. V.V. Apollonov, in Symposium HPLS@A-2012, Istanbul, 10 Sept 2012
- 5. V.V. Apollonov, Nat. Sci. 4, 713 (2012)
- 6. N.G. Basov, O.V. Bogdankevich, A.Z. Grasiuk, IEEE J. Quantum Electron 2, 9 (1966)
- 7. SPIE Events Europe, TRUMPF's R@D (2012)
- A. Giesen, H. Hugel, A. Voss, K. Wittig, U. Brauch, H. Opower, Appl. Phys. B 58, 365 (1994)
- 9. V.V. Apollonov , A.I. Barchukov, A.M. Prokhorov, JEEE J. Quantum Electron 6, 10 (1974) (Report of FIAN, 1971)
- 10. V.V. Apollonov, Nat Sci. 4, 719 (2012)

Chapter 13 High Power/Energy Lasers and New Applications



13.1 Introduction

At the beginning of 1973 in the USSR, the study of designing possible LJE systems was conducted. A reflector located in the tail of the rocket prototype concentrated the obtained radiation in air, creating reactive thrust through the resulting micro-burst. The results from successful tests of different reflectors that also acted as laser light receivers were obtained. One should note that all of these experiments were conducted with the use of electric discharge CO₂ lasers with power up to 10 kW. However, to inject technologically effective equipment (global network connections, Internet, photo-monitoring of Earth surface, debris cleaning) into orbit, the necessary radiated power is substantially higher. For example, for KA launching with a weight of 1000 kg, a laser with a power no less than 10–15 MW is necessary [1, 2].

13.2 Lasers for Laser Jet Engine Development

Presently, gas-dynamic lasers (GDL) are the only capable systems for LJE applications, since only in this case does the laser technology significantly intersect rocket technology, which has evolved considerably in the last 50 years towards the creation of super-power gas generators and poses similar problems. Furthermore, the laser must work in the P-P regime with a high repetition frequency of short pulses in order to avoid laser emission screening by the plasma, which appears in such engines, and therefore for an increase in the working effectiveness [3]. In the opinion of specialists such as classical missile designers, LJE can be effectively used for inexpensive single-stage launches of nano- and micro-satellites with masses of 5–50 kg. In the first stage of flight, KA use atmospherinc air as the working medium in the engine at heights up to 30 km. Above this altitude, injection

of the satellite into orbit requires the use of an onboard reserve of special fuel or ablating substance in quantities not exceeding 15–20% of the KA starting weight. According to expert opinions, such launches will be the fundamental basis of future commercial launch programs.

The A. M. Prokhorov General Physics Institute of RAS and other organizations of Russia have accumulated vast amounts of experience regarding the use and creation of powerful lasers. In the last few years, very successful experimental studies of the P-P regime in powerful and continuous laser systems were conducted. This has enabled the experimental realization of a super-powered P-P laser source on the basis of gas-dynamic principles and a LJE composed of a light carrier with a control system. This collection of work represents a major step towards the future of launching super-lightweight KA into low/near Earth orbit. The completion of this project will make it possible to create highly economical and reusable LJE for the delivery of a wide variety of payloads into space. The key advantage of this new approach is the fact that the source of kinetic energy and the payload are decoupled in space, thereby reducing the launched weight of the KA to that of only the payload weight. As predicted by K. E. Tsiolkovskii, the first KA will be achieved with the aid of electromagnetic waves directed from an external energy source. At the time, laser technology had yet to be discovered. As confirmed in recent symposia in this field of research, various scientists and specialists in our country have suggested that the problems of the creation of powerful lasers can be solved with a high repetition rate (50–100 kHz) of pulses of short duration (150– 250 ns). Recently Arthur Kantrowits, the "the father of laser reactive motion", wrote:

Dear Victor, thank you for the pleasure of reading your articles from the last symposium on the motion with the aid of laser energy which are now accessible for the scientific community. After considering these works, I believe that these remarkable ideas regarding the quasi-stationary wave, the light-detonation waves, and the matrix of reflectors that were introduced into your new examination are very important for the development of the theory and technology of motion with the aid of the light. With great admiration, I control the start of development of the laser technology in the world and in Russia, in particular. I hope that your publications will stimulate significant activity in the field of laser engine creation and its applications. It would be very interesting to hear about the continuing progress in this hot field of research. Thanks for your energetic contribution. **A. Kantrowits**

The high-frequency P-P mode of laser operation was developed and tested on the basis of powerful CO₂—GDL, Nd YAG with lamp pumping and can be successfully used for other types of the powerful lasers, such as: HF/DF, Nd YAG with LD pumping, COIL and CO. The results of computer modeling for high repetition rate P-P lasers are presented in our review. The data from modeling depends on the characteristics of media, method of pumping, resonator geometry, and many other parameters of the laser under consideration [4].

1. COIL: P-P mode starts at frequencies >20 kHz. Pulse duration <250 ns. Depth of modulation—100% starts at frequencies >100 kHz. Ratio: *P* peak./ *P* aver. = 100–1000.

- 2. HF/DF: P-P mode starts at frequencies >100 kHz. Depth of modulation—100% starts at frequencies >250 kHz. Pulse duration <150 ns. Ratio: *P* peak./ *P* aver. = 1000–10,000.
- 3. Nd YAG: P-P mode starts at frequencies >4 kHz. Depth of modulation—100% starts at frequencies >40 kHz. Pulse duration <250 ns. Ratio: *P* peak./ *P* aver. = 100–1000.
- 4. CO: P-P mode starts at frequencies >10 kHz. Depth of modulation—100% starts at frequencies >100 kHz. Pulse duration <250 ns. Ratio: *P* peak./ *P* aver. = 100–1000.

The project of the GDL with an output power of 20 MW with the varied high-frequency structure of emission is presently located in Russia. Meaningful results were obtained for a notable increase in the effectiveness of laser energy used in a developed mode of emission, which, according to our estimations, made it possible to launch payloads from tens of kg to a hundreds, or even a thousand kg. Due to the different potential applications of this technology, similar work has already begun in Germany, Japan, England, France, China, S. Korea, Brazil and a number of other countries. Practically all participants of those projects note the unique position of GDL as one of the most promising systems because of its scalability with respect to rocket technology up to the level of several ten megawatts and also for other important parameters.

To date, the possibility of applying laser emission to aerospace tasks has been investigated in two ways: launching light KA to orbital space and the reduction of aerodynamic drag on flying bodies moving through the atmosphere at high speeds. To develop LJE, periodic repetitive laser sparks are created by P-P laser emission that is focused on the reflector near the rear end of KA. Sparks generate shock waves which transfer a part of their mechanical pulse to the reflector located near the tail of the rocket. Recent gas-discharge laser systems have demonstrated a characteristic pulse repetition frequency that was limited within the range of 100-300 Hz by the time of gas exchange in the discharge zone. To achieve high average powers up to 10 MW, it is necessary to use laser pulses with an energy of about 100 kJ. With reduced air pressure encountered at altitudes higher than 15 km, each pulse creates a long living plasma sphere that occupies practically the entire volume of reflector, which leads to the screening of the subsequent pulses within 10 ms. One further technical difficulty of the corresponding method of energy extraction from the laser is that they apply very strong impact loads due to the high energy of the pulses. Additionally, the use of high energy pulses with a small repetition frequency and, consequently, with a very high peak power is limited by optical breakdown en route to the surface of reflector. The method that we have proposed overcomes all of these difficulties through the usage of laser emission with pulses having short durations, with a high pulse repetition frequency, and with a mechanism of generated by OPD shock waves that are resonant. Under these conditions, the LJE energy of laser pulses with short durations (100 ns) can be effectively (95%) absorbed and converted (\sim 30%) into shock waves. In addition to this, it is shown that the specific thrust can be increased several times due to the artificial transformation of the radial component of shock waves into the longitudinal direction. There are many other advantages of high repetition rate P-P lasers that should be mentioned here as well [5], including:

- A much higher efficiency of energy extraction from a media and conversion into laser light, which is important for high aperture lasers scale up.
- Decreasing of the plasma screening effect due to the reduction of the duration of laser pulses and the increase of the number of pulses up to a few tens of kHz.
- Decreasing the thermal defocusing of the laser beam due to the use of an optimal temporal structure of laser radiation.
- Localization of energy deposition in space and time and the elimination of the stressed state of solids under laser action due to the replacement of melting by ablation.
- Possibility of unrolled 3d geometry of breakdowns in space due to a very high repetition rate generation of laser pulses, creation of optical, acoustical and electromagnetic fields far away of laser source.
- Much longer distances of optical breakdown conditions for the same optical systems.

13.3 Long Conducting Channel and New Set of Applications

In this case, the displacement of the optical focusing system and interaction between the P-P laser radiation with the energy in the focus of the optical system that is sufficient for breakdown ensures the formation of a continuous current-conducting channel in the air medium due to its ionization. Calculations show that the frequency band of laser pulses ensures the continuity of the formed current-conducting channel in the appropriate speed range of the moving focusing system, which can be realized in this particular medium. With the help of the focusing system, each pulse of the laser creates a region of plasma that extends in the relatively small section of space following the trajectory the device. If the pulses follow each other at a repetition rate of low frequency, then the plasma regions will be displaced in a manner similar to a dotted line. However, at higher frequencies that are optimal for the particular medium and speed, for example more than 10 kHz, then the displacements of ionized regions will no longer have breaks and this process will form a continuous conducting channel (Fig. 13.1).

However, after the moving optical system enters into much less dense layers of the atmosphere and further into the vacuum, then the problem of the scarcity of medium appears. This leads to a deficiency in the ionized gas both as the source of conducting medium and as the means of shock wave accumulation and means of energy transfer that is necessary for motion. Consequently, the moving optical system must be supplied with a source of medium that is created near the focus of

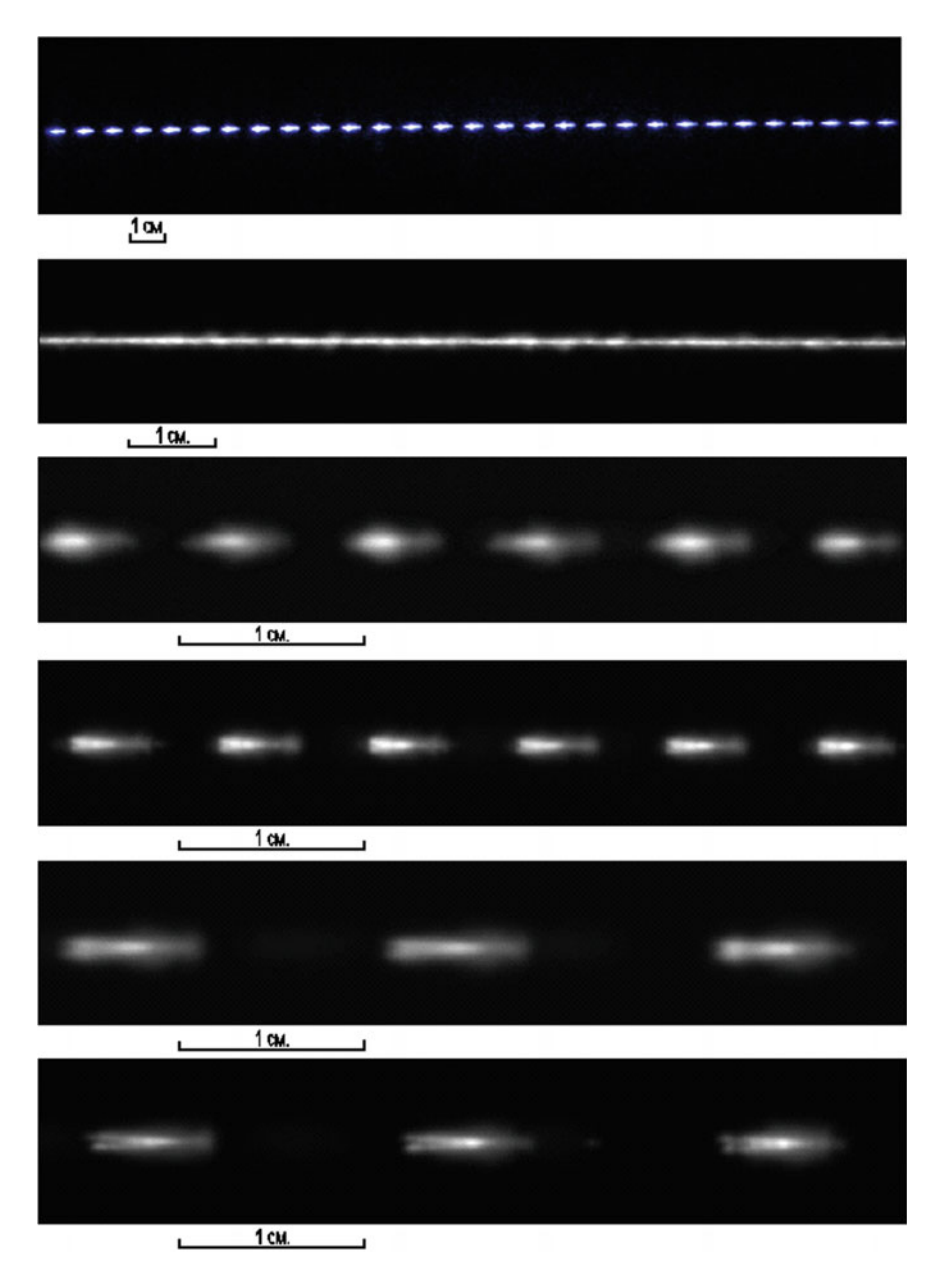


Fig. 13.1 Time controlled evolution of trains in the space for F = 20 Hz, 50 cm/s and for F = 25 kHz, 250 cm/s correspondingly

the laser and is sublimated under the action of incident laser radiation. This source is made from an easily ionized substance containing nano-particles of metal or a substance which, under the action of laser emission, ensures the synthesis of such nano-particles. In this case, the presence of such a source of easily ionized substance makes it possible to form a continuous current-conducting channel in a vacuum. Simultaneously, the presence of metallic nano-particles in the sublimated material improves the conductivity of the channel and increases the specific thrust of the laser jet engine (LJE). This device contains the mobile optical system and reservoir with the sublimated substance, which essentially determines the time of reaching the required length of an electrical power transmission channel [6].

Introducing a high voltage electrode into the current-conducting channel formed by the moving optical focusing system both stabilizes and transfers energy along the length of the channel. To facilitate the breakdown conditions of the medium in the focal point of the optical system with the appearance of not only a conducting channel but also with high energy shock waves, it is expedient to use a source of easily ionized substances that can form the steam-gas medium with a low breakdown threshold. Correspondingly, this decreases the breakdown energy requirements for the laser pulse.

The moving focusing system can be executed in the form of a conical body or the combination of a cylinder and cone, the apex of which is inverted from the direction of motion. Special optics are mounted on the end of the moving system. These optics can be selected from the number of known optical systems and ensure the focusing of the laser light which arrives at a certain distance from its surface. An easily ionized substance containing nano-particles of metal or a substance that ensures their synthesis is placed in the body of the moving system. This substance is sublimated by the incident laser radiation. Examples of such substances include wax, paraffin, delrin (high-quality acetate homopolymer) and other polymeric substances. The nano-particles of metal can be of significant dimensions, for example 10-100 nm, and can be prepared from metals such as aluminum, tin, copper, sodium, potassium, caesium, and lead. Sources that combine carbon with alkali metals can also be used to synthesize nano-particles of metal or the metal-composite materials that possess sufficiently high electrical conductivity. These materials are well reported in literature and include fullerenes on the basis of alkali metals or copper, which demonstrate high-temperature superconductive properties with $T_c > 140$ K. To obtain nano-crystalline powder, both plasma and laser heating methods can be used. As a result, nano-particles of carbides, oxides, and nitrides were obtained with the aid of pulse laser heating of metals in rarefied atmospheres of methane (in the case of carbides), oxygen (in the case of oxides), and nitrogen or ammonia (in the case of nitrides). The pulsed laser evaporation of metals in an atmosphere of inert gas (He or Ar) and a reagent gas (O₂, N₂, NH₃, CH₄) makes it possible to obtain mixtures of nano-crystalline oxides of different metals, oxides, nitrides or carbide-nitride mixtures. The composition and size of nano-particles can be controlled by changing the pressure and composition of the inert gas atmosphere and reagent gas, by changing the power of the laser pulse, and by changing the temperature gradient during the cooling process.

There are two reasons for the high conductivity of the fine powder. One reason is that the size and shape of the particles increases the strength of the electric field. The second reason is the concentration of particles in the dust of the plasma track of

"Impulsar" [4, 5]. The content of nano-particles in the sublimated substance is usually 10–15% of the mass. High repetition rate P-P laser should be used as the source of laser emission. The moving focusing system is launched directly from the Earth's surface with the aid of high repetition rate P-P laser emission with energy sufficient for the breakdown of the medium in the focus of optical system (Fig. 13.2).

As a result of the concentration of laser radiation in a relatively small volume, the breakdown of the medium occurs. Air breakdown appears in the region of ionization that follows behind the moving focusing system at a certain distance and the shock wave provides additional momentum, accelerating the system. Upon entry into the rarefied layers of the atmosphere or open space, the breakdown and appearance of shock waves can only be achieved using an onboard supply of easily ionized substance. Once the focusing system arrives at an assigned distance or when it reaches the current conducting channel, the energy transfer process is initiated by placing an electrode of the high voltage source into the channel. The conductivity of such a channel has proven to be sufficient for the discharge of a capacitor bank on the ground after the optical system reached the apogee in its trajectory [7, 8].

The results of electrical breakdown tests of dust plasma are presented here with a detailed explanation of the experimental arrangements. The most simple and effective dust plasma production methods were incorporated into our investigation. The best specific voltage result for dust plasma breakdown was measured for an electrical Cu wire explosion approach. The results of dust plasma modeling are [10]:

- P-P CO₂ laser with train of pulses and total energy—20 J. Dust particles size 50-250 nm and concentration N = 10 to the 10-12 power;
- For dust plasma produced by laser ablation: paraffin wax + graphite or permalloy powder—300 V/cm;

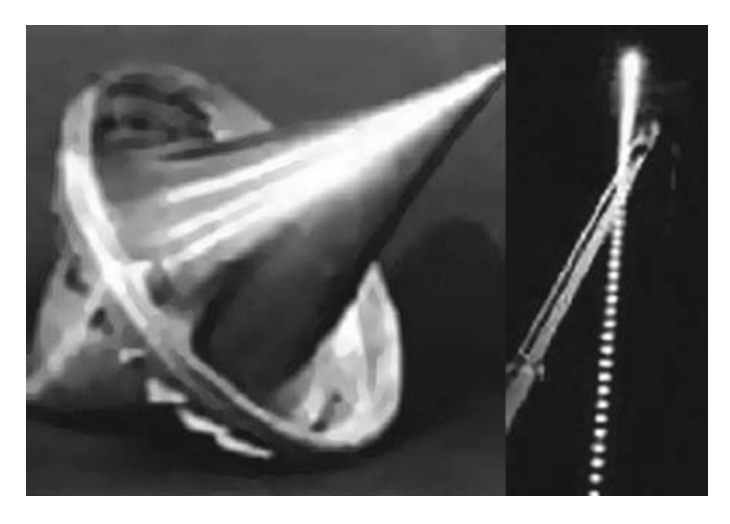


Fig. 13.2 Launch of vehicle by low rate P-P laser (Rep. rate—20 Hz, P = 10 kW)

- For nano-particles of Al, Fe, segnetoelectrics—350 V/cm;
- CO₂ single pulse laser channel, produced by conical optics—100 Ω /m, 100 V/cm;
- Long channel (filaments) produced by solid state laser—0.1 M Ω /m, 7.5 kV/cm:
- Long channel produced by wire explosion —10 Ω/m , 45–50 V/cm;
- Data for wire explosion channel, corresponding to the delays: 10–50–75 mks;
 97–124–166 V/cm.

It should be mentioned here that the minimum resistance value depends on the cross-section of the envelope of dust particles, the concentration and size of particles, the repetition rate of laser pulses, the average power of the laser, gas pressure, humidity, and many other parameters.

It is necessary to say several words about the interrelation between atmospheric electricity with the composition of the atmosphere and the climate of the planet. Many years were undertaken attempting to create conducting channels long enough to study the air in the upper atmosphere and to solve specialized problems. Accordingly, these problems can be solved with the program "Impulsar" because of its use of a high-voltage high-frequency Tesla's source. Simultaneously, the results from investigations of LJE show solutions to the following problems:

- Creation of an interceptor of manmade space debris and other dangerous space objects, such as asteroids, comets, meteorites and so on [9];
- Launch of micro-objects with the super-high acceleration to the space;
- Realization of orbital scale conducting channels for energy delivery from space to the ground [10, 11].

Powerful pulsed lasers are capable of creating large scale current conducting channels that can be located at arbitrary distances from the source of radiation. Channels with lengths of hundred of meters can be achieved with the low energy of single laser pulse. Starting in the 1970s, successful attempts were undertaken to intercept lightning bolts and to block over-voltage waves on electric power lines.

13.4 Lightning Control

The first and the most natural application for high power/energy lasers is lightning! Lightning is an electrical spark discharge that is usually manifested by its bright flash of light and by its accompanying thunder. While the average length of lightning is 2–5 km, some discharges can stretch across distances in the atmosphere up to 150 km. Let us pause to examine the process of how lighning appears in greater detail. Most frequently, lightning appears in rain clouds, which are appropriately called thunderstorms. Furthermore, lightning can be formed in layered rain clouds, within volcanic eruptions, tornados, and dust storms. Usually, linear lightning is observed, which is related to electrode-less discharges because they

begin and end in accumulations of charged particles. Until now, this phenomenon has given lightning some unclear properties that distinguish it from discharges between electrodes. For example, lightning does not occur at distances shorter than several hundred meters. Also, they appear in electric fields that are considerably weaker than those of inter-electrode discharges. Furthermore, the collection of charges transferred by lightning lasts only for thousandths of a second between a huge number of small and well isolated particles located within a volume of several km³. In lightning the electrical energy of cloud is converted into heat and light.

The most well known process is how lightning develops in thunderstorm clouds, in particular intra-cloud lightning, lightning that passes between clouds and ground-based lightning which strikes into the earth. For lightning to appear, it is necessary to form a relatively small but critical volume of an electric field within the cloud that has a tension sufficient for discharge to begin, of about 1 MV/m. In the rest of the cloud, there must also be an average tension for maintaining the discharge, which is about $0.1{\text -}0.2$ MV/m.

The process of the development of ground-based lightning consists of several stages. In the first stage, impact ionization begins in the zone where the electric field reaches a critical value. This is created first by free electrons that always exist in small quantities in air and, under the action of the electric field, are accelerated to significant speeds towards the earth. As these electrons collide with air molecules, they ionize them. Consequently, electrical discharges or streamers flow along electron avalanches, which can merge to create the brightly thermo-ionized channel with high conductivity known as the stepped leader of lightning. All of these steps are accompanied by a bright glow that dims only when the leader stops moving. This process is repeated during motion of the leader towards the earth's surface at an average speed of 200 km per second. The field strength is strengthened proportional to the action the reciprocal streamer that extends from objects protruding from the earth's surface. This special feature of lightning is used for the creation of lightning rods. The final stage of lightning is characterized by the reverse discharge from the bottom to top of the ionized channel. This discharge has currents from tens to hundreds of thousands of amperes and is noticeably brighter than the leader. Additionally, it advances at high speeds that range from 100 km per second to 10,000 km per second. The temperature within the channel of main discharge can exceed 25,000 °C and this channel can extend from 1 to 10 km with a diameter of several centimeters. Afterwards, the pulse of ionized current advancing along the channel and its glow are weakened. The final stage can last a hundredth or even tenths of a second long and the current can reach hundreds and thousands of amperes. Such lightning strikes are called "protracted" and frequently cause fires. The main discharge, however, frequently occurs only within the cloud. Charges at high altitudes can form an arrow-shaped leader that moves continuously with a speed of thousands of kilometers per second and shares a similar brightness to that of a stepped leader. When the arrow-shaped leader reaches the surface of the earth, a second strike follows shortly thereafter in a manner similar to the first. This can repeat several times, usually, but can occur as many as several tens of times. The duration of repeated lightning can exceed 1 s. Displacement of the channel of repeated lightning strikes by wind creates a luminous strip of so-called strip-lightning. The entry of lightning directly into soil forms sintered quartz sand into a unique mineral known as a fulgurite. Intra-cloud lightning usually only includes leader stages with lengths varying from 1 to 150 km. The probability of intra-cloud lightning grows in proportion to distance from the equator, changing from 0.5 at temperate latitudes to 0.9 in the equatorial strip. Lightning is accompanied by changes in electrical and magnetic fields and by radio emission through so-called atmospheric disturbances. The probability that lightning can kill depends on its height and on the electrical conductivity of soil at certain depths. The electrical conduction of lightning is based on all of these factors. If there is an electric field within the cloud that is sufficient for maintaining discharge but insufficient for initiation, then wire cables or the products of the combustion of aircraft or rocket engines can be used to trigger a lightning strike. Specifically, lightning can be provoked in layered rain and cumulus congestus clouds.

13.5 Manifestation of Atmospheric Electricity Existence

Why does lightning thunder and sparkle? Electric charges that accumulate in clouds lead to the breakdown of air, which is accompanied by a flash of light and the formation of an acoustic shock wave. In other words, thunder and lightning are the manifestation of atmospheric electricity. Over the last two and one-half of centuries, the fundamental connection between thunderstorm phenomena and electricity was reliably confirmed by numerous studies of geophysicists, meteorologists, specialists on lightning protection. However, in the last two decades, a qualitative jump in the improvement of the methods of observations has led to many unexpected discoveries in the study of thunderstorm clouds, lightning, and the orbital scale of the atmospheric electrical chain. The renewed interest in the problems of atmospheric electricity has made it possible to look differently at the mechanisms of shaping of electric field and its role in the dynamics of the atmosphere and ionosphere of the Earth.

The heart of atmospheric electrical machine, the thunderstorm cloud, is more precisely the totality of thousands of thunderstorms that are simultaneously "working" together which are distributed in the lower part of the atmosphere, known as the troposphere. Thunderstorm clouds do not last for long, only existing for several hours. However, the occurance of a few thunderstorms will draw others which form nearby in the troposphere. Contemporary satellite measurements and ground-based systems of the registration of lightning give researchers sufficiently reliable maps of the allocation of frequencies of lightning flashes over the Earth's surface. The flash rate above the surface of ocean is on average lower than that above the continents in the tropics. The reason for this asymmetry is the intense convection in the continental regions, where the land is effectively heated by solar radiation. The quick ascent of thoroughly heated air that is saturated by moisture contributes to the formation of powerful convective clouds that develop vertically,

the upper part of which has temperatures lower than 40 °C. As a result, particles of ice are formed known as soft hail or hail, whose interaction against the background of rapidly ascending air current leads to the separation of charges. Cloud heights over large bodies of water are typically lower than those above the continents and the processes of electrization are less effective above the ocean. Recently, the differences in the concentrations of the aerosols found above the ocean and above the continents have been discussed. Since aerosols serve as condensation nuclei, which are necessary for forming the particles in the supercooled air, their abundance above the land increases the probability of the strong electrization of cloud. However, the quantitative analysis of this factor requires detailed experiments.

Approximately 78% of all lightning is recorded between 30°S and 30°N. The study of the statistical features of specific regions requires further improvement of satellite and ground based mapping of thunderstorms. These studies are conducted with the consideration that lightning activity is extremely sensitive to the climate of the planet, reacting to changes in the temperature, humidity, radiation conditions, and the composition of the atmosphere.

Progress in the studies of atmospheric electricity is connected, first of all, with the mechanisms of the generation and dissipation of electrical energy in the atmosphere. The main concept here is the so-called electrical dynamo, or the generation of a quasi-stationary electric field and the space charge in the moving weakly conductive medium. In the simplest formulation of a dynamo, very wide intervals of time-spatial scales are manifested. This means that an electric field would arise on the scale of several kilometers with a strength of about 30 kV/cm, allowing for the breakdown of dry air under standard conditions and the random traffic of charges due to the collisions of cloud solid or liquid particles. This leads to the addition of micro-currents into the macroscopic current with a relatively high value (several amperes) that is required for the rapid (tens of seconds) process of the separation of charges. It is evident from casual observation that within ripe thunderstorm cells, lightning discharges occur regularly every 15–20 s. In essence, the mechanism of charging acting in the cloud is very effective although the average electric charge density rarely exceeds several nCl/m³.

As showed by measurements of the electric field on the earth's surface and also inside the cloud medium (on balloons, aircraft, and rockets), the "main" negative charge of a typical thunderstorm cloud is on average several tens of coulomb and occupies the interval of heights corresponding to temperatures from -10 to -25 °C. The "basic" positive charge is also several tens of coulombs and it is located above basic negative charge. Therefore, a large part of cloud-earth lightning discharges return to the earth as a negative charge. The lower part of the cloud frequently reveals small positive charges of approximately 10 Cl. To explain the 3-layer structure of the field and charge in thunderstorm clouds, one must examine the mechanisms of the separation of charges. These mechanisms depend on factors such as temperature, phase composition of medium, and the spectrum of the sizes of cloud particles. The value of the charge that is transferred from the electric field for one collision is very important. From this parameter, all mechanisms can be subdivided into inductive and non-inductive classes. For the inductive class of

mechanisms, the charge q depends on the value and direction of an external electric field and is connected with the polarization of the interacting particles. Meanwhile, non-inductive charge exchanges between particles in an explicit form that does not depend on the field strength. In spite of the abundance of different microphysical mechanisms of electrization, many authors now consider non-inductive charge exchanges to be the main form, involving the collisions between small crystals of ice with sizes up to tens of micrometers and particles of soft hail with dimensions on the order of several millimeters.

Experiments have established the presence of a characteristic temperature at which the sign of charge q reverses, which typically lies between -15 and -20 °C. This feature has gained popularity, because the typical temperature profile in the cloud can be used to explain the 3-layer distribution of charge density. Recent experiments showed, however, that many thunderstorm clouds possess an even more complex structure of space charge. It is especially interesting to note that mesoscale convective systems (having horizontal scales from ten to hundreds of kilometers) serve as an important source of thunderstorm activity. Their characteristic feature is the presence of a united electrical structure, which includes the region of intensive convection and is sometimes extended several hundred kilometers beyond the stratified region. In the region of stratification the ascending currents are relatively weak but the electric field has a steady multilayer structure. Near the zero isotherm, a narrow layer of space charge is formed with a thickness of several hundred meters and a critical charge for the high lightning activity of mesoscale convective systems. However, the mechanisms and laws governing the formation of the layer of positive charge near the zero isotherm remains the subject of debate.

Other examples of the work of electrical dynamos include the electrization and discharge phenomena within dust and snow storms, within volcanic eruptions, in nuclear explosions in the atmosphere, and in technological processes that involve the mixture of aerosol flows, for example in the flour-grinding and cement industries. The presence of powerful convective and turbulent flows in thunderstorm clouds and the aforementioned cases of electrization suggest that the interaction of large charged particles with the sizes of 0.1–10 mm with the particles of micrometer size in the moving conducting gas medium plays an important role for electrical dynamos. The poly-phase and multi-flow nature of the medium leads to the effective transformation of mechanical energy into electrical energy.

The problem of the initiation of lightning discharge remains unanswered and involves many complex questions. Let us pause briefly to examine two of them. First, as measurements on balloons, rockets, and aircraft have shown, the maximum tension of electric field in the thunderstorm clouds does not usually exceed 2 kV/cm, which is substantially lower than the threshold of the breakdown of dry air at the heights in question, which is on the order of 10 kV/cm. In the thunderstorm cloud, however, the discharge is developed in humid air, which contains particles of different size. It is natural to assume that the threshold of the field is reached in a compact spatial domain on the scale of less than 10 m or more generally on the microscale because of field strengthening on the particles. Furthermore, it happens

in a sufficiently short period, so that common sensors of field do not have that required spatial or time resolutions for proper measurement. The development of avalanches of fast "run-away" electrons with energies on the order of 1 MeV can serve as the alternative explanation to initiation of spark in the sufficiently weak field. Such electrons can be accelerated in the field of cloud because of a drop in braking power occurs with an increase in the energy of particle. The threshold for the development of an avalanche is almost an order of magnitude lower than the usual threshold for the breakdown of dry air. Therefore, when seeding particles that are highly energized by cosmic rays are present, the development of avalanches in the cloud can give birth to localized regions of high conductivity that are capable of initiating a spark.

The second question arises because the classical theory of gas discharge cannot explain the cloud medium's rapid passage into the conducting state during the preliminary stage of lightning. Recently, a new scenario of this stage had been proposed and investigated that is connected with the cloud reaching a regime of self-organized criticality. In this model, electrical cells with significant dimensions of 1–30 m randomly grow in space and time. Small-scale breakdowns between pairs of cells can cause "chain reaction" of intra-cloud micro-discharges, or the development of the stochastic process "of the metallization" of intra-cloud medium. This model describes the experimentally observed features of the preliminary stage of the lightning discharge through the dynamics of micro-discharges and characteristics of its radio emission.

The study of thunderstorm phenomena includes experiments on the artificial initiation of lightning, or triggered lightning. In order to create a discharge in the atmosphere under the thunderstorm cloud, a rocket is used which leaves behind a significant trail of soot in the spent oxidizer that is capable of conducting electricity. Initiation occurs with the sufficiently high tension of field on the earth's surface under the cloud, not less than 5-10 kV/m. The first classical diagram of the initiation of discharges was realized with a rocket pulling a wire from onboard of research vessel in 1960. Since then, thousands of successful experiments have been carried out studying the physics of the ascending and arrow-shaped leaders, the return shock, and the mechanism of the sudden strengthening of the luminosity of lightning channel because of the sharp current amplification have all been investigated in great detail. Today, new possibilities of controlling lightning discharges have been opened with the aid of lasers. Powerful lasers are capable of organizing extensive plasma cylinders in air which can initiate and direct the lightning discharges similar to the conducting channels used to trigger lightning from metallic wires or from the products of the combustion of special geodetic rockets.

In 1925, Ch. Wilson indicated the possibility of accelerating electrons to relativistic energies in the field of a thunderstorm cloud. This hypothesis was confirmed recently through a series of experiments showing the generation of relativistic particles and quanta of high-frequency emission in the atmosphere that correlate with thunderstorm activity. Measurements on balloons revealed an anomalous increase in the intensity of X-ray and gamma-radiation more than two or three orders of magnitude over the course of approximately one minute with a maximum

of the spectrum in the region 50-60 keV. Ground observations also revealed intense flashes of X-radiation with energy of quanta of several hundred keV, whose appearance coincided with the creation of the lightning leader's flash and with the arrow-shaped leader of trigger lightning. Finally, publications in the last several years have shown results from satellite observations of the splashes of gamma-quanta MeV-foot level, X-ray, and ultraviolet radiation of atmospheric origin. To explain these phenomena, a number of works investigate the atmospheric electrodynamics, or more precisely, the generation of the run-away electrons and their breakdown. Energetic quanta can arise from the bremsstrahlung of the fast electrons which interacts with air molecules. Models describe different situations, including the development of avalanches of fast electrons when the extensive air is showered by cosmic rays and the breakdown of run-away electrons in the strong field of the stepped leader of lightning. One should note that an increase in the number of fast electrons in the field of a thunderstorm cloud in the presence of extensive air showers is accompanied by the generation of a large quantity of secondary particles, leading to the generation of current pulses and radio emission. If the energy of the primary particles are sufficiently great $(10^{17}-10^{19} \text{ eV})$, the short (several microseconds) pulses of radio emission can have enormous energy (up to 1 MeV), which explains the appearance of the so-called narrow bipolar pulses that are sometimes observed during ground-based and satellite measurements and correlate with thunderstorm activity. The formation of such intensive current pulses is of interest both for understanding of the mechanism of the generation of lightning and for studying cosmic rays with extremely high energies. It is interesting that in thunderstorm clouds where the cellular structures of the electric field have amplitudes exceeding the threshold "of running away" proves to be essential for the process of accelerating electrons to relativistic energies. The randomly oriented electrical cells together with this acceleration greatly increase the time of life of relativistic electrons in the cloud because of the diffusive nature of their trajectories. This makes it possible to explain the significant duration of the splashes of X-ray and gamma-radiation and the nature of their interrelation with the lightning flashes. The role of cosmic rays for atmospheric electricity must be further clarified experimentally to study their correlation with thunderstorm phenomena.

13.6 Sprites and Jets Investigation

At the end of the last century, a strong surge in studies of atmospheric electricity gave rise to observations of various discharge phenomena in the middle atmosphere. The first of which are known as sprites, which occur in the middle atmosphere and correlate with daily thunderstorm activity where the glowing region stretches up to 85–90 km above the earth and whose flash durations last from ones to tens of milliseconds. Similarly, elves are observed stretching to heights of 70–90 km with durations less than 100 s. Finally, jet discharges have been observed starting from the upper part of clouds and extend sometimes to mesospheric heights

with a speed of about 100 km/s [12]. Measurement of high-altitude discharges and diagnostics of their characteristics are complicated by their short time of life and the sporadic nature of lightning discharges. Therefore, until now the physical models of sprites, elves, and jets remain the subject of intense discussions. Perhaps the information about the physical nature of sprites and jets could have the greatest application for the development of future high conductivity channel technology.

The optical flash of sprites in the mesosphere appears several milliseconds after discharge from the cloud to the earth, sometimes across distances of tens of kilometers horizontally from the channel of lightning. Discharge ignites above a critical altitude, since the threshold of the breakdown of air falls exponentially with its height. Conversely, the amplitude of the disturbances of the electric field, which appear when powerful lightning flashes in the cloud-earth capacitor, decreases relatively slowly with altitude following a power law and at heights extending approximately 75 km into the atmosphere that exceed the threshold of breakdown. In the last decade, the study of high-altitude discharges in the atmosphere became the subject of extensive investigations and greatly developed the direction of geophysical electrodynamics. Although the accumulation of data characterizing the morphology of these phenomena is by no means completed, it is already possible to switch over to a study of more specific features of the structure and dynamics of high-altitude discharges and their role in the orbital electrical chain and the balance of low components of the atmosphere. Experiments and theoretical calculations show that these discharges must be considered as a part of the dynamic process which includes the formation of the structure of the field, the charge in the cloud, and lightning discharges to the earth.

Different approaches to simulations are widely discussed, including the attraction mechanism of the run-away electrons. Models of the generation of electric field in the middle atmosphere have been generated in great detail that consider the special features of the charge distribution and its dynamics in convective systems at orbital scales which serve as the basic source of positive discharges to the earth. Accordingly, a physical model has been developed that describes the fine structure and dynamics of sprites. Sprites are represented as the network of micro-discharges—streamers—and as a self-sustaining process in an external field. Together with the metallizing process of thunderstorm clouds that was already mentioned, yet another example of self-organizing behavior is found when the dynamics of high-altitude discharge is caused by reaching the threshold of the so-called directed flow along the branched conducting channels which overlap the entire length of a sprite. The immediate prospects for studying high-altitude discharges in the atmosphere involve conducting coordinated ground-based and space experiments and also with the development of new methods of measurement of the parameters of high-altitude discharges through the use of radio-wave and laser diagnostics.

The electrical field of the atmosphere is extremely variable. The tension of the vertical component of the field sags due to ground-winds and thunderstorm cloudiness that can reach several kV/m horizontally.

Therefore, the growth of clear weather corresponds to conditions where wind speeds do not exceed 6 m/s and in the absence of any sediments, hoarfrost, fog, or

lower cloudiness. But even under these conditions near the earth's surface there is an electric field with a tension of approximately 150 V/m, along which the weakly conducting air flows with electric current having a density of several pa/m². This field changes in time and space and these fluctuations range up to tens of percent relative to the average value. The measurements of electric field, current, and conductivity under the conditions of clear weather serve as powerful means of studying the electrical state of the atmosphere. However, this information is only useful when divided between planetary and orbital scales, from the order of the height of neutral atmosphere at 100 km to the local disturbances of the electrical parameters. The latter, in turn, are directly connected with both the changes in the ionic-aerosol composition and with the dynamics of the conducting medium. Various studies have established that the boundary layer of the atmosphere is characterized by the presence of aeroelectrical structures which are manifested by pulsations of an electric field with a power-law spectrum with short-term periods from ones to several hundred seconds.

The electrodynamics of fog is of special interest. Full-scale observations show that under the conditions of fog in the frequency band 10^{-2} to 1 Hz, power-law spectra of the pulsations of field also occur, but the intensity of these pulsations increases more an order of magnitude compared to the conditions for clear weather. This is explained by the diffusion of charged drops in the lowest layer of the atmosphere. The result of structural-temporal analysis made it possible to isolate two forms of the electrical state of fog, the first of which is characterized by the formation of intensive aeroelectrical structures and the second by chaotic variations in the field and current.

13.7 Conclusions

The successful development of powerful high repetition rate P-P laser technology and of the "Impulsar" system make it possible to create conducting channels capable of energy transfer across tens or hundreds of kilometers. As a result, this will enable the creation of new and promising systems that master power engineering in outer space and will motivate future improvements to the global ecology of our planet.

References

- 1. V.V. Apollonov, High Power Molecular Lasers (Springer, Berlin, 2016)
- 2. V.V. Apollonov, To the space by laser light. Vestnik RANS 1 (2008)
- 3. V.V. Apollonov, Yu.S. Vagin, Conducting channel creation in a non-conductive media, RF Patent № 2009118874 (2009)
- 4. V.V.Apollonov, Yu.S.Vagin, A.B. Egorov, V.V. Kiyko, V.I. Kislov, Patent РФ № 2175159

References 187

 V.V.Apollonov, High power lasers for "Lightcraft" applications, in *Proceedings of ISBEP-6*, Santa Fe, NM, USA (2009)

- V.V. Apollonov, Yu.S. Vagin, A.B. Egorov, V.V. Kiyko, V.I. Kislov, High-frequency pulse-periodic mode for high-power laser, in *Proceedings of ISBEP-2*, Sendai, Japan (2003)
- 7. V.V. Apollonov, Vpered k Tciolkovskomu, in RTSoft, Moscow (2010)
- 8. V.V. Apollonov, V.R. Sorochenko, Yu.A. Shakir, in *Experimental investigation of resonance* single wire line of energy transfer. Report of GPI RAS, (2009)
- V.V. Apollonov, High power lasers for space debris elimination, in HPLS@A-2012, Istanbul, Turkey (2012)
- V.V. Apollonov, N.V. Pletnev, Formation of extended conducting channels in atmosphere. QE 42(2) (2012)
- 11. V.V. Apollonov, N.V. Pletnev, Formation of extended directional breakdown channels produced by a copper wire exploding in the atmosphere. Tech. Phys. **58**(12) (2013)
- 12. H.T. Su, R.R. Hsu, A.B. Chen, Y.C. Wang, W.C. Hsiao, L.C. Lee, M. Sato, H. Fukunishi, Gigantic jets between a thundercloud and the ionosphere. Nature **423**, 974–976 (2003)

Chapter 14 High Power/Energy Disk Lasers



14.1 Introduction

It has long been customary that as new technologies emerge into the light, potential users and experts start wondering whether these new techs will replace the old, well-established approaches to the solution of known problems. When we look back at the time when the first laser was created, it becomes clear that each new and more advanced technology usually replaces the pre-existing and well-proven technologies. However, a more differentiated and balanced assessment of the many innovations in the field of laser shows that there is no such thing as a perfect design, or an ideal laser. There is always room for improvement and further development. It is possible that in the near future a laser with the disk geometry of the active medium will become the dominant technology. However, despite this, a number of existing laser technologies (with some exceptions, of course) will continue to improve for quite a long time. Based on these considerations, we must continue to develop most types of lasers, each time clearly specifying their undeniable technological niche and knowing well their advantages and disadvantages.

High efficiency and excellent beam quality of disk lasers mean that they can be widely used in modern science and industry for a very large range of applications, including treatment of the surface of dielectric materials in microelectronics, cutting, drilling, welding, polishing and cleaning of the surface, other technological operations with superhard and fragile metals and composite materials, etc. Pulse-periodic (P-P) Q-switched disk lasers and high-average-power, mode-locked laser systems ensure optimal conditions for ablation (sublimation) of a material. A number of advantages of high repetition rate P-P lasers emitting short pulses, as applied to a wide range of industrial technologies, is the basis of many modern concepts of disk lasers. High-intensity light with an insignificant thermal lens effect in the central high-loaded zone of the active medium have led to the lifting of restrictions on the brightness of the pump diode. This has reduced the cost of laser sources, and thus has significantly improved the efficiency of electro-optical

conversion, especially in the regime of high average power. The power of the laser source is varied by scaling the cross sectional area of the generated radiation. It should be noted that its ratio to the thickness of the active material in the disk geometry is much larger than the ratio of the cross section of typical core elements of the active medium to their length in any conventional solid-state laser systems. This eliminates the problems associated with nonlinear distortions of the geometry of the active medium, and enables realizing superhigh peak values and average powers of laser sources with the disk geometry and the same parameters of the radiation in the far-field region.

14.2 Disk and Fiber Lasers

It is clear that each laser source has its advantages and disadvantages. Beam quality of modern solid-state lasers (disk and fiber lasers) is pretty good, and their efficiency is very high. A fiber laser has significant advantages at low, average and peak output powers, while a disk laser, on the contrary, is preferable in those applications which require high and super-high output powers.

Among high repetition rate P-P sources emitting coherent high average and peak output radiation, disk lasers will undoubtedly dominate today and in the future. They provide the best solution for many industrial applications in the multi-kilowatt power range. A disk is a simple and easily excited laser element, which allows cost-effective generation of radiation with improved parameters. It has a lot of potential for the future. The advantage of the disk laser over the fiber laser is already obvious in the kilowatt power range. Having a large radiating surface, the power density of the disk laser is not critical even at high peak powers. On the contrary, in fiber lasers the increase in the peak power negatively affects the reliability of the resonator. The main disadvantage of the fiber laser is also its high sensitivity to the reflected beam, which often appears in the laser due to the interaction of the generated light with matter. If the radiation reflected from the target affects the fiber laser resonator, then it should be immediately shut down to preserve the cavity.

At the same time, the disk laser resonator is insensitive to the penetration of reflected beams. Even in the case of highly reflective materials, technological operations can be performed without the risk of an emergency switching off of the laser. Another advantage of kilowatt disk lasers is their modular design. This design allows one to replace laser modules during after-sales service, thereby ensuring that in the event of failure of the laser, the downtime as well as the cost of repairs will be minimal.

On the contrary, in fiber lasers, the single-unit design of the resonator makes it impossible to replace easily the failed unit without extensive alteration of the system as a whole. At the same time, the use of fiber laser technology offers certain advantages, especially in the power range (up to several hundreds of watts). This laser is suitable for micromachining of dielectric surfaces and composite materials. However, only the disk laser has a high potential in the case of high peak powers,

i.e., when it is necessary to provide a train of short pulses with the highest peak power. In a typical disk laser, as opposed to a fiber laser, the power density inside the cavity is far below the critical damage threshold of the laser active medium and surfaces of auxiliary optical elements, even at a high peak power. For this reason, a disk laser allows, among other things, a better use of the laser medium in general, and significantly improvement in laser efficiency.

Thus, in the future solid-state diode-pumped disk lasers will play the dominant role. Laser diode structures are central elements in many new types of lasers. Today, the decisive factor is the acquisition of the necessary experience and skills to design most efficiently new laser systems. Semiconductor-based technologies and applications of laser equipment on new physical principles are key technologies of modern times. For many years, the world has accumulated the experience needed today in this field of knowledge. The challenge is to ensure technological excellence in the application of laser systems, not only today but in the future.

14.3 Design and Physical Foundations of Disk Laser Operation

The principle of the disk laser operation is based on the use of an active element in the form of a disk with a cooled surface. High cooling efficiency of the laser medium is provided by a large area of the disk surface, which is important from the point of view of the heat transfer process. Therefore, the average power in the beam can reach quite high values. It is important to note that due to effective heat transfer within the disk area there is no thermal lens effect, characteristic of 'rod' and 'slab' (optical range) geometries of the active element. In this case, cooling is performed through a side surface of the active element; a two-dimensional heat flow, forming a parabolic profile of thermal distortion, propagates through this side surface. The temperature dependence of the refractive index in this case leads to the emergence of a strong thermal lens effect. Such a lens deteriorates the directivity of the output and significantly limits the effectiveness of its action. The thin disk, in contrast, is cooled through a thin contact region on one side and generates a one-dimensional axial heat flow on the other side. As a result, the temperature gradient is distributed parallel to the laser beam, which does not result in the thermal lens effect. In practice, a thin laser element in high power/energy disk lasers is either connected to a porous heat sink or is cooled by forced convection [1, 2].

In both cases, the undesirable thermal lenses are eliminated by the optimum layout of structural elements of the disk laser. Integral heat transfer from the active material to the porous heat sink depends directly on the area of the pump zone and on the geometry of the heat transfer contact. At a constant temperature of the active laser element, the average output power achieved is directly proportional to the area of the pump zone and, consequently, to the cross-sectional area of the laser beam on the disk. This is a unique feature of disk lasers, which allows one to change the power density at a constant energy of the beam on the disk. This property is

particularly important for multi-kilowatt sources, because it makes it possible to adjust the value of the peak output power without changing many other parameters that affect the performance of the overall system.

At first glance, the basic challenge is the disk thickness needed for efficient heat dissipation, because the conventional scheme involves low absorbance of the active disk material. However, the pump scheme allows one to find an elegant solution to this problem. The process of excitation in the active material of the disk can be represented in the form of multi-channel optical configuration [3, 4] consisting of a parabolic mirror and a pump deflection system. The parabolic mirror focuses a collimated beam of the laser cavity containing an active element. After partial absorption of radiation passing through the disk body, some energy of the beam is reflected from a highly reflective mirror located on the backside of the disk. As a result of multiple reflections through prisms and the parabolic mirror in general we deal with 20 iterations of radiation passes through the body of the disk, which ensures high efficiency of absorption of light energy of the pump beam. The optical scheme of such resonators tolerates limitations on the brightness of the pump source. Generally, pumping of a high average power disk laser does not require a beam of high optical quality. That is why both laser diodes and rather complex laser diode structures with a uniform intensity distribution can be used in this case. In terms of the practical use laser diodes with a uniform intensity distribution are more preferable due to much lower energy consumption per one watt of the pump power.

For efficient processing of materials: cutting, drilling, polishing and removal of a thin film from the surface of various materials laser pulses with a high peak power and high repetition rate are needed. Typical pulse duration of a Q-switched Yb: YAG disk laser lies within one microsecond. Q-switching is provided by means of an acousto-optic modulator. Depending on the resonator geometry it is possible to generate pulses with duration from a few hundred picoseconds to a microsecond. To date, the best results achieved with the help of P-P disk lasers having high average power are as follows: pulse repetition rate—up to 10 kHz; maximum pulse energy—100 mJ; peak power—200 kW; average power—up to 1000 W. However, there are fundamental physical limitations on further scaling of the disk lasers, which we will discuss below.

14.4 Laws of Scaling of Disk Lasers

The power of disk lasers is limited not only by the power of the pump and overheating of the medium but also by the losses due to the ASE and the background radiation losses in the resonator. To avoid overheating, the size of the active medium should vary in accordance with the law of power scaling. Then, to avoid large losses caused by their exponential growth during the ASE, amplification of radiation corresponding to transverse round trips should not be large. This requires a reduction in gain G. Gain is determined by the reflectivity of the output mirror and disk thickness. Amplification of radiation per round trip, however, should not be

substantially greater in magnitude than the radiation loss per round trip along the same optical path. The difference between the gain and losses per round trip of radiation determines the optical energy that is coupled out from the laser cavity. Reduction of the gain at this loss level requires an increase in the disk thickness. In this case, at a certain critical size, the disk becomes optically too thick and cannot be pumped above the threshold without overheating. Some features of scaling can be shown on a simple model. Suppose M is the saturation intensity of the medium. The corresponding optimal thickness of the disk can be estimated as $h \sim T/Mb$. The corresponding optimal lateral dimensions of the disk can be represented in the form: $D \sim T/Mb2$, where T is a parameter of the heat load. Roughly speaking, the loss per round trip of radiation must be scaled inversely proportional to the cube root of the power required: $P \sim n T2/Mb3$.

An additional problem is the efficient delivery of pump energy. In cases with a small-signal gain, single-pass absorption of the pump is also low. It follows that the effective utilization of the pump energy is very necessary for the effective operation of the laser disk. To scale the output power, the medium must be optically thin, which requires a large number of passes of the pump energy through the medium. Besides, the pump energy coupled in through the lateral side of the disk can also be a possible solution for efficient pumping.

To reduce the effects of the ASE, it was proposed to use an optical cover consisting of an undoped material on the surface of the laser disk. This cover allows the spontaneously emitted photons to escape from the active layer and prevents their resonance in the bulk of active material. Rays cannot be reflected from the surface, as in the case of an open disk. This allows the maximum power achievable by the disk laser to be increased by an order of magnitude. Reflection of the ASE from the disk edge should also be suppressed. This can be done through the absorbing layer at the generatrix of the disk cylinder. In the regime when output power is close to maximal, much of the energy is used in the ASE; therefore, the absorbing layers must also have radiators accumulating heat. In the case of the maximum pump density of the disk laser its efficiency is quite low: Most of the pump power is used in the ASE and is absorbed at the edges of the device. In this case, the distribution of the pump energy between several disks can significantly improve the performance of the laser system. Indeed, lasers, consisting of several modules with disk elements in a single cavity, have been repeatedly reported. One of these lasers, fabricated by the TRUMPF Group [4]—a world leader in this class of laser systems—is presented at Fig. 14.1.

In the history of electrical discharge CO₂-lasers output power scaling a very similar geometry had been investigated carefully. This is a "Zig-Zag"—CO₂ laser which was created in FIAN by Barchukov in the beginning of 70s. The future of "Zig-Zag" multi-module geometry disk laser probably will be the same. At the Fig. 14.2 "Zig-Zag"—CO₂-laser created by Barchukov FIAN 1970 [2] is presented. With the help of this laser we have forecasted a lot of new effects which later on made significant difficulties to the scientists involved into high power mono-module laser creation. There are: deformation of the high power laser mirrors surface and distortion of phase front of the beam during propagation and as the result-high

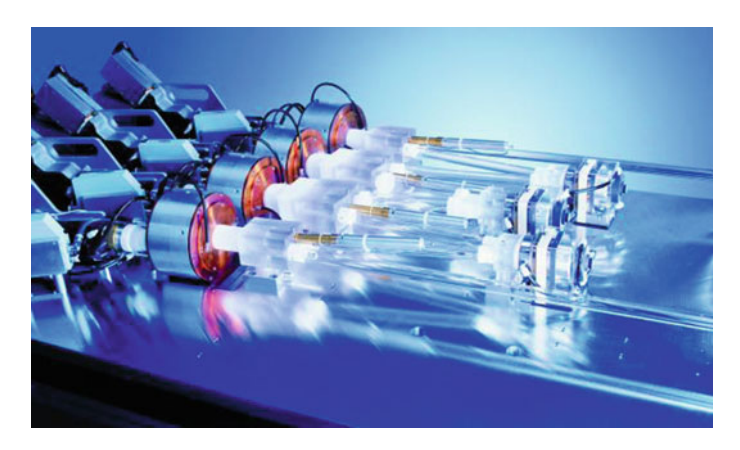


Fig. 14.1 "Zig-Zag" disk laser consisting of a series of disk modules in a single cavity (TRUMPF [1])



Fig. 14.2 "Zig-Zag"—CO₂-laser created by Barchukov FIAN 1970 [1]

power static and adaptive optics, big scale water cooled optics for telescopes based on SiC, high power CW plasmotrone in air and as the result—crusibleless growing of crystals, high quality laser beam and as the result—high quality laser based hard materials welding and cutting and so on.

In the quasi-continuous regime, the power can be estimated by scaling the saturation intensity with a duty cycle of the pump and by multiplying the duration of the pump by the pulse repetition rate. At moderate repetition rates (e.g., higher

than 1 Hz), the maximum energy of the output pulses is approximately inversely proportional to the cube of background losses b. The undoped cover can increase the average output power by an additional order of magnitude, provided that this cover does not increase the background loss. At low pulse repetition rates (in the single-pulse regime) and sufficient pump power, there is no general limitation on the energy, but the required size of the device increases rapidly with increasing pulse energy, thereby establishing a practical limit of energy. One active element, according to the estimates, can generate an optical pulse with energy of a few thousand joules, depending on the level of internal signal loss in the disk.

Disk lasers, as well as fiber lasers, have a large ratio of the cooling surface area to the gain of the laser. However, these two different concepts of the laser design also differ by the values of the achievable peak power. Beam quality of fiber lasers is determined by properties of waveguides, the refractive index difference between the core and the cladding, and the size of the internal diameter of the fiber that transmits light. On the other hand, beam quality of disk lasers depends on the design of the resonator. With increasing size of the optical pump region (its diameter is usually a few millimeters) at a constant optical power density on the disk surface, scaling of the output power becomes possible. Adjustment of the resonator also has similar features. Self-phase modulation defines the typical limit of nonlinear amplification of ultrashort pulses. It leads to an extension of the spectral line proportional to the ratio of the effective optical path in the material with nonlinear characteristics to the effective cross-sectional area of the beam multiplied by the square of the pulse duration. An electro-optical switch in a regenerative amplifier of the disk laser makes a substantial contribution to the nonlinear characteristics of the gain which is greater than the contribution from the disk. It must be emphasized that the values of the peak power, achieved today in single disk modules, are much smaller than the values obtained in 'rod' and 'slab' solid-state laser systems. However, the level of the average power generated by a single disk module also leaves much to be desired.

14.5 Regenerative Amplification of Pulses

At present, in the scientific and technical research and manufacturing processes relying on the use of high average power lasers, only sources operating in two regimes find applications, i.e., CW and P-P laser sources with a pulse repetition rate up to hundreds of Hz and pulse duration from tens of microseconds to tens of milliseconds. In most processes, purely thermal mechanism of action is mainly implemented, since use is made of the possibility of a laser source to deliver quite a lot of energy to a small area of the surface of the work piece. High-frequency, high-average-power laser systems operating in the Q-switched regime, which provides the pulse duration in a periodic train from a few to hundreds of nanoseconds, allows for a fundamentally different mechanism of interaction of radiation with matter, i.e., ablation, ensuring local release of energy not only in space but also in

time [5]. This results in an explosive local evaporation of the substance without an intermediate liquid phase. This mechanism can significantly extend the range of technological applications of laser sources. Today, it has found a real use in practice, only at an insignificant level of output power in the range of 1000 W. However, there arises a reasonable question: Why are high-power P-P lasers not available at the international laser market? The answer is simple: The complexity of their manufacturing consists in the inability of application of the classical modulation methods to laser systems with high average and peak powers. At the same time, it is quite clear that the creation of high-power (>1 kW) P-P lasers with frequencies up to 100 kHz or higher (with a peak power exceeding the average power by two to three orders of magnitude) would significantly expand the field of application of laser sources, increase their efficiency, and implement qualitatively new effects.

One of the successful trends in implementation of new methods of highfrequency modulation of the output from high-power laser sources is due to the regenerative amplification of a small signal injected into the cavity of a high-power gas or solid-state laser with the classical rod geometry. Use of intracavity modulators in high power/energy laser systems is hindered, because high power density inside the cavity leads to the appearance of plasma on the surface elements of the modulator, to the screening of radiation and to the destruction of the optical elements of the modulator. Quite promising is the method of realization of the P-P regime in high power/energy lasers, which is based on the use a self-filtering cavity. This cavity is a confocal resonator consisting of two confocal spherical mirrors of different curvatures; in the common focal plane there is an annular output mirror with a hole. Because of the high degree of discrimination of the higher modes with respect to the resonator losses, the lower mode is reliably generated. The spherical resonator mirror is placed outside the active medium and contains a modulation unit comprising spherical mirrors. The laser mode should be formed quickly enough in the leading edge of a giant pulse. The problem of laser micromachining usually involves cutting, drilling, surface cleaning and polishing, as well as removal of thin layers due to the ablation of the material. Micromachining relies on lasers emitting pulses of different duration. The geometry of the beam and the pulse repetition rate are crucial: usually the pulse duration does not exceed a few tens of nanoseconds, and in some cases reaches several hundreds of picoseconds. Disk laser technology provides excellent flexibility in the scaling of the output power by combining it with a high pulse energy and excellent beam quality.

14.6 Prospects for Scaling the Power/Energy of Disk Lasers

As mentioned above, the design of the disk laser generating a continuous and relatively high power is ideal for cutting and welding metals, where high optical quality of the beam is required. It is important for such industries as automotive, transportation, aerospace and heavy engineering. However, the design of the disk

laser is more suitable for a range of new technologies that are currently in demand. Today, a multi-module laser with a power up to 16 kW and beam quality of > 2 mm mrad, fabricated by the TRUMPF Group, is the undisputed leader in this class of laser systems. CW solid-state diode-pumped disk lasers demonstrate highly efficiency. Beam quality of the laser disk is outstanding, which makes it possible to work with a target from a large distance, while providing an extremely high concentration of radiation in the interaction region with the help of the focusing optics. In this design of the laser module the disk size is no more than 4–5 mm, because at larger sizes the energy loss due to the amplified spontaneous emission increases at an absolutely unacceptable rate. The above-presented laser system consists of a set of disk modules in a single cavity. This geometry of the laser system allows implementation of the P-P regime with a fairly high peak power, but the average power lies within a kilowatt. Parallel operation of disk lasers can increase the peak power of the entire system, but the phase-locking of the disk channels in the P-P regime requires additional scientific research. Further expansion of the power to the megawatt level of both the average and peak power in both geometries is very problematic.

At the same time, a different approach is known to the implementation of scalable solid-state laser systems, which consists of a set of active elements in the form of 'slabs', followed by phase-locking of the generated radiation. The team of the Northrop Grumman Corporation has created a laser with a power of >100 kW and high laser beam quality equal to the diffraction limit of 1.5 (averaged value) with the exposure time of 300 s [6]. The laser efficiency reaches 30%. The authors of the project point to the easy replacement of individual laser channels in case of failure. They also mentions some of the advantages of the parallel structure of the amplifying channels in terms of ease of further increasing output power, if necessary, to 100 kW. Beside, the laser assembled according to this scheme provides the divergence at the level of two diffraction limits from the common (composite) aperture. From general physical considerations, we can assume that for a given power level and a reasonable value of radiation resistance of optical elements, the divergence of the laser radiation at the level of 2×10^{-5} rad can be achieved for the CW generation regime and 0.6×10^{-5} rad for the P-P regime. A further increase in the number of channels in order to obtain an output power of 1 MW will require the coherent summation of the power from at least 80 channels, which seems an elusive task.

The question arises as to how the average power of a few megawatts can be achieved on the basis of solid-state lasers. And it is this power that is needed to address many problems associated with the removal of debris from near-Earth space, with launching of missiles with the help of lasers, with the creation of long-range conducting channels and others. Fiber lasers are not applicable for these purposes because of the smallness of the area of the exit pupil of the fibers and hence the impossibility of operation of such lasers in the high-frequency P-P regime with high peak power at an average power of a few megawatts [7, 8]. The laser system based on 'slabs' also seems hard to implement as adjustment of the system and its maintenance in a safe operation mode are comparable to the complexity of

working with a multi-element system for the solution to the problem of controlled thermonuclear fusion (CTF) at Livermore (USA). Proceeding from the above, the answer is quite clear: Such a laser can and should be based on the mono-module disk laser geometry!

This is due to the indisputable advantages of the disk geometry in terms of the minimal thermal lens in the active media and the high radiation resistance of the disk in the P-P regime because of the large area of the optical surface to couple out the radiation. But first it is necessary to find a solution to the problem of the suppression of ASE along the diameter of the disk. In this case, the size of the disk at a megawatt level of the average output will be at least 50 cm, i.e., at least hundred times bigger the size of the disk that is used today in existing systems. Radiation from such a laser, obtained during generation in the active medium of a single disk, does not require additional phase-locking. At the same time, such a laser in a mono-module geometry will be very well combined with a large diameter telescope for ensuring high peak power density of the laser pulse on space debris. It is known that the disk geometry of a laser was proposed 46 years ago. Recently the solution to the problem of the ASE suppression with increasing transverse dimensions of the active medium in the mono-module disk geometry has been found! Thus, the prospect of creation of a superlaser for new class of cutting edge problems is open!

14.7 Conclusions

Only the future will show the physical-technical solution for the mono-module disk laser which will be used effectively for the processing of materials and for the solution of other important challenges faced by science and technological advances. It is important to say that creation of megawatt class high repetition rate P-P disk lasers with a large cross section of the active medium is real and opens up great prospects for their use in solving the problems of launching of small satellites with lasers, formation of super-long conducting channels in space and atmosphere, cleaning of the near-Earth space from the space debris, etc. [9–11].

References

- 1. V.V. Apollonov, A.I.Barchukov, A.M.Prokhorov, JEEE Quantum Electron. 6, 10 (1974)
- 2. V.V. Apollonov, A. M. Prokhorov, A. H. Guenther, Laser Phys. 11, 8 (2001)
- 3. N.G. Basov, O.V. Bogdankevich, A.Z. Grasiuk IEEE J. Quantum Electron. 2(9), 594 (1966)
- 4. SPIE Events Europe, TRUMPF's R@D, (2012)
- 5. V.V. Apollonov, P.B. Corkum, R.S. Teylor, Appl.Phys.Lett. 35, 147 (1979)
- 6. SPIE Events Europe, Nothrop's R@D, (2012)
- 7. V.V. Apollonov, in Symposium HPLS@A-2012, Istanbul, 10 Sept (2012)
- 8. V. V. Apollonov, V. I. Kislov, A. M. Prokhorov, Quantum Electron. 23, 5 (1996)

References 199

- 9. V.V. Apollonov, Natural science 4, 705 (2012)
- 10. V.V. Apollonov, Nat. Sci. 4, 713 (2012)
- 11. V.V. Apollonov, Nat. Sci. **4**, 719 (2012)
- 12. V.V. Apollonov, Nat. Sci. **4**, 725 (2012)

Chapter 15 High Power/Energy Molecular Lasers



15.1 Introduction

A SSVD can be established in a gas by creating primary electrons the density of which should exceed a certain minimum value n_{\min} throughout the discharge gap [1, 2]. Various methods for preionization of a gas in the discharge gap have been developed for this purpose [3, 4]. Primary electrons are created by these methods directly in the discharge gap, which sometimes causes difficulties in the establishment of conditions necessary for the formation of a SSVD. For example, high voltages are needed for the formation of an initial plasma when the preionization source and the active medium are combined in the same volume [5], where as preionization with ultraviolet radiation may be ineffective because of strong absorption of such radiation in a medium [6], and if soft X-rays are used, it is necessary to ensure rigid synchronization of the X-ray and pump sources [7]. In mixtures of gases typical of CO₂ lasers, losses of electrons due to trapping are relatively small at low values of E = p, where E is the electric field intensity and p is the gas pressure. The trapping coefficient is considerably less than the absorption coefficient of ultraviolet radiation for the same mixtures [7]. It follows that, in principle, it should be possible to create primary electrons in a density needed for the formation of a self-sustained volume discharge at a considerable distance from an ionization source and then transport the electrons to the gap by drift in an electric field. A method of formation of a self-sustained volume discharge by filling the discharge gap with a flux of electrons drifting in an electric field, without preliminary ionization of the whole discharge volume, was proposed and implemented [8]. The source of electrons was a plasma formed in an auxiliary discharge initiated under a grid cathode. This method made it possible also to establish a SSVD in a system of electrons with a strongly inhomogeneous electric field in the discharge gap.

15.2 Physical Model of SSVD Formation

The SSVD formed by filling the discharge gap with primary electrons was studied in the electrode system with a uniform initial distribution of the electric field (the anode with the Chang profile [9]—a flat mesh cathode) with a discharge gap measuring 6–10 cm in length. In these experiments use was made of the configuration presented in Fig. 15.1. When U_0 was less than the static breakdown voltage of the discharge gap, $U_{\rm eT}$, use was made of a scheme with pulsed application of the voltage exceeding $U_{\rm CT}$ to the discharge gap. In the latter case, the filling of the discharge volume with electrons from the plasma of the auxiliary discharge was performed either by applying a bias to the discharge gap [10], or by artificially increasing the duration of the leading edge of the voltage pulse applied to the discharge gap [10, 11]. The value of U was chosen so that the electrons can reach the anode before the onset of the ionization processes in the discharge gap.

The conditions of the SSVD formation in initial highly nonuniform field distribution in the discharge gap were performed using the setup schematically shown in Fig. 15.1b. The electrode system ($d=10~\rm cm$) was formed by a planar anode 1 (a rectangular plate measuring $18\times 50~\rm cm$ in size, curved along a radius of 10 mm) and a cathode 2 with sharp edges (a rectangular brass mesh measuring $10\times 40~\rm cm$ in size). The surface area covered by auxiliary discharge 3 under the mesh was slightly larger than the cathode area. In order to reduce the working voltage [12, 13] and increase the duration of stable combustion of the SSVD [14, 15], easily ionizable substances such as tripropylamine and triethylamine at a vapor pressure were added into the mixture.

In the experiments we controlled the lower limit for the SSVD ignition with respect to the voltage $U_{\rm min}$ (determined by the voltage of the pump source), and the SSVD stability limit with respect to the CO₂–N₂–He gas mixture composition and the energy input. The SSVD uniformity was monitored visually by photos of the glow discharge, as well as by the small-signal gain and its distribution over the

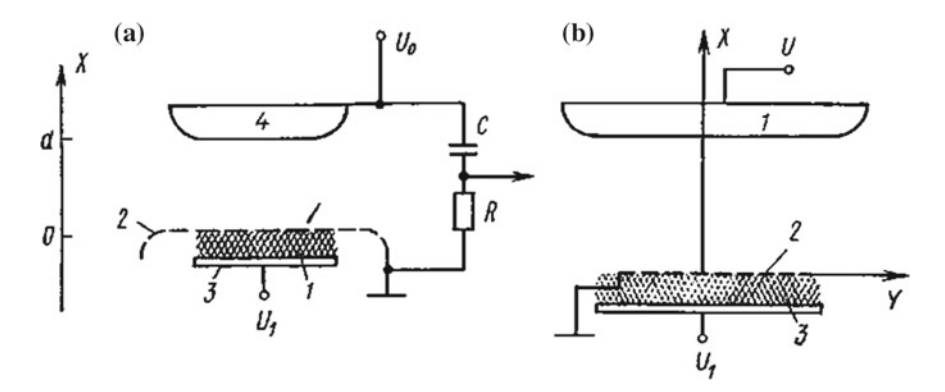


Fig. 15.1 Discharge systems with profiled (a) and nonprofiled (b) electrodes

aperture of the amplifier. The electron flux current in the discharge gap was deduced from the voltage drop across a resistor R. The charge carried by the flux was found from the change in the voltage across a capacitor C for R = 0. The contribution to the gap conductance made by the photoionization of the gas in the gap by the auxiliary-discharge radiation was estimated from the charge of the positive ions formed in the gap (these measurements were carried out by applying a negative bias voltage U_0).

The following types of an auxiliary discharge were investigated:

- (1) A barrier discharge [16] in which a wire insulated with polyethylene was used as the electrode.
- (2) A corona discharge initiated by a multipin electrode, stabilized by limiting the current through the pins by a ballast resistor [17].
- (3) A volume discharge between a grid (discharge gap cathode) and a metal cathode, initiated as described in [18].
- (4) A volume discharge between a semiconductor cathode (carbon-filled rubber with a bulk resistivity [19] and a grid (discharge gap cathode) initiated without preionization [20].
- (5) A multichannel discharge on the surface of a high-permittivity insulator limited by the insulator capacitance [21].
- (6) A multichannel discharge on the surface of a semiconductor (carbon-filled rubber [19]) limited by the semiconductor resistance (this auxiliary discharge was realized in the same way as a multichannel discharge on the surface of a ceramic described in [21]).

In all these auxiliary discharges, an electric field was applied to auxiliary discharge plasma. A special auxiliary electrode was not essential. The auxiliary electrode is the one used to apply the voltage pulse to ignite the auxiliary discharge.

The propagation of primary electrons in the discharge gap (one-dimensional case) in the absence of ionization multiplication is described by the system of equations and boundary conditions for the electric field E(x, t), the density of electrons n(x, t) and negative ions $N_t(x, t)$ [22]:

$$\partial n/\partial t + \partial (n\mu E)/\partial x = -\alpha n\mu |E|;$$
 (15.1)

$$\partial N_i/\partial x = \alpha n\mu |E|; \tag{15.2}$$

$$\partial E/\partial x = -(N_i + n)e/\varepsilon_0;$$
 (15.3)

$$\int_{0}^{d} E \, \mathrm{d}x = -U_0; \tag{15.4}$$

$$n(0,t) = \text{const} = n(0);$$
 (15.5)

$$N_i(x,0) = 0; (15.6)$$

$$n(x,0) = 0$$
 when $x > 0$, (15.7)

where α , μ , and e are the attachment, mobility and charge of electrons, respectively; ε_0 is the dielectric constant. The *X*-axis is directed from the cathode (x = 0) to the anode (x = d); the electron density at the cathode surface n(0) is assumed to be constant over time (the escape of the electrons from the cathode to the displacement field is compensated for by the influx from the plasma of the auxiliary discharge). In expressions (15.1)–(15.7) the mobility of the negative ions is negligible.

System (15.1)–(15.7) was solved using an explicit difference scheme [10]. To simplify the calculations we assumed that $\alpha = \text{const.}$ Figure 15.2a shows the dependences n(x) and E(x) for various time points at $U_0 = 400 \text{ kV}$, d = 40 cm, $\mu = 10^3 \text{ cm}^2/\text{Vs}$, $n(0) = 10^9 \text{ cm}^{-3}$. It is seen that in the absence of the electron loss through the attachment, stationary distributions n(x) and E(x) are established in the discharge gap for $t > t_0 = d/E_0\mu$, where $E_0 = U_0/d$. The discharge gap accumulates a volume charge of negative ions, which prevents the propagation of primary electrons. Calculations performed for different a and d showed that at the time $t = t_0$, the electron densities near the anode n_{α} (d) (at $\alpha \neq 0$) and n(d) (at a = 0) are related as by the expression:

$$n_{\alpha}(d) \approx n(d)e^{-\alpha d}$$
. (15.8)

In conventional CO₂ lasers utilizing atmospheric pressure CO₂–N₂–He gas mixtures, $E_0 \le 3$ kV/cm is less than 10^{-2} cm⁻¹ [23, 24]. Therefore, when d < 1 m

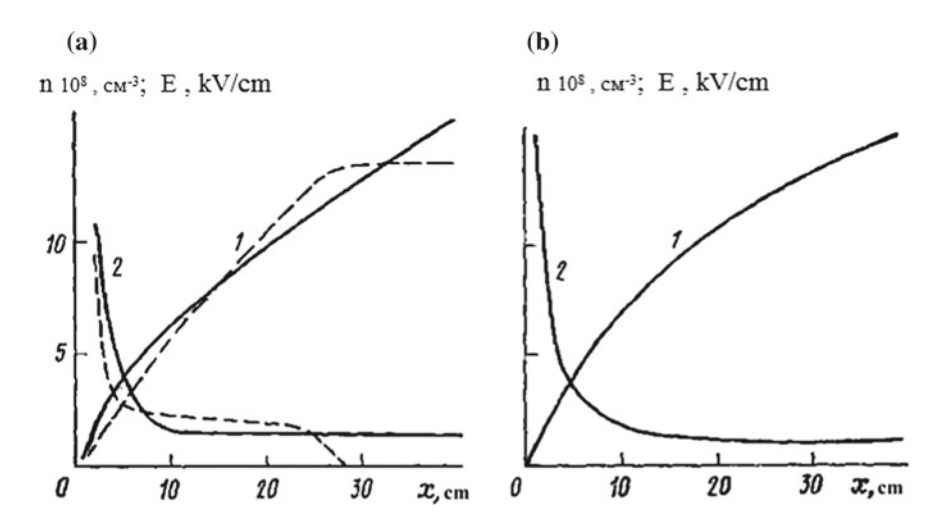


Fig. 15.2 Calculated dependences E(x) (curves denoted by 1) and n(x) (curves denoted by 2): **a** t = 2 mks (dashed curves) and 4–6 mks (continuous curves); **b** U = 400 kV, $\mathbf{T_f} = t = 8$ mks, $n(0) = 10^{10}$ cm⁻³

and $E_0 \le 3$ kV/cm, the loss of electrons through the attachment does not affect significantly the propagation of primary electrons, and the analysis of the possibilities of the method can rely on the model of a stationary primary electron (a = 0 and $t > t_0$). Approximate steady-state solution to system (15.1)–(15.7) at large n(0), when

$$\delta = 3\varepsilon_0 E_0 / 4en(0)d \ll 1 \tag{15.9}$$

has the form [24]

$$E(x) = \frac{3}{2}E_0\sqrt{\frac{x}{d} + \delta^2};$$
(15.10)

$$n(x) = \frac{3}{4} \frac{\varepsilon_0 E_0}{ed} \sqrt{\frac{d}{x + \delta^2 d}};$$
(15.11)

$$j = \frac{9}{8}\mu\varepsilon_0 \frac{E_0^2}{d} (1 - 3\delta^2), \tag{15.12}$$

where j is the current density of primary electrons.

Let us perform estimations. Let $E_0 = 1 \text{ kV/cm}$, d = 50 cm, then from (15.11) $n(d) \approx 10^7 \text{ cm}^{-3}$ clearly exceeds Nmin, required for the SSVD formation [10]. In this case, condition (15.9) is fulfilled already at $n(0) \approx 10^8 - 10^9 \text{ cm}^{-3}$. It will be shown below that such low densities of the electrons at the cathode can provide almost any type of the auxiliary discharge. Thus, our estimates confirm the possibility of obtaining the SSVD by filling the discharge gap with primary electrons, which are necessary for the SSVD formation process by realization of high concentrations of primary electrons at large distances from the cathode. Note some features of this method which follow from the considered model.

It is seen from (15.11) that at a certain distance from the cathode $(x \gg \delta^2 d \approx 10^{-3} d \text{ when } E_0 = 1 \text{ kB/cm}, d = 40 \text{ cm}, n(0) = 10^9 \text{ cm}^{-3})$ under the condition of (15.9) n(x) is independent of n(0). Therefore, the discharge gap will be filled by electrons uniformly (in a plane perpendicular to x), even in the case of a significant nonuniformity of the n(0) distribution over the cathode area. This makes it possible to produce a SSVD without small-scale inhomogeneities (typical of systems with UV preionization) caused by shading of the discharge volume by a mesh cathode [25], and to increase the small-signal gain and efficiency of CO_2 lasers.

It follows from (15.10) that, despite the relatively low concentration of the primary electrons in the discharge volume, the presence of the uncompensated negative charge of primary electrons leads to a significant distortion of the electric field in the discharge gap. As a result, the ionization processes will develop in the first place at the anode, where the electric field can be enhanced by 1.5 times compared to E_0 . At the same time, the development of ionization at the cathode is difficult, because the field is close to zero due to the screening of the cathode by the

volume charge of primary electrons. Obviously, the effect of the cathode screening when filling the discharge gap with electrons should manifest itself in the real geometry of the discharge gap. Therefore, it is advisable to try to find the conditions for obtaining the SSVD in systems of nonprofiled electrodes, which would greatly simplify the creation of electric discharge lasers. Distortion of the electric field in the discharge gap by a volume charge of primary electrons should result in a voltage drop (this voltage is used to produce a SSVD), which is an obvious advantage of the proposed method. However, in a system with preliminary displacement U_0 , which is used to fill the discharge gap with electrons, and subsequent to apply the voltage pulse with the amplitude U to the discharge gap, degree of enhancement of the electric field at the anode (with respect to the U/d) $K_v = 1 + U_0/2U$ may be small, because it is not always acceptable increase U_0 to values close to $U_{\rm st}$. The degree of distortion of the electric field can be increased by using a scheme with an artificially prolonged voltage front [11]. Figure 15.2b shows the results of numerical solutions of (15.1)–(15.3), (15.5)–(15.7) for $\pi(x)$ and E(x) at a = 0 with the boundary condition

$$\int_{0}^{d} E \, \mathrm{d}x = -\frac{U}{2} \left(1 - \cos \frac{\pi t}{\tau_f} \right),\tag{15.13}$$

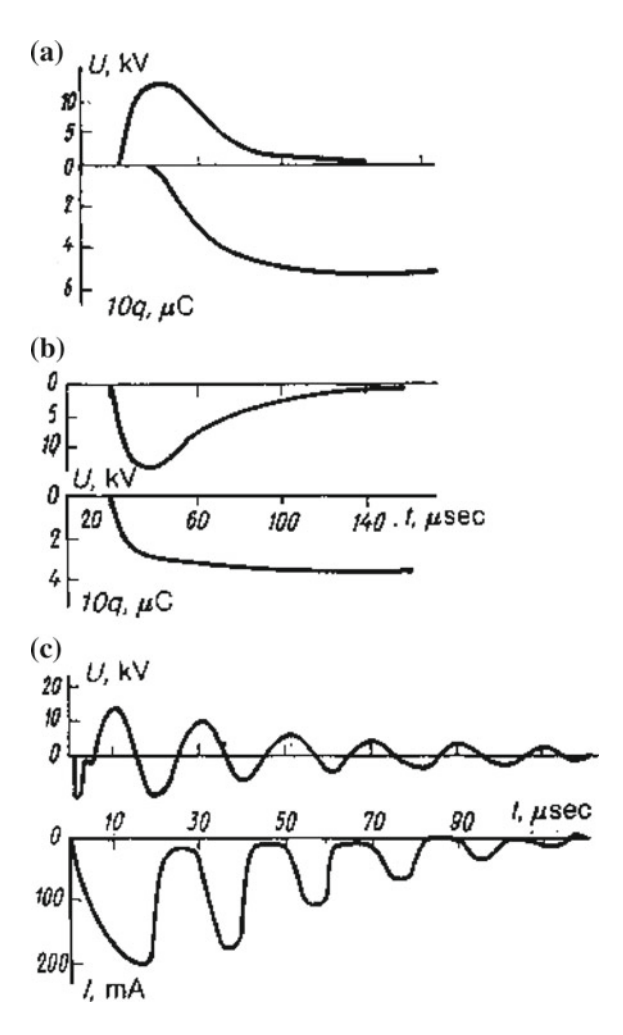
which corresponds to the law slew of the voltage rise in the discharge gap in this scheme. To completely fill the discharge gap with the electrons, it is needed also to satisfy the condition $\mathbf{T_f} \geq 2d^2/\mu U$. It is seen from Fig. 15.2b that when $t = \mathbf{T_f} = 2d^2/\mu U$, as in the case of constant displacement in the discharge gap, the gain E(d) is reached, which U/d is 1.5 time higher relative to U/d at multiple reductions of E(0).

15.3 Experiments

Figures 15.3a, b show oscillograms of the electron charge q(t) extracted from the discharge gap and of the voltage U(t) between the gap cathode and the auxiliary-discharge electrode, recorded for a mixture of N_2 with tri-propylamine obtained for the case when d=2 cm and the electrode area was S=200 cm². The auxiliary discharge was a multichannel discharge on the surface of a ceramic (with the permittivity $\varepsilon=2000$), limited by the capacitance of the ceramic itself [21]. The shape of U(t) was set by the parameters of a special RC circuit. A comparison of the q(t) oscillograms recorded for different polarities of the voltage U(t) indicated that the main rise of q(t) occurred in the region where dU/dt < 0. When a negative bias voltage was applied to the discharge gap, the form of the q(t) oscillograms was independent of the sign of dU/dt. In accounting for these results one should bear in mind that the sign of the electric field in the gap between the ceramic surface and

15.3 Experiments 207

Fig. 15.3 Oscillograms of the voltage U(t) on the auxiliary electrode, of the electron charge q(t), and of the electron flux current I(t) in the case of positive (a) and negative (b) polarities, and also in the case of oscillatory nature of the voltage U(t) (c)



the discharge gap cathode was the same as the sign of $\mathrm{d}U/\mathrm{d}t$. Therefore, for $\mathrm{d}U/\mathrm{d}t < 0$ some of the electrons were expelled from the auxiliary-discharge plasma into the discharge gap across the grid cathode and drifted toward the anode in the bias field $(U_0 > 0)$. For $\mathrm{d}U/\mathrm{d}t > 0$ or $U_0 < 0$ it was not possible to drive electrons beyond the grid and in the discharge gap the flux of the current was then entirely due to the photoionization of the gas by the auxiliary-discharge radiation.

Figure 15.3c shows the oscillograms of the voltage U(t) and of the electron current in the discharge gap I(t) for an oscillatory form of the voltage U(t). It is clear from these oscillograms that a considerable current in the discharge gap was recorded only for dU/dt < 0, irrespective of the sign of U(t).

It should be stressed that we investigated long-duration discharges in order to identify the conditions for the formation of an electron flux from the long-duration auxiliary-discharge plasma itself. Under these conditions, in spite of the presence of

an easily ionizable substance in the gas, the contribution to the discharge gap conductance of the electrons arriving from the auxiliary-discharge plasma was (for suitable signs of dU/dt and U_0) approximately ten times higher than the contribution made by the photoionization of the gas by the auxiliary-discharge radiation even when the latter was of the surface type. Under these conditions the contribution of the photoionization to the charge of the electrons crossing the gap did not exceed 10% of the contribution of the electron flux for a corona discharge and it was not greater than 1% in the case of barrier volume discharges (these values were obtained for d=6 cm, $U_0=30$ kV, mixture of N_2 with tripropylamine, P=1 atm) and the presence of an easily ionizable substance in the gas had practically no influence.

When the auxiliary discharge pulse was shortened (by reducing the inductance or the active resistance in the circuit of this discharge), the contribution of the photoionization to the discharge-gap conductance increased and, in principle, it was possible to form an electron flux from a plasma created by the ultraviolet radiation of the auxiliary discharge in the cathode region (and also from a plasma on the surface of a plasma cathode [26] or a barrier discharge plasma in systems described in [18]).

As already pointed out, the homogeneity of a SSVD could be improved by selecting the auxiliary discharge characteristics in such a way as to satisfy the condition (15.9). Naturally, one would then have to ensure a certain minimum density of the electron current in the auxiliary gap. In this case, the possibility of SSVD igniting in a discharge plasma is determined by the condition $\mathbf{T_{dd}} \geq t_0$ ($\mathbf{T_{dd}}$ is the auxiliary discharge duration); otherwise, the near-cathode zone can lose electrons before the ionization processes in the discharge plasma are developed.

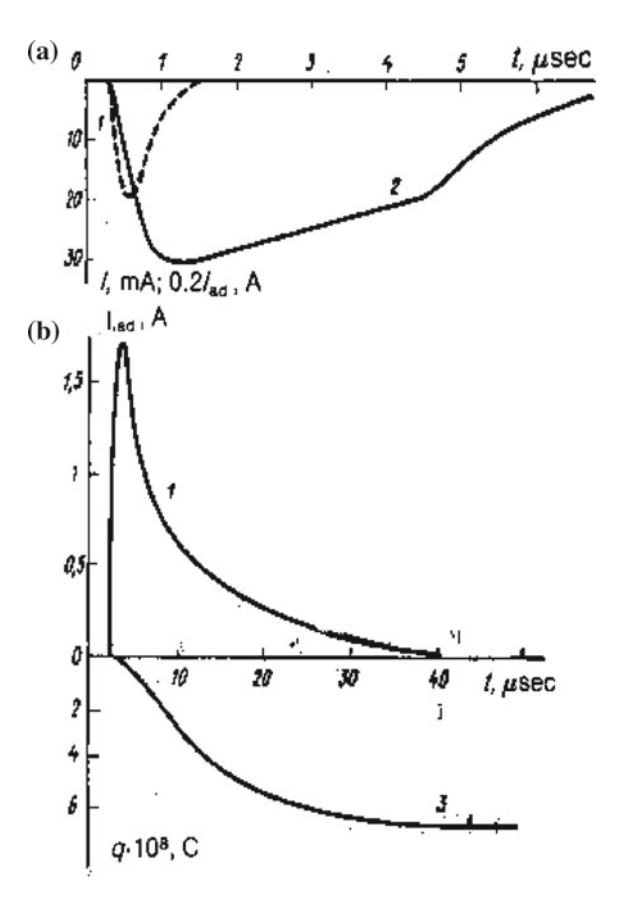
Figure 15.4a shows oscillograms of the electron flux current and of the auxiliary discharge current (this was a volume type of discharge) obtained for a mixture of gases of the $CO_2:N_2=1:3$ composition at a pressure of p=0.3 atm when the gap was d=2 cm and the applied bias voltage was $U_0=12$ kV. The distance between the auxiliary discharge electrodes was 1 cm and the area of the auxiliary electrode was S=200 cm². It is clear from Fig. 15.4a that change in the auxiliary discharge current by an order of magnitude altered I(t) by just 10%, indicating that the condition (15.9) was satisfied. The measurements showed that the saturation I(t) is reached at

$$I_{\rm dd}/S = i_{\rm dd} \ge (20 - 30)i_{\rm lim} = (20 - 30)\varepsilon_0 \mu E_0^2 d,$$
 (15.14)

where i_{lim} is the limiting current density of the primary electron from (15.12) when (15.9) is met. Condition (15.14) is an empirical criterion, equivalent to (15.9). Note also that the fulfillment of these conditions becomes simpler when d increases. Condition (15.14) can be also easily met when use is made of a pulsed corona discharge as an auxiliary discharge. However, the limiting duration of the stable burning out of both a corona and a volume auxiliary discharge, when condition (15.14) is met without any special measures taken into account, does not exceed 5–10 μ s.

15.3 Experiments 209

Fig. 15.4 Oscillograms of the volume auxiliary discharge current (1) from metal (a) and semiconductor (b) electrodes, of the electron flux current (2), and of the charge carried by this flux (3)



Both volume and corona discharges could be stabilized by utilizing electrodes made of semiconductor materials [20]. Figure 15.4b shows oscillograms of the volume discharge current in a mixture of gases of the $CO_2:N_2:He = 8:32:60$ composition with an admixture of triethylamine at p = 1 atm, ignited without a preliminary ionization between a semiconductor material cathode (which was a disk 5 cm in diameter and 2 cm thick) and a grid (discharge gap cathode); it also includes an oscillogram of the charge q(t) of the electrons extracted from the discharge gap in the case when $U_0 = 5$ kV, d = 8 cm, and the distance between the auxiliary discharge electrodes was 1 cm. The density of the auxiliary discharge current obtained in this way was ~ 50 mA/cm² and the duration of the stable burning of the discharge in gas mixtures of various compositions exceeded 30 μ s.

In the case of a discharge of the surface of an insulator, which was limited by the capacitance of the insulator itself, our measurements indicated that the electron current in the gap between the insulator surface and the grid was an order of magnitude less than via an auxiliary electrode. Therefore, (15.14) is equivalent to the condition

$$dU/dt \ge (2-3) \cdot 10^2 \mu E_0^2 \varepsilon_0/dC_d$$
 (15.15)

Condition (15.15) is easily fulfilled at $\mathbf{T}_{\mathbf{dd}} = t_0$ and $C_{\mathbf{d}} = 100 \text{ pF/cm}^2$ ($C_{\mathbf{d}}$ is the specific capacity of the dielectric). Stable burning of long duration discharge, when (15.14) is met, is realized also in a multichannel discharge grazing along the surface of a semiconductor material limited by the intrinsic resistance of the material due to a choice in the discharge capacitance.

When the necessary condition was satisfied, stable long-term burning of the discharge was achieved also for a multichannel auxiliary discharge on the surface of a semiconductor material, which was limited by the resistance of the material itself, when the charging capacitor was suitably selected It therefore follows that when special measures were taken, all the types of the auxiliary discharge discussed above were capable of forming an electron flux with the maximum parameters specified by (15.12).

Figure 15.5a shows the dependence of the electron flux current $I(U_0)$, recorded under the same conditions as the oscillograms in Fig. 15.4a. Clearly, at low values of $U_0 I \sim U_0^2$ this dependence is in agreement with (15.12). When U_0 exceed a certain minimum value I, the current rise steeply and this was accompanied by volume radiation in the discharge gap, indicating the onset of the ionization processes and the formation of a SSVD. This minimum value of U_0 amounted to (2/3) $U_{\rm at}$, as expected on the basis of (15.11), according to which the electric field at the anode was enhanced by the space charge of the electron flux by a factor of 1.5 compared with E_0 . We could assume that the possibility of igniting a SSVD at a $U_{\rm st}$ voltage lower than mentioned in [10, 25, 27], was also due to distortion of the electric field by the space charge of the electron flux and in [10] this flux could be formed both from an auxiliary-discharge plasma under the cathode or from the photoplasma in the cathode region, because the discharge on the surface of a ceramic used in [10] was of relatively short duration ($\sim 1.5 \, \mu$).

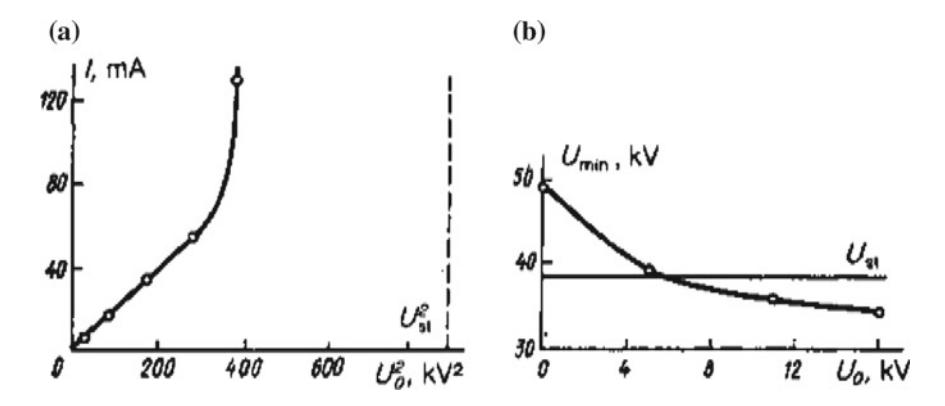


Fig. 15.5 Dependences of the amplitude of the electron flux current (a) and of the minimum ignition voltage of a SSVD (b) on U_0

15.3 Experiments 211

The influence of the distortion of the electric field on the conditions of formation of a SSVD is manifested also by the results in Fig. 15.5b, which gives the dependence of the minimum voltage U_{\min} on U_0 for the ignition of such a discharge in the circuit with a preliminary bias of the discharge gap. The sign of this bias was opposite to the sign of U_0 in order to avoid formation of an electron flux on application of a voltage pulse to the discharge gap. In this case the auxiliary discharge was of the barrier type. Experiments were carried out on a mixture of the $CO_2:N_2:He=1:1:3$ composition and the other parameters were d=6 cm and p=0.5 atm. A voltage pulse was applied to the discharge gap after the delay $T=t_0=d^2/\mu U_0$ relative to the beginning of the auxiliary discharge. It is clear from Fig. 15.5b that Umin decreased monotonically on increase in U_0 in accordance with the above model.

At low overvoltages across the discharge gap the distortion of the electric field by the space charge of the electron flux had a considerable influence on the conditions of energy deposition in the plasma of the SSVD and on the residual voltage across the gap after the end of the discharge.

Figure 15.6a gives oscillograms of the voltage U(t) and current in a SSVD formed when the density of the electron current was too low for a significant distortion of the field and the condition (15.9) was not obeyed (d = 6 cm, gas mixture of the CO₂:N₂:He = 1:1:3 composition, p = 0.5 atm, charging voltage $U_{\rm ch} = 45$ kV, $T_{\rm f} = 0.8$ µs). Figure 15.6b shows oscillograms of U(t) and I(t) recorded under the same conditions as in Fig. 15.6a, but in this case the condition (15.9) was satisfied. A comparison of Fig. 15.6a, b indicated that distortion of the electric field by the space charge of the electron flux resulted in some reduction in the amplitude of the voltage pulse across the discharge gap and also increased the amplitude of the current in the SSVD; it also increased the energy deposited in the discharge by a factor of about 2. This could be important under conditions when it would be difficult to establish a high overvoltage across the discharge gap.

All the forms of the auxiliary discharge investigated by us using a system of profiled electrodes made it possible to form a SSVD when the energy deposited was

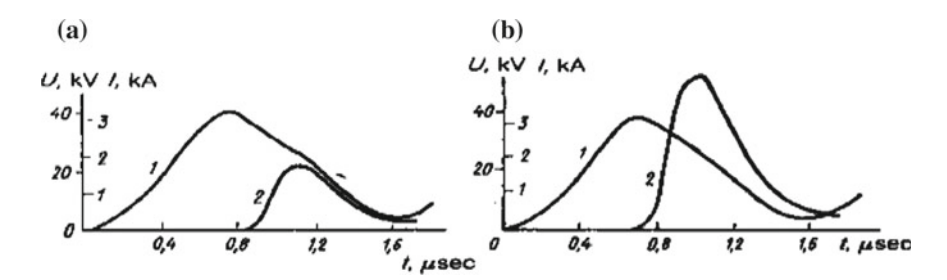


Fig. 15.6 Oscillograms of the voltage U (curves denoted by 1) and of the current (curves denoted by 2) for a SSVD when the condition (9) is not satisfied (a) and when it is satisfied (b)

up to 300 J/l. The content of CO_2 in CO_2 – N_2 –He gas mixtures (with the addition of easily ionizable substances) at atmospheric pressure reached 40% when the total content of all the molecular gases was up to 70%, whereas in helium-free mixtures it was up to 30%. We also established a SSVD in atmospheric air (p = 0.4 atm, d = 10 cm) by the addition of triethylamine, which was evidence of the high efficiency of the method of formation of a SSVD by filling the discharge gap with an electron flux, and this was true also of gases characterized by strong electron trapping.

The best characteristics of a SSVD in a system of nonprofiled electrodes (Fig. 15.1b) did not differ from the characteristics of the corresponding discharge observed when the initial distribution of the electric field in the discharge gap was homogeneous. The discharge formed using such electrodes could be ignited employing any of the listed types of the auxiliary discharge, with the exception of a volume discharge utilizing metal electrodes (this type of the auxiliary discharge was difficult to realize using nonprofiled electrodes because of the inhomogeneity of the electric field in the auxiliary gap). The investigated system was characterized by a strongly inhomogeneous initial distribution of the electric field in the discharge gap, which was close to the field distribution between one of the electrodes and a plane of symmetry in a parallel-plate capacitor of limited size (as shown in cross section in Fig. 15.1b); the field on the anode decreased monotonically along the normal to the symmetry axis of the discharge gap, whereas the field on the cathode increased reaching its maximum at the edge. Consequently, the static breakdown voltage in the system with nonprofiled electrodes was approximately half the corresponding voltage in the quasi-steady phase of a SSVD. When the discharge gap was subjected to a voltage pulse of amplitude $U > U_{si}$ (representing the regime with a deliberately delayed leading edge of the voltage pulse), a spark breakdown at the cathode edge was observed in the absence of an auxiliary discharge. When the auxiliary discharge $U_{\rm st} < U < 1.8 U_{\rm st}$ was started and the static voltage was in the required range, a spark did not appear during the period T_{dd} even when the formation of such a spark in the absence of an auxiliary discharge was less than T_f . A weak electron flux current was then observed in the discharge gap. When the amplitude of the voltage pulse exceeded required level and an auxiliary discharge was started simultaneously with the leading edge of the pulse a volume discharge appeared in the gap.

It therefore follows that the distortion of the initial distribution of the electric field by the space charge of the electron flux in the case of nonprofiled electrodes resulted, in contrast to the case of profiled electrodes, in an increase (rather than a reduction) of the pulsed breakdown voltage of the discharge gap and the breakdown was of volume nature. A strongly inhomogeneous initial distribution of the electric field in the presence of nonprofiled electrodes was corrected in the process of profiling the discharge gap with electrons, i.e., a dynamic profiling of electrodes by the space charge of the electron flux took place. We shall now consider qualitatively this phenomenon.

Screening of the cathode by the negative charge of electrons reduced several-fold the electric field on the cathode surface, compared with the average 15.3 Experiments 213

field U(t)/d in the discharge gap at a given moment, so that ionization processes could not develop near the sharp edges of the cathode. The field at the anode was then enhanced and the relative magnitude of the enhancement should be highest at the center of the electrode, since the electron flux spread in the course of propagation in a discharge gap as a result of the electrostatic repulsion between the electrons. Bearing in mind also the initial distribution of the field in the discharge gap, we concluded that the ionization processes began to develop simultaneously from the anode to the cathode and from the center to the edges of the discharge gap, i.e., the propagation of an ionization wave, which formed a cathode layer when it closed the discharge gap, was not governed by the initial configuration of the electric field but by that configuration which was formed with the participation of the space charge of the electron flux This made it possible to prevent spark breakdown and to form in a system with nonprofiled electrodes a SSVD with a deposited energy distribution typical of such nonprofiled electrodes. Measurements of the small-signal gain at low pump energies, which represented the distribution of the energy deposited in the discharge in a plane perpendicular to the optic axis, demonstrated that the gain decreased away from the optic axis to the electrode edges. This provided an indirect confirmation of the above description of the formation of a SSVD. It should be stressed that a change in the voltage on the electrodes resulted in a redistribution of the electric field in the discharge gap at a finite rate governed by the electron mobility. Therefore, the condition for screening of the cathode by the space charge of the electron flux (where U/d is the instantaneous value of the field) could be disturbed if the voltage across the discharge gap rose too rapidly. In fact, it was not possible to create a SSVD using nonprofiled electrodes when the voltage was applied abruptly to the electrodes and this was true even when the application of a bias resulted in a preliminary filling of the discharge gap with electrons. Sparks were observed at the corners of the cathode, i.e., in the regions with the maximum concentration of the electric field in the absence of screening. The discharge was stable in the case when the leading front of the voltage pulse was delayed deliberately [10, 11] so that the duration of this front was >2 µs, for d=10 cm. A classical example of nonprofiled electrodes with a strongly inhomogeneous initial distribution of the electric field in the discharge gap was the first transversely excited CO₂ laser [18]. The present experiments indicated that the electron flux in such a system was formed by a barrier discharge plasma created directly on the cathode surface and this made it possible to satisfy quite readily the saturation (15.9) and screening conditions. One should stress also that an increase of the stability of a SSVD [11] in systems of the type described in [18] and considered in the present study, which was observed when easily ionizable substances were added to the gas mixtures, was not due to photoionization of these additives because in the case of regimes used to form a SSVD by filling the gap with an electron flux the contribution of the photoionization to the conductance of the discharge gap during the filling process was unimportant compared with the contribution of the electron flux from the auxiliary discharge plasma and this was true for the majority of the auxiliary discharges. Our investigations made it possible to increase the aperture of SSVD based lasers and amplifiers up to 80 cm and to obtain a radiation energy of CO_2 lasers more then 5 kJ for the electric efficiency more than 10%.

15.4 High Power/Energy HF (DF) Lasers

The main problem arising in the construction of powerful wide-aperture nonchain HF(DF) lasers in which a chemical reaction is initiated by a SSVD is the implementation of the SSVD itself in mixtures of SF_6 with hydrogen carriers (deuterium carriers). The possibility of applying for such purposes the usual methods based on the preliminary ionization of the gas in a homogeneous electric field with the subsequent application of a high-voltage pulse to the discharge gap [28] is limited by the high electro-negativity of the SF_6 molecules.

A new approach to the solution of the problem of increasing the volume of the active medium and the energy of the radiation emitted by nonchain HF(DF) lasers was found in our earlier studies [29–31]. In a study [30] of a nonchain HF(DF) laser with preionization by soft X-rays, it was observed that the SSVD characteristics and the laser output characteristics are independent of the presence of preionization if the cathode surface has been subjected to a treatment involving the deposition on it of small-scale inhomogeneities. In other words, if the cathode has a rough surface, preionization is not essential in order to obtain an SSVD in the mixtures of an HF (DF) laser.

The possibility of achieving an SSVD without preionization and with an energy input homogeneous throughout the volume under the conditions of a high edge inhomogeneity of the electric field in the discharge gap of an HF(DF) laser has also been demonstrated [31]. These investigations made it possible to increase the aperture of a nonchain HF(DF) laser based on SF₆—hydrocarbon (deuterocarbon) mixtures up to 27 cm and to obtain a radiation energy of ~ 400 J for an electric efficiency of approximately 4% [32]. An SSVD without preionisation in SF₆ and in mixtures containing it, i.e. a selfinitiated volume discharge (SIVD) [33], has a number of properties unusual for volume discharges. The observation of a discharge of this kind opens up unique opportunities for the development of simple and effective nonchain HF(DF) lasers operating in both pulsed and repetitively pulsed regimes. Further investigations of the SIVD in order to establish the principal mechanisms determining its development is therefore of undoubted interest. To review the results of our investigations is in fact the subject of the present chapter.

The SIVD characteristics were investigated in discharge gaps with electrodes having different configurations (Fig. 15.7) with the ratio of the partial pressures of the mixture components $SF_6:C_2H_6=10:1-10:3$ and pd=0.02-0.7 cm bar (p is the pressure of the mixture and d the interelectrode distance). The integral characteristics of the discharge and the dynamics of its development were studied by using a system of plane electrodes illustrated schematically in Fig. 15.7a. The SIVD was struck with d=2-6 cm between an aluminium cathode 6 cm in diameter, rounded

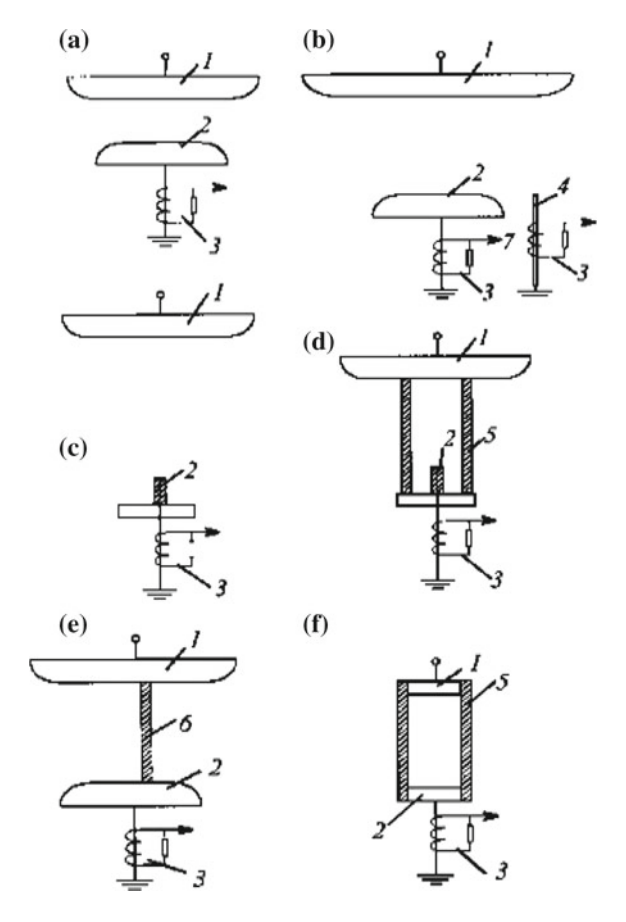


Fig. 15.7 Discharge gaps with electrodes having different configurations: (1) anode; (2) cathode; (3) Rogowski loop; (4) initiating electrode; (5) glass tube; (6) glass plate

(1 cm radius) along the perimeter, and an aluminium anode 12 cm in diameter. The surface of the cathode, including the rounded parts, was sandblasted.

In order to investigate the SIVD dynamics, an artificial (transmission) line with a variable number of cells was discharged across this gap [34]. This made it possible to follow, by varying the duration of exposure to the voltage across the gap in the range 40–400 ns at a constant current, the development of the discharge in time and in space by photographing it for various exposures to the voltage. In the remaining SIVD studies in which the above and other electrode systems shown in Fig. 15.7 were used, the discharge a capacitor was used to strike the volume discharge. The discharge gaps (Fig. 15.7a, b) were additionally illuminated from the side by a low-current (I < 3 A) spark enclosed in a quartz envelope. This spark could not ensure the volume photoionisation of the gas, but, as a result of the initiation of electrons at the cathode, it made it possible to stabilize the scatter of the

gap-breakdown delay times. The discharge gaps in the configurations shown in Fig. 15.7c–f were not additionally illuminated.

The dynamics of the development of the SIVD was also investigated in an electrode system with a sectioned cathode (Fig. 15.7b). Here, the main cathode and anode were the same as in Fig. 15.7a, but an earthed conductor 1.5 mm in diameter (the initiating electrode) was connected in parallel to the main cathode at a distance 5 mm in a horizontal plane extending from its edge. The vertical distance between the cathode surface and the tip of the conductor was chosen in such a way that, during the initiation of the discharge by a low-current spark, the electrical breakdown of the gap extended initially to the conductor. A conductor with polyethylene insulation and a core diameter of 1.5 mm served as the cathode in the electrode system in Fig. 15.7c, d (the discharge occurred between the rod and the plane). In these experiments, the SIVD was investigated under conditions such that not more than one cathode spot could be formed on the cathode. In the discharge gap shown in Fig. 15.7d, the discharge cross section on the anode was confined by a glass tube 6–8 mm in diameter (confined discharge), placed between the electrodes in such a way that its upper edge touched the surface of the anode.

In the configuration presented in Fig. 15.7e, the plane electrodes (the same as in Fig. 15.7a) were linked by a dielectric plate 2 mm thick with a transverse dimension of 5 cm. In the electrode system shown in Fig. 15.7f, the SIVD was struck for an interelectrode distance (the distance between two aluminium disks 3.6 cm in diameter) of 5.5 cm; the disks were placed in a quartz tube with an internal diameter of 3.8 cm, the electrodes had sharp edges, and the cathode surface was sandblasted.

The SIVD dynamics was studied in discharge gaps with different geometry. The scheme of the setup for investigating the discharge in a gap with a linear cathode geometry is shown in Fig. 15.7a. The SIVD with a total duration of \sim 370 ns was ignited in the SF₆:C₂H₆ = 10:1 mixture at a pressure p=33 Torr and an interelectrode distance of 4 cm. The electrodes were a 0.5-mm thick copper bar 16 cm in length (a knife-edge cathode) placed edgewise and a disk anode 6 cm in diameter rounded over the perimeter with a radius of curvature of 1 cm. The breakdown was forcedly initiated at the center of the cathode with a weak-current spark limited with an R=900 Q resistor. This spark could not provide an initial electron density in the gas high enough for the development of a volume discharge, but allowed fixing the position of the primary gap breakdown. The SIVD glow was recorded with a single-frame streak camera tube with a frame exposure time of 20 ns, which was triggered with a variable delay T relative to the instant of gap breakdown.

To study the SIVD dynamics in the plane gap geometry, we used the circuit with a sectioned cathode shown in Fig. 15.7b. In this case, the interelectrode distance, the working mixture pressure, and the electrical circuit of the setup were the same as in the previous experiment, except that the cathode was not a copper bar, but a disk 6 cm in diameter rounded over the perimeter with a radius of curvature of 1 cm and subjected to sandblast processing [29–31, 33]. Insulated conductors 1 mm in diameter were inserted into holes 2 mm in diameter drilled 4 cm apart through the cathode in its plane region. One of the conductors (1) protruded above the cathode surface by 1 mm to ensure the occurrence of the primary gap breakdown at

precisely this point. By comparing the oscilloscope traces through the ignitor (7) and monitoring (2) electrodes, we could trace the SIVD spread over the gap.

The dynamics of an individual diffusion channel was investigated using the setup shown in Fig. 15.7c. The diffusion channel was simulated by a discharge with a rod (cathode)—plane gap geometry at a pressure p=16.5–49.5 Torr of the SF₆: $C_2H_6=10:1$ mixture for an interelectrode distance of 4 cm. The cathode was the end of a polyethyleneinsulated wire with a core diameter of 1.5 mm, and the anode was a disk 10 cm in diameter. The SIVD development was monitored with the streak cameras, as in the experiments performed using the setup of Fig. 15.7a.

In the circuits shown in Fig. 15.7a, b, the capacitor *C* discharged into the gap via inductance *L* upon switching spark gap. In the circuit of Fig. 15.7c, an artificial line discharged into the gap. The currents in the circuits of Fig. 15.7 were monitored with Rogowski coil Rc, the voltage across the gaps was measured with resistive dividers. A typical photograph of an SIVD in a plane-electrode system is presented in Fig. 15.7a.

Figure 15.7b shows the corresponding current (I) and voltage (U) oscillograms. It is seen from Fig. 15.8 that the SIVD does not outwardly differ from the usual SVD with preionisation. It consists of a set of diffuse channels, linked to bright cathode spots and expanding towards the anode. By overlapping, the diffuse channels generate an overall diffuse glow. Despite the appreciable strengthening of the electric field on the edge of the gap, this region is scarcely distinguishable and the cathode spots cover the entire surface of the cathode. The SIVD voltage and current oscillograms are also typical for SSVD in electronegative gases. Energy is deposited in the SIVD plasma at a quasi-steady-state voltage The voltage in mixtures of SF₆ with hydrocarbons, when the content of the latter is not greater than 17%, depends only slightly on their partial pressure. The dependence of $U_{\rm qs}$ on pd for pd = 0.05–2.5 cm bar and specific energy inputs in the discharge plasma up to 0.2 J cm⁻³ is described satisfactorily by the expression [35] where $U_{\rm qs} = A + Bp$ (SF₆)d is the partial pressure of SF₆ in the mixture. For pure SF₆ and SF₆:

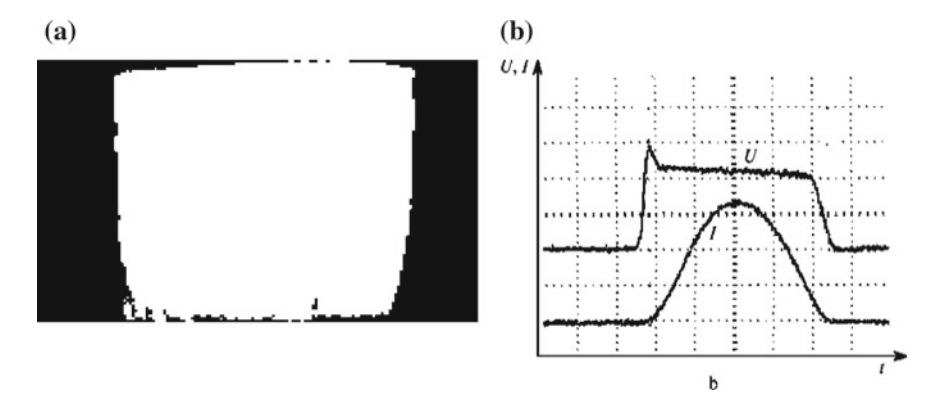


Fig. 15.8 Photograph of an SIVD in a system of plane electrodes (a) and typical current (I) and voltage (U) oscillograms for the SIVD; scan|100 ns division-[1] (b)

 $C_2H_6 = 10:1$, 10:2 mixtures, we have respectively A = 0.72 and 0.79 and 1.1 kV and B = 92.7, 94.8 and 96.4 kV cm bar. The value of B obtained in the present experiments is close to the known [35] critical reduced electric field strength $(E/p)_{cr} = 89 \text{ kV/cm}$ bar (the difference is $\sim 8\%$).

The differences between SIVD and SSVD are manifested in the dynamics of their development. Figure 15.9 presents the results of studies on the dynamics of the development of an SIVD in a plane-electrode system (Fig. 15.7a) for the discharge across the gap of an artificial line with a variable number of cells. As can be seen from Fig. 15.9, in contrast to SSVD, an SIVD is struck initially in the zone of the maximum amplification of the electric field on the gap edge in the form of one or several diffuse channels linked to the cathode spots. The radiation from the

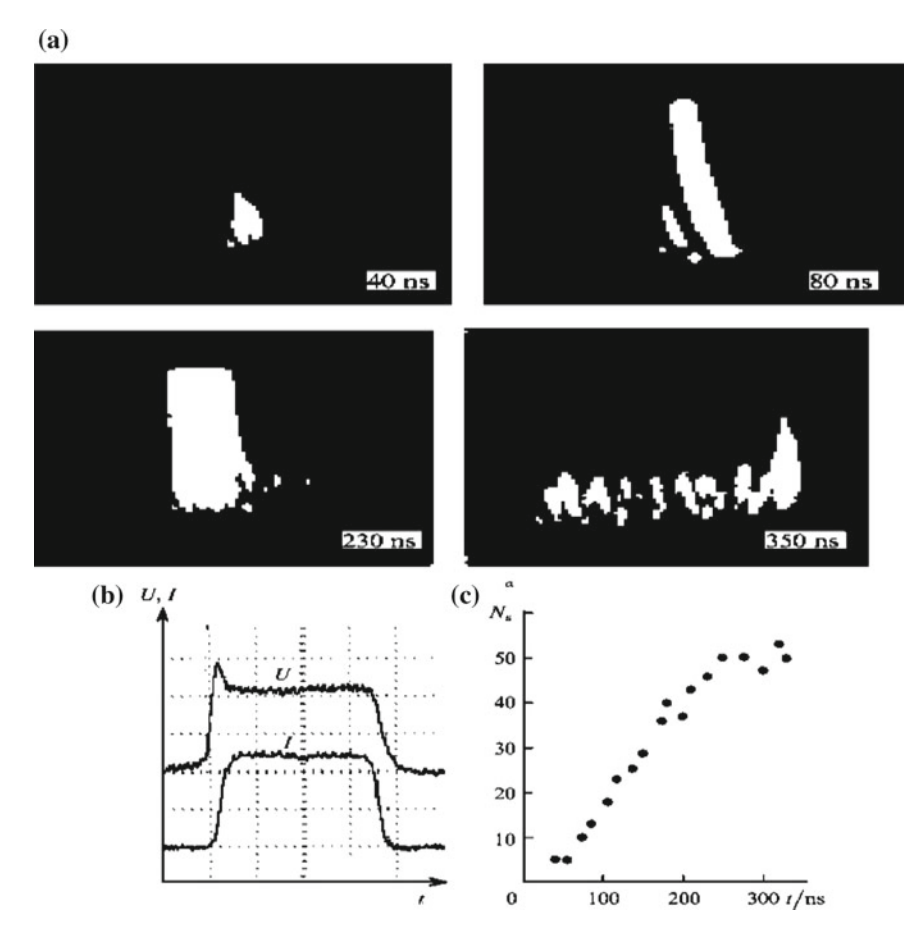


Fig. 15.9 Characteristics of an SIVD: photographs of an SIVD in a system of plane electrodes at different times (spark illumination from the left) (**a**), voltage (*U*) and current (*I*) oscillograms for the SIVD during the discharge across the gap of an artificial line consisting of 20 cells (scan—100 ns division-[1] (**b**) and time dependence of the number of spots on the cathode N_s (**c**)

discharge in the remainder of the gap is not detected at this instant. The channels formed first initiate the appearance of the subsequent channels and the SIVD spreads over the gap perpendicular to the direction of the electric field at $U_{\rm qs}$ constant voltage, gradually filling the entire gap. The total number of spots on the cathode increases from the instant of the electrical breakdown of the gap virtually in proportion to time, i.e. in proportion to the energy injected into the discharge when account is taken of the experimental conditions.

Since the SIVD develops at a constant current (with the exception of the leading and rear edges) under the experimental conditions described, the current through channels formed earlier should diminish after the appearance of new ones. The characteristic features of the development of an SIVD listed above suggest the operation of current-limiting mechanisms in SF₆ and in mixtures based on it, which hinders the transfer of the entire energy through a single channel. It appears that precisely these mechanisms are in fact responsible to a large extent for the existence of the unusual form of the discharge such as the SIVD, including the possibility of achieving it in gaps with a strong edge inhomogeneity of the field.

The existence of such mechanisms is also indicated by the results of experiments in an electrode system with simulation of the first diffuse channel by the initiating electrode (Fig. 15.7b). Figure 15.10a, which presents characteristic oscillograms of the discharge current through the initiating (curve 1) and main (curve 2) cathodes, shows that the current through the initiating cathode does indeed appear appreciably earlier than the current through the main cathode and its maximum is attained at an instant when the main current still continues to grow.

Figure 15.10b illustrates the dependence of the fraction of the energy A, transmitted by the initiating cathode, relative to the total energy W injected into the discharge. The quantity A decreases monotonically with increase in W, reaching saturation, which yet again constitutes evidence in favour of the existence of mechanisms preventing the transfer of the entire SIVD energy through one channel.

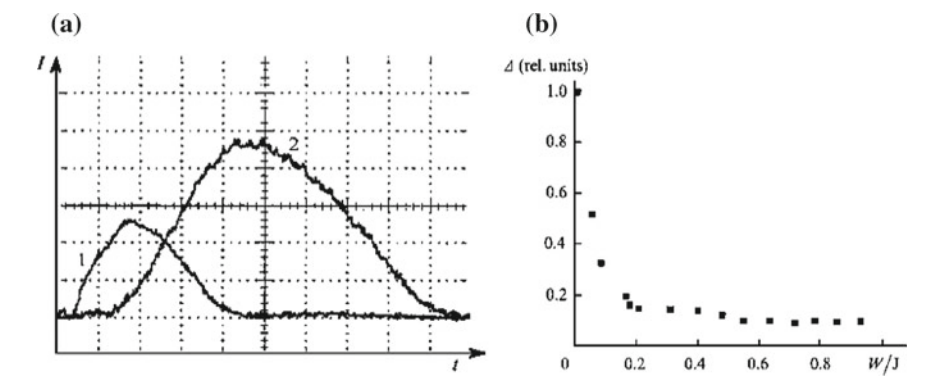


Fig. 15.10 Oscillograms of the current through the initiating (1) and main (2) cathodes (39.7 A division-[1], scan \mid 50 ns division-[1] (a) and dependence of the fraction of energy A transmitted through the initiating electrode relative to the total energy $W(\mathbf{b})$

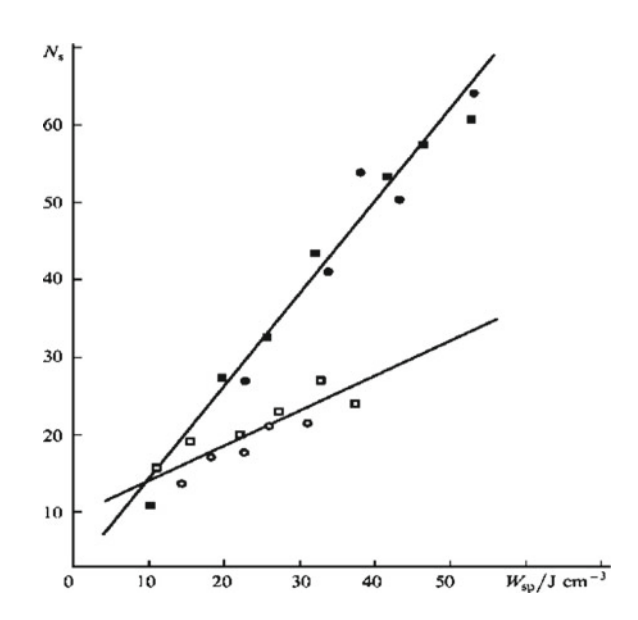
However, we may note that that in the experiment under consideration, the simulation of the initial diffuse channel with the aid of a special electrode is not entirely equivalent to the real conditions, because, in order to guarantee that the discharge begins from the initiating cathode, it would be necessary to raise it by approximately 1 mm above the surface of the main cathode. For this reason, the brightness and transverse dimensions of the simulated initial diffuse channel differed appreciably from those of channels in the main gap, whereas under real conditions this was not observed (Fig. 15.8).

Figure 15.11 presents a typical dependence of the total number of spots on the cathode NS on the average specific energy $W_{\rm sp}$ injected into the plasma. It was recorded in a system of plane electrodes for different values of d and p. $W_{\rm sp}$ was varied during the experiments by varying the charging voltage and charging capacitance. The duration of the discharge current was also varied. Evidently, for a fixed value of p, $N_{\rm s}$ depends only slightly on d. Within the limits of error, the points t satisfactorily on a linear dependence of $N_{\rm s}$ on $W_{\rm sp}$.

Consequently, for a fixed value of p, the number of spots on the cathode is determined by $W_{\rm sp}$ and not the density and duration of the current, $W_{\rm sp}$ actually specifying the total number of spots on the cathode. For a short duration (less than 100–150 ns) of the current, the spots may not cover the entire surface of the cathode but only its section near the site of the primary electrical breakdown of the gap. In short discharges, the local density of spots may therefore be greater than in long discharges.

The dependence of N_s on p may be more complex: N_s increases with increase in p and the increase is nonlinear. A diminution of the transverse dimensions of the spots on the cathode and of the diffuse channels on the anode is also observed under

Fig. 15.11 Dependence of the number of cathode spots $N_{\rm s}$ on the specific input energy $W_{\rm sp}$ for the SF₆: $C_2H_6=10:1$ mixture with d=6 cm and p=33.6 Torr (square black), d=2 cm and p=33.6 Torr (dot black), d=6 cm and p=16.8 Torr (n), and d=2 cm and p=16.8 Torr (\bigcirc)

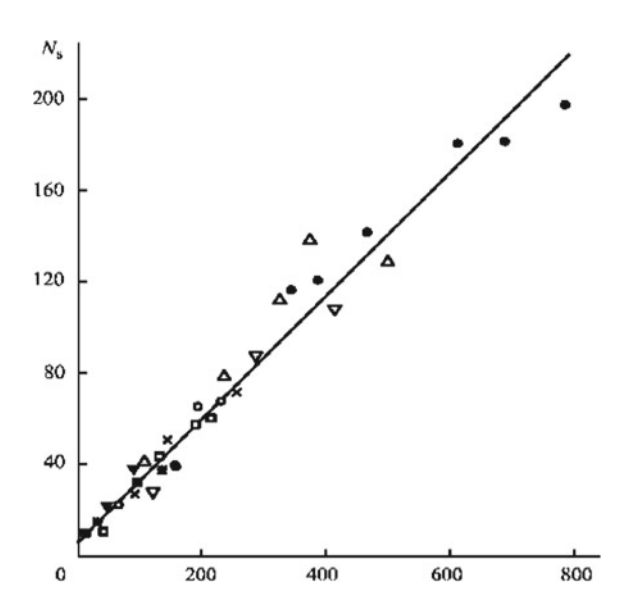


these conditions, i.e. the volume occupied by each channel decreases simultaneously with increase in $N_{\rm s}$. One may postulate that such influence of the growth of p on $N_{\rm s}$ is associated with the increase in the electric field strength (defined as $E_{\rm qs} = U_{\rm qs}/d$) for which an SIVD develops and which is known [1] to determine the probability of the formation of a cathode spot. The dependence of $N_{\rm s}$ on the parameter $W_{\rm sp}$ $E_{\rm qs}$ plotted for different values of p and p taking into account this hypothesis, is presented in Fig. 15.12. It is satisfactorily fitted by the linear function $N_{\rm s} = a + bW_{\rm sp}E_{\rm qs}$, in which the constant p is in its turn a function of the state of the cathode surface and of the hydrocarbon content in the mixture [32]. A conclusion important for the further interpretation of the mechanisms of the development of an SIVD follows from Figs. 15.11 and 15.12: the volume occupied by the discharge increases with increase in the amount of energy injected into the plasma and almost in proportion to the energy.

Figure 15.13a, b present photographs of an SIVD in a rod-plane electrode system (Fig. 15.13c) for d = 5 cm and p = 34 Torr in the SF₆:C₂H₆ = 10:1 mixture recorded for two energies W deposited in the discharge plasma. In this geometry, the SIVD consists of a diffuse plume, expanding towards the anode, with formation of a bright plasma on the cathode. Under conditions such that new spots cannot be formed on the cathode, the volume V of the glowing part of the plume (an analogue of a diffuse channel) increases with increase in W.

The dependence of V on W obtained under the same conditions as in Fig. 15.13 is presented in Fig. 15.14. A linear growth of V with increase in W can be seen. For W = 5 J, the volume V is ~ 20 cm³, whereas the size of the plume on the anode is 3.6 cm. The high stability of the discharge in the gap geometry under consideration, despite the fact that the current density of the cathode is $j = 1.2 \times 10^5$ A cm⁻², is

Fig. 15.12 Dependence of the number of cathode spots $N_{\rm s}$ on $W_{\rm sp}E_{\rm qs}$ for the SF₆: $C_2H_6 = 10:1$ mixture with d = 6 cm and p = 33.6 Torr (square black), d = 6 cm and p = 16.8 Torr (square light), d = 4 cm and p = 23.3 Torr (*), d = 3 cm and p = 23.3 Torr (dot black), d = 3 cm and p = 33.6 Torr (O), d = 3 cm and p = 50.4 Torr d = 3 cm and p = 67.2 Torr (triangle), and d = 2 cm and p = 33.6 Torr (\times)



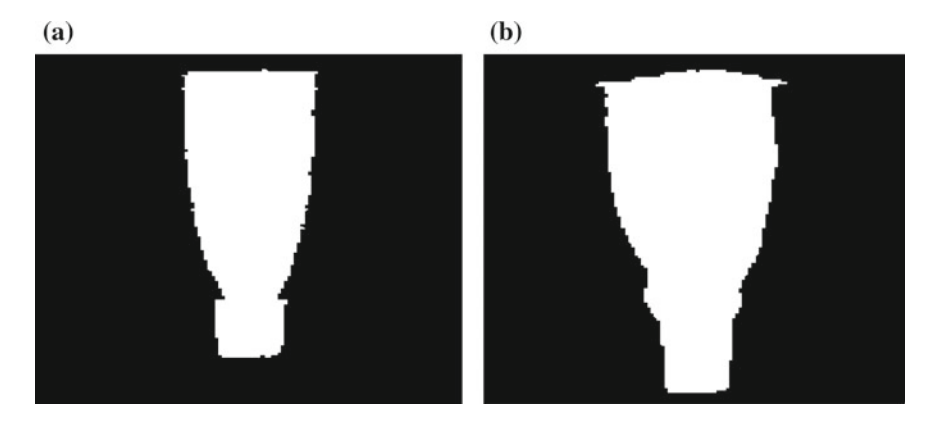
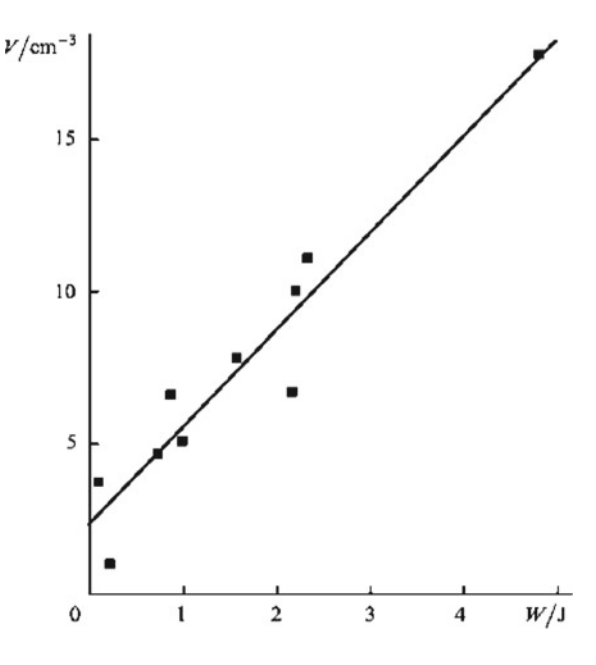


Fig. 15.13 Photographs of an SIVD in the rod-plane electrode system with W = 0.73 J (a) and 2.33 J (b)

striking. It is noteworthy that the influence of the duration of the discharge current on V is also appreciable in this geometry. This accounts for the considerable scatter of the points in Fig. 15.14 because in the experiments the duration of the current varied from 50 to 300 ns. Figure 15.15a, b present voltage (U) and current (I) oscillograms for an SIVD in the rod-plane electrode system (Fig. 15.7c) for current pulses of 100 and 200 ns duration with identical charging voltage and charging capacitance in the SF₆:C₂H₆ = 10:3 mixture (p = 40 Torr, d = 4.4 cm).

Fig. 15.14 Dependence of the volume V of an SIVD on the energy W in the rod-plane electrode system



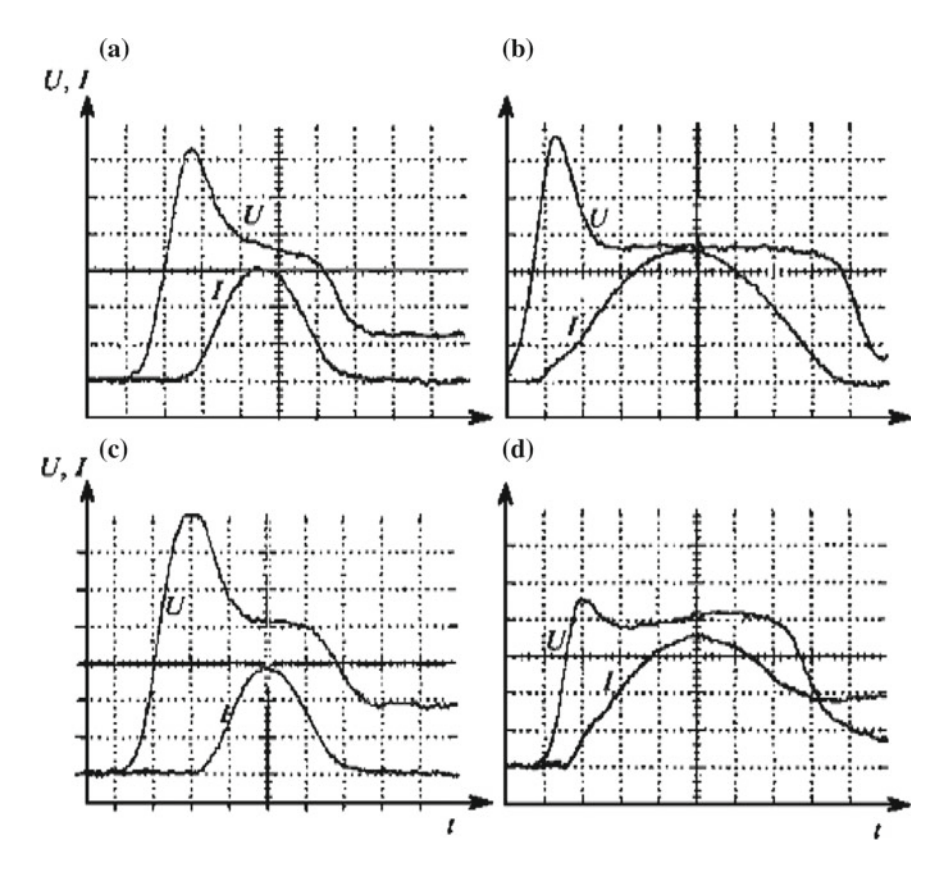


Fig. 15.15 Voltage (U) and current (I) oscillograms for an unconfined (\mathbf{a} , \mathbf{b}) and confined (\mathbf{c} , \mathbf{d}) SIVD in the rod-plane electrode system with T = 100 ns (\mathbf{a} , \mathbf{c}) and 200 ns (\mathbf{b} , \mathbf{d}). Oscillogram scales: 5.1 kV division-[1] (\mathbf{a} - \mathbf{d}), 79.4 A division [1] (\mathbf{b} , \mathbf{d}), 198.5 A division-[1] (\mathbf{a} , \mathbf{c}); time scan—25 ns division

Figure 15.15c and d show similar voltage and current oscillograms for an SIVD recorded under the same conditions but with confinement of the discharge on the anode by a tube 7 mm in diameter (Fig. 15.7d). As can be seen from Fig. 15.15a, b, the voltage and current oscillograms in the rod-plane system do not differ in any way from typical oscillograms obtained in a plane electrode system.

Confinement of the discharge leads to an appreciable change in the type of oscillograms. For a long duration of the current pulse (Fig. 15.15d), after the initial fall of the voltage, one observes its increase simultaneously with increase in the current, the current maximum being attained sooner than in the case of an unconfined discharge. The current amplitude also diminishes, whereas the voltage is appreciably higher at its maximum than in the case of an unconfined discharge. Voltage oscillograms of a similar type are obtained when the discharge characteristics are calculated taking into account the attachment of electrons to vibrationally excited SF_6 molecules [36]. However, the calculated oscillograms in [36]

do not agree with the experimental ones. We are not aware of other studies in which a similar form of the discharge voltage was observed in SF₆ and in mixtures based on it.

For T = 200 ns, the confined SIVD contracts after the current has reached a maximum. A decrease in the duration of the current makes it possible to obtain an uncontracted confined SIVD (Fig. 15.15c). In this case, there is no break in the voltage oscillogram and, following a general increase in the discharge voltage, the 'tail' becomes less tilted. We may note that the modification of the voltage pulse observed in Fig. 15.15c, d following the confinement of the SIVD is associated precisely with the increase in the specific energy input in the plasma because under the conditions of the discharge cannot expand during the energy deposition process.

Figure 15.16 presents dependences of $U_{\rm qs}$ on the energy $W_{\rm j/2}$ deposited in the discharge plasma before the attainment of the current maximum, in the rod-plane electrode system for confined (curve 1) and unconfined (curve 2) SIVD; was determined at the current maximum. Evidently, with increase in $W_{\rm j}/2$ an appreciable growth $U_{\rm qs}$ is observed in the confined SIVD, significantly more notable than in the unconfined SIVD. The relative increase $U_{\rm qs}$ (compared with $U_{\rm qs}$ for the unconfined SIVD) for the same values of $W_{\rm j}/2$ greater the smaller the value of p, i.e. the greater the energy deposited in the plasma per unit volume and the results presented in Figs. 15.15 and 15.16 indicate an increase in the electron attachment per molecule.

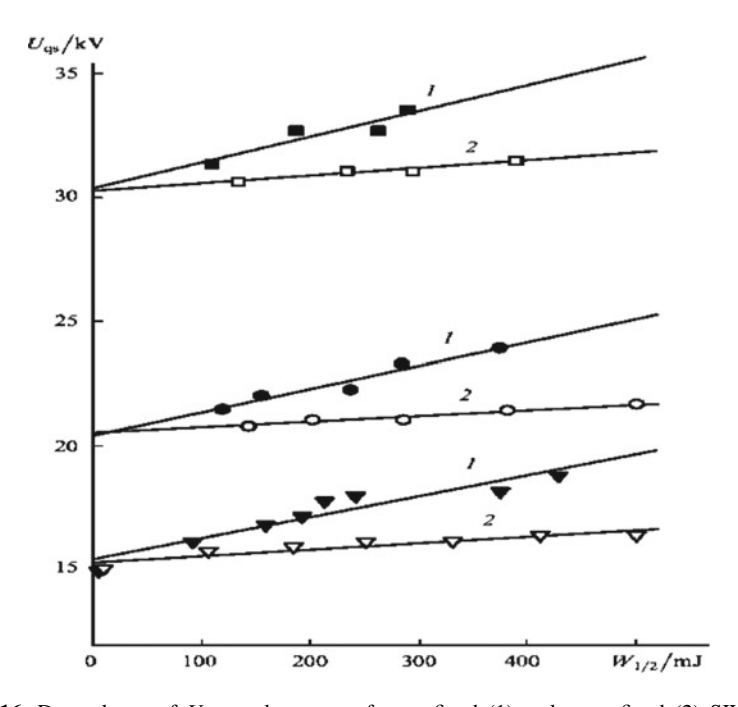


Fig. 15.16 Dependence of $U_{\rm qs}$ on the energy for confined (1) and unconfined (2) SIVD with p=33.6 Torr (triangles), 45.8 Torr (circles), and 67.2 Torr (squares); SF₆:C₂H₆ = 10:1 mixture, d=4 cm

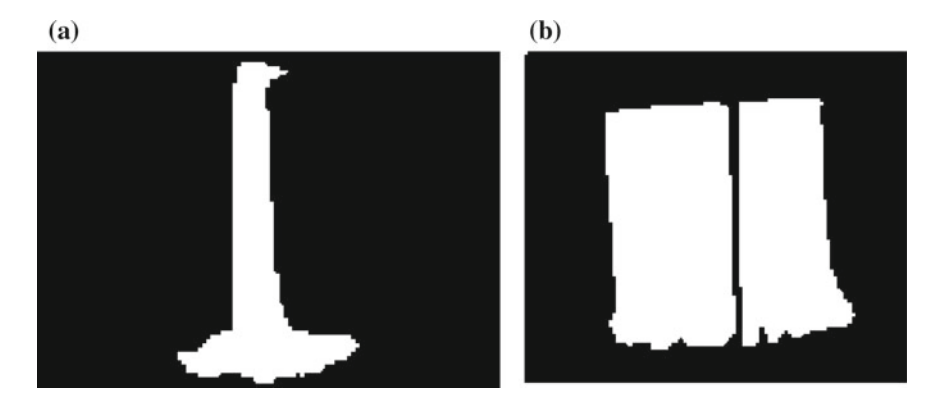


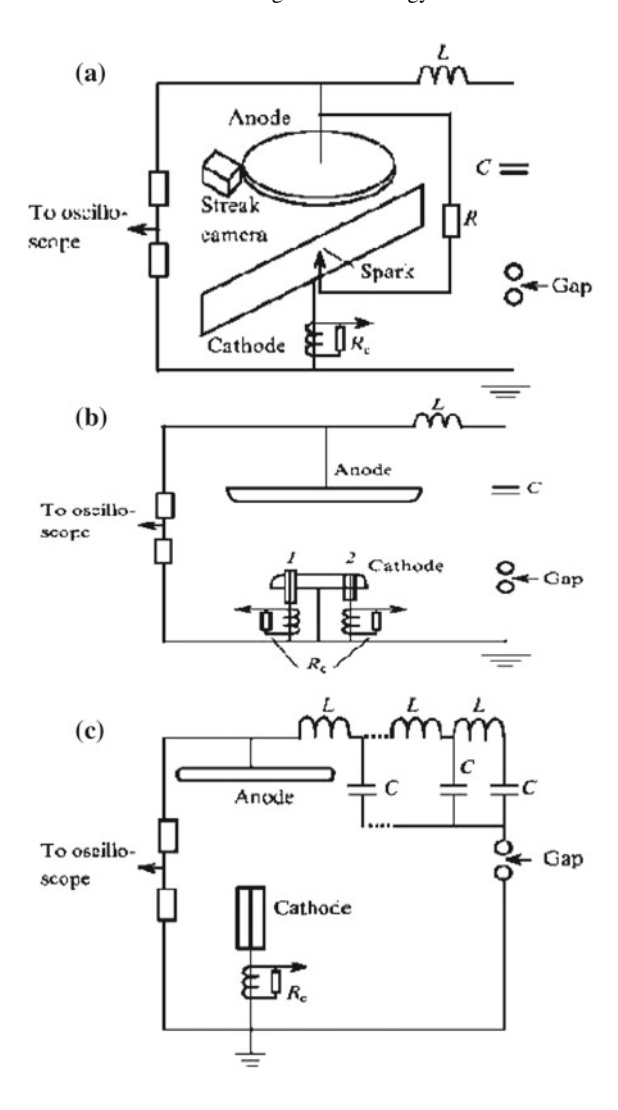
Fig. 15.17 Photographs of a discharge in a system of plane electrodes linked by a glass plate in air (a) and in the SF_6 : $C_2H_6 = 10:1$ mixture (b)

Coefficient in SF₆-based mixtures with increase in the specific energy input in the discharge plasma.

The possibility of obtaining a volume discharge in the electrode systems illustrated in Fig. 15.7e, f is a consequence of the existence of mechanisms restricting the SIVD energy transmitted by an individual diffuse channel and leading to an increase in the volume occupied by the discharge with increase in the input energy. Figure 15.17 presents photographs of a discharge in air and in the SF₆: $C_2H_6 = 10.1$ mixture, respectively, at a pressure of 65 Torr obtained in the system comprising plane electrodes linked by a dielectric plate (Fig. 15.7e). As was to be expected, the discharge in air develops in the form of the electrical spark breakdown of the gap along the surface of the dielectric plate, the bulk phase being entirely absent. In a SF₆– C_2H_6 mixture, the discharge is very much of the volume type, its external appearance and oscillograms being completely indistinguishable from an SIVD obtained in the same system in the absence of a plate (with the exception that the photograph shows a black band at the site where the plate is located).

In the system with transverse dimensions of the electrodes close to the internal diameter of the tube (Fig. 15.7f), the discharge is also very much of the volume $SF_6:C_2H_6 = 10:1$ mixture and p = 15-65 Torr. $W_{\rm sp} > 0.05 \text{ J cm}^{-3}$, the surface density of the cathode spots has a maximum in the central zone of the cathode, as in the usual gap with plane electrodes which are not linked by a dielectric surface. In the subsequent ignitions of an SIVD without change of mixture, an appreciable increase and a decrease in the current are observed in the above electrode system. Since in the case under consideration the SIVD occupies the entire volume of the discharge chamber (Fig. 15.7f), this fact indicates that, in the mixture of gases formed as a result of the dissociation of the starting materials, the effective ionization coefficient is smaller than in the initial mixture. We may note that a volume discharge in a tube with an internal diameter close to the diameter of the electrodes had been obtained earlier in a SF₆-H₂ mixture [37], but the authors [37] did not interpret this result.

Fig. 15.18 Schemes of experimental setups for studying the SIVD dynamics: ignitor (1) and monitoring (2) conductors



15.5 Discussion

Thus, the following processes are characteristic of SIVD: consecutive formation of diffuse channels (with a simultaneous decrease in the current through the channels which had arisen earlier) during the development of the SIVD in a gap with planar geometry, the expansion of the diffuse-glow zone in the rod-plane gap, an increase in the discharge voltage with increase in the specific energy. As already mentioned, these processes are apparently determined to a large extent by the mechanisms of the confinement of the current in the conducting channel, which depend on the specific energy input. We shall consider two possible mechanisms leading to this

15.5 Discussion 227

state of affairs, namely the dissociation of SF_6 by electron impact and the attachment of electrons to vibrationally excited SF_6 molecules.

In the first place we note that, for the ratios E/N close to the critical value, virtually the entire energy deposited in SF_6 is consumed in dissociation [38]. According to [35, 39], the $SF_6 = SF_4 + 2F$ channel is dominant.

The ionization potential of F atoms (17.42 eV) exceeds that for SF₆ (15.7 eV) [40], so that an appreciable contribution by the F atoms produced to the overall ionization should not be expected even at their considerable concentrations. As regards the attachment of electrons, the formation of F^{-1} ions via any of the possible mechanisms is known to be incapable of competing, as shown by estimates [41], with the attachment of electrons to SF6 molecules. The F excitation threshold is 12.7 eV [40] (the component of the main doublet with a threshold energy of \sim 0.05 eV may naturally be disregarded in the given instance), i.e. it is in the region of the intense excitation of the SF₆ terms by electron impact [38]. Furthermore, there are grounds for the postulate that inelastic processes with participation of SF₄ molecules also do not influence in any way significantly the energy spectrum of the electrons in the discharge.

Thus, bearing in mind the qualitative nature of the models considered and neglecting therefore the difference between the cross sections for the elastic scattering of electrons by SF_6 molecules and their decomposition products, one may postulate that the influence of the dissociation of SF_6 may only affect the decrease in the reduced field strength E/N with increase in the total concentration of neutral particles N as the specific energy input increases.

It is possible to show that allowance for additional factors will significantly complicate the description without altering fundamentally the result: the dissociation of SF₆ by electron impact and the attachment of electrons to vibrationally excited SF₆ molecules may indeed serve as the mechanisms of the limitation of the current in the conducting channel in the active media of an HF laser. At the same time, the mechanisms of current limitation in the conducting channel are not sufficient for complete understanding of the processes observed in the experiment, in particular the propagation of the discharge into the interior of the gap in the direction perpendicular to the applied field [20]. Figure 15.19 shows the streak-camera images of a SIVD in the gap with a knife-edge cathode obtained at different instants of time. The corresponding oscilloscope traces of discharge current and voltage are given in Fig. 15.20. One can see from Fig. 15.19 that the gap is broken down at the center (at the region of the auxiliary spark discharge). At this instant of time, the SIVD has the form of one diffusion channel, with a cathode spot already formed. Then, new channels appear near the first channel, which have a significantly lower brightness, and are developing at a voltage close to the static breakdown voltage for SF₆.

The number of new channels increases with time, they 'disperse' from the middle to the periphery of the gap, and their brightness gradually achieves that of the first channel, the channels closest to the first channel being the brightest. All the channels become equally bright with time, while the brightness of the first channel decreases significantly. Upon a further SIVD development, the brightness of the

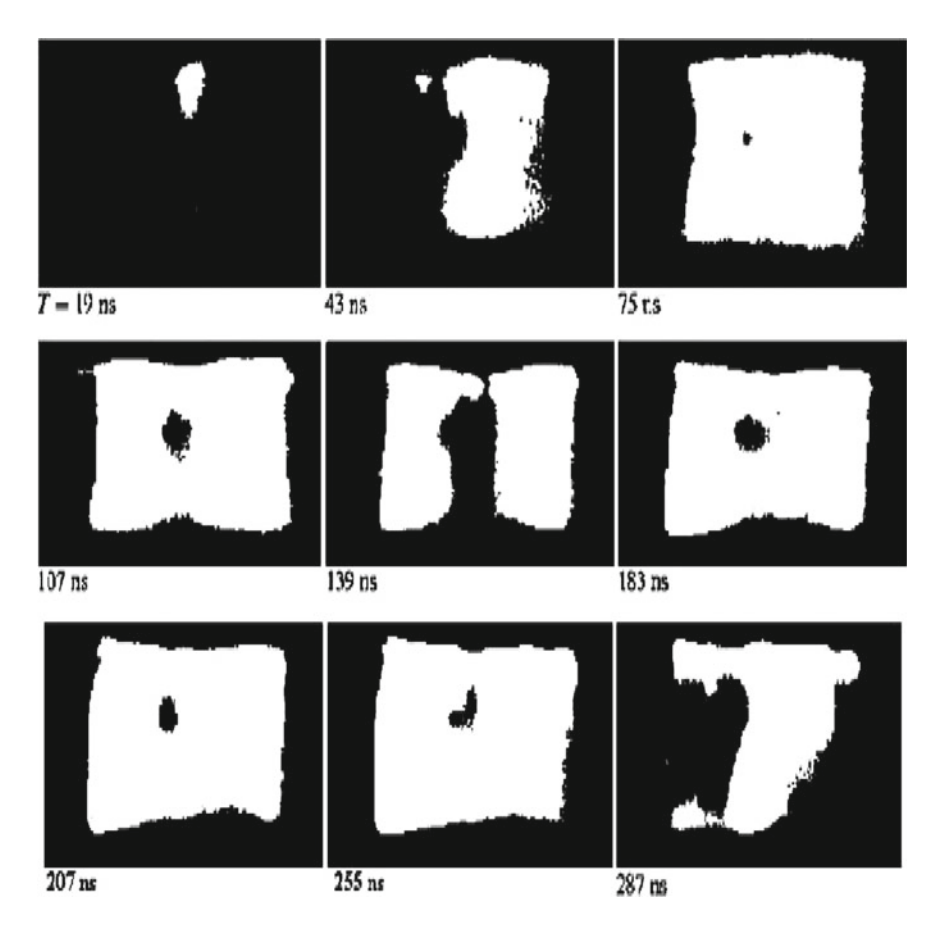
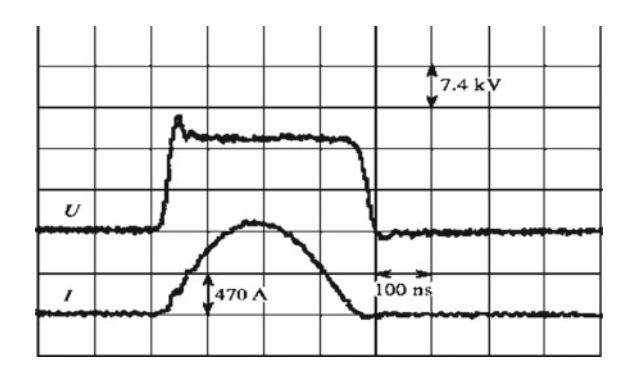


Fig. 15.19 Streak camera images obtained at different instants of time T

Fig. 15.20 Oscilloscope traces of the voltage and current of a SIVD



channels at the gap periphery (i.e., the channels removed from the primary breakdown region) gradually increases. However, for T > 210 ns the glow becomes uniform again over the cathode length, the glow in the first channel also being

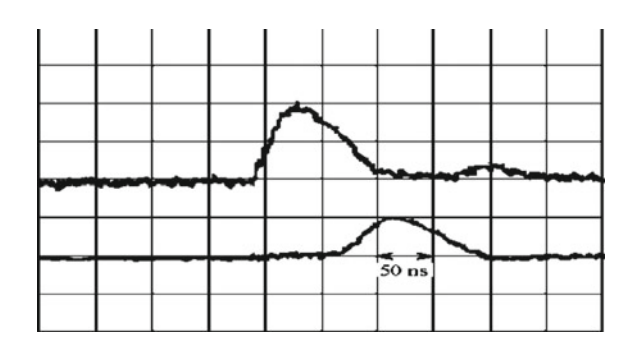
15.5 Discussion 229

restored. This effect will be referred to as a current return (to the channel). Then, we observed the development of discharge instability against the background of the total diffusion glow.

Therefore, the results outlined above confirm directly the fact that the SIVD spreads over the gap at a voltage close to the static breakdown voltage in the form of a sequence of diffusion channels. In this case, the first channel, which was produced upon the gap breakdown, fades away as new channels emerge. Note also that the current return (see Fig. 15.19), which is manifested in the equalization of the brightness of all the channels and in the increase in the brightness of the first channel following its initial decrease, is observed only when the energy introduced into the plasma is high enough. This effect vanishes when the energy is lowered or the linear size of the cathode is increased. For high energy inputs (150–200 J/L) typical of HF (DF) lasers, the SIVD spreading over the gap is so fast that the time resolution of our streak camera is insufficient A similar pattern of SIVD development is also observed with the plane discharge gap geometry. Figure 15.21 shows the oscilloscope traces from the igniter and monitoring conductors (see Fig. 15.18b) obtained in the experiment with the sectioned cathode. One can see from Fig. 15.21 that the current begins to flow through the monitoring conductor with a significant delay relative to the current through the ignitor.

By the time of onset of the current through the monitoring conductor, the amplitude of the current through the ignitor lowers by more than a factor of two, i.e., in this experiment, too, we observed quenching of the initially produced channel upon the emergence of subsequent channels. One can also see from the oscilloscope trace of the current through the ignitor (Fig. 15.21) that a current returns to the first channel after its almost complete quenching in the case of a plane gap as well, provided the energy input is high enough. In the rod-plane gap, the spreading of the frame, which simulated a single diffusion channel, was observed to occur in two stages. During the first 20–30 ns following the gap breakdown, the discharge volume rapidly increased, out of proportion to the energy inputted. Then, the discharge volume increased approximately linearly with the energy. For a constant total energy W introduced into the plasma, the largest volume V occupied by the SIVD by the instant of energy input termination increased with lowering the mixture pressure p. Figure 15.22 shows the dependence of V on the parameter

Fig. 15.21 Oscilloscope traces of the current through the ignitor (the upper trace) and monitoring (the lower trace) conductors



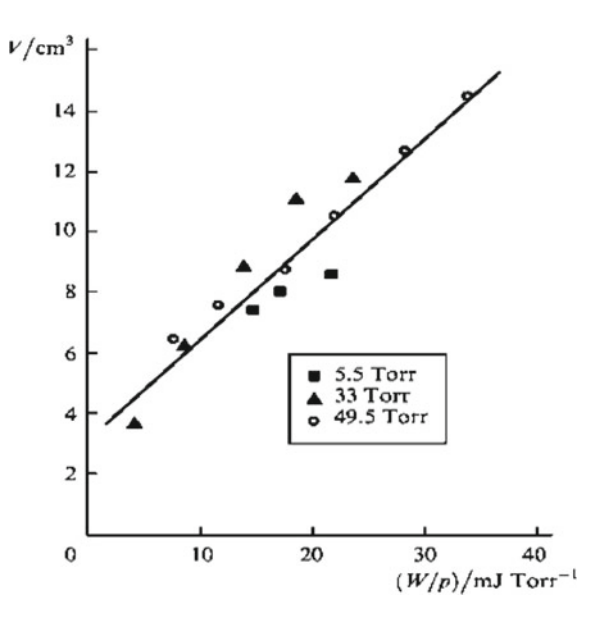
W/p obtained for different p. One can see that this dependence is satisfactorily, to within the error of experimental determination of V, described by a linear function.

The results presented above confirm assumptions that there exist mechanisms of current density limitation in the diffusion channel of a discharge in SF_6 and SF_6 -based mixtures [28, 33, 41–45] (and also in several other strongly electronegative gases [33, 45]). It would be reasonable to attempt to relate these mechanisms to the specific feature of SF_6 , namely, with its strong electronegativity.

Strongly electronegative gases have highly reduced electric field strengths of E/N, where E is the field strength and N is the concentration of neutral molecules, at which an electrical breakdown occurs and the energy is inputted into the plasma. They also have large electronegativity parameters X_a defined as the ratio of concentrations of negative ions and electrons. For this reason, the following features of the charge kinetics inherent in these gases should be taken into account in the study of a volume self-sustained discharge in strongly electronegative gases such as SF_6 and SF_6 -based laser mixtures.

First, the electron-impact dissociation of SF_6 molecules and other components of the mixture plays a significant role in this discharge. Indeed, for high E/N close to the critical value $(E/N)_{Cr} = 360$ Td, the average energy of plasma electrons in the quasi-stationary stage of a self-sustained discharge approaches the SF_6 dissociation threshold and more than 80% of the energy inputted into the discharge is spent to the dissociation [41, 46] resulting in the production of an F atom. In the submicrosecond range typical for the discharge under study, decomposition products have no time to escape from the discharge channel, resulting in a local increase in the concentration N of particles, a decrease in E/N, and a decrease in the electric conductivity of the diffusion channel due to the increase in electron losses through attachment.

Fig. 15.22 Dependences of the volume V occupied by discharge on the parameter W/p for the SF₆:C₂H₆ = 10:1 mixture at a pressure p



15.5 Discussion 231

High negative ion concentrations are attained in the discharge, with the effect that the electron detachment from negative ions can make a significant contribution to the balance of charged particles. Usually the disintegration of negative ions in their collisions with neutral molecules and/or due to associative ionization is taken into account. However, for medium gas pressures (p = 10–100 Torr) and a submicrosecond discharge duration, these processes do not make any noticeable contribution to electron multiplication [47]. However, there are firm grounds to believe that the electron-impact detachment of electrons from negative ions can be an efficient channel of the delivery of secondary electrons to the discharge plasma [48].

Third, a significant influence on the parameters of an SF_6 -discharge plasma, including its conductivity, can be exerted by dissociative electron-ion recombination because high concentrations of positive ions are achieved in the discharge, and the energy is mainly inputted into the plasma. Ion-ion recombination must also be taken into account, because it may significantly limit the concentration of ions in the plasma.

Therefore, it follows from the above discussion that the main mechanisms of SIVD current density limitation are the dissociation of SF_6 molecules by electron impact resulting in a decrease in the ionization rate and an increase in the electron attachment rate due to the local reduction of the parameter E/N in the diffusion channel, and also electron-ion recombination, which is responsible for the growth of electron losses with increasing current density in the channel. It was shown qualitatively [45] that the current density can be also limited due to the attachment of electrons to vibrationally excited SF_6 molecules. However, the absence of reliable data on the rate constants for these reactions in the literature complicates a quantitative estimate of the role of this process in the balance of charged particles in the plasma.

We performed SIVD simulations to verify whether the above assumptions are consistent with the available experimental data. The channel structure of the discharge was modelled with a set of resistive elements connected in parallel. Similarly to [49], the concentrations of particles were determined by solving continuity equations for particles of each sort in combination with the Kirchhoff equations for the discharge circuit. The nonuniformity of initial conditions for the development of channels along the cathode length was simulated by prescribing different initial electron concentrations in each of the channels. In addition to the electron-impact ionization of SF6 and electron attachment to SF6 molecules, the following processes were included in the calculation.

- (1) SF₆ dissociation by electron impact. The number of dissociated molecules was defined as $N_d = W/qF$, where W is the energy inputted into the discharge and qF—4.5 eV is the energy spent to produce an F atom [37].
- (2) Electron detachment from negative ions by electron impact. It was assumed that SF₆—negative ions dominate in the plasma because the charge exchange reactions have no time to occur during the discharge period, while the cross sections for the electron-impact production of other negative ions are too small

- [46, 47]. The rate constant for the disruption of negative ions by electron impact should not be smaller than the rate constant for elastic electron scattering by molecules [48].
- (3) Dissociative electron-ion recombination. The rate constant for this process was estimated assuming that the SF₆ discharge plasma is dominated by SF₅⁺ ions (52).
- (4) Ion-ion recombination. In this case, the rate constant for the *E/N* values close to the critical value was taken from [47].

We simulated an SIVD with nine channels, which corresponds approximately to the conditions of the experiment performed using the setup of Fig. 15.18a. Figure 15.23 shows the oscilloscope traces of the voltage, the total discharge current and the current through a single channel for which we prescribed the maximum initial electron concentration, calculated for the energy density inputted into the discharge plasma equal to 80 and 40 J/L. One can see from Fig. 15.23a that the current through a single channel has two maxima when the energy input is high. This is in qualitative agreement with the oscilloscope trace of current through the ignitor (see Fig. 15.21) in the plane gap geometry and in agreement with the experimentally observed redistribution of the channel glow intensity upon the SIVD development in the knife edge-plane gap (see Fig. 15.19). The current return vanishes when the energy input is lowered (Fig. 15.23b).

Calculations also show that the electron detachment by electron impact and electronion recombination virtually compensate each other within the accuracy of estimates of the rate constants. The dissociation of SF₆ molecules and other components of the HF(DF)–laser mixture should therefore be considered as the principal mechanism responsible for current density limitation in the SIVD channel. However, it is reasonable to refine the magnitudes of the rate constants. Note that our model (like any zero-dimensional model which neglects the time variation of the SIVD volume) pretends only to a qualitative illustration of the current redistribution in the channels when account is taken of possible mechanisms of current density limitation.

Note also that the electron detachment from negative ions by electron impact should be taken into account in the analysis of the processes determining the instability development of the volume discharge in SF_6 and other strongly electronegative gases. Once again we draw attention to the result that follows from the investigation of the dynamics of a single diffusion channel: an SIVD develops at an approximately constant value of the energy parameter $W/(V_p)$.

15.6 Conclusions

We investigated the formation of the SSVD in CO_2 – N_2 –He mixtures by preliminary filling of the gap with an electron flux from an auxiliary discharge plasma. This method was suitable for large distances between the electrodes. A study was

15.6 Conclusions 233

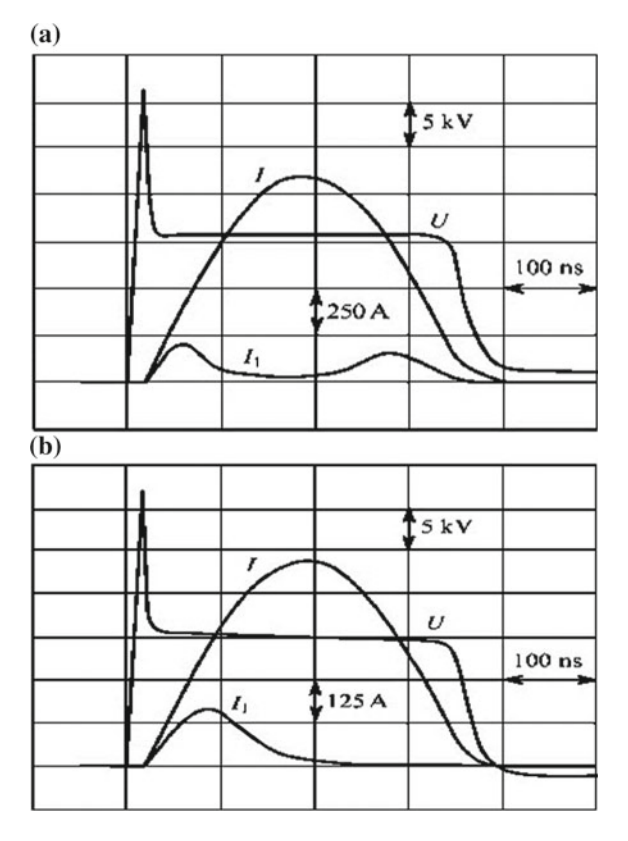


Fig. 15.23 Calculated oscilloscope traces of the voltage U, the total discharge current I, and the current I_n through the first channel for energy density 80 (a) and 40 J/L (b)

made of the characteristics of some of the discharges which could be used as auxiliary ones. It was established that the formation of a SSVD was affected significantly by the distortion of the electric field due to the presence of a space charge of the electron flux. Dynamic profiling of electrons was found to be possible and a SSVD was attained in systems with a strongly inhomogeneous initial distribution of the electric field in the gap [50–53].

The simplicity of the proposed methods is very promising for their applications in CO_2 lasers. Although the main results of the present investigation were obtained for CO_2 – N_2 –He gas mixtures, the methods can clearly be applied also to other gases like N_2O , for example. Due to our investigations the aperture of SSVD based lasers and amplifiers had been increased up to 80 cm. for the electric efficiency of more then 10%.

At the same time the SIVD in SF₆, used as the active media for nonchain HF lasers, has been investigated as well. The following features of the development of the SIVD have been established:

- After the primary electrical breakdown of the discharge gap, the SIVD spreads
 in the gap in the direction perpendicular to that of the electric field as a result of
 the consecutive appearance of overlapping diffuse channels. As the new channels appear, the current owing through the channels formed earlier diminishes.
- The volume occupied by the SIVD increases almost linearly with increase in the energy deposited in the plasma and, when the discharge volume is confined by a dielectric surface, the discharge voltage increases simultaneously with increase in the current.
- 3. The hypothesis was put forward that mechanisms exist for the limitation of the current in the conducting channel. They are associated with the specific energy released in the plasma and they prevent the transfer of all the deposited energy through a separate channel. It is shown that such mechanisms may be the dissociation of SF_6 and the attachment of electrons to vibrationally excited SF_6 molecules. Main result for SIVD based HF(DF) lasers looks very much promising and half of Kj level for energy output is very far from the natural limit for this type of the systems [53–56].

References

- V.Yu. Baranov, V.M. Borisov, A.A. Vedenov, S.V. Drobyazko, V.N. Knizhnikov, A. P. Napartovich, V.G. Niz'ev, A.P. Strel'tsov, in *Preprint No. 2248* (in Russian) (Institute of Atomic Energy, Moscow, 1972
- V.N. Karnyushin, A.N. Malov, R.I. Soloukhin, Kvantovaya Elektron. (Moscow) 5, 555 (1978); Sov. J. Quantum Electron. 8, 319 (1978)
- H. Seguin, J. Tulip, The article you requested is currently in production and will be available online at a later date. Appl. Phys. Lett. 21, 414 (1972)
- A.I. PavlovskiT, V.S. Bosamykin, V.I. Karelin, V.S. Nikol'skii. Kvantovaya Elektron. (Moscow) 3, 601 (1976); Sov. J. Quantum Electron. 6, 321 (1976)
- 5. A.I. Pavlovskii, V.F. Basmanov, V.S. Bosamykin, V.V. Gorokhov, V.I. Karelin, and P.B. Repin, in *Abstracts of Papers presented at Second All-Union Conf. on Physics of Electric Breakdown in Gases*, Tartu (in Russian) (1984), p. 330
- R.V. Babcock, I. Liberman, W.P. Partlov, Volume ultraviolet preionization from bare sparks. IEEE J. Quantum Electron. 12, 29–34 (1976)
- A.V. Kozrev, Yu.D. Korolev, G.A. Mesyats, Yu.N. Novoselov, A.M. Prokhorov, V.S. Skakun, V.F. Tarasenko, and S.A. Genkin: Kvantovaya Elektron. (Moscow) 11, 524 (1984); Sov. J. Quantum Electron. 14, 356 (1984)]
- 8. R.E. Beverly III, Appl. Phys. B **53**, 187–193 (1991)
- 9. T.Y. Chang, The article you requested is currently in production and will be available online at a later date. Rev. Sci. Instrum. **44**, 405 (1973)
- V.V. Apollonov, A.M. Prokhorov et al., Kvantovaya Elektron. (Moscow) 11, 1327 (1984);
 Sov. J. Quantum Electron. 14, 898 (1984)
- 11. V.V. Apollonov, A.M. Prokhorov, Ustinov et al., Kvantovaya Elektron. (Moscow) 12 (1985)
- 12. V.V. Apollonov, A.I. Barchukov, A.M. Prokhorov et al. Pis'ma Zh. Tekh. Fiz. 3 (1977)

References 235

- 13. V.V. Apollonov et al., Pis'ma Zh. Tekh. Fiz. 5 (1979)
- 14. V.V. Apollonov, A.M. Prokhorov et al., Kvantovaya Elektron. (Moscow) 10 (1983)
- 15. A.A. Kuchinskii (Kuchinsky), B.V. Lyubin, V.F. Shanskii, in *Proceedings of Sixteenth International Conference on Phenomena in Ionized Gases*, Dusseldorf (1983)
- 16. A.K. Laamme, Rev. Sci. Instrum. 41, 1578 (1970)
- 17. A.J. Beaulieu, Appl. Phys. Lett. 16, 504 (1970)
- 18. R. Dumanchin, J. Rocca-Serra, C. R. Acad. Sci. Ser. 269, 916 (1969)
- V.P. Gorelov, N.N. Minakova, V.A. Chagin, Elektrotekh. Promst. Ser. Elektrotekh. Mater. 5, 20 (1972)
- 20. P.A. Belanger, R. Tremblay, J. Boivin, G. Otis, Can. J. Phys. 50, 2753 (1972)
- 21. V.V. Apollonov, et al., Kvantovaya Elektron. (Moscow) 11 (1984)
- 22. A.L. Ward: J. Appl. Phys. 36 (1965)
- 23. O.P. Judd, J. Appl. Phys. 45, 4572 (1974)
- 24. A.H. von Engel, *Ionized Gases* (Clarendon Press, Oxford, 1955)
- I.L. Kamardin, A.A. Kuchinskii, V.A. Rodichkin, V.F. Shanskii, in Abstracts the Third All-Union Conference on Laser Optics, Leningrad (1982)
- 26. S.I. Andreev, N. M. Belousova, A.M. Prokhorov et al., Kvantovaya Elektron. 3 (1976)
- 27. Yu.D. Korolev, G.A. Mesyats, Physics of the Pulsed Electrical Breakdown of Gases (1991)
- 28. V.V. Apollonov et al., Pis'ma Zh. Tekh. Fiz. 22 (1996)
- 29. V.V. Apollonov et al., Quantum Electron. 27, 207 (1997)
- 30. V.V. Apollonov et al., Quantum Electron. 28, 116 (1998)
- 31. V.V. Apollonov et al., in *Proceedings of SPIE International Society for Optical Engineering*, vol. 374 (1998)
- 32. L. Richeboeuf et al., The influence of H₂ and C₂H₆ molecules on discharge equilibrium and F-atom production in a phototriggered HF laser using SF6. Phys. D **31** (1998)
- 33. V.V. Apollonov et al., in *Proceedings of the Second International Conference* (National Academy of Sciences of Belarus, Minsk, 1997)
- 34. G.D. Bortnik, The Physical Properties and the Electrical Strength of Sulfur Hexafluoride (1989)
- 35. V.V. Apollonov et al., in *Proceedings of the Ninth Conference on the Physics of Gas Discharges*, Ryazan (1980)
- 36. A.F. Zapol'skii, A.A. Yushko: Kvantovaya Elektron. (Moscow), Vol. 6, (1979)
- 37. E.B. Gordon, V.I. Matyushenko, P.B. Repin, V.D. Sizov: Khim. Fiz. 8 (1989)
- 38. A.A. Belevtsev, in *Proceedings of the Thirteenth International Conference on Dielectric Liquids*, Nara, Japan (1999)
- A.A Radtsig, M. Smirnov, Handbook of Atomic and Molecular Physics (Atomizdat, Moscow, 1980)
- 40. H.S. Massey, Negative Ions (Cambridge University Press, Cambridge, 1976)
- 41. D.I. Slovetskii, A.A. Deryugin, The Chemistry of Plasma (1987)
- 42. A.V. Melekhov, in Abstracts of Papers presented at Second Ail-Union Conference on Physics of Electric Breakdown of Gases, Tartu (1984) (in Russian)
- 43. V.V. Apollonov et al., Izv. Akad. Nauk, Ser. Fiz. 64 (2000)
- 44. V.V. Apollonov et al., in *Proceedings of SPIE International Society for Optical Engineering*, vol. 370 (1999)
- 45. V.V. Apollonov et al., Kvantovaya Elektron. 30 (2000)
- 46. N. Nakano, N. Shimura, Z.L. Petrovic, T. Makabe, Simulations of rf glow discharges in SF6 by the relaxation continuum model: physical structure and function of the narrow-gap reactive-ion etcher. Phys. Rev. E 49 (1994)
- 47. H. Hilmert, W.F. Schmidt, Electron detachment from negative ions of sulphur hexa uoride-swarm experiments. Phys. D: Appl. Phys. 24 (1991)
- 48. L.M. Biberman. Izv. Akad. Nauk SSSR, Ser. Energ. Tramp. 3 (1976)
- 49. V.V. Apollonov et al. Kvantovaya Elektron. 30 (2000)
- 50. A.J. Palmer. The article you requested is currently in production and will be available online at a later date. Appl. Phys. Lett. **25**, 138 (1974)

- 51. A.F. BelyatskiT, D.B. Gurevich, M.A. Kanatenko, I.V. Podmoshenski, T. Pis'ma. Zh. Tekh. Fiz. (Sov. Tech. Phys. Lett.) 6, 73 (1980)
- S.C. Lin, J.I. Levatter, X-ray preionization for electric discharge laser. Appl. Phys. Lett. 34, 505 (1979)
- V.V. Apollonov, G.G. Baitsur, A.M. Prokhorov, and K.N. Firsov: Pis'ma Zh. Tekh. Fiz. 11, 1262 (1985); Sov. Tech. Phys. Lett. 11, 521 (1985)
- V.V. Apollonov et al., in Proceedings of XIII Intern. Conference on Gas Discharge and their Applications, vol. 1 (2000)
- 55. V.V. Apollonov et al., in *Proceedings of XXV International Conference on Phenomena in Ionized Gases*, vol. 1 (2001)
- 56. V.V. Apollonov et al., Kvantovaya Elektron. 31 (2001)

Chapter 16 High Power/Energy HF (DF) Lasers



16.1 Introduction

Non-chain HF (DF) lasers are the most suitable and ecologically safe source of powerful and energetic coherent radiation in the 2.6-3.1 µm (HF laser) and 3.5-4.1 µm (DF laser) spectral regions. Among the different methods of HF (DF) pulse and pulse-periodic laser creation suggested by our team under the guidance of Academician A.M. Prokhorov was self-sustained volume discharge (SSVD). It is well known that a SSVD can be established in a gas by creating a primary electron density that exceeds a certain minimum value n_{\min} throughout the discharge gap. Various methods for the preionization of the gas in the discharge gap have been developed for this purpose. Using these methods, primary electrons can usually be created directly in the discharge gas, which sometimes causes difficulties in the establishment of the conditions necessary for the formation of SSVD. For example, high voltages are needed for the formation of an initial plasma when the preionization source and active medium are combined in the same volume, whereas preionization with ultraviolet radiation may be ineffective because of the strong absorption of such radiation in a medium. In the case where soft x-rays are used, it is necessary to ensure rigid synchronization of the x-ray and pump sources.

In the mixtures of gases typical of CO₂ lasers, electron losses due to the trapping process are relatively small at low values of *E/p*. The trapping coefficient is considerably smaller than the absorption coefficient of ultraviolet radiation for the same mixtures. In principle, it should be possible to create primary electrons at the density needed for the formation of a SSVD at a considerable distance from an ionization source, and then to transport the electrons to the gap by drift in an electric field. We have investigated and confirmed this physical matter experimentally [1]. A SSVD formation method that works by filling the discharge gap with a flux of electrons drifting in an electric field, without preliminary ionization of the whole discharge volume, was proposed and implemented by our team. The electron source was a plasma formed in an auxiliary discharge initiated under a grid cathode. This

method also made it possible to establish a SSVD in a system with a strongly inhomogeneous electric field in the discharge gap [1].

The basic advantages of non-chain electric discharge HF (DF) lasers are high radiation pulse power, the ability to operate at reasonable pulse repetition frequencies, simple design and convenience of use. This method is one of the most attractive for applications and it is ecologically safe [2]. However, for an appreciable length of time these lasers were limited by their relatively low maximum radiation energy (<10 J). Evidently, the problem of improving the energy characteristics of similar lasers, as with most other electric discharge lasers operating at intermediate and high gas pressures, is readily connected to the challenge of performing SSVD itself. We investigated SSVD in the working mixtures of non-chain HF (DF) lasers with the aim of increasing their radiation energy to at least the level of a few hundred joules [2-12]. As a result of this study, a number of special features were found for non-chain HF (DF) lasers [3-12], which not only follow the traditional principles for forming a volume discharge at intermediate and high gas pressures [13, 14], but also largely contradict them. Specifically, it was found that SSVD can be ignited without any preliminary ionization in SF₆ and mixtures of SF₆ with hydrocarbons (deuteron-carbons) [2, 3]. We called this form of SSVD self-initiated volume discharge (SIVD) [5]. The realization of SIVD in large volumes allowed us to increase the radiation energy of non-chain HF (DF) lasers up to ~ 400 J at an electrical efficiency of $\sim 4\%$ [7–11].

An attempt has been made to obtain a deeper insight into the physics of SIVD, starting from the results of the investigations of non-chain HF (DF) lasers that we performed with A.M. Prokhorov at the GPI RAS, and analyze the potential of the method for further increasing the energy parameters of non-chain lasers.

16.2 A New Form of SSVD

Certain conditions should be met on the way to SIVD realization in dense gases, the following of which are the basic ones.

- (1) Primary electrons with number densities of no less than 10^6 – 10^9 cm³ must be created within a gas volume through its preliminary ionization.
- (2) In the special case where SSVD is employed for laser excitation, which imposes tight constraints on the uniformity of the active medium characteristics over the working volume, the primary electron multiplication should occur in a uniform electric field, which is usually provided by special shaping of the electrode surfaces. Clearly, the first condition cannot be observed in such a strongly electronegative gas as SF₆ [5, 7] because of the great primary electron losses from electron attachment, except for in the special 'photo triggered discharge' mode [15], which, however, is ineffective for energy input into molecular gases because of the low over-voltages at the gap and, in the case of large discharge gaps and active medium volumes, it is not realized at all. With increasing laser aperture and discharge volume, the problem of how to meet the second condition

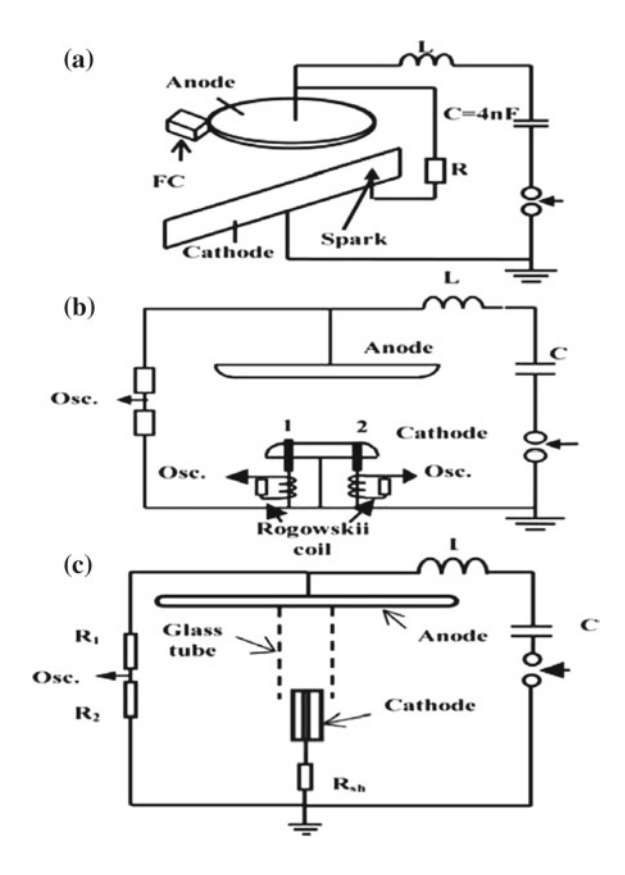
also arises—there are technical difficulties regarding the fabrication of large-sized intricate-shaped electrodes and the rise of the discharge circuit inductance caused by a useless growth in the transverse size of the electrodes [3, 4].

It clearly follows from the simplified analysis presented above that the possibilities for the creation of powerful electric discharge non-chain HF (DF) lasers while following the known physical principles for forming SSVD in dense gases are very limited. Moreover, when starting from these principles, all attempts to create non-chain HF (DF) lasers with a radiation energy of ~ 1 kJ and above seem to hold no promise. This appeared to restrain researchers' efforts to increase the energy parameters of non-chain HF (DF) lasers. Although there have been numerous works concerned with non-chain HF (DF) lasers, the radiation energy attained for them by 1996 was at the level of 10 J [16-18]. The incompleteness of the traditional understanding of the physics of forming SSVD in dense gases came to be understood after we found that it was possible to obtain discharge in SF₆ and mixtures of SF₆ with hydrocarbons (deuteron-carbons) in the systems of plane electrodes with high electric field enhancement at the edge without any preionization in a gas [2, 3]. The sufficient condition for the realization of SSVD in this case was the presence of small-scale ($\sim 50 \, \mu m$) roughness on the cathode. We called this form of discharge SIVD [5]. SIVD is not dissimilar to an ordinary SSVD with preionization. It comprises a set of diffuse channels that diverge in the direction of the anode and attach to bright cathode spots. When overlapped, these diffuse channels show a common diffuse glow [3, 5]. The SIVD current and voltage oscillograms are also typical of SSVD in electronegative gases [5]. In non-chain HF (DF) lasers with a rough cathode surface, preionization influences not only the discharge characteristics, but also the output laser energy [3, 5]. It should also be mentioned that analysis of the literature data indicates a negligible role for preionization in the formation of SSVD in non-chain lasers. For example, in [16], where a set of metal rods connected to a common busbar through a resistance (resistance uncoupling) served as the discharge gap cathode, preionization was absent, while in [18] it was performed through a high current dielectric surface discharge whose spectrum displayed not only UV radiation, but also soft x-ray radiation.

We have defined SIVD as a form of SSVD that is obtained without preionization in SF_6 and SF_6 based mixtures under SF_6 pressures of 30–150 Torr, which are typical for HF (DF) lasers. Based on analysis of the experimental results, the following questions are considered below.

- (1) What are the key features of the development of SIVD?
- (2) What are the physical mechanisms that determine the possibility of SIVD existing?
- (3) Is SF₆ a unique gas or can SIVD can be observed in other gases?
- (4) What are the active medium and output characteristics of non-chain HF (DF) lasers based on SIVD?
- (5) What are the prospects for further increases to the radiation energy of non-chain lasers?

Fig. 16.1 Scheme of the experimental setup for investigation of the SIVD dynamics



The setup used to investigate the dynamics of SIVD formation is represented schematically in Fig. 16.1a. A SIVD of ~ 500 ns duration was initiated in a SF₆:C₂H₆ = 10:1 mixture at a pressure of 33 Torr and an inter-electrode distance of 4 cm. The electrodes were a 0.5 mm thick and 16 cm long copper stripe (cathode) stood edgewise and a disk anode with a diameter of 6 cm rounded off along its perimeter to a radius of 1 cm. The breakdown was force initiated at the gap edge by a low-current spark restricted by resistance $R = 900 \Omega$. This spark could not in principle provide a sufficient number of primary electrons in the gas volume, but it allowed the site of the primary gap breakdown to be spatially stabilized. The luminosity of the SIVD was recorded by a single frame camera with an exposure time of 20 ns that was run with varying time delays relative to the instant of the gap breakdown.

The SIVD dynamics was also studied in the plane-plane gap geometry in experiments with the sectioned cathode depicted in Fig. 16.1b. In this case, the inter-electrode distance, the working medium pressure and the setup's electrical scheme were the same as in the former experiment, but the cathode was a flat disk rounded off along its perimeter to a radius of 1 cm. Isolated conductors with a diameter of 1 mm were inserted into holes with a diameter of 2 mm that had been

drilled within the flat part of the cathode and spaced at a distance of ~ 4 cm. The basic cathode and these conductors were connected to a common bus. The current through each conductor was recorded by Rogowskii coils. One of the conductors (1) extended ~ 1 mm above the cathode surface, which ensured a primary gap breakdown at that point, whilst comparing the oscillograms for the currents through the initial (1) and control (2) conductors allowed the SIVD extension over the gap to be followed.

The dynamics of a single diffuse channel was investigated using the setup represented schematically in Fig. 16.1c. The diffuse channel was initiated via discharge in the rod (cathode)-plane geometry in the SF₆:C₂H₆ = 10:1 mixture at pressures p = 16.5 + 49.5 Torr and an inter-electrode distance of d = 4 cm. The end of a 1.5 mm diameter rod dressed with polyethylene insulation was used as a cathode and the anode was a disk with a diameter 10 cm. Limitation of the cathode surface ensured the development of no more than one cathode spot. The SIVD dynamics was followed by a single frame camera, as in the experiments performed according to the scheme in Fig. 16.1a. The SIVD was also filmed with a video camera, which allowed exact calculation of the volume occupied by the discharge as a function of the energy put into the plasma, with the latter being calculated via the current and voltage oscillograms. With the aim of increasing the specific power input into the discharge plasma SIVD in the given gap, the geometry was bounded, in a number of experiments, by a glass tube with a diameter of 6-8 mm (bounded SIVD [6, 11]), as shown in Fig. 16.1c using a dashed line. This made it possible to bring up specific energy depositions to $\sim 1 \text{ J cm}^{-3}$.

The frames of the SIVD obtained via a single frame camera at different instants of time relative to the instant of the gap breakdown are shown in Fig. 16.2. Figure 16.3 gives the discharge voltage and current oscillograms that correspond to the process we have described. As can be seen from Fig. 16.2, the gap is broken down at the edge in the vicinity of an auxiliary electrode. At this instant in time, the SIVD constitutes a single diffuse channel with an already developed cathode spot. Then, near the first channel, much less bright new channels appear, which grow temporally in number while their brightness gradually becomes comparable to that of the first channel, with the brightest channel being the one located closest to the primary channel. In time, all the channels become equally bright, while the glow intensity of the first channel decreases noticeably. On further development of the SIVD, an increase in glow intensity is observed for the diffuse channels at the gap edge removed from the region of the first breakdown. However, at T > 250 ns the glow again becomes homogeneous throughout the length of the cathode, with the glow within the region of the first channel being recovered. Further, discharge instability begins to develop against the background of the total glow.

A very interesting picture of SSVD development is observed. Despite a local gap breakdown and the drop of the voltage across the gap to its quasi-stationary value (see Fig. 16.3), close to that of the static breakdown voltage in SF_6 [19], the initially formed channel is no longer capable of passing all the energy restored in the capacitor through itself, as takes place, for example, in air or nitrogen [7], where a local gap breakdown, even in the form of a diffuse channel, must be followed by

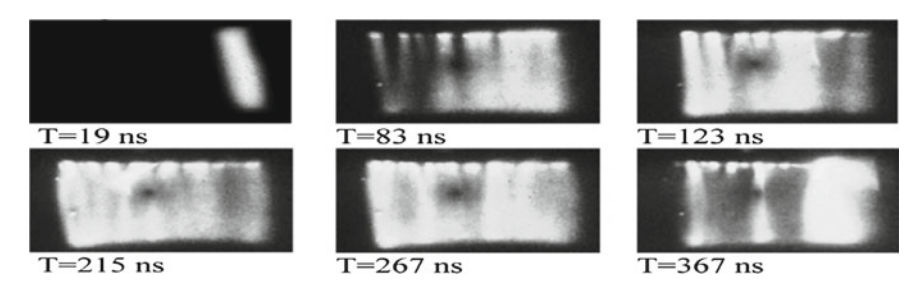


Fig. 16.2 SIVD frames for different T-values

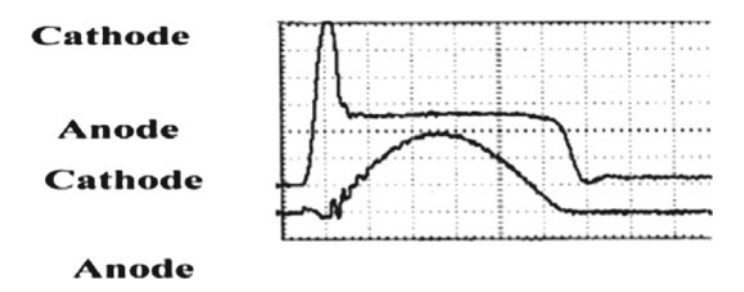


Fig. 16.3 Typical oscillograms for the voltage (upper trace) and current (bottom trace). Timescale: 100 ns div⁻¹

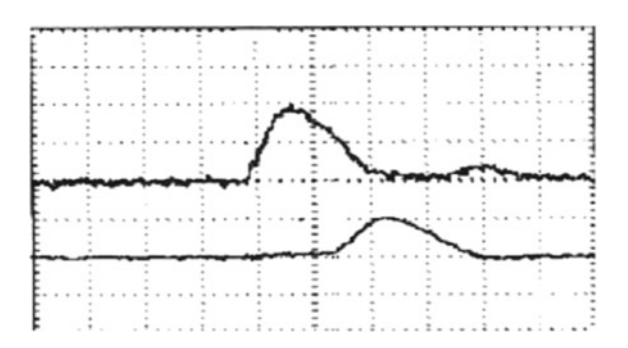
discharge instability and, at a sufficiently high restored energy, transition of the discharge from its diffuse to a constricted state. Instead, we see the formation of new diffuse channels after the appearance of the first one, and the extension of SIVD to the whole gap at the voltage close to the static breakdown value (see Fig. 16.3); in so doing, judging from the decrease of the brightness of the first channel in time, the current through it not only rises, but, conversely, falls with the appearance of new channels, i.e. an initially formed channel progressively quenches. It should be noted that the effect of current recovery, which is demonstrated in Fig. 16.2 and manifests itself by equalizing the brightness of all the channels after their initial drop, is only observed under sufficiently high deposited energies. With decreasing energy or cathode size growth (accompanied, naturally, by increased anode size), this effect is absent. However, when high energies are deposited in the discharge plasma (150–200 J I⁻¹), as is typical of HF (DF) lasers, SIVD extends to the whole gap so quickly that the single frame camera we use does not allow the process to be resolved.

A similar picture of SIVD development is observed in the discharge gaps with plane-plane geometry. Figure 16.4 shows the oscillograms for the currents through the initiating and control conductors (see Fig. 16.1b) obtained in the experiment with a sectioned cathode. It is seen from this figure that the current through a control conductor begins to flow with a noticeable delay relative to the current through the initiating conductor. It is also seen that the amplitude of the current

through the initiating conductor has reduced by half by the time that the current through the control conductor appears, i.e. in the given experiment we observe the effect of the quenching of the first channel through the next channels successively filling the discharge gap as they appear. The number of diffuse channels formed during the discharge current pulse duration, as shown in [5, 7], is proportional to the specific energy input into the discharge plasma. It is seen in the oscillograms in Fig. 16.4 that the effect of current recovery in the first channel also takes place in the plane–plane discharge gap geometry after its almost complete quenching. In the experiments described above, we observed an increase of the volume occupied by SIVD in the course of the energy input into plasma in the rod–plane geometry, i.e. the discharge volume depended directly on the energy deposited in this volume. Figure 3.5.5 gives the dependence of the volume V occupied by SIVD on the parameter W/p, where W is the energy put into the discharge and p is the gas mixture pressure. It is seen in Fig. 16.5 that the discharge volume grows linearly with the parameter W/p.

After the size of the SIVD in the rod-plane geometry was restricted by a glass tube, the discharge voltage and current oscillograms at energy depositions of up to $W_{\rm in} = 200 \text{ J I}^{-1}$ showed no changes, but at energy depositions in excess of 400 J I⁻¹, the oscillograms of a bounded SIVD displayed appreciable changes. Figure 16.6 shows the voltage and current oscillograms for bounded (U_b, h) and unbounded (U_b, h) I) SIVD in a SF₆:C₂H₆ = 10:2 mixture at pressure p = 33 Torr and d = 4 cm. As may be inferred from this figure, on restriction of the SIVD volume (equivalent to increasing a specific energy deposition), the voltage, just after its initial drop under breakdown, rises simultaneously with the current, even during a certain period of time after the current passes its maximum. As a whole, $U_b > U$ whilst $I_b < I$, i.e. an unusual situation is observed here-the gap conductivity decreases with increasing specific energy deposition. It should be pointed out that SF₆ and SF₆ based mixtures are not unique in this respect. Electric discharges in other strongly electronegative gases and their mixtures exhibit similar features. Figure 16.7a, b show the current and voltage oscillograms for a bounded SIVD in C₃F₈ and C₂HCl₃:C₂H₆ mixture, respectively. It is seen in Fig. 16.7a that the oscillogram $U_{\rm b}$ shows a more pronounced bend in C_3F_8 than in SF_6 .

Fig. 16.4 Oscillograms for the current through the initiating (upper trace) and control (bottom trace) wires. The timescale is 50 ns div⁻¹



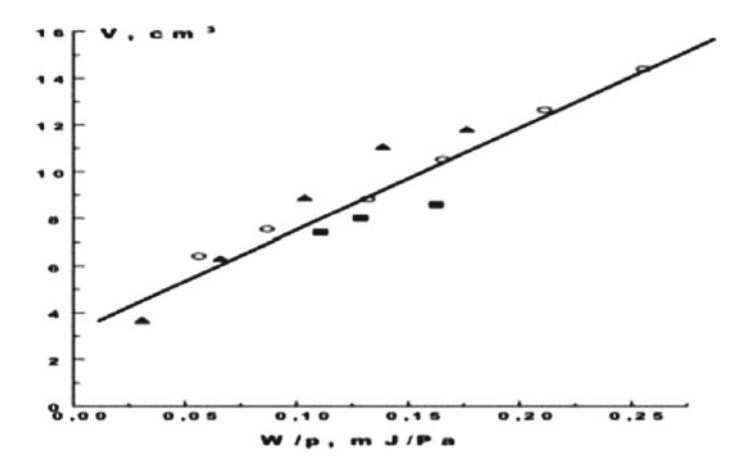
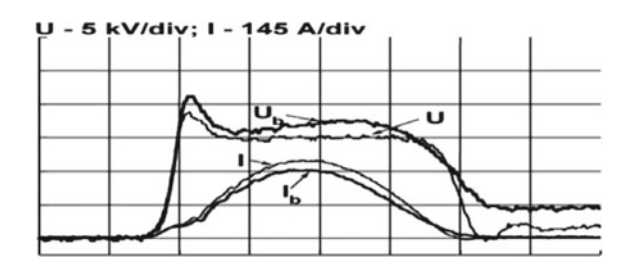


Fig. 16.5 Dependence of volume V occupied by SIVD on W/p. Mixture: $SF_6:C_2H_6 = 10:1$. I-p = 5 Torr; A-p = 30 Torr; and O-p = 45 Torr

The above-listed features of the development of SIVD allow one to assume that there are current restriction mechanisms in SF_6 and SF_6 based mixtures that make the passage of all the stored energy through a single channel difficult. It is clear that these mechanisms cause the existence of such an unusual form of discharge as SIVD, as well as the possibility of its generation in gaps with a high edge non-uniformity of the electric field. The results presented above are indicative of the presence of certain restriction mechanisms of the current density in diffuse channels in SF_6 and SF_6 based mixtures. It is natural to link the presence of these mechanisms to such a distinguishing feature of SF_6 as its high electro-negativity. Relative to other gases capable of attaching electrons to their molecules to form stable negative ions, strongly electronegative gases such as SF_6 are distinguished by (i) the high values of their operating reduced electric fields E/N and (ii) high magnitudes of electro-negativity χ_a , defined as the negative ion to electron concentration ratio. This gives rise to some special features for the discharge displays, which we summarize briefly below.

I. SF₆ molecule dissociation by electron impact becomes important. At E/N-values such that the electron impact ionization coefficient α is no less than the electron attachment rate η , high mean electron energies that approach the SF₆

Fig. 16.6 Experimental voltage and current oscillograms for bounded (U_b , I_b) and free (U, I) discharges. Timescale: 50 ns div⁻¹



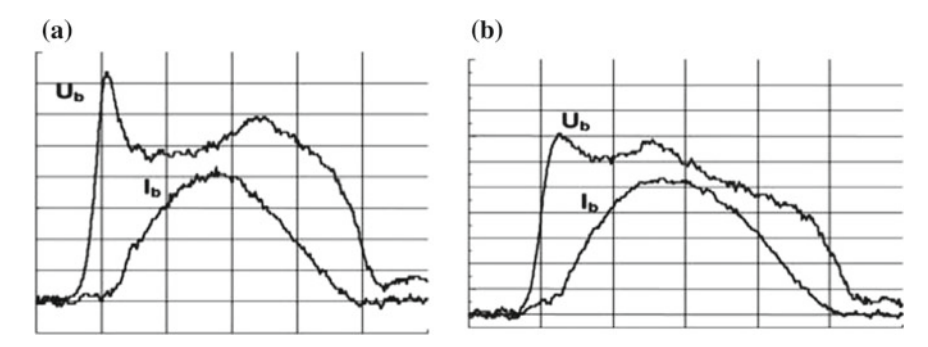


Fig. 16.7 Current (I_b) and voltage (U_b) oscillograms for a bounded SIVD. Timescale: 50 ns div⁻¹ **a** 30 Torr C_3F_8 and **b** mixture: 15 Torr $C_2HCl_3 + 3$ Torr C_2H_6

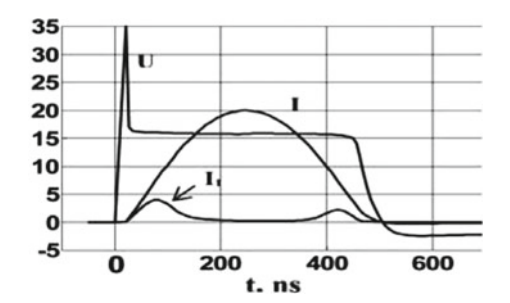
dissociation thresholds are attained. As a result, more than 80% of the energy deposited goes into dissociation [20]. Note that the dissociative ionization and electron attachment processes characteristic of SFg can contribute significantly to gas decomposition, and specifically to F-atom production [21]. On the sub-microsecond time-scale, the by-products formed have no time to leave the discharge channel, which leads to a local increase in the total gas number density N and, consequently, diminishing electric conductivity.

- II. Because χ_a is normally well over unity, large negative ion concentrations are achieved in SIVD, which means that electron generation processes via electron detachment from negative ions may come into play. Traditionally, detachment processes via negative ion-neutral molecule collisions or/and associative ionization are invoked. However, at intermediate gas pressures (10–100 Torr) on a microsecond timescale, the mechanisms mentioned do not contribute at all to electron multiplication, as follows from experiments and theoretical considerations [22]. On the other hand, there are strong grounds to believe that electron detachment by electron impact may be very efficient at producing secondary electrons in SFg. As applied to the development of electron avalanches in SF₆, this ionization mechanism was first proposed and quantitatively assessed in [23, 24]. It was also later considered for plasmas formed in other fluorine-containing gases.
- III. The high positive ion concentrations attained in SIVD, together with the fact that the relation $\alpha \approx \eta$ holds under the working conditions, mean that dissociative electron–ion recombination can strongly influence the SF₆ discharge plasma parameters, both qualitatively and quantitatively. At the SF₆ plasma decay stage (the trailing edge of the voltage impulse), ion-ion recombination also affects the discharge characteristics considerably. It should, however, be stressed that both of the recombination processes in SF₆ are poorly known, so that no firm data on the corresponding rate constants at elevated reduced electric fields close to $(E/N)_{cr}$ can be found in the literature at this time.

To describe SF₆ dissociation, the energy spent for F-atom production is taken to be equal to 4.5 eV. Further, it is suggested that the negative ion SF₆⁻ dominates under the conditions of interest, because charge transfer reactions have no time to be accomplished [22] and the cross-sections for the direct production of other negative ions by electron impact are too small [21]. The rate constant for electron impact detachment from negative ions is assessed as $k_d = 10^{-7}$ cm⁻³ s⁻¹, on the assumption that this quantity is no less than that of the elastic electron scattering in SF₆ [23]. The rate constant b_{ei} for dissociative electron-ion recombination is derived with regard to the fact that the positive ion SF₅⁺ predominates in SF₆ electric discharge plasma [21]. In addition, it is assumed that $b_{\rm ej} \sim T_{\rm e}^{-1/2}$, where $T_{\rm e}$ is the electron temperature. As a result, $b_{\rm ei} = 10^{-7}~{\rm cm}^{-3}~{\rm s}^{-1}$ is taken. To determine the ion-ion recombination rate constant \vec{b}_{ii} , special experiments are carried out [25, 26]. Without going into detail, here we give = 10^{-8} cm⁻³ s⁻¹ as an adequate value for the conditions of interest. It is clear that all the processes considered above, when taken into account with their actual rate constants, may influence the SIVD voltage oscillograms considerably. It can be inferred that dissociative electron-ion recombination and electron detachment by electron impact seem to equilibrate each other, at least within the accuracy to which the corresponding rate constants are presently known. This seems to lend additional support to the estimates for the rate constants $k_{\rm d}$ and $b_{\rm ei}$ presented in this chapter.

Advanced studies on a submicrosecond intermediate pressure SIVD in SF₆ and SF₆-C₂H₆ mixtures are presented. It is found that the decomposition of SF₆ molecules-either immediately through electron impact or through dissociative ionization and electron attachment-influences the discharge characteristics (specifically the voltage and current oscillograms) greatly. The breakup of C₂H₆ molecules may also be thought of as a notable dissociation mechanism. Electronion dissociative recombination and electron impact detachment from negative ions are felt to balance each other in pure SF₆ and in SF₆ with small C₂H₆ additives. The considered processes enable one to explain such a unique phenomenon as SIVD qualitatively. It should also be noted that electron detachment from negative ions because of electron impact is one of the most probable mechanisms for the development of SSVD instability in SF₆ and SF₆ based mixtures. Taking into account the influence of the listed processes enables one to describe the dynamics of SIVD formation qualitatively. In our calculations the channel structure of SIVD is modeled by a set of paralleled pure resistances whose conductivity is determined in accord with [10, 19]. The differences in the initial conditions when developing the channels lengthwise of the cathode are specified by different initial electron number densities n_0 for each of the channels. A total of nine channels are taken into account, which corresponds to using a knife cathode in the experiment. Figure 16.8 gives the calculated oscillograms for voltage U, total current I and the current through the first channel. It is seen that a current through an individual channel displays two maxima, which correlates qualitatively with the results of the experiments that investigated the SIVD dynamics, wherein the effect of current recovery was observed.

Fig. 16.8 Oscillograms for voltage U and general current I, and the current through the first channel I_b scales: current–25 A div⁻¹, voltage–5 kV div⁻¹ and time–200 ns div⁻¹



By this means, it is the presence of the mechanisms that restrict current through a conducting channel that makes it possible to form SSVD without preionization—SIVD. However, a sufficiently high uniformity and stability should also be ensured for SIVD to be used in non-chain HF (DF) lasers. SIVD can only conventionally be assigned to ordinary volume discharges. A volume nature is attained for SIVD by overlapping individual diffuse channels attached to cathode spots, i.e. in principle SIVD has a jet structure. What is important for the uniformity and stability of such discharges is, therefore, not the initial electron number density as such, but the surface density of the cathode spots, which is to a large extent determined by the surface state, in addition to a number of other factors. The results of experiments performed with the aim of revealing these factors are discussed below.

Experiments were carried out in a dielectric discharge camera filled with a mixture of SF₆ and hydrocarbons (C_2H_6 or C_3H_8) at a total pressure of p=5+15 Torr. A volume discharge was burnt between an A1 Ø6 cm cathode rounded off to a radius 1 cm along its perimeter and an A1 Ø12 cm anode at values $p_d=0.02-0.7$ cm atm. In the experiments we used both cathodes that had been polished and cathodes that had been subjected to sandblasting. A capacitor was discharged through the gap. Changing the capacitance and the capacitor's discharge voltage varied the energy inserted into the SIVD plasma.

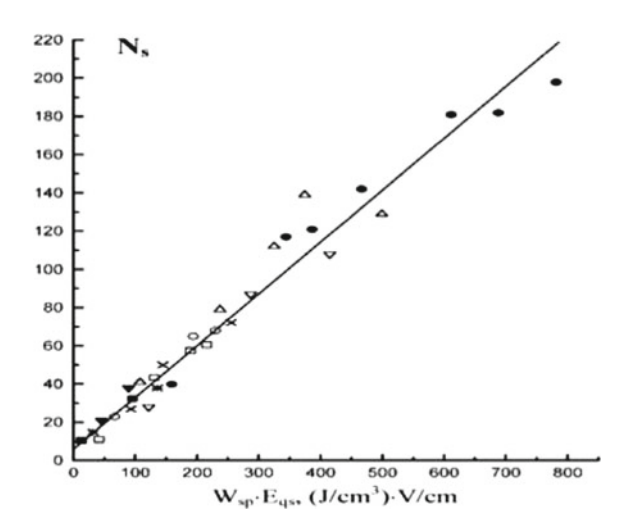
Figure 16.9 shows the number $N_{\rm s}$ of spots on the cathode that had been subjected to sandblasting as a function of the parameter $W_{\rm sp}$, $E_{\rm qs}$, $W_{\rm sp}$ is the deposited energy per unit gas volume and $E_{\rm qs}$ is the electric field strength in the quasi-stationary phase of SIVD. As can be seen in Fig. 16.9, this relationship is satisfactorily approximated by a linear function:

$$N_{\rm s} = a + bW_{\rm sp} - E_{\rm qs}.\tag{16.1}$$

The rise of the quantity $N_{\rm s}$ and, consequently, of the cathode spots surface density—which is observed not only when a specific energy deposition is increased, but also when the electric field strength is—reflects the fact that the electric field strength magnitude determines the probability of the formation of a cathode spot to a considerable extent [14]. The constant b in expression (16.1) is in turn a function of the cathode surface state and the hydrocarbon content in the mixture.

Figure 16.10 shows the dependences of N_s on a partial pressure of C_2H_6 in the mixture at an SF₆ pressure of 30 Torr while d = 4 cm, obtained using a polished

Fig. 16.9 Dependence of the number of cathode spots N_s on $W_{\rm sp}$ $E_{\rm qs}$ for the SF₆: $C_2H_6=10:1$ mixture with d=6 cm and p=33.6 Torr (\square), d=6 cm and p=16.8 Torr (\blacksquare), d=4 cm and p=23.3 Torr (\P), d=3 cm and p=23.3 Torr (\P), d=3 cm and p=33.6 Torr (o), d=3 cm and p=33.6 Torr (Δ), d=3 cm and d



cathode (curve 1; a mechanical polish of the surface is followed by aging via approximately 100 discharges) and a cathode subjected to sandblasting (curve 2). These dependences were obtained at constant energy depositions in the SIVD plasma. As is seen in Fig. 16.10, the quantity $N_{\rm s}$ increases appreciably with increasing hydrocarbon partial pressure. From this figure it is also evident that the roughness of the cathode surface comes to play a role in increasing the density of the cathode spots and, correspondingly, the effective volume occupied by the SIVD. In accordance with expression (16.1), the density of the cathode spots in the SF₆–C₂H₆ mixture can also be increased by stepping up the discharge burning voltage through adding small quantities of gases that are more electronegative than SF₆, for example, CCl₄ or C₂HCl₃. Note that 2 Torr C₂HCl₃ addition to the SF₆–C₂H₆ mixture does not lead to a noticeable decrease in the SIVD stability.

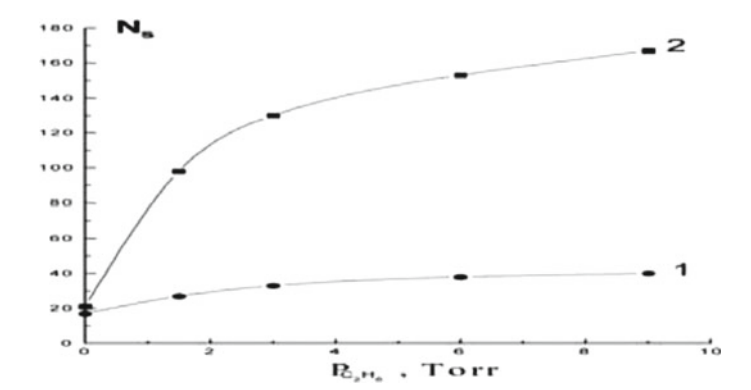


Fig. 16.10 Dependences of the cathode spots number N_s on a partial pressure of C_2H_6 in SF₆: C_2H_6 mixture. SF₆ pressure p=30 Torr. 1–polished cathode and 2–cathode subjected to sandblasting

The problem of increasing the stability of SIVD in SF_6 based mixtures is adequately covered in [5–10], and so it is not covered in detail in this paper. We only report on the basic results in this area. In [5], it was shown that the addition of hydrocarbons and deuteron–carbons to SF_6 allows specific energy depositions to be increased by a factor of 5–6 at a given discharge duration, for which reason it is preferable to employ these hydrogen (deuterium) donors in a non-chain HF (DF) laser, rather than H_2 and D_2 . In addition, it was shown in [8, 10] that the stability of SSVD in a mixture of SF_6 with hydrocarbons or deuteron–carbons does not in practice depend on whether there are sites of local electric field enhancement at the discharge gap, which enables us to use identical flat electrodes rounded off to small radii $r \ll d$ along the perimeters as the anodes and cathodes–i.e. to employ essentially compact electrodes–in non-chain HF (DF) lasers. This makes it possible to substantially decrease the size of the discharge camera and, correspondingly, the discharge circuit inductance, which is of great importance in scaling the characteristics of non-chain HF (DF) lasers.

We should point out that the detachment of electrons from negative ions, which is taken into account by us when considering the mechanisms of electric current density restriction, may be one of the possible mechanisms leading to the development of instability in SF_6 and SF_6 based mixtures. However, such an analysis is very challenging because of the severe difficulty of exactly accounting for the plasma composition within the channel growing from a cathode spot, wherein the initial components of the working mixture are strongly dissociated owing to great current densities (up to 10^4 A cm⁻²).

16.3 Non-chain HF (DF) Lasers Pumped by SIVD

SIVD has great potential for the creation of extremely simple and compact non-chain HF (DF) lasers. However, in the absence of preionization, setups with working medium volumes of less than 21 at a relatively small cathode surface exhibit an appreciable scatter in the pulse breakdown voltage amplitudes that is especially undesirable under the pulse-periodic working mode. Therefore, in the given case, it is expedient to initiate SIVD by, for example, a low-current spark located either outside the discharge gap or in a hole on the cathode [5]. In principle, this regime is similar to a 'photo triggered discharge' mode [15, 17, 27]. However, in classical photo triggered discharge schemes being applied to excimer lasers, a powerful illumination of the gap is necessary, since this illumination serves the dual function of initiating the breakdown and producing the necessary primary electron number density in a gas medium. In mixtures of SF₆ with hydrocarbons, powerful illumination is not needed, because the distinguishing feature of SIVD is that a discharge after a local gap breakdown spreads, as shown above, over the whole surface of the cathode, wherever it first occurs [5]. This means that a local illumination of the cathode by a low-current spark is quite sufficient to stabilize the electric and output characteristics of HF (DF) lasers. With reference to an unusual

operating mode, some special features of an HF (DF) laser with an aperture of 5 cm are considered in this section in detail.

In the laser (Fig. 16.11), flat A1 electrodes with dimensions of 20×80 cm (anode) and 7×60 cm (cathode), rounded off to a radius of 1 cm in their perimeters and separated by a distance of d = 5 cm, were used. The cathode surface was subjected to sandblasting. To obtain SIVD, the Fitch scheme was used with capacitors C_1 and C_2 of 0.1 μ F and a maximum discharge voltage of 50 kV. The discharge gap was laterally illuminated with a spark limited by two resistances of $r = 5 \text{ k} \Omega$ connected directly to the electrodes. The spark was located symmetrically relative to the electrodes at a distance of ~ 5 cm from the cathode edge. Ten blowers ensured the operation of the laser in a pulse-periodic regime with a frequency of up to 10 Hz. The laser worked with mixtures SF₆-C₂H₆ and C₆D₁₂ at pressures of 45–70 Torr. In the majority of the experiments, a resonator formed by an A1 mirror with a radius of curvature of 20 m and a plane-parallel plate of BaF₂ was used. The laser radiation divergence was measured using an unstable telescopic resonator with the amplification M = 3. To rule out the influence of the near-electrode regions on the results, the laser aperture in these measurements was limited to a diameter of 4 cm. The radiation divergence measurements were carried out via the focal spot method using a mirror wedge [28].

Note that in contrast to a typical photo triggered discharge system, breakdown initiation in our case occurred spontaneously as soon as the voltage across the gap exceeded a certain critical magnitude. With the separation of the illumination scheme from the laser-pumping scheme, it was possible to initiate breakdown at an arbitrary instant of time.

Typical oscillograms for the pulses of the laser generation, current and voltage across the gap are presented in Fig. 16.12 (curves 1, 2 and 3, respectively). As is seen in this figure, discharge gap breakdown occurs due to photo initiation at the leading edge of the voltage pulse, a laser pulse maximum delaying slightly relative to the current maximum. Without the initiating spark, the scatter in the gap breakdown voltage amplitudes is as high as 20%, which, correspondingly, causes a spread of 15% in the magnitudes of the output laser energies.

Figure 16.13 shows the dependence of the output laser energy (W_{out}) (generation on HF) on the energy W deposited in the discharge plasma for mixtures with different proportions of C_2H_6 . It can be seen that in the mixtures with the

Fig. 16.11 Electrical scheme of the non-chain HF (DF) laser

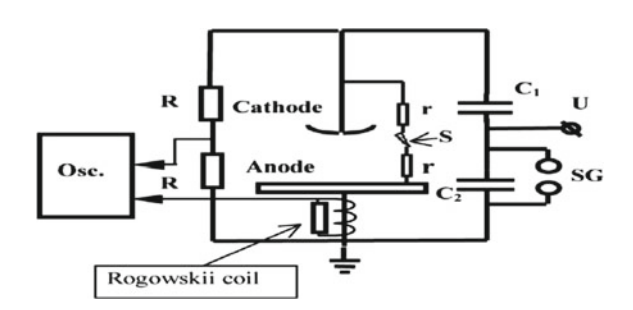
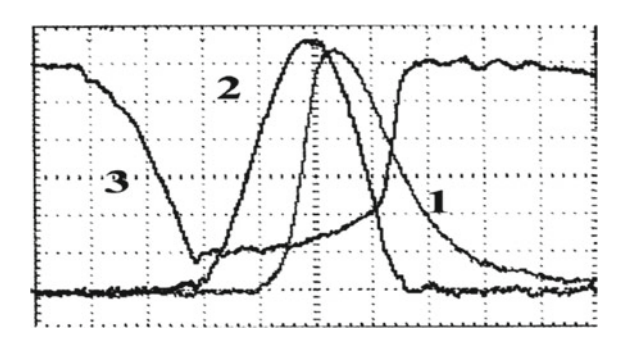


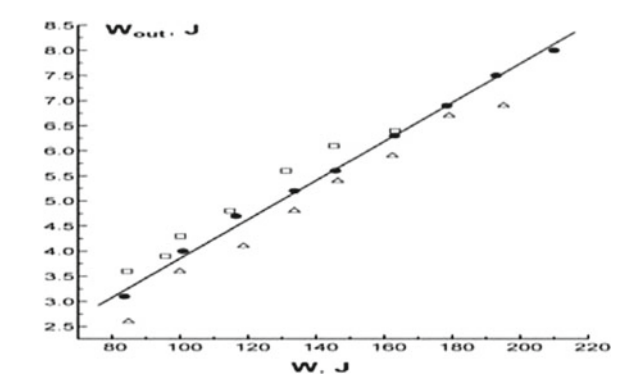
Fig. 16.12 Typical oscillograms of laser pulse (1), current pulse (2) and voltage across the discharge gap (3) for the mixture 66 Torr SF₆ + 6 Torr C₂H₆. Scales: current–3 kA div⁻¹, voltage–10 kV div⁻¹ and time–100 ns div⁻¹



component ratios C_2H_6 :SF₆ = 1.5:22 and 2:22 the output energy rises with the increase of the deposited energy practically linearly. In the experimental conditions, the mixture C_2H_6 : $SF_6 = 1.5:22$ turned out to be optimal, with a maximum value of the generation energy of $W_{\text{out}} = 8$ J obtained at an electrical efficiency of 3.2%. The discharge volume assessed by the laser radiation print on thermal paper was -1.51, which corresponds to a specific energy deposition in the plasma of $\sim 220 \text{ J l}^{-1}$. A decrease of W_{out} with increasing W in mixtures with a lower content of C_2H_6 (mixture C_2H_6 :SF₆ = 1:22) arose from discharge instability at high energy depositions. Indeed, in this mixture, when operating at energy depositions of $\sim 200 \text{ J}$ 1⁻¹, we observed bright plasma stems growing from the cathode edge, which sometimes bridged the gap. For mixtures with a higher C₂H₆, content, there was no decrease in laser efficiency with increasing W until the discharge remained stable, and the lengths of the plasma channels were not in excess of d/2. This causes us to anticipate that the increase of the electrical efficiency with increasing inter-electrode distance takes place because the SIVD becomes more uniform due to a greater overlapping of diffuse channels [5, 7].

In the investigated electrode system, a great enhancement of the electric field takes place at the gap edge. In such gases as CO₂, air and N₂, this results in the discharge concentrating at the gap edge [4]. In mixtures of SF₆ with hydrocarbons this is not the case, because of the distinguishing feature of SIVD—even though

Fig. 16.13 Dependences of the output laser energy (W_{out}) (generation on HF) on energy W deposited in the discharge plasma obtained for mixtures of C_2H_6 :SF₆ with different component ratios: \Box -1:22, \bullet -1.5:22 and Δ -2:22



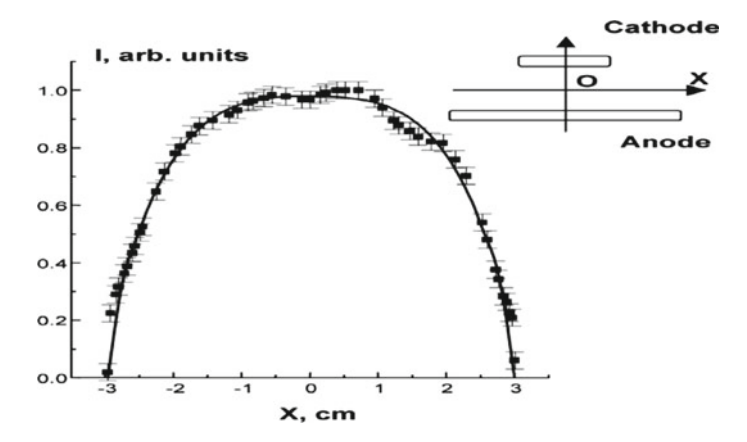


Fig. 16.14 Plasma intensity distribution over the optic axis-contained plane placed in parallel to the electrode surfaces

SIVD originates at the edge, it then displaces into the interior of the gap because of the existence of the mechanisms that limit the current density in a diffuse channel. The SIVD plasma intensity distribution over the optic axis-contained plane parallel to the electrode surfaces is shown in Fig. 16.14. The maximum of the SIVD luminosity intensity is attained at the axis. The radiation energy is also distributed over the laser aperture in a similar manner, i.e. the edge's electric field enhancement does not appreciably influence the distribution of the output laser radiation.

By this means, a local illumination of the cathode is quite sufficient to obtain a uniform SSVD in mixtures of SF_6 with hydrocarbons, and the presence of regions displaying high edge non-uniformity does not worsen the SIVD stability and only influences the distribution of the laser radiation energy over the aperture slightly. Therefore it is possible to use plane electrodes rounded off to small radii along their perimeters. We have not found any appreciable features for the P-P operating mode that have not been mentioned previously elsewhere [27–29].

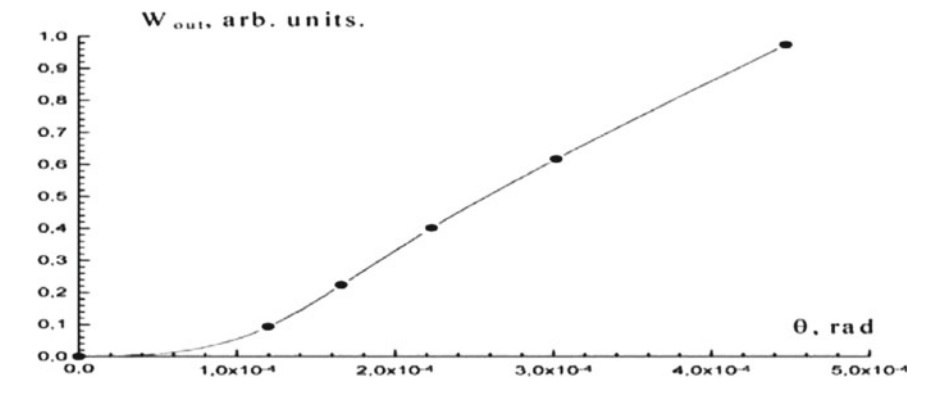


Fig. 16.15 Angular distribution of the radiation energy in the far zone

The radiation divergence was measured in the special case where the laser operated on DF molecules (Fig. 16.15). As can be seen from Fig. 16.15, the radiation divergence at a level of 0.5 is $\theta_{0.5} = 2.9 \times 10^{-4}$ rad, which corresponds to four diffraction limits. Further improvement of the given parameter can be expected from increasing the laser aperture, because lengthening the inter-electrode distance should improve the discharge uniformity through greater overlapping of diffuse channels.

16.4 Wide Aperture Non-chain HF (DF) Lasers

On increasing the cathode surface and active medium volume, the necessity of initiating the gap breakdown disappears. In this case, the breakdown delay becomes so negligible that it cannot be inferred from the oscillogram, and the breakdown occurs at the voltage leading edge. Therefore, when dealing with setups with great active medium volumes, there is no necessity for additional units to initiate the gap breakdown, since a sufficiently uniform discharge forms spontaneously.

We considered the scaling problems for non-chain HF (DF) in previous papers [6, 8, 10] in greater detail.

16.5 Conclusions

So, in this chapter we touch on the necessary conditions for obtaining SIVD in large volumes.

- (1) The cathode surface should posses a small-scale ($\sim 50 \mu m$) roughness;
- (2) It is important to match the circuit wave impedance to the discharge plasma resistance at a given inter-electrode distance, and a mixture pressure should be chosen in such a way that the discharge burning voltage determined by the conditions of the gap breakdown in SF₆ [19] is two times smaller than the voltage fed to the gap;
- (3) The increase of electrical energy produced via the increase in the generator's capacitance at a given maximum generator voltage should be followed by the growth of the discharge volume V as $V \sim C^{3/2}$, where C is the generator's capacitance [8, 10]. On fulfillment of all these conditions, one should also try to maximally decrease the time period of the energy deposition in the discharge plasma.

The maximum generation energies obtained for non-chain HF (DF) lasers in our experiments were 407 J (HF) and 325 J (DF), with electrical efficiencies of 4.3 and 3.4%, respectively. The active medium volume was \sim 60 l at an aperture of 27 cm (Fig. 16.16a, b).

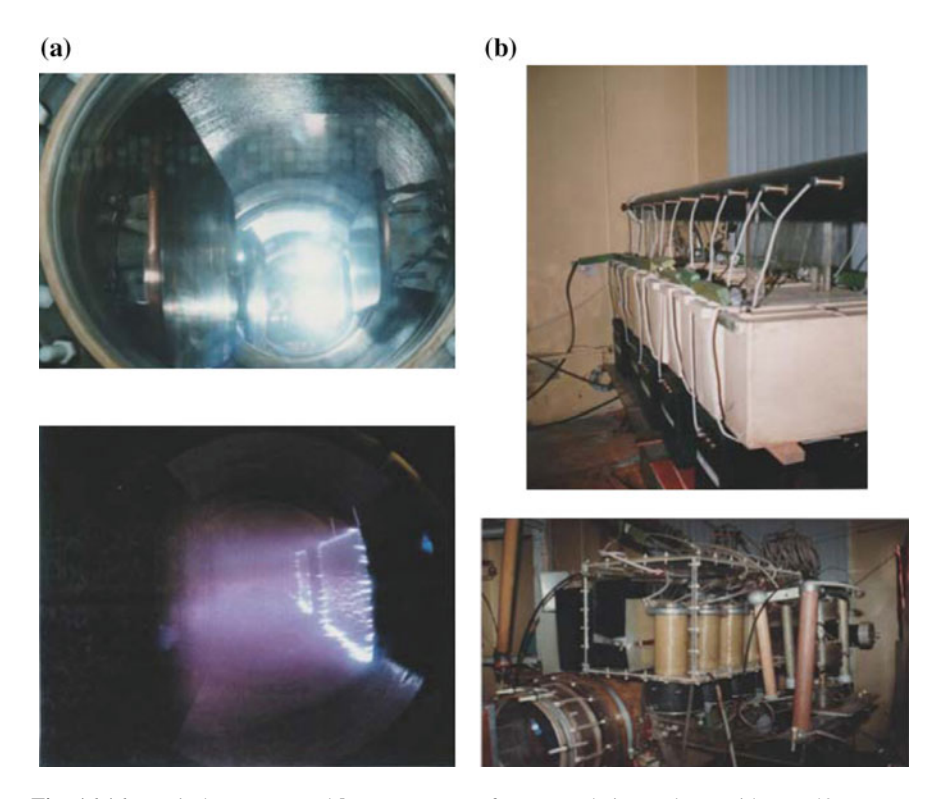
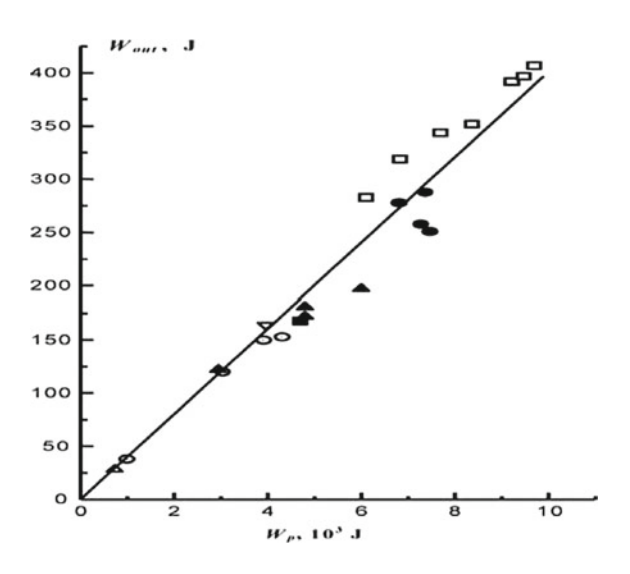


Fig. 16.16 a Discharge gap and b power source for a non-chain HF laser with P = 407 J

Fig. 16.17 Dependence of the output HF laser energy $W_{\rm out}$ on the energy stored in the generator's capacitors



16.5 Conclusions 255

Of natural interest is the problem of further increasing the laser radiation energy. Figure 16.17 shows the dependence of the output HF laser energy $W_{\rm out}$ on the energy $W_{\rm p}$ stored in the capacitors of a high-voltage generator. This figure reflects the data we obtained using setups with different volumes of active medium. This allows us to predict the possibility of further increases to the output energy of non-chain HF (DF) lasers through the creation of setups that operate at energy depositions above a few tens of kJ using the methods we developed during that very productive period of time [30–32].

References

- V.V. Apollonov et al., SSVD in CO₂-N₂-He gas mixtures Proc. Int. Conf. Lasers 85, 681 (1985)
- 2. V.V. Apollonov, SSVD based chemical lasers. Laser Focus World 12, 84 (2003)
- 3. V.V. Apollonov et al., Feasibility of increasing the output energy of a non-chain HF (DF) laser. Quantum Electron. **24**, 213 (1997)
- 4. V.V. Apollonov et al., Non-chain electric discharge HF (DF) laser with high radiation energy. Quantum Electron. **25**, 123 (1998)
- 5. V.V. Apollonov et al., High-power non-chain HF (DF) lasers initiated by SSVD, in *Proceedings of SPIE, XII International Symposium on Gas Flow and Chemical Lasers and High-Power Laser Conference*, vol. 3574 (St Petersburg, Russia, 1998), p. 374
- 6. V.V. Apollonov et al., SSVD based pulse non-chain HF (DF) laser, in *Proceedings of SPIE, High-Power Laser Ablation*, vol. 3343 p. 783 (1998)
- V.V. Apollonov et al., SIVD in non-chain HF lasers based on SF₆-hydrocarbon mixtures. Quantum Electron. 30, 207 (2000)
- V.V. Apollonov et al., SSVD for initiated wide aperture non-chain HF (DF) lasers. Izv. RAN Ser. Fiz. 64, 1439 (2000)
- V.V. Apollonov et al., SSVD in mixtures of SF₆ with hydrocarbons to excite non-chain HF lasers, in *Proceedings of SPIE, International Conference on Atomic and Molecular Pulsed Lasers III*, vol. 4071, p. 31 (2000)
- V.V. Apollonov et al., Scaling up of non-chain HF (DF) laser initiated by SSVD, in Proceedings of SPIE, High-power Lasers in Energy Engineering vol. 3886, p. 370 (2000)
- 11. V.V. Apollonov et al., Generation and properties of SSVD in strongly electronegative gases, in *Proceedings of XXV International Conference on Phenomena in Ionized Gases, ICPIG-2001*, vol. 1 (Nagoya, Japan), p. 255 (2001)
- 12. V.V. Apollonov et al., Volume discharge in SFj mixtures with gydrocarbons, in *Proceedings of XIII International Conference on Gas Discharge and their Applications, GD-2000*, vol. 1 (Glasgow, UK), p. 409 (2001)
- 13. E.W. McDaniel, Gas lasers, in *Applied Atomic Collision Physics*, vol. 3 (Academic, New York, 1982)
- 14. Yu.D. Korolev, G.A. Mesyats, Physics of Pulse Discharge in Gases (Nauka, Moscow, 1991)
- H. Brunet et al., Pulsed HF chemical laser using a VUV phototriggered discharge, in SPIE, VIII International Symposium on Gas Flow and Chemical Lasers, vol. 1397, p. 273 (1990)
- H. Pummer et al., Parameter study of 10-J hydrogen fluoride laser. Appl. Phys. Lett. 22, 319 (1073)
- 17. V. Puech, High-efficiency, high-energy performance of a pulsed HF laser pumped by phototriggered discharge. Appl. Phys. B **55**, 183 (1992)

- 18. N.N. Burtsev et al., 1984 On simultaneous formation of volume and sliding discharges of millimicrosecond duration for gas lasers pumping, in *Proceedings of VII All-Union Conference on Physics Low-temperature Plasma (Tartu)* (1984)
- 19. V.V. Apollonov et al., Discharge characteristics of a nonchain HF (DF) laser. Quantum Electron. **30**, 483 (1987)
- D.I. Slovetskii, A.A. Deryugin, Electron energy distribution functions and interaction of electrons with polyatomic molecules of fluorine-containing gases, in *Plasma Chemistry*, vol. 13, ed. by B.M. Smirnov (Energoizdat, Moscow, 1987), p. 240
- N. Nakano et al., Simulation of RF glow discharges in SF₆ by the relaxation continuum model: physical structure and function of the narrow-gap reactive-ion etcher. Phys. Rev. E 49, 4455 (1994)
- H. Hilmert, W. Schmidt, Electron detachment from negative ions of sulfur hexafluoride-swarm experiments. J. Phys. D: Appl. Phys. 24, 915 (1991)
- 23. A.A. Belevtsev, L.M. Biberman, About some nonlinear effect in development of electron avalanches in electronegative gases Izv. Akad. Nauk SSSR Energ. Transp. 6, 74 (1997)
- D. Hayashi et al., Role of reaction products in F-production in low-pressure, high-density CF₄ plasmas. Japan. J. Appl. Phys. 38, 6084 (1999)
- V.V. Apollonov et al., Ion-ion recombination in SF₆ and SF₆-C₂H₆ mixtures at high values of E/N. Quantum Electron. 31, 629 (2001)
- V.V. Apollonov et al., Ion-ion recombination in SF₆ and SF₆-C₂H₆ mixtures at high values of E/N, in *Proceedings of XXV International Conference on Phenomena in Ionized Gases,* ICPIG-2001, vol. 3 (Nagoya, Japan), p. 277 (2001)
- 27. B. Lacour, High average power HF (DF) lasers, in *Proceedings of SPIE, III International Conference on Atomic and Molecular Pulsed Lasers* vol. 4071, p. 9 (1997)
- 28. Yu.M. Abrosimov et al., Measuring of a divergence of a pulsing laser radiation by a method of a focal spot with application of a reflecting wedge Tech. Measure. 4, 30 (1982)
- 29. S.D. Velikanov et al., Physical aspects of the operation of HF (DF) lasers with a closed active-medium replacement cycle. Quantum Electron. 24, 11 (1997)
- V.V., Apollonov, A.M. Prokhorov, Ecologically safe high power lasers Keynote address at Int. Conf. Lasers Tucson, AX, USA, (2001)
- V.V. Apollonov, High power self-controlled volume discharge based molecular lasers. Opt. Eng. 43, 16–33 (2004)
- 32. V.V. Apollonov, High Energy Molecular Lasers (Springer, Berlin, 2016)

Chapter 17 High Power/Energy Optics



17.1 Introduction

History of high power/energy optics is inextricably associated with the creation of a single-mode CO_2 laser (P = 1.2 kW), operating in the master oscillator-power amplifier regime and employing the principle of a quasi-optical transmission line, at the Laboratory of Oscillations of the P. N. Lebedev Physics Institute headed at that time by A. M. Prokhorov. Its creator was A. I. Barchukov, who worked with a team of young scientists on the problem of scaling of single-mode electric-discharge laser systems [1–5]. Due to the research conducted on such a laser system, we managed to study many physical phenomena occurring when high intensity radiation interacts with matter, including with the elements of the optical path of laser systems, which subsequently greatly facilitated creation of high-power lasers. Then, in the early 1970s, we paid attention to a phenomenon that was to limit undoubtedly the further growth of the power generated by lasers being developed [6]. More than twenty years of fundamental and applied research devoted to the study of this phenomenon and to the solution of problems associated with it allow a conclusion that its essence consists in the following. An optical surface of a highly reflecting power/energy optics element (POE) or any element of an optical path does not fully reflect radiation falling on it. A small portion of energy (fractions of a percent, depending on the wavelength) is absorbed by this reflecting element and turns into heat. As the output power increases, even a small amount of it is sufficient to induce thermal stresses in a POE. Thermal stresses distort the geometry of the reflecting surface, affecting thereby, for example, the possibility of long-distance delivery of radiation and its concentration in a small volume. The discovered effect of thermal deformations of a POE required a theoretical study of the problem that had not been solved in such a setting ever before. Very useful was the experience in solving the problems of thermo elasticity, gained by the theoretical department headed at that time at by B. L. Indenbom at the Institute of Crystallography, USSR Academy of Sciences. Minimisation of the thermoelastic response of the optical surface of the POE exposed to intense laser radiation is one of the key problems of power optics. Improving the efficiency of laser systems, increasing the output power/energy and imposing stricter requirements to the directivity of generated radiation fluxes are inextricably linked with the need to design and create a POE with elastic distortions $\lambda_0/10 - \lambda_0/20$ (λ_0 is the wavelength) at specific radiation loads up to several tens of kW cm⁻² [7–10].

Interest in high power/energy optics and its physical, technical and technological solutions is unabated to this day. An almost simultaneous creation of first lasers in the USA and the USSR gave birth to annual symposia on Optical Materials for High-Power Lasers (Boulder, USA) and Nonresonant Laser–Matter Interaction (Leningrad, USSR). Regular meetings of scientists and engineers, as well as proceedings of the symposia have had a significant impact on the development of research in the field of power optics in many countries [11–13].

The data presented in this review allow one to reconsider important aspects of temperature fields, thermoelastic stresses and thermal deformations in POEs, resulting from the exposure of their surfaces to high power/energy laser radiation. In this case, use is made of the relations (which are similar to Duhamel's integral formula from the theory of heat conduction) between the quantities characterising the thermal stress state in any nonstationary regimes of energy input into a solid. A peculiar feature of the analysis of the thermal stress state in this case consists in the fact that these relations comprise time t not as an independent variable, which is used in the differentiation (as, for example, in review [14]) but as a parameter, which is a consequence of incoherence of the quasi-stationary problem of thermoelasticity presented below. Thus, by using the theory we developed in the early 1970s, we consider in this review a wide range of phenomena related to the thermal stress state of a solid-body surface exposed to radiation arbitrarily varying in time [15–21]. This consideration is particularly important for the optics of high power/ energy, high-pulse repetition rate laser systems that are being actively developed. The review published [14] contains data (important for the development of high power/energy optics) on the use of capillary porous structures with a different degree of the surface development, which can be efficiently employed to increase the heat exchange at a temperature below the boiling point of the coolant. The evaporation-condensation mechanism of heat transfer in the POE on the basis of porous structures and the idea of lowering the boiling temperature under reduced pressure of the coolant in cellular materials, developed by us at the same time [14, 21], are not considered in this review.

17.2 Static POEs Based on Monolithic Materials

Consider the most important aspects of the problem of static POE fabrication, namely, the conditions needed to achieve high optical damage thresholds for a mirror surface. Note that in our first studies [4–9] we obtained only stationary

expression for the limiting intensities, leading to the optical destruction of POEs, and the stability parameters of optical surfaces based on them.

17.2.1 Thermal Stress State of a Solid Body Exposed to Laser Radiation

Temperature field. We considered a strongly absorbing isotropic body, which at the initial moment of time has a fixed temperature. The body surface with the absorption coefficient A is exposed to an axisymmetric radiation flux of arbitrary temporal shape. It is assumed that the intensity distribution in the laser beam cross section obeys the Gaussian law: $I(r) = I_0 \exp(-K_0 r^2)$, where $K_0 = 2/r_0^2$. Energy absorption takes place directly on the irradiated surface. Physically, this means that the skin-layer depth δ is smaller than the depth of the temperature field penetration in the body under consideration during the characteristic times τ of changes in the radiation intensity, i.e., $\delta \ll \sqrt{a^2 \tau}$, where a^2 is the thermal diffusivity of the material.

The problem of determining the temperature field was considered in the linear formulation: it was assumed that all thermal and mechanical characteristics of the materials are independent of temperature and energy loss by radiation and convection was neglected. Provided that the characteristic size of the beam is $r_0 < L$, where L is the characteristic size of the irradiated body, and the energy input time is $t < L^2/a^2$, in solving this problem one can use the half-space model. The heating of the sample material is described in this case by the heat conduction equation [22]

$$\frac{\partial T}{\partial t} = a^2 \Delta T \tag{17.1}$$

at the following initial and boundary conditions:

$$\frac{\partial T}{\partial z}\Big|_{z=0} = -\frac{I_0 A_0}{\lambda} f(t) \exp(-K_0 r^2),$$

$$T(r, z, 0) = 0,$$

$$\lim_{\substack{r, z \to \infty \\ r, z \to \infty}} T < M,$$
(17.2)

where M is the finite quantity; f(t) is the time function of the laser beam intensity normalised to I_0 ; A_0 is the absorption coefficient of laser radiation on a metal surface; λ is the thermal conductivity of the body material; and T is the temperature.

Using the method of successive integral Hankel and Laplace transforms, we obtain the solution to (17.1):

$$T(r,z,t) = T^* \frac{I_0 A}{2\lambda \sqrt{K_0}},$$

$$T^* = \frac{1}{2\pi i \sqrt{K_0}} \int_{\sigma-i\infty}^{\sigma+i\infty} dp \Psi(p) \exp(pt) \int_0^{\infty} \xi \frac{\exp(-\xi^2/4K_0)}{\gamma} \exp(-yz) J_0(\xi r) d\xi,$$
(17.3)

where p and ξ are the parameters of Laplace and Hankel transforms; $\gamma^2 = p/a^2 + \xi^2$; $\Psi(p)$ is the Laplace transform of f(t); and J_0 is the zero-order Bessel function.

This expression allows us to describe the thermal state of a solid body heated by laser radiation, whose intensity varies with time in an arbitrary manner.

Thermoelastic stresses. The thermoelastic behaviour of the body is analysed by using the system of equations [22, 23]

$$\mu \nabla^2 u + (\lambda' + \mu) \operatorname{grad} \operatorname{div} u - (3\lambda' + 2\mu) \alpha_{\mathrm{T}} \nabla T + F - \rho \ddot{u} = 0,$$

$$\nabla^2 T - \frac{1}{a^2} \frac{\partial T}{\partial t} + \frac{W_0}{\lambda} - \frac{(3\lambda' + 2\mu) \alpha_{\mathrm{T}} T}{\lambda} \operatorname{div} u = 0,$$
(17.4)

where λ' and μ and are the Lame coefficients [24]; μ is the deformation vector; ρ is the density of the material; F is the external force; α_T is the coefficient of thermal expansion; and W_0 is the density of volume heat sources.

In considering the deformation of an elastic metal halfspace whose surface is exposed to pulsed laser radiation, when the inequalities

$$|\rho \ddot{u}| \ll (3\lambda' + 2\mu)\alpha_{\rm T}|\nabla T|,$$

$$\nabla^2 T \sim \frac{1}{a^2} \frac{\partial T}{\partial t} \gg \frac{(3\lambda' + 2\mu)\alpha_{\rm T} T}{\lambda} \operatorname{div} u$$
(17.5)

are fulfilled, we can pass to the system of equations of the quasi-stationary thermoelasticity theory:

$$\mu \nabla^2 u + (\lambda' + \mu) \operatorname{grad} \operatorname{div} u - (3\lambda' + 2\mu) \alpha_{\mathrm{T}} \nabla T = 0,$$

$$\nabla^2 T - \frac{1}{a^2} \frac{\partial T}{\partial t} = 0.$$
(17.6)

In this case, from the first inequality we obtain the duration of a single pulse

$$\tau \gg \max\left(\frac{\rho a^2}{\lambda'}; \frac{\rho a^2}{\mu}\right) \sim 10^{-6} - 10^{-8} \,\mathrm{s},$$
 (17.7a)

and from the second-

$$\tau^{3/2} \ll \frac{\rho^2 c^2 a}{\mu \alpha_{\rm T}^2 I_0 A}.$$
(17.7b)

We represented the stress tensor components in the general form [21]:

$$\hat{\sigma}_{zz} = 2GD \int_{0}^{\infty} \xi^{2} J_{0}(\xi r) \phi(\xi) \left\{ e^{-\gamma z} - e^{-\xi z} [1 + z(\xi - \gamma)] \right\} d\xi,$$

$$\hat{\sigma}_{rr} = 2GD \int_{0}^{\infty} \phi(\xi) \left\{ J_{0}(\xi r) \left[\xi(\xi z - 2)(\xi - \gamma) e^{-\xi z} + \xi^{2} e^{-\xi z} - \gamma^{2} e^{-\gamma z} \right] \right.$$

$$\left. + \frac{J_{1}(\xi r)}{r} \left[\xi e^{-\gamma z} - \left[(\xi - \gamma)(\xi z - 2(1 - \nu)) + \xi \right] e^{-\xi z} \right] \right\} d\xi,$$

$$\hat{\sigma}_{rz} = 2GD \int_{0}^{\infty} \xi \phi(\xi) J_{1}(\xi r) \left[\gamma \left(e^{-\gamma z} - e^{-\xi z} \right) - \xi z(\xi - \gamma) e^{-\xi z} \right] d\xi,$$

$$\hat{\sigma}_{\phi\phi} = 2GD \int_{0}^{\infty} \phi(\xi) \left\{ J_{0}(\xi r) \left[(\xi^{2} - \gamma^{2}) e^{-\gamma z} - 2\nu \xi(\xi - \gamma) e^{-\xi z} \right] \right.$$

$$\left. + \frac{J_{1}(\xi r)}{r} \left[\left\{ \left[(\xi - \gamma)(\xi z - 2(1 - \nu)) \right] + \xi \right\} e^{-\xi z} - \xi e^{-\gamma z} \right] \right\} d\xi,$$
(17.8)

where G is the shear modulus; J_1 is the first-order Bessel function;

$$D = \frac{\alpha_{\mathrm{T}}}{2} \frac{1 + \nu}{1 - \nu} \frac{I_0 A a^2}{K_0 \lambda p} \Psi(p); \quad \phi(\xi) = \frac{\xi}{\nu} \exp(-\xi^2 / 4K_0);$$

and v is Poisson's ratio. Analysis of the expression reveals the nature of the time changes at any point in the half-space.

Thermal deformations. The stress state occurring in a solid body is accompanied by its deformation, its largest amplitude being achieved on the irradiated surface. The expression for the normal displacement of the surface, corresponding to a given temperature distribution, has the form:

$$W(r,z,t) = W^* \frac{(1+\nu)\alpha_{\rm T} I_0 A}{\lambda K_0},$$
(17.9)

$$W^* = \frac{F_0}{2\pi i} \int_0^\infty d\nu \int_{\sigma - i\infty}^{\sigma + i\infty} dp \frac{\Psi(p/t)}{p} \exp(p - \nu) J_0(\sqrt{\nu} \delta_r) \frac{\sqrt{\nu} - \sqrt{\nu + p/F_0}}{\sqrt{\nu + p/F_0}}, (17.10)$$

where $F_0 = 4K_0a^2\tau$. The resulting expression allows us to trace the changes in the surface shape during irradiation.

Thus, this consideration has made it possible to describe fully the characteristics of temperature fields, thermoelastic stresses and thermal deformations occurring in solids whose surface is exposed to high-power laser radiation varying with time in an arbitrary manner. In addition, the following relations are fulfilled between the quantities characterising the thermal stress state in the continuous-wave and any other nonstationary regime of energy input into the solid [22, 24]:

$$T^{\text{tr}} = \int_{0}^{t} f(t - \tau) \frac{\partial T^{\text{st}}}{\partial \tau} d\tau,$$

$$\sigma_{ik}^{\text{tr}} = \int_{0}^{t} f(t - \tau) \frac{\partial \sigma_{ik}^{\text{st}}}{\partial \tau} d\tau,$$

$$W^{\text{tr}} = \int_{0}^{t} f(t - \tau) \frac{\partial W^{\text{st}}}{\partial \tau} d\tau.$$
(17.11)

These relations are similar to Duhamel's integral formula from the theory of heat conduction. It should be noted that the local deformation of the POE surface is the determining factor of the laser impact and the bending deformation component of the POE as a whole can be reduced to zero due to the large thickness of its effectively cooled base. Later, both components of the POE deformation were examined in the book of Tsesnek et al. [25].

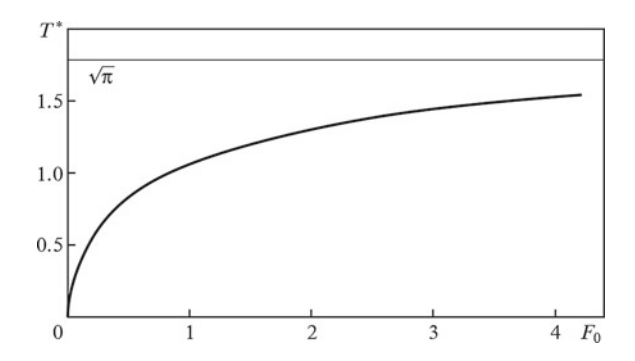
17.2.2 Continuous-Wave Irradiation

Temperature field. If the time of laser irradiation satisfies the inequality $r_0^2/a^2 \le t \le L^2/a^2$, a steady-state temperature field can be established in the sample material. The main property of the process of its establishment is described by the expression [21]

$$T^* = \frac{2}{\sqrt{\pi}} \arctan \sqrt{F_0}.$$
 (17.12)

It follows from (17.12) that for instants of times t, at which $F_0 \ge 4$, the current temperature is 10% less than the steady-state value. We therefore assume that, starting at time t, at which $F_0 > 4$, a stationary thermal state is established in the sample material (Fig. 17.1).

Fig. 17.1 Time dependence of the sample surface temperature at the centre of the region (number F_0) exposed to cw radiation



The expression for the temperature field in the half-space has the form [21]

$$T^* = \int_{0}^{\infty} J_0(\sqrt{\nu}\delta_r) \exp\left[-\sqrt{\nu}(\delta_z + \sqrt{\nu})\right] \frac{d\nu}{\sqrt{\nu}},$$
 (17.13)

where $\delta_z = 2\sqrt{K_0}z$ and $\delta_r = 2\sqrt{K_0}r$. From this expression we obtain the locality of the temperature field, the characteristic values of which decrease with increasing distance from the centre of the surface irradiation region and inside the material (Figs. 17.2, 17.3 and 17.4).

Thermoelastic stresses. In the steady-state regime $(p \to 0)$, nonzero are only the components of the tensor of thermal stresses σ_{rr}^* and $\sigma_{\varphi\varphi}^*$ [21]:

$$\sigma_{rr}^{*} = 2(1 - v) \int_{0}^{\infty} \exp\left[-\sqrt{v}\left(\sqrt{v} + \delta_{z}\right)\right] \left[J_{1}\left(\sqrt{v}\delta_{r}\right) - J_{0}\left(\sqrt{v}\delta_{r}\right)\right] \frac{dv}{\sqrt{v}},$$

$$\sigma_{\varphi\varphi}^{*} = 2(1 - v) \int_{0}^{\infty} \exp\left[-\sqrt{v}\left(\sqrt{v} + \delta_{z}\right)\right] \left[-J_{1}\left(\sqrt{v}\delta_{r}\right)/(v\delta_{r})\right] dv,$$
(17.14)

Fig. 17.2 Temperature field distribution on the z axis

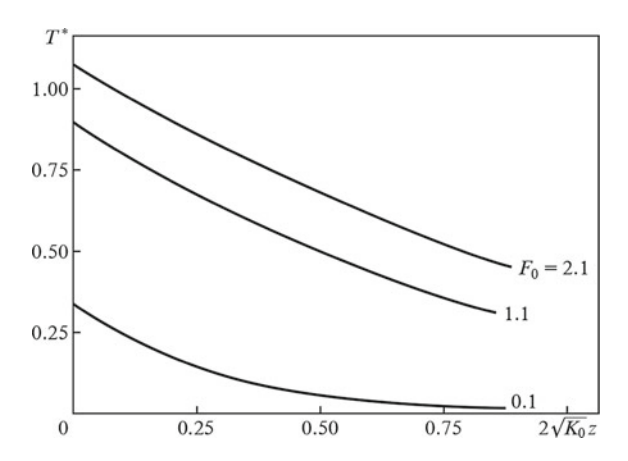


Fig. 17.3 Temperature field distribution on the sample surface

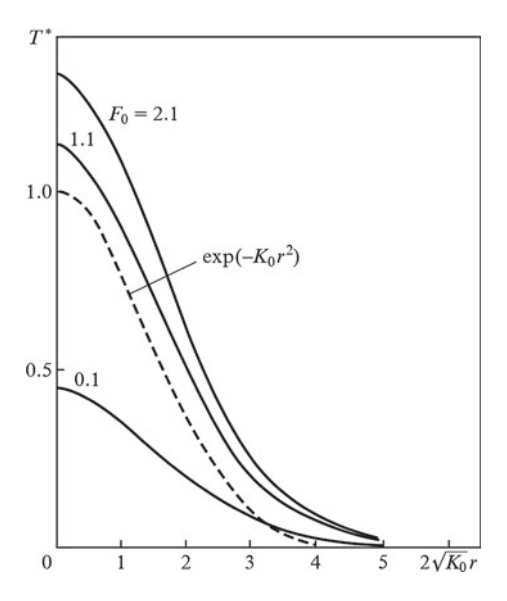
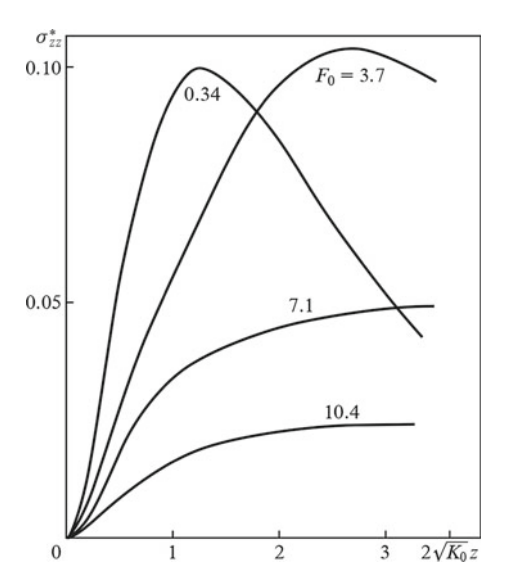


Fig. 17.4 Dependence of the axial stress σ_{zz} on the exposure time of laser irradiation

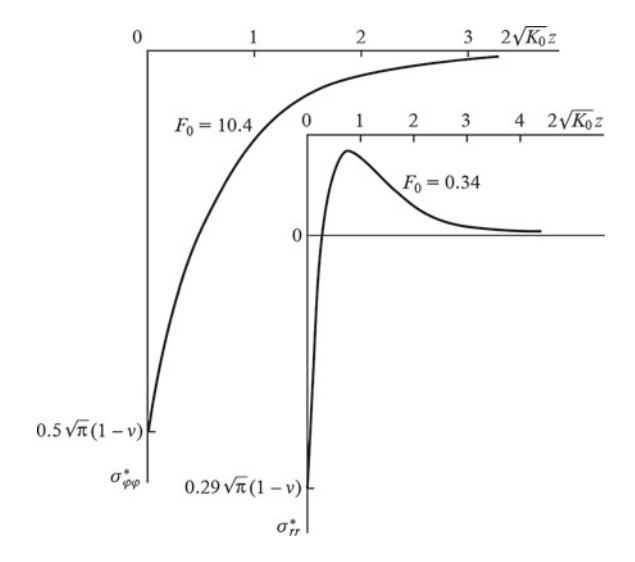


where

$$\sigma_{ik}^* = rac{\lambda \sqrt{K_0}(1-v)}{I_0 A G lpha_{
m T}(1+v)} \sigma_{ik}(r).$$

The maximum values of these components are achieved in the centre of the irradiated region (Fig. 17.5) on the surface of the half-space, where the stationary field of thermoelastic stresses have the form (Figs. 17.6 and 17.7)

Fig. 17.5 Distribution of the peripheral $(\sigma_{\varphi\varphi})$ and radial (σ_{rr}) tensor components on the z axis for different exposure times of laser irradiation



$$\sigma_{rr}^{*} = \frac{\sqrt{\pi}(1-\nu)}{2} {}_{1}F_{1}\left(\frac{1}{2}; 2; -\delta_{r}^{2}/4\right),$$

$$\sigma_{\varphi\varphi}^{*} = \frac{\sqrt{\pi}(1-\nu)}{2} \left[{}_{1}F_{1}\left(\frac{1}{2}; 2; -\delta_{r}^{2}/4\right) - {}_{1}F_{1}\left(\frac{1}{2}; 1; -\delta_{r}^{2}/4\right) \right].$$
(17.15)

The main property in establishing a steady state for σ_{rr} and $\sigma_{\phi\phi}$ are characterised by the dependence shown in Fig. 17.8:

Fig. 17.6 Stress field σ_{rr} on the surface of the half-space.

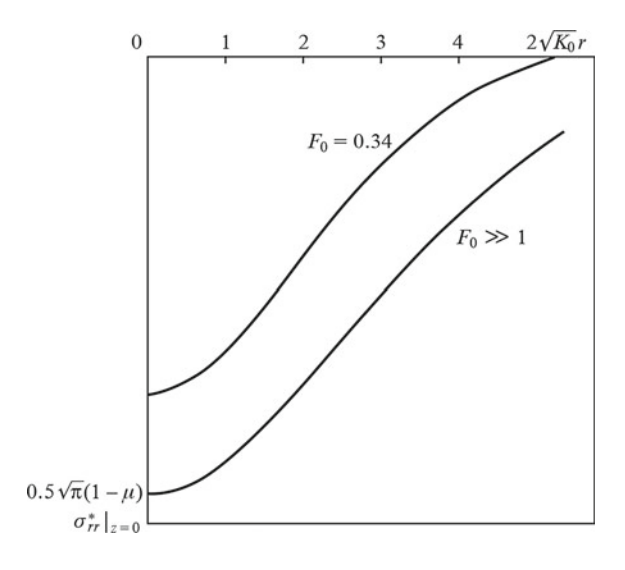
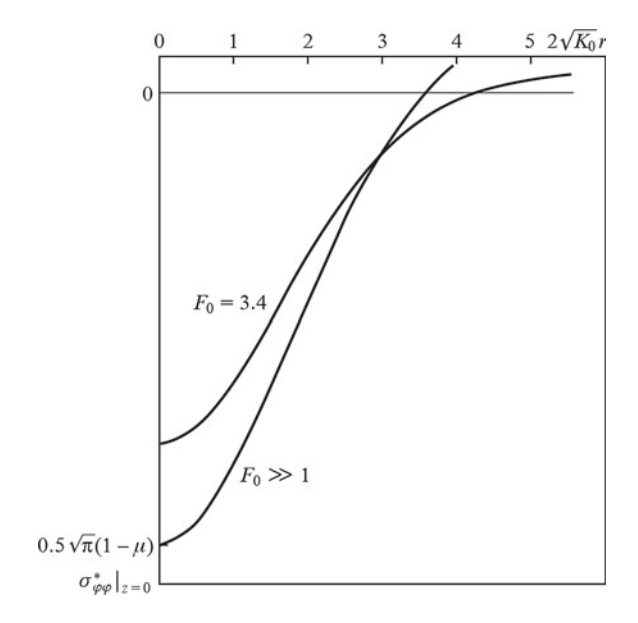


Fig. 17.7 Stress field $\sigma_{\phi\phi}$ on the surface of the half-space.



$$\sigma_{ii}^{*}(\delta_{r} = \delta_{z} = 0) = \frac{1+\nu}{\sqrt{\pi}} \left[F_{0} \left(\arctan \frac{1}{\sqrt{F_{0}}} - \frac{1}{\sqrt{F_{0}}} \right) - \frac{1-\nu}{1+\nu} \arctan \sqrt{F_{0}} \right]. \quad (17.16)$$

This expression completely describes the characteristics of the stressed state arising in a solid when its surface is irradiated by cw laser radiation.

Thermal deformation of the surface. The expression for the displacement W^* of the reflective surface in the half-space model has the form [21]:

$$W^* = -\frac{1}{2} \left\{ F_0 \exp\left(-\delta_r^2/4\right) - \left[\frac{4\sqrt{F_0}}{1+F_0} - 2\ln\left(\sqrt{F_0} + \sqrt{F_0+1}\right)\right] {}_1F_1\left(\frac{3}{2}; 1; -\frac{\delta_r^2}{4}\right) \right\}.$$
(17.17)

Fig. 17.8 Establishment of a stationary stress sate on the surface, in the centre of the irradiated region

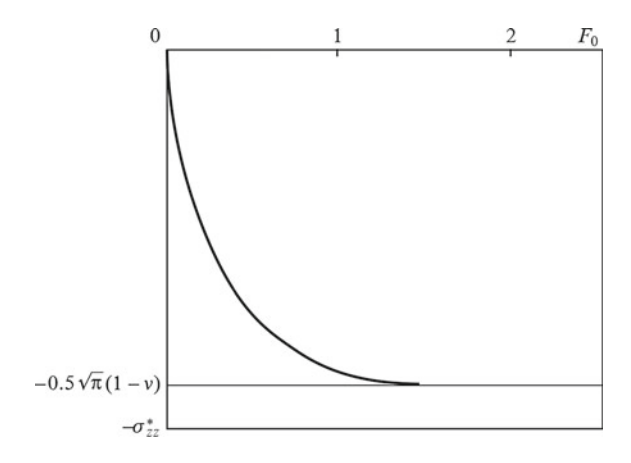
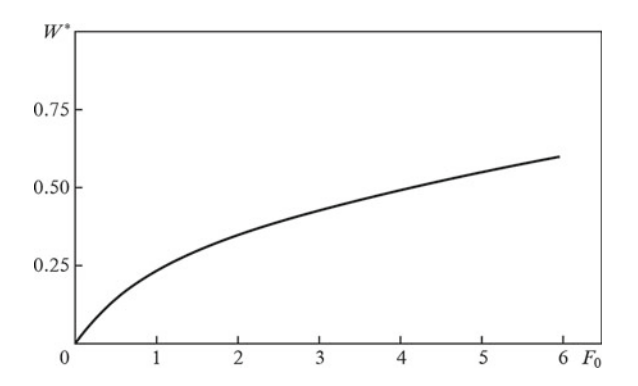


Fig. 17.9 Establishment of a quasi-stationary deformation state on the surface, in the centre of the irradiated region



Deformation surface profiles for different exposure times are shown in Fig. 17.9.

17.2.3 Pulsed Irradiation

Temperature field. In the case of short irradiation times, the depth of the temperature field penetration into the material is proportional to $\sqrt{a^2t} \ll r_0$; therefore, the radial heat spreading can be ignored, and the temperature distribution over the surface repeats the laser beam intensity distribution profile [26]:

$$T^* = \frac{2}{\sqrt{\pi}} \left[\Theta(t^*) \arctan\left(\sqrt{F_0 t^*}\right) - \Theta(t^* - 1) \arctan\left(\sqrt{F_0 (t^* - 1)}\right) \right] \exp\left(-K_0 r^2\right), \tag{17.18}$$

where $\Theta(t^*)$ is the Heaviside function; $t^* = t/\tau$; and τ is the pulse duration.

Thermoelastic stresses. Thermoelastic stresses arising in a solid irradiated by laser light play an important role in the destruction of the optical surface of the POE. Under pulsed irradiation ($F_0 \ll 1$) the expressions for the stress tensor components are given by (17.15), because in this case the propagation of heat in a solid is of quasi-one-dimensional character and the radial heat spreading can be neglected. The depth of penetration of thermal stresses in the material is $\sqrt{a^2\tau} \ll r_0$, which follows from the form of σ_{ik} on the z axis:

$$\sigma_{rr}^{*}(\delta_{r}=0) = -\frac{2}{\sqrt{\pi}}\sqrt{F_{0}}\left[\exp\left(-\delta_{z}^{2}/4F_{0}\right) - \frac{\sqrt{\pi}\delta_{z}}{2F_{0}}\operatorname{erfc}\left(\frac{\delta_{z}}{2\sqrt{F_{0}}}\right)\right]$$

$$\approx \frac{8F_{0}^{3/2}}{\sqrt{\pi}\delta_{z}^{2}}\exp\left(-\frac{\delta_{z}^{2}}{4F_{0}}\right),$$
(17.19)

where

$$\frac{\delta_z}{2\sqrt{F_0}} \gg 1.$$

The maximum values of the components σ_{rr}^* and $\sigma_{\alpha\alpha}^*$ are achieved on the surface,

$$\sigma_{rr}^* = \sigma_{\varphi\varphi}^2 = -2\sqrt{F_0/\pi} \exp(-\delta_r^2/4), \qquad (17.20)$$

i.e., the distribution of the components σ_{rr}^* and $\sigma_{\varphi\varphi}^*$ on the surface repeat the laser beam intensity distribution. The components σ_{rr}^* and $\sigma_{\varphi\varphi}^*$ on the surface z=0 are equal, and the expression for $\sigma_{ii}^*(\delta_r,\delta_z=0)$ has the form:

$$\sigma_{ii}^* = -\frac{2}{\sqrt{\pi}} \left[\Theta(t^*) \sqrt{F_0 t^*} - \Theta(t^* - 1) \sqrt{F_0 (t^* - 1)} \right]. \tag{17.21}$$

In the case of small irradiation times

$$\sigma_{zz}^* = 2\delta_z F_0 t^* \int_0^\infty V^3 \exp\left(-V^2 - V\delta_z\right) dV,$$

$$\sigma_{rz}^* = -\frac{\delta_r}{2} \exp\left(-\frac{\delta_r^2}{4}\right) \left[F_0 t^* \operatorname{erf}\left(\frac{\delta_z}{2\sqrt{F_0 t^*}}\right) + \frac{\sqrt{F_0 t^*}}{\pi} \delta_z \exp\left(-\frac{\delta_z^2}{4F_0 t^*}\right) \right],$$
(17.22)

where V is a transform variable. The difference in signs of the components means that in the case of thermal deformation of the sample by laser radiation, for σ_{zz} tension of a material is realised, whereas for σ_{rz} —compression. The maximum value of σ_{zz} is achieved on the z axis; in this case, $\delta_z^{\rm max} \approx 4\sqrt{12}$, i.e., $z_0^{\rm max} \approx 0.66r_0$, and $\sigma_{zz}^{*\rm max} \approx 1.9F_0$. The component σ_{rz}^* reaches its maximum value at point $r_0^{\rm max} = r_0/2$ and $z_0^{\rm max} \approx 2\sqrt{a^2t}$:

$$\sigma_{r_2}^{*\text{max}} \approx -0.5F_0. \tag{17.23}$$

A distinctive feature of the behaviour of the σ_{zz}^* component is that if the inequality $F_0 \ll 1$ is fulfilled, the position of its maximum on the z axis is determined by the spatial characteristics of the laser beam rather than the irradiation time. The maximum of this component is achieved by the end of the laser pulse. This feature is explained by the fact that at $F_0t^* \ll 1$ the region of thermoelastic perturbations lies on the sample surface and localises in the irradiation region, because heat due to heat conduction has no time to spread over the sample material. In the opposite case, i.e., at $F_0t^* > 1$, the point of this component maximum is determined from the condition $\delta z^2/(4F_0t^*) = 1$.

Thermal deformations. The expression for the thermal deformation of the reflecting surface irradiated by a rectangular laser pulse, whose duration satisfies the condition $F_0 \ll 1$, has the form [21]:

$$W^* = -\frac{F_0}{2} \exp(-K_0 r^2) [\Theta(t^*) t^* - \Theta(t^* - 1) (t^* - 1)]. \tag{17.24}$$

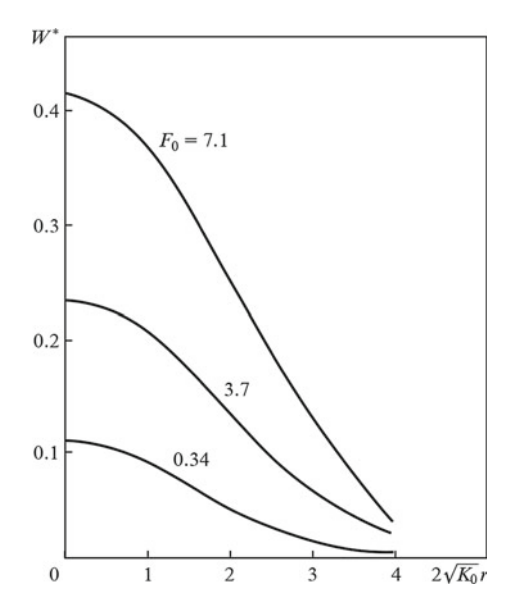
The distribution of thermal deformations of the reflecting surface repeats the laser beam intensity distribution (Fig. 17.10), which we used in our method of the dynamic control of the intensity distribution of laser radiation [27].

17.2.4 Repetitively Pulsed Irradiation

Thermal deformations of a solid body exposed to repetitively pulsed laser radiation were analysed by using the previously derived relations that are similar to Duhamel's integral formulas. The energy flow was treated as a train of rectangular pulses having a duration r, period T_0 (repetition rate $v_0 = 1/T_0$) and off-duty ratio $SQV = \tau/T_0$. It was assumed that $F_0 = 4K_0a^2T_0 < 1$. The arising thermal stresses and deformations of the temperature field are expressed in terms of the integrals (typical of the cw regime) that are similar to Duhamel's integrals [28]:

$$F^{\text{PP}} = \int_{0}^{t} f(t - \tau) \frac{\partial F^{\text{cw}}}{\partial \tau} d\tau.$$
 (17.25)

Fig. 17.10 Deformation surface profiles for different exposure times



At the initial instants of time, i.e., when $F_0t^* < 1$, repetitively pulsed irradiation is similar to pulsed irradiation. The geometric meaning of (17.25) is characterised by the area of the integrals in Fig. 17.11. (For the temperature and the components $\sigma_{\varphi\varphi}$ and σ_{rr} , the value of $\partial F^{\rm cw}/\partial \tau$ tends to infinity as $1/\sqrt{t}$ at $t\to 0$ and to zero at $t\to \infty$; for deformation $\partial F^{\rm cw}/\partial \tau$ tends to const at $t\to 0$ and to zero at $t\to \infty$.) In the case of long irradiation times, i.e., when $F_0t^*>1$, the temperature and thermal stresses reach their quasi-steady states, i.e., a constant component of these values becomes similar to that in the cw regime of energy input with a reduced intensity I_0 SQV. In this case, against the background of this component, along with changes in the laser beam intensity, there will be the characteristic peaks of temperature and stress, which are similar to peaks during pulsed irradiation. A separate 'pulse' of thermal deformations of the reflecting surface exists against the background of a 'stationary component' tending to infinity.

Temperature field. The expression for the temperature has the form [21]

$$T* = \frac{1}{2\pi i} \int_{\sigma_{i} + i\infty}^{\sigma_{i} - i\infty} dp \Psi(p) e^{p} \int_{0}^{\infty} \frac{e^{-V} J_{0}(\sqrt{V}\delta_{r}) \exp\left[-\sqrt{V}(\sqrt{V} + \delta_{z})\right]}{\sqrt{8/F_{0} + V}} dV, \quad (17.26)$$

since for a train of pulses

$$\Psi(p) = \frac{[1 - \exp(-p\tau)]\{1 - \exp[-p(N+1)T]\}}{p[1 - \exp(-pT)]}$$
(17.27)

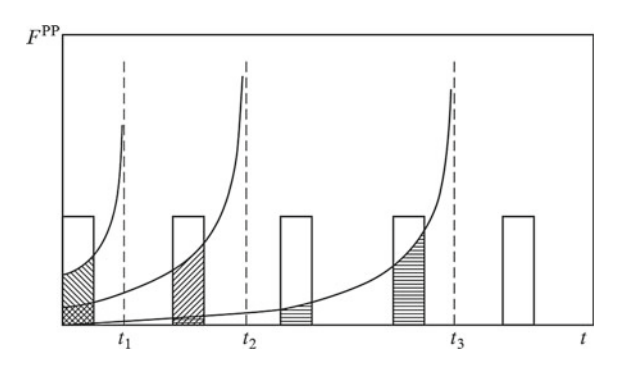
is the Laplace transform of f(t); and N is the number of propagated laser pulses.

In the centre of the irradiation region the temperature reaches a maximum value by the time the next pulse terminates $(F_0 > 1)$:

$$T_{\text{max}}^* = \sqrt{\pi} \text{SQV} + \frac{2}{\sqrt{\pi}} \arctan \sqrt{F_0 \text{SQV}},$$
 (17.28)

where SQV is the off-duty ratio of the temporal structure of radiation.

Fig. 17.11 Geometrical interpretation of Duhamel's integrals



Thermoelastic stresses. Maximum values of the radial and circumferential tangential stress are achieved in the centre of the irradiation region, where they are equal to each other:

$$\sigma_{ii}^{\text{PP}} = \int_{0}^{t} f(t - \tau) \frac{\partial \sigma_{ii}^{\text{cw}}}{\partial \tau} d\tau$$
 (17.29)

 $[\sigma_{ii}^{cw}]$ is determined from (17.16)]. The field distribution of stresses σ_{ii}^{*} on the surface by the time when the next laser pulse terminates has the form:

$$\sigma_{ii}^* = \text{SQV}\sigma_{ii}^{*(1)} + \sum_{n=0}^{N} \Theta(n+1-t^*) \big[\Theta(t^*-n)$$

$$\times \sigma_{ii}^{*(2)}(t^*-n) - \Theta(t^*-n-\text{SQV}) \sigma_{ii}^{*(2)}(t^*-n-\text{SQV}) \big],$$
(17.30)

where $\sigma_{\varphi\varphi}^{*(1)}$ and $\sigma_{rr}^{*(1)}$ are determined from (16), and $\sigma_{\varphi\varphi}^{*(2)} = \sigma_{rr}^{*(2)}$ —from (17.21). Because in the steady stress state σ_{zz} and σ_{rz} are identically zero, their values in the case of repetitively pulsed irradiation are the same as in the case of pulsed irradiation (accuracy \sim SQV).

Deformation of the surface. The displacement of a solid-body surface exposed to repetitively pulsed radiation also has stationary' and pulse components [21]: $W^* = \text{SOV}W^{*(1)} + W^{*(2)}$.

When the quasi-stationary state is reached

$$W^* = -\operatorname{SQV} \ln 2\sqrt{F_0} F 1 \left(\frac{3}{2}; 1; -\frac{\delta_r^2}{\pi}\right)$$

$$-\frac{F_0}{2} \sum_{n=0}^{N} \Theta(n+1-t^*) [\Theta(t^*-n)(t^*-n)$$

$$-\Theta(t^*-n-\operatorname{SQV})(t^*-n-\operatorname{SQV})] \exp(-K_0 r^2).$$
(17.31)

17.2.5 Criteria for the Optical Surface Stability

Expressions given for the characteristics of the thermal stress state of a solid whose surface is irradiated by high-power cw, pulsed and repetitively pulsed laser radiation allowed us to determine the limiting intensities corresponding to different stages of the optical damage of mirror surfaces [21, 29]. To this end, the parameters of the optical surface stability include not only the thermophysical and mechanical properties of the material but also the parameters of a Gaussian-like beam, namely the intensity in the centre of the irradiation region, the size of the irradiation region and the duration of a single pulse and, in the case of repetitively pulsed irradiation,

—the pulse train off-duty ratio. The stability parameters of the reflector contain the ratio of a maximum value of the thermal stress state characteristic to its value at which the solid material experiences irreversible macroscopic changes—melting, plastic (brittle) or fatigue deformation or achievement of a critical value $\lambda_0/20$ by the amplitude of thermal deformation of the optical surface, where λ_0 is the wavelength of the laser used. The thus introduced stability parameters of mirrored POE surfaces made it possible not only to compare different pure metals and their alloys in terms of applicability in power optics but also to create specific types of combined POEs capable of withstanding high-power fluxes of cw, pulsed and repetitively pulsed laser radiation.

Continuous-wave regime. A solid body whose surface is exposed to cw laser radiation is destroyed when the temperature field in the centre of the irradiation region reaches the melting point of the material and the components of the stress field reach the yield point. The stability of the optical surface under cw irradiation is by the parameters

$$\gamma_{T_{\text{melt}}}^{\text{cw}} = \frac{\sqrt{\pi I_0 A}}{2\lambda \sqrt{K_0} T_{\text{melt}}}, \quad \gamma_{\sigma_{\text{T}}}^{\text{cw}} = \frac{\sqrt{3\pi} (1+\nu) I_0 A G \alpha_{\text{T}}}{2\lambda \sqrt{K_0} \sigma_{\text{T}}}$$
(17.32)

If $\gamma_{T_{\rm melt}}$ and $\gamma_{\sigma_{\rm T}}$ < 1, the material will undergo no irreversible changes. The values of these parameters in the case of cw laser radiation at a power density $I_0A=1~{\rm kW~cm^{-2}}$ and $K_0=8\times10^2~{\rm m^{-2}}$ are shown in Table 17.1 for Cu, A1 and Mo. The main reason for the damage of the optical surface can be determined from the relation

$$\gamma_{\text{rel}}^{\text{cw}} = \frac{\gamma_{\sigma_{\text{T}}}^{\text{cw}}}{\gamma_{T_{\text{molt}}}^{\text{cw}}} = \frac{\sqrt{3}(1+\nu)G\alpha_{\text{T}}T_{\text{melt}}}{\sigma_{\text{T}}}.$$
(17.33)

If $\sigma_{\rm rel}^{\rm cw} > 1$, the material will be destroyed when the component σ_{ii} reaches the yield point, or when the melting point of the material, $T(0,0,\infty)$ is reached.

For the materials in question (Table 17.1), the main reason for the deterioration of the optical surface at lower laser intensities is irreversible plastic deformations of the POE in the centre of the irradiation region. There is another important reason for the deterioration of the optical surface—excess of the critical value $\lambda_0/20$ by the value of thermal deformation of the optical surface—which is implemented at long exposure times of high power laser radiation and in the range of the parameters corresponding to the elastic deformation of the material. In this case, phase and energy characteristics of the reflected laser beam are markedly impaired. The criterion for the optical surface stability to such changes in the optical characteristics of the reflector is given by parameter

$$\gamma_{\lambda_0/20}^{\text{cw}} = \frac{20(1+\nu)\alpha_{\text{T}}I_0A}{\lambda K_0\lambda_0} \ln 2\sqrt{F_0}.$$
 (17.34)

Parameter	Material		
	Cu	Mo	Al
CW regime			
$\gamma_{T_{\text{melt}}} = \frac{\sqrt{\pi I_0 A}}{2\lambda \sqrt{K_0}} \frac{1}{T_{\text{melt}}}$	0.74	0.8	2.3
$I_{\rm th} = \frac{1}{\gamma_{T_{\rm melt}}} / {\rm kW cm^{-2}}$	1.4	1.3	0.44
$\gamma_{\sigma_{\mathrm{T}}} = \frac{\sqrt{3\pi}I_{0}AG\alpha_{\mathrm{T}}(1+\nu)}{2\lambda\sqrt{K_{0}}\sigma_{\mathrm{T}}}$	19.3	10 ⁴	38.3
$I_{\mathrm{th}} = \frac{1}{\gamma_{\sigma_{\mathrm{T}}}} / \mathrm{kW cm^{-2}}$	0.05	10 ⁻⁴	2.6×10^{-2}
Pulsed regime			
$\gamma_{T_{\text{melt}}} = \frac{\sqrt{\pi I_0 A}}{2\lambda \sqrt{K_0}} \frac{1}{T_{\text{melt}}}$	2.0×10^{-3}	1.45×10^{-3}	5.4×10^{-3}
$I_{\rm th} = \frac{1}{\gamma_{T_{ m melt}}} / { m kW cm^{-2}}$	500	700	190
$\gamma_{\sigma_{\mathrm{T}}} = \frac{\sqrt{3\pi}I_{0}AG\alpha_{\mathrm{T}}(1+\nu)}{2\lambda\sqrt{K_{0}}\sigma_{\mathrm{T}}}$	0.16	55	0.28
$I_{\rm th} = \frac{1}{2} / {\rm kW cm^{-2}}$	6.3	1.8×10^{-2}	3.6

Table 17.1 Parameters of stability and threshold intensities for Al, Mo and Cu at $I_0A = 1 \text{ kW cm}^{-2}$, $r_0 = 5 \text{ cm}$, and $t = 5 \times 10^{-5} \text{ s}$

The value $\gamma_{\lambda_0/20}^{\text{cw}} < 1$ can be reached if use is made of some types of reflector designs with efficient cooling [30].

Pulsed regime. The parameters of the optical surface stability under pulsed irradiation by a Gaussian-like laser beam having a duration τ and intensity I_0 in the centre of the irradiation region, determined by the ability to reach critical values T_{melt} , σ_{T} and $\lambda_0/20$ by temperature $T(0,0,\tau)$, thermoelastic stresses $\sigma_{ii}(0,0,\tau)$ and thermal deformations $W(0,0,\tau)$, have the form [29]:

$$\gamma_{T_{melt}}^{P} = \frac{2I_{0}A}{\sqrt{\pi}\lambda T_{melt}} \sqrt{a^{2}\tau},
\gamma_{\sigma_{T}}^{P} = 4\sqrt{\frac{3}{\pi}} \frac{I_{0}AG\alpha_{T}(1+\nu)}{\lambda G_{T}(1-\nu)} \sqrt{a^{2}\tau},
\gamma_{\lambda_{0}/20}^{P} = \frac{40(1+\nu)I_{0}A\alpha_{T}a^{2}\tau}{\lambda\lambda_{0}}.$$
(17.35)

The values of these parameters, found for copper, aluminium and molybdenum at $I_0A = 1 \text{ kW cm}^{-2}$, $K_0 = 2.82 \times 10^2 \text{ m}^{-2}$ and $\tau = 50 \, \mu \text{s}$, and the heat flow values I_0A , at which $\gamma_i^p = 1$, are presented in Table 17.1. In the cw regime, the optical surface properties are mainly degraded due to irreversible plastic deformations in the centre of the irradiation region. Under pulsed irradiation the behaviour of the thermal stress state is more complicated than under cw irradiation. Thus, in contrast to the stationary thermal stress state, the nonstationary state in the material of a solid is characterised by the presence of the nonzero components σ_{zz} and σ_{rz} . In this case, the highest value is reached by the component σ_{zz} on the z axis at a distance of $\sim 0.66r_0$ from the optical surface. If at some level of these I_0A values the

component σ_{zz} is greater than the strength modulus σ_b , it is possible to implement the conditions of brittle fracture, at which the surface layer of the POE material will be detached. For this type of destruction the parameter of the optical surface stability has the form:

$$\gamma_{\sigma_{\rm b}}^{\rm p} = \frac{4I_0 A E \alpha_{\rm T} a^2 \tau \sqrt{K_0}}{(1-\nu)\lambda \sigma_{\rm b}},$$

and the stability parameter defined with respect to plastic deformation, has the form:

$$\gamma_{\sigma_{\rm T}}^{\rm p} = \frac{\sqrt{3}I_0 A E \alpha_{\rm T} F_0}{\lambda \sqrt{K_0} (1 - \nu) \sigma_{\rm T}} \left[1 + 2 \frac{\sqrt{F_0}}{3\pi} \exp\left(-\frac{\sqrt{3}}{2F_0}\right) \right],\tag{17.36}$$

The values of the parameters and their corresponding intensities for Al, Mo and Cu are listed in Table 17.1.

Repetitively pulsed regime. The state of a solid body, whose surface is irradiated by repetitively pulsed laser pulses, combines the characteristic features of thermal stress states under pulsed and cw irradiation. In this case, for the temperature fields, the fields of the components σ_{rr} and $\sigma_{\varphi\varphi}$, the stress tensor and the thermal deformation fields the realisable temperature and thermal stress states are a combination of stationary and nonstationary states. In this regard, the stability parameters of the reflecting surfaces, defined by the ability of the temperature to reach the melting point of the material, of the components σ_{rr} and $\sigma_{\varphi\varphi}$ to reach the yield point and of thermal deformation to reach the threshold $\lambda_0/20$, are as follows [21]:

$$\gamma_i^{\text{PP}} = \text{SQV}\gamma_i^{\text{cw}} + \gamma_i^{\text{p}}.\tag{17.37}$$

Under repetitively pulsed irradiation, a nonstationary, cyclically repeated stress state arises on a solid surface in the material. As a result, the material of the solid body may experience irreversible fatigue damage. The conditions under which the POE surface undergoes macroscopic fatigue fracture can be assessed by Wohler curves, determining the dependence of modulus of the amplitude of fatigue stresses on the number of cycles of the loading pulses N_p [21, 31].

17.2.6 Irreversible Changes in the Optical Surface

Dynamics of the fatigue and brittle fracture is characterised by the emergence and extension of microcracks. Therefore, inadmissibility of destruction of the optical POE surface is dictated by the need to preserve the diffusely scattered component of laser radiation at negligible levels. Moreover, the origin and development of microcracks is accompanied by microstructural and phase transformations of the material, leading to a change in the structural and phase composition of the reflecting surface and, as a consequence—to an increase in its absorption coefficient *A*, whereas the adsorption of various substances on the resulting system of

microcracks initiating an optical breakdown leads to a decrease in radiation resistance of the reflecting surface. Furthermore, the optical breakdown of air near the target can occur without the segregation of impurities directly in the vicinity of emergence of microcracks, because they become the nucleus of the electric fields, etc. We considered sequentially the basic mechanisms of microstructural and phase transformations preceding the stage of plastic, fatigue and brittle fracture or accompanying these stages, as well as analysed the possible reasons for the change in the optical surface quality. The expressions obtained are important not only for the problems of power optics. They are effectively used today for the analysis of the conditions of fracture of solids of different nature due to excess of limiting stresses for the various components of the stress tensor.

17.3 Static OPEs Based on Materials with a Porous Structure

The feasibility of using porous structures for cooling thermally stressed POEs was justified theoretically and experimentally in our papers [32–39]. An increase in the optical damage threshold of laser reflectors based on porous structures was provided by a 'minimum' thickness of the separating layer (tens of microns), by the heat transfer intensification, by high permeability of the heat exchanger for the selected coolants pumped through the porous structure and by the use of the heat exchanger with a significantly developed surface. The test results of water-cooled POEs that are based on the porous structures indicated the possibility of removal of high heat flows at low values of the mirror surface deformations. The maximum density of the heat flow being removed, which does not lead to destruction of the mirror surface, was equal to 8.2 kW cm⁻². At q = 2 kW cm⁻² the value of thermal deformation was $\sim \lambda_0/20$, where $\lambda = 10.6 \,\mu\text{m}$ [32, 33].

A further increase in the optical damage threshold of cooled mirror surfaces can be realized by the optimization of the porous structure parameters [34, 38, 39], the appropriate choice of the coolant [21], the development of the technology of fabrication of a thin separating layer based on intermetallic compounds [32] and the rational design of the POE on the whole [35–37]. The development of a cooled POE requires a detailed study of heat and mass transfer in porous structures. These processes at the beginning of research in the field of high power/energy optics were either insufficiently studied or not studied at all.

17.3.1 Temperature Field in Porous Structures Under Convective Cooling

The temperature fields in porous structures are calculated in the one-dimensional formulation under the following assumptions: the incident radiation is uniformly

distributed over the irradiated surface; the thickness of the porous layer Δ_p is much greater than the depth of heating, which makes it infinitely large $(\Delta_p \to \infty)$ and allows consideration of the half-space model; and the temperature and velocity of the flow through the thickness the porous layer are constant. The heat transfer equation, which describes the temperature distribution over the thickness of the porous layer, can be written in the dimensionless form:

$$\frac{\mathrm{d}^2 \Theta}{\mathrm{d}\bar{\mathbf{r}}^2} = N(\Theta - 1),\tag{17.38}$$

where $\Theta=t/t_{\rm T}, \ \bar{x}=x/d_{\rm m}$ and $N=\tilde{\rm N} u N'$ are the dimensionless temperature, coordinate and Nusselt number, respectively; $d_{\rm m}$ is the mean diameter of the structure particles; $\tilde{\rm N} u=h_{\rm m}d_{\rm m}/\tilde{\lambda}$ is the modified Nusselt number, which characterises the ratio of the convective cooling to the heat transfer due to skeleton thermal conductivity; $N'=S_{\rm V}d_{\rm m}$ is a dimensionless parameter; and $S_{\rm V}$ is the heat transfer surface.

The boundary conditions of this equation can be written in the form:

$$\bar{x} = 0, \quad d\Theta/d\bar{x} = -\tilde{N}u\bar{q}\bar{x} \to \infty, \quad \Theta \to 1,$$
 (17.39)

where $\bar{q} = q/(h_{\rm m}t_{\rm T})$ is the dimensionless heat flux density and q is the heat flux density transmitted through the separating layer. The solution to this equation has the form [21, 34]

$$\Theta(\bar{x}) = 1 + \bar{q}\sqrt{\tilde{N}u/N'}\exp(-\sqrt{Nx}). \tag{17.40}$$

It follows from (17.40) that the rate of temperature decrease over the thickness of the porous structure is determined by the parameter \sqrt{N} . The maximum heat flux density, removed from the reflector due to convective cooling, follows from the condition of equality of the coolant temperature Θ_p at a fixed pressure to the boiling temperature Θ_{boil} of the coolant ($\Theta_p = \Theta_{\text{boil}}$) at a chosen pressure and has the form:

$$\bar{q}_{\text{max}} = (\Theta_{\text{boil}} - 1) \sqrt{N'/\tilde{\text{Nu}}}.$$
 (17.41)

The degree of heat transfer intensification in a porous structure as a result of the turbulent flow circulation and the surface development is determined by the coefficient K_{int} , which characterises the ratio of the amount of heat removed by the coolant in the structure under consideration to the amount of heat that would be removed directly from the cooling surface of the separating layer by the coolant when it flows in a slot gap of depth Δ [40]:

$$K_{\text{int}} = q/h_{\Delta}(t_{\bar{x}=0} - t_{\text{T}}),$$
 (17.42)

where h_{Δ} is the coefficient of convective heat transfer in the coolant flow in a slot gap. For example, for the turbulent regime of the coolant flow the Nusselt number has the form

$$Nu_{\Delta} = 0.023 Re^{0.8} \Pr^{0.4}, \tag{17.43}$$

where Re and Pr are the Reynolds and Prandtl numbers.

In the case of removal of heat fluxes, the depth of heating is [41]

$$\bar{\Delta}_{\text{max}} = N^{-1/2} \ln 10^2 (\Theta_{\text{boil}} - 1).$$
 (17.44)

In combination with the expressions describing the flow hydrodynamics, the obtained dependences are the basis for optimising the parameters of porous structures, ensuring minimal thermal deformations of POE surfaces or, if necessary, the maximum heat fluxes, removed in the case of convective cooling.

17.3.2 Convective Heat Transfer in a Porous Structure

The regime of the coolant flow in porous materials, which is of interest for high-power optics, is a transition between laminar and turbulent regimes. The criterion equation of the interporous convective heat transfer for gases and droplets can be represented in the form [41]

$$Nu = c(Re Pr)^n, (17.45)$$

where c and n are the constants depending only on the structural characteristics of the porous material.

Using known experimental data from the literature [42], we analysed the dependences of c and n on the structural characteristics of porous structures for which these constants are quite authentically known. As a result, we found that c and n depend mainly on the bulk porosity $\Pi_{\rm V}$. Thus, relation (17.45) for the dimensionless Nusselt number with account for correlation expressions $c(\Pi_{\rm V})$ and n ($\Pi_{\rm V}$) allows one to calculate the coefficient of convective heat transfer in porous structures.

17.3.3 Hydrodynamics of a Single-Phase Flow in a Porous Structure

The temperature field and thermal deformation of the POE are largely determined by the flow rate of the coolant pumped through a porous layer, which depends on the hydrodynamic characteristics and conditions of the coolant inlet and outlet. Hydrodynamic characteristics of a single-phase fluid flow in porous structures, mainly in the region $\Pi_V \le 0.5$, were studied in many experimental papers [41, 42]. In the general case, the hydrodynamics of the flow in porous structures is described by the modified Darcy's equation (Dupuit–Reynolds–Forchheimer equation) [43–45]:

$$-\frac{\mathrm{d}p_0}{\mathrm{d}r} = \alpha\mu_0 u + \beta\rho u^2,\tag{17.46}$$

where p_0 is the flow pressure; u is the filtration rate, equal to the ratio of the specific mass flow rate of the coolant G_0 to the density ρ ; α and β are the viscous and inertial resistance coefficients, respectively; and μ_0 is coefficient of dynamic viscosity of the coolant

From (17.46) we obtained the equation for the coefficient of friction, C_f , in the form

$$C_{\rm f} = 2/({\rm Re} + 2),$$
 (17.47)

where $C_{\rm f}=-2({\rm d}p_0/{\rm d}x)\rho/G_0^2\beta$ and ${\rm Re}=G_0\beta/\mu_0\alpha$ (the characteristic size β/α). Known also is a slightly different approach to the calculation of C_{f} : as a characteristic size use is made of \sqrt{K} , where K is the permeability coefficient, characterising the hydrodynamics of the flow according to Darcy's law $({\rm Re}_{\sqrt{K}}G\sqrt{K}/\mu)$, then

$$C_{\rm f} = 2\left(1/\text{Re}_{\sqrt{K}} + c\right)/c. \tag{17.48}$$

The relationship between the coefficients α , β and parameters c and K can be represented as $\alpha=1/K$ and $\beta=c/\sqrt{K}$. The parameter c is a universal constant for identical porous structures. For example, for all the materials made of metal powders with spherical or close-to-spherical particles $c\approx0.55$, and for materials made of powders of arbitrary particle shape 0.45 < c < 0.566. Thus, when calculating the hydraulic characteristics of the structures we assumed c=0.55, although in our case this provides a somewhat higher value of the friction coefficient $C_{\rm f}$.

The permeability coefficient K, which is a structural characteristic of a porous structure, does not depend on the flow regime and is determined experimentally from Darcy's law. In connection with the development of works in the field of heat pipes, many experimental data are currently available to determine K for powder and metal fibrous structures. The dependence of the permeability coefficient for metal fibrous structures on bulk porosity has the form [46]:

$$K = A\Pi_{V}^{m}, \tag{17.49}$$

where A and m are the coefficients depending on the relative length of the fibers Ud. Similar expressions can be obtained for powder porous structures. In addition,

the permeability coefficient is calculated from the known Carman–Kozeny relation [41]:

$$K = \varphi \Pi_{\rm V}^3 d_{\rm m}^2 / (1 - \Pi_{\rm V})^2 \approx \Pi_{\rm V}^3 / 5 S_{\rm V},$$
 (17.50)

where φ is a constant depending on the structure.

We used the expressions presented to determine the hydraulic characteristics of power optics elements utilising porous structures made of metal powders and metal fibrous structures.

17.3.4 Effect of the Coolant Inlet and Outlet Conditions on the Hydraulic Characteristics of the POE

Usually, in cooled POEs the coolant is supplied to and removed from the porous structure through evenly distributed alternating channels on the surface being cooled. In the case of inlets and outlets in the form of alternating holes we may deal with a significant nonuniformity of the velocity field in calculating the flow in radial directions. This leads to additional pressure drops in the circulation of the coolant, which are accounted for by the coefficient K_g . In this case, the total pressure drop in a porous structure has the form

$$\Delta P_0 = \Delta p_0 K_g,\tag{17.51}$$

where Δp_0 is the pressure drop in the case of a uniform velocity field.

The coefficient K_g , characterising the influence of collector effects on hydraulic resistance during the motion of the fluid in a porous structure, can be written as:

$$K_g = \frac{F}{\pi s^2 n (1 - a)} \frac{cG(1/a - 1)/\pi n \rho s \Delta - (v/\sqrt{K}) \ln a}{v\sqrt{K} + cv}.$$
 (17.52)

Here F is the area of the irradiated surface; n is the number of channels for the inlet (outlet) of the coolant; and $a = 2r_0/s$ is a relative spacing between the holes. One can see from (17.52) that K_g depends both on the geometric characteristics of the supply and removal of the coolant (on a) and on G; with increasing a and G, the coefficient K_g increases. Thus, the coefficient K_g characterises the design excellence of the inlet and outlet system of the POE coolant.

When K_g is known, the total pressure drop in the porous structure is calculated by formula (17.51), taking into account the expression for calculating Δp_0 :

$$\Delta p_0 = \nu \rho s (1 - a) \left(\nu / \sqrt{K} + c \nu \right) / \sqrt{K}, \tag{17.53}$$

where $v = Cs/(\rho F \Delta)$ is the coolant filtration rate.

17.3.5 Thermal Conductivity of Porous Structures in POEs

As for the problems of cooling of POEs, of interest is to study the thermal conductivity of a porous structure skeleton. In most cases, data are summarised in the form of the dependence $\tilde{\lambda}(\Pi_V)$ for the samples, manufactured using the single technology and the same type of material. In calculations use can be made of the Odolevsky equation [47]:

$$\tilde{\lambda} = \lambda_c \frac{1 - \Pi_V}{1 + \Pi_V},\tag{17.54}$$

where λ_c is the thermal conductivity of a compact material.

Effective thermal conductivity of metal fibrous felt structures may have a considerable anisotropy depending on the direction of the fibres in the felt. Usually, $\tilde{\lambda}$ is generalised by the relations [47]:

$$\tilde{\lambda}_{||} = \lambda_c (1 - \Pi_{V}) \exp(-\Pi_{V}), \tag{17.55a}$$

$$\tilde{\lambda}_{\perp} = \lambda_c (1 - \Pi_{\rm V})^2,\tag{17.55b}$$

where $\tilde{\lambda}_{||,\perp}$ is the effective thermal conductivity in the direction parallel and perpendicular to the felt-making plane. In the latter case one can also use the expression

$$\tilde{\lambda}_{\perp} = \lambda_c (1 - \Pi_{\rm V})^3. \tag{17.56}$$

The expressions presented satisfactorily approximate the experimental data [40, 47] and can be used in the determination of the thermal characteristics of cooled POEs made of metal fibrous structures. In this case, expression (17.55b) describes the upper limit of the experimental data (an optimistic estimate), and (17.56)—the lower (a pessimistic estimate).

17.3.6 Thermal Deformation of the Optical Surface

To assess small distortions of the optical surface, which are characteristic of POE deformation, we made an assumption of free expansion of the porous structure and the separating layer according to the temperature fields. Then, the thermal deformation of the mirror surface W^* is the sum of expansions of the separating (thickness Δ_s) and porous (thickness Δ) layers:

$$W^* = \alpha_s \Delta_s t_T [1/2(\Theta_1 + \Theta_2) - \Theta_0] + \alpha_p \Delta t_T [(1 - \Theta_0) + \bar{q} d_m / (N'\Delta)], \quad (17.57)$$

where α_s and α_p are the temperature coefficients of linear expansion of the separating and porous layers, respectively; $\Theta_i = t_i/t_T$ is the dimensionless temperature;

 t_0 is the coolant temperature at the inlet of the reflector; and t_1 and t_2 are the temperatures of the outer and inner surfaces of the separating layer, respectively.

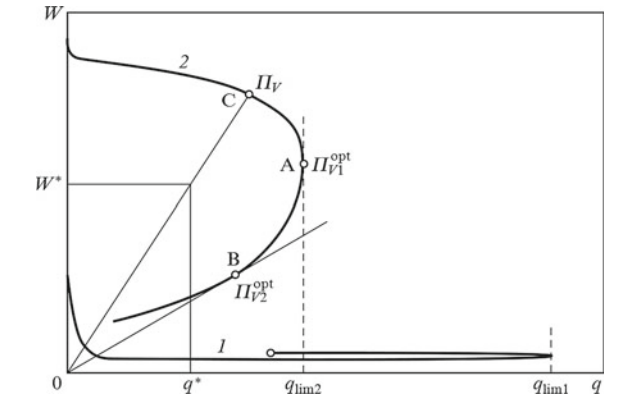
The above-derived expressions describing the processes of heat and mass transfer in porous structures were used to calculate the characteristics of cooled POEs.

Figure 17.12 shows the qualitative dependence of thermal deformation on the maximum density of the heat flow being removed (the variable Π_V at a constant d_m) for two selected regions of the reflector, corresponding to the regions of injection $[W_1^*(q_{\lim 1})]$ and outflow $[W_2^*(q_{\lim 2})]$ of the coolant. Varying the average grain size d_m (or the diameter of the fibre), we can construct a family of curves, characterised by a constant value of d_m and variable porosity V, for reflectors with the same type of the capillary structure. The curves were plotted at a constant pressure drop and by taking into account the coolant heating in the porous structure; in addition, the temperature of the coolant at the inlet was assumed equal to the POE temperature.

The deformation of the optical surface in the coolant outflow region is $W_2^* > W_1^*$; hence, crucial to the selection of the structural characteristics of the porous structure is curve (17.2), and the difference between curves (17.1) and (17.2) characterises the degree of perfection of the cooling system. The curves are the envelopes of the working thermal deformation characteristics of a family of reflectors with this type of structure. The performance characteristic of the reflector with a given porosity of the structure Π_V is obtained by connecting the straight line from point C with the origin of the coordinates. Point C corresponds to the maximum density of the heat flow, removed due to convective cooling, and the line segment 0C is a dependence of thermal deformations of the mirror surface on the heat load.

In general, curve (17.2) has two points: point A corresponding to optimal porosity Π_{V1}^{opt} which facilitates removal of the heat flow having the maximum density for the selected grain size, the coolant pressure drop, and coolant inlet and outlet conditions; and point *B* [the point of tangency of curve (17.2) with the straight line from the origin of the coordinates] corresponding to the porosity Π_{V2}^{opt} ,

Fig. 17.12 Qualitative dependence of thermal deformations on the maximum power density for the heat flow removed from two POE zones, corresponding to the regions of (1) injection and (2) outflow of the coolant



for which in the porous structure the optimal thermal distortions of the mirror surface are realised.

The choice of material and the basic parameters of the structure ($d_{\rm m}$ and $\Pi_{\rm V}$) must be based on a comparison of a family of curves (17.2) with possibilities of obtaining the desired porous structures and separating layers. In our review [14] we presented the results illustrating the feasibility of the experimental method and numerical calculations of thermal deformation characteristics of water-cooled POEs made of widely used copper and molybdenum powders.

17.3.7 Liquid-Metal Coolants in POEs Based on Porous Structures

In 1978, we were first to suggest that a further increase in the optical damage threshold of mirror surfaces of POEs based on porous structures is possible when liquid alkali metals and their alloys are used as coolants [38]. Prospects of utilising liquid-metal coolants in POEs were determined by the possibility of achieving a high heat transfer coefficient in the porous structure due to a favourable combination of thermophysical properties of liquid metals. This allowed one to lessen the requirements to the thermal conductivity of the porous structure material, which opened up the possibility of using new structural materials with a low thermal expansion coefficient and thermal conductivity in reflectors. Of particular interest was the employment of eutectic alloys of liquid metals with low melting points in POEs.

Consider some results of theoretical and experimental investigations of heat and thermal deformation characteristics of POEs cooled by the eutectic alloy Na–K. As part of earlier assumptions the heat transfer equation can be written as

$$\frac{\mathrm{d}^2 t}{\mathrm{d}x^2} = \frac{h_{\mathrm{e}}}{\tilde{\lambda}} S_{\mathrm{V}}(t - t_{\mathrm{T}}),\tag{17.58}$$

where $h_{\rm e}$ is the heat transfer coefficient between the porous structure material and the coolant. Due to the lack of published data on the heat transfer of liquid metals in porous structures, the lower bounds of the heat transfer coefficient were estimated by using the known data on the heat transfer of liquid-metal coolants in triangular arrays of nuclear reactor fuel elements [48]. To calculate the heat transfer of liquid metals in the nuclear fuel assemblies, use was made of the relations:

in densely packed structures (s/d = 1)

$$Nu = Nu_{lam} + 0.0408 \Big(1 - 1/\sqrt{1.24\epsilon + 1.15}\Big) Pe^{0.65}; \eqno(17.59)$$

in not densely packed structures (1.0 < s/d < 1.2)

$$Nu = Nu_{lam} + \frac{3.67}{90(s/d)^2} \times \left\{ 1 - \left[\frac{1}{\left[(s/d)^{30} - 1 \right]/6 + \sqrt{1.24\varepsilon + 1.15}} \right] Pe^{m_1} \right\};$$
 (17.60)

in not densely packed structures (1.2 < s/d < 2)

$$Nu = Nu_{lam} + 3.67Pe^{m_2}/90(s/d)^2.$$
 (17.61)

Here, $m_1 = 0.56 + 0.19s/d - 0.1/(s/d)^{80}$; Pe is the Peclet number;

$$Nu_{lam} = \left[7.55 \left(\frac{s}{d} - \frac{6.3}{(s/d)^{17(s/d)(s/d - 0.81)}}\right)\right] \left[1 - \frac{3.6}{(s/d)^{20}(1 + 2.5\epsilon^{0.86}) + 3.2}\right]$$

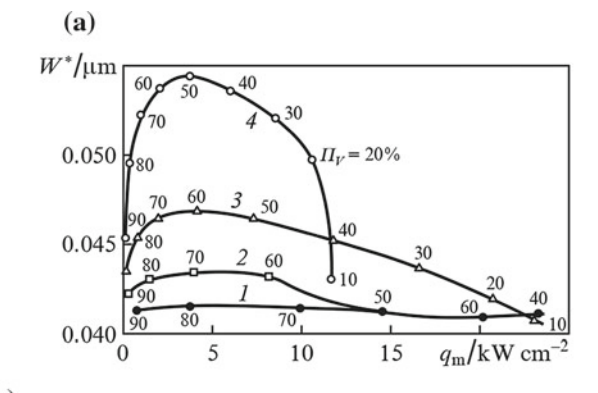
is the Nusselt number for the laminar flow; s/d is the relative spacing of the fuel elements in the array; and $\varepsilon = \lambda_{st}/\lambda_T$ is the ratio of the thermal conductivity of the fuel element cladding material to the thermal conductivity of the coolant. The relations (17.59)–(17.61) are valid for $\varepsilon > 0.01$ and 1 < Pe < 4000.

Assuming that the hydraulic diameter of the array of the fuel elements corresponds to the hydraulic diameter of the POE porous structure ($d_s = d_p$), and the diameter of a set of rods – to the wire diameter (for metal-fibrous porous structures), we can obtain the dependence $d_s = d_m \Pi_V / (1 - \Pi_V)$ for felt porous structures.

Figures 17.13 and 17.14 show the results of numerical calculations of thermal deformation characteristics of the POE cooled by the eutectic coolant Na–K. It was assumed that the porous structures of the reflectors were made of molybdenum and invar felt. The mean diameter of the felt and the bulk porosity of the structure varied within $20 \le d_{\rm m} \le 200~\mu{\rm m}$ and $0.1 \le \Pi_{\rm V} \le 0.9$. The curves in Figs. 17.13 and 17.14 are the envelopes of the thermal deformation characteristics of the POE family and plotted at a constant pressure drop of the coolant and a maximum temperature of the cooling surface equal to $100~^{\circ}{\rm C}$.

One can see from Fig. 17.13 that the deformation of the optical surface in the region of the coolant outlet, calculated with account for its heating in the porous structure, substantially exceeds the deformation in the region of the coolant inlet $(W_2^* > W_1^*)$. The maximum power densities of the heat flux for the POE in question are as follows: $q_1 > 20 \text{ kW cm}^{-2}$ in the region of the coolant inlet and $q_1 = 6.6 \text{ kW cm}^{-2}$ in the region of the coolant outlet; in this case, $W_2^* = 0.3 \,\mu\text{m}$. The minimum deformation W_2^* in the region of the coolant outflow at a power density of 4.2 kW cm⁻² is 0.12 $\,\mu\text{m}$, which is significantly lower than the optical damage threshold of the POEs for CO₂ lasers.

Analysis of the data in Fig. 17.14 shows that the use of porous structures made of materials with a low thermal expansion coefficient (invar fibres) allows one to significantly (approximately by 3–4 times) reduce thermal deformations of the



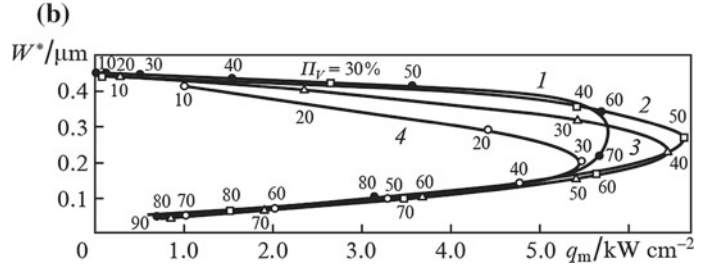


Fig. 17.13 Nomograms of thermal deformation characteristics of POEs based on metal-fibrous porous structures made of molybdenum, which are cooled by a Na–K coolant in the regions of its inlet (a) and outlet (b) at $d_{\rm m}$ = (1) 20, (2) 50, (3) 100 and (4) 200 μm

mirror surface both in the region of the coolant inlet and outlet in the case of liquid-metal cooling. Thus, the maximum thermal loads, experimentally allocated from the mirror surface, exceeded $10~kW~cm^{-2}$. The experimentally measured thermal deformations of POEs made of invar fibres in the region of minimum deformations were less than $0.5~\mu m$.

It should be noted that the results presented in Figs. 17.13 and 17.14 clearly show that liquid metals are very promising for POE cooling. Such cooling in combination with porous structures made of materials with relatively low coefficients of thermal expansion opens up fundamentally new possibilities for creating a class of very precise POEs with a high optical damage threshold.

Today, due to the accumulation of experimental data on convective heat transfer and hydrodynamics in porous structures, such structures are widely used in space instrumentation and nuclear power systems exposed to high radiation doses. Due to the structural features, metal porous structures have no blind pores, which eliminates unwanted thermal processes. They provide good permeability, high thermophysical characteristics, ability to use POEs at a boiling point of working fluids in heated regions, high heat transfer rates and high limiting values of critical heat fluxes. Metal porous structures exhibit good physicomechanical and performance characteristics. Metallurgical production technology ensures their stability and

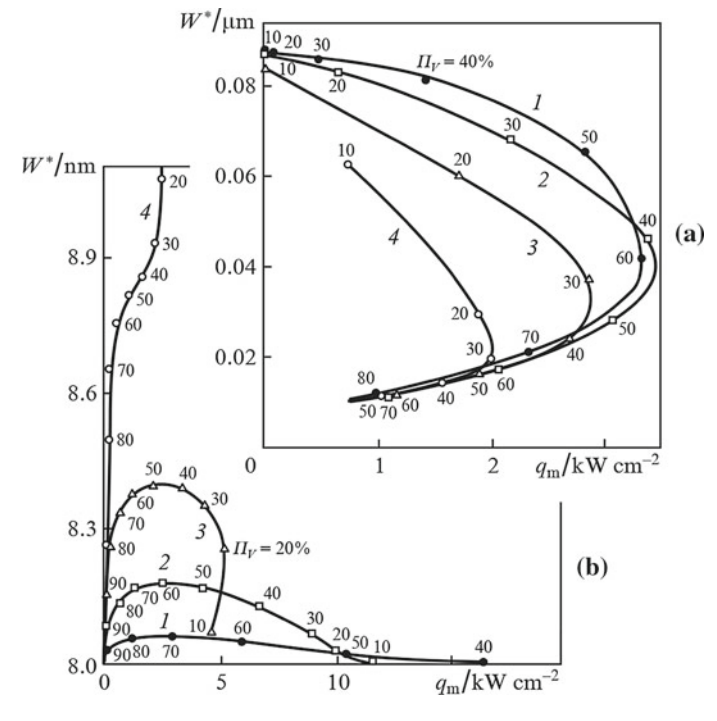
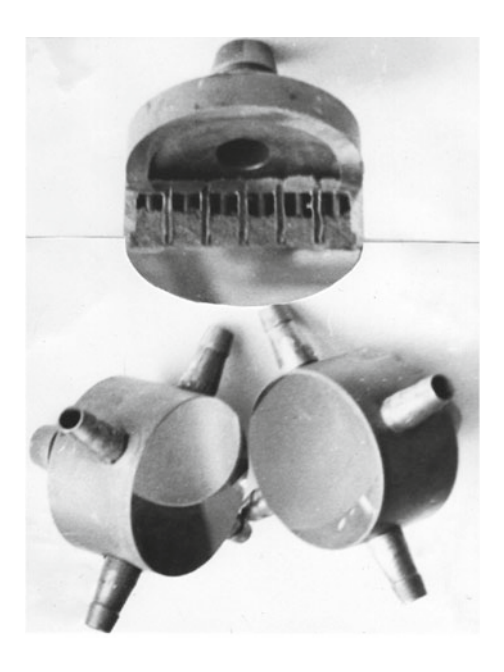


Fig. 17.14 Nomograms of thermal deformation characteristics of POEs based on metal-fibrous porous structures made of invar, which are cooled by a Na–K coolant in the regions of its inlet (a) and outlet (b) at $d_{\rm m}$ = (1) 20, (2) 50, (3) 100 and (4) 200 μm

Fig. 17.15 Cooled POE with a powder porous structure



reproducibility, long service life, and high reliability. One of the first mirrors based on porous structures is shown in Fig. 17.15.

The new areas of research, which have been successfully developed recently, include the study of boiling on surfaces with porous coatings with their structural and hydrodynamic characteristics taken into account, the study of the influence of these characteristics on the contact thermal resistance between the porous and solid layers, and the study of heat transfer during condensation of liquids on the working surfaces of porous structures. It should be noted that our investigations of heat transfer in porous structures made it possible to develop the technological basis for creating a series of water-cooled mirrors for power lasers by employing chemical etching of metal foils with subsequent soldering to fabricate a multilayer heat exchanger with a moderate degree of development of the heat exchange surface [49–52].

17.4 Adaptive POEs and Optical Systems Based on Them

The variety of the phenomena that change the optical characteristics of the medium in the propagation path of radiation and in the optical system of the laser-leads to degradation of the quality of the wavefront (WF), which is manifested by a significant increase in the angular divergence of the generated beam and by a reduction in the peak intensity upon focusing. Most fully the entire range of requirements to WF correctors in adaptive optics systems is met by POEs with adjustable shape of the reflecting surface, in which the WF distortion are compensated for by changing the shape of the mirror surface. In this case it is possible: (1) to fabricate cooled and uncooled adaptive POEs with a high optical damage threshold in a wide range of radiation exposures [21, 53]; (2) to produce adaptive optics systems for the entire set of currently known schemes for generation of cw and repetitively pulsed laser radiation in wavelengths ranging from far-IR to ultraviolet; and (3) to manufacture adaptive POEs for correcting and measuring non-stationary phase distortions in the time interval up to several milliseconds, by selecting the substrate materials of the mirror surface which provide their predetermined static and dynamic deformation properties [54–56].

The most challenging, in our view, is the realisation of adaptive POEs with a high optical damage threshold of the reflecting surface, because it is necessary in this case to combine the shape and cooling control systems in the reflector. Our approach to creating adaptive POEs was based on the methods of forced heat removal for cooling the mirror surface while shaping the reflecting surface by controlled elastic deformation of the porous structure of the heat exchanger.

Prospects of our proposal consisted in the possibility of providing the necessary static and dynamic deformation and thermal characteristics of adaptive POEs, because the use of porous structures allows one to implement the optical damage threshold (up to several tens of kW cm⁻²) of the mirror surface, whereas their use as a substrate material of the mirror surface having low stiffness enables control of the

shape of the reflecting surface in a wide range of local displacement amplitudes of its individual regions. Moreover, since in the operating condition the material of the porous heat exchanger of an adaptive POE is filled with a liquid coolant, natural resonant oscillations of the mechanical design of the adaptive POE may be effectively damped in the dynamic regime of the device operation.

Studies on modelling the correction of basic WF distortions by the adaptive POE, determining the optical quality of the intense laser radiation flux (including the WF tilt, defocusing, spherical aberrations), showed that at a consistent satisfaction of the power optics requirements, involving realisation of high values of the optical damage threshold (the porous structure thickness of the exchanger must be several millimetres), inaccuracy of conjugation of the WF shape with the shape of the reflecting surface for CO_2 laser radiation is $\lambda_0/10 - \lambda_0/20$ using a control system with 50–60 actuators on the aperture of the adaptive POE up to 100 mm in length.

Along with the well-known solutions [56, 57], our approach to creating adaptive POEs is very promising in the development of adaptive optics systems for high-power lasers [58–63]. However, its implementation required complex investigations to establish the peculiarities of dynamic and static regimes of deformation of porous structures, to study the influence of the processes of internal friction in porous materials on the dynamics of their cyclic loading, to determine the effect of anisotropy of mechanical properties of the structure on the form of the response function of the reflecting surface, to establish an optimal (for these devices) control of an adaptive optical system, and to create new types of actuators with high energy capacity. It is important to note the major role of the design bureaus headed at that time by B. V. Bunkin and N. D. Ustinov in achieving these goals.

Great importance in the development and creation of adaptive POEs with specified static and dynamic characteristics was given to actuators providing the required amplitudes of deformation over a wide dynamic range. Solutions related to the use of piezoelectric materials in physical problems associated with adaptive POEs are not free from drawbacks. These include the need for high strains required for the realisation of amplitude displacements and the inevitability of hysteresis phenomena that hinder the formation of a phase-conjugated laser beam WV by the relief of the reflecting surface. In the regimes of 'modulation' and 'phase conjugation' the amplitudes of local displacements of the reflecting surface should reach $0.1-0.5\lambda_0$ and $1-5\lambda_0$, respectively. To ensure such displacement amplitudes we proposed adaptive POE actuators of new types, which are made of magnetostrictive materials and implement the conditions for the Joule and Wiedemann effects [62, 63]. At the same time we pointed out the prospect of creation of compact highly efficient actuators, providing a stable amplitude displacement in the frequency range up to 10 kHz.

The employment of the designed and built adaptive POEs utilising porous structures is not confined to adaptive optics, although in this field they solve a number of important problems. According to the results of modelling intracavity optical systems [64–68], the use of adaptive POEs allows one to obtain the diffraction angular divergence of radiation fluxes when use is made of unstable resonators in high-power carbon dioxide laser systems. Adaptive POEs were

essentially a new type of devices ensuring the local control of phase characteristics of coherent radiation fluxes. As a result, they served as prototypes for different laser beam modulation, selection and scanning devices. For example, the use of an adaptive POE in the laser cavity made it possible to convert high-power cw radiation into high-frequency repetitively pulsed radiation by *Q*-switching [68], and the employment of adaptive POEs in a Fabry–Perot interferometer allowed for automated analysis of spectral and modal composition of laser radiation, etc. Undoubted are the advantages of this class of adaptive POEs in traditional applications of adaptive systems, such as laser ranging. Here we should mention paper [57], which presents the characteristics of a number of adaptive mirrors.

17.5 Large POEs Based on Multilayer Honeycomb Structures

Actual operating conditions of large POEs put forward in most cases contradictory requirements, significantly complicating the process of their manufacture. With low weight and high specific stiffness, large POEs should continue to operate under intense unilateral heating and rapidly changing ambient temperature. However, increasing the size of the POEs, while preserving the predetermined level of the optical surface distortion, dramatically increases their mass. To reduce the weight of large POEs while maintaining the stiffness of their structures, along with new approaches such as the use of materials with synthesised physical and technical properties promising is also the search for new solutions to the problem. In some cases, the POE weight is reduced by creation of internal voids with relatively large cells. This allows one to decrease the POE weight by 6–7 times for the value of optical surface distortion by its own weight, which is 0.7–0.8 of monolithic mirror distortion. However, it is difficult to create a system of thermal stabilisation without significant loss of rigidity in POEs with large internal voids.

An alternative way to reduce the weight of bulky POEs, as in the case of highly loaded POEs, is the use of highly porous honeycomb materials [69, 70]. We theoretically and experimentally investigated the possibility of creating lightweight bulky POEs based on multilayer honeycomb structures. Such structures have a relatively small mass at high specific stiffness, good thermal insulation properties and high absorption of elastic vibrations. Multilayer structures also provide the ability to create a highly efficient system of thermal stabilisation.

In the case of axisymmetric thermal loading the problem of thermal distortions of the optical surface of a cooled multilayer honeycomb POE was solved in [71]. In this case, to calculate the temperature fields in a large POE, we considered the problem for a multilayer cylinder whose end and side surfaces were heated, and inside the layers the heat was removed by a coolant. Thermal deformations W^* of the optical surface were determined as the sum of the normal thermal expansion of the POE and its bending

$$W* = W_{\rm n}^* + W_{\rm bend}^*, \tag{17.62}$$

where $W_n^* = \int_0^H \beta(z) T(z, r) dz$ is the normal extension; $\beta(z)$ is the linear expansion coefficient; T(z, r) is the temperature; and H is the POE thickness.

Bending was determined from the equation

$$abla^4 W_{\mathrm{bend}} = -
abla^2 \frac{M_{\mathrm{T}}}{D},$$

where

$$M_{\rm T} = \int\limits_{z_0-H}^{z_0} \frac{E\beta z}{1-\nu} T(z,r) \mathrm{d}z$$

is the temperature moment;

$$D = \int_{z_0 - H}^{z_0} \frac{Ez^2}{1 - v} \mathrm{d}z$$

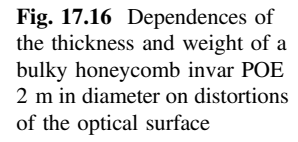
is the bending stiffness; and E is Young's modulus. Poisson's ratio \tilde{v} and the position of the neutral surface were determined from the conditions

$$\int_{z_0 - H}^{z_0} \frac{E}{1 - v^2} (\tilde{v} - v) dz = 0, \qquad \int_{z_0 - H}^{z_0} Ez dz = 0,$$

$$W_{\text{bend}}(r) = C_1 + C_2 \ln r + C_3 r^2 + C_4 r^2 \ln r + \frac{1}{D} \int_0^2 \frac{1}{\rho} \int_0^{\rho} \xi H(\xi) d\xi d\rho,$$
(17.63)

and the constants C_1 , C_2 , C_3 and C_4 -from the boundary conditions.

Studies showed [72, 73] that for the absorbed heat flux equal to $\sim 10~\rm W~cm^{-2}$ the optical surface distortions of the POE based on multilayer honeycomb invar structures do not exceed 0.7 μm at the POE diameter of 1 m. Constant thermal stabilisation (time needed to reach steady-state operation), which is determined from the solution of the nonstationary problem, for such structures is a few tenths of a second. A peculiar feature of lightweight honeycomb POEs is the fact that a relatively non-rigid filling material may experience a shear strain and transverse compression, significantly affecting the POE operation. In this connection, there appeared a problem of its optimisation, which was considered in the framework of nonlinear programming. The relative displacement of the POE surface under the influence of gravitational, mechanical and thermal loadings was determined by the finite element method [73].



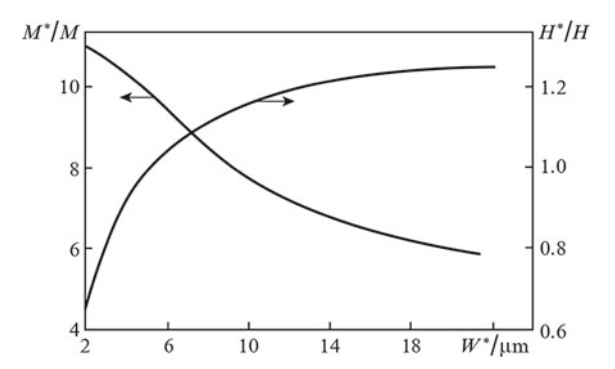


Figure 17.16 shows the dependence of M^*/M and H^*/H on the allowable distortion W^* of the optical surface of the POE under its own weight. Here M^* and H^* are the weight and thickness of a circular monolithic plate, and M and H are the weight and thickness of the three-layer honeycomb invar structure with a diameter of 2 m. It can be seen that the effectiveness of the multilayer honeycomb structure increases with toughening the requirements for an acceptable distortion of the optical surface. Figure 17.16 also shows that for certain ratios of the structural parameters, the optical surface distortion can be minimised. The example of employment of multilayer honeycomb structures during the manufacture of large POEs 1 m in diameter is shown in Fig. 17.17. Lightweight bulky POEs made of invar are currently used in laser facilities and confirm their high efficiency. This class of POEs is described in detail in [74].

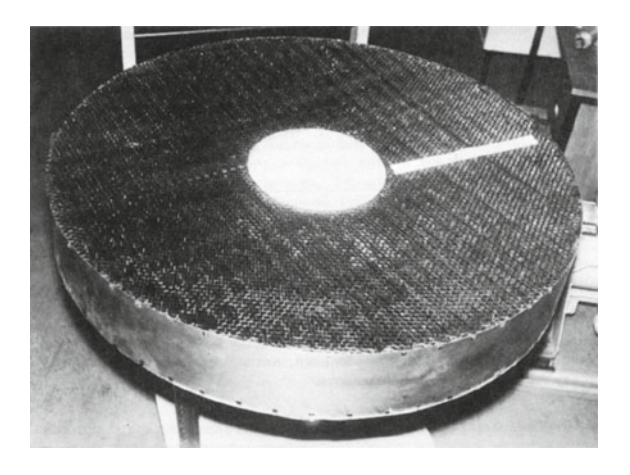
17.6 Large POEs Based on Composite Materials

Progress in this area is largely provided by the rapid development of new technologies and the synthesis of materials with fundamentally new properties. The need for such a development is associated with an ever-expanding range of problems faced by modern science and practice.

A common disadvantage of large POEs made of glass, glass ceramics, fused quartz and other materials, which are used in optical astronomy and laser technology, is their low thermal conductivity. Such mirrors cannot be used effectively in unilateral heating and technological features of their production do not allow one to significantly reduce weight and ensure effective thermal stabilisation.

Good results in the fabrication of lightweight large POEs have been achieved using composite materials, the methods of their manufacture being well developed [75–78]. Of greatest interest is the silicon infiltrated carbon-fibre-reinforced silicon carbide composite. The process is based on the deposition of carbon on a free surface during gas phase pyrolysis. Precipitating carbon strengthens frame filaments and combines them into a rigid three-dimensional lattice. The thus obtained porous

Fig. 17.17 Preform of a large multilayer honeycomb invar POE 1 m in diameter



silica preforms are impregnated with silicon melt in an inert atmosphere. By varying the amount of silicon and impregnation temperature, one can produce samples, significantly different in porosity and phase composition. One can also fabricate virtually carbide porous structures with advanced open porosity, which, except for weight reduction, provides an effective system for thermal stabilisation. Heat treatment removes residual stresses in the composite, increasing its structural stability.

A significant weight reduction of POEs while maintaining their specific rigidity can be achieved also by creating a honeycomb structures. For a honeycomb frame to be manufactured, we used the slip-casting method. Specially prepared slip mass was poured into a mold and polymerised. After removal of the mold the preform was annealed and siliconized.

Fig. 17.18 Honeycomb frame of the POE

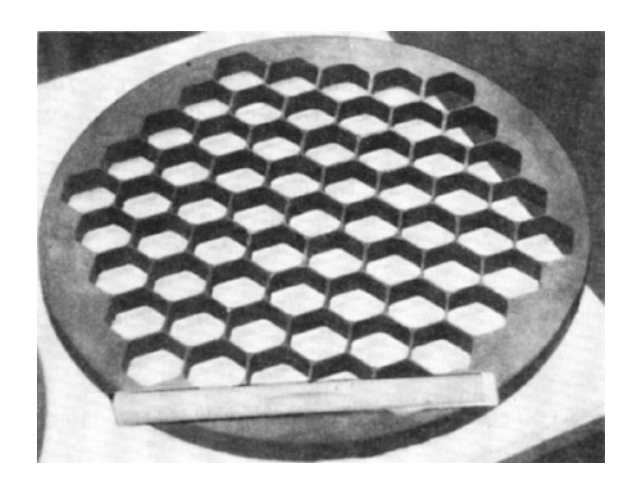
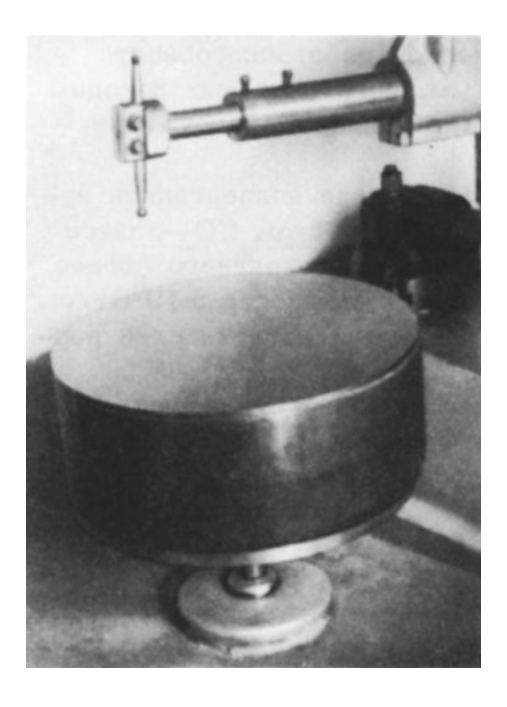


Figure 17.18 shows a honeycomb frame, produced by the slip-casting method. By joining the resultant honeycomb frame with monolithic plates made of the same material one can form a multilayer honeycomb structure with highly efficient thermal stabilisation.

Figure 17.19 shows a photograph of a lightweight uncooled POE 500 mm in diameter, placed on a polishing/lapping machine. A highly reflecting coating was deposited on the optical surface of the silicon carbide wafer having a surface roughness of $0.010~\mu m$.

The optical damage threshold of cooled and uncooled POEs based on silicon infiltrated carbon-fibre-reinforced silicon carbide composites was measured experimentally, high power densities being simulated by the electron beam heating facility we developed [79–81]. The POE was installed in a vacuum chamber and served as an anode of an electro-optical system. The optical damage threshold of the cooled POE 500 mm in diameter was achieved under thermal loading by an electron beam with a power density of $\sim 300~{\rm W~cm^{-2}},$ which at characteristic values of the reflection coefficients of the POE materials for laser radiation is equivalent to a power density up to a few tens of kW cm $^{-2}$. Significant expansion of the range of new materials and the development of modem processing methods and technologies of their connection favours the manufacture of effective large POEs made of C/SiC materials based with record-high thermal stabilisation and high optical performance.

Fig. 17.19 Large POE 500 mm in diameter on a polishing dapping machine



17.7 High Power/Energy Optics and Its New Applications

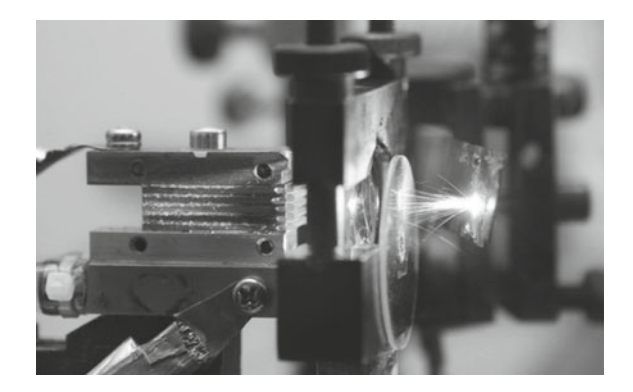
17.7.1 Cooling of Laser Diode Assemblies

One of the brightest and most promising implementations of the ideas of power optics is now the introduction of forced heat transfer in high power/energy semi-conductor lasers, which are widely used today to pump solid-state lasers having active elements of different geometry: rods, disks, slabs, fibres [82–86]. Solid-state lasers have the highest efficiency reaching 80% in some case. Modem manufacturing technologies of semiconductor structures made it possible to significantly increase the laser lifetime (tens of thousands of hours of continuous operation). The variation of the semiconductor material composition can change the wavelength range of radiation from the near-IR to the UV. These lasers are very compact, reliable and easy to operate. The power output can be increased by the simultaneous use of a large number of laser diodes, which are formed in one-dimensional or two-dimensional effectively cooled structures (Fig. 17.20).

Cooled laser diode assemblies possess almost all the remarkable properties of single semiconductor lasers: high intensity, high reliability and long lifetime. These lasers have much smaller weight and size dimensions in comparison with other types of lasers, can easily be fed from independent low-voltage power supplies (solar, nuclear energy) without bulky transformers. Equipment based on laser diode assemblies really becomes a reliable high-performance instrument that can be used in industry, medicine, research and military applications.

The stability of operation of laser diode assemblies and the value of their output are completely determined by the heat transfer efficiency. Laser diode arrays are soldered with a low-temperature solder to the surface of the heat exchanger, which is produced in accordance with high-power optics technology. It should be noted that the levels of heat fluxes which are to be removed from the contact region of the array with the heat exchanger have already approached the characteristic values of the power optics and are equal to several hundreds of W cm⁻² [87, 88].

Fig. 17.20 Cooled laser diode assembly



17.7.2 New Generation of High Power/Energy Optics Based on Silicon Carbide

Currently, the development of high-power optics stimulates three trends of efficient use of its technical and technological solutions:

- lightweight, highly stable, large ground- and space-based telescopes for studying the universe and transmitting energy over long distances;
- astronomical optical instruments for remote sensing of the Earth and near space from spacecrafts;
- highly efficient cooled POEs for high-power lasers and laser systems.

All the three trends are based on cutting-edge technologies. The choice of the POE material is a key issue in production of a new generation of optical objects. Thus, a bulky silicon carbide POE has a weight that is 7–10 times lower than that of the POE made of glass ceramics, the best quality in terms of radiation scattering, high thermal stability and a minimum time constant (Fig. 17.21). Comparative evaluation of materials with the help of optical quality criteria developed by us in the early 1970s showed that silicon carbide has a distinct advantage over traditional materials [19, 20]. This conclusion is consistent with more recent conclusions of foreign experts from Germany, France, Japan and China. It is appropriate here to note the contribution of acad. E. P. Velikhov, who initially supported the creation of the technology of silicon carbide production and the development of large optics [89–93].

Obviously, the development of bulky POEs for high power/energy lasers and transition to a new generation of space-based telescopes is accompanied by the introduction of silicon carbide and related technologies into everyday practice.

Fig. 17.21 Silicon carbide POE



17.8 Conclusions 295

17.8 Conclusions

In concluding this chapter of theoretical and experimental works in the field of high power/energy optics we should note one very important point: Effective development of any of the areas of modem cutting-edge technologies, as a rule, gives a result not only in the related fields of technological applications, but also in completely different branches of science and technology. Thus, the appearance of one-and two-dimensional cooled high-power laser diode arrays, large astronomical cooled POEs based on silicon carbide and complex composite materials is largely a consequence of the success of power optics [94–99]—a recognized effective donor for many areas of science and advanced technology of the XXI century. Its successful development continues.

References

- A.I. Barchukov, N.V. Karlov, V.K. Konyukhov, Y.B. Konev, B.B. Krynetskii, V.M. Marchenko, Y.N. Petrov, A.M. Prokhorov, D.V. Skobel'tsyn, A.V. Shirkov, *Otchel FIAN (FIAN Report)* (Moscow, 1968–1970)
- A.I. Barchukov, Y.B. Konev, A.M. Prokhorov, Radiotekh. Electron. 15, 2193 (1970)
- 3. A.I. Barchukov, Y.B. Konev, A.M. Prokhorov, Radiotekh. Electron. 16, 996 (1971)
- V.V. Apollonov, A.I. Barchukov, V.K. Konyukhov, A.M. Prokhorov, Otchel FIAN (FIAN Report) (Moscow, 1971)
- V.V. Apollonov, A.I. Barchukov, V.K. Konyukhov, A.M. Prokhorov, Otchel FIAN (FIAN Report) (Moscow, 1972)
- V.V. Apollonov, A.I. Barchukov, V.K. Konyukhov, A.M. Prokhorov, Pis'ma Zh. Eksp. Teor. Fiz. 15, 248 (1972)
- 7. V.V. Apollonov, A.I. Barchukov, A.M. Prokhorov, *Proceedings of the First European Conference on 'Lasers and Applications'* (Drezden, GDR, 1972)
- 8. V.V. Apollonov, A.I. Barchukov, V.K. Konyukhov, A.M. Prokhorov, Kvantovaya Elektron. **3**(15), 103 (1973) [Sov. J. Quantum Electron. **3**(3), 244 (1973)]
- V.V. Apollonov, A.I. Barchukov, A.M. Prokhorov, Proceedings of the Second European Conference on 'Lasers and Applications' (Drezden, GDR, 1973); Preprint FIAN No. 157 (Moscow, 1973)
- V.V. Apollonov, A.I. Barchukov, A.M. Prokhorov, Otchet FIAN (FIAN Report) (Moscow, 1973)
- 11. A J. Glass, A.H. Guenther, Appl. Opt. 12, 34 (1973)
- 12. S.J. Cytron, *Memorandum Report M73-I7-1* (Philadelphia, PA, 1973)
- D.H. Jacobson, W. Bickford, J. Kidd, R. Barthelemy, R.H. Bloomer, AIAA paper no. 75-779 (1975)
- 14. V.V. Apollonov, Laser Phys. 23, 1 (2013)
- 15. V.V. Apollonov, A.I. Barchukov, A.M. Prokhorov, Radiotekh. Electron. 19, 204 (1974)
- V.V. Apollonov, A.I. Barchukov, A.M. Prokhorov, IEEE J. Quantum Electron. 10, 505 (1974)
- 17. V.V. Apollonov, Preprint FIAN no. 105 (Moscow, 1973)
- 18. A.I. Barchukov, Doctor Dissertation (Moscow, FIAN, 1974)
- 19. V.V. Apollonov, A.I. Barchukov, A.M. Prokhorov, Kvantovaya Elektron. 2, 380 (1975)
- 20. V.V. Apollonov, Cand. Dissertation (FIAN, Moscow, 1975)
- 21. V.V. Apollonov, *Doctor Dissertation*. (FIAN, Moscow, 1982)

- 22. H. Parkus, *Instalionare Warmespannyngen* (Springer, Wien, 1959; Fizmatgiz, Moscow, 1963)
- 23. W. Nowacki, *Problems of Thermoelasticity* (PWM-Polish Scientific Publishers, Warszawa, 1960; Izd. AN SSSR, Moscow, 1962)
- 24. E. Jahnke, F. Emde, F. Losch, *Tafeln Hoherer Funktionen* (Verlagsgesellschaft, Stuttgart, 1960; Nauka, Moscow, 1964)
- L.S. Tsesnek, O.V. Sorokin, A.A. Zolotukhin, Metallicheskie zerkala (Mashinostroenie, Moscow, 1983)
- V.V. Apollonov, F.V. Bunkin, S.A. Chetkin, Tez. Dokl. I Vsesoyuz. Konf. 'Problemy upravleniyaparametrami lazernogo izlucheniya' (Proceedings. I All-Union Conference on Problems of Controlling Parameters of Laser Radiation) (Tashkent, 1978)
- V.V. Apollonov, A.I. Barchukov, A.M. Prokhorov, Tez. Dokl V Vsesoynzn. Soveshchaniya po neresonansnomu vzairnodeistviyu opticheskogo izlucheniya s veshchestvom (Proceedings. V All-Union Meeting on Nonresonant Interaction of Optical Radiation with Matter) (Leningrad, 1978)
- 28. H.E. Bennet, J.O. Porteus, J. Opt. Soc. Am. 51, 123 (1961)
- 29. V.V. Apollonov, A.M. Prokhorov, S.A. Chetkin, Kvantovaya Elektron. 8, 2208 (1981)
- 30. V.V. Apollonov, P.I. Bystrov, V.F. Goncharov, A.M. Prokhorov, *Aulh. Cert. No. 135237* (priority date 08 Dec 1978)
- 31. T. Yokobori, An Interdisciplinary Approach to Fracture and Strength of Solids (Wolters-Noordhoff, Groningen, 1968; Mir, Moscow, 1971)
- 32. V.V. Apollonov, A.I. Barchukov, A.M. Prokhorov, *Otchet FIAN (FIAN Report)* (Moscow, 1977)
- V.V. Apollonov, A.I. Barchukov, A.M. Prokhorov, Auth. Cert. No. 103162 (priority date 24 May 1977)
- 34. V.V. Apollonov, A.I. Barchukov, A.M. Prokhorov et al. *Kvantovaya Elektron.* 5, 1169 (1978) [Sov. *J. Quantum Electron.* 8, 672 (1978)]
- 35. V.V. Apollonov, A.I. Barchukov, A.M. Prokhorov et al. Auth. Cert. No. 135238 (priority date 08 Dec 1978)
- V.V. Apollonov, A.I. Barchukov, A.M. Prokhorov, Auth. Cert. No. 144371 (priority date 19 Jan 1979); V.V. Apollonov, A.M. Prokhorov et al. Auth. Cert. No. 142696 (priority date 29 May 1979)
- V.V. Apollonov, A.I. Barchukov, A.M. Prokhorov, Proc. Laser Opt. Conf. (Leningrad, 1980)
 p. 43
- 38. V.V. Apollonov, A.M. Prokhorov, *Kvantovaya Elektron.* **8**, 1328 (1981) [Sov. *J. Quantum Electron.* **11**, 796 (1981)]
- V.V. Apollonov, A.M. Prokhorov, *Kvantovaya Elektron.* 8, 1331 (1981) [Sov. J. Quantum Electron. 11, 798 (1981)]
- 40. V.P. Isachenko, V.A. Osipov, A.S. Sukomel, *Teploperedacha (Heat Transfer)* (Energiya, Moscow, 1969)
- 41. V.A. Mayorov, Teploenergetika 1, 64 (1978)
- 42. W.M. Kays, A.L. London, *Compact Heat Exchangers* (McGraw Hill, New York, 1984; Moscow: Energiya, 1967)
- 43. J. Dupuit, Eludes Theoretiques et Pratiques sur le Movement des Eaux (Paris, 1863)
- 44. P. Deitrich et al., Flow and Transport in Fractured Porous Media (Springer, Berlin, 2005)
- 45. P. Forcheimer, Vereines deulscher Ingenieure, 45 (1901)
- 46. G.S. Beavers, E.M. Sparrow, J. Appl. Mech. 36, 711 (1969)
- 47. S.V. Belov, *Poristye materialy* v *mashinoslroenii* (Porous Materials in Mechanical Engineering) (Mashinostroenie, Moscow, 1967)
- 48. V.I. Subbotin, M.K. Ibragimov, P.A. Ushakov, *Gidrodinamika i teploobmen v atomnykh reactorakh* (Hydrodynamics and Heat Exchange in Nuclear Reactors) (Atomizdat, Moscow, 1975)
- V.V. Apollonov, B.V. Bunkin, L.N. Zakhar'ev, N.N. Polyashev, A.M. Prokhorov, Auth. Cert. No. 152944 priority date 14. Feb 1980

References 297

- 50. V.Y. Khomich, Cand. Dissertation (FIAN, Moscow, 1981)
- 51. V.V. Apollonov et al., Kvantovaya Elektron. 8, 2208 (1981)
- 52. Y.P. Voinov, Cand. Dissertation (NPO 'Almaz', Moscow, 1982)
- 53. S.A. Chetkin, Cand. Dissertation (FIAN, Moscow, 1983)
- 54. V.V. Apollonov, A.M. Prokhorov, Izv. Akad Nauk SSSR. Ser. Fiz. 8, 48 (1984)
- V.V. Apollonov, S.A. Chetkin, A.M. Prokhorov, Proceedings of the Boulder Laser Damage Symposium. XVI (NBS-Boulder, Colorado, USA, 1984)
- 56. A.G. Safronov, Cand. Dissertation (GPI, Moscow, 1996)
- 57. O.I. Shanin, *Shirokoaperturnaya silovaya adaptivnaya optika* (Wide-Aperture Adaptive Power Optics) (Fotonika, Moscow, 2012)
- 58. V.V. Apollonov, S.A. Chetkin, *Kvantovaya Elektron.* 15, 2578 (1988) [Sov. J. Quantum Electron. 18, 1621]
- 59. V.V. Apollonov, A.M. Prokhorov, Pis'ma Zh. Tekh. Fiz. 14, 3 (1988)
- V.V. Apollonov, A.M. Prokhorov et al., Kvantovaya Elektron. 18, 358 (1991) [Sov. J. Quantum Electron. 21, 325 (1991)]
- 61. V.V. Apollonov, A.M. Prokhorov, *Proceedings of the Boulder Laser Danuige Symposium.* XX (NBS-Boulder, Colorado, USA, 1989)
- 62. V.V. Apollonov, V.I. Borodin, A.S. Brynskikh, S.I. Zienko, S.V. Murav'ev, S.N. Temnov, Kvantovaya Elektron. 16, 386 (1989)
- 63. V.V. Apollonov, A.M. Prokhorov, Kvantovaya Elektron. 17, 1496 (1990)
- 64. V.V. Apollonov, D.V. Artemov, V.I. Kislov, Kvantovaya Elektron. 203 (1993)
- 65. V.V. Apollonov, D.V. Artemov, V.I. Kislov, Kvantovaya Elektron. 577 (1994)
- 66. V.V. Apollonov, V.I. Kislov, Kvantovaya Elektron. 23, 999 (1996)
- 67. V.V. Apollonov, V.I. Kislov, A.M. Prokhorov, Kvantovaya Elektron. 23, 1081 (1996)
- 68. V.V. Apollonov, V.I. Kislov, A.G. Suzdaltsev, Kvantovaya Elektron. 33, 753 (2003)
- 69. V.V. Apollonov, A.M. Prokhorov, Pis'ma Zh. Tekh. Fiz. 14, 236 (1988)
- 70. V.V. Apollonov et al., Pis'ma Zh. Tekh. Fiz. 15, 3 (1989)
- 71. V.V. Apollonov, A.M. Prokhorov, G.I. Babayants, Pis'ma Zh. Tekh. Fiz. 16, 2 (1990)
- 72. V.V. Apollonov, A.M. Prokhorov, Pis'ma Zh. Tekh. Fiz. 17, 655 (1991)
- 73. V.A. Shmakov, *Doctor Dissertation* (GPI, Moscow, 1997)
- 74. V.A. Shmakov, Silovaya optika (Nauka, Moscow, 2004)
- V.A. Alekseev, V.N. Antsifirov, V.V. Apollonov, S.V. Bilibin, M.G. Gadzhiev, A. P. Kunevich, E.A. Narusbek, A.M. Prokhorov, Pis'ma Zh. Tekh. Fiz. 11, 1350 (1985)
- 76. V.V. Apollonov, V.S. Kolesov, A.M. Prokhorov et al., Pis'ma Zh. Tekh. Fiz. 16, 79 (1990)
- 77. V.V. Apollonov, G.I. Babayants, M.V. Gartman, V.M. Golomazov, Y.D. Loktionov, Y.M. Pirogova, G.V. Plotsev, A.M. Prokhorov, Pis'ma Zh. Tekh. Fiz. 16, 83 (1990)
- 78. V.V. Apollonov, Tech. Dig. 'Lasers 2001' (Tucson, Arizona, USA, 2001)
- 79. V.V. Apollonov, A.M. Prokhorov, Auth. Cert. No. 4250382 (priority date 17 Mar 1987)
- 80. V.A. Shurygin, Cand. Dissertation (NPO Almaz', Moscow, 1992)
- 81. V.V. Apollonov et al., Proceedings of the 1st World Conference on Experimental Heat Transfer, Fluid Mechanics and Thermodynamics (Dubrovnik, Yugoslavia, 1988)
- 82. V.V. Apollonov, G.I. Babayants, A.A. Kazakov, BSh Kishmakhov, A.M. Prokhorov, Kvantovaya Elektron. 24, 869 (1997)
- 83. V.V. Apollonov et al., Quantum Electron. 27, 850 (1997)
- 84. V.V. Apollonov, A.M. Prokhorov et al., Phys. Rev. A 58(3), 42 (1998)
- 85. V.V. Apollonov et al., Kvantovaya Elektron. 25, 355 (1998)
- 86. V.V. Apollonov et al., Patent No. 2399130 (priority date 22 Jan 2007)
- 87. S.I. Derzhavin, Cand. Dissertation (GPI, Moscow, 1988)
- 88. V.V. Kuz'minov, Cand. Dissertation (GPI, Moscow, 2002)
- 89. A.N. Schul'ts, Doctor Dissertation (LTI, Moscow, 2003)
- 90. V.V. Apollonov, A.M. Prokhorov, A.H. Guenther, Laser Phys. 11, 930 (2001)
- 91. N. Kageyama, K. Torii, T. Morita, M. Takauji, T. Nagakura, J. Maeda, H. Miyajima, H. Yoshida, *Hamamatsu Photonics Report* (Hamamatsu, 2011)
- 92. V.V. Apollonov, Nat Sci 5, 556 (2013)

- 93. www.Northropgrumman.com/SolidStateHighEnergyLaserSystems/
- 94. M.N. Libenson, E.B. Yakovlev, G.D. Shandybina, *Konspekt lektsii (Lecture Notes)*. ed. by V. P. Veiko (Izd ITMO, St. Petersburg, 2008)
- 95. V.V. Apollonov, A.M. Prokhorov, A.H. Guenther, Laser Focus World 1, 101 (2003)
- 96. V.V. Apollonov, Eksp Soyuz 3, 36 (2012)
- 97. V.V.J. Apollonov, Sci. Tsrael-Technol. Adv. 4, 3 (2012)
- 98. V.V. Apollonov, Chinese J. Opt. 6, 1 (2013)
- 99. V.V. Apollonov, *Program of Symposium HPLS@A-2012* 6 (Istanbul, 2012)

Chapter 18 New Technologies for High Power/ Energy Lasers Based on LD-Structures, New Technologies and Materials



18.1 Introduction

At the present, high power/energy lasers are often treated as laboratory equipment requiring constant maintenance by specially trained personnel. In this regard, the most promising now are semiconductor lasers. To date, they have the record-high efficiency reaching 70%. Modern technologies of fabrication of semiconductor structures have made it possible to significantly increase the lifetime of the laser, which is tens of thousands of hours of continuous operation. Besides the variation of the semiconductor material can change the wavelength range of the radiation from the infrared to the ultraviolet.

Currently, semiconductor lasers are the only lasers used in household appliances, namely, in communication and electronic devices. The cost of semiconductor lasers is still high, but falling from year to year as the production grows up. Semiconductor lasers are very compact and easy to operate.

The main feature of lasers based on semiconductor structures (LD-structure), which allowed them to work at room temperature, is a small amount of the active medium. Therefore, the output power of a single diode is low. Currently, it does not exceed 10 W. To increase the output power, one needs to use at the same time a large number of laser diodes, which form one-dimensional (bars) or two-dimensional (arrays) structures. This direction in the development of high-power semiconductor laser systems is being exploited relatively recently, but very rapidly.

The assembly of laser diodes has almost all the remarkable properties of single semiconductor lasers, such as high intensity, high reliability, long lifetime (up to 10^{12} cycles). These lasers have much smaller weight and size dimensions (up to 10 times) in comparison with other types of lasers. They can be easily fabricated with an independent low-voltage power supply (solar, nuclear) without bulky transformers. Equipment based on laser diode assemblies really becomes a reliable

high-performance tool that can be used in industry, medicine, and military hardware.

Almost all developed countries are, in one way or another, involved in the design and development of such laser systems. The leading role is played by the USA, Germany, England, and France. Interest in the creation of these systems is huge. Suffice it to say that just in the last two years, many small companies, specializing exclusively in the production of these lasers, have been established in the USA and China. This proves that their commercial benefits come to the fore.

To date, there are three main areas of use of cooled high power/energy laser diode assemblies.

- (i) Pumping of solid-state crystal lasers. These lasers, having high-quality output radiation, work as light transformers. The efficiency of such lasers is much higher than the efficiency of solid-state lamp-pumped lasers, because pumping by semiconductor lasers makes it maximal. For kilowatt lasers, the efficiency has already exceeded the value of a few tens of percent. Radiation of semiconductor lasers does not deteriorate the gain medium of solid-state lasers, thereby extending significantly the lifetime of the entire laser system. Weight and size dimensions of such systems are small, which makes them transportable. The main purpose of modern research is to develop and fabricate diode arrays with the highest possible power density. The record of 200 W from a 1-cm-long diode array has been demonstrated recently thanks to the improvement in technology and assembly structure and to a highly efficient heat transfer in the porous structure of the heatsink. The maximum output power from one array, according to calculations, can reach 500 W. This is especially important for further scaling of the power of laser systems and for increasing their efficiency. A diode-pumped laser with an output power of 100 kW and higher has been recently developed and fabricated in the US.
- (ii) Coupling of the diode array radiation into the fiber for puming fibre lasers or for further transport to the processing facility. Radiation losses in the laser diode assembly-optical fibre system are about 15–20% and mainly determined by the heat transfer, which does not allow one to effectively combine the lasing zones of separate diodes of the array into a minimal spot on the aperture of the fiber with the help of cylindrical optics.
- (iii) Development of phase-locked ID and 2D diode arrays. The output radiation of such lasers is a set of narrowly focused interference peaks (in particular one peak) with a low divergence. Based on theoretical estimates, the output power of such systems can be as high as the power of a conventional out-of-phase diode array. Therefore, such lasers are a source of light with a high efficiency inherent in semiconductor lasers and with a low divergence characteristic of solid-state crystal lasers. At present, such systems are being actively studied. The possibility of scaling the process of phase-locking of arrays and bars of laser diodes has already been shown and high-power laser diode assemblies have been produced.

18.1 Introduction 301

(iv) Recent advances in solid-state, fiber, and diode laser technologies along with various beam combination techniques resulted in a rapid increase of output power available from these devices. Design of high-power laser systems exceeding limits of single-aperture emitters relies on coherent and incoherent combination of radiation from multiple emitters into a single beam with enhanced brightness. Coherent combination requires mutual phase locking of multiple emitters. Therefore, coherent oscillation of a multichannel laser system requires conversion of all emitters to a single-frequency regime (single transverse and single longitudinal modes) and precise control of relative phases of all emitters. There are several approaches to mode selection and phase locking. In this chapter, we would like to stress the importance of passive methods that require narrow spectral and angular selectivity of locking elements. Several methods of incoherent combination of laser beams are currently under investigation. The most interesting approach under development in our days is the high-density spectral beam combining (SBC), which requires extremely high spectral selectivity of combining elements. Low efficiency of a laser system means that excessive amount of heat is generated during operation. Maintaining low beam divergence (high brightness) under heat loading and providing efficient heat dissipation in a portable system are the main challenges associated with high-power laser systems. Semiconductor lasers are the highest efficiency laser sources demonstrated up to date. A number of manufacturers have developed high power/energy laser diodes with efficiency exceeding 70%. However, poor beam quality and high divergence of high-power diode laser systems prevent their use as primary sources of emission in a number of important applications. They have been extensively used to pump other lasers, particularly solid state (slab and disk) and fiber lasers capable of producing high-quality beams at the expense of reduced output power and overall system efficiency. Diode-pumped solid state and fiber lasers are essentially brightness converters for diode laser systems, providing enhanced brightness at the expense of overall system efficiency. While this approach has proved very useful and high efficiency of conversion has been achieved, dissipation of additional heat generated in the system requires significant increase in system size. Direct diode laser systems would make for more efficient and compact laser systems if higher brightness could be achieved without using intermediate lasers. Techniques of transverse mode selection and spectral narrowing of laser diodes together with efficient beam combining techniques enable a new generation of compact high-power laser systems. This high-efficiency portable direct diode system would produce a 10-kW laser beam with near-diffraction limited divergence, and even could be scalable up to the level of 100 kW and more.

Thus, the development and fabrication of water-cooled high power/energy laser diode bars and arrays are promising direction for the implementation of the ideas of power/energy optics in new high power/energy sources of coherent radiation.

18.2 New Approaches for High Power/Energy Lasers Development

(i) Pumping of solid-state crystal lasers

The use of LD-structures for pumping solid-state lasers leads to the high output optical quality and generally speaking use to work as a light transformer. The efficiency of such a system is low due to the low efficiency of solid-state lasers; however, pumping by semiconductor lasers makes it maximal. Radiation of semiconductor lasers does not spoil the working medium of crystal lasers, which makes it possible to significantly extend the life of the entire laser system. Weights and dimensions of such systems are small, which allows them to be easily transported. The main purpose is to develop and fabricate diode arrays (bars) with the highest possible power density. Record-high values, i.e., 115 W from a 1-cm-long single diode array, were obtained by Coherent Inc., USA. The limiting power from one bar, as calculations show, can reach 500 W. At the Department of High-Power Lasers of the A.M. Prokhorov General Physics Institute of the Russian Academy of Sciences a 1-cm-long diode array with an 100 W output was fabricated. Solid-state diode-pumped lasers are being increasingly studied and developed by a large number of firms in the various countries. High-power diode-pumped laser systems are being developed mainly in such major companies as Rofin-Sinar Technologies Inc. (Germany), Coherent and Newport Corporation (USA).

(ii) Coupling radiation from a diode array into a fiber

An important problem here is the coupling of radiation from a diode array into the fiber for further transport to the work piece to be processed. Radiation losses in such a laser–fiber system reach more than 30%. At the same time, 500-W laser systems are known to be produced industrially in the U.S., France and Germany.

(iii) Phase-locking of a diode array

In our opinion, the most promising application of laser diode assemblies is the creation of a phase-locked diode array. The output radiation of such a laser is a set of narrowly focused interference peaks (in particular one peak) with a small divergence. The estimated output power can reach the power of a conventional diode array producing one set of beams that are out of phase with those of another set of beams. This laser is a light source with high efficiency and low divergence that are characteristic of semiconductor lasers and solid-state crystal lasers, respectively. By analogy with the technique of phase-locked antennas in the radio range, the beam divergence in the case of phase-locked diode arrays can easily be increased to 10^{-6} rad without expensive telescopic systems, which provides ultra-long communication and transmission of energy over long distances.

At present, these systems are being actively studied. For example, Closed Joint-Stock Company Energomashtekhnika has been conducting research in this field since 1997 and has produced a prototype of a ~ 20 W phase-locked laser. The possibility has been shown of scaling the process of phase-locking of the arrays and

bars of laser diodes. Arrays of laser diodes with an output power up to 500 W have been fabricated. The effect of phase-locking of high power/energy laser diode structures is being increasingly investigated. According to the press in other countries, the maximum output power in a phase-locked array is reported to be only 1.5 W.

(iv) Spectral beam combining

The fiber SBC architecture maintains the high efficiency, high surface-to-volume ratio for simplified thermal management, and flexible packaging of fiber lasers. Furthermore, the architecture provides the same exceptional ruggedness and reliability of fiber lasers since the majority of the path length is in fiber without requiring adjustments or alignment. Fiber delivers light from the different fiber lasers up to a beam combiner module containing the free space optics. The simple optical layout combines the outputs from different wavelength fiber lasers on a single reflective multi-layer dielectric grating without requiring active adjustments or control loops. The outputs from an array of fibers are collimated with a transform mirror and directed on to a dielectric grating with each beam at a unique angle. The wavelength of each beam is selected to diffract into the same output angle, such that the ensemble of beams are overlapped into a single beam of multiple wavelengths. The architecture produces near-diffraction limited Gaussian profile beams in the near and far field, nearly identical to that of the individual fiber lasers. We previously demonstrated this approach at >3 kW output power with excellent beam quality and high efficiency by combining twelve fiber lasers of approximately 300 W each. Below we describe recent work where we extended the SBC approach to 96 fiber lasers of approximately 300 W each to produce more than 30 kW output power.

18.3 Laser Systems of Propellant Ignition

One of the most important applications of laser diodes is the creation of a system of multiple ignition of rocket propellant in the combustion chamber of a launcher. Apart from the fact that the parameters of the laser system should provide multiple ignition of the mixture with 100% certainty, the laser design must meet the requirements specific to onboard lasers that are currently used in space technology:

- Compactness
- 2. Small size and weight
- 3. Absence of high-voltage in the power supply system
- 4. Resistance to vibrations and g forces
- 5. Absence of active cooling (including the closed circuit with a refrigerant and a pump)
- 6. Long service life.

A new and specific requirement for the launcher-related design of the laser is the need to deliver the laser radiation into the combustion chamber through an optical fiber. Accordingly, the peak and average power of the laser must permit delivering its radiation into the fiber with a minimal chance of the fibre damage.

Since July 2002 works have been on the way for a laser system ensuring multiple ignition of rocket propellant components in the prechamber (or ignitor) of the third-stage rocket motor. In the course of these works the following sources of laser radiation were used:

(A) Solid-state laser

A solid-state laser operating in a modified spike regime, first proposed and patented by CJSC Energomashtekhnika, with the following radiation parameters:

```
Wavelength—1.054 µm; output energy—4–10 J; temporal shape of radiation—a train of 100–150 pulses with an irregular period; pulse train repetition rate—a single pulse; duration of the pulse train—600–700 ms; duration of a single pulse—200–400 ns; pulse spacing—4–7 ms; peak output power \sim \! 100 kW; divergence—4 \times \ 10^{-4} rad; type of the active element pumping - lamp pumping.
```

Figure 18.1 shows the oscillograms of a train of pulses (Fig. 18.1a) and of single spike (Fig. 18.1b) of a laser operating in a modified spike regime. A characteristic feature of the temporal shape is the irregular spacing between neighboring spikes within the pulse train and the high contrast of the spikes with respect to the pedestal (significantly higher than in the pulse of a conventional free-running solid-state laser). It should be noted that the duration of the spikes is by about order of magnitude shorter than in the traditional pulse. These differences in the temporal shape of the modified spike regime made it possible to realize a much higher peak output power compared to a traditional pulse of the same energy.

The laser is a laboratory model with a rather bulky power supply and cooling module. The dimensions of the laser head are as follows: $200 \times 200 \times 1400$ mm. The appearance of the laser head is shown in Fig. 18.2.

(1) A solid-state Q-switched pulsed laser:

```
wavelength, 1.06 \mu m; pulse energy, up to 1 J; peak power, up to 100 MW; pulse duration, 10 ns; repetition rate, a single pulse or 10 Hz. The laser however was a rather cumbersome laboratory bench.
```

(2) A serial ytterbium fiber laser (YPL1/100/20):

```
wavelength, 1.062 μm; average output power, 20 W;
```

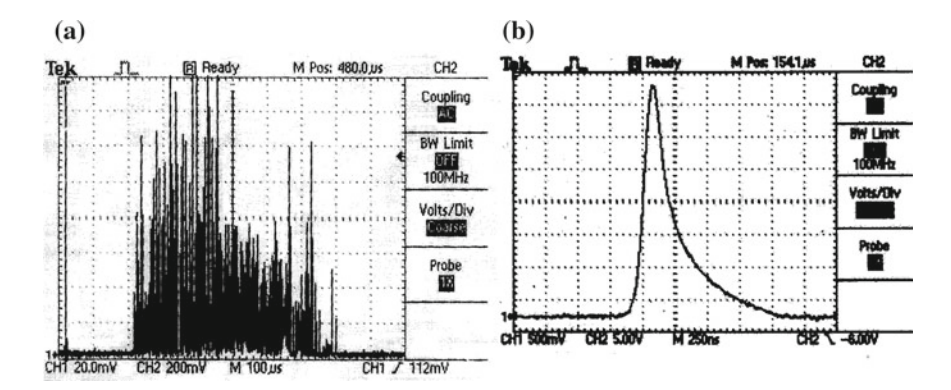


Fig. 18.1 a Oscillogram of a "ruff pulse" (100 mks/div); **b** oscillogram of single pulse from "ruff pulse" structure (250 ns/div)



Fig. 18.2 Laser head and power supply

pulse duration, 120–150 ns; pulse repetition rate, 20–80 kHz; maximum pulse energy, 1 mJ; maximum peak power, 10 kW; divergence, 10^{-3} to 3×10^{-3} rad.

The laser was significantly smaller in size than the two above-mentioned lasers, the total weight of the power unit and the laser head was 8 kg. Neither water cooling nor a high-voltage power supply was used in the laser.

Experiments were performed to study the ignition of different fuel mixtures (oxygen-kerosene, oxygen-alcohol, oxygen-hydrogen) in the prechamber (or ignitor) of the third-stage rocket motor. In the first stage of the research, the radiation

was delivered into the prechamber through an optical window, which was installed in the seat of a standard spark plug. The radiation was focused by a lens mounted outside the chamber onto the target placed inside the chamber. In the experiments a metal mesh was installed in the channel of the input laser beam. This target made it possible to successfully ignite the fuel mixture. Due to the large capillary resistance. the target in the form of a mesh effectively protected the sapphire window (through which the laser beam is delivered) from condensation. The disadvantages of this target include the problem of maintaining its thermal stability during the operation of the combustion chamber. A graphite rod, mounted in a brass ring, is inserted into the combustion chamber. This target can be moved along the axis of the combustion chamber, thereby determining the optimal zones to initiate ignition. This target makes it possible to ignite the fuel mixture at very low levels of laser energy. The downside of the target is the possibility of its destruction in the high oxidizing environment; the wall of the subsonic part of the exit nozzle is covered with oxides, special targets in the combustion chamber are absent. The laser beam was focused on the wall with a long-focus lens. This variant is the most reliable one for ignition, as no high requirements are imposed on focusing and there are no changes in the scheme of the combustion chamber (Fig. 18.3).

The experimental results showed a significant advantage of laser (1) over other lasers: the use of this laser made it possible to ignite all the above-mentioned mixtures with a large margin of the radiation energy. In particular, the threshold of ignition for the oxygen-hydrogen mixture was 90 mJ.

Laser (2) ignited only the hydrogen—oxygen mixture (this mixture is known to be the most flammable one), and the ignition threshold was 60 mJ.

Laser (3) ignited all the above-mentioned mixtures. However, reliable ignition was achieved using the full laser power of 20 W, optimal repetition rate of 50 kHz and conical target, which provided cumulation of the material evaporated from the target and, accordingly, its additional heating.

Fig. 18.3 Laser head YPL1/ 100/20



In our opinion, in experiments with two lasers, (1) and (3), the optical breakdown threshold for the gas mixture near the target was not reached; the basic mechanism of ignition was the contact of the gas mixture with heated vapors of the target material formed near it by laser ablation. Because in the case of laser (1) the peak power was about 10 times higher, the higher was the temperature of the vaporized material. Most likely, this parameter played a crucial role in the successful ignition of less flammable mixtures such as oxygen–kerosene and oxygen–alcohol.

Because of a significantly higher peak power, in experiments with laser (2) the optical breakdown threshold of the gas mixture was substantially exceeded. The plasma, produced near the target on the leading edge of the laser pulse, shields it from the rest of the pulse and no target material is significantly evaporated. Therefore, the main ignition mechanism is the ignition of the gas mixture at its contact with the laser plasma. However, based on the experimental results, this type of ignition is less effective because it does not allow one to ignite less flammable mixtures. Based on these experiments, we can draw the following conclusions:

- The mechanism of laser ablation is more effective to ignite the rocket propellant mixtures than the optical breakdown of the mixture. An additional argument in favor of ablation is the fact that the propellant itself is not involved in the process. Therefore, hot vapors of the target can be produced either before or during the injection of the propellant components. In the case of the optical breakdown of the mixture, its threshold depends strongly on the gas composition and pressure in the chamber. In this case, the breakdown can occur after filling the chamber with the mixture. Such a regime is ideal in the case of a small combustion prechamber, but can lead to self-ignition of the mixture and to an explosion in a large combustion chamber.
- The laser pulse energy (and, hence, its peak power) significantly affects the temperature of the evaporated material, and the total energy of the pulse train influence its mass. An increase both in the temperature and the mass of the evaporated material provides more reliable ignition of propellant mixtures. Therefore, in designing an ideal laser for ignition, it is needed to optimize both the peak power of a single pulse and the energy of the pulse train (in the case of a pulse-periodic laser, high power).
- It is also likely that an important parameter is the laser pulse repetition rate. At the optimal repetition rate additional heating of the target vapors by subsequent pulses is also possible, but in such a way that the target vapors would not fully absorb the incident radiation and allow for ablation in all the pulses of the train. Thus, when working with laser (3), optimal was the frequency of 50 kHz, at which a continuous optical discharge was observed near the target (Fig. 18.4).

(B) Fiber-optic coupling system for ignition

The use of optical fibers for coupling light into the combustion chamber eliminates the installation of an optical window in the wall of the chamber and delivers radiation through a small hole in the housing, comparable in diameter to those used



Fig. 18.4 Optical igniter with optical discharge

for the injection of fuel mixtures of components (hundreds of μm). Installation of the optical window is often impossible due to design reasons; besides, an additional risk is due to the possibility of explosion of the window at very high temperatures and pressures in the combustion chamber.

Therefore, in the second stage of the works an original construction has been designed and manufactured to couple optical radiation into the fiber and place the fiber inside the combustion chamber. This design ensures high reliability of the fiber attachment, long service life without re-polishing of the end that is in the combustion chamber, and the optimal delivery of radiation to the target. The optical scheme of the ignition system with fiber-optic input is shown in Fig. 18.5. Subsequently, this design was used to deliver the radiation of lasers. The radiation of laser could not be coupled into the fiber due to the very high peak power that damages the fiber end. The power can be splitted by seven channels and delivered to the igniter.

Thus, a single-pulse Q-switched solid-state laser with pulse duration of ~ 10 ns is not optimal for igniting the propellant mixtures and causes big problems when coupling the laser beam into an optical fiber. We consider it inappropriate to use

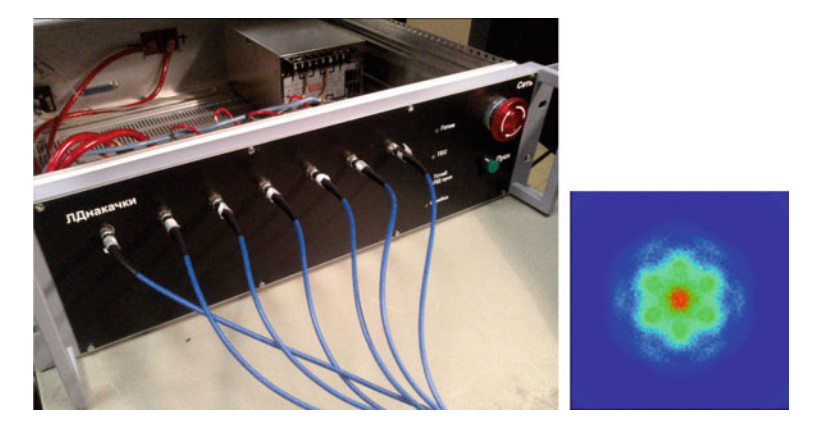


Fig. 18.5 Seven channels pumping block with near field pattern

such lasers for igniting propellants. Based on the above considerations, it is proposed to test sequentially the lasers developed and designed by CJSC "Energomashtekhnika" for igniting propellants in the combustion chamber of the rocket booster (the oxygen-hydrogen mixture). The lasers have the following parameters:

I. A solid-state laser with semiconductor pumping:

```
wavelength, 1.06 \mum; pulse duration, 100–200 ns; pulse energy, 10–50 mJ; peak power, 50–500 kW pulse repetition rate, 5–100 \mus (the optimal interval is determined for each working mixture); continuous operating time, 5 s.
```

Based on the experience in designing solid-state diode-pumped lasers and laser diode arrays at CJSC Energomashtekhnika, we came to the conclusion that such parameters can be demonstrated by a transversely diode-pumped solid-state laser with a passive optical switch (e.g., LiF with color centers) to ensure modulation and by laser diode arrays in phase-locked and out-of-phase regimes. The proposed laser can make use of the original patented diode-pumped laser with the following parameters: pulse energy, 50 mJ; pulse repetition rate, 100 Hz; a special design for fixing the active element and diode laser arrays, which eliminates water cooling. At present, the laser emits pulses with an energy of 50 mJ and a repetition rate of 50 Hz. If long-term continuous operation is required (the laser operates from 1 to 5 s), a substantial increase in the pulse repetition rate (up to 1 kHz) is possible without reducing the pulse energy.

II. A laser diode array in an out-of-phase oscillation mode (intermediate stage):

```
wavelength, 0.808 \mu m; operation mode, pulse-periodic; pulse duration, 100 \mu s; pulse energy, 0.2 J; peak power, 2 kW; maximum peak power density during focusing, 2 MW/cm²; pulse repetition rate, 1 kHz; continuous operation time (without cooling), 5 s.
```

III. An array of laser diodes in a phase-locked oscillation mode

```
wavelength, 0.940 µm; operation mode, continuous; power, 40 W; maximum peak power density during focusing, 40 MW/cm<sup>2</sup>; continuous operation time (without cooling), 5 s.
```

In comparison with diode-pumped solid-state lasers, the laser diode array, operating both in the out-of-phase (cheaper) and phase-locked oscillation modes is even more compact and reliable ignition device. Since, as shown above, the mechanism of laser ablation is more effective to ignite rocket propellants than the optical breakdown, the devices based on the array technology must take a critical position in the solution of the above problems. It should be noted that the first samples of laser diode arrays developed for other purposes, have already been produced at CJSC Energomashtekhnika. Currently, work is underway to ensure phase-locking of laser diode structures.

Estimates show that the radiation of the proposed lasers can be coupled into an optical fiber without the risk of its damaging. A significant increase in the pulse energy and pulse duration at a high repetition rate within 5 s or a transition to the continuous regime with sharp focusing of the radiation under conditions of its phase-locking suggests that the proposed ultra-compact laser systems are ideal devices for solving the problem of reliable multiple ignition of various components of the rocket propellant in combustion chambers of the launchers.

Thus, high-power diode arrays are promising sources of radiation, the dominant role of which in the new millennium is ensured by a unique set of basic features and characteristics.

18.4 New SiC-Mirror Manufacturing Technology Capabilities

For many years, Russia has been developing new materials based on refractory metals and ceramics. Results of works have been widely used in the development of a nuclear jet engine and fuel elements of nuclear reactors. In the early 1970s, researchers at the Lebedev Physical Institute of the USSR Academy of Sciences (the General Physics Institute of the USSR Academy of Sciences was organized later in 1983 on the basis of the Laboratory of Oscillations of the Lebedev Physical Institute) discovered the physical effect of local deformation of the reflective mirror surface and began to actively conduct research to design power optics for high-power laser systems. The solution of this problem required a material that under conditions of radiation exposure, alternating temperatures and inertial accelerations, retains high geometric stability and has high corrosion resistance in aggressive environments, such as hydrogen fluoride (Table 18.1).

Analysis of a wide range of materials on the basis of stability parameters proposed in [1–3] has shown that silicon carbide produced either by reaction bonding or sublimation has an advantage over other materials in all criteria. Specific heat loads under cw, repetitively pulsed and pulsed irradiation (kW/cm²) also play an important role. The data obtained are in good agreement with the results of similar studies carried out much later by US specialists [4].

Table 18	Table 18.1 Properties	s of diffe	rent ma	terials, and	ties of different materials, and results of their evaluation by the stability criteria [1, 2]	r evalua	tion by ti	e stability	criteria [1, 2	_			
Mate-rial	Properties				Constant loading					Pulsed loading	5.0		Stiffne
					Criterion $(\tau > 0.1)$	<u> </u>				Criterion ($\tau < 0.1$ s)	: 0.1 s)		criterion
	$\alpha \times 10^6 \; \mathrm{K}^{-1}$		C (J/ kg K)	$ \lambda \qquad \qquad C (J) \qquad \gamma \times 10^{-3} $ $ (W/\mu K) \qquad \text{kg K}) \qquad \text{kg/m}^3 $		(MPa)	$\lambda \alpha E \times 10^{-6} \text{ W/}$	$\sigma_{0.01}\lambda \alpha E imes 10^{-4} ext{ W/m}$	q (kW/cm²)	$C \cdot \gamma/\alpha \times 10^{-10} \text{ W s/}$ m^3	$ \begin{array}{c ccccccccccccccccccccccccccccccccccc$	q (kW/cm²)	$\gamma \times 10$
-	2	3	4	5	9	7	8	6	10	11	12	13	4
Cu	17	400	380	6.8	13	185	24	3.4	2.6	20	31	4	14.7
Мо	5.1	130	260	10.2	32	280	25	2.2	1.6	52	34	5	32.3
W	4.6	170	134	19.3	41	750	37	8.9	2.5	56	83	10	21.2
SiCpe	2.8	130	1200	2.7	40	230	46	2.7	2.3	116	43	5	131
SiC	2.8	230	1200	3.2	45	330	82	0.9	3	137	92	=	143

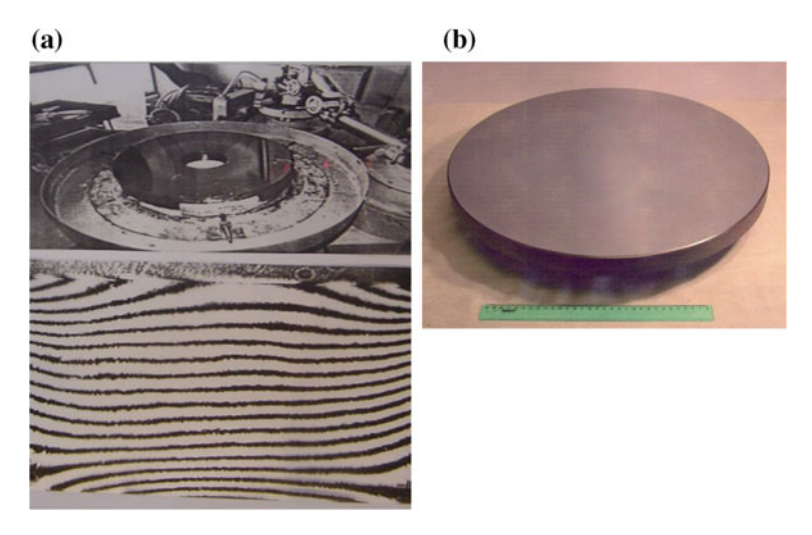


Fig. 18.6 a SiC laser mirror (1 m in diameter) cooled via a porous heat exchanger; **b** Reaction-bonded non-cooled SiC mirror

The technology we developed in the late 1980s allows [5–8] to fabricate mirrors with a high specific radiation resistance while maintaining the geometric stability of the reflecting surface (Fig. 18.6).

Currently, SiC is recognized worldwide as a highly promising material for mirror substrate fabrication and development of all the telescope components due to its many attractive properties, such as:

- high specific stiffness (high rigidity and low density);
- low thermal sensitivity (low thermal expansion coefficient and very high thermal conductivity); and
- extreme hardness and stiffness, which allow for good mechanical property retention in the micron range and ultimate characteristics for mirror forming and polishing.

Currently available equipment makes it possible to produce meter-class monolithic silicon carbide mirror blanks. The methods developed for the manufacture of cellular silicon carbide substrates allow for fabrication of lightweight space- and ground-based laser mirrors (Fig. 18.7).

The original welding technology of SiC ceramics enables the manufacture of complex structures having low weight and high rigidity, such as, for example, optical benches, mounts (racks, farms, etc.) and other elements of laser mirrors (Fig. 18.8).

The developed welding technology provides vacuum-tight connection, which enables the production of hermetic containers made of silicon carbide for long-term storage of spent nuclear fuel (SNF). Widely known is the inertness of silicon

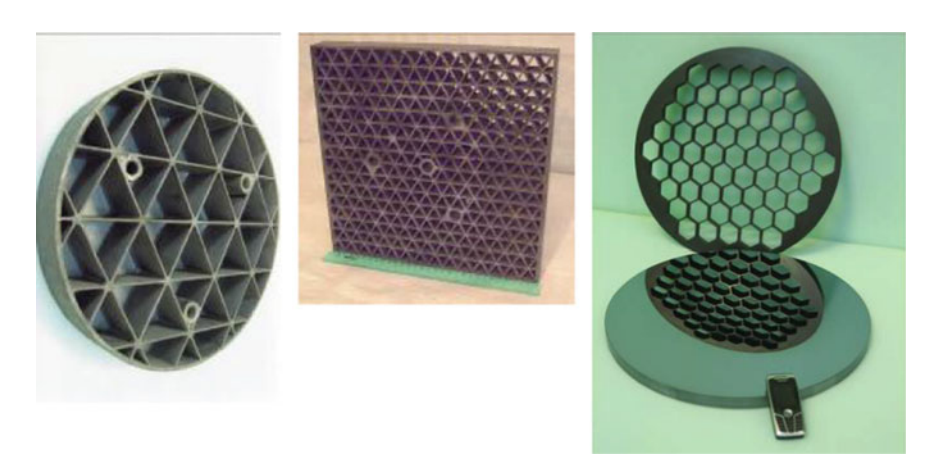


Fig. 18.7 Honeycomb structure of lightweight laser mirrors

Fig. 18.8 Elements of a cooled mirror



carbide to corrosion and high resistance to all types of ionizing radiation (gamma rays, neutrons, protons), which ensures reliable storage of SNF that is in contact with groundwater for thousands of years. In cooperation with the OJSC SPII VNIPIET we have designed and manufactured a full-size prototype of a silicon carbide cask for long-term storage and disposal of absorbing elements of nuclear submarine reactors and unreprocessible SNF of nuclear-powered ice-breaker fleet.

The methods of silicon carbide purification and high production standards elaborated in Russia made it possible to design and build tooling for manufacturing processes of very-large-scale integrated circuits (VLSICs). The manufactured products meet world standards (NORTON company) as evidenced by the growing volume of purchases of tooling in Europe and the United States. The plant that is friendly to our organization makes accessories that enable to deposit VLSICs on silicon wafers with a diameter from 75 to 300 mm (Fig. 18.9).

The high thermal conductivity of silicon carbide ($\lambda > 250$ W/mK for sublimated and $\lambda \sim 490$ W/mK for single-crystal SiC) enables the use of silicon carbide as a

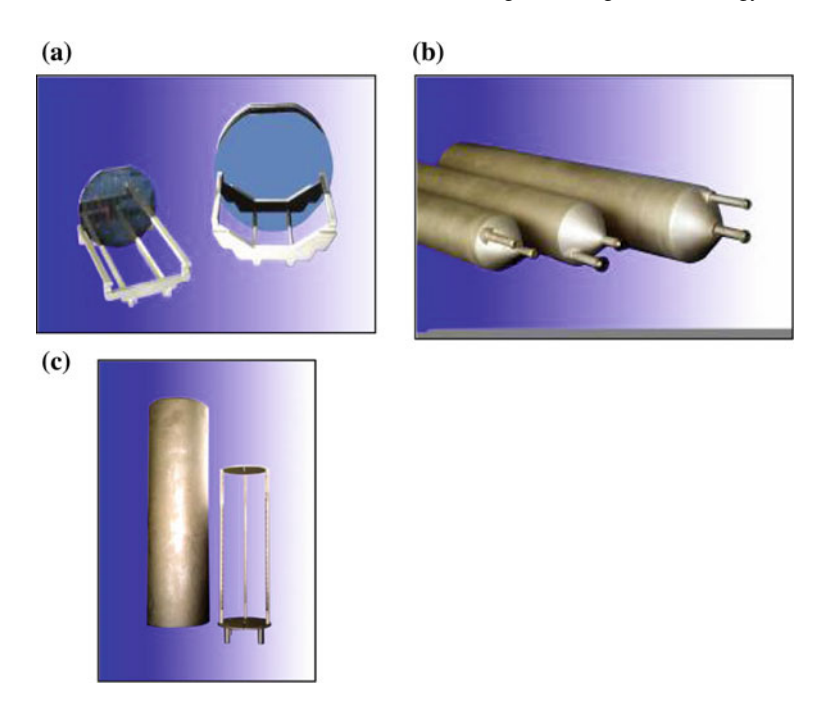


Fig. 18.9 Accessories made of high purity silicon carbide for VLSIC production. **a** Cassette for silicon wafers up to 200 mm in diameter; **b** reactor for annealing wafers up to 200 mm in diameter and **c** reactor and cassette for wafers 300 mm in diameter (presented by G. I. Babayants)

Fig. 18.10 SiC heat exchanger for an array of semiconductor laser diodes



heat exchanger. Currently, the technology of manufacturing high-performance SiC heat exchangers for semiconductor laser diode arrays has been perfected. Thus, in close cooperation with industrial enterprises we have produced and tested samples of laser diode arrays (Fig. 18.10) with a radiated power from one array at the level of 115 W.

18.5 Conclusions 315

18.5 Conclusions

The use of silicon carbide as a heat conductive material is also important because its thermal expansion coefficient is close to the thermal expansion of gallium arsenide (GaAs), a substrate of a semiconductor laser array, which prevents its cracking during brazing to the body of the heat exchanger. Studies are under way and positive results have been obtained in the implementation of radiation phasing on two-dimensional arrays of semiconductor laser diodes. Currently, research is under way to develop technology for growing silicon carbide single crystals of much bigger size for the manufacture of microelectronic and optoelectronic devices operating at high temperatures and fluxes of ionizing radiation.

References

- V.V. Apollonov, A.I. Barchukov, N.V. Karlov, A.M. Prokhorov, E.M. Shefter, Sov. J. Quantum Electron. 5, 216 (1975)
- 2. V.V. Apollonov, High-Power Optics (Springer, New York, 2014)
- 3. N.N. Bochkov, V.F. Gordeev, V.S. Kolesov et al., *Poverkhnost'*, *Fizika*, *Khimiya*, *Mekhanika* 11 (1983)
- D. Castel, B. Calvel, P. Lamy, K. Dohlen, M. Bougoin, Monolithic SiC telescope of the OSIRIS narrow-angle camera for cometary mission ROSETTA, in *Part of the SPIE Conference on Advanced Telescope Design, Fabrication, and Control*, Denver, Colorado, SPIE vol. 3785, July 1999
- V.V. Apollonov, G.I. Babayants, B. Sh. Kishmakhov, High Power SiC Based Technologies (International Forum on Advanced High Power Lasers and Applications, Osaka, 1999), p. 23
- 6. V.V. Apollonov, High power optics and its new manifestations. Nat. Sci. 5(N5), 653 (2013)
- V.V. Apollonov, A.M. Prokhorov, A.H. Guenther, High power optics. Laser Phys. 11, 930 (2001)
- 8. V.V. Apollonov, High Power Lasers in Our Life (NOVA, New-York, 2015)

Conclusions

Powerful pulsed and pulse-periodic lasers are capable to create the current-conducting channels of a large length, which are located at the arbitrary distances from the source of radiation. Length of channels about hundreds of meters can be achieved with low energy of the single pulses. Beginning from the 70's, successful attempts at their use for the solution of problems by the interception of lightning and blocking of the waves of overvoltage on the electric power lines were undertaken. Successful developments of the technology of high-frequency P-P regime of high power/energy lasers and technology of "Impulsar" make it possible to foresee the possibility of the realization of the well conducting channels with length into several ten and hundreds of kilometers for the purpose of the energy transfer up to the significant distances, creation by new promising for the mastery of outer space of power engineering and to contribute to an essential improvement in the global ecology of planet.

The book based on our previous works has shown that, in spite of the discontinuous structure of the long laser spark created by pulsed laser in the vicinity of a grounded electrode, it may capture the channel of leader discharge developing in the gap between the electrode and the charged aerosol cloud. The capture takes place for quite high electric field strength at the electrode, its value being close to that of the field required for the emergence of an ascending positive leader in the absence of a laser spark in the gap. The creation of a laser spark near the tip of an earthed electrode enables a considerable decrease in the time of formation of a stable leader, which starts propagating toward the cloud and captures a part of the laser spark. As a result, its velocity increases compared to the case when the discharge develops in the absence of a laser spark in the gap. The continuous laser-induced spark that has been demonstrated in our experiments for such applications is the next step for a reliable lightning protection system development. Indeed, owing to the interaction process with the continuous laser-induced spark, the leader discharge developing from the tip of the lightning rod may much better precede the ascending discharges from the object being protected during its advance 318 Conclusions

toward an approaching descending leader, capture the latter, and thus protect the object.

We determined the range of sizes of dust nanoparticles (from 50 nm to 300 µm) and their minimum volume density that are necessary to provide an electric breakdown in order to form a plasma channel according to the "Impulsar" program. The results of the model experiments showed that nana-particles in the plasma channel can merge into larger aggregates during the laser reactive engine operation. The experiments on electric breakdown showed also that a high conductivity of a plasma channel with a diameter of ~ 8 mm and a minimum specific resistance of $\sim 5 \Omega$ /m is implemented at the maximum introduced specific energy: $\sim 200 \text{ J/m}$. At a larger channel diameter, the specific energy is proportional to the squared ratio of diameters. The minimum average electric field strength ($\sim 52 \text{ V/cm}$) in the channel, at which a streamer-leader electric breakdown of the discharge gap begins, is due to the following factors: (1) the presence of dispersion and condensation aerosols of hot particles of copper oxide (CuO, Cu2O) and copper with oxidized surface (smaller than 300 µm in diameter) in the channel for a long time (1–10 µs) due to their low mobility; (2) the presence of superheated metal drops at the centre of plasma formations, which are in the metastable (unstable) state at temperatures $T \sim$ 3000-5000 °C and play a role of hot dots during thermionic emission; (3) formation of large linear aggregates of aerosol particles, which are formed during wire explosion; (4) low oxygen content in the channel as a result of fast oxidation of aerosol particles formed during wire explosion.

The use of silicon carbide as well as other new sophisticated materials as a heat conductive matter is also important because its thermal expansion coefficient is close to the thermal expansion of gallium arsenide, a substrate of a semiconductor laser array, which prevents its cracking during brazing to the body of the heat exchanger. Studies are under way and positive results have been obtained in the implementation of radiation phasing on two-dimensional arrays of semiconductor laser diodes.

Currently, research is under way to develop technology for growing silicon carbide single crystals of much bigger size for the manufacture of microelectronic and optoelectronic devices operating at high temperatures and fluxes of high power/energy laser radiation.

Only the nearest future will show the details of physical-technical solution for the best high power/energy laser which will be used effectively for many important challenges faced by science and technological advances of the future. However, today we can say that creation of high power/energy class high frequency pulse-periodic lasers with a large cross section of the active medium, high compactness and low weight will open up a great prospects for their use in solving the problems of launching of small satellites by lasers, formation of super-long conducting channels in space (vacuum and atmosphere), cleaning of the near-Earth space from space debris and other important tasks of our days.

A	В
Ablative material, 165	Background loss, 195
Absorbing elements, 313	Beam focus, 49
Acceleration, 140	Beam quality, 158
Acceleration regime, 141	Bessel function, 261
Acceleration stage, 75, 77, 80	Bipolar pulses, 32, 184
Accumulated energy, 104	Black body, 125
Acousto-optic modulators, 154	Breakdown, 100, 104, 152
Active media, 227	Breakdown characteristics, 145
Active rear mirror, 154	Breakdown fields, 12
Actuators, 287	Breakdown of air, 27
Adaptive, 286	Breakdown trajectory, 106
Adaptive systems, 288	
Adiabatic expansion, 51	C
Aerodynamic resistance, 86	Capacitor bank, 121
Aeroelectrical structures, 34, 186	Capturing ring, 122
Aerosol particles, 113	Cathode area, 205
Air gap breakdown, 10	Cathode edge, 251
Amplified Spontaneous Emission (ASE), 160,	Cathode spots, 248
193	Cavern radius, 139
Angular aperture, 106	Cellular materials, 258
Annealed and siliconized, 291	Ceramic capacitor, 5
Annealing wafers, 314	Channel boundary, 119
Arbitrary temporal shape, 259	Channel conductivity, 99, 112, 145
Argon jet, 49	Channel diameter, 125
Array reflector, 81, 82	Channel expansion, 118, 124
Atmospheric pressure, 212	Channel glow intensity, 232
Attachment of electrons, 234	Channels, 197
Auxiliary discharge, 203, 205, 207, 237	Channel structure, 104
Auxiliary discharge plasma, 210	Chaotic, 34, 157, 186
Average power, 84, 139, 163, 164	Charged aerosol, 16
Axicon, 150	Charged aerosol cloud, 317
Axisymmetric approximation, 46	Charged particles, 101

Charge transfer reactions, 246	Curvature, 166
Charging voltage, 11	Cutting, drilling, 192
Chemical etching, 163, 167	Cutting-edge technologies, 294
Chemical fuel,, 65	CW laser, 156
Chemical lasers, 95	Cyclically repeated stress, 274
Cladding material, 283	Cyclic loading, 287
Cleaning, 169	Cylinder walls, 77
Climate of planet, 36	Cylindrical shock wave, 117, 126
Coherent radiation, 288	
COIL, 157	D
CO ₂ -laser radiation, 6	Damage threshold, 275
Collector effects, 279	Damping decrement, 112
Combustion chamber, 303, 306, 309, 310	Decomposition of SF ₆ , 246
Combustion chamber of a launcher, 303	Decomposition products, 230
Composite materials, 290, 295	Deformation, 260, 269, 274
Compression phase length, 47	Deformation characteristics, 281
Com-pression phases, 50	Deformation component, 262
Computations in air, 53	Deformation surface profiles, 267
Condensation nuclei, 28, 181	Demolition, 58
Conducting air flows, 34, 186	Dense gases, 239
Conducting the nows, 54, 166 Conducting channel, 151, 174, 176, 318	Density of plasma, 7
Conducting electricity, 31, 183	Deposited energy, 234, 251
Conductive channel, 53	Deposition process, 224
Conductivity, 10	Descending leader, 22
Conductivity channel, 120	Deterioration, 272
Conductivity of air, 35	Detonation regime, 68
Cone angle, 14	Detonation wave, 58
Conical focusing optics, 112	
	Development of channels, 231
Conical optics, 95	Development of instability, 249 Diameter of the channel, 118
Conic optics., 4	•
Continuous operation, 293, 299	Dielectric materials, 189
Continuous quasi-cylindrical, 98	Diffraction energy loss, 150
Conversion, 74	Diffractionless' wave beam, 96
Coolant, 258	Diffuse channel, 218, 221, 239, 241, 242, 247
Coolant flow, 277	Diffusion channel, 227, 232
Coolant inlet, 283	Dimensionless form, 276
Coolant outlet, 283	Dimensionless velocity, 73
Cooled and uncooled adaptive, 286	Diode arrays, 302
Cooling efficiency, 191	Diode-pumped disk lasers, 191
Cooling module, 304	Diode-pumped lasers, 309
Cooling surface, 283	Diode-pumped solid state, 301
Copper, 176	Discharge channel, 105, 111, 121, 144
Copper oxide, 103	Discharge concentrating, 251
Copper oxide particles, 113	Discharge cross section, 216
Cosmic rays, 30, 35, 183	Discharge current, 18, 19, 209, 222
Coupling coefficient, 134	Discharge gap, 101, 112, 201, 202, 206, 213,
Cross section, 169	237
Crystal, 159	Discharge geometry, 122
Current amplitudes, 21	Discharge inductance, 112
Current breakdown, 106	Discharge instability, 229, 241
Current-limiting mechanisms, 219	Discharge plasma, 232, 243
Current pause, 104	Discharge uniformity, 253
Current recovery, 242	Discharge voltage, 234
Current restriction mechanisms, 244	Discharge voltage source, 120

Discharge volume, 243	Expansion coefficient, 312
Disk and fiber lasers, 190	Expansion of the channel, 118
Disk elements, 193	Expansion rate, 120, 126
Disk geometry, 198	Exploding wire, 124
Disk laser, 158	Explosion, 130, 308
Disk material, 192	Explosion centre, 70
Dissociation, 244	Explosion channel, 107
Divergence of radiation, 70	Explosive charge, 119
Duhamel's integral, 269	Externally injected, 167
Dupuit–Reynolds–Forchheimer, 278	3
Dust plasma, 145	F
Dynamic loads, 92, 141	Far-field region, 190
Dynamic processes, 10	Femtosecond laser, 96
Dynamic profiling of electrons, 233	Fiber, 308
Dynamics of SIVD, 240, 246	Fiber lasers, 190, 303
Dynamic time, 70	Fibrous felt structures, 280
Dynamic viscosity, 278	Field strength, 29, 182
Dynamic Viscosity, 270	Flexible hose, 132
E	Flight velocity, 137
	•
Ecologically safe, 238	Flux density, 276
Electrical breakdown, 177, 219, 220	Focusing reflector, 52
Electrical discharges, 27	Focusing system, 177
Electrical dynamos, 30, 182	Fraunhofer diffraction, 99
Electrical efficiencies, 253	Frequency, 73
Electrical energy, 36, 179, 253	Fuel elements, 283
Electrical spark breakdown, 225	Fundamental harmonic, 50
Electric breakdown, 5, 9, 12, 97, 103, 106, 111,	
113	G
Electric conductivity, 245	Gain, 195
Electric discharges, 5, 151, 257	Gallium arsenide, 318
Electric field, 17, 26, 29, 101, 181, 244	Gamma-radiation, 31, 183
Electric field strengths, 230	Gap geometry, 232
Electric field strengths, 230 Electrization, 29, 182	Gap geometry, 232 Gap periphery, 228
Electric field strengths, 230 Electrization, 29, 182 Electrode rod, 18	Gap geometry, 232 Gap periphery, 228 Gas density, 45
Electric field strengths, 230 Electrization, 29, 182 Electrode rod, 18 Electrodes, 217	Gap geometry, 232 Gap periphery, 228 Gas density, 45 Gas-dynamic CO ₂ , 168
Electric field strengths, 230 Electrization, 29, 182 Electrode rod, 18 Electrodes, 217 Electron current, 208	Gap geometry, 232 Gap periphery, 228 Gas density, 45 Gas-dynamic CO ₂ , 168 Gas-dynamic lasers, 79, 86, 98
Electric field strengths, 230 Electrization, 29, 182 Electrode rod, 18 Electrodes, 217	Gap geometry, 232 Gap periphery, 228 Gas density, 45 Gas-dynamic CO ₂ , 168
Electric field strengths, 230 Electrization, 29, 182 Electrode rod, 18 Electrodes, 217 Electron current, 208	Gap geometry, 232 Gap periphery, 228 Gas density, 45 Gas-dynamic CO ₂ , 168 Gas-dynamic lasers, 79, 86, 98
Electric field strengths, 230 Electrization, 29, 182 Electrode rod, 18 Electrodes, 217 Electron current, 208 Electron density, 96, 216	Gap geometry, 232 Gap periphery, 228 Gas density, 45 Gas-dynamic CO ₂ , 168 Gas-dynamic lasers, 79, 86, 98 Gas medium, 249
Electric field strengths, 230 Electrization, 29, 182 Electrode rod, 18 Electrodes, 217 Electron current, 208 Electron density, 96, 216 Electron detachment, 232, 246	Gap geometry, 232 Gap periphery, 228 Gas density, 45 Gas-dynamic CO ₂ , 168 Gas-dynamic lasers, 79, 86, 98 Gas medium, 249 Gas mixtures, 209
Electric field strengths, 230 Electrization, 29, 182 Electrode rod, 18 Electrodes, 217 Electron current, 208 Electron density, 96, 216 Electron detachment, 232, 246 Electron flux, 212	Gap geometry, 232 Gap periphery, 228 Gas density, 45 Gas-dynamic CO ₂ , 168 Gas-dynamic lasers, 79, 86, 98 Gas medium, 249 Gas mixtures, 209 Gas pressure, 74
Electric field strengths, 230 Electrization, 29, 182 Electrode rod, 18 Electrodes, 217 Electron current, 208 Electron density, 96, 216 Electron detachment, 232, 246 Electron flux, 212 Electron impact, 231	Gap geometry, 232 Gap periphery, 228 Gas density, 45 Gas-dynamic CO ₂ , 168 Gas-dynamic lasers, 79, 86, 98 Gas medium, 249 Gas mixtures, 209 Gas pressure, 74 Gas velocity, 63
Electric field strengths, 230 Electrization, 29, 182 Electrode rod, 18 Electrodes, 217 Electron current, 208 Electron density, 96, 216 Electron detachment, 232, 246 Electron flux, 212 Electron impact, 231 Electron—ion recombination, 245	Gap geometry, 232 Gap periphery, 228 Gas density, 45 Gas-dynamic CO ₂ , 168 Gas-dynamic lasers, 79, 86, 98 Gas medium, 249 Gas mixtures, 209 Gas pressure, 74 Gas velocity, 63 Geodetic rockets, 31, 183
Electric field strengths, 230 Electrization, 29, 182 Electrode rod, 18 Electrodes, 217 Electron current, 208 Electron density, 96, 216 Electron detachment, 232, 246 Electron flux, 212 Electron impact, 231 Electron—ion recombination, 245 Electron multiplication, 245	Gap geometry, 232 Gap periphery, 228 Gas density, 45 Gas-dynamic CO ₂ , 168 Gas-dynamic lasers, 79, 86, 98 Gas medium, 249 Gas mixtures, 209 Gas pressure, 74 Gas velocity, 63 Geodetic rockets, 31, 183 Geometric factor, 76
Electric field strengths, 230 Electrization, 29, 182 Electrode rod, 18 Electrodes, 217 Electron current, 208 Electron density, 96, 216 Electron detachment, 232, 246 Electron flux, 212 Electron impact, 231 Electron—ion recombination, 245 Electron multiplication, 245 Electron scattering, 232, 246	Gap geometry, 232 Gap periphery, 228 Gas density, 45 Gas-dynamic CO ₂ , 168 Gas-dynamic lasers, 79, 86, 98 Gas medium, 249 Gas mixtures, 209 Gas pressure, 74 Gas velocity, 63 Geodetic rockets, 31, 183 Geometric factor, 76 Geometric stability, 312
Electric field strengths, 230 Electrization, 29, 182 Electrode rod, 18 Electrodes, 217 Electron current, 208 Electron density, 96, 216 Electron detachment, 232, 246 Electron flux, 212 Electron impact, 231 Electron—ion recombination, 245 Electron multiplication, 245 Electron scattering, 232, 246 Electro-optical system, 292	Gap geometry, 232 Gap periphery, 228 Gas density, 45 Gas-dynamic CO ₂ , 168 Gas-dynamic lasers, 79, 86, 98 Gas medium, 249 Gas mixtures, 209 Gas pressure, 74 Gas velocity, 63 Geodetic rockets, 31, 183 Geometric factor, 76 Geometric stability, 312 Gigantic spherical capacitor, 35 Glass ceramics, 290
Electric field strengths, 230 Electrization, 29, 182 Electrode rod, 18 Electrodes, 217 Electron current, 208 Electron density, 96, 216 Electron detachment, 232, 246 Electron flux, 212 Electron impact, 231 Electron—ion recombination, 245 Electron multiplication, 245 Electron scattering, 232, 246 Electro-optical system, 292 Elementary reflector, 85 Elevated pressure, 39, 73	Gap geometry, 232 Gap periphery, 228 Gas density, 45 Gas-dynamic CO ₂ , 168 Gas-dynamic lasers, 79, 86, 98 Gas medium, 249 Gas mixtures, 209 Gas pressure, 74 Gas velocity, 63 Geodetic rockets, 31, 183 Geometric factor, 76 Geometric stability, 312 Gigantic spherical capacitor, 35
Electric field strengths, 230 Electrization, 29, 182 Electrode rod, 18 Electrodes, 217 Electron current, 208 Electron density, 96, 216 Electron detachment, 232, 246 Electron flux, 212 Electron impact, 231 Electron—ion recombination, 245 Electron multiplication, 245 Electron scattering, 232, 246 Electro-optical system, 292 Elementary reflector, 85 Elevated pressure, 39, 73 Emission screening, 171	Gap geometry, 232 Gap periphery, 228 Gas density, 45 Gas-dynamic CO ₂ , 168 Gas-dynamic lasers, 79, 86, 98 Gas medium, 249 Gas mixtures, 209 Gas pressure, 74 Gas velocity, 63 Geodetic rockets, 31, 183 Geometric factor, 76 Geometric stability, 312 Gigantic spherical capacitor, 35 Glass ceramics, 290 Glass cutting, 166 Gravitational, 289
Electric field strengths, 230 Electrization, 29, 182 Electrode rod, 18 Electrodes, 217 Electron current, 208 Electron density, 96, 216 Electron detachment, 232, 246 Electron flux, 212 Electron impact, 231 Electron—ion recombination, 245 Electron multiplication, 245 Electron scattering, 232, 246 Electro-optical system, 292 Elementary reflector, 85 Elevated pressure, 39, 73 Emission screening, 171 Empirical criterion, 208	Gap geometry, 232 Gap periphery, 228 Gas density, 45 Gas-dynamic CO ₂ , 168 Gas-dynamic lasers, 79, 86, 98 Gas medium, 249 Gas mixtures, 209 Gas pressure, 74 Gas velocity, 63 Geodetic rockets, 31, 183 Geometric factor, 76 Geometric stability, 312 Gigantic spherical capacitor, 35 Glass ceramics, 290 Glass cutting, 166 Gravitational, 289 Ground-winds, 33, 185
Electric field strengths, 230 Electrization, 29, 182 Electrode rod, 18 Electrodes, 217 Electron current, 208 Electron density, 96, 216 Electron detachment, 232, 246 Electron flux, 212 Electron impact, 231 Electron—ion recombination, 245 Electron multiplication, 245 Electron scattering, 232, 246 Electro-optical system, 292 Elementary reflector, 85 Elevated pressure, 39, 73 Emission screening, 171 Empirical criterion, 208 Energy-accumulation region, 152	Gap geometry, 232 Gap periphery, 228 Gas density, 45 Gas-dynamic CO ₂ , 168 Gas-dynamic lasers, 79, 86, 98 Gas medium, 249 Gas mixtures, 209 Gas pressure, 74 Gas velocity, 63 Geodetic rockets, 31, 183 Geometric factor, 76 Geometric stability, 312 Gigantic spherical capacitor, 35 Glass ceramics, 290 Glass cutting, 166 Gravitational, 289
Electric field strengths, 230 Electrization, 29, 182 Electrode rod, 18 Electrodes, 217 Electron current, 208 Electron density, 96, 216 Electron detachment, 232, 246 Electron flux, 212 Electron impact, 231 Electron—ion recombination, 245 Electron multiplication, 245 Electron scattering, 232, 246 Electro-optical system, 292 Elementary reflector, 85 Elevated pressure, 39, 73 Emission screening, 171 Empirical criterion, 208 Energy-accumulation region, 152 Energy released, 106	Gap geometry, 232 Gap periphery, 228 Gas density, 45 Gas-dynamic CO ₂ , 168 Gas-dynamic lasers, 79, 86, 98 Gas medium, 249 Gas mixtures, 209 Gas pressure, 74 Gas velocity, 63 Geodetic rockets, 31, 183 Geometric factor, 76 Geometric stability, 312 Gigantic spherical capacitor, 35 Glass ceramics, 290 Glass cutting, 166 Gravitational, 289 Ground-winds, 33, 185
Electric field strengths, 230 Electrization, 29, 182 Electrode rod, 18 Electrodes, 217 Electron current, 208 Electron density, 96, 216 Electron detachment, 232, 246 Electron flux, 212 Electron impact, 231 Electron-ion recombination, 245 Electron multiplication, 245 Electron scattering, 232, 246 Electro-optical system, 292 Elementary reflector, 85 Elevated pressure, 39, 73 Emission screening, 171 Empirical criterion, 208 Energy-accumulation region, 152 Energy released, 106 Evaporation, 163	Gap geometry, 232 Gap periphery, 228 Gas density, 45 Gas-dynamic CO ₂ , 168 Gas-dynamic lasers, 79, 86, 98 Gas medium, 249 Gas mixtures, 209 Gas pressure, 74 Gas velocity, 63 Geodetic rockets, 31, 183 Geometric factor, 76 Geometric stability, 312 Gigantic spherical capacitor, 35 Glass ceramics, 290 Glass cutting, 166 Gravitational, 289 Ground-winds, 33, 185 Guiding electric discharges, 3, 4
Electric field strengths, 230 Electrization, 29, 182 Electrode rod, 18 Electrodes, 217 Electron current, 208 Electron density, 96, 216 Electron detachment, 232, 246 Electron flux, 212 Electron impact, 231 Electron-ion recombination, 245 Electron multiplication, 245 Electron scattering, 232, 246 Electro-optical system, 292 Elementary reflector, 85 Elevated pressure, 39, 73 Emission screening, 171 Empirical criterion, 208 Energy-accumulation region, 152 Energy released, 106 Evaporation, 163 Evolution of the discharge, 19	Gap geometry, 232 Gap periphery, 228 Gas density, 45 Gas-dynamic CO ₂ , 168 Gas-dynamic lasers, 79, 86, 98 Gas medium, 249 Gas mixtures, 209 Gas pressure, 74 Gas velocity, 63 Geodetic rockets, 31, 183 Geometric factor, 76 Geometric stability, 312 Gigantic spherical capacitor, 35 Glass ceramics, 290 Glass cutting, 166 Gravitational, 289 Ground-winds, 33, 185 Guiding electric discharges, 3, 4 H Half-space, 263–266
Electric field strengths, 230 Electrization, 29, 182 Electrode rod, 18 Electrodes, 217 Electron current, 208 Electron density, 96, 216 Electron detachment, 232, 246 Electron flux, 212 Electron impact, 231 Electron-ion recombination, 245 Electron multiplication, 245 Electron scattering, 232, 246 Electro-optical system, 292 Elementary reflector, 85 Elevated pressure, 39, 73 Emission screening, 171 Empirical criterion, 208 Energy-accumulation region, 152 Energy released, 106 Evaporation, 163	Gap geometry, 232 Gap periphery, 228 Gas density, 45 Gas-dynamic CO ₂ , 168 Gas-dynamic lasers, 79, 86, 98 Gas medium, 249 Gas mixtures, 209 Gas pressure, 74 Gas velocity, 63 Geodetic rockets, 31, 183 Geometric factor, 76 Geometric stability, 312 Gigantic spherical capacitor, 35 Glass ceramics, 290 Glass cutting, 166 Gravitational, 289 Ground-winds, 33, 185 Guiding electric discharges, 3, 4

Heat conductive material, 315	Injection, 66
Heat exchanger, 293	Injection beam, 155
Heat fluxes, 277	Integrated circuits, 313
Heating mechanism, 136	Intensity distribution, 97
Heating of aerosols, 70	Inter-electrode discharges, 25
Heating radiation, 97	Inter-electrode distance, 240
Heat load, 281	Intra-cavity elements, 166
Heatsink, 300	Intra-cavity loss, 153
Heat transfer, 277, 293	Intricate-shaped electrodes, 239
Heavy-metal particles, 100	Invar, 290
HF/DF laser, 157	Invar felt, 283
High, 275	Ion-ion recombination, 231
High-altitude discharges, 32, 185	Ionization at the cathode, 205
High-average-power, 195	Ionization current, 26
High conductivity, 108	Ionization of the channel, 118
High conductivity channel, 95, 101, 126	Ionization threshold, 101
Higher powered/energy radiation, 137	Ionized channels, 149
High frequencies, 135	Irradiation region, 271–273
High-frequency generators, 100	Irradiation time, 268
High-frequency modulation, 196	Isolated sparks, 40
High-frequency P-P, 167	isolated sparies, 10
High optical damage threshold., 284	L
High power/energy, 40, 161, 196	Laboratory bench, 304
High power/energy lasers, 155, 299	Lamp pumping, 304
High- pressure region, 45	Large optics, 294
High rigidity, 312	Laser ablation, 177
High specific stiffness, 288	Laser beam, 272
High-voltage high-frequency, 36	Laser diode assemblies., 300
Homogeneous plasma, 99	Laser diodes, 192, 301
Honeycomb structures, 288	Laser disk., 193
Hot particles, 103	Laser engine, 40
Humidity, 18, 178	Laser equipment, 191
Hydraulic characteristics, 279	Laser hyperboloids, 108
•	Laser-induced breakdown, 15
Hydrocarbon, 247 Hydrogen fluoride, 310	Laser irradiation, 265
rydiogen nuonae, 310	
T	Laser jet engine, 53, 55, 129, 176
I Imition 206	Laser plasma, 57, 83, 141
Ignition, 306	Laser-plasma channel, 150
Ignition mechanism, 307	Laser pulse, 49
Ignitor, 305	Laser radiation, 3, 42, 83
Ignitron, 103, 123	Laser spark, 4, 17, 21, 40, 317
Illumination of the cathode, 252	Laser-spark-controlled, 149
Immobile air, 76	Laser technologies, 165
Immobile gas, 132	Launching, 86
Impact detachment, 246	Launching light KA to orbital space, 173
Impulsar program, 99, 113	Leader channel, 107
Individual diffuse channel, 225	Leader charge, 21
Industrial lasers, 154	Leader discharge, 21
Inelastic processes, 227	Leader segment, 21
Inertial accelerations, 310	Leading edge, 103, 212
Inhomogeneous electric, 201	Light-detonation mode, 45
Initiating a streamer, 106	Lightning, 144
Initiation of electrons, 215	Lightning activity, 28
Injected low-power beams, 155	Lightning conduction, 27

Lightning discharge channel, 15	Negative ions, 231
Lightning protection, 22	Non-chain HF (DF), 214, 238, 249
Lightning protection system, 3, 16, 149, 317	Nonequilibrium plasma, 101
Lightning rods, 144	Nonlinear amplification, 195
Light storm, 27	Nonlinearity, 45
Light transformer, 302	Nonprofiled electrodes, 213
Lightweight honeycomb, 289	Nonuniform field, 202
Liquid metals, 282	Nozzle, 16
Liquid phase, 164	
Local displacements, 287	0
Locking elements, 301	Odolevsky equation, 280
Long-focus lens, 306	One-dimensional case, 203
Low-frequency modulation, 50	Open porosity, 291
Low-pressure region, 41	Operating mode, 169
Luminescence, 43	Optical breakdown, 13, 76, 174
	Optical damage threshold, 282, 287
M	Optical discharge, 39, 307
Mach numbers, 125	Optical elements, 167
Manmade space debris, 178	Optical fiber, 310
Mass transfer, 92, 141, 281	Optical pattern, 17
Mechanical energy, 30, 182	Optical pulse, 195
Mechanism of interaction, 153	Optical resonator, 168
Megawatts, 197	Optical surface, 259, 272, 273
Merging, 58	Optoelectronic, 318
Merging mechanism, 40	Oscillation mode, 309
Metal balls, 97	Oscilloscope trace, 13
Metallization, 145	Output characteristics, 249
Metallizing process, 33, 185	Output power, 303, 304
Metal mesh filters, 5	Output radiation, 166
Metal rods, 10	Overheating, 193
Microelectronic, 315	Oxygen–kerosene and oxygen–alcohol, 307
Microstructural, 275	Oxygen mixture, 306
Mirror surface, 286	D
Mixture pressure, 253	P
Mode selection, 301	Paraffin, delrin, 176
Modulation, 196	Paraxial beam region, 168
Modulator, 156, 168	Payloads, 66
Molecular gases, 238	Payload weight, 67
Molybdenum, 283	Peak power, 197
Momentum increment, 90	Peclet number, 283
Monochromatic images, 151	Periodic laser pulses, 42
Mono-module, 198	Periodic laser pulse train, 81
Monoreflector, 60, 84	Periodic trains, 42
Multichannel discharge, 203	Permalloy, 108
Multilayer heat exchanger, 286	Permeability coefficient, 278
Multi-mode operation, 160	Perturbation field, 46
	Phase composition, 274
N	Phase-locked, 300
Nanoparticles, 176, 318	Phase-locked array, 303
Nanopowder, 99	Phase-locked laser., 302
Nanosecond pulse, 8, 164	Phase-locked oscillation, 309
Nanoseconds, 195	Photodetonation regime, 68
Natural discharge, 96	Photoionization, 117, 207, 208, 213
Near-diffraction, 303	Physicomechanical, 284
	J

Piezo-electric transducer, 42	Pulsed lasing, 129
Pin photodiode, 104	Pulsed radiation, 132
Plane-parallel plate, 250	Pulsed train., 157
Planetary, 34, 186	Pulse duration, 50, 308
Plasma channel, 98, 99, 251	Pulse energy, 57, 305
Plasma density, 107	Pulse-periodic, 98
Plasma formation, 107	Pulse-periodic laser, 99, 144, 318
Plasma nuclei, 12	Pulse-periodic radiation, 142
Plasma plume, 110	Pulse repetition rate, 55, 72, 75, 83, 138
Plasma region, 89	Pulse train, 56, 307
Plasma trace, 46	Pump zone, 191
Polished cathode, 248	
Polyethylene, 203	Q
Polyethylene insulation, 216	Quasi-one-dimensional, 267
Polymer material, 65	Quasi-stationary currents, 35
Porous layer, 276, 277	Quasi-stationary phase, 247
Porous structure, 275, 278, 282, 286, 300	Quasi-stationary pressure, 75
Portable direct diode system, 301	
•	Quasi-stationary problem, 258
Positive leader, 22	Quasi-stationary wave, 71, 72, 82, 130
Potential transfer, 5	Quasi-steady phase, 212
Powder, 278	Quasi-steady-state voltage, 217
Power density, 272	Quasi-three-level, 159
Power/energy lasers is lightning, 178	Quenching, 229, 243
Power/energy optics, 257, 275, 301	n
Powerful lasers, 172	R
Power supply, 129, 293, 303, 304	Radiation boundary, 118
P-P disk, 160	Radiation divergence, 108, 253
P-P laser emission, 177	Radiation energy, 73, 238, 239, 255, 306
P-P mode, 157, 172	Radiation intensity, 53, 143
P-P operating, 156	Radiation loads, 258
P-P operation, 167	Radiation losses, 83
P-P regime, 197	Radiation parameters, 133
P-P solid-state, 154	Radiation power, 93
Prechamber, 305	Radiation resistance, 155
Preionization, 214	Radiatively heated area, 119
Preliminary bias, 211	Rain clouds, 25
Pressure distribution, 46	Random trajectory, 112
Pressure drop, 281	Realisable temperature, 274
Pressure fluctuations, 134	Receiving reflector, 72
Pressure jumps, 42	Reflective mirror surface, 310
Pressure pulsations, 49	Reflector, 53, 73, 78, 131, 138
Primary channel, 241	Reflector diameter, 137
Primary electrons, 204, 240	Reflector surface, 58
Probability of discharge, 20	Regenerative amplification, 195
Profiling the discharge gap, 212	Relaxation of the plasma, 151
Propagation time, 119	Repetition frequency, 173
Propagation velocity, 69	Repetition rate, 42, 85, 89, 141, 309
Propellant mixtures, 307	Repetitively pulsed, 66, 271, 272, 310
Propulsion, 137, 139	Repetitively pulsed irradiation, 269
Pulsation source, 45	Repetitively pulsed propulsion, 92
Pulse and pulse-periodic, 237	Repetitively pulsed radiation, 134
Pulse breakdown, 249	Repetitively pulsed regime, 129
Pulse components, 271	Residual aerosol, 112
Pulsed laser radiation, 138	Residual current, 104
1 dised fasel fadiation, 130	Residual Cultelli, 104

Resistance uncoupling, 239	Solar radiation, 28, 180
Resonance, 92	Solar to terrestrial connections, 35
Resonator geometry, 172	Solid body, 274
Resonator region, 155	Solid-state crystal lasers, 300
Restriction mechanisms, 244	Solid-state laser, 109, 165, 190
Rocket, 91, 138	Sophisticated materials, 318
Rocket motor, 304	Sound speed, 46, 91
Rocket prototype, 171	Source circuit, 121
Rocket technology, 173	Space-based telescopes, 294
Rod-plane electrode, 224	Space charge, 211
Rogowskii coils., 241	Space charge, 211 Spacecraft, 78, 138
	•
Rogowski loop, 101	Space debris, 161, 169
Roughness, 253	Spark, 17, 21, 41, 68, 90, 240, 250
Run-away, 33, 185	Spark channel, 119
Run-away electrons, 31, 184	Spark length, 8
	Spark of the train, 78
S	Spatial-temporal, 168
Sandblasting, 247	Special electrode, 220
Saturation intensity, 193	Specific conductivity, 97
Scaling, 192	Specific energy, 126, 220, 241
Scaling the power, 137	Specific energy deposition, 125, 243
Scattering, 100	Specific force, 63, 86
Screening, 205	Specific impulse, 100
Selectivity, 301	Speed of cutting, 165
Self - guiding laser burst, 144	Speed of sound, 140
Selfinitiated, 214	Spending channels, 143
Self-organized criticality, 30, 183	Spherical mirrors, 156
Semiconductor lasers, 293, 299	Spherical optics, 95, 97
Semiconductor material, 210, 299	Spike regime, 108
Separating layer, 276	Splashes of X-ray, 32, 184
Separation of charges, 29, 181	Spontaneous emission, 197
SF ₆ -discharge plasma, 231	Spontaneous modelocking, 5
Sharp edges, 216	Sprites, 32
Shielding, 63	Stability criteria, 145
Shock ionization., 101	Stable leader, 20
Shock wave, 67, 72, 74, 78, 92, 132, 134,	Static breakdown, 229
138–141, 174 Sheek ways companying 00	Stationary gas, 42
Shock-wave compression, 90	Stationary propulsion, 92
Shock-waves merging, 132	Steady-state solution, 205
Short-circuit mode, 117	Stepped leader, 26
SiC, 194	Step shape, 10
Signal from, 12	Streak camera, 42, 217, 229
Silicon carbide, 294, 315	Streamer corona, 20
Silicon wafers, 313	Streamer-leader, 318
Single beam, 301	Streamers overlap, 112
Single crystals, 315	Stressed state, 266
Single frame camera, 242	Stress-induced birefringence, 159
Single-mode CO ₂ , 257	Stress tensor, 261, 275
SIVD dynamics, 215	Strong electric field, 112
SIVD stability, 248	Strongly inhomogeneous, 212
Slot gap, 276	Structure of emission, 173
Small divergence, 302	Subsonic radiation, 69
Small-mass rocket, 140	Super-long conducting channels, 198
Smooth transition, 49	Supersonic velocity, 63, 118
*	· //

Supply and removal 270	Transfer energy 112
Supply and removal, 279 Surface stability, 274	Transfer energy, 113 Transformation efficiency, 60
Surrounding air, 79	Triggered discharge system, 250
Surrounding an, 79	Tri-propylamine, 206
Т	
	Trotyl equivalent, 67
Tapered elements, 97	Turbulence in atmosphere, 100
Technological applications, 295	Turbulent cooling, 76
Technological niche, 189	Turbulent mixing, 71
Telecommunication equipment, 15	Turbulent regimes, 277
Telescope components, 312	TT
Temperature distribution, 267	U
Temperature field, 259, 262	Ultraviolet radiation, 237
Temperature, humidity, 28, 181	Unconfined discharge, 223
Temporal structure, 161	Uniform discharge, 253
Temporal structure of radiation, 270	Uniform electric field, 238
Tension of a material, 268	Unique phenomenon, 27
Thermal characteristics, 280	
Thermal conductivity, 259, 280	V
Thermal deformation, 262, 269, 270, 273, 280,	Vapor pressure, 202
282	Velocities in the atmosphere, 67
Thermal distortions, 282	Velocity of the flow, 276
Thermal expansion, 50	Vertical current, 35
Thermal ionization, 96, 101, 150	Voltage and current oscillograms, 243
Thermal lensing, 159	Voltage divider, 120
Thermal mechanism, 163	Voltage growth, 10
Thermal processes., 284	Voltage polarity, 110
Thermal regime, 164	Voltage pulse, 101
Thermal stabilisation, 288, 290, 292	
Thermal stresses, 257	W
Thermoelasticity, 257, 260	Water-cooled heat sink, 159
Thermoelastic stresses., 263	Water-cooled mirrors, 286
Thermo-ionized channels, 26	Wide-aperture beams, 70
Thermooptical generation, 39	Wiedemann effects, 287
Thin wire, 100, 131	Wire explosion, 103
Thrust, 53, 66, 143	Wire-explosion products, 107
Thunderhead, 144	Wireless energy transfer, 86
Thunderstorm cloud, 28, 31, 180, 184	Without preionization, 247
Thunderstorm generators, 35	
Thunderstorm patterns, 17	Y
Time resolution, 30, 183	Young's modulus, 289
Traction force, 62	
Train, 304	Z
Train frequency, 60	Zig-Zag, 161, 193
Train of pulses, 154	